Physicochemical Problems of Mineral Processing

Volume 48, Issue 2
2012

www.minproc.pwr.wroc.pl/journal
www.dbc.wroc.pl/dlibra/publication/11251

Oficyna Wydawnicza Politechniki Wrocławskiej
Wrocław 2012

The papers published in the Physicochemical Problems of Mineral Processing journal are abstracted in BazTech, Chemical Abstracts, Coal Abstracts, EBSCO, Google Scholar, Scopus, Thomson Reuters (Science Citation Index Expanded, Materials Science Citation Index, Journal Citation Reports) and other sources

This publication was supported in different forms by
Komitet Górnictwa PAN (Sekcja Wykorzystania Surowców Mineralnych)
Akademia Górniczo-Hutnicza w Krakowie
Politechnika Śląska w Gliwicach
Politechnika Wrocławska

ISSN 1643-1049 (print)
previously 0137-1282
ISSN 2084-4735 (online)

OFICYNA WYDAWNICZA POLITECHNIKI WROCŁAWSKIEJ
Wybrzeże Wyspiańskiego 27, 50-370 Wrocław, Poland

CONTENTS

Physicochem. Probl. Miner. Process. 48(2), 2012, 329–339

www.minproc.pwr.wroc.pl/journal/

Physicochemical Problems of Mineral Processing

ISSN 1643-1049 (print)
ISSN 2084-4735 (online)

Received February 28, 2012; reviewed; accepted March 16, 2012

THE OPTIMAL BALL DIAMETER IN A MILL

Nedeljko MAGDALINOVIC*, Milan TRUMIC, Maja TRUMIC****
Ljubisa ANDRIC***

* Megatrend University, Faculty of Management, Park suma kraljevica bb, Zajecar, Serbia
** University of Belgrade, Technical Faculty, VJ 12, Bor, Serbia, mtrumic@tf.bor.ac.rs, Tel.: +381 30 421 749; fax: +381 30 421 078
*** Institute for Technology of Nuclear and Other Mineral Raw Materials, Bulevar Franš d'Eperea 86, Belgrade, Serbia

Abstract. This paper covers theoretical and experimental explorations for the sake of determining the optimal ball charge in mills. In the first part of the paper, on the basis of the theoretical analysis of the energy-geometric correlations, which are being established during the grain comminution by ball impact, as well as on the basis of the experiment carried out on grinding quartz and copper ore in a laboratory ball mill, there has been defined a general form of the equation for determining: the optimal ball diameter depending on the grain size being ground; and the parameter of the equation through which the influence of a mill is being demonstrated; then the parameter of the grinding conditions; and the parameter of the material characteristics being ground in relation to the ball size. In the second part of the paper, the process of making up the optimal ball charge has been defined providing the highest grinding efficiency, as well as its confirmation by the results of the experimental explorations.

keywords: mineral processing, optimal ball diameter, optimal ball charge, grinding

1. Introduction

The ball size in a mill has a significant influence on the mill throughput, power consumption and ground material size (Austin et al., 1976; Fuerstenau et al., 1999; Kotake et. al., 2004).

The basic condition, which must be met while grinding the material in a mill is that the ball, while breaking the material grain, causes in it stress which is higher than the grain hardness (Bond, 1962; Razumov, 1947; Supov, 1962). Therefore, for the biggest grain size, it is necessary to have a definite number of the biggest balls in the charge, and with the decreased grain size, the necessary ball size also decreases (Olejnik, 2010; 2011). For each grain size there is an optimal ball size (Trumic et. al., 2007).

The bigger ball in relation to the optimal one will have an excess energy, and consequently, the smaller ball mill has less energy necessary for grinding. In both cases, the specific power consumption increases and the grinding capacity decreases (Concha et al. 1992; Katubilwa and Moys, 2009; Erdem and Ergun, 2009).

http://dx.doi.org/10.5277/ppmp120201

A great number of explorers were dealing with the questions of determining the maximal ball diameter depending on the material size being ground. A few empirical formulae have been proposed, out of which some are recommended for industrial mills (Bond, 1962; Razumov, 1947; Olevskij, 1948), but some of them have been defined on the basis of investigations carried out in laboratory mills and they have not been applied to industrial mills (Belecki, 1985; Supov, 1962).

All suggested formulae fit into the general form given by:

$$d_{b\max} = Kd^n, \tag{1}$$

where: $d_{b\,max}$ is the maximum ball diameter in a charge, d is the characteristic top limit of the material size which is being ground (d_{95} or d_{80} in the formulae is recommended for industrial mills); K and n are parameters, for which all authors say to be dependent on the mill characteristics, grinding conditions and characteristics of the material being ground. They are determined experimentally.

Even a simplified theoretical analysis clearly defines the influential factors on parameters K and n. The topic of this paper is, first of all, this kind of analysis and then the determination of the optimal ball charge model in a mill.

2. Theoretical background

Each grain size corresponds to a definite optimal ball size. The diameter of a ball is determined by the condition that, at the moment of breaking the grain, it has energy E, which is equal to energy E_0 necessary for grain comminution:

$$E = E_0. \tag{2}$$

The ball impact energy on grain is proportional to the ball diameter to the third power:

$$E = K_1 d_b^3. \tag{3}$$

The coefficient of proportionality K_1 directly depends on the mill diameter, ball mill loading, milling rate and the type of grinding (wet/dry). None of the characteristics of the material being ground have any influence on K_1.

The ball impact energy on the grain is turned into the action of comminution, which according to the Rittinger comminution law is directly proportional to the newly formed grain surface while being ground. We can suppose that the grain has got the form of a ball with diameter d and that the area of comminution occurs along the equator cross section. Then, the comminution energy E_0 is proportional to the surface of equator circle, that is, the grain diameter to the second power:

$$E_0 = K_2 d^2. \tag{4}$$

It is clear that the coefficient of proportionality K_2 is not influenced by any of the characteristics of the material being ground.

In accordance with Eq. 2, the necessary condition for grain comminution is:

$$K_1 d_{bo}^3 = K_2 d^2 . \tag{5}$$

So, we have got the following: the optimal ball diameter d_{bo} is proportional to the grain diameter d to the exponent $n = 0.67$:

$$d_{bo} = \left(\frac{K_2}{K_1} \right)^{1/3} d^{2/3} = K_3 d^{0.67} . \tag{6}$$

The conclusion that can be drawn from Eq. 6 is quite clear and it shows that exponent n is neither influenced by mill's characteristics, grinding conditions, nor the characteristics of material being ground. All these influential factors are reflected only through the numerical value of parameter K, while the numerical value of exponent $n = 0.67$ has resulted from the theoretical energy–geometry relations shown by Eq. 2 to 6, which cannot be disputed.

In the formulae of the above mentioned authors, the numerical value of exponent n ranges from 0.2 up to 1.0 (Olevskij $n = 0.2$; Razumov $n = 0.3$; Bond $n = 0.5$; Baleski and Supov $n = 1.0$). Such great discrepancies in numerical values of exponent n are the result of the statistical data processing obtained from practice and investigations performed according to the model defined by Eq. 1, as well as the conviction that parameter n depends on mill's characteristics, grinding conditions and characteristics of the material being ground. If constant value $n = 0.67$ had been adopted in these result analysis, we would have obtained equally valid correlations, but only with the different values for proportionality coefficient K. Let us point out once again that the following issues have got an influence on the coefficient K: mill's characteristics, grinding conditions, and characteristics of the material being ground. Now, we have the right to put the following question: have not we attributed insufficient knowledge of the influence of the ball charge sliding in a mill under the different grinding conditions to the change of exponent n? There are some more similar justified questions.

This paper, describing a first part of investigation, aims at checking the hypothesis defined by Eq. 6 as well as its preference in relation to the hypothesis defined by Eq. 1.

Let us look back at the optimal ball charge in a mill. The necessary number of balls having the definite diameter N_b in a mill should be proportional to grain number N having the definite diameters which they can grind:

$$N_b \sim N . \tag{7}$$

The number of grains of the material with determined diameters depends on the grain size distribution. For a great number of materials the grain size distribution at the ball mill feed has been described by Gaudin-Schumann's equation:

$$d^* = \left(\frac{d}{d_{\max}} \right)^m , \tag{8}$$

where d^* is the filling load of grains less than d, d is the grain diameter, d_{max} is the maximum grain diameter, m is the exponent which characterizes the grain size distribution.

The number of balls, having the determined diameter in a mill, depends on the ball size distribution in the charge. Let us suppose that the ball size distribution in the charge can also be depicted by Gaudin-Schumann's equation:

$$Y = \left(\frac{d_b}{d_{b\max}} \right)^c , \qquad d_{b\min} < d_b < d_{b\max}, \tag{9}$$

where Y is the load of the balls having diameters less than d_b, d_b is the ball diameter, d_{bmax} is the maximum ball diameter in charge, d_{bmin} is the minimum ball diameter which can grind efficiently in a mill, c is the exponent which characterizes the ball size distribution.

The condition for efficient grinding, defined by Eq. 7, will be fulfilled when the grain size distribution and the ball size distribution are the same, which means that the parameters of both distributions are equal in Eqs. 7 and 9:

$$m = c . \tag{10}$$

In the second part of the paper, we will investigate the hypothesis defined by Eqs. 8, 9 and 10.

3. Experimental

Investigations were carried out in a laboratory ball mill having the size of DxL = 160x200 mm with a ribbed inside surface of the drum. The mill ball loading was 40% by volume, the rotation rate was equal to 85% of the critical speed.

Balls were made from steel: S4146, extra high quality, having hardness 62 ± 2 HRC according to Rockwell. Grinding tests were carried out with the samples of quartz having high purity of >99% SiO_2 as well as samples of copper ore consisting of 0.37% Cu, 67.48% SiO_2 and 15.02% Al_2O_3. Bond's working index for quartz is W_i = 14.2 kWh/t and for for copper ore W_i = 14.9 kWh/t.

The first part of this investigation has been oriented towards testing the hypothesis defined by Eq. 5. For that purpose, there has been observed the grinding kinetics of narrow size fractions of quartz and copper ore sizes (-0.80/+0.63 mm; -0.63/+0.50 mm; -0.50/+0.40 mm and -0.40/+0.315 mm) with the ball charge of different diameters (Table 1). The dry mill grinding has been conducted. The volume of grinding samples was equal to the volume of the interspaces of balls and the interstitial gaps between the balls charge.

The grinding efficiency of the narrow particle size fractions with ball charge of various diameters has been observed through the constant of milling rate k in the equation of the grinding kinetics law for the first order grinding $R=R_0e^{-kt}$, where R is the unground remainder of the sample after grinding time t, and R_0 is the sample mass for grinding. The first order kinetics of grinding occurred for all ball charges and for all samples.

As the ball charges and narrow, the size fractions of the samples have different masses. In this research, the grinding efficiency has also been observed through the specific mill throughput per ground product, per unit mass of the ball charge Q_s (kg/h/kg). The specific throughput has been calculated at grinding time t = 3 min.

Tables 2 and 3 give the numeric values of constant grinding rate k of the narrow size fractions of quartz and copper ore as well as the specific mill throughput with the ball charge of various sizes.

Table 1. Characteristics of ball charge and sample mass of quartz and copper ore

Symbol of ball charge	Ball diameter in charge d_b (mm)	Charge mass (g)	Number of balls in charge N_b	Sample mass (g) quartz and copper ore			
				-0.80+0.63	-0.63+0.50	-0.50+0.40	-0.40+0.315
A	6	7171	8149	1080/827	1073/792	1100/770	1072/792
B	11	6920	1277	1116/869	1139/832	1148/809	1140/832
C	15	6729	482	1136/900	1140/862	1136/838	1153/861
D	20	6475	199	1155/991	1142/950	1124/923	1168/949

Table 2. Constants of milling rate k and specific throughput of mill Q_s for grinding narrow particle size fractions of quartz

Symbol of the ball charge	Ball diameter in charge d_b (mm)	Size fraction (mm)							
		-0.80+0.63		-0.63+0.50		-0.50+0.40		-0.40+0.315	
		k	Q_s	k	Q_s	k	Q_s	k	Q_s
A	6	0.098	0.726	0.132	0.828	0.137	0.889	0.156	0.930
B	11	0.222	1.224	0.216	1.220	0.180	1.142	0.149	0.989
C	15	0.281	1.381	0.216	1.229	0.167	1.101	0.133	0.943
D	20	0.233	1.418	0.159	1.169	0.122	0.979	0.084	0.780

Figures 1 and 2 show the dependence of milling rate constant k upon the ball diameter in the charge d_b while grinding different quartz and copper ore size fractions. In Figs. 1 and 2, one can see that for each size fraction there is a proper ball diameter, which provides the highest efficiency of grinding, in terms of the milling rate constant k and that it is the optimal ball diameter d_{bo} for grinding the given grain size.

By means of graphic interpolation, from Figs. 1 and 2, there has been determined optimal ball diameter d_{bo}, which provides the highest grinding efficiency of the corresponding size fraction and the results have been shown in Table 4. We can notice

that the values for d_{bo} are very close in terms of both parameters for grinding efficiency.

Table 3. Constants of milling rate k and specific mill throughput Q_s for grinding narrow particle size fractions of copper ore

Symbol of the ball charge	Ball diameter in charge d_b (mm)	Size fraction (mm)							
		-0.80+0.63		-0.63+0.50		-0.50+0.40		-0.40+0.315	
		k	Q_s	k	Q_s	k	Q_s	k	Q_s
A	6	0.072	0.586	0.126	0.882	0.107	0.749	0.118	0.754
B	11	0.152	1.060	0.177	1.188	0.139	0.938	0.122	0.867
C	15	0.189	1.248	0.202	1.287	0.148	1.033	0.121	0.848
D	20	0.171	1.242	0.168	1.220	0.129	0.927	0.111	0.763

Table 4. Optimal ball diameter

Size fraction (mm)	Mean grain diameter, d (mm)	Optimal ball diameter d_{bo} (mm)				Mean value of the optimal ball diameter d_{bo} (mm)	
		In terms of constant milling rate, k		In terms of specific mill throughput, Q_s			
		Quartz	Copper ore	Quartz	Copper ore	Quartz	Copper ore
-0.80+0.63	0.715	16.0	16.5	16.5	17.5	16.25	17.0
-0.63+0.50	0.565	13.5	15.0	14.0	16.0	13.75	15.5
-0.50+0.40	0.450	12.5	14.2	13.0	15.0	12.75	14.6
-0.40+0.315	0.357	8.0	12.0	9.0	13.0	8.50	12.5

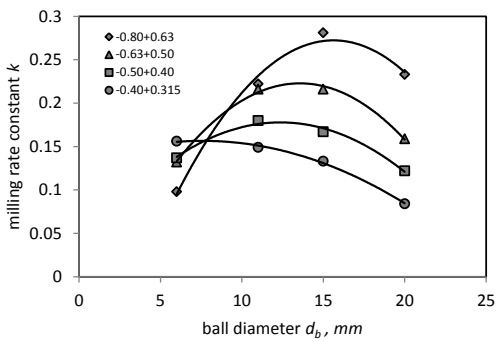

Fig. 1. Dependence of milling rate constant k while grinding particular size fractions of quartz upon ball diameter d_b in the charge

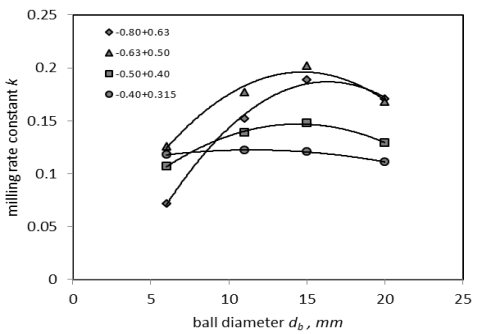

Fig. 2. Dependence of milling rate constant k while grinding particular size fractions of copper ore upon ball diameter d_b in the charge

Figure 3 shows the dependence of optimal ball diameter d_{bo} on mean grain quartz diameter d in a fraction, in the coordinate system [ln$d$; lnd_{bo}]. The linear arrangement of points in Fig. 3 points to the fact that there is a strong correlating connection of forms given by Eq. 1.

By the method of the least squares, it was possible to determine the numerical values of parameters *K* and *n* in Eq. 1, with a very high degree of correlation *r*, so that they, for the conditions of our experiment, would be as follows:

$$\text{quartz: } d_{bo} = 22.67 d^{0.87},\ r=0.95, \tag{11}$$

$$\text{copper ore: } d_{bo} = 19.77 d^{0.42},\ r=0.98. \tag{12}$$

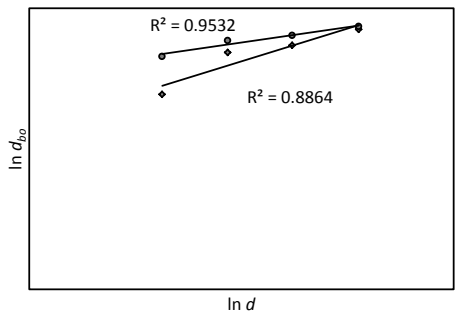

Fig. 3. Dependence of optimal ball diameter d_{bo} on mean grain diameter d in a fraction

The grinding tests on all samples have been performed under identical conditions. The only difference is in the characteristics of quartz and copper ore, in terms of Bond's working index. In other words, copper ore has got a higher Bond's working index and this should have been expressed in Eq. 12 in terms of a higher value for coefficient *K* compared to the value in Eq. 11 for quartz. However, this didn't happen. The value of *K* in Eq. 12 is less than the value in Eq. 11. This happened because of the incorrect hypothesis, which says that the exponent *n* depends on the characteristics of a mill, grinding conditions and raw material characteristics. It was incorrect to emphasize higher influence of Bond's working index on exponent *n* instead on parameter *K*.

In this paper, in our theoretical analysis, we have come to the concision, that parameter *n* has got the constant value: $n = 0.67$ and that it does not depend on the characteristics of a mill, the grinding conditions and raw material characteristics. Thus, consequently, the optimal ball size is defined by Eq. 6.

By means of the least squares, we have determined the numerical values of parameters *K* in Eq. 6, so that they, for the conditions of our experiment and with a very high degree of correlation *r*, are as follows:

$$\text{quartz: } d_{bo} = 19.69 d^{0.67},\ r=0.94, \tag{13}$$

$$\text{copper ore: } d_{bo} = 23.45 d^{0.67},\ r=0.97. \tag{14}$$

Equations 13 and 14 confirm our theoretical hypothesis that exponent *n* has got the constant value $n = 0.67$ and that the influence of the mill characteristics, grinding conditions and raw material characteristics has been demonstrated only in terms of the

numerical value of parameter *K*. The higher value of the Bond's working index for copper ore has led to the higher value of parameter *K* in Eq. 14 in relation to the value of the same one in Eq. 13 for quartz, and that is the theoretically expected issue.

The second part of this paper refers to the testing of the hypothesis for modeling the optimal ball charge in a mill, defined by Eqs. 8 to 10. The optimal ball charge in a mill has been formed in the following way.

1. We define the value of the exponent in Eq. 8 for the material to be ground
2. We define maximum ball diameter d_{bmax}, according to one of the known formulae
3. The ball load with different diameters in the charge ranging from d_{bmax} to d_{bmin} is to be calculated according to Eq. 9, where the exponent $m=c$.

The grinding tests were carried out on artificially formed samples of quartz and copper ore having the grain size of -0.80/+0.315 mm, whose particle size distribution is described by Eq. 8 so that, for both samples, it is as follows

$$d^* = \left(\frac{d}{0.8}\right)^2. \tag{15}$$

The maximum and minimum ball diameters in the charge, in accordance with Eqs. 14 and 15 are as follows:

quartz: $$d_{b\max} = 19.69 d^{0.67} = 19.69 \cdot 0.8^{0.67} = 17.0\,\text{mm}, \tag{16}$$

$$d_{b\min} = 19.69 d^{0.67} = 19.69 \cdot 0.315^{0.67} = 9.1\,\text{mm}, \tag{17}$$

copper ore: $$d_{b\max} = 23.45 d^{0.67} = 23.45 \cdot 0.8^{0.67} = 20.2\,\text{mm}, \tag{18}$$

$$d_{b\min} = 23.45 d^{0.67} = 23.45 \cdot 0.315^{0.67} = 10.8\,\text{mm}. \tag{19}$$

In accordance with the available ball load used or making the charge, the balls with the following diameters have been used: 10.3 mm; 12.7 mm; 15 mm; and 19 mm. There have been formed there different charges: *E*, *F* and *G*. The charge *E* was made up according to the hypothesis of this paper according to the equation:

$$Y_E = \left(\frac{d_b}{19}\right)^2, \quad 10.3 < d_b < 19.0. \tag{20}$$

In charge *F*, the larger balls prevail and their size distribution follows the equation:

$$Y_F = \left(\frac{d_b}{19}\right)^4, \quad 10.3 < d_b < 19.0. \tag{21}$$

In charge *G*, the smaller balls prevail and their size distribution follows the equation:

$$Y_G = \left(\frac{d_b}{19}\right)^{1.5}, \quad 10.3 < d_b < 19.0. \tag{22}$$

In Table 5 we have given the composition of samples in the charge according to the size distribution. The ball mill loading is 40% by volume. The quartz sample mass for grinding is 915 g and for copper ore 787 g.

The grinding efficiency with ball charges *E*, *F* and *G*, has been observed in terms of the constant milling rate of the first-order k and the specific throughput of mill Q_s per ground product per unit mass of the charge, on the controlling screen with the mesh size of d = 0.315 mm at the grinding time of t = 3 min. The results of grinding are shown in Table 6 and they confirm our hypothesis that the highest grinding efficiency is provided by charge *E*, where the ball size distribution is identical with the one with the grain size distribution of the material being ground.

The accomplishment of this principal in industrial mills is possible by loading the mills with the balls of different diameters, in the proper correlation, where the value of exponent c in Eq. 9 is brought closer to the value of the exponent m in Eq. 8.

Table 5: Composition of samples and charges according to the size distribution

Particle size distribution, d (mm)	Weight W (%)	Ball diameter d_b (mm)	Charge E		Charge F		Charge G	
			W (%)	M (g)	W (%)	M (g)	W (%)	M (g)
-0.80+0.63	38	19	38	2732	58	4157	29	2090
-0.63+0.50	23	15	23	1653	21	1480	16	1159
-0.5+0.40	14	12.7	14	1006	12	853	15	1089
-0.40+0.315	25	10.3	25	1797	9	667	40	2898
	100		100	7188	100	7147	100	7236

Table 6: Milling rate constant k and specific throughput of mill Q_s, with different ball charges

Indicator for the grinding efficiency	Charge E		Charge F		Charge G	
	Quartz	Copper ore	Quartz	Copper ore	Quartz	Copper ore
k	0.119	0.078	0.108	0.072	0.105	0.073
Q_s	0.890	1.084	0.821	1.075	0.796	1.071

4. Conclusion

All proposed formulae for determining the ball diameter, depending on the diameter of the grain size material being ground, fit into the general form given in the equation:

$$d_b = Kd^n,$$

where d_b is the ball diameter, d is the diameter of the grain size material being ground, K and n are parameters, for which all authors say, depend on mill characteristics,

grinding conditions and characteristics of the material being ground and which are consequently determined by experiments.

By means of theoretical analysis of energy–geometry correlations, which are being established during the process of grain comminution by ball impact, it has been clearly proved that exponent *n*, by which grain diameter *d* has been raised to a power, does not have any influence on the characteristics of mill characteristics, grinding conditions and characteristics of the material being ground. All these influential factors have only been reflected by numerical value of parameter *K*, while the numerical value of exponent *n* is constant and amounts to 0.67. This result has been proved by the results of our investigation in this paper. Thus, the general form of the formula for determining the ball diameter, depending on the diameter of the grain size material being ground is:

$$d_b = Kd^{0.67}.$$

Starting from the physical fact that the required number of balls of determined diameter N_b in a mill should be proportional to number of grains *N* of determined diameters which will be ground, we have come to the theoretical hypothesis that, in order to achieve effective grinding, the ball size distribution in the charge should be the same with the material grain size distribution being ground.

In a great many cases, the grain size distribution of a ball mill feed is well described by Gaudin-Schumann's equation:

$$d^* = \left(\frac{d}{d_{\max}} \right)^m,$$

where d^* is the grain fill level less than *d*, *d* is the grain diameter, d_{max} is the maximum grain diameter, *m* is the exponent which characterizes the grain size distribution.

The optimal ball charge in a mill should be made up in such a way that the ball size distribution of a charge should be in accordance with Gaudin-Schumann's equation:

$$Y_E = \left(\frac{d_b}{d_{b\max}} \right)^c, \; d_{b\min} < d_b < d_{b\max},$$

where *Y* is the ball fill level having the diameter less than d_b, d_b is the ball diameter, d_{bmax} is the maximum ball diameter in the charge, d_{bmin} is the minimum ball diameter which can grind efficiently in a mill, *c* is the exponent which characterizes the ball size distribution so that the most efficient grinding can be achieved if the condition $m=c$ is fulfilled.

The results of this experiment in this paper have completely proved the given hypothesis.

Acknowledgements

Part of results, used in this work, were obtained from the work on the project: TR 33023 - Development of the Technology for the Copper Ore and Precious Metals Flotation Processing for the

Sake of Achieving better Technological Results and TR 33007 - Implementation of Advanced Technological and Ecological Solutions in Existing Product Systems of Copper Mine Bor and Copper Mine Majdanpek, It was financed by the Ministry of Education and Science of the Republic of Serbia.

References

AUSTIN, L.G., SHOJI, K., LUCKIE, P.T., 1976, *The effect of ball size on mill performance*, Powder Technol. 14 (1), 71–79.

BELECKI, E.P., 1985, *Vibor razmera šarov dlja šarovih meljnic*, Obogaščhenie rud, 11, 40-42.

BOND, F.C., 1961, *Crushing and Grinding Calculations*, Allis Chalmers Tech. Pub. O7R9235B.

CONCHA, F., MAGNE, L., AUSTIN, L.G., 1992, *Optimization of the make-up ball charge in a grinding mill*, Int. J. Miner. Process. 34 (3), 231–241.

ERDEM, A.S. ERGUN, S.L., 2009, *The effect of ball size on breakage rate parameter in a pilot scale ball mill*, Miner. Eng. 22, 660–664

FUERSTENAU, D.W., LUTCH, J.J., DE, A., 1999, *The effect of ball size on the energy efficiency of hybrid high-pressure roll mill/ball mill grinding*, Powder Technol. 105, 199–204.

KATUBILWA, F. M., MOYS, M.H., 2009, *Effect of ball size distribution on milling rate*, Miner. Eng. 22, 1283–1288

KOTAKE, N., DAIBO, K., YAMAMOTO, T., KANDA, Y., 2004, *Experimental investigation on a grinding rate constant of solid materials by a ball mill—effect of ball diameter and feed size*, Powder Technol. 143– 144, 196– 203

OLEJNIK, T.P., 2010, *Kinetics of grinding ceramic bulk considering grinding media contact points*, Physicochem. Probl. Miner. Process. 44, 187–194.

OLEJNIK, T.P., 2011, *Milling kinetics of chosen rock materials under dry conditions considering strength and statistical properties of bed*, Physicochem. Probl. Miner. Process. 46, 145–154.

OLEVSKIJ, V.A., 1948, *Najvigodesni razmer šarov dlja šarovih meljnici*, Gornij žurnal, 1,1–5.

RAZUMOV, K.A., 1947, *Racionirovanoe pitanie meljnic šarami*, Gornij žurnal 3, 31–35.

ŠUPOV, L.P., 1962, *Udarnoe dejstvie šarov v meljnice*, Obogašshenie rud, 4, 15–20.

TRUMIC, M., MAGDALINOVIC, N., TRUMIC, G., 2007, *The model for optimal charge in the ball mill*, Journal of Mining and Metallurgy A, 43, 19–32.

Physicochem. Probl. Miner. Process. 48(2), 2012, 341–353

www.minproc.pwr.wroc.pl/journal/

Physicochemical Problems of Mineral Processing

ISSN 1643-1049 (print)
ISSN 2084-4735 (online)

Received November 14, 2011; reviewed; accepted February 17, 2012

INVESTIGATION OF RADIOACTIVE CONTENT OF MANISA-SOMA AND ISTANBUL-AGACLI COALS (TURKEY)

Ismail DEMIR, Ilgin KURSUN

Istanbul University Engineering Faculty Mining Engineering Department, Istanbul, Turkey, dismail@istanbul.edu.tr, ilginkur@istanbul.edu.tr

Abstract. Coal, the world's most abundant, most accessible and most versatile source of fossil energy was brought to the forefront of the global energy scene by the industrial revolution of the 19th century. Like any fossil fuel, coal is associated with naturally occurring radioactive materials. This is due to their U, Th, and K content. This certainly has radiological implications not only for the miners but also for the immediate environment of the mines and the users. In this study, the radioactive elements in Manisa-Soma and Istanbul-Agacli coals and their ashes were studied. In the experimental section, the coal and thermal power plant ashes which were taken from Manisa-Soma were used. Sieve, moisture, ash, calorific value, volatile amount, total carbon, total sulphur, major element and radioactive element analysis of the samples were carried out. The float and sink analyse and flotation tests were carried out on the samples which were taken from Manisa-Soma and Istanbul-Agacli. Thus, radioactive elements changes and moving mechanisms were investigated with coal preparation and burning methods. Furthermore, the pre-investigation of the assessment of the thermal power plant ashes was carried out with the experiments on the ash samples, which were taken from the Soma thermal power plant.

keywords: coal, radioactive elements, coal properies

1. General information

Social and technological development changes are in direct proportion to the amount of energy that is consumed. As a result of the fast growth of world population, the consumed energy naturally increases alongside. Especially, the fact that population growth of Turkey is higher than the worldwide average means that the requirement for energy will increase more every day. In 2008, petroleum has the highest share in energy consumption in Turkey with 32.8%, which is followed by natural gas with 30.4%, coal with 28% and the remaining 10% is occupied by renewable resources including hydraulic (Teias, 2008).

A clean environment is needed for a healthy life and energy is needed for a comfortable life, which requires utilisation of resources by minimising their impact.

http://dx.doi.org/10.5277/ppmp120202

The fact that even ashes of burned coal is usable is an important point both for economic benefit and environmental impact, and this may only be possible due to proper features of coal. When coal is burnt in thermal power stations, toxic trace elements in the coal like As, Cd, Ga, Ge, Pb, Sb, Se, Sn, Mo, Ti and Zn, which have the potential of contaminating, are transferred to the waste products (cinder, ash and gas). Volatile ashes containing many poisonous elements may be collected in ash collection pools under furnaces or as piles. Because soluble metal ions and compounds may leak from the ash pools or piles, then have the potential to contaminate soil, surface and underground water. Then, severe environmental problems may occur (Karayiğit et al., 2000; Perçinel, 2000; Esenlik, 2005; Tuna et al., 2005).

When coal is combusted, toxic trace elements like arsenic (As), cadmium (Cd), lead (Pb), antimony (Sb), selenium (Se), stannum (Sn) and zinc (Zn) are transferred to waste products like cinder, ash and gases. When the waste products are disposed contained poisonous (toxic) trace elements may be conveyed to the atmosphere, earth surface and oceans. These elements may be seriously threatening for living organisms by creating environmental, and health problems when the waste products are washed with rain and these elements are carried away with underground water to the soil, and surface and underground waters (Baba, 2001; Ateşok, 2004; Demir, 2009).

Some of the human diseases occurring near thermal power plants, due to the toxic elements spread in the neighbourhood are given below (Perçinel, 2000):

As: Anaemia, nausea, renal symptoms, ulcer, skin and pulmonary cancer, defective births.

Be: Malfunction of respiration and lymph, lungs, spleen and kidneys, carcinogenic effects.

Cd: Lung emphysema and fibrosis, kidney diseases, cardiovascular effects, carcinogenic effects.

Hg: Nervous and kidney damages, cardiovascular effects, birth problems.

Mn: Respiratory problems.

Ni: Skin and intestinal diseases, carcinogenic effects.

Pb: Anaemia, nervous and cardiovascular problems, delayed growth, gastric and intestinal problems, carcinogenic effects, birth problems.

Se: Gastric and intestinal nausea, pulmonary and splenic damages, anaemia, cancer, teratogenic effects.

V: Acute and chronic respiratory malfunction (Perçinel, 2000).

Radon gas forms in the area in which ashes of the thermal power plant collect (ash chambers) reach the air. Even if these ashes are buried in soil, radon gas infiltrates through the pores of the soil and blends in the air. Radon gas may transform into polonium and active lead in 3.8 days. Therefore, piles of ash emit radioactivity. Perhaps the most critical material that is disposed through the chimneys is uranium, that is contained in lignite and released during combustion to spread around. Uranium is also a serious problem (Özyurt, 2006).

1.1. Major and trace elements contained in coal and coal ash

C, H, O, N and S contained in the structure of coal, contents of which are generally higher than 1000 ppm, form the organic matrix and they are called major elements. Al, Fe, Mg, As, Zn, Cu, F, Th, V etc. with a concentration that is generally less than 1000 ppm are called trace elements in coal (Ateşok, 2004; Özyurt, 2006). There are some elements in coal which are inorganic, which may form inorganic or organometalic compounds, and which may be recovered if they are at an economic level. In the sediments containing coal layers and in coal formations, Ge, Ga, U and Cu may be found at economic levels. Coal also contains toxic trace elements like Be, Mo, V, Zn, W, Co, Cd, As, Pb, Se, and Cr, which are contaminants (Kural, 1998; Özyurt, 2006; Demir, 2009; Demir and Kurşun, 2010).

During combustion of coal, trace elements such as Pb, Cu, Zn, V, As and Th become volatile and concentrate in the furnace ash (Özyurt, 2006; Riley, 2008; Demir, 2009; Demir and Kurşun, 2010). When coals are combusted at high temperatures, their molecular structure is demolished, and an important portion of Cl and F is disposed into air as gases together with smoke (Özyurt, 2006). When coal dust is combusted in thermal power plants, carbon, nitrogen and sulphur contained in the coal structure oxidise and transform into carbon oxide (CO_x), nitrogen oxide (NO_x) and sulphur oxide (SO_x). Some water vapour forms during this transformation, too. Whereas cinder is collected under combustion furnaces, volatile ashes are caught by electro-filters and some are transported with the chimney gas. Researches show that trace elements mostly collect on volatile ashes (Karayiğit et al., 2000; Özyurt, 2006).

In thermal power plants that use coal, combustion in the furnaces occurs at around 900-1400°C depending on the type of coal. Coal pieces heat up in the furnace, vaporizable materials convert into gases and combustion occurs. Minerals disintegrate and melt under heat, start decomposing and agglomerate (Kural, 1998; Özyurt, 2006).

Hg, As, Se, Ni, Pb, Ce are Zn mostly related to sulphide minerals and organic substances. Combination (formation) of coal minerals or organic substances with trace elements may seriously affect vaporisation limit and consequently its ratio in the chimney gas disposed by the plant. Trace elements detected in chimney gases are mostly associated to sulphide minerals (Riley, 2008; Shah et al., 2008).

During combustion of coal, some trace elements contained in coal like As, Cd, Ga, Ge, Pb, Sr, Mo, Zn, Ba transfer to the waste products (cinder, ash and gases). Especially fly ashes of such wastes produce very convenient media for adhesion of elements in liquids and gases because they have clayish structure, endure high temperatures and have large surface area (Özyurt, 2006; Demir, 2009; Demir and Kurşun, 2010).

2. Findings

2.1. Results of particle size analysis

Coal samples collected from the site for the research were crashed in the laboratory type jaw crusher and roll crusher in Istanbul University, Mining Engineering

Department, Mineral Processing Laboratory, and then applied dry particle size analysis to study particle size distribution.

Particle size curves were drawn according to the particle size analysis performed using 8 mm, 4 mm, 2 mm, 1 mm and 0.5 mm laboratory type Retsch brand stainless steel sieves of square section and d_{80} particle dimensions were calculated.

Figure 1 shows particle size curves drawn according to the results of particle size analysis made after crashing of coal samples collected from Manisa-Soma and İstanbul-Agacli region in roll crusher. As the curves show, d_{80} of roll crusher outputs of Manisa – Soma and Istanbul-Agacli coals are 5.4 mm and 5.9 mm, respectively.

Figure 2 shows particle size curve of the coal samples collected from Manisa-Soma and Istanbul-Agacli Region, which were used in float and sink experiments, according to the results of particle size analysis. The curves show that d_{80} of Manisa-Soma and Istanbul-Agacli coals are 1900 μm and 2100 μm, respectively.

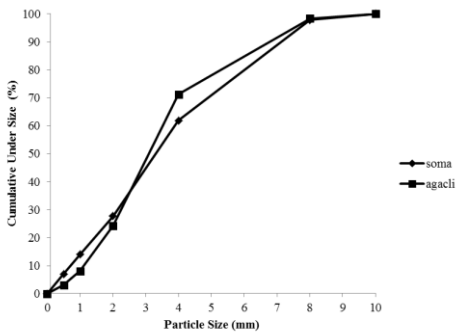

Fig. 1. Manisa-Soma and Istanbul-Agacli particle size distribution after roll crushing

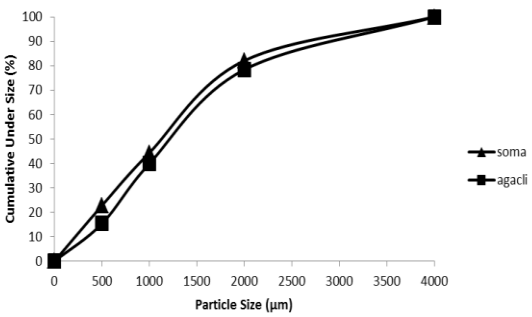

Fig. 2. Particle size curves of "float and sink experiments" samples of Manisa-Soma and Istanbul-Agacli coals

2.2. Results of Proximate and Ultimate Chemical Analysis

Ash samples and coal samples collected for the study were brought to the Mineral Processing Laboratory of Istanbul University, and humidity, ash, density, volatile matter, total sulphur and thermal value analyses were made on these samples. Evaluation and interpretation of the chemical analysis results of the coal and ash samples are summarised below.

Humidity. Coal samples collected from the TKI (Turkish Coal Enterprises) Ege Lignite Enterprises (Manisa-Soma) for the study were brought to the Mineral Processing Laboratory of Istanbul University, and total humidity analysis was made on these samples. Analysis was made according to standard TS 690 ISO 598 (Method-C). Total humidity analysis was made after bringing samples to the laboratory in closed nylon bags without losing time. Due to the high temperature at electro-filters, humidity values of ash samples are mostly almost zero.

Figure 3 shows the percentage curves of the humidity that is lost in time when coal samples collected from Manisa-Soma and Istanbul-Agacli region are heated in drying oven at 105ºC. It was calculated that coal samples collected from Manisa-Soma and Istanbul-Agacli contain 15.49% and 31.75% humidity, respectively. The analyses show that almost entire humidity contained in the samples may be removed in 3 hours for Manisa-Soma coal samples and 5 hours for Istanbul-Agacli coal samples.

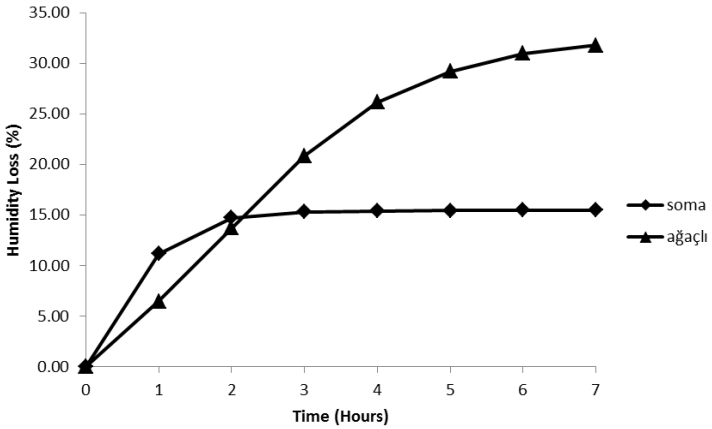

Fig. 3: Graphic of humidity loss (%) as a function of time (hours) for Manisa-Soma and Istanbul-Agacli coals

Volatile Matter. It was observed that volatile matter content of ash samples is lower than coals'. Whereas, Manisa-Soma coal sample contains 31.32% volatile matter, its thermal power plant ashes contain 1.2% because of the unburned coal pieces. Agacli sample contains 57.27% volatile matter.

Ash. Ash analyses of the coal samples within the study were realised in Istanbul University, Department of Mine Engineering, Mineral Processing Laboratory. According to the results of this analysis, coals collected from Manisa – Soma region are coals with high ash ratio.

Theoretically, ash content of waste products formed as the result of combustion in thermal power plants (volatile ash and bottom ash) must be 100%. However, depending on characteristics of combusted coal and conditions of combustion systems, it is always possible to find some unburned coal remnants in these wastes. As a matter of fact, Manisa – Soma thermal power plant ash contains 1.2% unburned pieces.

Total Sulphur. Dry base total sulphur contents of thermal Power Plant ash and coal samples collected for the study in air were analysed by Acme Analytical Laboratories Ltd. in Canada. Leco carbon sulphur device was used in total sulphur analysis (Acme, 2009).

When coals used in Manisa-Soma thermal power plant and ashes formed by combustion are examined for total sulphur contents, it is observed that a little portion is disposed into the air by burning and the rest is concentrated in ash.

Thermal Value. Upper thermal values and lower thermal values of the coal samples were analysed in the Environment and Fuel Analysis Laboratory approved by TÜRKAK belonging to Istanbul Metropolitan Municipality, Department of Environmental Protection & Development. IKA C7000 device was used for thermal value analyses.

Density Analysis. Density analysis with a pycnometer was performed to determine densities of the coal samples collected for the study and to compare optimum sorting density used in float and sink experiments. Density Analysis was performed in Istanbul University, Department of Mine Engineering, Ore Preparation and Concentration Laboratory. TS ISO 5072 Brown Coal and Lignite – Assessment of Real and Apparent Relative Density standard was utilized in the analysis method.

The heavy mediums used in float and sink experiments of Soma and Agacli coals were selected as 1.6 and 1.3 g/cm^3, respectively.

Elementary Analyses. Elementary Analyses of the coal samples collected for the study were performed in Advanced Analyses Laboratory of Istanbul University. Based on the air dried elementary analysis results of the analysed samples are given in Table 2.

Table 1. Based on the air dried chemical analysis results of Istanbul-Agacli, Manisa- Soma coal samples and Manisa- Soma power plant ash samples

Sample	Amount of volatile substances (%)	Ash Content (%)	Total sulphur content (%)	Upper thermal value (Kcal/kg)	Lower thermal value (Kcal/kg)	Density (g/cm^3)
İstanbul-Agacli	57.27	8.12	1.37	4742	4499	1.301
Manisa-Soma coal	31.32	35.88	0.67	2942	2761	1.553
Manisa-Soma ash	1.2	98.80	1.26			

Table 2. Based on the air dried elementary analysis results of Istanbul-Agacli, Manisa-Soma coal samples

	C, %	H, %	N, %	S, %
İstanbul - Agacli	48.19	4.92	0.36	0.56
Manisa – Soma	43.13	2.75	0.42	0.28

Methods used in elementary analyses are explained below:

1DX Analysis. In 1DX analysis, 0.5g of the sample is leached with royal water heated up to 95ºC (Aqua Regia in Latin; it is generally obtained by mixing one third concentrated hydrochloric acid and nitric acid) and the solution placed in ICP-MS device to read the values (Acme, 2009).

Elements detected by 1DX analysis are: Mo, Cu, Pb, Zn, Ni, As, Cd, Sb, Bi, Ag, Au, Hg, Tl, Se.

Leco TOT/C and TOT/S analysis. Total C and Total S analyses are performed with Leco carbon sulphur device (Acme, 2009).

4A Analysis. In 4A analysis, 0.2g coal and ash samples are applied lithium metaborate/tetraborate fusion and decomposed with diluted nitric acid, and then major oxides they contained were detected with the ICP-ES device (Acme, 2009).

Minerals that are analysed with 4A are: SiO_2, Al_2O_3, Fe_2O_3, MgO, CaO, Na_2O, K_2O, TiO_2, P_2O_5, MnO, Cr_2O_3.

4B Analysis. In 4B analysis, 0.2g coal and ash samples are applied lithium metaborate/tetraborate fusion and decomposed with diluted nitric acid, and then rare soil elements and refractor elements they contained were detected with the ICP-MS device. In addition, 0.5g samples were decomposed in royal water, and precious metals and base metals were detected with ICP-MS (Acme, 2009).

Elements that are analysed with 4B are (nitric acid and ICP-MS): Ba, Be Co, Cs, Ga, Hf, Nb, Rb, Sc, Sn, Sr, Ta, Th, U, V, W, Y, Zr, La, Ce, Pr, Nd, Sm, Eu, Gd, Tb, Dy, Ho, Er, Tm, Yb, Lu.

Elements that are analysed with 4B are (Royal Water and ICP-MS): Au, Ag, As, Bi, Cd, Cu, Hg, Mo, Ni, Pb, Sb, Se, Tl, Zn.

Combustible efficiency analysis. It is used in interpretation of combustible efficiency washing performance. Combustible efficiency has been calculated with the formulae as below (Ateşok, 2004):

$$\text{Combustible Efficiency} = \frac{(100-c)(t-f)}{(100-f)(t-c)}100, \quad (1)$$

where, *t* represents waste schist ash %, *f* raw coal ash %, *c* clean coal ash %.

Float and sink experiments. Trace element analysis results of the products obtained from float and sink experiments are given in Attachments 1 and 3.

Combustible efficiencies of samples according to the float and sink experiment results are given in Table 3.

Combustible efficiencies of the flotation experiment results are given in Table 4.

Table 3. Combustible efficiencies of the coal samples that floated and sank in float and sink experiments

Float and Sink (-4mm+0,5mm)	Quantity,%	ΣC Content,%	Ash, %	Combustible Efficiency,%
Soma +1,6 floating	47.51	63.35	9.90	66.76
Soma -1,6 sinking	52.49	15.37	59.40	33.24
Soma feed	100.00	38.17	35.88	100.00
Agacli +1,3 floating	68.06	58.86	7.90	68.23
Agacli -1,3 sinking	31.94	57.28	8.60	31.77
Agacli feed	100.00	58.36	8.12	100.00

Table 4. Combustible efficiencies of the floating and sinking coal samples in flotation results

Flotation, (-0,5mm)	Quantity, %	ΣC Content, %	Ash, %	Combustible Efficiency, %
Soma floating	61.21	31.44	45.70	61.12
Soma sinking	38.79	30.81	45.50	38.88
Soma feed	100.00	31.20	45.62	100.00
Agacli floating	49.93	60.27	7.30	50.01
Agacli sinking	50.07	59.59	7.60	49.99
Agacli feed	100.00	59.93	7.45	100.00

Combustible efficiencies according to total coal dressing works, in which results of float and sink experiments and flotation experiments are evaluated together, are given in Table 5.

Table 5. Combustible efficiencies of floating and sinking coals in total after coal dressing processes

Total Coal Dressing (-4mm)	Quantity, %	ΣC Content, %	Σ Ash, %	Σ Combustible Efficiency, %
Soma ΣFloating	50.92	53.80	45.70	50.83
Soma ΣSinking	49.08	18.41	45.50	49.17
Soma ΣFeed	100.00	36.43	45.60	100.00
Agacli ΣFloating	65.44	59.02	7.30	65.51
Agacli ΣSinking	34.56	57.76	7.60	34.49
Agacli ΣFeed	100.00	58.58	7.40	100.00

Flotation Experiments. Trace element analysis results of the products obtained by flotation experiments performed in the study are given in Appendices 1 and 3.

Combustible efficiencies of Manisa – Soma coal is low because it is high ash coal and lignite flotation is difficult.

Trace element analysis results of Manisa Soma Coal, Ash and Thermal Power Plant Ash, are given in Appendix 2. Trace element analysis results of İstanbul Agacli Coal and Ash are given in Appendix 3.

3. Conclusions

Because Manisa-Soma lignite is low in thermal value, they can only be used in thermal power plants. It has been observed that trace element sedimentations settling in coal during geological formation of the area is higher than worldwide coal average.

In the Float and Sink Experiments performed on Manisa-Soma coal, which has a relative density of 1.553 g/cm^3, $ZnCl_2$ solution of 1.6 g/cm^3 density has been used. It has been calculated that it is very easy to sort at this density, 47.51% of the coal feed with 35.88% ash content floats, and floating coal contains 9.90% ash and sinking coal contains 59.40% ash. When sorting is made at 1.6 g/cm^3 density, combustible efficiency of floating coals has been calculated to be 66.76%.

As a result of flotation experiments applied on Manisa-Soma coal, it has been found that 61.21% of the coal feed with 45.62% ash content floats, and floating coal

contains 45.70% ash and sinking coal contains 45.50% ash. At the end of flotation, it has been calculated that combustible efficiency of floating coal is 61.12%.

It has been aimed to obtain a total coal preparation conclusion by combining the results of float and sink experiment and flotation experiment. According to these results, total floating ratio of the coal with 45.60% total ash content is 50.92% and ash content is 45.70%. Total combustible efficiency has been calculated to be 50.83%.

According to the major and trace element results of the Float and Sink Experiment made on Manisa-Soma coal, whereas radioactive element content of Th is 3.26 ppm in the feeding coal, it is 1.00ppm in floating coal and 5.30 ppm in sinking coal. Furthermore, when post-combustion ashes of these coals are examined, the value found in Floating Coal ash is 12.40 ppm, in Sinking Coal ash 8.80ppm and in Unsorted Coal ash 8.20 ppm respectively. This shows that Th element collects in the sinking part after coal dressing, and gets concentrated in the ash after combustion. In the same way, when the samples are analysed in respect to U element, the values are 7.19 ppm in Unsorted Coal, 7.40 ppm in the floating part and 7.00 ppm in the sinking part after float and sink experiment. When they are analysed with respect to ash, the value is 11.50 ppm in the feeding coal ash, and they concentrate in Floating Coal ash as 72.60 ppm and 12.1 ppm in Sinking Coal ash.

When samples are analysed with respect to air polluting elements, it was observed that As, Co and Mn concentrated in floating coals, Be, Cd, Hg and Ni concentrated in the ashes of these coals, and Se concentrated in sinking coal and its ash.

Th and U values for Soma run-of-mine coal samples are 5.70 ppm and 8.30 ppm, respectively. Th and U values for Soma coal samples were determined as 8.20 ppm and 11.50 ppm respectively according to the results of ash test. Th and U values were observed as 26.20 ppm and 26.50 ppm respectively in Soma thermal power plant ashes.

Because Istanbul-Agacli lignite is low in thermal value, they can only be used in thermal power plants. It was observed that the trace element sedimentations settling in coal during geological formation of the area is higher than worldwide coal average.

In the Float and Sink Experiments performed on Istanbul-Agacli coal, which has a relative density of 1.301 g/cm^3, $ZnCl_2$ solution of 1.3 g/cm^3 density was used. It was calculated that it is very easy to sort at this density, 68.06% of the coal feed with 8.12% ash content floats, and floating coal contains 7.90% ash and sinking coal contains 8.60% ash. When sorting is made at 1.3 g/cm^3 density, combustible efficiency of floating coals was calculated to be 68.23%.

After the flotation experiments applied on Istanbul-Agacli coal samples, it has been found that 49.93% of the coal feed with 7.45% ash content floats, and floating coal contains 7.30% ash and sinking coal contains 7.60% ash. At the end of the flotation, it was calculated that the combustible efficiency of floating coal is 50.01%.

The aim of this study was to obtain a total coal preparation conclusion by combining the results of float and sink experiments and flotation experiments. According to these results, total floating ratio of the coal with 7.40% total ash content

is 64.44% and ash content is 7.30%. Total combustible efficiency was calculated as 65.51%.

According to the major and trace element results of the Float and Sink Experiment made on Istanbul-Agacli coal, whereas the radioactive element content of Th is 3.05 ppm in the feeding coal, it is 2.60 ppm in floating coal and 4.00ppm in sinking coal. Furthermore, when post-combustion ashes of these coals are examined, the value found in Floating Coal ash is 32.30 ppm, in Sinking Coal ash 36.00 ppm and in Unsorted Coal ash 43.40 ppm. This shows that Th element collects in the sinking part after coal dressing, and gets concentrated in the ash after combustion. In the same way, when the samples are analysed in respect to U element, the values are1.16 ppm in Unsorted Coal, 0.90 ppm in the floating part and 1.70 ppm in the sinking part after float and sink experiment. When they are analysed with respect to ash, the value is 11.60 ppm in the feeding coal ash, and they concentrate in Floating Coal ash as 13.70 ppm and 13.4 ppm in Sinking Coal ash.

When samples were analysed with respect to air polluting elements, it was observed that As, Co and Mn were concentrated in floating coals, Be, Cd, Hg and Ni were concentrated in the ashes of these coals, and Se was concentrated in sinking coal and its ash.

Acknowledgement

A part of this work was supported by Scientific Research Projects Coordination Unit of Istanbul University under the project number T-2324.

References

ACME, 2009, Acme Labs Schedule of Services & Fees.

ATEŞOK, G., 2004, *Coal preparation and technology*, Publications of the Foundation for Development of Mining, ISBN-975-7946-22-2, İstanbul, Turkey.

BABA, A., 2001, *Effect of Yatağan (Muğla) thermal power plant waste product storage area on underground water*, Dokuz Eylül University Journal of Geology Engineering 25 (2), İzmir, Turkey.

DEMIR, İ., 2009, *Investigation of evaluation possibilities of Turkish Coals in terms of their trace element contents by use of coal preparation methods*. Istanbul University, Institute of Science, Mining Engineering Department, Master's Thesis, İstanbul, Turkey.

DEMIR, İ., KURŞUN, İ., 2010, *An investigation of trace element content of the Zonguldak-Kozlu coal washery plant's feed coal*, Proceedings of the 17th Coal Congress of Turkey, June 02-04, 2010 Zonguldak, Turkey, 415–429.

ESENLIK, S., 2005, *Mineralogy, petrography and element contents of coal combusted in Orhaneli thermal power plant and waste Products, Bursa, Turkey*. Hacettepe University, Institute of Sciences, Geological Engineering Department, Master's Thesis, Ankara, Turkey.

KARAYIĞIT, A.I., GAYER, R.A., QUEROL, X., ONACAK, T., 2000, *Contents of major and trace elements in feed coals from Turkish coal-fired power plants*, Int. J. Coal Geol., 44, 169–184.

KURAL, O., (Ed.) 1998, *Properties, technology and environmental impacts of coal.* ITU Faculty of Mining, İstanbul, Turkey.

ÖZYURT, Z., 2006, *Environmental effect of the trace elements in thermal power plants' waste products*, Eskişehir Osmangazi University, Mining Engineering Department, Master's Thesis, Eskişehir, Turkey.

PERÇINEL, S., 2000, *Effect of coal use in thermal power plants on human health*, Proceedings of the 12th Turkish Coal Congress, 23-26 May 2000, Zonguldak, Turkey.

RILEY, K., 2008, *Analysing for trace elements*, http://www.ccsd.biz/products/traceelementdb.cfm.

SHAH, P., STREZOV, V., PRINCE, K., NELSON, P. F., 2008, *Speciation of As. Cr. Se and Hg under coal fired power station conditions*, Elsevier Fuel 87, 1859–1869.

SWAINE, D.J., 1990, *Trace elements in coal*, Butterwarh, London.

TEIAS, 2008, Web page of Turkish Electricity Transmission Co. (Türkiye Elektrik İletim A.Ş.) http://www.teias.gov.tr/ (visiting date: 12.09.2008).

TSE, 1992, TS 10091/April 1992, *Mineral coal foamy flotation experiment, section 1, laboratory process*, Turkish Standards Institute, Ankara, Turkey.

TSE, 1999, TS ISO 5072/April 1999, *Brown coal and lignite – assessment of real and apparent relative density*, Turkish Standards Institute, Ankara, Turkey.

TSE, 2002a, TS 690 ISO 589/March 2002, *Assessment of total humidity in mineral coal*, Turkish Standards Institute, Ankara, Turkey.

TSE. 2002b, TS 711 ISO 562/March 2002, *Assessment of volatile substances in mineral coal and coke*, Turkish Standards Institute, Ankara, Turkey.

TSE. 2003, TS 3037 ISO 7936/March 2003, *Definition and display of mineral coal float and sink experiment requirements, general definitions for device and processes*, Turkish Standards Institute, Ankara, Turkey.

TSE, 2006, TS ISO 1171+Tech Cor 1/November 2006, *Solid mineral fuels – quantity of ash*, Turkish Standards Institute, Ankara, Turkey.

TUNA, A. L., YAĞMUR, B., HAKERLERLER, H., KILINÇ. R., YOKAŞ, İ., BÜRÜN, B., 2005, *Research on pollution caused by the thermal power plants in Muğla region*, Muğla University, Scientific Research Projects Final Report, Muğla, Turkey.

Appendix 1. Analysis results and average trace elements table for Manisa Soma coal

		Method	4A-4B	4A-4B	4A-4B	4A-4B	4A-4B	4A-4B	4A-4B	4A-4B	4A-4B	4A-4B	4A-4B	4A-4B	4A-4B	4A-4B	4A-4B	4A-4B
		Analyte	SiO2	Al2O3	Fe2O3	MgO	CaO	Na2O	K2O	TiO2	P2O5	MnO	Cr2O3	Sc	Ba	Be	Co	Cs
		Unit	%	%	%	%	%	%	%	%	%	%	%	ppm	ppm	ppm	ppm	ppm
		MDL	0.01	0.01	0.04	0.01	0.01	0.01	0.01	0.01	0.01	0.01	0.002	1	1	1	0.2	0.1
Float and Sink Coal	Soma -4+0.5mm +1.60 Floating	Coal	1.71	1.05	0.49	0.23	3.23	0.06	0.07	0.05	0.03	<0.01	0.00	<1	113.00	<1	1.10	2.80
	Soma -4+0.5mm -1.60 Sinking	Coal	21.81	6.01	3.02	1.11	21.78	0.11	0.65	0.16	0.08	0.04	0.00	6.00	196.00	1.00	2.50	9.50
Float and Sink Ashes	Soma -4+0.5mm +1.60 Floating Ash	Ash	N.A.	N.A.	N.A.	N.A.	N.A.	N.A.	N.A.	N.A.	N.A.	N.A.	N.A.	N.A.	1239.00	5.00	16.80	5.10
	Soma -4+0.5mm -1.60 Sinking Ash	Ash	32.00	10.34	5.56	1.74	33.79	0.26	1.02	0.28	0.13	0.07	0.008	11.00	350.00	<1	4.80	14.70
Unsorted Coal	Soma Unsorted Coal	Coal	17.91	7.26	2.33	0.84	13.08	0.11	0.77	0.20	0.08	0.03	0.005	6.00	250.00	<1	3.30	10.40
Unsorted Coal Ashes	Soma Unsorted Coal Ashes	Ash	21.06	8.70	2.51	2.47	58.14	0.23	0.98	0.30	0.19	0.06	0.007	7.00	425.00	<1	6.80	13.80
Flotation	Soma -0.5mm Floating	Coal	19.49	8.69	2.09	0.86	13.15	0.14	0.89	0.24	0.07	0.02	0.009	7.00	298.00	<1	3.50	10.70
	Soma -0.5mm Sinking	Coal	17.99	7.01	2.95	0.90	15.33	0.18	0.73	0.20	0.08	0.04	0.005	7.00	287.00	<1	3.20	9.00
Flotation Ashes	Soma -0.5mm Floating Ash	Ash	41.37	17.88	4.43	1.77	26.50	0.32	1.93	0.51	0.16	0.05	0.013	15.00	604.00	2.00	7.90	21.10
	Soma -0.5mm Sinking Ash	Ash	N.A.	N.A.	N.A.	N.A.	N.A.	N.A.	N.A.	N.A.	N.A.	N.A.	N.A.	N.A.	584.00	3.00	7.20	18.90
World Average*		Coal												1.00	200.00	2.00	5.00	1.00
Lowest		Coal												1.00	20.00	0.10	0.50	0.30
Highest		Coal												10.00	1000.00	15.00	30.00	5.00
Turkey Average		Coal														1.00	9.40	
Lowest		Coal	0.67	0.07	0.26	0.04	0.06	0.01	0.01	0.01	0.01	0.01				0.20	1.00	
Highest		Coal	28.27	12.00	12.57	3.17	14.08	2.34	1.85	0.57	0.24	0.07				7.00	55.00	

*Swaine (1990)

		Method	4A-4B	4A-4B	4A-4B	4A-4B	4A-4B	4A-4B	4A-4B	4A-4B	4A-4B	4A-4B	4A-4B	4A-4B	4A-4B	4A-4B	4A-4B	4A-4B
		Analyte	Ga	Hf	Nb	Rb	Sn	Sr	Ta	V	Th	U	W	Zr	Y	La	Ce	Pr
		Unit	ppm	ppm	ppm	ppm	ppm	ppm	ppm	ppm	ppm	ppm	ppm	ppm	ppm	ppm	ppm	ppm
		MDL	0.5	0.1	0.1	0.1	1	0.5	0.1	8	0.2	0.1	0.5	0.1	0.1	0.1	0.1	0.02
Float and Sink Coal	Soma -4+0.5mm +1.60 Floating	Coal	2.10	0.30	2.00	4.40	<1	77.40	<0.10	51.00	1.00	7.40	<0.5	13.90	1.80	2.10	4.00	0.47
	Soma -4+0.5mm -1.60 Sinking	Coal	6.60	1.10	3.30	37.90	<1	135.10	0.20	45.00	5.30	7.00	0.80	37.80	9.50	11.80	22.40	2.68
Float and Sink Ashes	Soma -4+0.5mm +1.60 Floating Ash	Ash	18.30	4.80	24.70	8.90	4.00	753.00	1.00	617.00	12.40	72.60	4.90	163.70	21.30	24.10	43.00	5.19
	Soma -4+0.5mm -1.60 Sinking Ash	Ash	10.50	2.00	6.20	58.90	3.00	231.10	0.40	83.00	8.80	12.10	1.40	65.50	18.80	21.50	41.60	4.98
Unsorted Coal	Soma Unsorted Coal	Coal	7.70	1.40	4.80	41.20	1.00	152.40	0.40	74.00	5.70	8.30	0.70	44.90	9.10	13.70	25.10	3.01
Unsorted Coal Ashes	Soma Unsorted Coal Ashes	Ash	8.80	1.90	6.30	48.40	2.00	426.40	0.40	75.00	8.20	11.50	0.90	68.10	13.10	18.80	35.00	4.14
Flotation	Soma -0.5mm Floating	Coal	8.70	1.60	5.00	47.60	<1	179.20	0.40	72.00	7.10	9.00	0.60	53.70	9.50	14.80	28.30	3.36
	Soma -0.5mm Sinking	Coal	7.90	1.40	4.40	39.40	2.00	180.70	0.30	66.00	5.70	8.60	0.80	43.90	9.20	13.00	24.10	2.94
Flotation Ashes	Soma -0.5mm Floating Ash	Ash	19.00	3.50	10.50	100.90	3.00	362.10	0.80	155.00	14.30	17.90	1.60	118.20	19.90	30.20	56.90	6.81
	Soma -0.5mm Sinking Ash	Ash	15.10	2.80	8.90	79.10	2.00	350.80	0.70	132.00	12.60	17.70	1.30	93.20	19.00	27.60	51.10	6.06
World Average*		Coal	5.00	1.00	5.00	40.00	2.00	200.00	0.20	40.00	4.00	2.00	1.00	50.00		10.00	20.00	
Lowest		Coal	1.00	0.40	1.00	2.00	1.00	15.00	0.10	2.00	0.50	0.50	0.50	5.00	2.00	1.00	2.00	1.00
Highest		Coal	20.00	5.00	20.00	50.00	10.00	500.00	1.00	100.00	10.00	10.00	5.00	200.00	50.00	40.00	70.00	10.00
Turkey Average		Coal								87.00	6.00	13.00						
Lowest		Coal								6.00	1.00	0.40						
Highest		Coal								287.00	29.00	132.00						

*Swaine (1990)

		Method	4A-4B	4A-4B	4A-4B	4A-4B	4A-4B	4A-4B	4A-4B	4A-4B	4A-4B	4A-4B	4A-4B	2A	2ALeco	4A-4B	4A-4B
		Analyte	Nd	Sm	Eu	Gd	Tb	Dy	Ho	Er	Tm	Yb	Lu	Leco	TOT/S	LOI	Sum
		Unit	ppm	ppm	ppm	ppm	ppm	ppm	ppm	ppm	ppm	ppm	ppm	TOT/C %	%	%	%
		MDL	0.3	0.05	0.02	0.05	0.01	0.05	0.02	0.03	0.01	0.05	0.01	0.02	0.02	-5.1	0.01
Float and Sink Coal	Soma -4+0.5mm +1.60 Floating	Coal	1.80	0.32	0.07	0.31	0.06	0.27	0.07	0.18	0.03	0.21	0.03	63.35	0.70	90.10	97.00
	Soma -4+0.5mm -1.60 Sinking	Coal	10.00	2.02	0.48	1.83	0.28	1.50	0.31	0.85	0.14	0.96	0.15	15.37	0.65	40.60	95.41
Float and Sink Ashes	Soma -4+0.5mm +1.60 Floating Ash	Ash	20.40	3.78	0.92	3.72	0.63	3.54	0.65	2.12	0.27	2.13	0.36	N.A.	N.A.	N.A.	N.A.
	Soma -4+0.5mm -1.60 Sinking Ash	Ash	20.00	3.76	0.89	3.29	0.55	3.02	0.62	1.81	0.30	1.82	0.28	0.22	1.18	7.30	92.48
Unsorted Coal	Soma Unsorted Coal	Coal	11.60	2.07	0.47	1.67	0.28	1.48	0.30	0.93	0.14	0.95	0.15	33.93	0.75	57.30	99.89
Unsorted Coal Ashes	Soma Unsorted Coal Ashes	Ash	16.40	2.85	0.62	2.33	0.39	2.16	0.43	1.32	0.20	1.34	0.19	0.97	0.73	5.20	99.81
Flotation	Soma -0.5mm Floating	Coal	12.40	2.08	0.49	1.84	0.30	1.64	0.33	0.99	0.16	1.00	0.16	31.44	0.76	54.30	99.90
	Soma -0.5mm Sinking	Coal	10.50	1.91	0.46	1.63	0.27	1.57	0.31	0.98	0.15	0.93	0.15	30.81	0.81	54.50	99.88
Flotation Ashes	Soma -0.5mm Floating Ash	Ash	25.00	4.64	0.99	3.77	0.61	3.49	0.67	2.12	0.32	2.18	0.33	1.49	1.52	4.80	99.77
	Soma -0.5mm Sinking Ash	Ash	23.20	4.25	0.99	3.67	0.57	3.31	0.63	1.97	0.31	2.03	0.30	N.A.	N.A.	N.A.	N.A.
World Average*		Coal	10.00	2.00	0.50							1.00					
Lowest		Coal	3.00	0.50	0.10	0.40	0.10	0.50	0.10	0.50	0.50	0.30	0.03				
Highest		Coal	30.00	6.00	2.00	4.00	1.00	4.00	2.00	3.00	3.00	3.00	1.00				
Turkey Average		Coal															
Lowest		Coal															
Highest		Coal															

*Swaine (1990)

		Method	1DX	1DX	1DX	1DX	1DX	1DX	1DX	1DX	1DX	1DX	1DX	1DX	1DX	1DX
		Analyte	Mo	Cu	Pb	As	Cd	Sb	Bi	Ag	Au	Hg	Tl	Se	Ni	
		Unit	ppm	ppm	ppm	ppm	ppm	ppm	ppm	ppm	ppb	ppm	ppm	ppm	ppm	
		MDL	0.1	0.1	0.1	0.5	0.1	0.1	0.1	0.1	0.5	0.01	0.1	0.5	0.1	
Float and Sink Coal	Soma -4+0.5mm +1.60 Floating	Coal	0.70	9.50	3.90	20.90	0.10	0.10	<0.10	<0.10	<0.50	0.06	0.70	0.80	7.60	
	Soma -4+0.5mm -1.60 Sinking	Coal	0.50	15.00	8.90	66.60	0.30	<0.10	0.10	<0.10	0.70	0.06	0.90	2.80	7.10	
Float and Sink Ashes	Soma -4+0.5mm +1.60 Floating Ash	Ash	12.00	61.00	5.50	219.00	0.90	1.70	0.40	<0.10	8.30	<0.01	<0.10	2.10	54.20	
	Soma -4+0.5mm -1.60 Sinking Ash	Ash	1.40	21.80	10.40	102.30	0.50	0.20	0.30	<0.10	<0.50	<0.01	0.10	3.10	15.20	
Unsorted Coal	Soma Unsorted Coal	Coal	0.60	18.90	8.60	52.00	0.20	0.20	0.20	<0.10	<0.50	0.07	<0.10	0.70	9.40	
Unsorted Coal Ashes	Soma Unsorted Coal Ashes	Ash	1.60	20.80	16.40	58.90	0.30	0.10	0.20	<0.10	1.00	<0.01	0.20	1.10	21.50	
Flotation	Soma -0.5mm Floating	Coal	0.70	21.90	10.60	46.90	0.30	0.20	0.20	<0.10	<0.50	0.08	<0.10	0.60	12.10	
	Soma -0.5mm Sinking	Coal	0.90	21.10	10.40	56.10	0.20	0.20	0.20	<0.10	<0.50	0.10	<0.10	0.60	13.20	
Flotation Ashes	Soma -0.5mm Floating Ash	Ash	2.10	45.50	16.80	99.50	<0.10	0.30	<0.10	<0.10	0.90	<0.01	0.50	1.70	29.70	
	Soma -0.5mm Sinking Ash	Ash	2.20	42.20	16.90	114.40	0.10	0.30	<0.10	<0.10	<0.50	<0.01	0.30	1.50	25.30	
World Average*		Coal	3.00	15.00	20.00	10.00	0.50	1.50						1.00	20.00	
Lowest		Coal	0.10	0.50	2.00	0.50	0.10	0.10	2.00			0.02	0.20	0.20	0.50	
Highest		Coal	10.00	50.00	80.00	80.00	3.00	10.00	20.00			1.00	1.00	10	50.00	
Turkey Average		Coal			12.00	53.00	1.00					0.10		2.00	126.00	
Lowest		Coal			0.10	2.00	0.01					0.03		0.10	3.00	
Highest		Coal			286.00	686.00	45.00					0.70		26.00	1700.00	

*Swaine (1990)

Appendix 2. Trace element analysis results of Manisa Soma coal, ash and Thermal Power Plant ash

	Method	4A-4B		4A-4B		4A-4B		4A-4B		4A-4B		4A-4B		4A-4B		4A-4B	
	Analyte	SiO2	Si	Al2O3	Al	Fe2O3	Fe	MgO	Mg	CaO	Ca	Na2O	Na	K2O	K		
	Unit	%	(%)	%	(%)	%	(%)	%	(%)	%	(%)	%	(%)	%	(%)		
	MDL	0.01		0.01		0.04		0.01		0.01		0.01		0.01			
Soma (-4mm) Coal	Coal	17.91	8.37	7.26	3.84	2.33	1.63	0.84	0.51	13.08	9.35	0.11	0.08	0.77	0.64		
Soma (-4mm) Coal Ash	Ash	21.06	9.85	8.70	4.61	2.51	1.76	2.47	1.49	58.14	41.56	0.23	0.17	0.98	0.81		
Soma Thermal Power Plant Ash	Ash	44.97	21.02	21.25	11.25	4.10	2.87	1.67	1.01	23.67	16.92	0.54	0.40	1.29	1.07		

	Method	4A-4B		4A-4B		4A-4B		4A-4B		4A-4B	4A-4B	4A-4B	4A-4B	4A-4B	4A-4B
	Analyte	TiO2	Ti	P2O5	P	MnO	Mn	Cr2O3	Cr	Ni	Sc	Ba	Be	Co	Cs
	Unit	%	(%)	%	(%)	%	(%)	%	(%)	ppm	ppm	ppm	ppm	ppm	ppm
	MDL	0.01		0.01		0.01		0.002		20	1	1	1	0.2	0.1
Soma (-4mm) Coal	Coal	0.20	0.12	0.08	0.03	0.030	0.023	0.005	0.003	<20	6.00	250.00	<1	3.30	10.40
Soma (-4mm) Coal Ash	Ash	0.30	0.18	0.19	0.08	0.060	0.046	0.007	0.005	27.00	7.00	425.00	<1	6.80	13.80
Soma Thermal Power Plant Ash	Ash	0.73	0.44	0.22	0.10	0.04	0.031	0.02	0.010	37.40	15.00	893.00	3.00	15.20	25.10

	Method	4A-4B	4A-4B	4A-4B	4A-4B	4A-4B	4A-4B	4A-4B	4A-4B	4A-4B	4A-4B	4A-4B	4A-4B	4A-4B	4A-4B
	Analyte	Ga	Hf	Nb	Rb	Sn	Sr	Ta	Th	U	V	W	Zr	La	Ce
	Unit	ppm	ppm	ppm	ppm	ppm	ppm	ppm	ppm	ppm	ppm	ppm	ppm	ppm	ppm
	MDL	0.5	0.1	0.1	0.1	1	0.5	0.1	0.2	0.1	8	0.5	0.1	0.1	0.1
Soma (-4mm) Coal	Coal	7.70	1.40	4.80	41.20	1.00	173.60	0.40	5.70	8.30	74.00	0.70	44.90	13.70	25.10
Soma (-4mm) Coal Ash	Ash	8.80	1.90	6.30	48.40	2.00	426.40	0.40	8.20	11.50	75.00	0.90	68.10	18.80	35.00
Soma Thermal Power Plant Ash	Ash	22.60	4.00	20.30	94.80	3.00	381.10	1.50	26.20	26.50	275.00	3.80	167.60	50.90	95.40

	Method	4A-4B	4A-4B	4A-4B	4A-4B	4A-4B	4A-4B	4A-4B	4A-4B	4A-4B	4A-4B	4A-4B	4A-4B	1DX	1DX
	Analyte	Pr	Nd	Sm	Eu	Gd	Tb	Dy	Ho	Er	Tm	Yb	Lu	Mo	Cu
	Unit	ppm	ppm	ppm	ppm	ppm	ppm	ppm	ppm	ppm	ppm	ppm	ppm	ppm	ppm
	MDL	0.02	0.3	0.05	0.02	0.05	0.01	0.05	0.02	0.03	0.01	0.05	0.01	0.1	0.1
Soma (-4mm) Coal	Coal	3.01	11.60	2.07	0.47	1.67	0.28	1.48	0.30	0.93	0.14	173.60	0.15	0.60	18.90
Soma (-4mm) Coal Ash	Ash	4.14	16.40	2.85	0.62	2.33	0.39	2.16	0.43	1.32	0.20	1.34	0.19	1.60	20.80
Soma Thermal Power Plant Ash	Ash	10.58	39.50	7.30	1.53	6.52	0.96	5.26	1.11	3.05	0.46	3.34	0.48	2.40	29.20

	Method	1DX	1DX	1DX	1DX	1DX	1DX	1DX	1DX	1DX	1DX	1DX	2ALeco	2ALeco	
	Analyte	Pb	Zn	As	Cd	Sb	Bi	Ag	Au	Hg	Tl	Se	TOT/C	TOT/S	Ash
	Unit	ppm	ppm	ppm	ppm	ppm	ppm	ppm	ppb	ppm	ppm	ppm	%	%	%
	MDL	0.1	1	0.5	0.1	0.1	0.1	0.1	0.5	0.01	0.1	0.5	0.02	0.02	
Soma (-4mm) Coal	Coal	8.60	28.00	52.00	0.20	0.20	0.20	<0.1	<0.5	0.07	<0.1	0.70	33.93	0.75	42.70
Soma (-4mm) Coal Ash	Ash	16.40	38.00	58.90	0.30	0.10	0.20	<0.1	1.00	<0.01	0.20	1.10	0.97	0.73	94.80
Soma Thermal Power Plant Ash	Ash	25.00	81.00	144.90	1.60	0.40	0.70	<0.1	<0.5	0.02	0.30	2.20	0.71	1.26	98.80

Appendix 3. Analysis results and average trace elements table for Istanbul Agacli coal

		Method Analyte Unit MDL	4A-4B SiO2 % 0,01	4A-4B Al2O3 % 0,01	4A-4B Fe2O3 % 0,04	4A-4B MgO % 0,01	4A-4B CaO % 0,01	4A-4B Na2O % 0,01	4A-4B K2O % 0,01	4A-4B TiO2 % 0,01	4A-4B P2O5 % 0,01	4A-4B MnO % 0,01	4A-4B Cr2O3 % 0,002	4A-4B Sc ppm 1	4A-4B Ba ppm 1	4A-4B Be ppm 1	4A-4B Co ppm 0,2	4A-4B Cs ppm 0,1
Float and Sink Coal	Agacli -4+0.5mm +1.30 Floating	Coal	0.42	0.70	1.10	0.28	2.08	0.08	0.01	<0,01	<0,01	<0,01	0.00	1.00	47.00	2.00	2.10	<0.10
	Agacli -4+0.5mm -1.30 Sinking	Coal	1.35	1.20	1.33	0.25	1.82	0.09	0.05	0.04	<0,01	<0,01	0.00	2.00	46.00	2.00	1.80	0.30
Float and Sink Ashes	Agacli -4+0.5mm +1.30 Floating Ash	Ash	N.A.	N.A.	N.A.	N.A.	N.A.	N.A.	N.A.	N.A.	N.A.	N.A.	N.A.	N.A.	610.00	21.00	34.60	0.30
	Agacli -4+0.5mm -1.30 Sinking Ash	Ash	N.A.	N.A.	N.A.	N.A.	N.A.	N.A.	N.A.	N.A.	N.A.	N.A.	N.A.	N.A.	460.00	10.00	19.70	1.20
Unsorted Coal	Agacli Unsorted Coal	Coal	0.87	0.94	1.22	0.31	2.17	0.09	0.02	0.02	0.04	0.01	<0.002	2.00	57.00	2.00	2.60	0.20
Unsorted Coal Ashes	Agacli Unsorted Coal Ashes	Ash	N.A.	N.A.	N.A.	N.A.	N.A.	N.A.	N.A.	N.A.	N.A.	N.A.	N.A.	N.A.	609.00	17.00	36.60	0.90
Flotation	Agacli -0.5mm Floating	Coal	1.28	1.26	1.56	0.34	2.56	0.09	0.04	0.03	0.01	0.01	0.002	3.00	63.00	2.00	2.70	0.30
	Agacli -0.5mm Sinking	Coal	1.20	1.15	1.41	0.31	2.38	0.11	0.03	0.03	0.04	0.01	0.004	3.00	61.00	2.00	2.30	0.20
Flotation Ashes	Agacli -0.5mm Floating Ash	Ash	N.A.	N.A.	N.A.	N.A.	N.A.	N.A.	N.A.	N.A.	N.A.	N.A.	N.A.	N.A.	654.00	15.00	27.70	2.00
	Agacli -0.5mm Sinking Ash	Ash	N.A.	N.A.	N.A.	N.A.	N.A.	N.A.	N.A.	N.A.	N.A.	N.A.	N.A.	N.A.	659.00	13.00	26.30	2.30
World Average*		Coal												1.00	200.00	2.00	5.00	1.00
Lowest		Coal												1.00	20.00	0.10	0.50	0.30
Highest		Coal												10.00	1000.00	15.00	30.00	5.00
Turkey Average		Coal														1.00	9.40	
Lowest		Coal	0.67	0.07	0.26	0.04	0.06	0.01	0.01	0.01	0.01	0.01				0.20	1.00	
Highest		Coal	28.27	12.00	12.57	3.17	14.08	2.34	1.85	0.57	0.24	0.07				7.00	55.00	

*Swaine (1990)

		Method Analyte Unit MDL	4A-4B Ga ppm 0,5	4A-4B Hf ppm 0,1	4A-4B Nb ppm 0,1	4A-4B Rb ppm 0,1	4A-4B Sn ppm 1	4A-4B Sr ppm 0,5	4A-4B Ta ppm 0,1	4A-4B V ppm 8	4A-4B Th ppm 0,2	4A-4B U ppm 0,1	4A-4B W ppm 0,5	4A-4B Zr ppm 0,1	4A-4B Y ppm 0,1	4A-4B La ppm 0,1	4A-4B Ce ppm 0,1	4A-4B Pr ppm 0,02
Float and Sink Coal	Agacli -4+0.5mm +1.30 Floating	Coal	2.60	0.30	0.80	0.10	<1	462.70	<0.10	11.00	2.60	0.90	1.20	9.70	6.50	1.90	4.80	0.55
	Agacli -4+0.5mm -1.30 Sinking	Coal	3.30	0.40	2.50	1.90	<1	373.10	<0.10	16.00	4.00	1.70	1.30	14.60	7.20	4.10	9.00	1.01
Float and Sink Ashes	Agacli -4+0.5mm +1.30 Floating Ash	Ash	27.10	3.20	13.90	2.10	12.00	5672.00	0.40	259.00	32.30	13.70	14.40	113.00	91.90	24.90	56.90	7.42
	Agacli -4+0.5mm -1.30 Sinking Ash	Ash	28.00	4.40	20.50	10.00	3.00	3435.00	1.00	202.00	36.00	13.40	11.90	148.80	60.30	32.10	71.30	7.89
Unsorted Coal	Agacli Unsorted Coal	Coal	2.60	0.30	1.60	0.90	1.00	445.50	<0.10	47.00	3.60	1.30	1.10	11.00	6.80	3.10	6.20	0.81
Unsorted Coal Ashes	Agacli Unsorted Coal Ashes	Ash	22.10	3.70	11.10	7.20	7.00	5792.00	0.70	227.00	43.40	11.60	10.50	140.60	91.80	43.30	95.60	11.03
Flotation	Agacli -0.5mm Floating	Coal	2.80	0.40	2.00	1.10	<1	491.40	<0.10	21.00	4.00	1.50	1.10	14.50	7.70	3.70	7.90	0.95
	Agacli -0.5mm Sinking	Coal	2.50	0.40	1.80	1.10	<1	476.70	<0.10	35.00	3.90	1.30	0.90	13.80	7.10	3.50	7.50	0.88
Flotation Ashes	Agacli -0.5mm Floating Ash	Ash	28.40	4.80	18.60	8.40	2.00	4744.00	0.80	219.00	38.60	15.40	11.10	153.30	79.60	35.80	78.50	9.18
	Agacli -0.5mm Sinking Ash	Ash	28.90	4.20	19.00	8.80	2.00	4746.00	0.80	225.00	36.80	15.70	10.90	147.90	78.80	35.70	77.40	8.93
World Average*		Coal	5.00	1.00	5.00	40.00	2.00	200.00	0.20	40.00	4.00	2.00	1.00	50.00		10.00	20.00	
Lowest		Coal	1.00	0.40	1.00	2.00	1.00	15.00	0.10	2.00	0.50	0.50	0.50	5.00	2.00	1.00	2.00	1.00
Highest		Coal	20.00	5.00	20.00	50.00	10.00	500.00	1.00	100.00	10.00	10.00	5.00	200.00	50.00	40.00	70.00	10.00
Turkey Average		Coal								87.00	6.00	13.00						
Lowest		Coal								6.00	1.00	0.40						
Highest		Coal								287.00	29.00	132.00						

*Swaine (1990)

		Method Analyte Unit MDL	4A-4B Nd ppm 0,3	4A-4B Sm ppm 0,05	4A-4B Eu ppm 0,02	4A-4B Gd ppm 0,05	4A-4B Tb ppm 0,01	4A-4B Dy ppm 0,05	4A-4B Ho ppm 0,02	4A-4B Er ppm 0,03	4A-4B Tm ppm 0,01	4A-4B Yb ppm 0,05	4A-4B Lu ppm 0,01	2A Leco TOT/C % 0,02	2ALeco TOT/S % 0,02	4A-4B LOI % -5,1	4A-4B Sum % 0,01
Float and Sink Coal	Agacli -4+0.5mm +1.30 Floating	Coal	2.60	0.58	0.19	0.78	0.13	0.79	0.18	0.51	0.07	0.49	0.07	58.86	1.18	92.10	96.75
	Agacli -4+0.5mm -1.30 Sinking	Coal	3.60	0.95	0.22	0.95	0.15	0.93	0.22	0.60	0.10	0.54	0.09	57.28	1.77	91.40	97.56
Float and Sink Ashes	Agacli -4+0.5mm +1.30 Floating Ash	Ash	32.80	7.99	2.48	9.72	1.81	10.52	2.46	6.80	1.00	6.33	1.09	N.A.	N.A.	N.A.	N.A.
	Agacli -4+0.5mm -1.30 Sinking Ash	Ash	32.20	6.64	1.81	7.13	1.21	6.94	1.58	4.80	0.72	4.41	0.64	N.A.	N.A.	N.A.	N.A.
Unsorted Coal	Agacli Unsorted Coal	Coal	2.80	0.67	0.28	0.90	0.21	0.86	0.21	0.63	0.14	0.58	0.14	59.36	1.19	93.20	98.91
Unsorted Coal Ashes	Agacli Unsorted Coal Ashes	Ash	45.30	10.02	2.72	11.12	1.85	10.92	2.39	6.60	0.87	5.84	0.89	N.A.	N.A.	N.A.	N.A.
Flotation	Agacli -0.5mm Floating	Coal	4.10	0.87	0.23	0.93	0.16	1.05	0.22	0.62	0.09	0.58	0.08	60.27	1.18	92.70	99.92
	Agacli -0.5mm Sinking	Coal	3.80	0.85	0.21	0.94	0.15	1.04	0.21	0.62	0.09	0.51	0.07	59.59	1.49	92.40	99.06
Flotation Ashes	Agacli -0.5mm Floating Ash	Ash	38.60	8.47	2.33	9.41	1.55	9.66	2.07	6.53	0.92	5.54	0.83	N.A.	N.A.	N.A.	N.A.
	Agacli -0.5mm Sinking Ash	Ash	37.40	8.26	2.31	9.26	1.54	9.36	2.06	6.23	0.92	5.48	0.82	N.A.	N.A.	N.A.	N.A.
World Average*		Coal	10.00	2.00	0.50							1.00					
Lowest		Coal	3.00	0.50	0.10	0.40	0.10	0.50	0.10	0.50	0.50	0.30	0.03				
Highest		Coal	30.00	6.00	2.00	4.00	1.00	4.00	2.00	3.00	3.00	3.00	1.00				
Turkey Average		Coal															
Lowest		Coal															
Highest		Coal															

*Swaine (1990)

		Method Analyte Unit MDL	1DX Mo ppm 0,1	1DX Cu ppm 0,1	1DX Pb ppm 0,1	1DX As ppm 0,5	1DX Cd ppm 0,1	1DX Sb ppm 0,1	1DX Bi ppm 0,1	1DX Ag ppm 0,1	1DX Au ppb 0,5	1DX Hg ppm 0,01	1DX Tl ppm 0,1	1DX Se ppm 0,5	1DX Ni ppm 0,1
Float and Sink Coal	Agacli -4+0.5mm +1.30 Floating	Coal	0.50	7.10	3.00	28.90	<0.10	0.10	<0.10	<0.10	<0.50	0.04	2.40	1.20	12.80
	Agacli -4+0.5mm -1.30 Sinking	Coal	0.70	10.20	6.80	32.50	<0.10	0.20	0.10	<0.10	<0.50	0.05	2.70	1.50	13.40
Float and Sink Ashes	Agacli -4+0.5mm +1.30 Floating Ash	Ash	10.70	82.70	0.60	307.20	<0.10	2.10	<0.10	0.10	8.10	<0.01	<0.10	2.70	119.80
	Agacli -4+0.5mm -1.30 Sinking Ash	Ash	7.40	105.30	5.90	235.60	0.50	1.50	<0.10	0.10	<0.50	<0.01	<0.10	4.90	94.30
Unsorted Coal	Agacli Unsorted Coal	Coal	0.50	10.70	5.30	30.90	<0.10	0.20	0.10	<0.10	0.60	0.05	<0.10	1.00	14.00
Unsorted Coal Ashes	Agacli Unsorted Coal Ashes	Ash	7.60	75.10	27.40	311.70	0.10	1.30	0.30	0.20	2.50	<0.01	<0.10	0.90	130.40
Flotation	Agacli -0.5mm Floating	Coal	0.60	15.20	6.60	30.30	<0.10	0.20	0.10	<0.10	<0.50	0.05	<0.10	1.10	16.20
	Agacli -0.5mm Sinking	Coal	0.50	14.00	7.40	29.00	<0.10	0.20	0.10	<0.10	<0.50	0.06	0.10	0.90	15.20
Flotation Ashes	Agacli -0.5mm Floating Ash	Ash	10.00	162.00	22.60	312.80	<0.10	2.40	<0.10	0.30	3.20	<0.01	0.50	3.50	136.70
	Agacli -0.5mm Sinking Ash	Ash	9.90	135.10	21.80	310.60	0.40	2.60	<0.10	0.30	1.10	<0.01	0.40	3.90	136.60
World Average*		Coal	3.00	15.00	20.00	10.00	0.50	1.50						1.00	20.00
Lowest		Coal	0.10	0.50	2.00	0.50	0.10	0.10	2.00			0.02	0,20	0.20	0.50
Highest		Coal	10.00	50.00	80.00	80.00	3.00	10.00	20.00			1.00	1.00	10.00	50.00
Turkey Average		Coal			12.00	53.00	1.00					0.10		2.00	126.00
Lowest		Coal			0.10	2.00	0.01					0.03		0.10	3.00
Highest		Coal			286.00	686.00	45.00					0.70		26.00	1700.00

*Swaine (1990)

Physicochem. Probl. Miner. Process. 48(2), 2012, 355−367

www.minproc.pwr.wroc.pl/journal/

Physicochemical Problems of Mineral Processing

ISSN 1643-1049 (print)
ISSN 2084-4735 (online)

Received November 12, 2011; reviewed; accepted January 27, 2012

INVESTIGATION OF COPPER CEMENTATION KINETICS BY ROTATING ALUMINUM DISC FROM THE LEACH SOLUTIONS CONTAINING COPPER IONS

Ahmet EKMEKYAPAR*, Mehmet TANAYDIN, Nizamettin DEMIRKIRAN***

* Chemical Engineering Department, Faculty of Engineering, Inonu University, 44280, Malatya, Turkey, nizamettin.demirkiran@inonu.edu.tr

** Chemical Engineering Department, Faculty of Engineering, Tunceli University, 62000, Tunceli, Turkey

Abstract. Recovery of metallic copper from the leach solution containing copper (II) ions by cementation process using aluminum disc has been examined. Solutions obtained from the leaching of malachite in aqueous acetic acid solutions were used in the study. It was determined that the cementation rate increased with increasing solution concentration, temperature and rotating speed, and decreasing solution pH. The reaction rate fits to the first order pseudo homogeneous reaction model and is controlled by diffusion. The activation energy of this process was calculated to be 32.6 kJ/mol.

keywords: copper cementation, leaching, malachite, activation energy

1. Introduction

Most of metals are found in nature as complex mixtures of their sulfides, oxides, carbonates, silicates etc. Metals are generally produced after being extracted from an ore or its concentrates. The extraction of metals from the metal sources is carried out either by pyrometallurgy or hydrometallurgy (Venkatachalam, 1998; Gupta and Murkherjee, 1990). Hydrometallurgical methods in processing ores, concentrates, and secondary metal sources (various industrial wastes) have gained recently increasing importance in the extraction of nonferrous metals from ores.

Hydrometallurgy is essentially concerned with methods whereby metals, metal salts, or other metal compounds are produced by means of chemical reactions involving aqueous and organic solutions (Gupta and Murkherjee, 1990). It covers a large variety of processes ranging from the leaching of metal values in an aqueous solvent through the purification of the solutions to the recovery of the metals or their compounds by chemical or electrochemical precipitation (Venkatachalam, 1998; Rosenqvist, 2004).

Leaching is the first step of any hydrometallurgical process. Leaching is the term applied to the process of recovering a metal from the metal source by a solvent or lixiviant. The metallic value in a metal source passes into the solution by dissolving in

http://dx.doi.org/10.5277/ppmp120203

the leaching step. During this step, in addition to the desired metal, other metals present in the ore matrix may also pass into the solution. Therefore, before the final recovery of the desired metal, purification processes are applied to remove the impurities from the leach liquor. There are many ways to achieve this goal (Venkatachalam, 1998; Gupta and Murkherjee, 1990; Han, 2002). Metal value can be directly obtained from the leach liquor without purification in some cases.

The final part of a hydrometallurgical flow sheet concerns the recovery process. The acquired product is either the elemental metal or its suitable compound. The various techniques available for the recovery of a metal from the leach liquors with or without purification are crystallization, ionic precipitation, reduction with a gas, electrochemical reduction (cementation), and electrolytic reduction (Gupta and Murkherjee, 1990).

Among the metal gaining processes, cementation, which is basically an electrochemical reduction process, is one of the most effective and economic methods applied successfully for obtaining of valuable metals from industrial solutions. The advantages of this technique are its relative simplicity, ease of control, and low energy consumption (Venkatachalam, 1998; Gupta and Murkherjee, 1990; Naubactep, 2010; Kuntyi et al., 2011). That process involves the chemical reduction of metal ions by galvanic interaction between noble metal ions and a more active metal in an aqueous solution medium. (Venkatachalam, 1998; Gupta and Murkherjee, 1990**)**. For any cementation reaction the overall reaction equation can be written as follows

$$N^{n+} + M^{0} \longrightarrow N^{0} + M^{m+} \quad (1)$$

where, N is the noble or precipitating metal, M is the reductant metal.

Copper is among the most intensively applied and valuable metals used by industry. It is used mostly in the electrical and electronics industries because of its high electrical conductivity. In addition, copper and its alloys are utilized in the engine, communication, and aviation industries, for electricity production and distribution, in measuring devices, in chemical industry etc. (Dib and Makhloufi, 2004; Arzutug et al., 2004).

Copper generally is found in nature in the form of sulfide and oxide minerals, such as azurite, malachite, tenorite, chrysocolla, bornite, brochantite, enargite, chalcopyrite, chalcocite, covellite (Akçıl, 2002; Arzutug et al., 2004; Bingöl et al., 2005). Metallic copper is produced from these ores by pyrometallurgical and hydrometallurgical methods. In production of copper from low-grade oxidized copper ores, hydrometallurgical methods are commonly preferred because pyrometallurgy is not feasible for these type ores.

Among the oxidized copper ores, malachite is the most popular. The leaching and kinetics of malachite has been investigated by various researchers (Oudenne and Olson, 1983; Künkül et al., 1994; Yartaşı and Çopur, 1996; Ekmekyapar et al., 2003; Bingöl and Canbazoğlu, 2004; Arzutuğ, 2004; Bingöl et al. 2005; Lui et al., 2010). Malachite ore can be used to produce metallic copper and copper compounds by

hydrometallurgical techniques. After leaching of malachite with a convenient lixiviant, copper in the purified leach solution can be precipitated by cementation, deposited by direct electrowinning or solvent extraction-electrowinning methods. In cementation and direct electrowinning methods copper is obtained in metallic state, while in solvent extraction-electrowinning method, copper is first selectively recovered from the solution by chelating Cu^{2+} and dissolving in an organic solvent, and then the solvent is stripped off from the chelat by a strong acid to give a solution to be amenable to electrowinning process (Ekmekyapar et al., 2003; Elamari et al., 2006).

In the recovery of copper from the leach solution by cementation process, when aluminum is used as reductant metal, copper ions are easily reduced to its metallic state due to the difference between the electrode potentials of these two metals. The standard reduction potentials of copper and aluminum are 0.34 and -1.67 V, respectively. During the cementation process, the half-cell reactions occurring are:

$$Cu^{2+} + 2e^- \leftrightarrows Cu^o \quad \text{(reduction reaction)} \qquad E^o = 0.34 \text{ V} \tag{2}$$

$$Al^o \leftrightarrows Al^{3+} + 3e^- \quad \text{(oxidation reaction)} \qquad E^o = -1.67 \text{ V} \tag{3}$$

Thus, the whole cementation reaction of copper ions onto aluminum disc may be expressed by the following reaction equation:

$$3Cu^{2+} + 2Al^o \longrightarrow 3Cu^o + 2Al^{3+} \qquad \Delta E^o = 2.01 \text{ V} \tag{4}$$

As can be seen from Equation (4), the potential of this cementation reaction is positive, and the standard free energy, ΔG^o, is negative ($\Delta G^o = -nF\Delta E^o$). The negative value of the standard free energy indicates that this process is favorable thermodynamically, and thus a spontaneous heterogeneous reaction takes place in the galvanic cell.

Recovery of copper from various solutions containing copper (II) ions by cementation reaction has been studied by many researchers. In these studies related to copper cementation iron has been generally used as sacrificial metal because of its cheapness. However, zinc and aluminum have been also used as precipitant or reductant metals (MacKinnon and Ingraham, 1970; MacKinnon and Ingraham, 1971; MacKinnon et al., 1971; Annamalai et al., 1978; Annamalai and Murr, 1978; Chen and Lee, 1994; Wei et al., 1994; Masse and Piron, 1994; Djokic, 1996; Stefanowicz et al., 1997; Dönmez et al., 1999; Kanungo et al., 2001; Stankoviç et al., 2004; Dib and Makhloufi, 2004; Kanungo et al., 2003; Karavasteva, 2005; Fouad and Abdel Basir, 2005; Hung et al., 2005; Demirkıran et al., 2007; Amin and El-Ashtoukhy, 2011).

In most of works in the literature copper cementation with a reductant metal has been mostly carried out using synthetic pure solutions containing copper ions. In the present study, metallic copper was recovered by using the actual solution which is derived from after the leaching of malachite ore in acetic acid solution. For the recovery of copper a rotating aluminum disc was used as the reductant metal. In the experiments the influence of copper ion concentration, reaction temperature, solution pH, and disc rotation speed on copper cementation were investigated. The kinetics of

the cementation reaction was evaluated by measuring the rate of decrease of copper concentration in the solution.

2. Materials and Methods

Before recovery of metallic copper from the leach solution by cementation reaction, malachite ore was leached in aqueous acetic acid solution. The aim of the leaching experiment is to produce the liquor required for cementation tests.

Malachite ore sample, an oxidized copper ore, used in the leaching process was supplied from Palu region Elazığ, Turkey. The ore sample was crushed, ground, and then sieved using ASTM sieves to obtain the desired particle size fractions. The fraction of 164 µm was utilized for the leaching tests in our experiment. The mineralogical analysis of the malachite ore sample was performed by means of a Rigaku RadB-DMAX II X-ray diffractometer. The results of X-ray analysis are given in Fig. 1. The chemical composition of the sample is shown in Table 1.

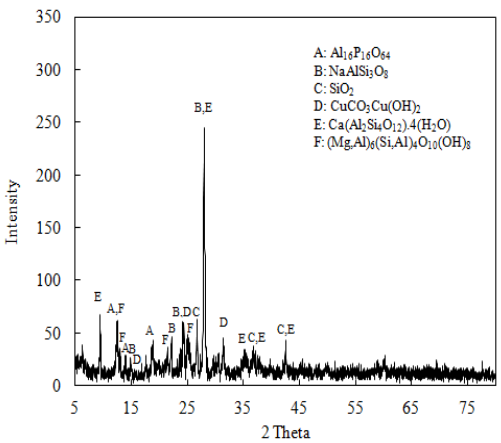

Fig. 1. X-ray diffractogram of malachite ore used in the study

Table 1. Chemical analysis of malachite ore used in the study

Component	SiO_2	Al_2O_3	MgO	Fe_2O_3	CuO	CaO	Na_2O	TiO_2	Ignition loss	Other oxides
Value, %	46.40	17.00	7.30	6.87	5.20	3.30	2.30	1.30	8.00	2.33

The leaching experiment was carried out in a glass reactor of 1 dm^3 volume equipped with a mechanical stirrer having a digital controller, a thermostat and a back-cooler. The optimum conditions of leaching determined by preliminary tests were temperature 40ºC, solution concentration 1 mol/ dm^3, stirring speed of 400 rpm, solution volume 500 cm^3, particle size of 164 µm, ore amount 2 g, leaching time 120 min.

After pouring 500 cm^3 of acetic acid solution (1 mol/dm^3) into the reactor and bringing it to the desired reaction temperature (40ºC), a given amount of malachite ore

(2 g) was added to the solution, and the stirring speed was set to 400 rpm. The leaching process was carried out for 120 min of reaction time. At the end of this operation the content of the reactor was immediately filtered. The amount of copper (II) ion in the filtrate was determined by complexometric titration using EDTA as a titrant and murexide as an indicator. The amount of extracted copper from the ore after 120 min of leaching time was calculated as 1.58 g/dm^3. The solution attained in the leaching step was considered as the mother liquid and it was diluted by adding distilled water to reach the desired concentration of copper(II) ion for utilization in the cementation stage. Process variables chosen for cementation process are given in Table 2. Cementation studies were performed in a 1 dm^3 glass reactor equipped with a mechanical stirrer, a reaction temperature control unit, and a cooler to avoid loss of solution by evaporation. The leach solution containing copper(II) ion of 500 cm^3 volume was added into the reaction vessel. The pH of the solution was adjusted to the desired value by diluted sulfuric acid solution. When the reactor content reached the desired reaction temperature, aluminum disc (height of 0.005 m, diameter of 0.05 m, working surface area $1.73 \cdot 10^{-2}$ m^2) was immersed in the solution. The disc was screwed onto the end of a thin stainless steel rod which was attached to the mechanical stirrer. The disc was rotated at controlled speeds in the solution. The progress of the cementation reaction was followed by measuring the concentration of copper ions in the solution. Aliquots of 5 cm^3 each were withdrawn at regular intervals during the reaction and immediately filtered using filter paper. The filtered samples were analyzed for copper ion content by titrating with EDTA in the presence of murexide indicator. The amount of deposited copper was calculated according to difference between the initial and final copper concentrations of the solution. The fraction of cemented copper was calculated as follows:

x = initial copper concentration/copper concentration at time t.

Table 2. Parameters and their ranges used in the experiments

Parameter	Value
Concentration, mol/dm^3	0.0025, 0.005, 0.010, 0.020
Temperature, ºC	20, 30, 40, 50, 60
Rotating speed, rpm	200, 300, 400, 500
pH	1.0, 1.5, 2.0, 2.5, 3.26

3. Results and Discussion

In order to observe the effect of rotation speed of Al disc on the cementation rate of copper the experiments were carried out at different rotation speeds in the range of 200 to 500 rpm. The results obtained from these tests showed that the cemented copper fraction increased with increasing the disc rotation speed. This result indicates that the copper cementation rate is probably the diffusion controlled under these

experimental conditions. During cementation reaction, a solid layer of metallic copper is formed onto the surface of aluminum disc. This solid layer prevents the contact of copper ions with aluminum disc surface. If the rotation speed of the disc is strong enough, the deposit formed onto the disc can peel off from aluminum surface. This fact can facilitate the diffusion of ions towards the metal disc surface, and thus the cemented fraction of copper increases as the rotation speed of the disc increases. Furthermore, the diffusion layer thickness decreases as the rotation speed of the disc increases, which facilitates the diffusion of copper ions towards disc surface.

The effect of the initial pH of the leach solution on the copper cementation was investigated using different initial pH values in the range of 1.00-3.26. The experimental findings exhibited that the solution pH had a considerable effect on the copper cementation rate. During the experiments, it was observed that the fraction of cemented copper increased with decreasing the initial pH of leach solution. The recovery of metallic copper from the leach solution involves two main processes: adsorption of copper ions on the surface of metallic aluminum disc and the cementation of copper ions on the disc. The presence of a passive oxide layer on aluminum surface inhibits the cementation reaction rate generating a resistance to diffusion of copper ions towards the metal disc surface. This oxide film formed on the disc surface can be destroyed by the acidity of solution. Hence, the oxide film dissolves more readily at low pH values, and it may cause an increase in the cementation rate with increasing acidity (decreasing pH) of the leach solution (MacKinnon et al., 1971).

The effect of initial copper(II) ion concentration on the cementation rate was studied at the concentrations of 0.0025, 0.0050, 0.0100, and 0.0200 mol/dm^3. According to the results of the experiments the cementation rate increased with increasing copper concentration in the leach solution. During the cementation reaction the deposited copper accumulates onto the surface of the aluminum disc and a product layer (metallic copper) appears on the disc surface. This surface deposit shows a resistance to the diffusion of copper ions. Depending on the nature of the surface deposit its presence can enhance or diminish the cementation rate. If the metallic layer formed on the reductant metal is a coherent deposit the cementation rate decreases with increasing deposit mass. This case was observes at low initial copper ion concentration conditions. If the surface deposit formed on the reductant metal is a porous metallic layer the cementation rate may increase when the deposit layer thickness increases. When the initial copper ion concentration is high a coarse and porous precipitate on the metal disc surface appears. Under such conditions the diffusion of copper ions from the bulk of the solution to the disc surface occurs through the porous layer easily and the cementation rate can increase with the increase of the layer thickness. Besides, the coarse or dense precipitate formed onto the disc can be peeled off the disc surface by rotating the aluminum disc (Miller, 1973; Puvvada and Tran, 1995; Amin et al., 2007).

In order to investigate the effect of the reaction temperature on the copper cementation from the actual leach solutions some experiments were performed in the temperature range of 20 - 60ºC. The results showed that the deposited copper fraction increased with increasing the reaction temperature. At low temperatures the deposit on the disc surface was coherent. It was observed that the deposit formed on aluminum disc was thick and relatively coarse as the reaction temperature increased. This type of deposit is generally porous and it does not hinder the diffusion of copper ions to the disc surface. Furthermore, high temperatures help to strip the oxide layer off the disc surface, and therefore the cementation reaction proceeds at a faster rate (Kanungo et al., 2003; Lamya and Lorenze, 2005; Farahmand et al., 2009).

It has been reported that cementation reactions follow the first order kinetic with respect to the noble metal, and the rate limiting step is to be the transfer of mass to the reaction surface (Puvvada and Tran, 1995; Nosier and Sallam, 2000; El Batouti, 2003; Younesi et al., 2006; Demirkıran et al., 2007). In the present study, the kinetic analysis was performed according to the first order kinetics. The equation describing the kinetics of the first order reaction is:

$$-\ln(1-x) = k\,t \tag{5}$$

where x is the cemented copper fraction at time t. The influence of several parameters, such as solution concentration, reaction temperature, and stirring rate on the cementation rate should be considered because the cementation is a heterogeneous reactions. Hence, the effects of these parameters on the reaction rate were analyzed on the basis of the first order kinetic model.

The data on cemented copper fraction obtained from the experiments were used to perform $-\ln(1-x)$ versus time graphs. The constructed graphs can be seen in Figs. 2-5. As can be seen from the plots given in Figs. 2-5, the straight lines passing through the origin were obtained. The apparent rate constant values determined from the slopes of the lines in Figs. 2-5 and their correlation coefficients for each parameter are given in Table 3. The results in Figs. 2-5 and in Table 3 indicate that the kinetics of this process follows the first order kinetic model.

To deduce whether a cementation reaction is mass transfer limited (diffusion controlled), the relationship between the reaction rate and the disc rotation speed is usually determined. For this aim the Levich equation is usually used (Makhloufi et al., 1998; Makhloufi et al., 2000; Dib and Makhloufi, 2007):

$$k = 0.62\, D^{2/3}\, v^{-1/6}\, \omega^{1/2} \tag{6}$$

where k is the reaction rate constant or the mass transfer coefficient (cm/s), D is the diffusion coefficient of reactant species (cm^2/s), v is the kinematic viscosity of solution (cm^2/s), and ω is the angular velocity of disc (rad/s).

If the mass transfer is the rate determining step, then the plot of k versus $\omega^{1/2}$ in Eq. (6) must be a straight line. Using the apparent rate constants obtained for various rotation speeds (Table 3) a graph of k versus $\omega^{1/2}$ was drawn in Fig. 6. As shown in

Fig. 6, a linear relationship between the apparent rate constants and the square root of the disc rotational speeds was obtained. The linear dependence of the cementation rate on the square root of the rotation speed supports the conclusion that the cementation is mass transfer limited or diffusion controlled. It is clear that the rate of copper cementation increase with increasing disc rotation speed. This may be attributed to the decrease in the diffusion layer thickness as the rotational speed of the disc increases, thus giving a higher rate of transfer of copper ions from the bulk of the solution to the aluminum surface.

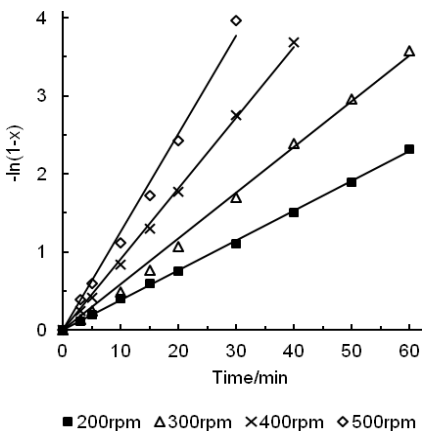

Fig. 2. Plot of –ln(1-*x*) versus *t* for different rotation speed

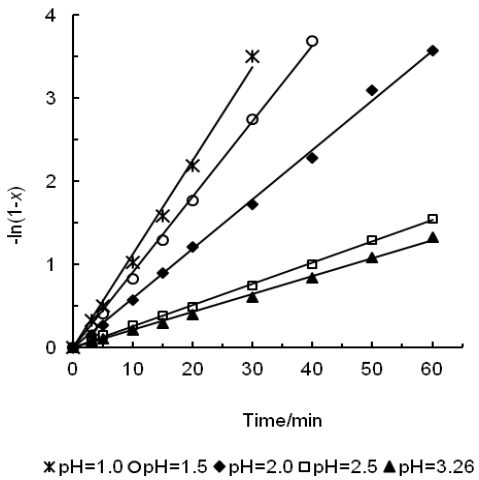

Fig. 3. Plot of –ln(1-*x*) versus *t* for different pH

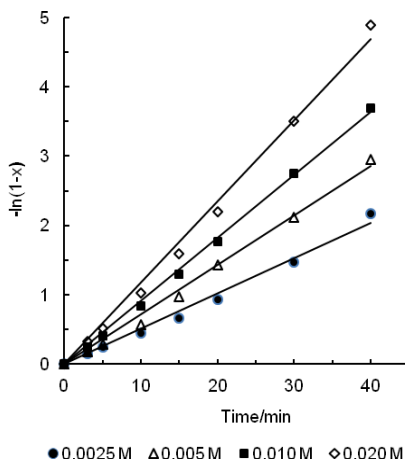

Fig. 4. Plot of –ln(1-*x*) versus *t* for different concentrations

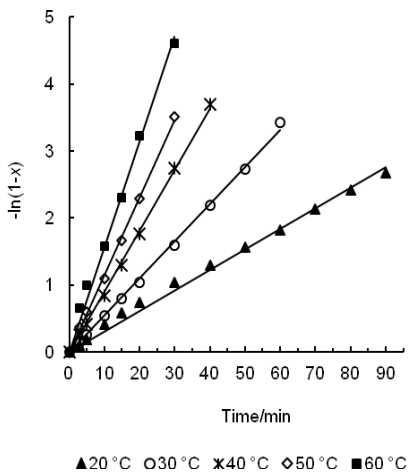

Fig. 5. Plot of –ln(1-*x*) versus *t* for different temperatures

Table 3. The apparent rate constants and their correlation coefficients

Parameter	First-order kinetic model	
	$k*10^3$, s^{-1}	R^2
Concentration, mol/dm^3		
0.0025	0.846	0.988
0.0050	1.188	0.993
0.0100	1.513	0.998
0.0200	1.956	0.994
Temperature, ºC		
20	0.513	0.993
30	0.920	0.998
40	1.513	0.998
50	1.938	0.998
60	2.612	0.994
Rotation speed, rpm		
200	0.635	0.999
300	0.975	0.997
400	1.513	0.998
500	2.097	0.992
pH		
1.0	1.883	0.995
1.5	1.513	0.998
2.0	0.993	0.998
2.5	0.427	0.998
3.26	0.358	0.997

To represent the influence of the cementation parameters on the rate constant of reaction, a mathematical model was proposed:

$$k=k_o\,(C)^a\,(RS)^b\,(pH)^c\,\exp(-E_a/RT) \tag{7}$$

where k_o is the frequency or pre-exponential factor (1/s), C is the initial copper concentration, RS is the rotational speed of aluminum disc (rpm), pH is the initial pH of solution, E_a is the activation energy of reaction (J/mol), R is the universal gas constant (J/molK), T is the reaction temperature (K), and a, b and c are the reaction orders according to concentration, rotational speed, and pH, respectively. Combining Eqs. (5) and (7), the following equation is obtained:

$$-\ln(1-x)= k_o\,(C)^a\,(RS)^b\,(pH)^c\,\exp(-E_a/RT)\,t \tag{8}$$

To calculate the values of constants a, b and c, the apparent rate constants given in Table 3 were used. Using the rate constant values for concentration a plot of ln k versus ln C was drawn in Fig. 7. The slope of straight line in Figure 7 is the reaction order with respect to solution concentration. The reaction order in respect to concentration is 0.40 with a correlation coefficient of 0.994. The orders of reaction with respect to rotation speed and pH were also calculated by means of data in Table 3. According to the obtained results the reaction order is 1.31 for rotation speed and -1.54 for pH. The correlation coefficients of these parameters are 0.99 and 0.91, respectively.

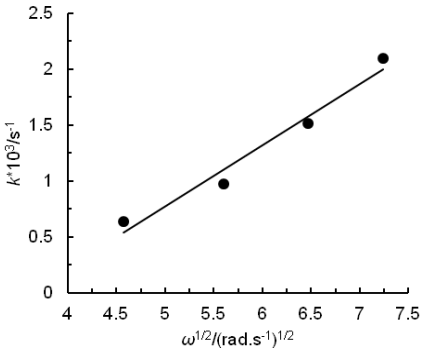

Fig. 6. Variations of apparent rate constant obtained for various rotation speeds with the square root of the disc rotation speed

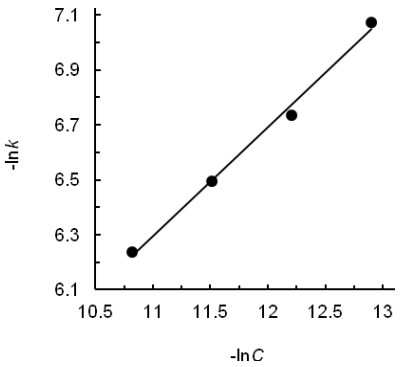

Fig. 7. Plot of ln *k* versus ln *C*

The activation energy of the cementation process was determined from the Arrhenius equation. The Arrhenius plot of the process is shown in Fig. 8. From the slope of the straight line in Fig. 8 the activation energy of reaction was calculated to be 32.6 kJ/mol. The intercept of the line was determined to be $2.7 \cdot 10^{-3}$. The value of the activation energy of process indicates that the copper cementation reaction by rotating aluminum disc is controlled by diffusion. The activation energy of diffusion controlled reactions is generally below 40 kJ/mol.

As a result, the mathematical model taking into account all parameters influencing the cementation reaction rate can be written as follows:

$$-\ln(1-x) = 2.7\text{x}10^{-3}\ (C)^{0.40}\ (RS)^{1.31}\ (\text{pH})^{-1.54}\ \exp(3924/T)\ t. \quad (9)$$

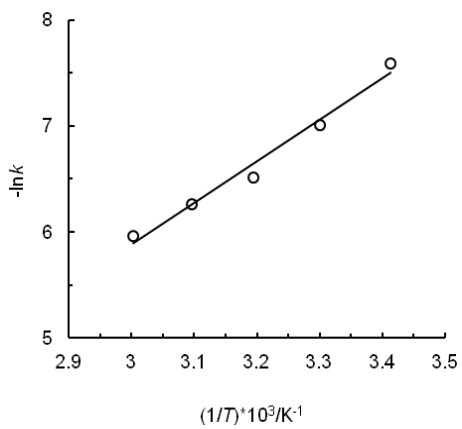

Fig. 8. Arrhenius plot for copper cementation reaction

4. Conclusions

In most of the papers published in the literature impurity-free copper solutions have been used for copper cementation. In the present paper, copper recovery has been

carried out using the solutions containing some impurities after the leaching of malachite ore in aqueous acetic acid solution. The effect of the experimental parameters on the copper cementation reaction have been examined. It was observed that the rate of copper cementation increased with increasing concentration, temperature and rotation speed, and decreasing with pH. The results of the experiments conform to previously published reports in the literature. In this paper, unlike many other studies, in order to represent the cementation kinetics a mathematical model was proposed. It was found that the cementation rate was diffusion controlled. The activation energy of the cementation process was calculated to be 32.6 kJ/mol.

Cementation process seems to be appropriate for the recovery of copper from the leach solutions containing various impurities without any additional purification process. But the copper obtained in this process has rather low purity, especially due to its tendency to form oxide during drying at the air. The copper deposit obtained in this study was brown and contained 88 percent copper. However, the impure cemented copper can be purified to increase the copper content and marketed as a powder. As a result, it can be said that cementation process is a reproducible and low cost approach that does not require expensive and complicated equipments.

References

AKÇIL, A., 2002. *A preliminary research on acid pressure leaching of pyritic copper ore in Kure Copper Mine, Turkey*, Minerals Engineering 15, 1193-1197.

AMIN, N.K., EL-ASHTOUKHY, E.S. Z., ABDELWAHAB, O., 2007. *Rate of cadmium ions removal from dilute solutions by cementation on zinc using a rotating fixed bed reactor*, Hydrometallurgy 89, 224-232.

AMIN, N.K., EL-ASHTOUKHY, E.S.Z., 2011. *Kinetic study of copper cementation onto zinc using a rotating packed bed cylindrical reactor*, Canadian Journal of Chemical Engineering 89, 609-616.

ANNAMALAI, V., HISKEY, J.B., MURR, L.E., 1978. *The effects of kinetic variables on the structure of copper deposits cemented on pure aluminum discs: A scanning electron microscopic study*, Hydrometallurgy 3, 163-180.

ANNAMALAI, V., MURR, L.E., 1978. *Effects of the source of chloride ion and surface corrosion patterns on the kinetics of copper-aluminum cementation system*, Hydrometallurgy 3, 249-263.

ARZUTUĞ, M.E., KOCAKERIM M.M., ÇOPUR M., 2004, Leaching of malachite ore in NH_3-saturated water, Industrial and Engineering Chemistry Research, 43, 4118-4123.

BINGÖL D., CANBAZOĞLU, M., 2004. *Dissolution kinetics of malachite in sulphuric acid*, Hydrometallurgy 72, 159-165.

BINGÖL, D., CANBAZOĞLU, M., AYDOĞAN, S., 2005. *Dissolution kinetics of malachite in ammonia/ammonium carbonate leaching*, Hydrometallurgy 76, 55-62.

CHEN, H.J., LEE, C., 1994. *Effects of the type of chelating agent and deposit morphology on the kinetics of the copper-aluminum cementation system*, Langmuir 10, 3880-3886.

DEMIRKIRAN, N., EKMEKYAPAR, A., KÜNKÜL, A., BAYSAR, A., 2007. *A kinetic study of copper cementation with zinc in aqueous solutions*, International Journal of Mineral Processing 82, 80-85.

DIB, A., MAKHLOUFI, L., 2004. *Cementation treatment of copper in wastewater: mass transfer in a fixed bed of iron spheres*, Chemical Engineering and Processing 43, 1265-1273.

DJOKIC, S.S., 1996. *Cementation of copper on aluminum in alkaline solutions*, Journal of Electrochemical Society 143, 1300-1305.

DÖNMEZ, B., SEVIM, F., SARAÇ, H., 1999. *A kinetic study of the cementation of copper from sulphate solutions onto a rotating aluminum disc*, Hydrometallurgy 53, 145-154.

EKMEKYAPAR, A., OYA, R., KÜNKÜL, A., 2003. *Dissolution kinetics of oxidized copper ore in ammonium chloride solution*, Chemical and Biochemical Engineering Quarterly 17, 261-266.

ELAMARI, K., JDID, E.A., BLAZY, P., 2006. *Copper solvent extraction from chalcopyrite concentrate acid leach solutions by LIX984*, Journal of Mining and Metallurgy Section B: Metallurgy 42B, 1-11.

EL BATOUTI, M., 2003. *Cementation reactions in the presence of nitrogen compounds*, Journal of Colloid and Interface Science 263, 548-553.

FARAHMAND, F., MORADKHANI, D., SAFARZADEH, M.S., RASHCHI, F., 2009. *Optimization and kinetics of the cementation of lead with aluminum powder*, Hydrometallurgy 98, 81-85.

FOUAD, O.A., ABDEL BASIR, S.M., 2005. *Cementation-induced recovery of self-assembled ultrafine copper powders from spent etching solutions of printed circuit board*, Powder Technology 159, 127-134.

GUPTA, C.K., MURKHERJEE, T.K., 1990. *Hydrometallurgy in extraction processes*. USA: CRC Press.

HAN, K.N., 2002. *Fundamentals of aqueous metallurgy*. USA: SME Inc.

HUNG, Y.P., MOHAMED, N., DARUS, H, 2005. *Recovery of copper from strong chloride-based solution*, Journal of Applied Science 5, 1328-1333.

KANUNGO, M., CHAKRAVARTY, V., MISHRA, K.G., DAS, S.C., 2001. *Influence of perchloric acid on the kinetics of immersion plating of copper onto aluminum*, Hydrometallurgy 61, 1-11.

KANUNGO, M., MISHRA, K.G., DAS, S.C., 2003. *Study on morphology of copper deposited onto aluminum by immersion plating from an oxalate bath containing perchloric acid*, Minerals Engineering 16, 1383-1386.

KARAVASTEVA, M., 2005. *Kinetics and deposit morphology of copper cementation onto zinc, iron and aluminum*, Hydrometallurgy 76, 149-152.

KUNTYI, O., ZOZULYA, G., SALDAN, I., KREE, V., KORNIY, S., STEL'MAKHOVYCH, B., 2011. *Nature of the silver precipitation obtained by cementation from thiosulphate solutions*, Central European Journal of Chemistry 9, 180-184.

KÜNKÜL, A., KOCAKERIM, M.M., YAPICI, S., DEMIRBAĞ, A., 1994. *Leaching kinetics of malachite in ammonia solutions*, International Journal of Mineral Processing 41, 167-182.

LAMYA, R.M., LORENZEN, L., 2005. *A study of factors influencing the kinetics of copper cementation during atmospheric leaching of converter matte*, Journal of the South African Institute of Mining and Metallurgy 105, 21-27.

LUI, W., TANG, M., TANG, C., HE, J., YONG, S., YANG, J., 2010. *Dissolution kinetics of low grade complex copper ore in ammonia-ammonium chloride solutions*, Transaction of Nonferrous Metal Society China 20, 910-917.

MACKINNON, D.J., INGRAHAM, T.R., 1970. *Kinetics of Cu(II) cementation on pure aluminum disc in acidic sulphate solutions*, Canadian Metallurgical Quarterly 9, 443-448.

MACKINNON, D.J., INGRAHAM, T.R., KERBY, R., 1971. *Copper cementation on nickel disc*, Canadian Metallurgical Quarterly 10, 165-169.

MACKINNON, D.J., INGRAHAM, T.R., 1971. *Copper cementation on aluminum canning sheet*, Canadian Metallurgical Quarterly 10, 197-201.

MAKHLOUFI, L., SAIDANI, B., CACHET, C., WIART, R., 1998. *Cementation of Ni^{2+} ions from acidic sulfate solutions onto a rotating zinc disc*, Electrochimica Acta 43, 3159-3164.

MAKHLOUFI, L., SAIDANI, B., HAMMACHE, H., 2000. *Removal of lead ions from acidic aqueous solutions by cementation on iron*, Water Resources 34, 2517-2524.

MASSE, N., PIRON, D.L., 1994. *Effects of temperature and powder morphologies on the cementation rate of copper in alkaline zinc solution*, Journal of Electrochemical Society 141, 664-669.

MILLER, J. D., 1973. *An analysis of concentration and temperature effects in cementation reactions*, Mining and Scientific Engineering 5, 242-254.

NOSIER, S.A., SALLAM, S.A., 2000. *Removal of lead ions from wastewater by cementation on a gas-sparged zinc cylinder*, Separation and Purification Technology 18, 93-101.

NOUBACTEP, C., 2010. *Elemental metals for environmental remediation: Learning from cementation process*, Journal of Hazardous Materials 181, 1170-1174.

OUDENNE, P.D., OLSON, F.A., 1983. *Leaching kinetics of malachite in ammonium carbonate solutions*, Metallurgical Transactions B 14B, 33-40.

PUVVADA, G., TRAN, T., 1995. *The cementation of Ag(I) ions from sodium chloride solutions onto a rotating copper disc*, Hydrometallurgy 37, 193-206.

ROSENQVIST, T., 2004. *Principles of extractive metallurgy*, USA: Tapir Academic Press.

STANKOVIÇ, V., SERBULA, S., JANCEVA, B., 2004. *Cementation of copper onto brass particles in a packed bed*, Journal of Mining and Metallurgy Section B: Metallurgy 40B, 21-39.

STEFANOWICZ, T., OSINSKA, M., STEFANIA N.Z., 1997. *Copper recovery by the cementation method*, Hydrometallurgy 47, 69-90.

VENKATACHALAM, S., 1998. *Hydrometallurgy*, India: Narosa Publishing House.

WEI, W.Y., LEE, C., CHEN, H.J., 1994. *Modeling and analysis of the cementation process on a rotating disk*, 10, 1980-1986.

YARTAŞI, A., ÇOPUR, M., 1996. *Dissolution kinetics of copper (II) oxide in ammonium chloride solutions*, Minerals Engineering 9, 693-698.

YOUNESI, S.R., ALIMADADI, H., ALAMDARI, E.K., MARASHI, S.P.H., 2006. *Kinetic mechanism of cementation of cadmium ions by zinc powder from sulphate solutions*, Hydrometallurgy 84, 155-164.

Physicochem. Probl. Miner. Process. 48(2), 2012, 369−380

www.minproc.pwr.wroc.pl/journal/

Physicochemical Problems of Mineral Processing

ISSN 1643-1049 (print)
ISSN 2084-4735 (online)

Received October 5, 2011; reviewed; accepted February 27, 2012

EVALUATION OF TURKISH BENTONITE FOR REMOVAL OF DYES FROM TEXTILE WASTEWATERS

Ilhan GULGONUL

Balikesir University, Mining Department, Cagis Yerleskesi, Balikesir, 10145, Turkey gulgonul@balikesir.edu.tr

Abstract. Removal of reactive dyes from textile industry wastewaters is a great economic and environmental challenge. In this study, systematic adsorption tests were carried out using natural and modified bentonites to remove a textile dye, Procion Navy HEXL. The results indicated an optimum at 0.1% solids concentration and 4 h of mixing time. The modified bentonite (hexadecyltrimethylammonium bromide, HTAB) had a 12-fold increase in the adsorption capacity compared to the natural bentonite. The zeta potential experiments revealed that the negative surface charge of natural bentonite at all pH values became positive upon modification with HTAB. These results clearly indicated that the negatively charged dye can adsorb onto bentonite surface via electrostatic attraction. In addition, adsorption isotherm models (Langmuir, Freundlich and Dubinin–Radushkevich) were used to analyze the adsorption in the dye-bentonite system. It is concluded that bentonite after surface modification can be conveniently used in the abatement of reactive azo dyes in textile wastewaters.

keywords: textile wastewater, dye, Procion Navy HEXL, bentonite, adsorption

1. Introduction

Wastewaters from textile industry cause considerable environmental pollution in the world. Particularly, wastewaters containing soluble dyes must be cleaned before they are discharged to nature. Therefore, textiles dyeing processes as well as the chemical content of dyeing components are very important. The dyed wastewaters consist of generally acids, bases, dissolved solid toxic compounds, and considerable colored pollutants (Armagan et al., 2004). Moreover, many dyes are toxic, and obstruct catalytic effects and also cause severe damages to the human bodies (Baskaralingam et al., 2006; Ozcan et al., 2007). While reactive dyes are fairly soluble in water, their removal from wastewater by conventional coagulation and activated sludge process is rather difficult (Ozdemir et al., 2004).

Oxidation and adsorption are two basic techniques used in the treatment of textile industry wastewater. UV/o zone and UV/H_2O_2 oxidation methods are used to make wastewater colorless (Espantaleón et al., 2003; Baskaralingam et al., 2006; Ozcan et al., 2007; Eren and Afsin, 2008; Turabik, 2008). Adsorption is an important method commonly used for cleaning of wastewater for treatment and separation of colorants in

http://dx.doi.org/10.5277/ppmp120204

industrial processes (McKay, 1982). It is claimed that activated carbon and polymer resin are good but relatively expensive for the removal of chemicals from wastewater (McKay, 1982; Ozcan et al., 2007; Turabik, 2008).

Activated carbon is known to have a fairly low adsorption capacity for some reactive dyes (Juang et al., 1997). There are also a number of studies on decolorization of wastewater using cost-effective adsorbent systems, chitosan/reactive (Juang et al., 1997), montmorillonite and sepiolite/methylgreen (Rytwo et al., 2000), sepiolite/rhodamine (Arbeloa et al., 1997), and natural zeolite/basic dye (Armagan et al., 2004; Ozdemir et al., 2004; Benkli et al., 2005; Ozcan et al., 2007; Turabik, 2008). In recent years, since activated carbon adsorbent is expensive, low-cost natural clays such as sepiolite (Espantaleón et al., 2003; Ozdemir et al., 2004; Alkan et al., 2007), bentonite (Espantaleón et al., 2003; Baskaralingam et al., 2006; Ozcan et al., 2007; Eren and Afsin, 2008; Turabik, 2008), zeolite (Espantaleón et al., 2003; Baskaralingam et al., 2006; Ozcan et al., 2007; Eren and Afsin, 2008; Turabik, 2008), and montmorillonite (Wang et al., 2004) have been used directly or modified for cleaning of textile industry wastewater.

Meanwhile, the adsorption isotherm is one of the most important data to understand the mechanism of the adsorption systems. For this purpose, several isotherm models have been widely used for the systems (Espantaleón et al., 2003; Baskaralingam et al., 2006; Ozcan et al., 2007; Eren and Afsin, 2008; Turabik, 2008). For example, in our study, three important adsorption models, namely Freundlich (Freundlich, 1906), Langmuir (Langmuir, 1918), and Dubinin–Radushkevich (D-R) (Dubinin and Radushkevich, 1947) were used in the analysis of adsorption data.

The aim of this study is to examine the adsorption mechanism of reactive Procion Navy HEXL dye by natural and modified bentonites, and find out their applicability to textile waste waters. The effects of parameters such as solids concentration, mixing time, and dye concentration on the adsorption capacity of bentonite were systematically investigated. Additionally, the adsorption isotherms, Langmuir, Freundlich, and D-R, were used to find the best-fitted model for the adsorption results. The results will help provide a basis for removal of colorants through the use of bentonite.

2. Materials and methods

2.1. Materials

The bentonite sample, Na-bentonite, used for the experiments was obtained from Samaş Bentonite Company in Reşadiye-Tokat region of Turkey. The chemical analysis of Na-bentonite sample (<63 μm) was performed by inductively coupled plasma (ICP, Perkin Elmer Model 3800). The mineralogical composition of the sample was identified by XRD technique using air-dried and ethylene-glycol treated samples (Rigakudiffractometer with Cu(K_α) radiation). The chemical and mineralogical composition of Na-bentonite was given elsewhere (Bulut et al., 2009).

The bentonite sample has an average particle size (d_{50}) of 3 μm as determined by Fritsch Particle Sizer. The raw bentonite has a cation exchange capacity (CEC) of 76.45 meq/100 g whereas the purified bentonite was found to have a CEC of 99.2 meq/100 g.

A quaternary amine, hexadecyltrimethylammonium bromide (HTAB, C19H42BrN, 99% purity), purchased from SIGMA, was used for modifying the surface of bentonite. The chemical structure of HTAB and the procedure for the preparation of modified bentonite are given elsewhere (Sabah, 1998). Briefly, the modification process involves mixing of 3% solids with $3 \cdot 10^{-2}$ M HTAB followed by solid–liquid separation and drying. When the surface of bentonite was modified with HTAB, the clay surface was converted from polar to nonpolar properties. First, 3% bentonite was conditioned at 60ºC for 1 h in water and then treated with HTAB at 25ºC for 2 h. Distilled and deionized water with a conductivity value of $2 \cdot 10^{-6}$ mohms/cm was used in all experiments.

A commercial dye, Procion Navy HEXL with reactive azo group and aminochlorotriazine was used for the adsorption experiments. It contains an anionic sulfonate group. This dye is a commercial sample, and its structure is not given in the Color Index.

2.2. Methods

2.2.1. Zeta potential experiments

The zeta potential measurements of the bentonite samples were carried out with the Zeta Meter 3.0 equipped with a microprocessor unit, which automatically calculates the electrophoretic mobility of particles, and then converts it to zeta potential. First, a bentonite sample of 0.1 g was conditioned in 100 cm^3 of distilled water for 10 min. Then, the suspension was kept for 5 min to allow the large particles to settle down. Finally, the zeta potential measurements were carried out with the natural and modified bentonite samples. Each data point was taken as an average of approximately 10 measurements. All measurements were made at room temperature (22.5±1ºC).

2.2.2. Adsorption experiments

The adsorption tests were carried out using the natural and modified bentonite samples in 20 cm^3 glass vials at 0.1% solids concentration. The vials were shaken at 400 rpm using an orbital shaker (Edmund Buhler KL-2) for 4 h followed by centrifugation for 10 min. The equilibrium concentration of the dye Procion Navy HEXL was determined by UV automatic spectrophotometer (UV-2000). The samples for UV analysis were filtered to remove the suspended matters. The adsorption density was calculated by the following formula:

$$\Gamma = \frac{(C_i - C_e)\cdot V}{m1000}, \tag{1}$$

where Γ is the amount of dye adsorbed per g of adsorbent in mg/g, C_i is the initial dye concentration in mg/dm^3, C_e is the equilibrium (residual) dye concentration in mg/dm^3, V is the volume of the solution in dm^3, m is the mass of adsorbent (g).

2.2.3. Adsorption models

Langmuir, Freundlich, and D-R isotherm models, which are two-parameter equations, were used to identify the adsorption mechanism of dye-bentonite system. The Langmuir isotherm is represented as below (Espantaleón et al., 2003; Baskaralingam et al., 2006; Ozcan et al., 2007; Eren and Afsin, 2008; Turabik, 2008):

$$q_e = \frac{\mathrm{K}_L a_L C_e}{1 + a_L C_e} \tag{2}$$

where K_L is the constant of the Langmuir model related to the adsorption capacity, a_L is the constant of the Langmuir model related to the energy of adsorption.

The theoretical maximum monolayer adsorption capacity q_m (mg/g) is numerically equal to (KL/a_L). Freundlich equation is based on the equation (Espantaleón et al., 2003; Baskaralingam et al., 2006; Ozcan et al., 2007; Eren and Afsin, 2008; Turabik, 2008):

$$q_e = \mathrm{K}_f C_e^{1/\mathrm{n}} \tag{3}$$

where K_f is Freundlich constant with indicators of adsorption capacity, n is Freundlich constant with indicators of adsorption intensity.

D–R isotherm is expressed as follows (Espantaleón et al., 2003; Baskaralingam et al., 2006; Ozcan et al., 2007; Eren and Afsin, 2008; Turabik, 2008):

$$q_e = q_m \exp\left\{\frac{\left[RT\ln\left(1 + 1/C_e\right)\right]^2}{\left(-2E^2\right)}\right\} \tag{4}$$

where q_m is the maximum adsorption capacity (mg/g), E is the energy of adsorption (kJ/mole).

In addition, nonlinear regression technique was performed to optimize the isotherm parameters of reactive Procion Navy HEXL dye adsorption on bentonite surface. The solver add-in function of the Microsoft Excel was used for nonlinear regression method (Corporation, 2002).

3. Results

3.1. Effect of solids concentration on adsorption

In order to obtain the optimum solids concentration for the adsorption tests with the natural bentonite sample, a series of adsorption experiments were carried out at different solid concentrations at 25 mg/dm^3 dye concentration. The conditioning time was kept at 4 h. The results from these experiments shown in Fig. 1 indicate that as the solids content is increased, the adsorption density decreases with increasing solid concentration down to 0.1% solids concentration (1 mg/g). Beyond this point, there was a slight decrease in solids concentration. According to these results, 0.1% solids concentration was chosen for further studies with the natural and modified bentonite samples.

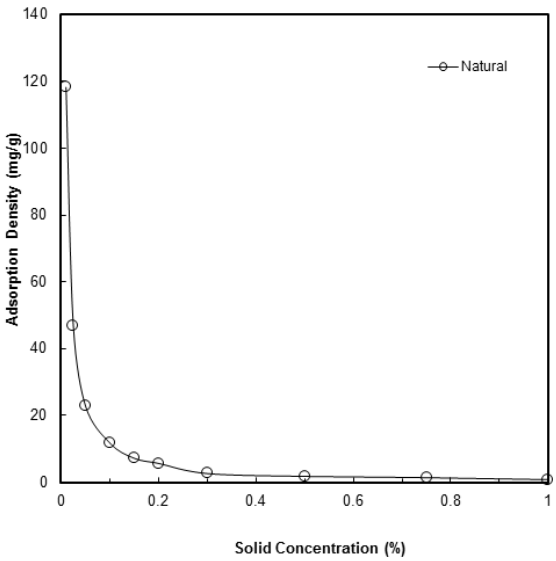

Fig. 1. Variation of adsorption of Procion Navy HEXL dye on natural bentonite with solids concentration

3.2. Effect of mixing time on adsorption

A series of adsorption experiments with the natural bentonite were also carried out as a function of time in order to find the optimum time. The experiments were carried out at an initial dye concentration of 25 mg/dm^3 and 0.1% solids concentration. As seen from Fig. 2, the adsorption density sharply increased up to 1 h, further increased with increasing the time and finally reached the plateau at 2 h. As seen from Fig. 2, even though the adsorption density reached a plateau at 2 h, 4 h of conditioning time was chosen for further studies taking into consideration some factors such as pH, concentration, and temperature etc. (Armagan et al., 2004; Ozdemir et al., 2004).

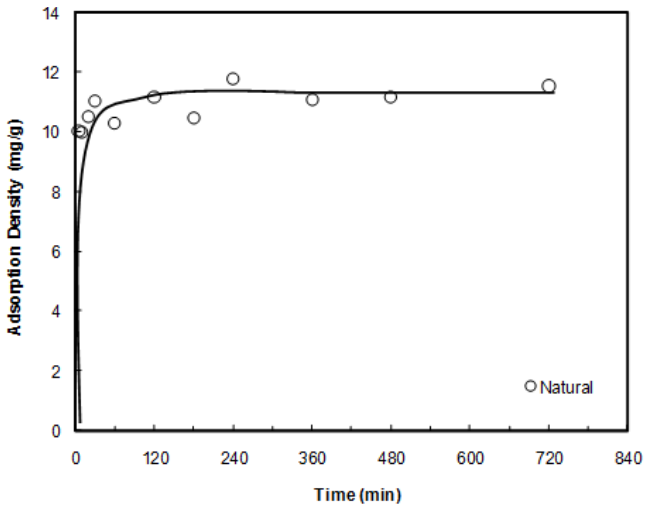

Fig. 2. Adsorption of Procion Navy HEXL dye onto natural bentonite against conditioning time

3.3. Effect of dye concentration on adsorption

The adsorption experiments were carried out with the natural and modified bentonite samples at different dye concentrations to obtain the adsorption isotherms of bentonite/dye system. The experiments were conducted at 0.1% solids concentration and mixing time of 4 h. Figure 3 shows the adsorption isotherms of dye Procion Navy HEXL on the natural and modified bentonites. As seen from Fig. 3, in the case of the natural bentonite, the adsorption density increased up to 20 mg/g, and then reached a plateau. Meanwhile, as can be clearly seen from Fig. 3, the modification of bentonite with HTAB led to about a 12-fold increase in the adsorption capacity of bentonite.

4. Discussion

Wastewaters in textile industry cause a detrimental effect to the environment, and this problem must be solved economically and efficiently. Therefore, many physical, chemical, and biological methods have been used, in the industry. However, these methods are expensive, and there is a need for low cost methods to reduce the contamination in wastewaters. For example, it has been suggested that low-cost natural clays such as bentonite (Ozcan et al., 2007; Eren and Afsin, 2008; Turabik, 2008), sepiolite (Ozdemir et al., 2004; Alkan et al., 2007), and zeolite (Armagan et al., 2003; Armagan et al., 2004; Ozdemir et al., 2004; Benkli et al., 2005) can been used either directly or after modification for wastewater treatment.

In this study, the ability of bentonite to uptake the reactive Procion Navy HEXL dye was investigated in detail, and the optimum conditions for the dye-bentonite system was obtained. The results from these studies showed that the optimum solids

concentration and conditioning time was 0.1% and 4 h, respectively. These data are also in agreement with the literature. For example, Ozdemir et al. (2004) and Armagan et al. (Espantaleón et al., 2003; Baskaralingam et al., 2006; Ozcan et al., 2007; Eren and Afsin, 2008; Turabik, 2008) showed that the optimum solids concentration of sepiolite and zeolite for reactive dyes was found 4 h at 25 mg/dm^3 dye concentration. In addition, the natural bentonite was modified with HTAB to increase its adsorption capacity. The adsorption tests with the modified bentonite showed that the modification process significantly increased the uptake of the bentonite. Based on the results from batch experiments, the modified bentonite yielded 12 times more adsorption capacity than the natural bentonite. The aim is to clarify fundamental details regarding the uptake of dye molecules from wastewaters using bentonite.

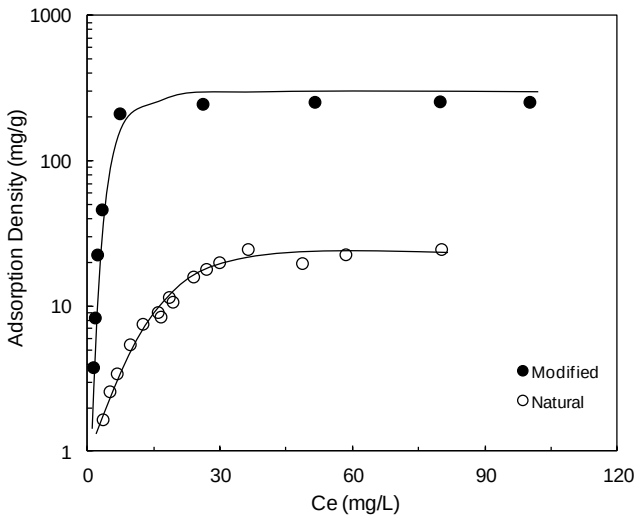

Fig. 3. Comparison of adsorption isotherms for natural and modified bentonite/Procion Navy HEXL dye

4.1. Zeta potential experiments

It is well known from the literature that zeta potential measurements are vitally important to determine the stability of clay-water system. For this reason, the zeta potential measurements with the natural and modified bentonites were carried out as a function of pH. The results presented in Fig. 4 clearly reveal that the natural bentonite was negatively charged at all pH values with no point of zero charge. On the other hand, the modified bentonite exhibited positive charges throughout the pH region (Fig. 4).

Procion Navy HEXL dye contains negative azo groups and thus exhibits negative surface charges. Since natural bentonite contains positive charges only at the edges, the overall net charge density is negative, particularly above pH 7. Adsorption of negatively charged dye molecule is weak at the natural bentonite surfaces. However,

the modification of bentonite with HTAB (quaternary amine surfactant) showed a considerable increase of the adsorption density. In this way, the bentonite surfaces became hydrophobic, and the negative charges of the surfaces were neutralized (Ozdemir et al., 2004).

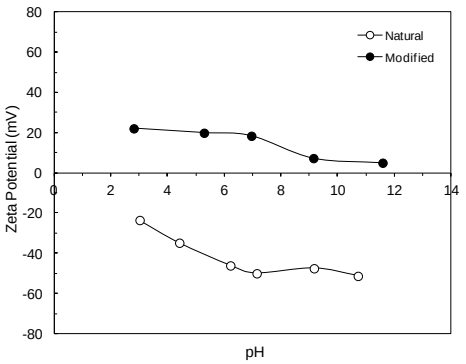

Fig. 4. Zeta potential profiles of natural and modified bentonites

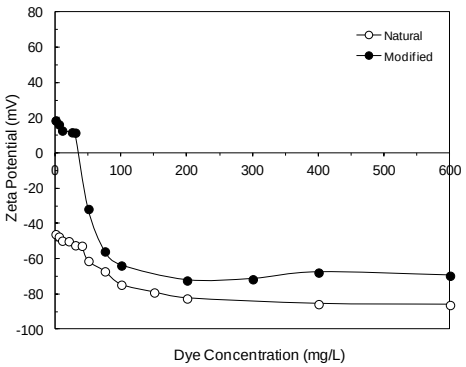

Fig. 5. Zeta potential profiles of the natural and modified bentonites vs. the dye concentration

The zeta potential measurements for natural and modified bentonites were also performed at different dye concentrations in order to understand the adsorption mechanism. The results presented in Fig. 5 show that the surface charges of the natural bentonite sample become more negative with an increase in dye concentration. This shows that the dye adsorbs on positive sites of the bentonite sample. At the same time, the positive charge of the modified bentonite decreased with increasing the dye concentration up to 25-30 mg/dm^3. Then, the surface charge sharply decreased, and became negative above 40 mg/ dm^3 dye concentration. When the dye concentration is further increased, the surface charge decreased slightly, and then reached a constant value. These results support the adsorption tests. Electrostatic attraction with negatively charged dye groups appeared to be instrumental in the uptake of dye onto the bentonite surface.

4.2. Adsorption models

The experimental data for absorbed Procion Navy HEXL dye onto natural and modified bentonites were compared using three of the two-parameter isotherm models, i.e. Langmuir, Freundlich, and D–R in order to find the best-fitted model for the data obtained. The different equation parameters and the underlying thermodynamic hypotheses of these models often provide insight into the adsorption mechanism, the surface properties and affinity of the adsorbent (Armagan et al., 2003). The isotherms obtained from the models are shown along with the isotherms from the experiments in Fig. 6. Finally, the equilibrium thermodynamic parameters were calculated for the dye-bentonite system, and the results for the isotherm constants and correlation coefficients (R^2) are presented in Table 1.

As seen from Fig. 6a, Langmuir, Freundlich, and D–R models fit very well the experimental equilibrium data for the natural bentonite. However, the Langmuir and D–R models give slightly better fitting than Freundlich model in the case of the modified bentonite (Fig. 6b). The reason for that can be attributed to the fast adsorption of dye molecules on the modified bentonite. As also seen in Table 1, all isotherms (Langmuir, Freundlich, and D-R) fit well with the experimental data (correlation coefficient R^2 = 0.975, 0.941, and 0.973) for the natural bentonite whereas the low correlation coefficient (R^2 = 0.804, 0.669, and 0.767) indicates poor agreement of isotherms with the experimental data for the modified bentonite. It may be due to the sorption that occurs at specific homogeneous sites within the adsorbent (Bouberka et al., 2006; Lian et al., 2009). Ma et al. (Espantaleón et al., 2003; Baskaralingam et al., 2006; Ozcan et al., 2007; Eren and Afsin, 2008; Turabik, 2008) found similar results, which exhibited a sharp initial rise in all the adsorbents (type I isotherm). They attributed predominant effect of strong electrostatic adsorbent–adsorbate forces of attraction, which meant a high affinity between the dye and the adsorbent surface (Ma et al., 2011).

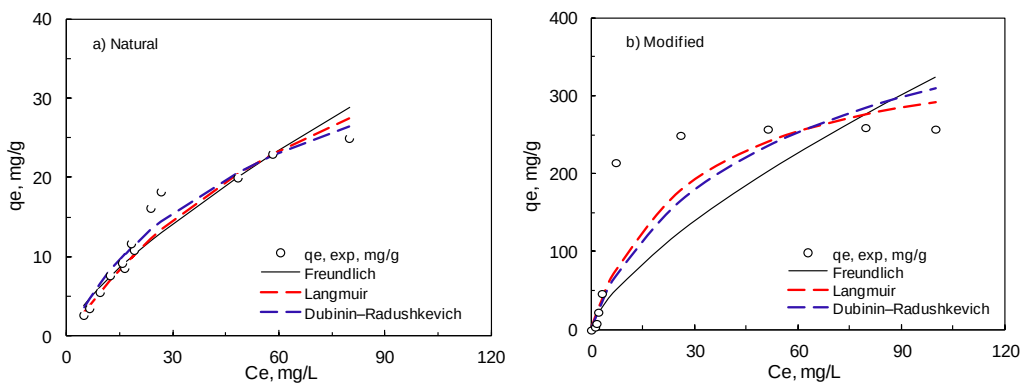

Fig. 6. Results for the adsorption models of dye-bentonite system: a) natural, and b) modified bentonite

Table 1. Parameters obtained from the adsorption models

	Langmuir				Freundlich			Dubinin–Radushkevich		
	K_L	a_L	$q_m=K_L/a_L$	R^2	K_f	1/n	R^2	q_m	E	R^2
Natural	0.784	0.018	43.747	0.975	1.161	0.728	0.941	49.758	5.644	0.973
Modified	13.103	0.035	375.163	0.804	12.947	0.699	0.669	494.804	6.463	0.767

According to Table 1, adsorption capacities were calculated from Langmuir (43.747 and 375.163 mg/g), Freundlich (1.161 and 12.947 mg/g), and D-R isotherm models (49.758 and 494.804 mg/g) for natural and modified bentonite, respectively. There are several similar studies in the literature. For example, the adsorption capacities of 98.6, 99.9, and 95.2 mg/g for Acid Yellow 194, Acid Blue 349, and Acid Red 423, respectively, on sepiolite were found to be higher than that on activated

carbon (49.2, 68.2, and 26.3 mg/g) but similar to that on natural bentonite (24.9, 92.7, and 29.1 mg/g) (Espantaleón et al., 2003; Baskaralingam et al., 2006; Ozcan et al., 2007; Eren and Afsin, 2008; Turabik, 2008).

Qiao et al. (2009) measured single dye adsorption equilibrium and analyzed the experimental data with the Langmuir, Freundlich and Redlich-Peterson isotherms. Their results fit well Redlich-Peterson model and provided the best correlation of the experimental data and also the adsorption capacities estimated from the Langmuir model for AR18 and AY23 were at 69.8 and 75.4 mg/g, respectively. Ozcan et al. (Ozcan et al., 2004) compared the results of natural and modified bentonite using dodecyl trimethylammonium bromide (DTMA) for the removal of acid blue 193. The adsorption capacity of DTMA-bentonite (740.5 mg/g) was found to be about 11-fold higher than that of Na-bentonite (67.1 mg/g) at 20°C. Ozcan et al. (2007) also found out that adsorption capacity was 206.58 mg/g for DTMA-bentonite in acidic solutions for the removal of reactive Blue 19, and adsorption isotherm data were fitted to the Langmuir model.

Ma et al. (2011) emphasized that the adsorption capacity of organobentonite was affected by the surfactant alkyl chain length. The longer chain surfactant of modified bentonite shows higher adsorption capacity. As the surfactant carbon chain length decreased from C16 to C8, the adsorption capacities of Orange II decreased from 298.39 mg/g to 144.08 mg/g. The adsorption capacities of Orange G showed the same tendency (from 170.46 to 94.72 mg/g). Eren (Eren, 2009) showed that Langmuir monolayer adsorption capacities of raw and manganese oxide modified bentonite as 131 and 457 mg/g, respectively. The Langmuir model with the maximum adsorption capacity of 227.27 mg/g agreed very well with experimental data whereas Freundlich model yielded 119.40 mg/g adsorption capacity (Lian et al., 2009).

For the D-R isotherm, E (kJ/mole) gives information about the type of adsorption (physical, chemical, and ion exchange). The energy of adsorption refers to transfer of one mole of ion from the bulk to the interface. When this value of free energy is in the range of 1-8 kJ/mole, the adsorption type can be classified as physical (Helferrich, 1962). An energy range between 8 and 16 kJ/mole indicates ion exchange (Cestari et al., 2007) and when the energy is more than 16 kJ/mole the type of adsorption can be stated as chemical adsorption (Basar, 2006; Tahir and Rauf, 2006). Because the magnitude of E calculated from the D-R isotherm is lower than 8 kJ/mole for both natural and modified bentonites, the adsorption mechanism of dye onto bentonite can be described by physical interactions. Tahir and Rauf (2006) found that the adsorption free energy from D-R isotherm for uptake of Malachite Green oxalate dye on bentonite at different temperatures were between 1.00 and 1.13 kJ/mole corresponding to physical adsorption. On the other hand Eren (2009) found that adsorption energy from D-R isotherm for Crystal Violet onto raw and modified bentonite were 11.47 and 19.55 kJ/mole, the adsorption type can be explained based on ion exchange and chemical adsorption, respectively.

5. Conclusions

The adsorption of Procion Navy HEXL on the bentonite sample was systematically investigated. The results showed that while the natural bentonite has an adsorption capacity of about 20 mg/g, bentonite modified with quaternary amines significantly increased its capacity (about 12 times, 250 mg/g). The zeta potential experiments indicated that the adsorption mechanism of dye on the modified bentonite is governed by electrostatic attraction of negatively charged dye groups on the positively charged surface. Finally, the adsorption data obtained from the experiments were analyzed using the adsorption models, i.e. Langmuir, Freundlich, and D–R. The results indicate that while all three models demonstrated a good correlation for the adsorption of dye molecules on the natural bentonite, it was not so good on modified bentonite.

These results clearly showed that modified bentonite could be used for the removal of dyes in textile wastewaters due to its low cost and high yield. This will be not only a good alternative to high cost absorbents such as activated carbon and polymer resins, but also help solve environmental problems.

References

ALKAN, M., DEMIRBAS, O., DOĞAN, M., 2007, *Adsorption kinetics and thermodynamics of an anionic dye onto sepiolite*, Micropor. Mesopor. Mat., 101(3), 388–396.

ARBELOA, F.L., ARBELOA, T.L., ARBELOA, I.L., 1997, *Spectroscopy of rhodamine 6G adsorbed on sepiolite aqueous suspensions*, J. Colloid Interf. Sci., 187(1), 105–112.

ARMAGAN, B., OZDEMIR, O., TURAN, M., CELIK, M.S., 2003, *Adsorption of negatively charged azo dyes onto surfactant-modified sepiolite*, J. Environ. Eng., 129(8), 709–715.

ARMAGAN, B., OZDEMIR, O., TURAN, M., CELIK, M.S., 2003, *The removal of reactive azo dyes by natural and modified zeolities*, J. Chem. Technol. Biot., 78(7), 725–732.

ARMAGAN, B., TURAN, M., ÇELIK, M.S., 2004, *Equilibrium studies on the adsorption of reactive azo dyes into zeolite, Desalination*, 170(1), 33–39.

BASAR, C.A., 2006, *Applicability of the various adsorption models of three dyes adsorption onto activated carbon prepared waste apricot*, J. Hazard. Mater. B, 135, 232–241.

BASKARALINGAM, P., PULIKESI, M., ELANGO, D., RAMAMURTHI, V., SIVANESAN, S., 2006, *Adsorption of acid dye onto organobentonite*, J. Hazard. Mater., 128(2–3), 138–144.

BENKLI, Y.E., CAN, M.F., TURAN, M., CELIK, M.S., 2005, *Modification of organo-zeolit surface for the removal of reactive azo dyes in fixed-bed reactors*, Water Res., 39(2–3), 487–493.

BOUBERKA, Z., KHENIFI, A., BENDERDOUCHE, N., DERRICHE, Z., 2006, *Removal of Supranol Yellow 4GL by adsorption onto Cr-intercalated montmorillonite*, J. Hazard. Mater., 133(1–3), 154–161.

BULUT, G., CHIMEDDORJ, M., ESENLI, F., CELIK, M.S., 2009, *Production of desiccants fromTurkish Bentonites*, Appl. Clay Sci., 46, 141–147.

CESTARI, A.R., VIEIRA, E.F.S., VIEIRA, G.S., ALMEIDA, L.E., 2007, *Aggregation and adsorption of reactive dyes in the presence of an anionic surfactant on mesoporous aminopropyl silica*, J. Colloid Interf. Sci., 309(2), 402–411.

CORPORATION, M., 2002, User's guide Microsoft Excel Version.

DUBININ, M.M., RADUSHKEVICH, L.V., 1947, *Equation of the characteristic curve of activated charcoal*, Chem. Zentr., 1875.

EREN, B., AFSIN, B., 2008, *Investigation of a basic dye adsorption from aqueous solution onto raw and pre-treated bentonite surfaces*, Dyes Pigments., 76(1), 220–225.

EREN, E., 2009, *Removal of basic dye by modified Unye bentonite, Turkey*, J. Hazard. Mater., 162(2–3), 1355–1363.

ESPANTALEŐN, A.G., NIETO, J.A., FERNÁNDEZ, M., MARSAL, A., 2003, *Use of activated clays in the removal of dyes and surfactants from tannery waste waters*, Appl. Clay Sci., 24(1), 105–110.

FREUNDLICH, H.M.F., 1906, *Over the adsorption in solution*, J. Phys. Chem., 57, 385–470.

HELFERRICH, F., 1962, *Ion-exchange*, McGraw Hill, New York, NY,

JUANG, R.S., TSENG, R.L., WU, F.C., LEE, S.H., 1997, *Adsorption behavior of reactive dyes from aqueous solutions on chitosan*, J. Chem. Technol. Biot., 70(4), 391–399.

LANGMUIR, I., 1918, *Adsorption of gases on plane surfaces of glass, mica and platinum*, J. Am. Chem. Soc. , 40, 1361–1403.

LIAN, L., GUO, L., WANG, A., 2009, *Use of $CaCl_2$ modified bentonite for removal of Congo red dye from aqueous solutions*, Desalination, 249(2), 797–801.

MA, J., CUIA, B., DAIB, J., LI, D., 2011, *Mechanism of adsorption of anionic dye from aqueous solutions onto organobentonite*, J. Hazard. Mater., 186 (2–3), 1758–1765.

MCKAY, G., 1982, *Adsorption of dyestuffs from aqueous solutions with activated carbon I: equilibrium and batch contact-time studies*, J. Chem. Technol. Biot., 32, 759–772.

OZCAN, A., OMEROGLU, C., ERDOGAN, Y., OZCAN, A.S., 2007, *Modification of bentonite with a cationic surfactant: an adsorption study of textile dye Reactive Blue 19*, J. Hazard. Mater., 140(1–2), 173–179.

OZCAN, A.S., ERDEM, B., OZCAN, A., 2004, *Adsorption of acid blue 193 from aqueous solutions onto Na-bentonite and DTMA-bentonite*, J. Colloid Interf. Sci., 280(1), 44–54.

OZDEMIR, O., ARMAGAN, B., TURAN, M., CELIK, M.S., 2004, *Comparison of adsorption characteristic of azo-reactive dyes on mezoporous minerals*, Dyes and Pigments, 62(1), 49–60.

QIAOA, S., HUA, Q., HAGHSERESHTA, F., HUB, X., LUA, G.Q.M., 2009, *An investigation on the adsorption of acid dyes on bentonite based composite adsorbent*, Sep. Purif. Technol., 67, 218–225.

RYTWO, G., NIR, S., CREPSIN, M., MARGULIES, L., 2000, *Adsorption and interactions of methyl green with montmorillonite and sepiolite*, J. Colloid Interf. Sci., 222(1), 12–19.

SABAH, E., 1998, *Adsorption mechanism of various amines onto sepiolite*, Ph.D. Thesis, Osmangazi University, Eskisehir,

TAHIR, S.S., RAUF, N., 2006, *Removal of a cationic dye from aqueous solutions by adsorption onto bentonite clay*, Chemosphere, 63(11), 1842–1848.

TURABIK, M., 2008, *Adsorption of basic dyes from single and binary component systems onto bentonite: simultaneous analysis of Basic Red 46 and Basic Yellow 28 by first order derivative spectrophotometric analysis methods*, J. Hazard. Mater., 158(1), 52–64.

WANG, C.C., JUANG, L.C., HSU, T.C., LEE, C.K., LEE, J.F., HUANG, F.C., 2004, *Adsorption of basic dyes onto montmorillonite*, J. Colloid Interf. Sci., 273(1), 80–86

Physicochem. Probl. Miner. Process. 48(2), 2012, 381−392

www.minproc.pwr.wroc.pl/journal/

Physicochemical Problems of Mineral Processing

ISSN 1643-1049 (print)
ISSN 2084-4735 (online)

Received December 10, 2011; reviewed; accepted February 8, 2012

BENEFICIATION OF LOW-GRADE FELDSPAR ORE USING CYCLOJET FLOTATION CELL, CONVENTIONAL CELL AND MAGNETIC SEPARATOR

Hasan HACIFAZLIOGLU, Ilgin KURSUN, Mert TERZI

Istanbul University, Engineering Faculty, Mining Engineering Department, Avcılar, Istanbul, ilginkur@istanbul.edu.tr

Abstract. In order to increase the quality of feldspar ore and to obtain sellable feldspar concentrate, it is necessary to remove coloring impurities such as iron and titanium contained in it. For the removal of coloring minerals from feldspar ore the most widely used method is reverse flotation method. Reverse flotation process is generally carried out in conventional mechanical cells. In this study, it was aimed to enrich low-grade feldspar by using cyclojet flotation cell which was developed as an alternative to conventional cell. Then, experiments were performed by using conventional cell and wet magnetic separator and the results were compared with the flotation results obtained by using cyclojet cell. In experimental studies, 200 micrometer grain sized feldspar (albite) ore obtained from Muğla province at the west side of Turkey was used. It was detected that the sample was containing 0.100% Fe_2O_3 and 0.360% TiO_2 as coloring minerals. Cyclojet cell, conventional cell and magnetic separator reduced the Fe_2O_3 content down to 0.010%, but TiO_2 content was different in the concentrates obtained by different devices. There was almost no reduction in TiO_2 content by magnetic separation method. Cyclojet cell reduced TiO_2 content down to 0.030% and mechanical cell reduced TiO_2 content down to 0.020%. The weights of the concentrate were detected as the highest (92.70%) in magnetic separator and as the lowest (75.40%) in cyclojet cell. Therefore, it is possible to say that cyclojet cell can compete with mechanical cell and removal of TiO_2 in cyclojet cell is much better than the removal of TiO_2 in magnetic separator. Generally, in the flotation process performed by using a reagent of Aero801 and Aero825 mixture in natural pH medium, both Fe_2O_3 and TiO_2 can be removed at a rate of up to 90%, but magnetic separator can only remove Fe_2O_3 mineral.

keywords: feldspar, separation, flotation

1. Introduction

Feldspar is an important industrial raw material used in ceramic, porcelain and glass industries. Sixty percent of the World feldspar production is used in ceramic industry, 35% is used in glass industry, and 5% is used in welding electrode, rubber, plastic and paint industry as filling material. It is known that total feldspar reserves of the World is $1.740 \cdot 10^6$ Mg and a large part of this reserve is located in Asia. Turkey

http://dx.doi.org/10.5277/ppmp120205

has a reserve of $240 \cdot 10^6$ Mg which is 14% of the World feldspar reserves and it has the largest Na-feldspar reserves among other countries in the World (Bayraktar et al., 1998; Kangal and Guney, 2002; Anonymous, 2010). Commercial and the most important ones of feldspar group minerals are albite ($NaAlSi_3O_8$), orthoclase ($KAISi_3O_8$) and anorthite ($CaAl_2Si_2O_8$) which are named according to the Na, K, and Ca contents in their structures. Since there are not many commercial anorthite deposits in the World, feldspar production mainly depends on albite and orthoclase minerals (Bayraktar et al., 2001; Karaguzel and Çobanoğlu, 2010).

Iron and titanium minerals existing in mineralogical structures of feldspar are known as unwanted impurities because of their coloring properties. Therefore, Fe_2O_3 and TiO_2 contents of 0.50% or below are required in feldspar. The main impurity minerals observed in feldspar ores are rutile and sphene for titanium, mica minerals and minerals such as garnet, hematite, hornblende, tourmaline, biotite, and muscovite for iron oxides. In case that the amounts of these minerals are higher than the specific values, the quality of glass and ceramic decreases and the color changes accordingly. Therefore, the main goal in enrichment of feldspars is based on removal of the coloring minerals from the ore. Magnetic separation appears to be the most appropriate method for enrichment of feldspars in terms of cost and simplicity. However, flotation method is generally preferred according to the mineralogical property because magnetic susceptibilities of titanium minerals such as sphene and rutile are very low and also magnetic separators used in this area can perform efficient separation down to a specific grain size. Conventional reverse flotation method is still the most widely used method in the World for the removal of the impurities in feldspars. On the other hand, chemical and biological methods also can be used for the removal of impurities. In chemical method, feldspar is leached by organic and inorganic acids and in biological method, microorganisms are used instead of chemicals (Styriakovaa et al., 2006; El-Rehiem and Abd El-Rahman, 2008). Agglomeration or selective flocculation methods are also used for enrichment of feldspar (Doğu and Arol, 2004).

In this study, Na-feldspar ore obtained from Muğla province (Turkey) was enriched by cyclojet cell which is an alternative jet flotation technique, conventional cell and magnetic separator and the results obtained from the devices were compared.

2. Experimental studies

2.1. Cyclojet flotation cell

Cyclojet cell is a high density jet flotation cell developed in Turkey in 2006 for the enrichment of coal slimes. In the previous studies, outstanding success of cyclojet for the enrichment of coal slime has been proven by many researches. It was observed that clean coals containing ash between 7% and 15% were obtained from coal slime having ash contents of about 45-55% fed into cyclojet cell (Hacıfazlıoğlu, 2009; Hacıfazlıoglu and Toroğlu, 2008). This device, which is effective in enrichment of

very fine particles, was used for the flotation of 200 micrometer grain sized Na-feldspar in this experiment.

Cyclojet cell, although it has some structural differences, mainly works with the principle of jet flotation. In this system, jet movement of pulp and centrifugal forces generated within the hydrocyclone and the cell are used. "Jet movement" is created linearly by a nozzle formed by a large number of holes in conventional jet flotation systems, but it is created as cone-shaped by a hydrocyclone apex in a cyclojet cell. In other words, pulp jet created in a cyclojet cell submerges into cell with a cyclonic move and creates a more efficient flotation providing more intensive shearing forces. Furthermore, intense mixing occurring within the cell and hydrocyclone minimizes the coating of particle with slime and it enables an effective flotation process without removing slime from the ore.

Schematic view of pilot-scale cyclojet cell test assembly installed in Istanbul University, Mining Engineering Department Mineral Processing Laboratory is shown in Figure 1. According to Figure 1, pulp conditioned in a 67 dm^3 conditioner for 10 minutes with the addition of collector and frother is fed tangentially into a hydrocyclone having a diameter of 16 cm with a pressure of 0.1-0.6 bar (10-60 kPa) by a centrifugal pump driven by a 1.5 kW motor. There are a conical tube with a height of 25 cm just below the hydrocyclone, and a separation cell having a diameter of 30 cm and height of 40 cm below conical tube. Upper flow outlet pipe of hydrocyclone is completely closed in order to prevent the upward movement of the pulp. In this case, high pressure pulp is first mixed thoroughly by swirling in hydrocyclone and then submerges into separation cell by forming a cyclonic jet. Meanwhile, an air gap created by the effect of the jet within the conical tube provides the suction of air from the atmosphere with a vacuum effect. Air from the atmosphere is sucked with a sectional velocity of 0.2 cm/sec through a circular hole with 1 cm diameter on the conical tube. Then, pulp jet mixed with the air sucked quickly submerges into the pulp in the separation cell and allows the formation of a large number of very fine-sized (300-500 microns) air bubbles by action of shear forces. Separation is performed by taking hydrophobic grains (coloring impurities) interfere with the bubbles in the separation cell from the upper part of the cell and taking hydrophilic grains (feldspar) which do not interfere with the air from the lower part of the cell. A by-pass was mounted into the system in order to ensure continuity in the cell and cleaning of feldspar ore over and over again. In other words, the bottom outlet pipe of the separation cell is connected to the conditioner with another pipe. In cyclojet flotation, sulphonate type collectors named as Aero801 and Aero825 manufactured by American CYTEC Company are used with a mixing ratios of 50% and dosages of 1000 and 2000 g/Mg. All experiments were performed by using tap water and at 24^0C room temperature and at natural pH value of (7-8). Solid content of the pulp and conditioning period were selected as 30% and 8 minutes respectively. Products obtained by reverse flotation were dried in the oven after filtration, and were

analyzed by XRD for Fe_2O_3 and TiO_2 content. Then, Fe_2O_3 and TiO_2 removal efficiencies were calculated by the following equations:

Fe_2O_3 removal efficiency (%) = [1- (Fe_2O_3 content in concentrate/Fe_2O_3 content in feed)]·100,

TiO_2 removal efficiency (%) = [1- (TiO_2 content in concentrate/TiO_2 content in feed)]·100.

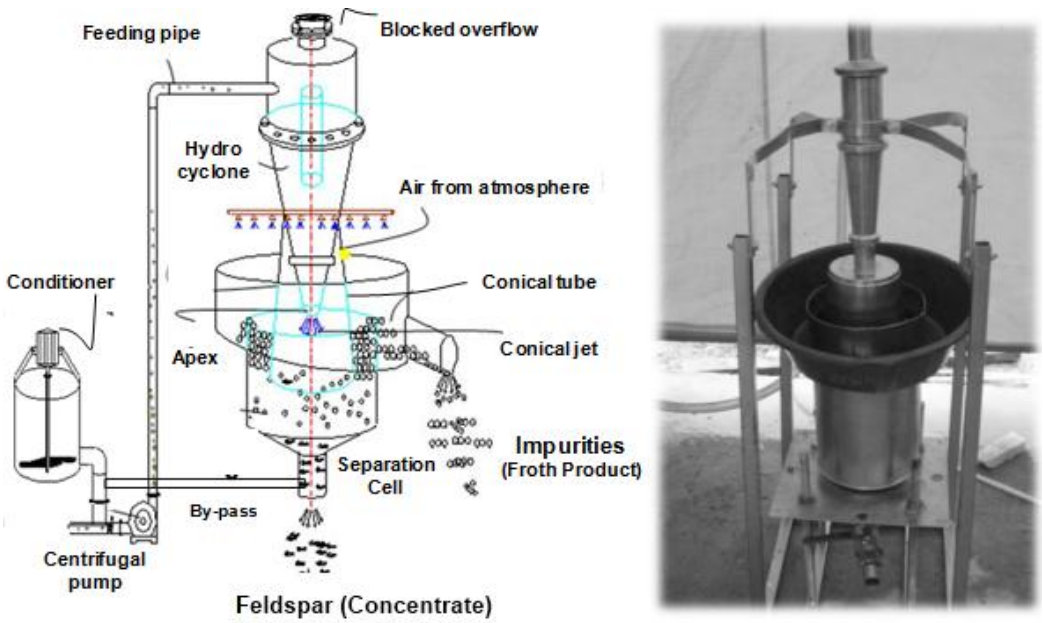

Fig. 1. Cyclojet flotation cell experimental set-up

2.2. Na-feldspar sample

A 50 kg Na-feldspar sample was taken from the feldspar enrichment plant owned by Esan Company operating in Muğla province located in the south-west part of Turkey. In this plant, the ore ground to 0.5 mm is enriched by using conventional mechanical mixing flotation cells. Before the enrichment, slime is removed from the Na-feldspar ore by 14 inch hydrocyclones and then feldspar is fed into flotation cell and coloring impurities are removed by reverse flotation. The main coloring impurities in the sample are minerals such as hematite, garnet, anatase, rutile, sphene, biotite and ilmenite containing iron and titanium. It was observed during microscopic observations done that 90% of the colored minerals were liberated from the feldspar grains with size under 200 micrometers. The whole sample was ground gradually by ceramic ball mill down to fine sizes under 200 micrometers in order to allow cyclojet cell to be effective at fine sizes (<200 μm) and to obtain high rate of liberation. According to the results of the chemical analysis of the sample used in the experimental studies done by using X-Ray diffractometer (XRD), the following were

detected: SiO_2 67.38%; Al_2O_3 19.28%, Fe_2O_3 0.10%, TiO_2 0.36%, MgO 0.25%, CaO 1.08%, K_2O 0.43% and Na_2O 10.07%.

3. Results and discussion

3.1. Optimization of cyclojet operation parameters

Some of the parameters of the study should be optimized in order to allow cyclojet cell to be effective in feldspar flotation. The most important ones are amount of reagent, pulp pressure, conical jet length and conical tube submerging depth. In the experiments performed to find the effect of the amount of reagent (collector), feeding pressure, conical jet height and conical tube submerging depth, solid concentration were set to 40 kPa, 10 cm, 30% respectively. In all experiments, total conditioning time was set to 8 minutes and total flotation time (froth removal time) was set to 10 minutes. Any additional frother or any chemical for pH adjustment were not used in the experiments since the Aero 801 and Aero 825 collectors have frothing characteristics. All experiments were performed by using tap water and at natural pH value of 7-8. The effects of various parameters on concentrate and waste characteristics during cyclojet flotation are given in Table 1. Every optimum parameter obtained was used in the next experiment.

Table 1. The effects of various parameters on concentrate and waste characteristics during cyclojet flotation

Parameters	Values	Concentrate (Feldspar)			Reject (impurities)		
		Fe_2O_3 content(%)	TiO_2 content(%)	Wt. (%)	Fe_2O_3 content(%)	TiO_2 content(%)	Wt. (%)
Reagent Aero801+825 (g/Mg)	750	0.070	0.230	76.600	0.198	0.786	23.400
	1500	0.020	0.040	67.200	0.264	1.016	32.800
Feed pressure (kPa)	10	0.090	0.270	82.200	0.146	0.776	17.800
	40	0.010	0.040	65.400	0.270	0.965	34.600
Conical jet lenght (cm)	10	0.010	0.030	66.100	0.275	1.003	33.900
	20	0.060	0.190	70.100	0.194	0.759	29.900
Conical tube submerging depth (cm)	10	0.010	0.030	67.000	0.283	91.667	33.000
	20	0.050	0.150	74.000	0.242	58.333	26.000

As shown in Table 1, removal of both Fe_2O_3 and TiO_2 increased with the increase in reagent amount. By increasing the reagent amount from a dosage of 750 g/Mg to a dosage of 1500 g/Mg, the Fe_2O_3 content in the concentrate was decreasing from 0.070% to 0.020%, while TiO_2 content decreased from 0,230% to 0,040%. Increase in the reagents amount provided flotation of greater amounts of impurities. On the other hand, with a fixed reagents dosage (1500 g/Mg), the Fe_2O_3 content in the concentrate

was reduced from 0.090% to 0.010% by increasing pulp pressure from 10 kPa to 40 kPa. The TiO_2 content in the concentrate was reduced from 0.270% to 0.040% by increasing the feeding pressure. Removal of Fe_2O_3 and TiO_2 minerals was lower at lower feeding pressure (10 kPa) because sufficient shear forces within the separation cell were not created. In other words, bubbles in cyclojet cell are formed by the pulp jet rapidly flushing from the apex. Here, the larger shear forces are generated as the pulp jet velocity gets higher, and consequently, a large number and relatively small-sized bubbles are formed within the cell.

Another important parameter affecting flotation efficiency in cyclojet cell is the conical jet length. As it can be seen clearly from the results indicated in Table 1 that concentrates having lower Fe_2O_3 and TiO_2 contents are obtained. The Fe_2O_3 content in the concentrate decreased from 0.060% to 0.010% by decreasing the jet length from 20 cm to 10 cm. The TiO_2 content in the concentrate decreased from 0.190% to 0.030%. The reason of this situation is related with the formation of sufficient number of bubbles as in the case of pressure effect. With the high jet length (20 cm), shear force was reduced due to jet activity and a smaller number of bubbles were formed in the cell. When the jet length was decreased to 10 cm, more bubbles were formed and more impurities were moved into froth product.

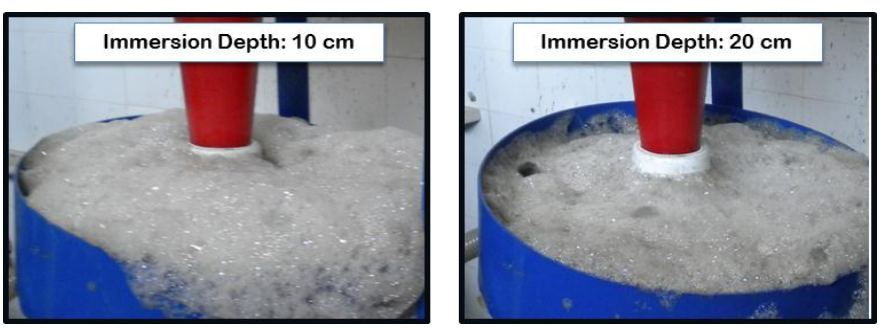

Fig. 2. Pictures of the froth at low and high conical tube submerging depths

In jet flotation systems, hydraulic pressure applied on the unit surface area at the outlet point of the tube increases as the depth of the sublance increases. Therefore, velocity of the pulp leaving the discharge point and the velocity of formation of the bubbles decrease. Furthermore, the sizes of the bubbles decrease because of high pressure (Güney et al., 2002; Cowburn et al., 2006; Çınar et al., 2007). A similar situation is also valid for the cyclojet cell, the sizes of the bubbles formed decrease as the depth of the sublance increases. However, the number of the bubbles formed decreases because of the changing medium conditions and high pressure. The pictures of the bubbles (froth) obtained at conical tube submerging depths of 10 and 20 cm are given in Fig. 2. It can be seen clearly in Figure 2 that a more intense layer of froth and therefore more number of bubbles were formed at an immersion depth of 10 cm and a thinner layer of froth was formed at an immersion depth of 20 cm. While Fe_2O_3

content was 0.010% at the immersion depth of 10 cm, the Fe_2O_3 content increased to 0.050% at the immersion depth of 20 cm. A possible reason is that grains cannot spread into the cell completely at higher immersion depths and they by-pass and mix with feldspar product. In other words, the impurities that must be moved with the froth could not pass over the conical tube and by going down to the bottom of the cell they entered the channel from which the feldspar concentrate is taken. Furthermore, as a result of formation of bubbles in insufficient number, less amount of impurity moved into froth product and a part of the impurities remained in the feldspar concentrate.

3.2. Cyclojet flotation tests performed under optimum conditions

Several flotation tests were performed in the cyclojet cell with a reagent amount of 1500 g/Mg at a feeding pressure of 40 kPa conical jet lenght and immersion depth of 10 cm, with solid concentration of 30%. Flotation tests were performed at 5 different foam skimming times such as 2, 4, 6, 8, and 10 minutes. In other words, the concentrate and the reject were taken separately at the end of 2, 4, 6, 8 and 10 minutes and they were dried and then analyzed. Characteristics of the concentrates obtained for different flotation times are shown in Fig. 3.

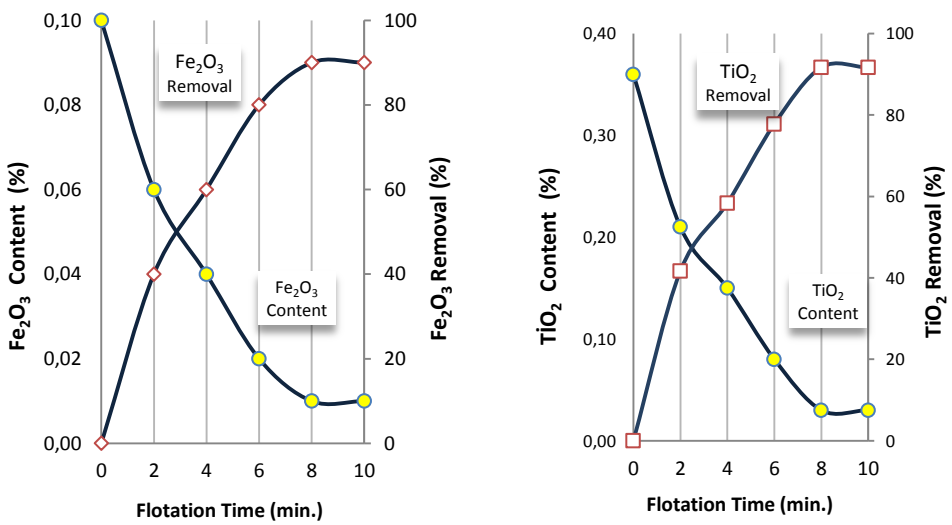

Fig. 3. Fe_2O_3 and TiO_2 content in concentrate and removal efficiency versus flotation time

As it was stated before, a by-pass was connected to the concentrate (feldspar) outlet pipe in the cyclojet cell. Feldspar concentrate obtained was transferred to the conditioner again through this by-pass pipe. Then, it was fed back to cyclojet cell by a centrifugal pump. Therefore, continuous flotation conditions are obtained in the cyclojet cell and products with different characteristics can be obtained with to the flotation time. As it can be seen in Fig. 3, the removal of both Fe_2O_3 and TiO_2

increased with increasing flotation time. While the Fe_2O_3 removal was 40% at the end of a flotation time of 2 minutes, it increased to 90% at the end of a flotation time of 10 minutes. A similar situation is also valid for TiO_2 because that the removal of TiO_2 at the end of flotation times of 2 and 10 minutes were 41.66% and 91.66%, respectively. Impurities which could not interfere with froth in the first stage interfere with froth in the second stage and then in the third stage and they were efficiently removed from the feldspar concentrate with increasing time of flotation. This situation has been clearly established in all the experiments. However, the contents of Fe_2O_3 and TiO_2 in the concentrates obtained at and after 8 minutes of flotation were similar. The amounts of the concentrate detected at the end of flotation times of 8 and 10 minutes were 75.40% and 66.10%, respectively. A further increase in the flotation time caused floating the feldspar grains and consequently a decrease in the weight of the concentrate. Therefore, the optimum flotation time for flotation of feldspar in cyclojet cell has been determined to be 8 minutes. At the end of this flotation time, the contents of Fe_2O_3 and TiO_2 have been detected as 0.010% and 0.030% respectively. The weights of the concentrate and the residue have been determined as 75.40% and 24.60%, respectively.

3.3. Comparison of the results obtained by cyclojet cell with the results obtained by mechanical cell and magnetic separator

Conventional flotation experiments were performed in Denver Model D-12 laboratory flotation cell having a volume of 3 dm^3. Following optimization studies, flotation was carried out under similar conditions with cyclojet cell. As reagent, a mixture of Aero 801 and Aero 825 with 50% mixing ratios and 1500 g/Mg dosage was used. Experiments were performed by using tap water and at natural pH (7-8). Mixer rotations and froth skimming time were chosen as 800 rpm and 10 minutes, respectively. Magnetic separation experiments were performed by using Boxmag Rapid LWHL type high field strength wet magnetic separator having maximum magnetic field strength of 1.9 T. This magnetic separator has a metal grade type matrix which can be moved between two fixed bobbin terminals. While the pulp was passing through the matrix, iron compounds are caught by the matrix. During preliminary experiments performed, pulp flow was too high because feeding size was too fine (-200 micrometers) and the hole between grade matrix was large (3000 micron meters). In this case, iron compounds could not be caught efficiently by the matrix. Therefore, periphery of grade matrix was surrounded with a wire matrix (Fig. 4) and the retention time of the grains in the matrix was increased. Then, the experiments have been carried out with a feeding velocity of 15 g/sec and at a solid rate of 30%. Obtained samples were passed through the magnetic separator 3 times. In other words, 3 stage cleaning process was performed.

Under similar conditions, the results obtained by cyclojet cell and mechanical cell are given together with the results obtained by magnetic separator in Table 2. Percentages of Fe_2O_3 and TiO_2 removal are shown in Fig. 5 comparatively. According

to Table 1, while cyclojet cell was producing a feldspar concentrate containing 0.010% Fe_2O_3 and 0.030% TiO_2, mechanical cell produced a concentrate containing 0.010% Fe_2O_3 and 0.020% TiO_2. The Fe_2O_3 contents of both types of cell are the same, but TiO_2 contents are different. TiO_2 content of the concentrate obtained from the mechanical cell is lower. Possible reason for this situation is that the mechanical cell has smaller sizes and more favorable conditions for the removal of TiO_2 were present. On the other hand, the magnetic separator showed a similar performance with the cyclojet cell and mechanical cell in respect to Fe_2O_3 removal. The Fe_2O_3 content of the concentrate was detected as 0.01% with 90% removal efficiency. However, the magnetic separator showed poor performance for the removal of TiO_2. Since the minerals such as rutile and sphene forming the TiO_2 content have no magnetic sensitivity or too low sensitivity, these minerals were not caught by magnetic separator and merged into the concentrate.

Fig. 4. View of wire matrix in wet magnetic separator

Table 2. Characteristics of the products obtained by cyclojet, mechanical cell and magnetic separator

Devices	Concentrate (feldspar)			Reject (impurities)		
	Fe_2O_3 content(%)	TiO_2 content(%)	Wt. (%)	Fe_2O_3 content(%)	TiO_2 content(%)	Wt. (%)
Cyclojet Flotation Cell	0.010	0.030	75.400	0.376	1.371	24.600
Mechanical Cell	0.010	0.020	78.500	0.429	1.601	21.500
Wet Magnetic Separator	0.010	0.340	92.700	1.243	0.614	7.300

When examining the weights of concentrate, it is observed that the highest efficiency was obtained by magnetic separator and the lowest efficiency was obtained by cyclojet cell. The amounts of the concentrates obtained by magnetic separator, mechanical cell and cyclojet cell were detected as 92.70%, 78.50% and 75.4% respectively. During flotation process, at normal pH (7-8) feldspars can float in the froth and emerge into froth product (impurities) in the course of time, but the lack of this problem in magnetic separation is the main cause for the high gravimetric efficiency. The complete chemical analyses of the final concentrates obtained by 3 different devices are shown in Table 3 together with the analysis of the feldspar

sample feed. As it can be seen from Table 3, the contents of the minerals such as SiO_2, Al_2O_3, CaO, MgO, Na_2O did not changed drastically as a result of the enrichment of feldspar ore by flotation and magnetic separation. While the flotation reagent was floating Fe_2O_3 and TiO_2 minerals, magnetic field in the magnetic separator affected only Fe_2O_3 mineral in feldspar which has magnetic sensitivity.

Because of this situation, as it can be seen clearly in Table 3 (foam products) that the Fe_2O_3 content in the residue was 0.146% at a feeding pressure of 10 kPa and it increased to 0.270% at a feeding pressure of 40 kPa. Similarly, TiO_2 content in the residue was 0.776% and 0.965% at feeding pressures of 10 and 40 kPa respectively.

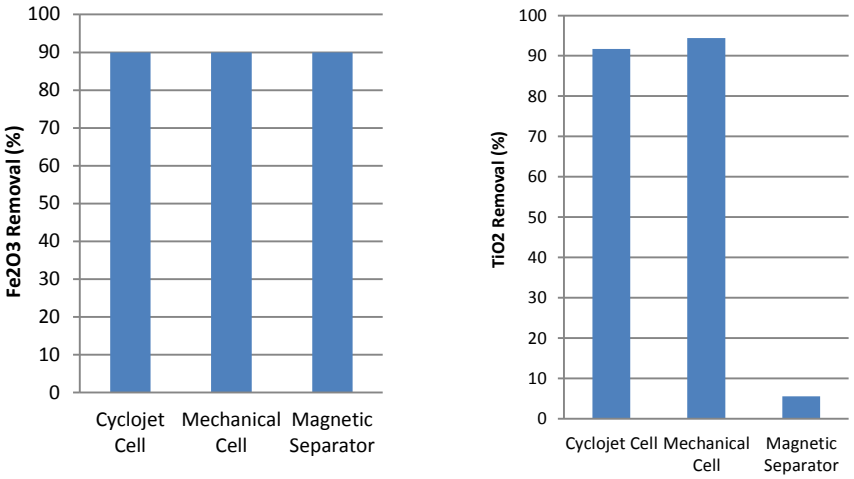

Fig. 5. Comparison of Fe_2O_3 and TiO_2 removal from feldspar by various devices

Table 3. Complete chemical analysis of feed and concentrates obtained from cyclojet, mechanical and magnetic separation

Component	Feed %	Cyclojet Cell Concentrate, %	Mechanical Cell Concentrate, %	Magnetic Sep. Concentrate, %
SiO_2	67.380	67.810	67.920	67.540
Al_2O_3	19.280	19.430	19.550	19.270
Fe_2O_3	0.100	0.010	0.010	0.010
TiO_2	0.360	0.030	0.020	0.340
MgO	0.250	0.010	0.010	0.100
CaO	1.080	0.950	0.940	1.150
Na_2O	10.070	10.310	10.300	9.970
K_2O	0.430	0.210	0.210	0.320
P_2O_5	0.080	0.010	0.010	0.020
MnO	0.010	0.010	0.010	0.010
Cr_2O_3	0.002	0.002	0.002	0.020
Others	0.058	0.060	0.060	0.078
L.O.I.	0.900	1.140	0.980	1.170

4. Conclusion

It is known that the coloring minerals found in feldspar ore can be removed by various methods. It has been observed that 90% of Fe_2O_3 can be removed by the performed flotation and magnetic separation processes, but TiO_2 content can only be removed by flotation. As a result of cyclojet flotation experiments TiO_2 content was reduced from 0.360% to 0.030%, and by magnetic separation TiO_2 content was reduced in a negligible amount down to 0.34%. Similarly, TiO_2 content was reduced down to 0.020% by the conventional flotation cell. On the other hand, all 3 devices showed similar performances in respect to Fe_2O_3 removal. The reason of this situation is that Fe_2O_3 mineral has magnetic sensitivity, but TiO_2 mineral have no magnetic sensitivity or low magnetic sensitivity. It is clearly seen from the results of this study that for the ores containing small amounts of $T\dot{I}O_2$ only magnetic separation is sufficient, but for the ores containing high amount of TiO_2 cyclojet or mechanical cell can be used.

Acknowledgement

The authors would like to give a special thanks to Esan Inc. for the supply of the samples and XRD analyses.

References

ANONYMOUS, 2010, *Feldspar Report*, TMMOB Chamber of Mining Engineers. No.169; ISBN:978-99444-89-905-5.

BAYRAKTAR, I., ERSAYIN, S., GÜLSOY, O.Y., 1998, *Magnetic separation and flotation of albite*, Innovations in Mineral Processing, Atak, Önal & Çelik (eds), Balkema, Rotterdam, ISBN:90-5809-013-2.

BAYRAKTAR, L., ERSAYIN, S., GÜLSOY, Ö.Y., 1997, *Upgrading titanium bearing Na-feldspar by flotation using sulphonates, succinamate and soaps of vegetable oils*, Miner. Eng. 12(1), 1363–1374.

COWBURN, J., HARBORT, G., MANLAPIG, E., POKRAJCIC, Z., 2006, *Improving the recovery of coarse coal particles in a Jameson cell*, Miner. Eng., 19 (6-8), 609–618.

ÇINAR, F., ŞAHBAZ, O., ÇINAR, M., ÖTEKAYA, B.,KELEBEK, Ş., 2007, *A parametric study on Jameson cell flotation of quartz*, XII Balkan Mineral Processing Congress, 10-14 June, Delphi, Greece, 251–256.

DOĞU, I., AROL, A.I., 2004, *Separation of dark-colored minerals from feldspar by selective flocculation using starch*, Powder Technol. 139, 258–263.

El-REHIEM, F.H., ABD EL-RAHMAN, M. K., 2008, *Removal of coloring materials from Egyptian albite ore*, Trans. Inst. Min. Metall., Sect. C. 117(3), 171–174.

GÜNEY, A., ÖNAL, G., ERGUT, Ö., 2002, *Benefication of fine coal by using the free jet flotation system*, Fuel Process. Technol. 15, 141–150.

HACIFAZLIOGLU, H., 2009, *Development of a new flotation machine (cyclojet cell) for flotation of fine coals*, Ph.D.Thesis, Karaelmas University, Zonguldak, Turkey.

HACIFAZLIOGLU, H., TOROĞLU, I., 2008, *Flotation of Bituminous Coal Slimes in the Cyclojet Cell and a Comparison of Cyclojet Cell and Jameson Cell in Terms of Their Flotation Performance*, Min. J. 47(1), 3–12.

KARAGÜZEL, C., ÇOBANOĞLU, G., 2010, *Stage-wise flotation for the removal of colored minerals from feldispathic slimes using laboratory scale Jameson cell*, Sep. Purif. Technol. 74, 100–107.

KANGAL, O., GUNEY, A., 2002, *Beneficiation of low-grade feldispars using free jet flotation*, Miner. Process. Extr. Metall. Rev. 23(3-4), 129–140.

STYRIAKOVAA, I., STYRIAK,I., MALACHOVSKY, P., LOVASA, M., 2006, *Biological, chemical and electromagnetic treatment of three types of feldspar raw materials*, Miner. Eng. 19(4), 348–354.

Physicochem. Probl. Miner. Process. 48(2), 2012, 393−401

www.minproc.pwr.wroc.pl/journal/

Physicochemical Problems of Mineral Processing

ISSN 1643-1049 (print)
ISSN 2084-4735 (online)

Received October 25, 2011; reviewed; accepted January 3, 2012

IMPROVING FLOATABILITY OF TAIXI ANTHRACITE COAL OF MILD OXIDATION BY GRINDING

Wencheng XIA, Jianguo YANG , Yuemin ZHAO, Bin ZHU, Yuling WANG

School of Chemical Engineering and Technology, China University of Mining & Technology, Xuzhou, Jiangsu 221116, China, xiawencheng@cumt.edu.cn, scetyjg@126.com

Abstract. Grinding is widely used in ore size reduction. In this investigation, grinding is proved to be advantageous in improving the floatability of anthracite coal of mild oxidation. FTIR was used to explain changes in the main functional chemical groups of anthracite coal of mild oxidation upon grinding. Improvements of the floatability of four size fractions, namely, +0.25 mm, 0.25-0.125 mm, 0.125-0.074 mm and -0.074 mm, were discussed respectively. The results show that the floatability of anthracite coal of mild oxidation can be improved by 30 minutes grinding. The anthracite coal of mild oxidation can obtain many fresh hydrophobic surfaces by scuffing. Besides, the anthracite coal of mild oxidation can be crushed and/or ground to form fines which also contain many fresh hydrophobic surfaces. Combustible matter recovery of anthracite coal of mild oxidation, ground by 30 minutes, can reach 72.14% with ash content of 8.63%, while combustible matter recovery of original coal is 56.65% with ash content of 9.90%.

keywords: anthracite; oxidation; grinding; floatability; FTIR

1. Introduction

Coal can be oxidized in air easily, i.e. underground, stored in coal bunkers, and even in the process of long distance transport (Huggins and Huffman, 1989). This oxidation process is known as weathering. Coal oxidation processes include three major aspects, i.e. oxygen adsorption, gas release, and heat release (Wang et al., 2003). The heat release causes coal to be oxidized to a further extent. All of these result in the formation of oxygen functional groups, such as carboxyl, phenolic and carbonyl functionalities on the coal surface, which reduce the hydrophobicity of the coal surface by increasing the number of sites that can form hydrogen bond with water molecules. Weathering processes make the coal more difficult to float with oily collectors (Aplan, 1988; Fuerstenau et al., 1992; Fuerstenau and Diao, 1990; Harris et al., 1995; Jia et al., 2000; Laskowski and Miller, 1984). Certainly, the oxidation processes also lead to many changes in the physical composition, besides chemical property, making coal porous and breakable.

http://dx.doi.org/10.5277/ppmp120206

Previous studies were focused on the oxidation mechanism by simulating the oxidation processes and show that the coal oxidation processes are concerned with oxidation temperature, coal particle size, and coal moisture (Chen, 1993; Coward, 1957; Sun, 1954). Oxidation rate decreases with the coal particle size and increases with the coal specific surface (Akgun and Arisoy, 1994; Carras and Young, 1994). The oxidation processes generally occur on the coal particle surface. Therefore, the physical composition and chemical property inside the coal particle change less (Somasundaran et al., 2000). It is generally acknowledged that the oxidation rate is inversely proportional to the degree of coalification (Diao and Fuerstenau, 1992; Schmal, 1989). Flotation tests of difficult-to-float oxidized coal were successfully accomplished by applying a direct coal and flotation reagents contact procedure with appropriate reagents (Ahmed and Drzymala, 2004). Coal stored at coarse size and then ground to fine size before flotation exhibits a higher flotation yield than that stored as fines (Fuerstenau et al., 1994). Recently, attrition has been used in improving the floatability of oxidized surface of anthracite waste coal (Sokolovic et al., 2012). Evidently, grinding generates sufficient fresh surface that minimizes the effects of the external oxidized surface, but grinding process may produce more ultra-fine coal particles, whose sizes are less than 10 micrometers, which are difficult to float (Forbes, 2011). Simultaneously, the ultra-fine coal particles need more flotation agent and the ultra-fine gangue particles adsorb on the coal surface leading to a more hydrophilic coal surface (Huynh et al., 2000; Oats et al., 2010). Optimal grinding time will be determined in this study. Coal particles of different sizes have different flotabilities which change through grinding. In this paper four size fractions, i.e. +0.25 mm, 0.25-0.125 mm, 0.125-0.074 mm and -0.074 mm of floatation concentrates will be compared for ground and original coal. In this regard, the paper investigates the flotation behavior and hydrophobicity of anthracite coal of mild oxidation before and after grinding using flotation. In addition, the Fourier Transform Infrared Spectroscopy (FTIR) analysis is used to explain the changes in the main functional chemical groups of anthracite coal of mild oxidation upon grinding.

2. Experimental method and procedure

In this investigation, dodecane was used as the oily collector and 2-octanol was used as the frother. Coal samples were provided by Taixi Coal Preparation Plant in China. Coal in this plant is stored outside and oxidizes mildly under the air, rain and sunshine. Coal samples were screened to pass 0.5 mm. The flotation tests were conducted in a 1.5 dm^3 XFG flotation cell using 100 g of coal at a pulp density of 6.25% solids. The impeller speed of the flotation machine was 1910 rpm and the airflow rate was 2 dm^3/min. Dodecane collector dose was 5 kg/Mg and 2-octanol frother 1 kg/Mg of coal. In each flotation test, the pulp was first agitated in the flotation cell for 3 min, after which dodecane collector (5 kg/Mg) was added and the pulp conditioned for an additional period of 3-min. 2-octanol frother (1 kg/Mg) was then added and the pulp was conditioned for an additional one minute.

The FTIR spectrum was obtained with KBr pellets prepared with 0.125-0.074 mm anthracite coal of mild oxidation samples (original coal) and the same anthracite coal of mild oxidation samples ground with KBr for an additional time in a mortar. For the FTIR analyses a Perkin Elmer Spectrum 2000 model spectrometer was used and the spectrum was obtained at 2 cm^{-1} resolution, between 4000 and 400 cm^{-1}. It is worth emphasizing that ash content influences the FTIR spectrum. The 0.125-0.074 mm anthracite coal of mild oxidation samples were separated by density separation using a centrifugal extractor with the density fraction of 1.4 kg/dm^3.

Grinding was conducted in a laboratory dry rod mill. Grinding times were 5 min, 10 min, 20 min and 30 min, respectively. The grinding products and flotation concentrate were screened to get four size fractions: +0.25 mm, 0.25-0.125 mm, 0.125-0.074 mm and -0.074 mm. Every size fraction was analyzed to determine parameters such as ash content, combustible matter recovery and yield. Eq. (1) was used to calculate the combustible matter recovery of the flotation experiments:

$$\text{Combustable matter recovery } (\%) = [M_c(100 - A_c)/M_F(100 - A_F)] \; x \; 100, \tag{1}$$

where M_C is weight of the concentrate (%), M_F is weight of the feed (%), A_C is the ash content of the concentrate (%), and A_F is the ash content of the feed (%).

3. Results and discussion

3.1. FTIR spectrum

The FTIR spectra of original and ground coal are showed in Fig. 1. After grinding, the FTIR spectrum shows five main functional chemical groups more than the original coal. The five main functional chemical groups are: 3030 cm^{-1}, 2910 cm^{-1}, 867 cm^{-1}, 797 cm^{-1} and 736 cm^{-1}. Among the five functional chemical groups, 3030 cm^{-1} and 2910 cm^{-1} are aliphatic hydrocarbons which are hydrophobic. Another three functional chemical groups 867 cm^{-1}, 797 cm^{-1} and 736 cm^{-1} indicate the presence of benzene rings which also are more hydrophobic than the oxygen functional groups. Oxygen functional groups detected at 3440 cm^{-1} and 1630 cm^{-1} are shown in Fig. 1. The FTIR image shows that grinding leads to more fresh surface and hydrophobic functional chemical groups on the surface of anthracite coal of mild oxidation than that of original coal. The absorbances of functional chemical groups are widely used for quantitative analysis (Jena et al., 2008; Yuh and Wolt, 1983). The absorbance is concerned with the functional chemical groups' content. Low absorbance is considered as a result of low functional chemical group content. After grinding, the anthracite coal of mild oxidation has low absorbance of the oxygen functional groups (3440 cm^{-1} and 1630 cm^{-1}). Thus, grinding causes anthracite coal of mild oxidation to be more hydrophobic than the original coal.

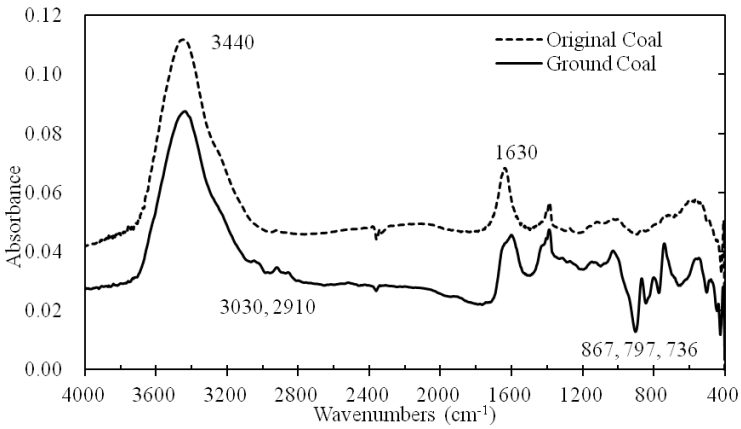

Fig. 1. FTIR spectrum of anthracite coal of mild oxidation before and after grinding

3.2. Size fractions changing

Figure 2 shows that the yield of the +0.25 mm fraction decreases and that of -0.074 mm increases with the grinding time. Middle size fractions (0.25-0.125 mm and 0.125-0.074 mm), should be crushed or ground to be fine, but the yield of the two size fractions increases with the increasing grinding time. It is so because the +0.25 mm size fraction during crushing and/or grinding forms three size fractions, namely, 0.25-0.125 mm, 0.125-0.074 mm and -0.074 mm. As shown in Fig. 3, the +0.25 mm size fraction during crushing or grinding becomes 0.25-0.125 mm, 0.125-0.074 mm and -0.074 mm fractions. Coal particles can be also surface ground and their sizes are less changed, so the size fractions of the coal particles are not changed.

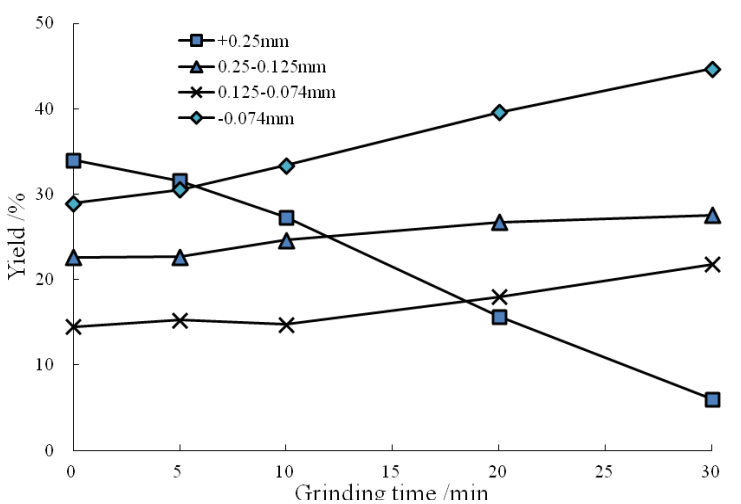

Fig. 2. Yields of size fractions before and after grinding

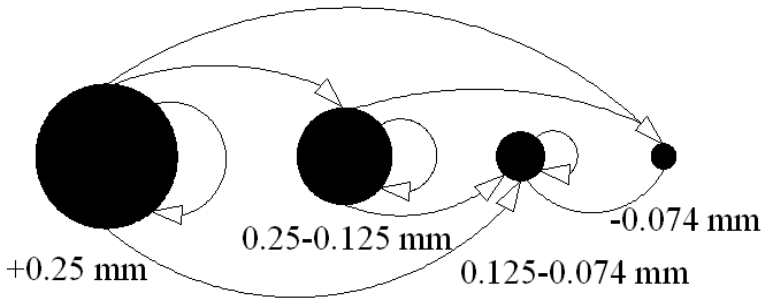

Fig.3. Size fractions changes due to grinding

As shown in Fig. 4, the ash content analysis of the four size fractions shows that the ash content of -0.074 mm decreases with the grinding time. Ash content of the +0.25 mm fraction reaches the highest after 5 min of grinding, and then decreases with the increasing of grinding time. Ash contents of the middle size fractions change less and in a random manner. Ash contents of the four size fractions of original coal decrease with the increasing of size, namely, +0.25 mm < 0.25-0.125 mm < 0.125-0.074 mm < -0.074 mm. Because low ash content coarse coals are crushed and/or ground to be small particles or fines, these small particles or fines make up the loss of middle size factions, so the middle size fractions and fines ash contents go down with the increasing grinding time.

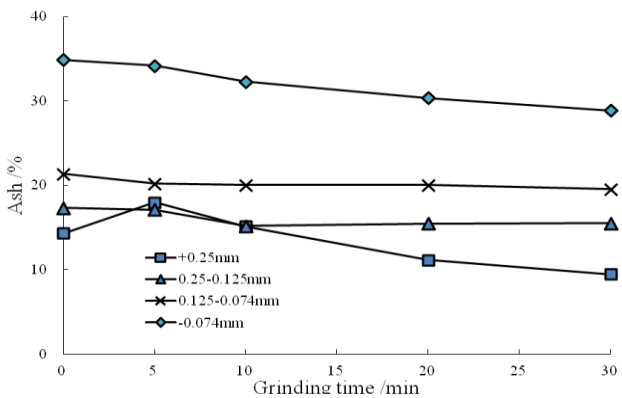

Fig. 4. Ash content of size fractions before and after grinding

3.3. Flotation tests

Figure 5 shows combustible matter recovery of anthracite coal of mild oxidation before and after grinding. The combustible matter recovery in concentrate increases

with the increasing grinding time for grinding time of 20 min and 30 min. The combustible matter recovery of +0.25 mm size fraction reaches the highest value after 20 min of grinding, and recovery after 30 min of grinding is smaller, but both are higher than these after 5 min or 10 min of grinding. The combustible matter recovery of different size fractions, namely, 0.25-0.125 mm, 0.125-0.074 mm and -0.074 mm, increases with the grinding time and is similar when the grinding time is either 20 min or 30 min. From the original coal flotation results, it can be seen that the size fractions, namely, 0.25-0.125 mm, 0.125-0.074 mm and -0.074 mm, have a similar combustible matter recovery, therefore, the size fraction has less effect on the floatability of anthracite coal of mild oxidation particles when the particles size is less than -0.25 mm. However, the combustible matter recovery of the 0.25-0.125 mm, 0.125-0.074 mm and -0.074 mm size fractions is different and becomes higher after grinding. All of these prove that grinding can improve floatability of anthracite coal of mild oxidation.

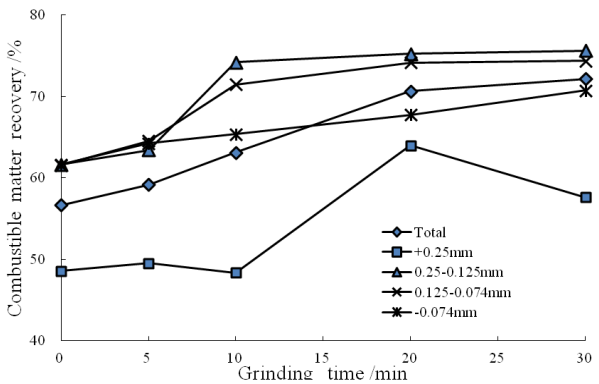

Fig. 5. Combustible matter recovery of size fractions before and after grinding

Figure 5 shows that anthracite coal of mild oxidation after 20 min or 30 min grinding time has higher combustible matter recovery and similar ash content. However, the combustible matter recovery of +0.25 mm size fraction decreases when the grinding time is more than 20 min. It may be explained that long time grinding produces many fines and ultra-fine coal particles which need more flotation agent dose. Ultra-fine gangue particles also adsorb on the coal surface causing the coal surface to be hydrophilic. Coarse coals need more hydrophobic surface for flotation than the middle size particles or fines because greater mass.

Figure 5 shows that the combustible matter recovery of different size fractions, namely, 0.25-0.125 mm, 0.125-0.074 mm and -0.074 mm, are higher than +0.25 mm. This phenomenon proves that the size fraction has a great effect on coal particles flotation, even though the coarse coals have been surface ground. In addition, the combustible matter recovery of size fractions, namely, 0.25-0.125 mm and 0.125-0.074 mm, is higher than -0.074 mm. It proves that fines from the surface of anthracite

coal of mild oxidation are more hydrophilic than small coal particles produced by surface grinding. Maybe the -0.074 mm anthracite coal fraction of mild oxidations is affected less by grinding as grinding has priority in coarse coals.

Figure 6 shows that ash contents of all size fractions first decrease with the increasing of grinding and then become similar when the grinding time is 20 min or 30 min. The ash content of the -0.074 mm size fraction reduces obviously from 19.03% to 13.63%. One of the reasons is that the low ash content of coarse coal particles (with the diameter between 0.5 mm and 0.125 mm) are crushed and/or ground to be fines (with the diameter less than 0.074 mm) which are easily floated.

Anthracite coal of mild oxidation surface has more oxygen functional groups causing the coal surface to be hydrophilic and prevents the coal surface from being covered by oily collectors, making coal difficult-to-float. Grinding is widely used to separate coal from gangue minerals. In addition, grinding can also produce fresh surface having higher hydrophobicity than the oxidized surface. As shown in Fig. 1, the FTIR spectrum indicates that grinding can produce fresh surface. The +0.25 mm coal particles have higher combustible matter recovery after grinding. It proves that grinding can improve the flotability of coarse coal particles. It appears that the floatability of other size fractions, such as 0.25-0.125 mm, 0.125-0.074 mm and -0.074 mm, are also improved by grinding.

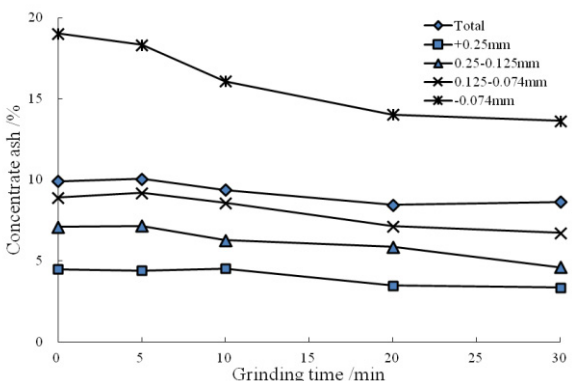

Fig. 6. Ash content of different size fractions of concentrate before and after

Grinding consists of two main processes: surface grinding and crushing, as shown in Fig. 7. Surface grinding changes the coal particle size not too much but has a great effect on the coal particle surface. Crushing changes the coal particle size more and also has the effect on the coal particle surface. Both the surface grinding and crushing produce many fresh hydrophobic areas on the coal surfaces of coal particles. Coal particles are crushed and/or ground to produce small particles and fines. The fines may also acquire many fresh spots as shown in Fig. 7. The original surfaces are more hydrophilic while the fresh surfaces, produced by crushing and/or grinding are more hydrophobic.

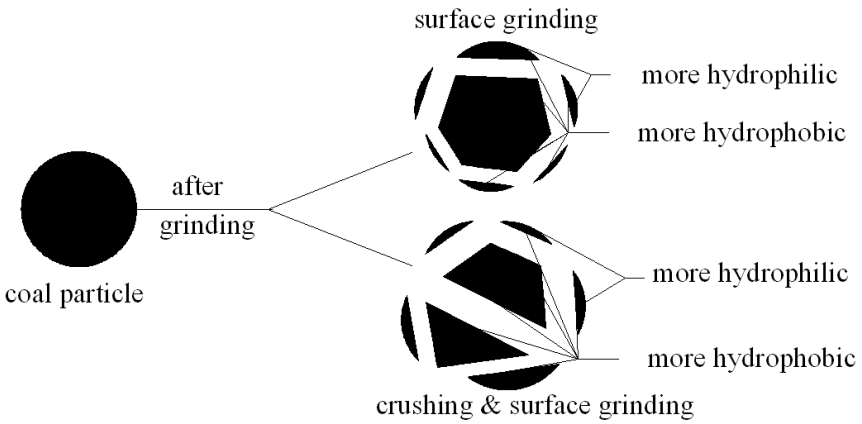

Fig.7. Surface properties changed by grinding

4. Conclusion

Oxidation processes occurring on the coal surface causes coal to be of low flotability. Grinding can be used to improve the floatability of anthracite coal of mild oxidation by producing many fresh surfaces areas. As shown in Fig. 7, grinding can be described as two main processes: surface grinding and crushing. Coal particles can be crushed and/or ground to form small particles or fines, some of which are formerly parts of the surfaces of anthracite coal of mild oxidation particles. These small particles or fines become more hydrophobic. Flotation tests show that the combustible matter recovery of anthracite coal of mild oxidation can research 72.14% with ash content of 8.63% by 30 minutes grinding, while that of original coal recovery is 56.65% with ash content of 9.90%. It is evident that the floatability of anthracite coal of mild oxidation can be improved by grinding.

Acknowledgements

This work was supported by the Fund from the Natural Science Foundation of China for Innovative Research Group (Grant 50921002).

References

AHMED, H.A.M., DRZYMALA, J., 2004, *Effect of flotation procedure and composition of reagents on yield of a difficult-to-float coal*. Physicochem. Probl. Miner. Process. 38, 53–63.

APLAN, F.F., 1988, *How the nature of raw coal influences its cleaning*. In: Klimpel, R.R., Luckie, P.T. (Eds.), Industrial Practice of Fine Coal Process. SME, Littleton, CO:99–111.

AKGUN, F., ARISOY, A., 1994, *Effect of particle size on the spontaneous heating of a coal stockpile*. Combust Flame 99, 137–46.

COWARD, H.F., 1957, *Research on spontaneous combustion of coal in mines—a review*. Research Report 142, Great Britain: Safety in Mines Research Establishment.

CHEN, X.D., STOTT, J.B., 1993, *The effect of moisture content on the oxidation rate of coal during near-equilibrium drying and wetting at 50˚C*, Fuel 72, 787–792.

CARRAS, J.N., YOUNG, B.C., 1994, *Self-heating of coal and related materials: models, application and test methods*. Prog. Energy Combust. Sci. 20, 1–15.

DIAO, J., FUERSTENAU, D.W., 1992, *Characterization of coal oxidation and coal wetting behavior by film flotation.* Coal Preparation 10, 1–17.

FORBES, E., 2011, *Shear, selective and temperature responsive flocculation: A comparison of fine particle flotation techniques*. Int. J. Miner. Process. 99, 1–10.

FUERSTENAU, D.W., SASTRY, K.V.S., HANSON, J .S., NARAYANAN, K.S., SOTILLO, F., DIAO, J. et al., 1992, *Coal Surface Control for Advanced Fine Coal Flotation*, Final Report.

FUERSTENAU, D.W., DIAO, J., 1990, *Surface Properties of Coal and Their Role in Coal Beneficiation*, Final Report.

FUERSTENAU, D.W., DIAO, J., HANSON, J.S., SOTILLO, F., SOMASUNDARAN, P., 1994, *Effect of weathering on the wetting behavior and flotation response of coal*. In: Blaschke, W.S., Gordon, Breach (Eds.), New Trends in Coal Preparation Technologies and Equipment, 747–753.

HUGGINS, F.E., HUFFMAN, G.P.,1989, *Coal weathering and oxidation: the early stages.* In: Nelson CR, editor. Chemistry of coal weathering, vol.14, 33–60. Elsevier, Amsterdam.

HARRIS, G.H., DIAO, J., FUERSTENAU, D.W., 1995, *Coal flotation with nonionic surfactants*. Coal Preparation 16, 135–147.

HUYNH, L., FEILER, A., MICHELMORE, A., RALSTON, J., JENKINS, P., 2000, *Control of slime coatings by the use of anionic phosphates: a fundamental study*. Miner. Eng. 13(10-11), 1059–1069.

JIA, R., HARRIS, G.H., FUERSTENAU, D.W., 2000, *An improved class of universal collectors for the flotation of oxidized and/or low-rank coal*. Int. J. Miner. Process.58, 99–118.

JENA M.S., BISWAL S.K., RUDRAMUNIYAPPA M.V, 2008,. *Study on flotation characteristics of oxidised Indian high ash sub-bituminous coal.* Int. J. Miner. Process. 87, 42–50.

LASKOWSKI, J.S., MILLER, J.D., 1984, *New reagents in coal flotation*. In: Jones, M.J., Oblatt, R. (Eds.), Reagents in the Mineral Industry. The Institution of Mining and Metallurgy, 145–154.

SOMASUNDARAN, P., ZHANG, L., FUERSTENAU, D.W., 2000, *The effect of environment, oxidation and dissolved metal species on the chemistry of coal flotation*. Int. J. Miner. Process. 58, 85–97.

SUN, S.C., 1954, *Effects of oxidation of coals on their flotation properties*. Trans. Am. Inst. Min. Metall. Eng. April, 396–401.

SCHMAL, D., 1989, *Spontaneous heating of stored coal*. In: Nelson C.R., (Ed.). Chemistry of coal weathering, 133–215. Elsevier, Amsterdam.

SOKOLOVIC, J.M., STANOJLOVIC, R.D., MARKOVIC, Z.S., 2012. *Activation of oxidized surface of anthracite waste coal by attrition*. Physicochem. Probl. Miner. Process. 48(1), 5–18.

WANG H. H., DLUGOGORSKI, B. Z., KENNEDY, E. M., 2003, *Coal Oxidation at Low Temperatures: Oxygen Consumption, Oxidation Products, Reaction Mechanism and Kinetic Modeling*, Progress in Energy and Combustion Science, 29, 487–513.

OATS, W.J., OZDEMIR, O., NGUYEN, A.V., 2010, *Effect of mechanical and chemical clay removals by hydrocyclone and dispersants on coal flotation*. Miner. Eng. 23, 413–419.

YUH, S.J., WOLT, E.E., 1983, *FTIR studies of potassium catalyst treated gasified coal chars and carbon*. Fuel 62, 252–255.

Physicochem. Probl. Miner. Process. 48(2), 2012, 403−412

www.minproc.pwr.wroc.pl/journal/

Physicochemical Problems of Mineral Processing

ISSN 1643-1049 (print)
ISSN 2084-4735 (online)

Received July 29, 2011; reviewed; accepted October 15, 2011

HYDROLYSIS OF SILICA SOURCES: APS AND DTSACl IN MICROENCAPSULATION PROCESSES

Krzysztof SZCZEPANOWICZ* , Grazyna PARA*, Aud M. BOUZGA, Christian SIMON**, Juan YANG**, Piotr WARSZYNSKI***

* Jerzy Haber Institute of Catalysis and Surface Chemistry, Polish Academy of Sciences, Niezpominajek st. 8, Krakow 30-239, Poland, ncszczep@cyf-kr.edu.pl

** SINTEF Material and Chemistry, Forskningsveien 1, NO-0314 Oslo, Norway

Abstract. The process of formation of silica shells around emulsion droplets was investigated. The ^{1}H-NMR spectroscopy was applied to follow the silica shell formation around emulsion droplets by hydrolysis and condensation of selected silanes in the emulsion system. (3- aminopropyl) triethoxysilane (APS) and dimethyloctadecyl [3-(trimethoxysilyl) propyl] ammonium chloride (DTSACl) were used as silica sources in microencapsulation process. The NMR analysis revealed strong dependence of the hydrolysis reaction rate on pH. Obtained information allowed selecting the optimal conditions for the formation of the capsules with silica shells. The obtained capsules' suspensions were stable for several weeks.

keywords: encapsulation, emulsions, silica shells, capsules, ^{1}H -NMR

1. Introduction

Microencapsulation can be defined as a process in which colloidal particles or droplets are being enclosed in inert shells of various materials to obtain capsules (Swapan, 2006). Encapsulation has a potential to improve the compatibility of lipophilic, poorly water-soluble or even water-insoluble compounds with aqueous media and it can protect active molecules from the negative effect of external environment. The development of the microencapsulation technology started with introduction of capsules containing dyes, which were incorporated into paper for copying purposes and replaced carbon paper (Schleicher and Green, 1956). Since then the number of processes used to produce microcapsules has continued to grow and the development of functional micro or nano-containers is currently one of the main topics in pharmaceutical research. In particular, nanocapsules can be used in specific drug delivery system as they can penetrate the cell membrane. Moreover they can be functionalized to achieve "intelligent targeting", i.e. delivery to the specific cells or organs (Donath and Moya, 2002; Radtchenko and Giersig, 2002; Shchukin and

http://dx.doi.org/10.5277/ppmp120207

Radtchenko, 2003; Shchukin and Sukhorukov, 2004; Georgieva and Moya, 2004; Sukhorukov and Dahne, 2000; Caruso and Fiedler, 2000; Schüler and Caruso, 2001). Application of mini- or micro-emulsion with silica sources as cores opens the possibility of formation of novel, oil core microcapsules with hydrolyzed silica shells with good control of their size (Grigoriev and Bukreeva, 2008; Szczepanowicz and Hoel, 2010) and functionality due to easy modification of the shell.

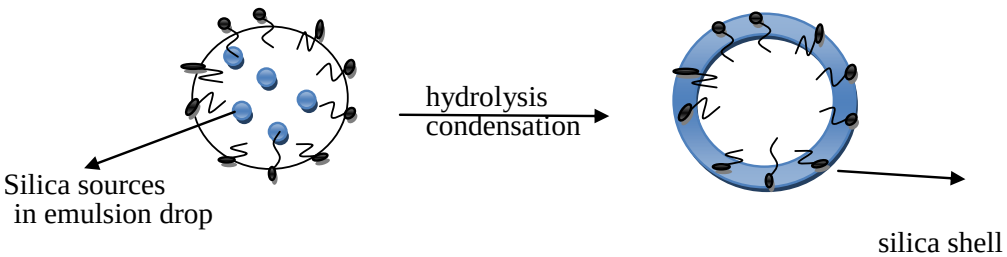

Fig. 1. Scheme of formation microcapsules with silica shells

In our previous work we have described the method of formation of emulsions containing silanes derivatives (Szczepanowicz and Dronka-Gora, 2009) for microencapsulation process, which is schematically presented in Fig. 1. The silanes undergo hydrolysis and condensation on the emulsion drop surface that leads to formation of a silica shell around liquid or semi-liquid core. We used APS and DTSACl as silica sources in emulsions of chloroform in water. The aim of our present work was to investigate the kinetics of the process of silica shell formation around emulsion droplets. We investigated the hydrolysis reaction of APS and DTSACl in chloroform emulsions systems in order to determine the conditions favorable for shell formation. The general scheme of polymerization reaction (hydrolysis and condensation) of silanes derivatives (alkoxysilanes) occurring at the interface and leading to silica shell formation is presented in Fig. 2 (Artaki and Bradley, 1985; Brinker and Scherer, 1990).

There are many works concerning the kinetics of TEOS (tetraethylorthosilicate) hydrolysis during the formation of monosize silica particles in the literature, but there are no reports concerning APS and DTSACl enclosed in emulsion systems. The following methods were used to determine the concentration of TEOS: ^{29}Si NMR (Bogush and Zukoski, 1991; Bailey and Mecartney, 1992), ^{13}C NMR (van Blaaderen and Geest, 1992) and Raman spectroscopy (Harris and Brunson, 1990; Matsoukas and Gulair, 1988). In order to study the kinetics of TEOS hydrolysis, Byers and Harris (1987) used gas chromatography for determining the concentration of ethanol, which is co-product of the reaction. Kinetic studies of the hydrolysis and condensation of TEOS were performed also by Chen (1996). That author determined concentration of TEOS by means of gas chromatography and conductometry and showed that both hydrolysis of TEOS and condensation of $Si(OH)_4$ are the first order reactions.

Relationships of the hydrolysis and condensation rate constants with reaction condition variables, such as temperature and H_2O concentration were also determined. In our study the progress of the shell formation by hydrolysis of silica sources was observed using NMR spectroscopy. Since we had found ^{29}Si-NMR spectra ambiguous, we proposed an alternative way to characterize the hydrolysis of silica sources in emulsion system by monitoring its progress by analysis of the ^{1}H-NMR signals from un-hydrolyzed APS and DTSACl and of the NMR spectra of co-products of their hydrolysis. Ethanol is a co-product of the hydrolysis of APS, while methanol is co-product of the reaction of DTSACl.

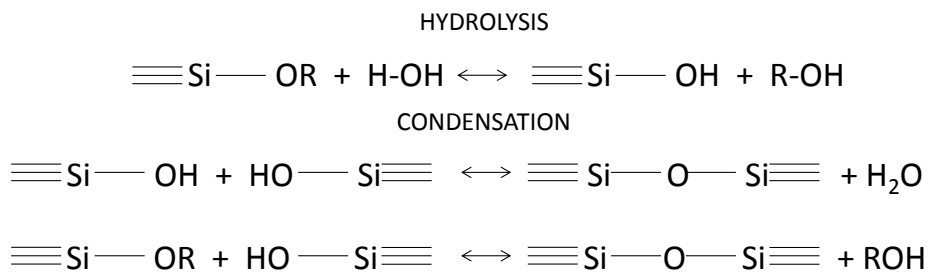

Fig. 2. The scheme of hydrolysis and condensation reactions of silanes (R is an alkyl group)

2. Materials and methods

APS ((3-aminopropyl)triethoxysilane), DTSACl (dimethyloctadecyl[3-(trimetho xysilyl)propyl]ammonium chloride), Tween 80 (polyoxyethylenesorbitan monooleate) were purchased from Sigma-Aldrich Co. Chloroform, HCl, NaOH were purchased from POCh SA. Water (Direct Q3 UV system, Millipore SA) was used for the preparation of solutions. All materials were used without further purification. Structural formulas of silica sources are shown in Fig. 3.

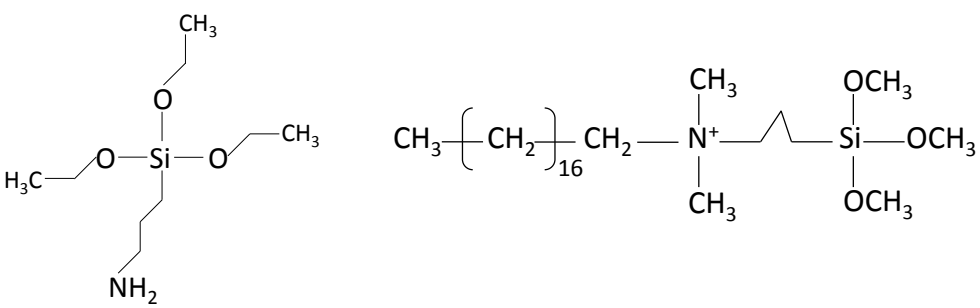

(a) (b)

Fig.3. Structural formulas of silica sources applied in our studies a) APS b) DTSACl

2.1. Emulsion preparation

The emulsions containing silanes (APS and DTSACl), and when it was necessary stabilized by addition of Tween 80, were prepared according to procedure described before (Szczepanowicz and Dronka-Gora, 2009) by continuous mixing of all components using magnetic stirrer.

2.2. Droplets size analysis

Size (hydrodynamic diameter) of emulsion droplets were determined by DLS (Dynamic Light Scattering) using Zetasizer Nano ZS from Malvern Instruments Ltd. with the detection angle of 173^{o} in optically homogeneous square polystyrene cells. Measurements of the average size of emulsion droplets were performed at 298 K. Each value was obtained as average from three runs with at least 10 measurements.

2.3. Zeta potential measurements

The zeta potential of emulsion droplets was measured by the microelectrophoretic method using Malvern Zetasizer Nano ZS apparatus. Each value was obtained as an average from three subsequent runs of the instrument with at least 20 measurements. The zeta potential of capsules was measured in 0.015M NaCl.

2.4. ^{1}H-NMR spectroscopy

NMR-spectroscopy was applied to characterise the hydrolysis of the silica sources in emulsion systems. Spectra were obtained using a Varian VXR S 300 MHz and Varian GEMINI 300 MHz instruments. The volume of 0.7 ml of the solution was used in the NMR-tube. C_6D_6 in a capillary was used to lock the instrument. First spectre were taken 15 minutes after preparing of the sample.

3. Results and discussion

The emulsions were prepared by mixing all components (water with surfactant and chloroform with silica sources) using magnetic stirrer. Figure 4 shows size distributions of emulsions drops containing 20% of APS in chloroform stabilized by Tween 80 with various oil to surfactant ratios. As it can be seen, quite monodisperse microemulsions with the average drop size of 20, 50 and 100 nm and zeta potential of +15 mV were obtained. Therefore, by changing the proportion between oil phase (chloroform) and surfactant it was possible to vary the average size of emulsion drops.

Because DTSACl exhibits strong surface activity as it was demonstrated before (Szczepanowicz and Dronk-Gora, 2009), lowering the interfacial tension between chloroform and water below 5 mN/m at the concentration 10^{-4} mol dm^{-3}, emulsions containing various amounts of DTSACl in chloroform were prepared without any additional surfactant. It is advantageous for biomedical application as in that way the amount of free surfactant, which can be toxic to cells, should be minimized. Figure 5

presents the example of the size distribution of emulsion drops obtained using the ratio between chloroform and DTSACl equal to1:1. The average size of emulsion droplets was 10 nm and their zeta potential was +22 mV. It can be seen that quite monodisperse emulsions can be obtained with this surface active silica source contained in the non-aqueous phase.

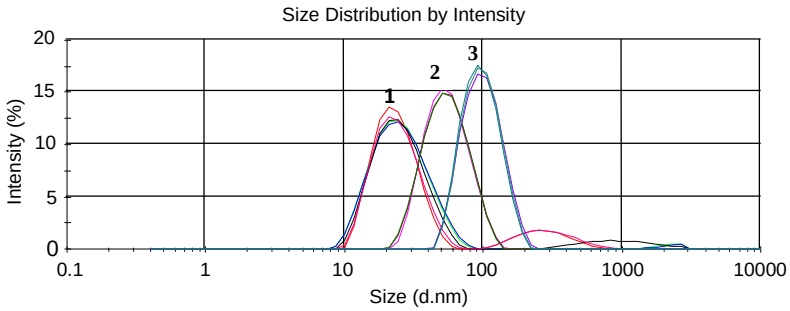

Fig. 4. Size distributions of emulsions - 20% APS in chloroform/Tween 80/water with various ratios between oil and surfactant: for 20 nm - 1:1, 50 nm – 3:1, 100 nm – 5:1.

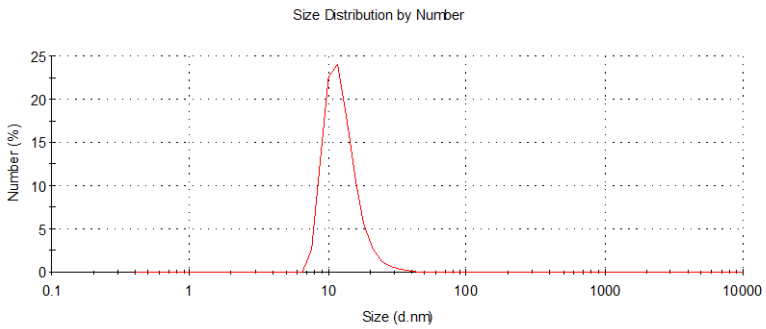

Fig. 5. Chloroform/DTSACl/water emulsions with the average drop size 10nm

NMR-spectroscopy was applied to characterise the hydrolysis of the silica sources in emulsion systems. However, since ^{29}Si-NMR spectra had been ambiguous, we proposed an alternative approach. The progress of the reaction was monitored by analysis of the ^{1}H-NMR signals from un-hydrolyzed APS/DTSACl and of ^{1}H-NMR spectra of co-products of their hydrolysis. Ethanol is a co-product of the hydrolysis of APS, while methanol is co-product of reaction of DTSACl. Progress of reaction was monitored at three conditions: basic (pH~10), acidic (pH~3) and natural (without any pH regulation). The spectra were taken immediately after the preparation of emulsion. In the ^{1}H-NMR spectra of the emulsion containing APS the quadruplet at 3.87 ppm was identified to belong to $–CH_3$ group from APS, the triplet at 1.26 ppm to $–CH_2$ group from APS and the triplet at 1.21 ppm to $–CH_2$ group from ethanol. Signals from

unhydrolyzed APS were missing in spectra regardless of hydrolysis conditions, whereas ones corresponding to the ethanol were visible for all conditions studied, which means that hydrolysis of APS in the emulsion system was very fast (Fig. 6). The time needed to prepare emulsions was always longer than time of the hydrolysis reaction so APS was fully hydrolyzed.

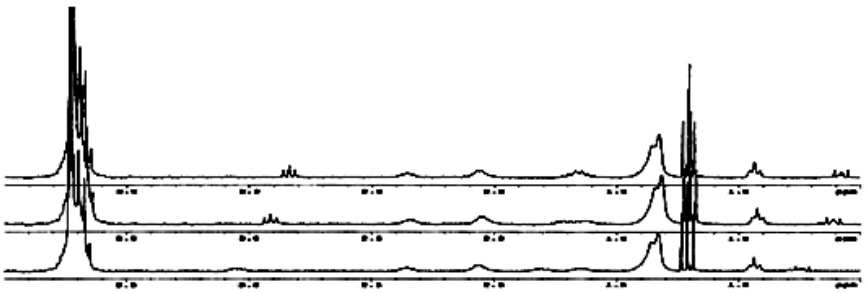

Fig. 6. The 1H-NMR spectra of emulsions containing APS. From the top: basic, natural, acidic

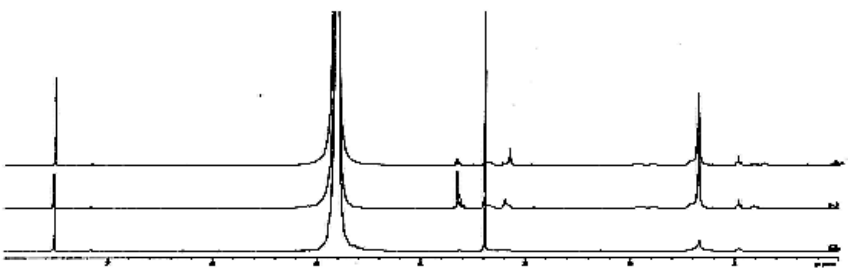

Fig. 7. The 1H -NMR spectra of emulsions containing DTSACl. From the top: acidic, natural, basic

In the case of DTSACl a convenient way to characterize the progress of hydrolysis was the analysis of the ^{1}H-NMR peak at 3.6 ppm from –O-CH_3 groups in DTSACl and the peak at 3.4 ppm of –CH_3 group from methanol. During the course of hydrolysis reaction the integrals of peaks from –O-CH_3 group in DTSACl decreased and integrals of methanol peaks increased. The kinetics of the reaction revealed strong dependence of its rate on pH of the emulsion. In the basic conditions (pH 10) hydrolysis was very fast, since the signal from DTSACl was not visible in the first spectra taken just after the sample preparation. In the natural and acidic conditions hydrolysis reaction was much slower (Fig. 7). In the acidic conditions (pH 3) no changes in spectra were observed even after 18 hours after sample preparation (see Fig. 8). Results obtained from NMR measurements of hydrolysis rate are collected in Table 1. This information allows selecting the optimal conditions for the formation of capsules with silica shells, in which hydrolysis of selected organosilanes is favorable. On the other hand it was found that DTSACl under the natural conditions (pH 6) was

almost fully hydrolyzed after 24 hours (Fig. 9). After two weeks, gradual growth of the emulsion containing APS in natural condition was observed due to continuing condensation of silica and thickening of the silica shell. The example of growth of the emulsion drops is illustrated in Fig. 10.

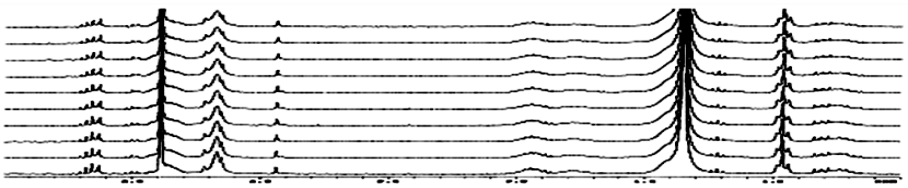

Fig. 8. The ^{1}H-NMR spectra of emulsions containing DTSACl in acidic conditions, sample has been tested over night with 1 hour period between spectra

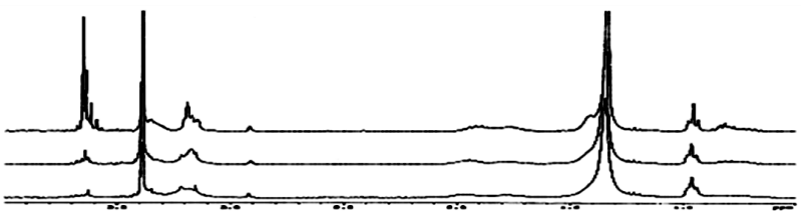

Fig. 9. The 1H -NMR spectra of emulsions containing DTSACl in natural condition, spectra taken just after preparing (top) after 3 hours (middle) and after 24 hours (bottom)

Table 1. Summary of results obtained from NMR measurements of hydrolysis of selected silanes

	APS	DTSACl
Acidic	fast	Slow (>12 days)
Neutral	fast	c.a. 24 h
Basic	fast	fast

One can see that the increase of the average size of the emulsion's drops is not accompanied by significant broadening of the size distribution. Thus, one can assume that the increase of the size is caused by the silica condensation on emulsion's drops instead of coalescence (or aggregation) of the emulsion. In the case of emulsion containing and stabilized by DTSACl, after half an hour in the alkaline conditions, growth of emulsion's drops was observed as it is illustrated in Fig. 11. Since that growth was not observed in acidic condition, we assumed that it was the result of silica condensation and shell thickening following its formation due to hydrolysis.

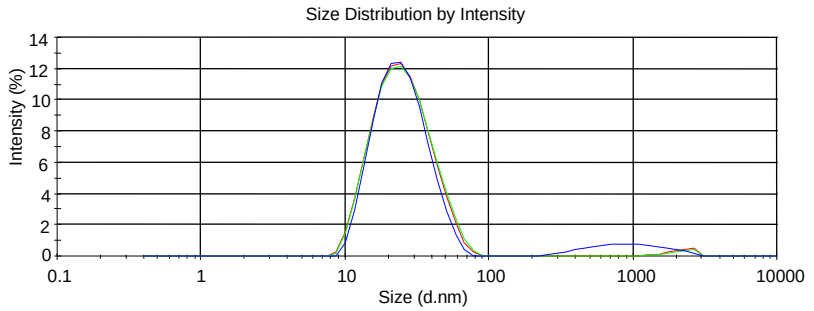

(a)

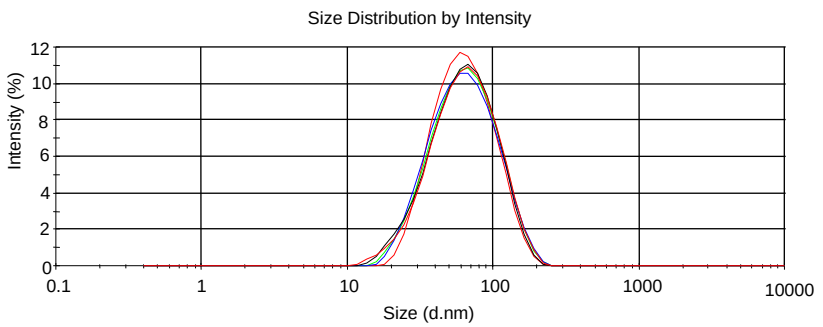

(b)

Fig. 10. Size distributions of emulsions - 20% APS in chloroform/Tween 80/water: (a) before and (b) after hydrolysis and condensation

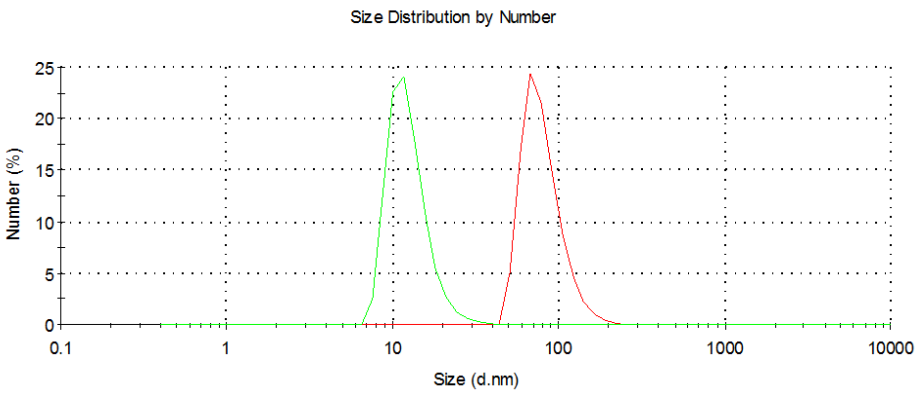

Fig. 11. Size distribution of emulsions - chloroform/DTSACl/water a) before (green line) and b) after hydrolysis and condensation (red line)

4. Conclusions

Chloroform solutions of silane derivatives APS or DTSACl were used as oil phase to prepare microemulsions, which play the role of cores for nanocapsules with silica shells. The size of obtained emulsion droplets ranged from 10 to 100 nm. The ^{1}H-NMR spectroscopy was applied to follow the silica shell formation around obtained emulsion droplets by the hydrolysis of silanes. The results revealed some dependence of the hydrolysis reaction rate on pH. In the case of the emulsion containing APS and stabilized by Tween 80, the rate was fast in all pH conditions studied, i.e., APS was fully hydrolyzed. On the other hand in the case of emulsion containing surface active DTSACl, the rate of its hydrolysis was strongly pH dependent - fast in the alkaline conditions, slow in acidic ones. The obtained information concerning the hydrolysis rate allows selecting the optimal conditions for the formation of capsules with silica shells. Gradual growth of the emulsion drop size observed under the conditions of fast hydrolysis, which was not accompanied by significant broadening of the size distribution by coalescence (or aggregation), was attributed to the silica condensation on emulsion's drops surface and shell thickening. Obtained nanocapsules with silica shells can be used for encapsulation and further surface modification (e.g. by layer-by-layer adsorption of polyelectrolytes).

Acknowledgements

The work was financed by MNiSW 'JUVENTUS' grant.

References

ARTAKI, F., BRADLEY, M., ZERDA, T.W., JONAS, J., 1985, *NMR and Raman study of the hydrolysis reaction in sol-gel process*. J. Phys. Chem. 89, 4399−4404.

BAILEY, J.K., MECARTNEY, M.L., 1992, *Formation of colloidal silica particles from alkoxides*. Colloids Surf. 63, 151−161.

BOGUSH, G.H., ZUKOSKI, I.V., 1991, *Studies of the kinetics of the precipitation of uniform silica particles through the hydrolysis and condensation of silicon alkoxides*. J. Colloid Interface Sci. 142, 1−18.

BRINKER, C.J., SCHERER, G.W., 1990, Eds. Sol-Gel Science; Academic Press: San Diego, p 108.

BYERS, C.H., HARRIS M.T., 1987, *Controlled microcrystalline growth studies by dynamic laser-light-scattering methods*. Ind. Eng. Chem. Res., 26, 1916−1923.

CARUSO, F., FIEDLER, H., 2000, *Assembly of Beta-Glucosidase Multilayers on Spherical Colloidal Particles and Their use as Active Catalysts*. Colloids Surfaces A: Physicochem. Eng. Aspects 169, 287−293.

DONATH, E., MOYA, S., 2002, *Hollow polymer shells from biological templates: Fabrication and potential applications*. Chem-Eur I vol. 8, (23) 5481−5485.

GEORGIEVA, R., MOYA, S.E., 2004, *Permeability and Conductivity of Red Blood Cell Templated polyelectrolyte Capsules Coated with Supplementary Layers*. Langmuir 20,1895−1900.

GRIGORIEV, D.O., BUKREEVA, T., 2008, *New method for fabrication of loaded micro- and nanocontainers: Emulsion encapsulation by polyelectrolyte layer-by-layer deposition on the liquid core.* Langmuir 24, 999−1004.

HARRIS, M.T., BRUNSON, R.R., 1990, *The base-catalyzed hydrolysis and condensation reaction of dilute and concentration TEOS solutions*. J. Non-Cryst. Solids 121, 397−403.

MATSOUKAS, T., GULAIR, E., 1988, *Dynamics of growth of silica particles from ammonia-catalyzed hydrolysis of tetraethylorthosilicate*. J. Colloid Interface Sci. 124(1), 252−261.

RADTCHENKO, I.L., GIERSIG, M., 2002, *Inorganic particle synthesis in confined micron-sized polyelectrolyte capsules.* Langmuir vol. 18, (21) 8204−8208

SCHLEICHER, L., GREEN, B.K., 1956. US Patent 2730456

SCHÜLER, C., CARUSO, F., 2001, *Decomposable Hollow Biopolymer Capsules.* Biomacromolecules, 2, 921−926

SHCHUKİN, D.G., RADTCHENKO, I.L., 2003, *Synthesis of nanosized magnetic ferrite particles inside hollow polyelectrolyte capsules.* J. Phys. Chem. B. 107(1), 86−90

SHCHUKIN, D.G., SUKHORUKOV, G.B., 2004, *Fabrication of fluorescent rare earth phosphates in confined media of polyelectrolyte microcapsules.* J. Phys. Chem. B. 108 (50), 19109−19113.

SHENG-LI, CHEN, 1996, *Kinetics of Formation of Monodisperse Colloidal Silica Particles through the Hydrolysis and Condensation of Tetraethylorthosilicate*. Ind. Eng. Chem. Res. 35, 4487−4493.

SUKHORUKOV, G., DAHNE, L., 2000, *Controlled precipitation of dyes into hollow polyelectrolyte capsules based on colloids and biocolloids*. *Adv mater* 12(2), 112−115.

SWAPAN K.G., 2006, *Functional Coatings by Polymer Microencapsulation.* Wiley-vch Verlag GmbH & Co. KGaA, Weinheim

SZCZEPANOWICZ, K., DRONKA-GORA, D., 2009, *Chloroform Emulsions Containing TEOS, APS and DTSACl as Cores for Microencapsulation*. Procedia Chem. 1, 1576−1583.

SZCZEPANOWICZ, K., HOEL, H.J., 2010, *Formation of Biocompatible Nanocapsules with Emulsion Core and Pegylated Shell by Polyelectrolyte Multilayer Adsorption*. Langmuir, 26(15), 12592–12597.

VAN BLAADEREN, A., VAN GEEST, J., 1992, *Monodisperse colloidal silica spheres from tetraalkoxysilanes: Particle formation and growth mechanism*. J. Colloid Interface Sci, 154(2), 481−501.

Physicochem. Probl. Miner. Process. 48(2), 2012, 413−424

www.minproc.pwr.wroc.pl/journal/

Physicochemical Problems of Mineral Processing

ISSN 1643-1049 (print)
ISSN 2084-4735 (online)

Received January 5, 2012; reviewed; accepted March 1, 2012

HEAT TREATMENT OF NATURAL DIATOMITE

Suzan S. IBRAHIM*, Ali Q. SELIM**

*Central Metallurgical R&D Institute CMRDI, P.O. Box 87, Helwan, Egypt, suzansibrahim@gmail.com
** Geology Dept., Faculty of Science, Beni Suif Univ., Egypt

Abstract. Heat treatment of an Egyptian natural diatomite was performed at different temperatures (600, 900, 1000, 1100, and 1200ºC). The samples were heated from room temperature 23±1ºC to the appointed temperature at a rate of 20^{o}C/ min, and kept at that temperature for 5 hour. The heat treated samples were examined by X-ray diffraction, scan-electro-microscopy, and other physical characters like sample color, texture, and weight reduction. Results showed that heat treatment of natural diatomite caused different forms of mineral modification and transformation to another mineral. At 1200ºC a new nano-metric silicate material was formed. These changes were mainly depending upon the treated temperature, diatomite genera, and the accompanied gangue minerals as well.

keywords: natural diatomite, heat treatment, porous structure

1. Introduction

Diatoms are belonging to the diploid eukaryotic unicellular algae (Bacillariophyta) with wide ranges of structures and shapes. Each of these has its own distinct shape and size (Sterrenburg et al., 2007). The outstanding feature of diatoms is their siliceous "shell" or frustule, which can be preserved for millions of years. In this manner, fossil deposits of microscopic diatom shells were built up as thick layers of "diatomaceous earth" or diatomite which could be extending over several miles (Sterrenburg et al., 2007).

Diatomite is formed by the closest packing of hydrous SiO_2 spheres and is classified as opal-A. Opaline minerals have been categorized into three general groups, including Opal-A, Opal-C, and Opal-CT, according to crystallinity and crystal structure (Jones and Segnit, 1971). Opal-A is predominantly amorphous. Opal-CT is semi-crystalline comprising of crystalline regions of cristobalite and tridymite, where opal-C is a well-ordered form of the silicate predominantly in the cristobalite form (Jones and Segnit, 1971). Diatomaceous silica, the amorphous silica with opal-A structure, exists in the form of frustule in the natural mineral assemblage of diatomite. Since the diatomaceous silica has properties such as high porosity with strong absorbability and excellent thermal resistance, diatomite has been widely used as filter aid, catalytic support, biological support, functional filler, and adsorbent, etc.

http://dx.doi.org/10.5277/ppmp120208

(Erdogan et al., 1996; Ibrahim and Selim, 2011; Li et al., 2003; Powers and Ibrahim, 2007; Vasconclos et al., 2000).

As is well known, the silica surface consists of siloxane bridges and different types of hydroxyl groups (i.e. silanols), which are key reactive sites for various surface reactions: wetting, dispersion in solutions, adsorption and surface modification (e.g. silylation) etc. (Ek et al., 2001; Takei et al., 1999). The distribution and evolution of different types of silanols and siloxanes largely depend on thermal treatment condition, as well as on ambient humidity and storage time (Bronnimann et al., 1988).

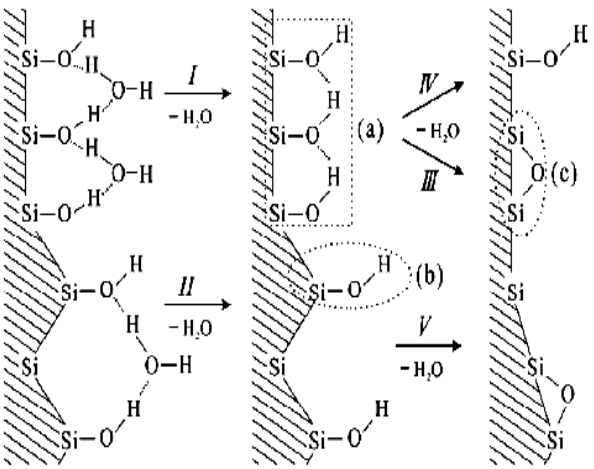

Fig. 1. The hydroxyl structure and the dehydration process of diatomaceous silica
(a) H-bonded silanols, (b) isolated silanols, (c) siloxane (Yuan et al., 2004)

At room temperature, both of the isolated and H-bonded silanols associate with the physically adsorbed water by hydrogen bond. After calcinations treatment, physically adsorbed water will be desorbed from the silanols, and the silanols will condense with the increase of temperature. Generally, the H-bonded silanols condense more easily than the isolated ones (Yuan et al., 2004). A model is proposed to elucidate the hydroxyl structure and the dehydration process of diatomite. At room temperature, both the isolated and H-bonded hydroxyl groups on the diatomite surface are H-bonded with physically adsorbed water. With the increase of temperature of 200 - 1000ºC, five dehydration processes are assumed, shown as scheme *I* to *IV* in Fig. 1 (Yuan et al., 2004).

At first, the desorption of water results in the decrease of intensity of the H_2O band and the appearance of the 3739 cm^{-1} shoulder band corresponding to the silanols (Fig. 1, *I* and *II*). With continuous desorption of water and the exposure of more and more silanols, the band becomes stronger with position progressively moving to higher wave number, and near the position of band corresponding to isolated silanol. This reflects that some strongly H-bonded silanols begin to condense to form siloxane

bridges (Fig.1, scheme *III* and *IV*) while most of the isolated silanols have not condensed. This shows that for the H-bonded silanol in diatomaceous silica, the weaker the hydrogen bond is, the closer its band nears that of isolated silanol, and more difficult the occurrence of condensation is. At 1000ºC, the intensity of 3745 cm^{-1} band reached its maximum, indicating the amount of isolated silanols reached the maximum. The asymmetry of this band toward the lower wave number reflects that there are some weakly H-bonded silanols remain on the surface (Yuan et al., 2004).

2. Experimental

A natural diatomite sample from Kom Osheem deposit, Egypt was subjected to heat treatment at temperatures from 600 to 900, 1000, 1100, and 1200ºC. Soaking time was kept constant at 5 hours through all experiments. The tests were carried out in programmable furnace, with a heating rate from a room temperature to the appointed temperature of 20^{o}C/min. Natural diatomite means that the crude ore was subjected to size disintegration and classified to remove extraneous matter coarser than 45 micron.

Phase analysis of the treated samples was applied using X-ray diffractmeter model "pw 1010" with CuKα radiation under target voltage 40kV and current 30 mA in a scanning rate of 5º 2θ/min. Elemental chemical analysis was conducted using "Perkin-Elmer Analyst 200" atomic absorption. Thermal analysis of the sample was carried out using "Netzsch STA 409 C/CD" unit. Particle size analysis of the sample was carried out using the 'Warman" cyclosizer. Structure skeleton of different samples have been microscopically viewed using scanning electron microscope (SEM) of the type JEM-1230, JEOL.

3. Results and discussion

3.1. Sample characterization

Phase analysis of the sample is illustrated in Fig. 2. Semi quantitative analysis of the sample showed that calcite [C], montmorillonite [M], and quartz [Q] were the main gangue minerals. They were found approximately at the ratio 4.45: 1.13:1, respectively (Table 1). Chemical analysis of the sample is shown in Table 2. From the Tables it could be concluded that diatomite mineral constituted about 80% of the sample. Particle size distribution showed that 100% of the sample was below 35 micron, whereas 94% was below 11 micron (Table 3).

Thermal analysis of the sample was depicted in Fig. 3. Figure 3 showed an endothermic pattern due to the release of diatomite absorbed water at the temperature range 100–200ºC, with a loss in sample weight reaching 0.7%. At temperature range 250- 600ºC, another endothermic reaction due to the release of the combined water of the clay mineral (300- 600°C) was recorded (Fig. 3). This endothermic reaction caused a loss in weight reaching 5.55%. An intense endothermic peak at the temperature range 600 to 750ºC due to calcite mineral break down, with a loss in weight reaching 8.95%, was depicted (Fig. 3). A loss in the sample weight reaching 1.75% was noticed

at 900-1200ºC that may be attributed to the complete dehydration of diatomite structure and the formation of a new silicate material.

SEM pictures of the sample showed that the most abundant diatomite genera types were epithemia argus (long diameter 70 um and short diameter 10 um), actinocyclus ehrenbergii (diameter 14 μm), and pinnularia brevicostata ((long diameter 20 μm and short diameter 10 μm) (Fig. 4). The presence of these diatomite genera indicated the fresh water environment origin of the deposit (Moyle and Dolley, 2003). Microscopic pictures of the sample revealed the presence of intact diatomite skeletons but not clearly observed. It was noticed that the skeletons surfaces were partly masked by the impurities; meanwhile the pores were filled with minute mineral particulates and organic matter, Fig. 4.

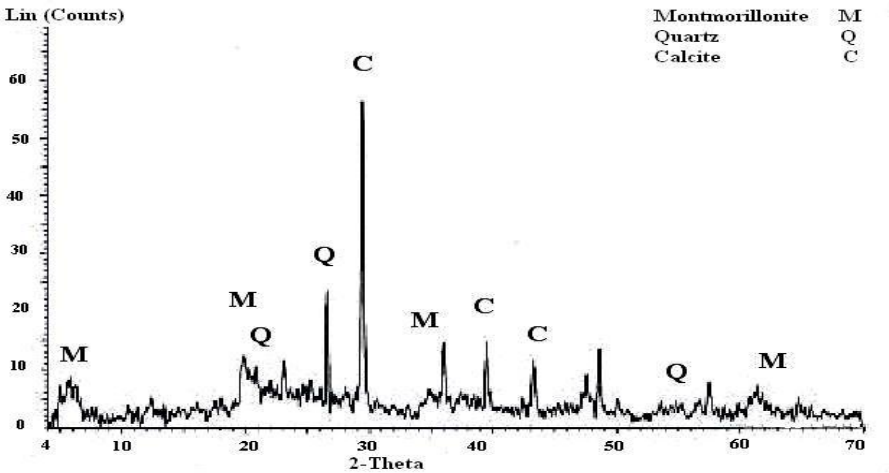

Fig. 2. XRD patterns of diatomite head sample

Table 1. Semi quantitative phase analysis of accompanied gangue minerals after XRD

Mineral	Wt.%
Quartz [Q]	15.20
Montmorillonite [M]	17.20
Calcite [C]	67.60

Table 2. Chemical analysis of the head sample

Constituent	Wt. %
SiO_2	83.60
Al_2O_3	4.24
CaO	6.17
Fe_2O_3	1.07
LOI	4.86

Table 3. Particle size distribution of the head sample

Size Fraction, um	Cum. Wt. % Retained
44	
35	
25	0.24
15	1.70
11	5.96
-11	100.00

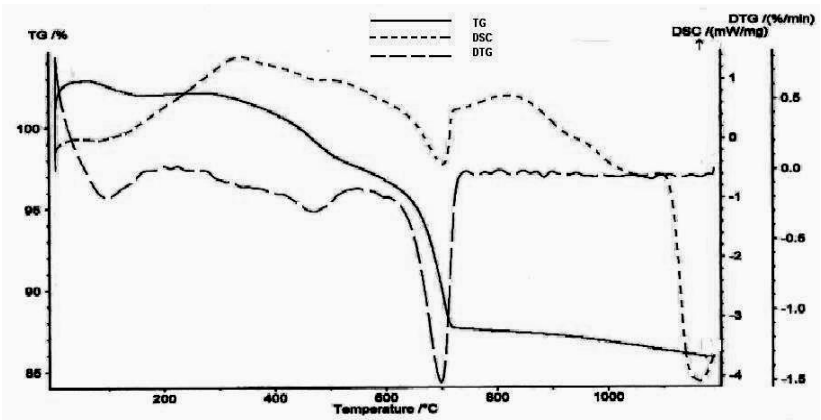

Fig. 3. Thermal analysis of diatomite sample

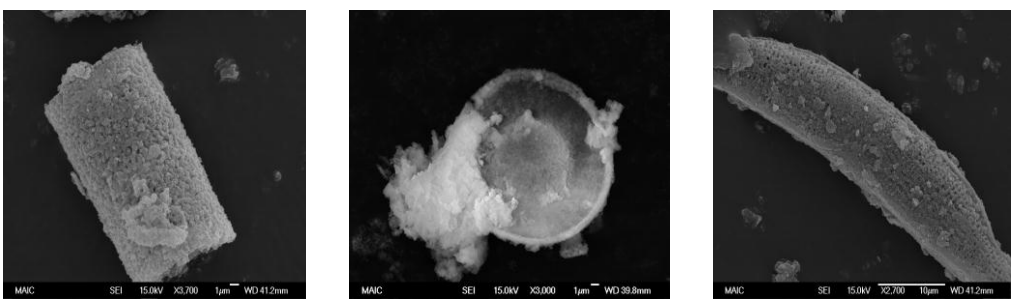

a b c

Fig. 4. Different diatomite genera, a: epithemia argus, b: actinocyclus ehrenbergii, c: pinnularia brevicostata, with complete blocked pore openings

3.2. Thermal behavior of the sample

On heating the sample at 600ºC for 5 hrs, dehydration process of diatomite surface was continued, where montmorillonite mineral was de-hydroxylated to form the amorphous meta kaolin according to the reaction (Balek and Murat, 1996):

$$Al_2O_3\,2SiO_2\,2H_2O = Al_2O_3\,2SiO_2 + 2H_2O.$$

Figure 5 illustrats the XRD pattern of the heated sample at 600ºC for 5 hrs. By comparing Figs. 2 and 5, it could be noticed that the main peak related to montmorillonite [M] at d-spacing = 15.0 (2θ=6º) disappeared due to the de-hydroxylation reaction to form metakaolin that appeared as broad noisy peaks at 2θ= 15º-30º (Balek and Murat, 1996) (Fig. 5). The fired sample at 600ºC for 5hrs showed a loss in sample weight reaching 6.39% and left behind a pink powder instead of the grey original color of the sample.

On heating the sample at 900ºC for 3 hrs wollastonite mineral was formed as a sole crystalline phase as shown in Figure 6. The mineral main peaks were shown at 2θ=30.06, 25.28, 23.20, (Fig. 6). On the other hand thermal decomposition of calcite was remarked, where complete removal of its main peaks at 2θ= 29.40, 43.14, and 39.40 was recorded (Fig. 6).

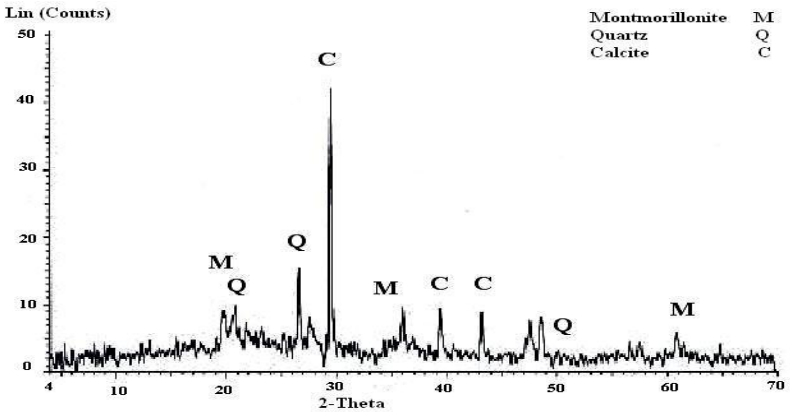

Fig. 5. XRD patterns of heated sample at 600ºC for 5hrs

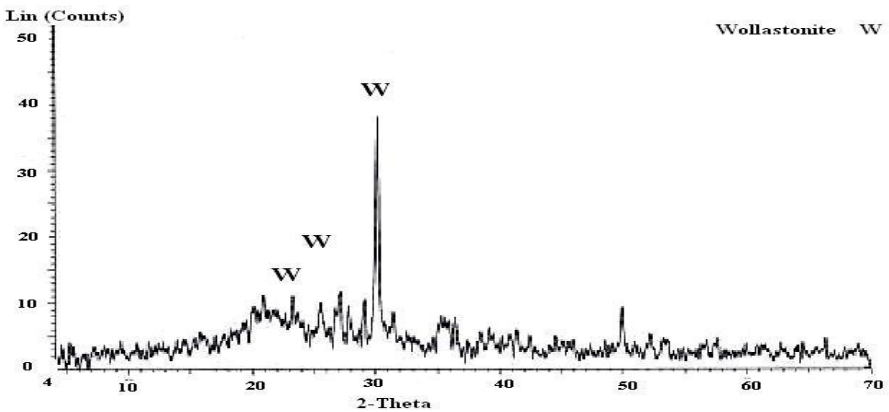

Fig. 6. XRD patterns of heated sample at 900ºC for 3hrs

The formation of wollastonite mineral [W] was explained after the reaction of the reactive lime species after calcite dissociation and reactive diatomaceous silica that was found in abundance in the heated sample (Ibrahim, 2009). A substantial increase in wollastonite peak intensity from 45% to 52.7% by increasing time of heating was remarked (Figs. 7 and 8), respectively.

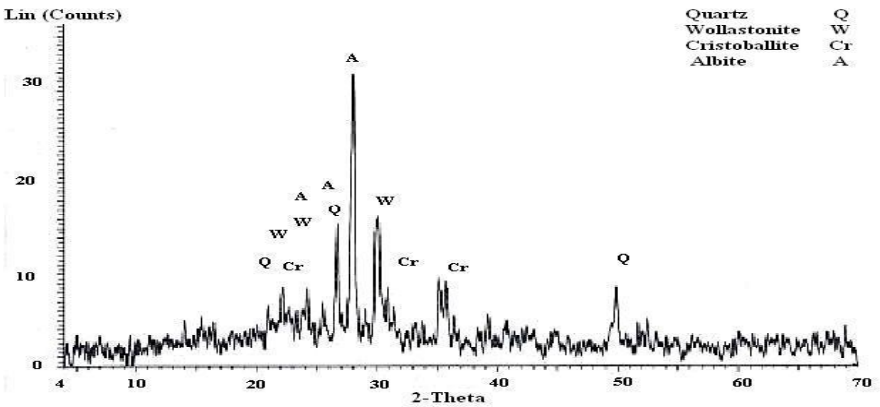

Fig. 7. XRD patterns of heated sample at 900ºC for 5hrs

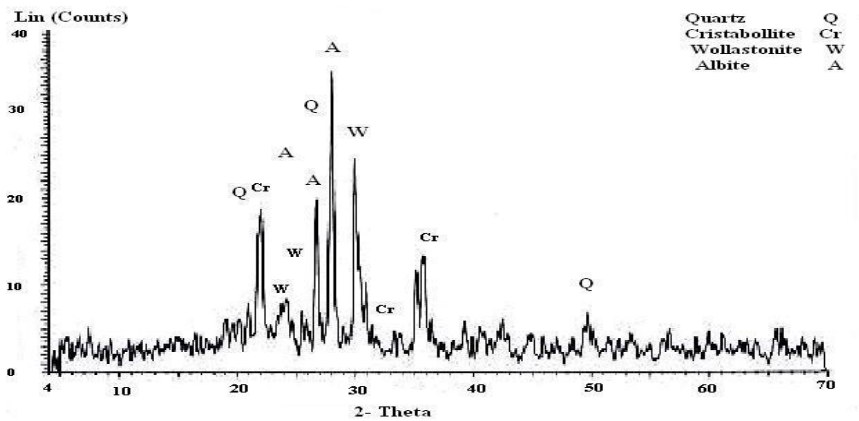

Fig. 8. XRD patterns of heated sample at 1000ºC for 5hrs

SEM pictures of the heated sample at 900ºC for 3 hrs showed that the pores openings of the diatomite porous structure became free from any blocking materials when compared to the original sample (Figs. 9 and 4), respectively. The temperature at which complete clearance of the porous structure of diatomite, i.e. calcinations temperature varied slightly from type to type, and presented an essential operation for diatomite when it was supposed to be directed to filter aid applications (Ibrahim and Selim, 2010; Ibrahim and Selim, 2011; Powers and Ibrahim, 2007).

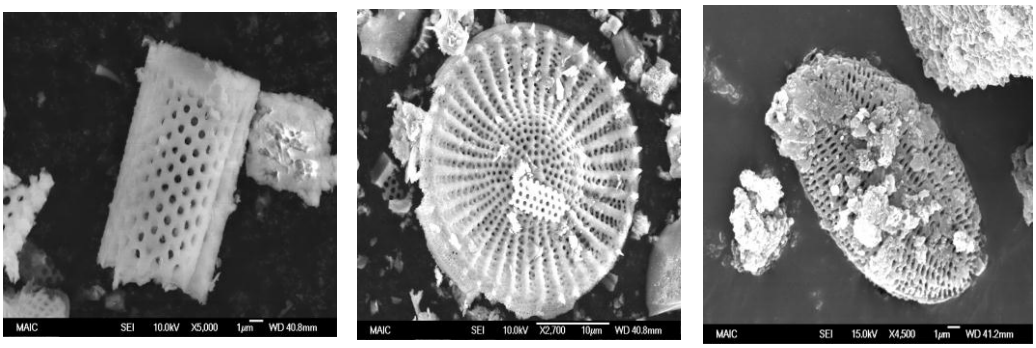

Fig. 9. SEM pictures showing the clean opened pores at 900ºC for 3 hrs

By increasing the firing soaking time to 5 hours at 900ºC, diatomite structure showed a sign of its original porous structure, but the concave and convex surfaces were almost all gone, and smoother surfaces were formed instead (Fig. 10).

On the other hand, XRD analysis of the fired sample showed a weak peak belonging to cristobalite mineral [Cr] at 2θ=21.93, 36.12, 31.46 (Fig. 8). It was suggested that the formation of cristobalite was in expense of diatomite silica, where crystalline silica formed cristobalite at 1200ºC, whereas amorphous silica like diatomite formed cristobalite at 900^{o}C (Wahl et al., 1961). Relative intensity of cristobalite peak (at 2θ=22^{o}) increased from 4.5% at 900^{o}C to 6.6% at 1000^{o}C (Figs. 8 and 9), respectively. The fired sample at 900ºC for 5hrs showed a loss in sample weight reaching 15.6% and left a faint brown powder behind, instead of grey original color of the sample.

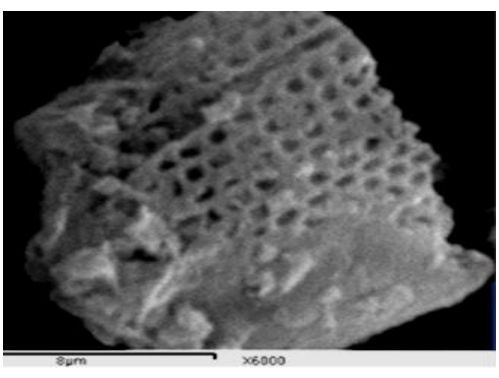

Fig. 10. Collapsing of diatomite porous structure at 900ºC for 5hrs

By increasing the firing temperature to 1000ºC for 5 hrs, complete dehydration of diatomite structure occurred which was accompanied by total collapsing and distortion of the porous structure as shown in Fig. 11. The left powder was brown in color and a pronounced loss in weight reached 19.82% was recorded.

By heating the sample at 1100ºC for 5 hrs, an olive green colored material was formed. The main XRD peaks of the product appeared at 2θ=21.93, 29.85, 35.48, and 30.88, that belonged to calcium alkali silicate mineral called diopside, (Fig. 12). Diopside is an inosilicate mineral composed of single chains of silica tetrahedra and belonging to pyroxene group. Pyroxenes have the general formula $XY(Si, Al)_2O_6$ (where X represents calcium, sodium, Fe^{+2} and magnesium and more rarely zinc, manganese and lithium and Y represents ions of smaller size, such as chromium, aluminium, iron (III), magnesium, manganese, scandium, titanium, vanadium and even iron (II). Although aluminium substitutes extensively for silicon in silicates such as feldspars and amphiboles, the substitution occurs only to a limited extent in most pyroxenes (Morimoto et al., 1989). The formed product showed loss on sample weight that reached 23.08% with a hard vitreous texture.

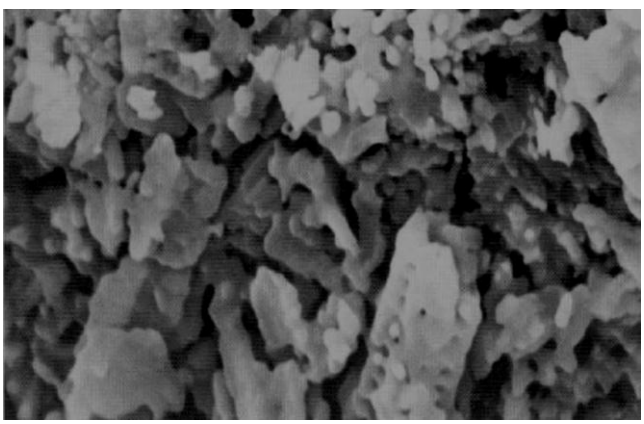

Fig. 11. Complete destroying of diatomite porous structure at 1000ºC

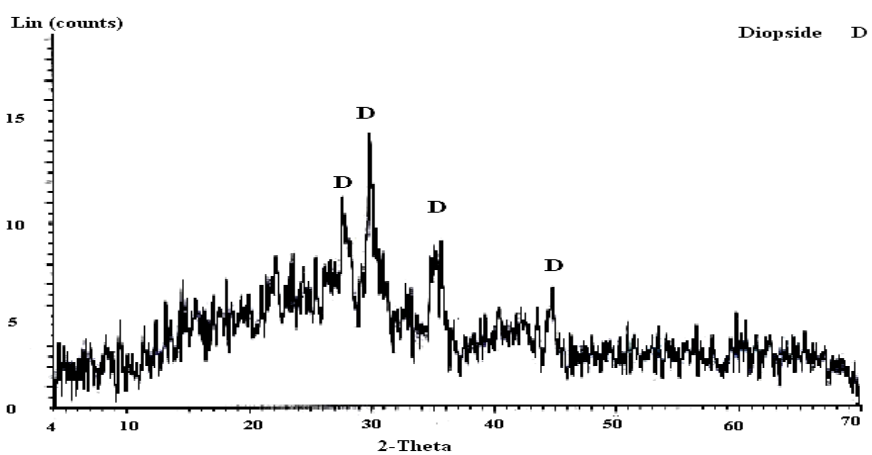

Fig. 12. XRD patterns of heated sample at 1100ºC for 5hrs

Figure 13 illustrates the XRD pattern of the sample after heating at 1200ºC for 5 hrs. The formed sample was a nano-metric vitreous glassy material (Fig. 14) that showed remarkable reduction in volume compared to the sample heated at 900ºC for 5 hrs (Fig. 15).

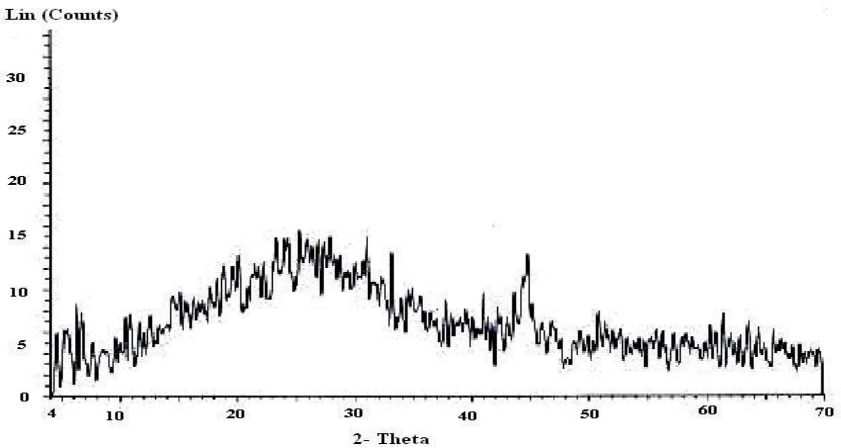

Fig. 13. XRD patterns of heated sample at 1200ºC for 5hrs

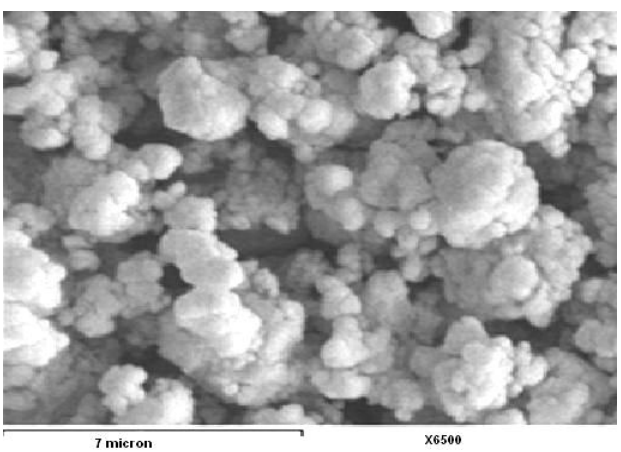

Fig. 14. SEM picture of the new material formed at 1200ºC

4. Conclusions

Natural diatomite sample from Kom Osheem Localiy, El-Fayoum Depression, Egypt was subjected to heat treatment. The main accompanied minerals were calcite, montmorillonite and quartz. The sample was soaked for 5 hrs at temperatures of 600, 900, 1000, 1100, and 1200ºC. Characterization of the heated samples was followed up

by using XRD and SEM techniques and other physical characterization like the detection of sample color, texture, and weight loss. Results showed that by heating the sample at different temperatures for 5 hrs, various transformation reactions from mineral to another was occurred. On the other hand, results showed that at 900ºC for 3 hrs the diatomite porous structure was completely calcined and improved. Partial collapsing of this porous structure started by heating the sample at 900ºC for 5 hrs, where complete destruction was remarked at 1100ºC with the formation of a nano-metric garnet like material at 1200ºC.

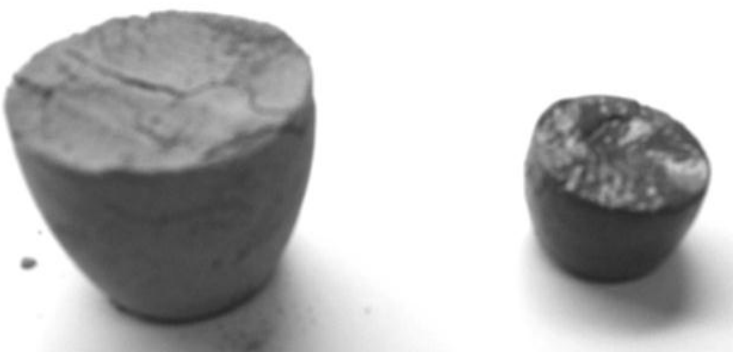

Fig. 15. Change in colour and volume of heated samples (A) at 900ºC and (B) at 1200ºC

References

BALEK V., MURAT M., 1996, *The emanation thermal analysis of kaolinite clay minerals*, Thermochim. Acta, 282–283, 385–397.

BRONNIMANN C.E., ZEIGLER R.C., MACIEL G.E., 1988, *Proton NMR study of dehydration of the silica gel surface*, J. Am. Chem. Soc., 110, 2023–2026..

EK S., ROOT A., PEUSSA M., NIINISTO L., 2001, *Determination of the hydroxyl group content in silica by the thermogravimetry and a comparison with HMAS NMR results*, Thermochim. Acta, 379, 201–212.

ERDOGAN B., DEMIRCI S., AKAY Y., 1996, *Treatment of sugar beet juice with bentonite, sepiolite, diatomite, and quartamin to remove color and turbidity*, Appl. Clay Sci. 11, 55–67.

IBRAHIM S.S., 2007, *Preparation of wollastonite mineral from Egyptian crude minerals*, Egyptian Academy of Scientific Research and Technology.

IBRAHIM S.S., SELIM A.Q., 2011, *Evaluation of Egyptian diatomite for filter aid applications*, Physicochem. Probl. Miner. Process., 47, 113–122.

IBRAHIM S.S., SELIM A.Q., 2010, *Producing a micro-porous diatomite by a simple classification-calcination process*, The Journal of Ore Dressing 2(23), 25–33.

JONES J.B., SEGNIT, E.R., 1971, *The nature of opal 1. nomenclature and constituents phases*, J. Geol. Soc., Aust. 18, 57–68.

LI X., BIAN C., CHEN W., HE J., WANG Z, XU N, XUE G, 2003, *Polyaniline on surface modification of diatomite: A novel way to obtain conducting diatomite fillers*, Appl. Surf. Sci. 207, 378–383.

MORIMOTO N., FABRIES J., FERGUSON A.K., GINZBURG I.V., ROSS M., SEIFEIT F.A., ZUSSMAN J., 1989, *Nomenclature of pyroxenes*, Canadian Mineralogist 27, 143–156.

MOYLE P.R., DOLLEY T.P., 2003, *A comparison of marine and continental-lacustrine diatomite deposits*, Industrial-Minerals Research.

POWERS K., IBRAHIM S.S., 2009, *Preparation of different diatomite concentrates for various industrial applications*, International Science and Engineering, NSF, USA.

STERRENBURG F., GORDON RJ., TIFFANY M.A., NAGY S.S., 2007, *Algae and cyan-bacteria in extreme environments*, Springer, 141–172.

TAKEI T., KATO K., MEGURO A., CHIKAZAWA M., 1999, *Infrared Spectra of Geminal and Novel Triple Hydroxyl Groups on Silica Surfaces*, Colloids and Surfaces, A: Physicochemical and Engineering Aspects, Vol. 150, No. 1, 77–84.

VASCONCELOS P.V., LABRINCHA J.A., FERREIRA J.M.F., 2000, *Permeability of diatomite layers processed by different colloidal techniques*, J. Eur. Ceram. Soc. 20, 201–207.

WAHL F.M., GRIM R.E., GRAF R.B., 1961, *Phase Transformations in Silica as Examined by Continuous X-ray Diffraction*, The American Mineralogist, 46, 1064–1076.

YUAN P., WU D.Q., HE H.P., LIN Z.Y., 2004, *The hydroxyl species and acid sites on diatomite surface: A combined IR and Raman study*, Applied Surface Science, 227, 30–39.

Physicochem. Probl. Miner. Process. 48(2), 2012, 425−439

www.minproc.pwr.wroc.pl/journal/

Physicochemical Problems of Mineral Processing

ISSN 1643-1049 (print)
ISSN 2084-4735 (online)

Received July 11, 2011; reviewed; accepted December 24, 2011

IRON REMOVING FROM TITANIUM SLAG FOR SYNTHETIC RUTILE PRODUCTION

Akbar MEHDILO, Mehdi IRANNAJAD

Department of Mining and Metallurgical Eng., Amirkabir University of Technology, Tehran, Iran, iranajad@aut.ac.ir, Phone: 0098-21-66419729, Fax: 0098-21-66405846

Abstract. Leaching with sulfuric and hydrochloric acids for upgrading titanium slag obtained from the Qara-aghaj ilmenite concentrate to a high grade titanium dioxide (TiO_2) was studied. The titanium slag containing 72.7% TiO_2 and 7.8% Fe_2O_3 was leached at varying solid/liquid (S/L) ratio, particle size, leaching time and acid concentration. The optimum amount of S/L ratio, particle size, acid concentration and leaching time using both acids were determined as 1:4, -100 μm, 8% and 2 h. Under optimum conditions, by using sulfuric acid, a titanium dioxide concentrate with 86.8% TiO_2 and 1.87% Fe_2O_3 was produced, while employing hydrochloric acid resulted in a concentrate containing 91% TiO_2 and 0.61% Fe_2O_3. The titanium dioxide concentrate prepared with hydrochloric acid, having acicular texture and by means of elongated separate particles; has less impurities than the one produced by sulfuric acid. The results demonstrate that hydrochloric acid dissolution of titanium slag and removing some impurities such as SiO_2 and MgO provide a product with good quality is prepared which is suitable as raw material for TiO_2 pigment production through the chloride process.

keywords: titanium slag, synthetic rutile, chloride process, sulfate process, acid leaching, TiO_2 pigment

1. Introduction

Titanium is relatively abundant in the earth's crust, which is usually found in igneous and metamorphic rocks as ilmenite ($FeTiO_3$), rutile (TiO_2) and titanomagnetite (Fe_2TiO_4–Fe_2O_4). A survey on the use of titanium in its various forms indicates that almost 95% is for the production of white TiO_2 pigment which has extensive application in paint, plastic and paper industries (Nayl et al., 2009; Nayl et al., 2009). Titanium dioxide also has high potential applications in environmental purification, gas sensors, and in photovoltaic cells due to its unique characteristics (Zang et al., 2009). Relatively minor quantities are used to produce metal and titanium chemicals (Lasheen, 2004).

Natural rutile, owing to its high titanium content and low levels of impurities, has traditionally been preferred as a feed stock for the production of titanium dioxide

http://dx.doi.org/10.5277/ppmp120209

pigment. Natural rutile is becoming scarcer and consequently more costly and alternative methods that use ilmenite are being favored. Ilmenite concentrates have relatively low titanium content (usually about 50% titanium dioxide compared to about 96% in the case of rutile) but have Fe as their major impurity and thus pose problems for pigment production. Nevertheless, ilmenite has been used as an alternate feed material for production of pigment through chemical routes (Samala et al., 2009).

Commercial production of TiO_2 pigment uses either the sulfate process or chloride process. In the former process, relatively low grade feedstock can be used, but it gives a higher volume of waste product that requires proper treatment and disposal. It is more preferable to use the chloride process which utilizes a feedstock of high TiO_2 grade as natural rutile mineral (94-98% TiO_2), synthetic rutile (92-95% TiO_2), anatase (90-95% TiO_2), leucoxene (>68% TiO_2), or titanium slag (80-90% TiO_2) as raw materials (Samala et al., 2009; El-Hazek et al., 2007; Lasheen, 2008, Zhang and Nicol, 2010; Nayl et al., 2009). The chloride process offers several advantages such as the yield of high quality products, a more eco-friendly process and the generation of a smaller amount of waste products (Zhang and Nicol, 2010).

The shortage of natural rutile and the need for higher grade titanium feedstocks has encouraged ilmenite upgrading by removing iron oxide and other impurities from the grain lattice, thus converting ilmenite into synthetic rutile for the chlorination process (El-Hazek et al., 2007; Mahmoud et al. 2004; Lasheen, 2009). There are several processes for the production of synthetic rutile from ilmenite and some of them were commercially applied. The most important of these processes are (Lasheen, 2004; El-Hazek et al., 2007; Mahmoud et al. 2004; Lasheen, 2009; Chun et al., 2008; Zhang and Nicol, 2009; Sasikumar et al. 2007; Kamala, 2006) given below.

(1) Smelting processes, where the iron part of the ilmenite is reduced and melted to separate iron from titanium. The titanium slag is then leached with sulfuric acid or with hydrochloric acid at elevated temperatures.

(2) Reduction of ilmenite to convert ferric iron partially to the ferrous form or completely to the metallic iron form followed by acid leaching.

(3) Reduction of the iron content of the ilmenite to the metallic iron followed by corrosion with oxygen and ammonium chloride.

(4) Oxidation and reduction of ilmenite followed by hydrochloric acid leaching (MURSO process).

(5) Roasting and magnetic separation followed by hydrochloric acid leaching (ERMS process).

In the first method, ilmenite ore can be smelted in the presence of carbonaceous reducing agents in an electric furnace where good quality pig iron is obtained together with titanium-rich slag which is chemically and mineralogically different than ilmenite (Nayl et al., 2009). In spite of high power consumption, smelting of ilmenite or titanium-bearing ore has several advantages over the synthetic rutile route by chemical process. The major advantages of the slag technology are: high titanium content, low waste generation, being suitable for sulphate and chloride processes, low chemicals

cost and converting the iron oxide as part of the concentrate to value-added iron metal (Kamala, 2006). The titanium slag produced from this process represents an important feedstock for the manufacture of titanium dioxide pigment by the sulphate process. In the case of the chloride process, the titanium-rich slag is further acid-leached by a hydrometallurgical process. As a leachant, hydrochloric acid is preferred to other acids because it allows comparatively easier recovery of the useful free acid from its waste solution. In addition, the recovery of a number of metal ions by liquid–liquid extraction from hydrochloric acid solutions is considerably easier than that from sulphuric acid solutions (Olanipekun, 1999).

On an industrial scale, the metallurgical complex of QIT-Fer & Titane Inc. (formerly named Quebec Iron & Titanium and later referred to the text as QIT), located in Sorel Tracy, Province of Quebec, Canada, is one of the largest producers of synthetic rutile by this method. In the acid-leaching plant of this company hydrochloric acid is used as a leachant (Guéguina and Cardarelli, 2007).

Fig. 1. Location map of Qara-aghaj deposit

In this work, the acid leaching process was studied using titanium slag obtained from the Qara-aghaj ilmenite concentrate. Beside Kahnoj beach sands in south of Iran, Qara-aghaj hard rock deposit which is located 36 km from Euromieh in Azarbayejan province, northwest of Iran (Fig. 1) has recently been explored as another titanium resource (Irannajad, 2002; Mehdilo, 2003; Irannajad, 1990). In the Qara-aghaj ore, titanium occurs mainly in the form of ilmenite partly as separated grains, exsolved lamellae in magnetite and dissemination in silicate minerals. The maximum amount of TiO_2 in ilmenite lattice is 48% (lower than the theoretical amount, 52.6%). The MgO and MnO contents of ilmenite are 0.74-1.48% and 0.38-2.4%, respectively which are relatively high. Magnetite is another valuable mineral in the ore. Pyroxene, olivine, hornblende and some plagioclase are the most important gangue minerals of the ore

(Mehdilo and Irannajad, 2010). Based on mineral processing tests an ilmenite concentrate by grading of 44.5% TiO_2 has been obtained by a combination of the gravity-magnetic separators (Mehdilo, 2003; Irannajad and Mehdilo, 2007; Irannajad and Mehdilo, 2004) and then converted to titanium slag by the carbothermic reduction smelting process in a DC electric arc furnace (Mehdilo and Irannajad 2006; Mehdilo et al., 2006; Irannajad and Montajam, 2005). In the present study, the iron removing from the produced titanium slag was investigated by sulfuric and hydrochloric acid leaching tests and the obtained titanium dioxide concentrate was characterized as a final product of both acids leaching.

2. Materials and procedure

2.1. Materials

The titanium rich slag prepared from ilmenite concentrate of Qara-aghaj hard rock titanium ore (Fig. 2) was used as the raw material. The chemical composition of the ore sample and ilmenite concentrate is presented in Table 1. Merck sulfuric and hydrochloric acids were employed for leaching tests. The chemical and phase composition of both raw material and the final residue of the leaching tests were carried out by X-ray fluorescence (Philips X Unique2) and X-ray diffraction (Philips X'Pert). The same materials were examined by scanning electron microscopy (Philips, model: XL30) equipped with EDS for morphological and spot analysis studies.

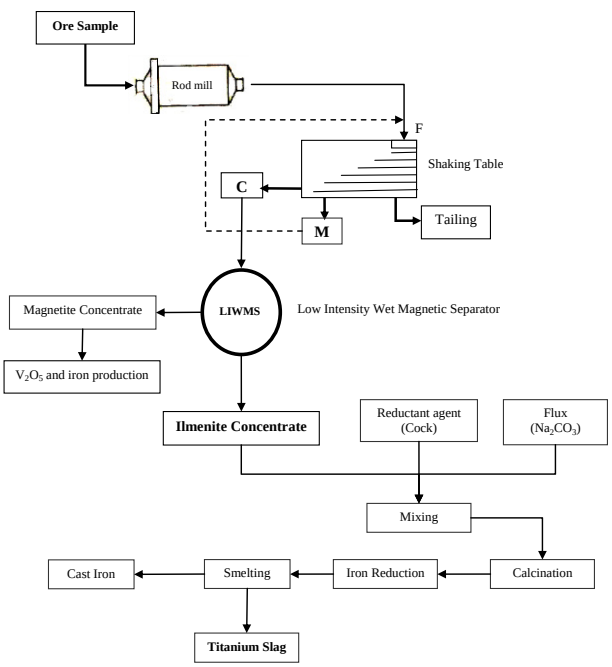

Fig. 2. Schematic diagram of ilmenite concentrate and titanium slag preparation from ore sample

Table 1. Chemical composition of ore sample and ilmenite concentrate

Composition, %	TiO_2	Fe_2O_3	MnO	MgO	SiO_2	Al_2O_3	CaO	P_2O_5	V_2O_5	Na_2O	Total
Ore sample	9.0	34.4	0.41	15.0	27.4	3.1	5.9	2.9	0.14	0.25	98.5
Concentrate	44.5	46.1	0.83	3.76	2.57	0.58	0.61	0.52	0.26	-	99.73

2.2. Procedure

The obtained titanium slag was crushed and ground below 100 μm and a representative sample was prepared. The samples with 100 g weight were used in the leaching tests by sulfuric and hydrochloric acids. After leaching and filtration, the residue as titanium dioxide concentrate was analyzed by XRF and the recoveries of TiO_2 and Fe_2O_3 were calculated based on feed and residue weight and grades. Finally, the product was characterized by analytical methods such as X-ray diffraction (XRD) and X-ray fluorescence (XRF), light microscopy and scanning electron microscopy.

3. Results and discussion

3.1. Slag characterization

The chemical and phase composition of the titanium slag are shown in Table 2 and Fig. 3, respectively. However, after slagging, the Fe_2O_3 content of the slag has been reduced to 7.8% but it is the most important of all impurities which should be removed. Fe_2O_3 is mainly in the form of iron metal which could not be separated from the slag. The other impurities are mainly light elements such as Si, Mg, Al, Ca, Mn and K which are concentrated in the slag product. SiO_2 and some of MgO, CaO and Al_2O_3 are sourced from silicate minerals. MnO and some of MgO, CaO and Al_2O_3 are related to impurities in ilmenite lattice. The high content of K_2O in the slag is due to potassium carbonate consumption as flux in the slagging process. The XRD pattern of the slag shows that rutile is the most important phase in the sample. The other titanium containing phases are Ti_2O_3, Ti_2O_5, anatase and negligible amount of pseudorutile ($Fe_2Ti_3O_9$). The impure phase of the slag was detected as FeO. The BSE images of the produced slag are shown in Fig. 4 and different parts or phases were chemically analyzed by EDX (Table 3). These results indicate that some parts of the slag have been transformed to titanium rich phases with spherical morphology (Fig. 4−b) containing up to 85% TiO_2 content (Table 3). The other titanium containing phase is probably pseudorutile which has been found by the EDX spot analysis (Table 3). The analysis of light particles shows that they are pig iron. These irons particles can be removed by the acid leaching process.

Table 2. The chemical composition of titanium slag

Composition	TiO_2	Fe_2O_3	MnO	MgO	SiO_2	Al_2O_3	V_2O_5	CaO	Na_2O	K_2O	Total
%	72.7	7.8	0.97	3.21	5.24	2.90	0.30	1.08	0.20	4.22	99.28

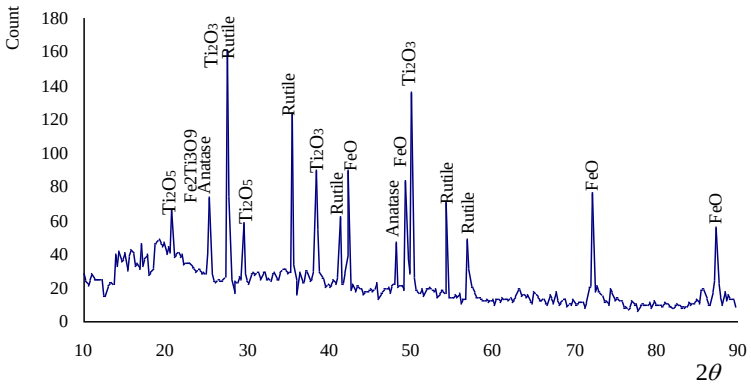

Fig. 3. XRD pattern of titanium slag used as raw material

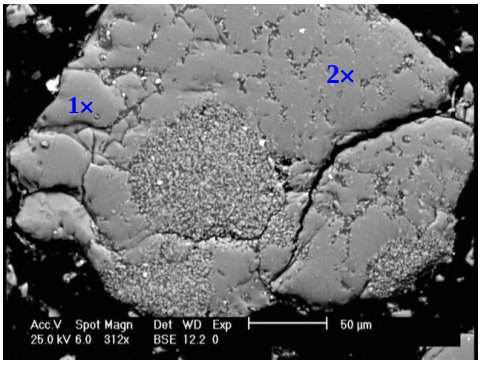

(a) BSE image of crushed titanium slag. Partial transformation of slag to titanium reached phases

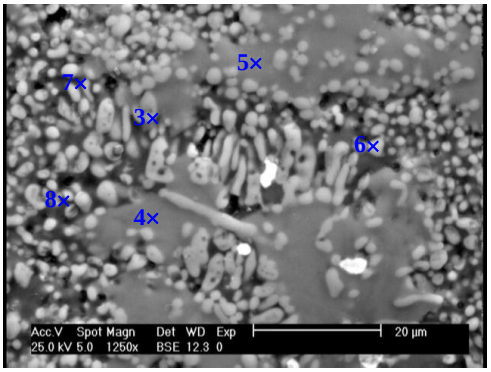

(b) titanium rich phases of image a) with higher magnification

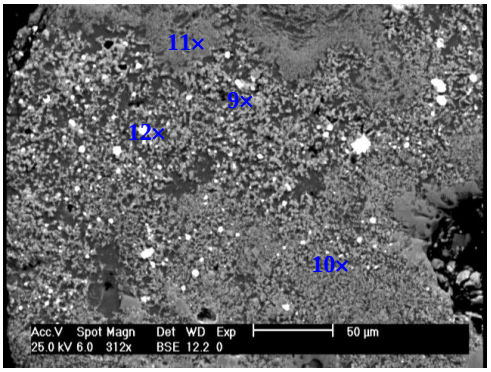

(c) presence of pig iron particles inside titanium slag

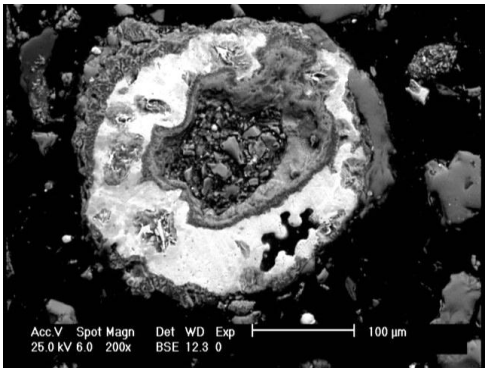

(d) larger grain of pig iron surrounding a titanium slag grain

Fig. 4. The BSE images of titanium slag

Table 3. Selected EDX analyses of titanium slag

Spot No.	Analyzed Points	Composition (%)										
		TiO_2	Fe_2O_3	MnO	V_2O_5	P_2O_5	CaO	MgO	SiO_2	Al_2O_3	Cr_2O_3	Total
1	compact parts of slag (spot 1- Fig 3a)	69.42	0.61	0.57	-	0.69	0.16	17.91	0.62	9.84	0.16	99.98
2	compact parts of slag (spot 2- Fig 3a)	70.45	0.44	1.18	0.20	0.75	2.40	4.55	13.40	6.32	0.27	99.96
3	pseudorutile (Fig 3b)	75.46	0.49	0.44	-	0.55	1.95	10.50	4.02	6.22	0.33	99.96
4	pseudorutile (Fig 3b)	77.72	0.55	1.17	-	0.44	2.24	0.97	12.66	3.92	0.32	99.98
5	pseudorutile (Fig 3b)	77.61	0.31	0.94	-	2.03	1.05	8.92	5.09	3.78	0.22	99.95
6	spherical particles (Rutile or Anatase) (spots 6, 7, 8- Fig 3b) (spots 9, 10- Fig 3c)	89.24	0.51	0.28	-	0.77	0.72	2.63	0.61	4.95	0.26	99.96
7		90.43	0.78	1.0	0.25	1.05	-	3.96	0.74	1.15	0.62	99.97
8		88.32	0.71	0.58	0.07	0.51	0.14	5.95	0.87	2.43	0.38	99.96
9		88.67	0.81	0.44	0	0.60	1.51	0.85	4.64	2.22	0.22	99.96
10		85.71	0.8	0.67	-	0.73	0.37	7.27	0.28	3.70	0.43	99.96
11	compact parts of slag (Fig 3c)	65.69	4.13	0.53	-	-	3.94	8.24	8.94	8.14	0.34	99.95
12	light grains- iron (Fig 3c)	4.60	90.53	0.33	0.17	0.85	0.13	0.60	1.11	0.95	0.71	99.98

3.2. Leaching tests

The leaching tests to remove iron were carried out on a titanium slag (Fig. 2) assaying 72.7% TiO_2 and 7.8% Fe_2O_3 using sulfuric and hydrochloric acid using different conditions. The parameters including solid/liquid (S/L) ratio, particle size, leaching time and acid concentration were investigated. Based on literature all leaching tests were carried out at a constant temperature of 95°C.

3.2.1. Effect of solid/liquid (S/L) ratio

Several leaching experiments were performed using sulfuric and hydrochloric acid, with S/L ratios of 1:1, 1:2, 1:4, 1:6 and 1:8. In these experiments, leaching was performed on the -100 μm feed material applying 60 minutes of agitation and using an acid concentration of 4%. From the results plotted in Fig. 5a and 5b, it is clearly evident that with increasing S/L ratio, the total iron leaching efficiency increased but its increasing after S/L=1:4 occurs slowly. By decreasing the S/L ratio or increasing acid consumption the titanium dissolution also increases. Therefore for decreasing acid consumption and titanium dissolution the S/L=1:4 is selected as optimum amount for the next experiments.

3.2.2. Effect of particle size

For investigation of the effect of particle size on leaching efficiency different samples were ground below 200, 150, 100 and 75 μm and were examined using both acids with the S/L ratio 1:4 applying 60 minutes of agitation and acid concentration of 4%. By increasing particle size the leaching efficiency is decreased as illustrated in Fig. 4. With -100 μm particle size, 81.7% of Fe_2O_3 and 9% of the TiO_2 was extracted

using sulfuric acid while in hydrochloric acid solution the leaching efficiency of Fe_2O_3 and TiO_2 were 88.3 and 3.9%, respectively. However, the iron recovery is increased for sample with -75 μm particle size but the titanium dissolution is also increased in this size fraction. So, in order to decrease titanium losses in solution and reduce grinding energy consumption, the -100 μm size fraction was used as the optimum particle size in the next experiments.

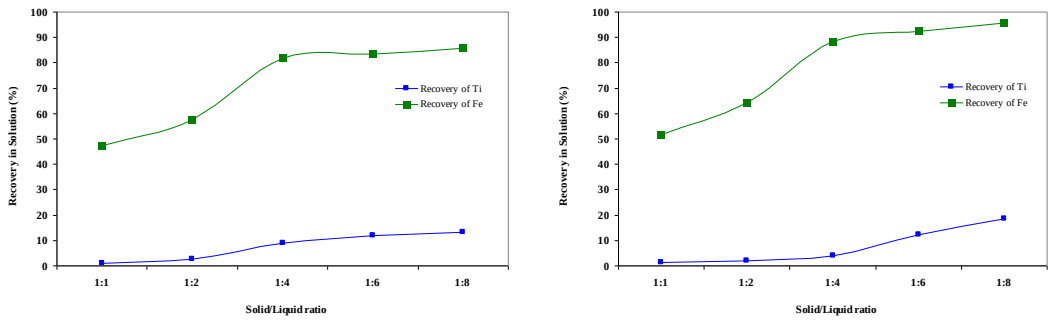

(a) (b)

Fig. 5. Effect of S/L ratio on leaching (60 minutes, 4% acid concentration, 95°C) efficiency; (a) recovery of TiO_2 and Fe_2O_3 in solution using sulfuric acid, and (b) recovery of TiO_2 and Fe_2O_3 in solution using hydrochloric acid

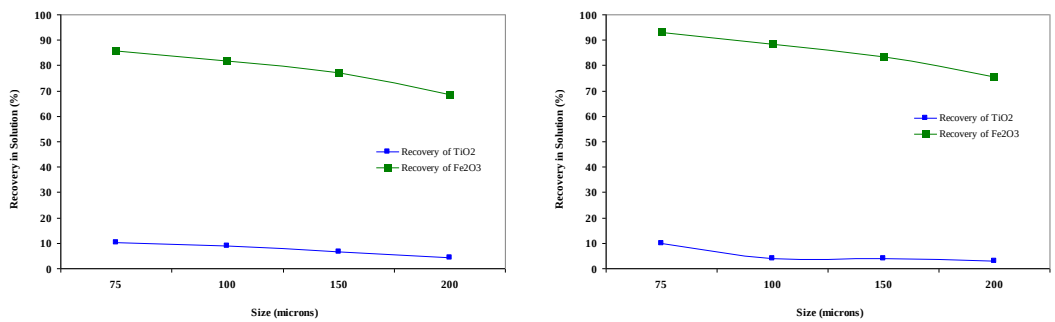

(a) (b)

Fig. 6. Effect of particle size on leaching (60 minutes, 4% acid concentration, 95°C) efficiency; (a) recovery of TiO_2 and Fe_2O_3 in solution using sulfuric acid, and (b) recovery of TiO_2 and Fe_2O_3 in solution using hydrochloric acid

3.2.3. Effect of leaching time

The effect of time on the leaching efficiency of titanium slag was examined between 0 and 240 minutes using the S/L ratio of 1:4 at 95°C. The results shown in Fig. 7a and 7b indicate that using sulfuric acid the residue obtained within 120 minutes has a maximum TiO_2 content (86.7%) and recovery (92%). At this time about 82% of Fe_2O_3 is brought into solution. With time, by increasing the iron dissolution

efficiency, the recovery of TiO_2 in the residue as titanium dioxide concentrate decreases from 92% to 88.5% by increasing the leaching time from 0 to 240 minutes. In the case of hydrochloric acid, the results presented in Fig. 8a and 8b indicate that the TiO_2 content in the residue (synthetic rutile) is greater than that produced by sulfuric acid leaching. This is due to higher solubility of iron in hydrochloric acid. With time, with increasing TiO_2 content in the residue from 88.7 to 91.3% the Fe_2O_3 content is decreased from 1.51% to 0.42%. The increase in leaching time results in the increase of titanium dissolution and decrease of titanium recovery in produced synthetic rutile. At 120 minutes leaching time, the Fe_2O_3 dissolution efficiency is about 94% and 95% of TiO_2 is recovered in the leaching residue as titanium dioxide concentrate.

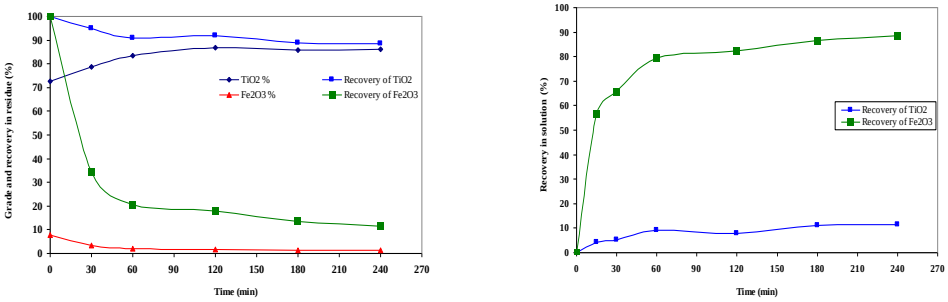

(a) (b)

Fig. 7. (a) Effect of time on TiO_2 and Fe_2O_3 contents and on their recoveries in residue, (b) Effect of time on recovery of TiO_2 and Fe_2O_3 in solution during sulfuric acid leaching (S/L ratio 1:4, 95°C)

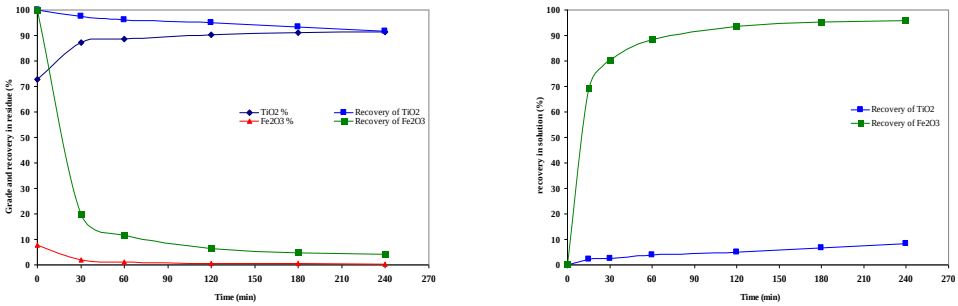

(a) (b)

Fig. 8. (a) Effect of time on TiO_2 and Fe_2O_3 contents and on their recoveries in residue, (b) Effect of time on recovery of TiO_2 and Fe_2O_3 in solution during hydrochloric acid leaching (S/L ratio 1:4, 95°C)

3.2.4. Effect of acid concentration

Several experiments were carried out using sulfuric and hydrochloric acid concentrations varying from 4 to 18% at 2 h leaching time and 95°C. From the results plotted in Figs. 9a and 9b it is clearly evident that, with increasing sulfuric acid

concentration, the total iron leaching efficiency increases steadily from 82.2% to about 90.4%. The Fe_2O_3 content of residue is reduced from 3.8% in 4% acid concentration to 1.85% in 18% acid concentration. The variation of the TiO_2 content in the residue at different acid concentrations is very negligible but its recovery is reduced from 92% to 88.2% due to the increase in titanium dissolution by increasing acid concentration. The results in Fig 10a and 10b revealed that by increasing hydrochloric acid concentration, more impurities are dissolved and the TiO_2 content in the residue is increased but the recovery is decreased due to high titanium losses in the solution. At 4% HCl, the recovery of Fe_2O_3 in the synthetic residue is 10.3% and this value dropped to 4.8% by increasing the HCl concentration to 8%. When the HCl concentration reaches 18%, the recovery of Fe_2O_3 is 3.5% and a higher increase in HCl concentration does not have a greater effect on the iron removal. Thus, 8% is the optimum HCl concentration where up to 95% of Fe_2O_3 is removed from the titanium dioxide concentrate and the TiO_2 and Fe_2O_3 contents are 91% and 0.61%, respectively.

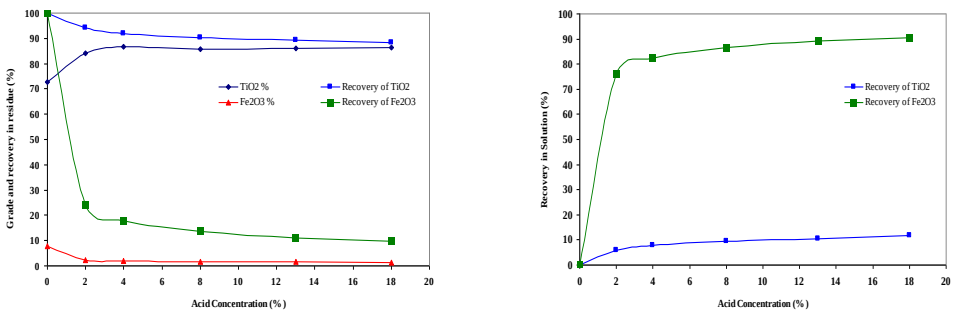

(a) (b)

Fig. 9. (a) Effect of acid concentration on TiO_2 and Fe_2O_3 contents and their recoveries in residue, (b) effect of acid concentration on recovery of TiO_2 and Fe_2O_3 in solution during sulfuric acid leaching (S/L ratio 1:4, 95°C, 120 minutes)

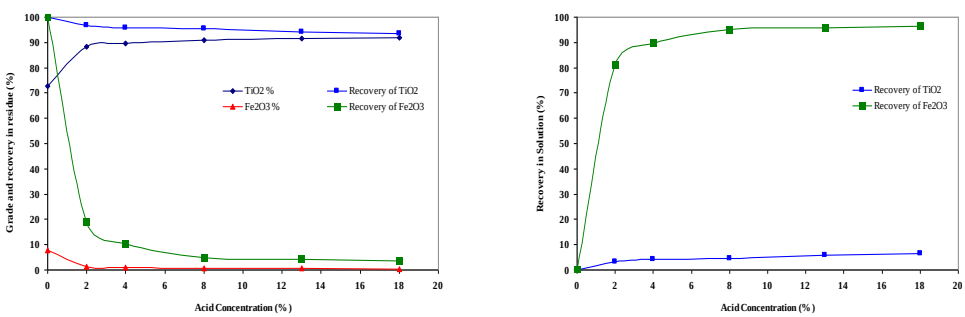

(a) (b)

Fig. 10. (a) Effect of acid concentration on TiO_2 and Fe_2O_3 contents and their recoveries in residue, (b) effect of acid concentration on recovery of TiO_2 and Fe_2O_3 in solution during hydrochloric acid leaching (S/L ratio 1:4, 95°C, 120 minutes)

3.3. Characterization of titanium dioxide concentrate

The produced titanium dioxide concentrate at the optimum conditions was washed and dried. In this concentrate rutile is the dominant phase but Ti_2O_3, anatase and iron oxide phases were also found. The chemical analysis of the dried product obtained under optimum conditions is presented in Table 4. The product of HCl leaching contains about 91% TiO_2 and only 0.6% iron as Fe_2O_3 while their content in the titanium dioxide concentrate obtained by H_2SO_4 leaching are 86.8 and 1.87, respectively. The contents of most impurities in the product of H_2SO_4 leaching are a little greater than the HCl leaching product. The BSE images of titanium dioxide concentrate produced by sulfuric and hydrochloric acid are compared in Fig. 11. These images indicate that the texture and morphology of the product obtained by HCl and H_2SO_4 are very different. The morphology of titanium dioxide produced by HCl leaching is more granular than that prepared by H_2SO_4 leaching (Fig. 11a and 11b). In the product of HCl leaching, the grains are mostly elongated with a clear and sharp boundary while the product of the H_2SO_4 process has grains with less elongation and unclear boundaries (Fig. 11c and 11d). Most of the particles produced by HCl leaching are needle-like crystals but the acicular texture is observed scarcely in the product of H_2SO_4 leaching (Fig. 11e and 11f). The particle size of the titanium dioxide concentrates produced by H_2SO_4 and HCl leaching was also determined by the image analysis method using a Clemex software. The cumulative percent of particles as a function of circular and spherical diameter is shown in Fig. 12 and 13. The information about size distribution of both products is presented in Table 6. The results indicate that the mean size of particles obtained from HCl leaching is a little smaller than that produced with H_2SO_4 leaching. Some of the particles shown in Fig. 11 were analyzed by EDX (Table 5). The chemical compositions of titanium dioxide particles produced by different acids leaching are closely similar. The maximum content of TiO_2 is 93% and the minimum content of iron as Fe_2O_3 is 0.48%. Among the coloring metals, the content of V_2O_5 and Cr_2O_3 in the produced material does not exceed 0.12% and 0.3%, respectively but the quantity of MnO_2 sourced from ilmenite lattice varies from 0.88 to 1.31% and could negatively affect the chlorination process. The content of other impurities (MgO, SiO_2, Al_2O_3, CaO and P_2O_5) is relatively high. Silica is not a major problem in the chloride process and could be removed with alkaline leaching (Nayl et al., 2009) but other impurities (MgO, Al_2O_3, CaO and P_2O_5) are the chlorine consuming components and should be removed before using this process.

Table 4. The chemical composition of produced titanium dioxide

%	TiO_2	Fe_2O_3	MnO	MgO	SiO_2	Al_2O_3	V_2O_5	CaO	K_2O	SO_3	Cl	Total
H_2SO_4	86.8	1.87	0.57	2.79	4.6	1.02	0.22	1.04	0.21	0.51	-	99.63
HCl	91.0	0.61	0.62	2.11	3.28	0.86	0.18	0.58	0.09	-	0.38	99.51

Table 5. Selected EDX spot analysis of synthetic rutile prepared by sulfuric and hydrochloric acids leaching

Product	Composition (%)										
	TiO_2	Fe_2O_3	MnO	V_2O_5	P_2O_5	CaO	MgO	SiO_2	Al_2O_3	Cr_2O_3	Total
Synthetic rutile produced by H_2SO_4 leaching	88.60	0.78	1.31	-	0.84	0.41	4.07	2.55	1.14	0.22	99.92
	91.42	0.68	1.14	-	0.39	0.11	4.23	0.95	0.90	0.14	99.96
Synthetic rutile produced by HCl leaching	92.23	0.58	0.88	-	0.47	0.61	2.08	1.89	0.77	0.27	99.85
	89.94	0.61	1.16	-	0.69	0.49	4.86	0.92	1.0	0.30	99.94
	93.01	0.48	0.96	0.12	0.13	0.45	3.05	0.58	0.90	0.22	99.99

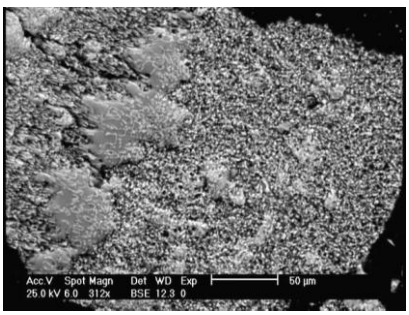

(a) Synthetic rutile produced by HCl leaching

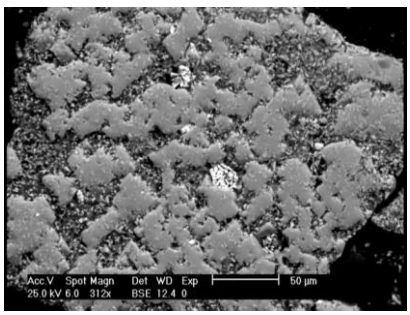

(a) Synthetic rutile produced by H_2SO_4 leaching

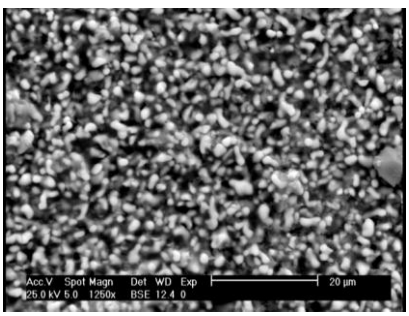

(c) Synthetic rutile produced by HCl leaching

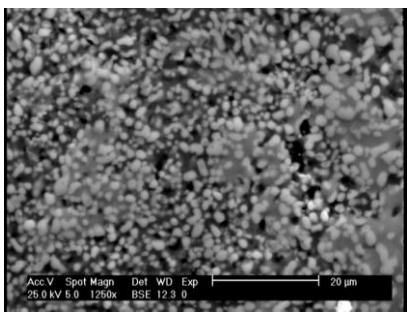

(d) Synthetic rutile produced by H_2SO_4 leaching

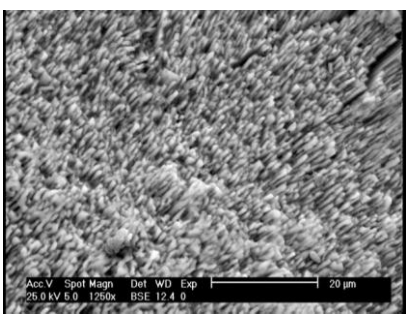

(e) Synthetic rutile produced by HCl leaching

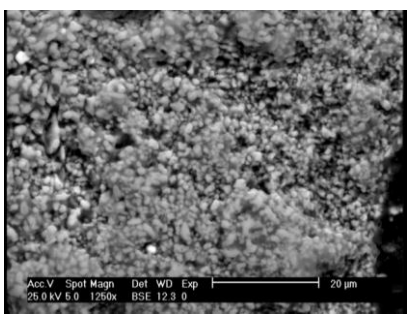

(f) Synthetic rutile produced by H_2SO_4 leaching

Fig. 11. Textural and morphological comparison of synthetic rutile particles prepared by sulfuric and hydrochloric acids leaching at the optimum conditions

Table 6. Information on size distribution of particles produced by H_2SO_4 and HCl leaching

Leaching solution	Diameter	Minimum size (μm)	Maximum size (μm)	Mean size (μm)	D80 (μm)	Standard Deviation (μm)
H_2SO_4	Circular	0.2	3.6	1.47	1.95	0.577
	Spherical	0.2	4.4	1.8	2.4	0.707
HCl	Circular	0.1	5.2	1.2	1.95	0.849
	Spherical	0.2	6.3	1.47	2.31	1.04

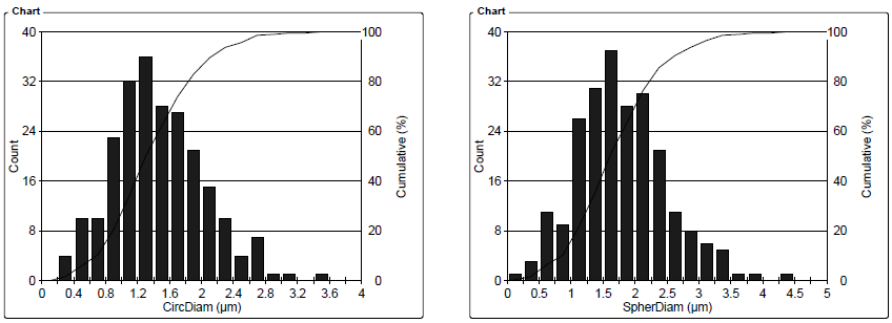

(a) Circular diameter (b) Spherical diameter

Fig. 12. Size distribution of titanium dioxide particles produced by H_2SO_4 leaching

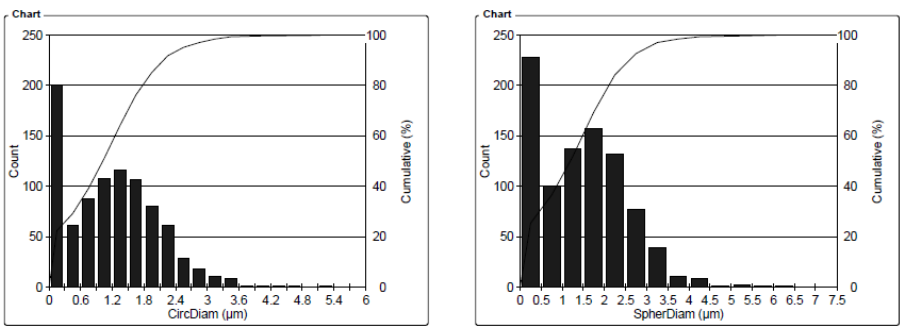

(a) (b)

Fig. 13. Size distribution of titanium dioxide particles produced by HCl leaching; (a) circular diameter, (b) spherical diameter

4. Conclusion

The leaching of titanium slag by both sulfuric and hydrochloric acid solutions at 95°C using an S/L ratio of 1:4 revealed that with a 2-hour leaching and 8% acid concentration, the Fe_2O_3 content in the residue is reduced to 1.87% and 0.61%, respectively. The increase in the leaching time and acid concentration does not have a great effect on iron removal efficiency. Under mentioned conditions, by using sulfuric

acid, the production of titanium dioxide concentrate containing more than 87% TiO_2 is not possible, while with hydrochloric acid as leachant, a product can be prepared containing up to 91% TiO_2. In addition to higher titanium purity and lower content of iron, the specific texture and morphology of titanium dioxide concentrate results in the hydrochloric acid being preferred. An easy recovery of hydrochloric acid from waste solutions is another profit of this reagent for upgrading titanium slag in order to produce suitable raw material for the chloride process. However, a high content of some impurities such as MgO and CaO may result in difficulties in chloride process and should be eliminated. More detailed investigation to remove these impurities is being performed by the authors.

References

EL-HAZEK N., LASHEEN T.A., EL-SHEIKH R., ZAKI SALAH A., 2007. *Hydrometallurgical criteria for TiO2 leaching from Rosetta ilmenite by hydrochloric acid*, Hydrometallurgy 87, 45–50.

GUEGUINA M. and CARDARELLI F., 2007. *Chemistry and mineralogy of titanium-rich slags. Part 1. hemo-ilmenite, sulphate, and upgrading titanium slags*, Mineral Processing and Extractive Metallurgy Review, 28, 1–58.

IRANNAJAD, M., 2002. *Mineral Processing Studies of Iranian Titanomagnetites Case Study: the Qara-aghaj Titanium Ore*, Report of investigation, Amirkabir University of Technology, Tehran, Iran.

IRANNAJAD, M., 1990. *Pilot Plant Flowsheet Development of the Kahnooj Titanium Ore Deposit, Report of investigation*, Amirkabir University of Technology, Tehran, Iran (In Farsi).

IRANNAJAD, M. and MEHDILO, A., 2007. *Laboratory-Based Flowsheet Development of Iranian Ilmenite Upgrading*, 20th International Mining Congress and exhibition of Turkey IMCET.

IRANNAJAD, M., MEHDILO, A., 2004. *Concentration of Iranian Titanium Ore by Physical Methods*, 2nd International Gravity Concentration Symposium (Gravity 04), Perth, Australia.

IRANNAJAD M., MONTAJAM M., 2005. *Upgrading of Ilmenite Concentrate from Uromieh Qara Aghaj by Smelting*, 1st Iranian Mining Engineering Conference, 2-5 February, Tehran, Iran (In Farsi)

KAMALA K. S., THOMAS C. A., DEVABRATA M., ARCHANA A., 2006. *An overview on the production of pigment grade titanium from titanium-rich slag*, Waste Management & Research 24, 74–79.

LASHEEN T. A., 2009. *Sulfate digestion process for high purity TiO2 from titanium slag*, Front. Chem. Eng. China 3, 155–160.

LASHEEN T. A., 2008. *Soda ash roasting of titanium slag product from Rosetta ilmenite*, Hydrometallurgy 93, 124–128.

LASHEEN T.A.I., 2004. *Chemical beneficiation of Rosetta ilmenite by direct reduction leaching*, Hydrometallurgy 76, 123–129.

LI C., LIANG B., WANG H. Y., 2008, *Preparation of synthetic rutile by hydrochloric acid leaching of mechanically activated Panzhihua ilmenite*. Hydrometallurgy 91, 121–129.

MAHMOUD M.H.H., AFIFI A.A.I., IBRAHIM I.A., 2004. *Reductive leaching of ilmenite ore in hydrochloric acid for preparation of synthetic rutile*, Hydrometallurgy 73, 99-109.

MEHDILO A. and IRANNAJAD M., 2010. *Applied Mineralogical Studies on Iranian Hard Rock Titanium Deposit*, Journal of Minerals & Materials Characterization & Engineering 9 (3), 247–262.

MEHDILO A., IRANNAJAD M., 2006, *Production of TiO_2 Pigment from Iranian Titanium Recourses*, Iran Surface Coatings Magazine 15, 16–22. (In Farsi)

MEHDILO A., IRANNAJAD M. and SHAFAEI S. Z., 2006. *Investigation about TiO_2 Pigment Production from ilmenite concentrate of Qarah-aghaj titanium deposit*, 1st international & 2nd national conference on color science and technology, 2-5 January, 2006. Tehran, Iran.

MEHDILO, A., 2003. M*ineral Processing Studies of the Qara-aghaj Titanium Ore by Physical Methods*, MSc Thesis, Amirkabir University of Technology, Tehran, Iran. (In Farsi)

NAYL A.A., AWWARD N.S., ALY H.F., 2009a. *Kinetics of acid leaching of ilmenite decomposed by KOH Part 2. Leaching by H_2SO_4 and $C_2H_2O_4$*, Journal of Hazardous Materials168, 793–799.

NAYL A.A., ISMAIL I.M. and ALY H.F., 2009b. *Ammonium hydroxide decomposition of ilmenite slag*, Hydrometallurgy 98, 196–200.

OLANIPEKUN E., 1999, *A kinetic study of the leaching of a Nigerian ilmenite ore by hydrochloric acid*, Hydrometallurgy, 53, 1–10.

SAMALA S., MOHAPATRA B.K., MUKHERJEE P.S. and CHATTERJEE S.K., 2009. *Integrated XRD, EPMA and XRF study of ilmenite and titanium slag used in pigment production*, Journal of Alloys and Compounds 474, 484–489.

SASIKUMAR C., RAO D.S., SRIKANTH S., MUKHOPADHYAY N.K., MEHROTRA S.P., 2007. *Dissolution studies of mechanically activated manavalakurichi ilmenite with HCl and H_2SO_4*, Hydrometallurgy 88, 154–169.

ZHANG S. and NICOL M. J., 2009. *An electrochemical study of the reduction and dissolution of ilmenite in sulfuric acid solutions*, Hydrometallurgy, 97, 146–152.

ZHANG S. and NICOL M. J., 2010. *Kinetics of the dissolution of ilmenite in sulfuric acid solutions under reducing conditions*, Hydrometallurgy 103, 196–204.

ZHANG Y., TAO Q., ZHANG Y., 2009. *A novel preparation of titanium dioxide from titanium slag*, Hydrometallurgy, 96, 52–56.

Physicochem. Probl. Miner. Process. 48(2), 2012, 441−454

www.minproc.pwr.wroc.pl/journal/

Physicochemical Problems of Mineral Processing

ISSN 1643-1049 (print)
ISSN 2084-4735 (online)

Received January 5, 2012; reviewed; accepted February 28, 2012

ADSORPTION AND DESORPTION KINETICS BEHAVIOUR OF METHYLENE BLUE ONTO ACTIVATED CARBON

Cigdem SARICI-OZDEMIR

Inonu University, Faculty of Engineering, Department of Chemical Engineering, 44280, Malatya, Turkey, Tel. : +90 422 3410010–4757, Fax: +90 422 3410046, cigdem.ozdemir@inonu.edu.tr

Abstract. In the present work investigations on a potential use of activated carbon for the removal of Methylene Blue (MB) from wastewater are presented. Adsorption kinetics of methylene blue has been studied using reaction-based and diffusion-based models. Three kinetic models, namely, pseudo-first-order, pseudo-second-order and the Elovich are analyzed at the temperature of 298 K for the reaction-based model. The kinetic studies showed that the data were well described by the pseudo-second-order kinetic model. Intraparticle diffusion, external-film diffusion, and internal-pore diffusion models characterizing MB were obtained. The results suggested that the activated carbon has a high potential to be used as an effective adsorbent for methylene blue adsorption. Pseudo first-order, pseudo second-order and the Elovich models were employed to describe the desorption mechanism. The experimental results showed that the pseudo second-order equation is the best model. About 99% of activated carbon has been regenerated by desorption.

keywords: activated carbon, adsorption, desorption, kinetic studies, methylene blue

1. Introduction

Environmental pollution is a problem both in developed and devoloping countries. Factors such as population growth, and urbanization, invariably place greater demands on the world. Industrial revolution brought, with technological progress such as discovery of how to make synthetic dye, virtually universal use by different industries. Cheaper to produce, more brighter color, fast and easy to apply to fabric, the new dyes changed world. The chemicals used to produce dyes today are often highly toxic, carcinogenic, or even explosive. Harmful chemicals are used in the dying process, including aniline, dioxin, toxic heavy metals (such as chrome, copper, zinc, formaldehyde). Almost all industrial dye processes involve a solution of a dye in water in which the fabrics are soak. So, the textile factories across the world are dumping millions of Mg of dye effluent into rivers. Therefore, it is necessary to remove them from the wastewater before discharging. For the removal of these materials, several methods such as physical, chemical and biological have been investigated. Among the methods, removal of dyes by adsorption is regarded as one of the competitive methods

http://dx.doi.org/10.5277/ppmp120210

because of high efficiency, economic feasibility and simplicity of design/operation (Chen et al., 2010; Rafatullah et al., 2010; Haque et al., 2011). Activated carbons, because of their large surface area and relatively high sorption capacity, for a wide variety of dyes, have become the most promising and effective adsorbent. Nevertheless, their applications are restricted, because activated carbons are prepared from natural materials such as wood or coal, which are expensive. Recently, low cost and easily available other carbonaceous materials have been used, for example apricot stone, almand barks, coffee seeds, tea waste, rice husk etc.) (Diao et al., 2001; Wei-Lung et al., 2011). Textile waste containing cotton, nylon and polymers creates a problem in the world. Activated carbon prepared from these wastes could be important for the regional economy. Because high value products are obtained from low cost materials, they simultaneously bring solution to the problem of wastes (Altenor et al. 2009).

Methylene blue (MB) is one of the well known basic/cationic dyes and has been widely used in wood, silk, cotton, pharmaceutical industries. In this work, activated carbon has been prepared from a mixture of textural waste by chemical activation with $ZnCl_2$ in the flow of N_2 at 500°C. The prepared activated carbon is used as an adsorbent to remove methylene blue from aqueous solutions. The kinetics and diffusion parameters of the adsorption and desorption processes have been investigated.

2. Materials and methods

2.1. Materials

The solute selected for this work was MB (chemical formula = $C_{16}H_{18}N_3SCl$, MW =320 g/mol). A stock solution of 1000 mg/dm^3 was prepared by dissolving the required amount of methylene blue in distilled water. The spectrophotometric determination of MB was carried out using a Shimadzu UV/Vis spectrophotometer at 662 nm (model UV-2100S, Japan).

2.2. Preparation of activated carbon (WZ)

Textural waste, provided by different textile fabrics in Malatya, Turkey, was used in this study as a source of activated carbon. The raw material was subjected to two steps of activation as follows.

a) The raw material was mixed with $ZnCl_2$ ($ZnCl_2$: waste=0.5/1), and the mixture was kneaded by adding distilled water. The mixture was then dried at 110°C to prepare the impregnated sample.

b) The impregnated sample was placed on a quartz dish, which was then inserted within a quartz tube (internal diameter = 60 mm). The impregnated sample was heated at the rate of 10°C/min up to the activation temparature (500°C) under N_2 flow (100 cm^3/min) and held at the activation temperature for 1 h. After activation, the sample was cooled under N_2 flow. The sample was washed sequentially several times with hot

distilled water to remove any residual chemical and until a pH of 7 was reached. The washed sample was dried at 110°C to prepare activated carbon.

2.3. Adsorption experiments

MB solutions were prepared in distilled water at the desired concentrations. Adsorption experiments were carried out by agitating 0.1 g of WZ with 50 cm^3 solutions of the desired concentration (50, 75 and 100 mg/dm^3) at different values of time (1 to 60 min) and 25ºC in a thermostatic bath operating at 400 rpm. The amount of MB adsorbed onto WZ, q_t (mg/g), was calculated by the mass balance relationship represented by equation:

$$q_t = (C_0 - C_t)\frac{V}{W}, \tag{1}$$

where C_0 and C_t are the initial and final (at time t) liquid and phase concentrations of MB (mg/dm^3), respectively, V is the volume of the solution (dm^3), and W is the weight of the dry WZ used (g).

The normalized standard deviation Δq_e (%) was calculated using Eq. (2):

$$\Delta q_e(\%) = 100\sqrt{\frac{\sum\left[\left(q_{e,\exp} - q_{e,cal}\right)/q_{e,\exp}\right]^2}{N-1}}, \tag{2}$$

where N is the number of data points, $q_{e,exp}$ and $q_{e,cal}$ (mg/g) are the experimental and calculated equilibrium adsorption capacities value, respectively.

2.4. Desorption experiments

For the desorption study, 0.5 g of activated carbon was added to 250 cm^3 of MB solutions (50, 75 and 100 mg/dm^3) and the mixture was stirred at 60 min. After mixing, the supernatant MB solution was discarded and the activated carbon alone was separated. Then, the MB-adsorbed activated carbon was added into 250 cm^3 of ethanol mixture (*v/v*, ethanol/water= 10/100). Ethanol and activated carbon (saturated with MB) solution samples were taken at specific time intervals (3, 5, 10, 60 min). The amount of MB desorbed from WZ, q_t (mg/g), was calculated at different values of time (1 to 60 min) and all concentrations and temperature of 25°C by the Eq. (1).

3. Results and discussion

3.1. Effect of initial concentration of methylene blue

Initial dye concentration provides an important driving force to overcome the mass transfer resistance of dye between the aqueous solution and activated carbon surface. Adsorption kinetic studies were performed by measuring methylene blue concentration and the results are illustrated in Fig. 1. The adsorption capacity

increased from 23.11 to 46.31 mg/g as the initial dye concentrations increased from 50 to 100 mg/dm^3. It can be seen that a rapid adsorption of MB by activated carbon occurred, after approximately 30 min for all concentrations. It was particularly interesting that the process showed an extraordinarily fast initial rate of adsorption, which can be verified by the fact that the amount of adsorbed MB onto activated carbon within 5 min almost achieved 90% of that at the equilibrium.

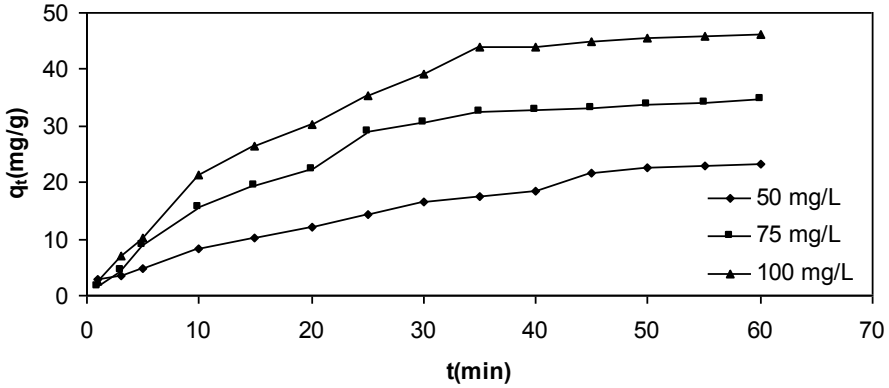

Fig. 1. Effect of initial dye concentration on the adsorption of MB as a function of time at 298 K

3.2. Adsorption kinetics

Kinetic mechanism of dye adsorption occurs through three consecutive steps:

1. external diffusion of dye molecules across the liquid film surrounding the porous adsorbent
2. adsorption of the dye on the adsorption site
3. internal diffusion of dye within the particle.

Due to the nature of adsorption, kinetic model for dyes could be divided into two types, namely reaction-based models and diffusion based models (Ho et al., 2000; Al-Degs et al., 2006).

3.2.1. Reaction-based models

To investigate the adsorption kinetics of MB three kinetic models, namely, pseudo first-order, pseudo second-order and Elovich models were analyzed at the temperature of 298 K.

The rate constant for the adsorption of MB onto activated carbon determined by the pseudo first-order equation is expressed as (Barrett et al.,1971):

$$\frac{dq_t}{dt} = k_1\left(q_e - q\right), \tag{3}$$

where k_1 (min^{-1}) is the pseudo first-order rate constant. Integrating Eq. (3) with respect to the integration conditions $q = 0$ to $q = q_t$ at $t = 0$ to $t = t$, the kinetic rate expression becomes:

$$\log(q_e - q_t) = \log q_e - \frac{k_1}{2.303} t, \tag{4}$$

where q_e and q_t are the amounts of MB adsorbed (mg/g) at equilibrium and time t (min), respectively.

The adsorption kinetics have also been determined by the pseudo second-order model using equation (Ho and McKay, 1998):

$$\frac{t}{q_t} = \frac{1}{k_2 q_e^2} + \frac{t}{q_e}, \tag{5}$$

where k_2 is the second order-rate constantn, g/(mg·min); and $h = k_2 q_e^2$, where h is the initial adsorption rate, mg/(g·min).

The Elovich model equation is generally expressed as (Low, 1960):

$$\frac{dq_t}{dt} = \alpha \exp(-\beta q_t). \tag{6}$$

To simplify the the Elovich equation, Chian and Clayton (1980) assumed that $\alpha\beta t >> t$ and by applying boundary conditions $t=0$ to $t=t$ and $q_t=0$ to $q_t=q_0$. Then, Eq. (6) becomes (Chien and Clayton, 1980):

$$q_t = \frac{1}{\beta}\ln(\alpha\beta) + \frac{1}{\beta}\ln t. \tag{7}$$

where α is the initial adsorption rate, mg/(g·min) and β is the desorption constant (g/mg).

The plot of log (q_e-q_t) versus t should give a linear relationship, from which k_1 and q_e can be obtained from the slope and intercept of the plot, respectively. The k_1 values, calculated q_e values, and correlation coefficients are provided in Table 1. The coefficient of correlation for the pseudo first-order kinetic model is not high for all concentrations. Moreover, the determined values of q_e calculated from the equation differ from the experimental values showing that adsorption of methylene blue onto WZ is not a first-order reaction and had low correlation coefficients (R^2<0.88).

The plot of (t/q_t) versus t of Eq. (5) should give a linear relationship, from which q_e and k_2 can be determined from the slope and intercept of the plot, respectively. The results are illustrated in Table 1. The experimental results were applied to the pseudo-second order model straight lines with high correlation coefficients (R^2=0.982). They indicate that adsorption of MB follows the pseudo-second order kinetic model. From the analysis of all kinetic models one can predict experimental behaviour of the MB-WZ system.

Table 1. Kinetic paramaters of adsorption

Concentration (mg/dm$^{3)}$	50	75	100
$q_{e,exp}$ (mg/g)	32.11	43.56	64.30
Pseudo-first order			
$q_{e,cal}$ (mg/g)	34.84	72.45	111.55
k_1 (min^{-1})	0.072	0.080	0.091
R^2	0.839	0.858	0.878
Δq_e (%)	40.2	31.1	28.0
Pseudo-second order			
$q_{e,cal}$ (mg/g)	32.36	42.63	68.49
k_2 (g·mg^{-1}·min^{-1})	0.00081	0.00078	0.00072
h (mg·g^{-1}·min^{-1})	0.848	1.417	3.377
R^2	0.915	0.962	0.982
Δq_e (%)	11.1	9.90	5.69
Elovich			
α (mg·g^{-1}·min^{-1})	3.947	6.537	8.864
β (g.mg^{-1})	0.178	0.106	0.079
R^2	0.900	0.953	0.958
Δq_e (%)	28.8	26.1	18.2

A comparison of the three kinetic models with experimental values for all concentrations can be seen in Figs. 2a-c. The normalized standard deviations Δq_e (%) are used to see the fit between the experimental data and theoretical values of MB onto activated carbon. It is clear from the figures and standard deviations (<11.10 %) that for pseudo-second-order (Table 1), there is a good agreement between the experimental and predicted values.

3.2.2. Diffusion-based models

Various diffusion models can be used to describe adsorption. These diffusion models have been developed to predict the dynamic character of adsorption. This work used the intraparticle diffusion, external-film diffusion, and internal-pore diffusion models to characterize adsorption of MB.

The intraparticle diffusion equation (Srivastova et al., 1989; Weber et al., 1973) can be written as follows:

$$q_t = k_{\text{int}} t^{1/2} + c\,, \tag{8}$$

where c is the intercept of the line, which is proportional to the thickness of the boundary layer and k_{int} is the intraparticle diffusion rate constant, mg/(g·min$^{-1/2}$). The intraparticle diffusion model rate constant, k_{int}, is obtained from the slope of the straight line of q_t versus $t^{1/2}$ (Fig. 3).

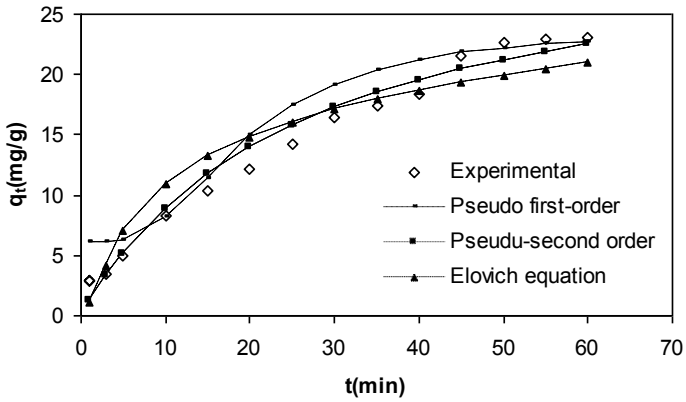

(a)

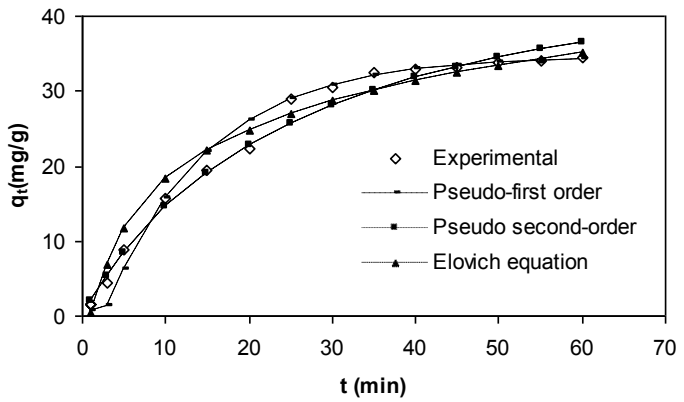

(b)

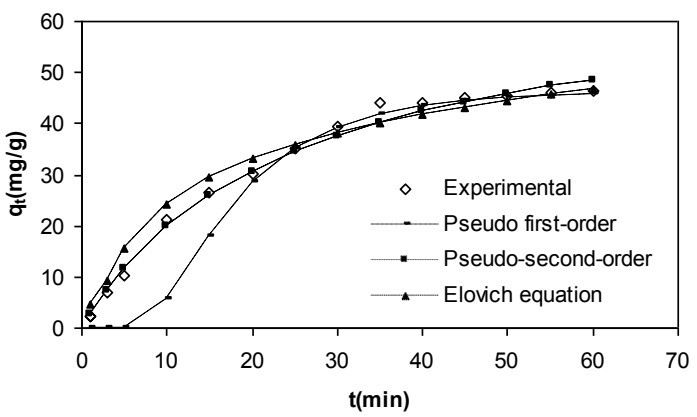

©

Fig. 2. Comparison of kinetic models at 298 K (a) Concentration of MB solutions: 50 mg/dm^3, (b) Concentration of MB solutions: 75 mg/dm^3 and (c) Concentration of MB solutions 100 mg/dm^3

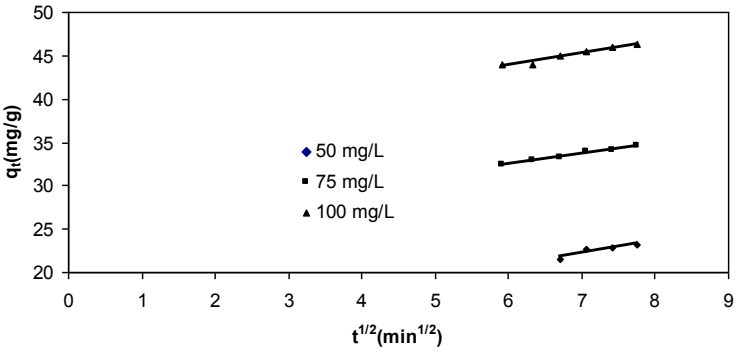

Fig. 3. Intraparticle diffusion plots of MB adsorption

During the initial adsorption period, description can be simplified by assuming that the concentration at the activated carbon surface tends toward zero (intraparticle diffusion negligible). External diffusion resistance is predominant and controls the adsorption of MB. Thus, the external diffusion models can be considered as follows (Dutta et al. 2011):

$$\left[\frac{d\left(C_t / C_0\right)}{dt}\right]_{t=0} = -k_f \frac{A}{V}. \tag{9}$$

and in the integrated form:

$$\ln \frac{C_t}{C_0} = -k_f \frac{A}{V} t, \tag{10}$$

where C_0 is the initial MB concentration (mg/dm^3), C_t MB concentration at time t (min), k_f external surface diffusion coefficient (m/min), A external surface area of the activated carbon (1750 m^2/g), V volume of solution (dm^3). Parameter k_f can be estimated from the slope of the $\ln(C_t/C_0)$ versus t curve at time $t \rightarrow 0$.

The internal-pore diffusion can be calculated by using equations which are derived from Fick's law (Hajjaji et al., 2001; Streat et al., 1995)

$$F(t) = \frac{C_0 - C_t}{C_0 - C_e} = \frac{q_t}{q_e} = \left[1 - \exp\left(-\frac{\pi^2 D t}{r^2}\right)\right]^{1/2}, \tag{11}$$

or

$$\ln\left[1 - \mathrm{F}(t)^2\right] = -\frac{\pi^2 D}{r^2} t, \tag{12}$$

where C_e is the MB equilibrium concentration (mg/dm^3), D is the internal-pore diffusion coefficient (m^2/min) and r is the particle radius assuming spherical geometry (2.10^{-6} m). A plot of $\ln[1\text{-}F(t)^2]$ versus time t should be linear with a slop of $-\pi^2 \cdot D/r^2$, which is commonly known as the diffusional rate constant.

Table 2 shows that the intraparticle diffusion model rate constant, k_{int}, which increases as the initial MB concentration increases. This could be attributed to the driving force of diffusion. The driving force changes with the MB concentration in the solution. The linear plots at various concentration do not pass through the origin, which shows that the intraparticle diffusion is not the only rate-controlling step (Fig. 3). If the plot is straight line passing through the origin, then the adsorption rate is governed by particle diffusion mechanism. Otherwise, it is governed by the film diffusion (Sarkar et al., 2003). The values of c are related to the boundary layer resistance. It is relatively high, and the greater is the contribution of the surface adsorption in the rate limiting step.

The values of external diffusion coefficient, k_f, increase by the increasing initial MB concentration (Table 2). The change in k_f, depends on the surface area and pore distribution of activated carbon. The activated carbon has micropores and external diffusion is more diffucult with the increasing initial concentration of MB.

The internal pore diffusivities were determined using Eq. (12). The adsorption data in Table 2 show that the internal pore diffusion coefficients is increasing with the increasing initial dye concentration.

A comparison of the adsorption capacities of MB adsorption estimated from the kinetic studies on various adsorbents is presented in Table 3. The variation in adsorption capacities and affinities can be mainly attributed to the differences in experimental condition and properties of the adsorbent. From Table 3, it can be observed, that the values of q_e of WZ for MB adsorption for the same initial concentration were higher than that for agricultural by-products (wood sawdust, rejected tea, carrot powder etc), zeolite, and activated carbon. The results demonstrated that WZ's could be employed as promising adsorbents.

Table 2. Diffusion parameters of adsorption

Concentration (mg/dm^3)	50	75	100
İntraparticle diffusion			
k_{int} (mg·g^{-1}·min$^{-1/2}$).	1.12	1.18	1.42
c	12.29	25.46	35.42
R^2	0.898	0.970	0.989
External-film diffusion			
$k_f \cdot 10^8$ (m/min)	13.10	14.50	15.10
R^2	0.976	0.980	0.993
Internal-pore diffusion			
$D \cdot 10^{15}$(m^2/min)	22.31	27.18	28.27
R^2	0.893	0.963	0.939

Table 3. Adsorption capacities of MB for adsorbents

Adsorbent	C_o (mg/dm^3)	q_e (mg/g)	Ref.
Wood sawdust	120	16.21	(Ofomaja, 2008)
Cotton stalk	475	104.82	(Deng et al., 20011)
	825	211.35	
Cotton stalk	950	240.96	(Deng et al., 20011)
(with H_2SO_4)	1415	381.68	
Cotton stalk	950	173.01	(Deng et al., 20011)
(with H_3PO_4)	1415	242.13	
Rejected tea	50	20.80	(Nasuha et al., 2010)
	100	40.50	
	200	80.00	
Kenaf care fibers	50	44.84	(Sajab et al., 2011)
	100	96.15	
	150	142.80	
Activated carbon	250	50.09	(Durala et al., 2011)
(from posidonia oceonica)	500	101.40	
	750	153.55	
Wheat straw	100	96.40	(Han et al., 2010)
Palm kernel fiber	20	7.67	(El-Sayed et al., 2011)
	40	7.22	
	80	27.22	
	160	31.26	
Peanut husk	80	35.52	(Song et al., 2011)
Carrot leaves powder	10	4.10	(Kushwaha et al., 2011)
Carrot stem powder	10	4.34	(Kushwaha et al., 2011)
J. curcas cake residue	200	160.85	(Kurniawan et al. 2011)
	500	282.31	
Titanate nanotubes	50	94.15	(Xionga et al. 2010)
	100	129.17	
NaOH-modified rejected	50	2.44	(Nasuha et al. 2011)
tea	100	3.99	
	200	19.80	
	300	71.42	
Lotus leaf powder	50	46.00	(Han et al., 2011)
	100	91.00	
Zeolite	30	4.81	(Han et al., 2009)
	55	8.27	
	113	14.90	
Jack fruit peel	35	10.58	(Hameed, 2009)
	80	25.48	
	130	40.70	
Tea waste	50	24.76	(Udin et al., 2009)
Activated carbon	50	32.36	This work
(from textural waste)	75	42.63	
	100	68.49	

3.3 Desorption kinetics

Desorption characteristics or regeneration of spent activated carbon is extremely important. Desorption experiments were carried out using activated carbon at 25^{o}C and initial concentration of 50, 75 and 100 mg/dm^3. As shown in Fig. 4 the desorption capacity at equilibrium of MB desorption increased from 0.08 to 0.23 mg/dm^3 with an increase in the initial dye concentration. The desorption reaches equilibrium with solid phase concentration of q_t at the shortest time of about 6 min. On the other hand, the

longest equilibrium time of about 12 min is needed for the case with the highest q_t values (Tseng et al., 2009). These values show that more than 99% of MB has been desorbed.

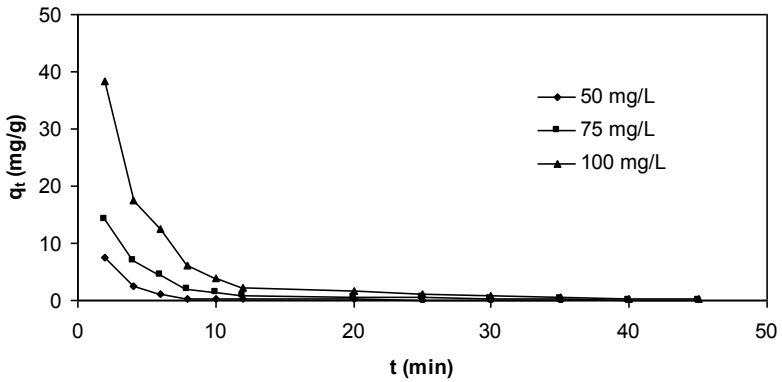

Fig. 4. Effect of initial dye concentration on the desorption of MB from activated carbons at 298 K

Desorption kinetics for activated carbon has not been determined in studies conducted to date. In this work, the kinetics of desorption has been considered using the pseudo-first order, pseudo-second order and Elovich model. Plots of the kinetic equation are shown in Figs. 5-7. The experimental results for the three kinetic illustrated equations are presented in Table 4. The behavior of k_1, k_2 and β could be attributed to the decrease in dye concentration in activated carbon. The R^2 values of the pseudo second-order model were >0.93, which is higher than the R^2 values obtained for the pseudo-first-order and the Elovich model. Therefore, the desorption kinetics could be better described by the pseudo-second-order kinetic model for MB desorption from activated carbon.

Table 4. Kinetic parameters of desorption

Concentration (mg/dm^3)	50	75	100
$q_{e,\exp}$ (mg/g)	0.08	0.09	0.23
Pseudo-first order			
$q_{e,\mathrm{cal}}$ (mg/g)	2.00	8.03	18.88
k_1 (min^{-1})	0.13	0.12	0.10
R^2	0.756	0.929	0.892
Pseudo-second order			
$q_{e,\mathrm{cal}}$ (mg/g)	0.11	0.29	0.51
k_2 (g·mg^{-1}·min^{-1})	2.11	0.61	0.31
h (mg·g^{-1}·min^{-1})	0.025	0.051	0.081
R^2	0.978	0.934	0.941
Elovich			
α (mg·g^{-1}·min^{-1})	38.67	102.4	305.27
β (g/mg)	0.32	0.22	0.09
R^2	0.800	0.875	0.849

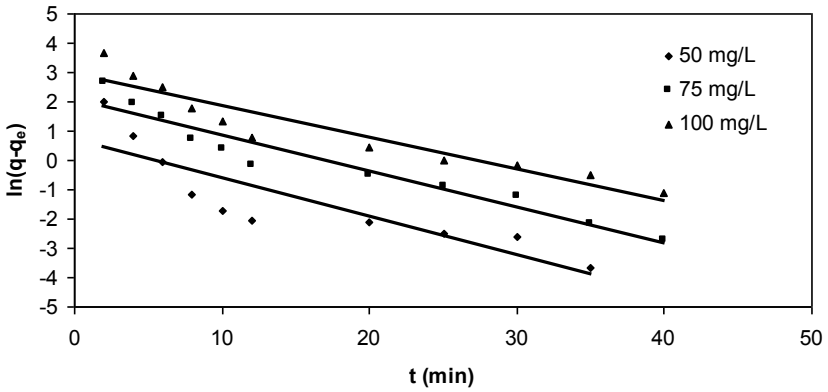

Fig. 5. Pseudo-first-order kinetics for the desorption of MB

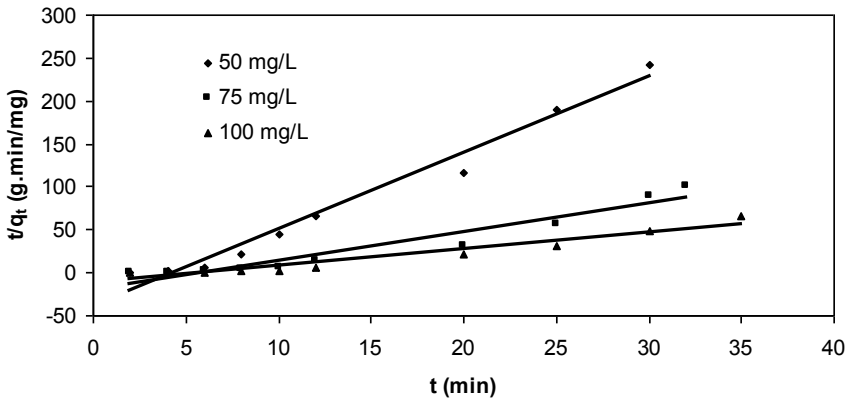

Fig. 6. Pseudo-second-order kinetics for the desorption of MB

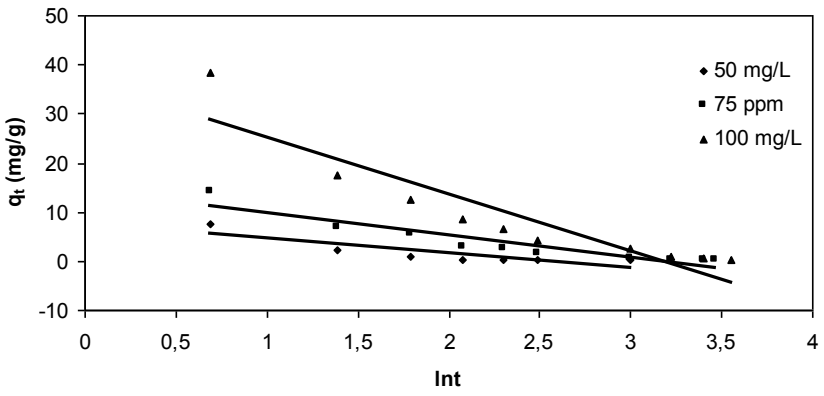

Fig. 7. The Elovich kinetics model for the desorption of MB

4. Conclusion

Activated carbon (WZ) can be used as adsorbent for removal of MB from its aqueous solution.

The kinetics of MB adsorption onto activated carbon was examined using the pseudo-first-order, pseudo-second-order and Elovich kinetics models. The adsorption kinetics followed the pseudo-second-order kinetic model.

The adsorption of MB onto activated carbon was controlled by external diffusion. The rate of adsorption of MB was very high during the first ten minutes. This was followed by a slower rate, and gradually approached a plateau.

Regeneration efficiency of activated carbon (or desorption of MB) was calculated to be 99%. The desorption kinetics followed the pseudo-second-order kinetic model.

References

AL-DEGS, Y.S., EL-BARGHOUTHİ, M.I., ISSA, A.A., KHRAİSHEH, M.A., WALKER, G.M., 2006, *Sorption of Zn(II), Pb(II) and Co(II) using natural sorbents: equilibrium and kinetic studies*, Water Res. 40, 2645–2658.

ALTENOR, S., CARENE, B., EMMANUEL, E., LAMBERT, J., EHRHARDT, J., GASPARD, S., 2009, *Adsorption studies of methylene blue and phenol onto vetiver roots activated carbon prepared by chemical activation* J. Hazard. Mater. 165, 1029–1039.

BARRETT, P.E.P, JOYNER, L.G., HALENDA, P.P. 1951, *The determination of pore volume and area distribution in porous substance. I. Computations from nitrogen isotherms*, J.Am. Chem. Soc. 73, 373–380.

CHEN, S., ZHANG, J., ZHANG, C., YUE, Q., Lİ, Y., Lİ, C. 2010, *Equilibrium and kinetic studies of methyl orange and methyl violet adsorption on activated carbon derived from Phragmites austries*, Desalination 252, 149–156.

CHİEN,S.H., CLAYTON, W.R., 1980, *Application of Elovich equation to the kinetics of phosphate release and sorption on soils*, Soil Sci. Soc. Am. J. 44, 265–268.

DENG, H., LU, J., Lİ, G., ZHANG, G., WANG, X. 2011, *Adsorption of methylene blue on adsorbent materials produced from cotton stalk*, Chemical Engineering Journal 172, 326–334.

DİAO, Y., WALAWENDER, W.P., FAN, L.T. 2002, *Activated carbons prepared from phosphoric acid activation of grain sorghum*, Bioresource Technology 81, 45-52.

DURALA, M.U., CAVASA, L., PAPAGEORGİOUC, S.K., KATSAROSC, F.K. 2011, *Ethylene blue adsorption on activated carbon prepared from Posidonia oceanica (L.) dead leaves: Kinetics and equilibrium studies*, Chemical Engineering Journal 168, 77-85.

DUTTA, S., BASU, J.K., GHAR, R.N. 2001, *Studies on adsorption of p-nitrophenol on charred saw-dust*, Sep. Purif. Technol. 21, 227–235.

EL-SAYED, G.O. 2011, *Removal of methylene blue and crystal violet from aqueous solutions by palm kernel fiber*, Desalination 272, 225–232.

HAJJAJI, M., KACIM, S., ALAMI, A., EL-BOUADILI, A., EL-MOUNTASSIR, M. 2001, *Chemical and mineralogical characterisation of a clay taken from the Moroccan meseta and a study of the interaction between its fine friction and methylene blue*. Applied Clay Science 20 1–12.

HAMEED, B.H., 2009, *Removal of cationic dye from aqueous solution using jackfruit peel non-conventional low-cost adsorbent*, Journal of Hazardous Materials 162, 344–350.

HAN, X., WANG, W., MA, X., 2011, *Adsorption characteristics of methylene blue onto low cost biomass material lotus leaf*, Chemical Engineering Journal 171, 1–8.

HAN, R., ZHANG, J., HAN, P., WANG, Y., ZHAO, Z., TANGA M., 2009, *Study of equilibrium, kinetic and thermodynamic parameters about methylene blue adsorption onto natural zeolite*, Chemical Engineering Journal 145 496–504.

HAN, R., ZHANG L., SONG C., ZHANG M., ZHU H., ZHANG L., 2010, *Characterization of modified wheat straw, kinetic and equilibrium study about copper ion and methylene blue adsorption in batch mode*, Carbohydrate Polymers 79, 1140–1149.

HAQUE, E., JUN, J.W., JHUNG, S.H. 2011, *Adsorptive removal of methyl orange and methylene blue from aqueous solution with a metal-organic framework material, iron terephthalate (MOF-235)*. J. Hazard. Mater. 185, 507–511.

HO, Y.S., MCKAY, G. 1998, *Sorption of dye from aqueous solution by peat*, Chem. Eng. J. 70, 115–124.

HO, Y.S., NG, J.C.Y., MCKAY, G. 2000, *Kinetics of pollutant sorption by biosorbents: a review*. Sep. Purif. Methods 29, 189–232.

KURNİAWAN, A., ISMADJİ, S., 2011, *Potential utilizationof Jatropha curcas L. press-cake residue as new precursor for activated carbon preparation:Application methylene blue removal from aqueous solution*, Journal of the Taiwan Institute of Chemical Engineers, in press.

KUSHWAHA, A.K., GUPTA, N., CHATTOPADHYAYA, M.C., 2011, *Removal of cationic methylene blue and malachite gren dyes from aqueous solution by waste materials of Daucus carota*, Journal of Saudi Chemical Society, in press.

LOW, M.J.D. 1960, *Kinetics of chemisorption of gases on solids*, Chem. Rev. 60, 267–317.

NASUHA N., HAMEED B.H., DİN A.T. 2010, *Rejected tea as a potential low-cost adsorbent for the removal of methylene blue*, Journal Hazard. Mater. 175, 126–132.

NASUHA, N., HAMEED, B.H., 2011, *Adsorption of methylene blue from aqueous solution onto NaOH-modified rejected tea*, Chemical Engineering Journal 166, 783–786.

OFOMAJA, A.E., 2008, *Kinetic study and sorption mechanism of methylene blue and methyl violet onto mansonia (Mansonia altissima) wood sawdust*, Chemical Engineering Journal 143, 85–95.

RAFATULLAH, M., SULAİMAN, O., HASHİM, R., AHMAD, A. 2010, *Adsorption of methylene blue on low-cost adsorbents: A review*, J. Hazard. Mater. 177, 70–80.

SAJAB, M.S., CHİA, C.H., ZAKARİA, S., JANİ, S.M., AYOB, M.K. 2011, *Citric acid modified kenaf core fibres for removal of methylene blue from aqueous solution*, Bioresource Technology 102, 7237–7243.

SARKAR M., KUMARACHARYA P., BHATTACHARYA B., 2003, *Modeling the adsorption kinetics of some priority organic pollutants in water from diffusion and activation energy parameters*, J. Colloid Interf. Sci. 266, 28-32.

SRIVASTOVA, S.K., TYAGI, R., PANT, N. 1989, *Adsorption of heavy metal ions on carbonaceous material developed from the waste slurry generated in local fertilizer plants*, Water Research 23, 1161–1165.

STREAT, M., PATRICK, J.W., CAMPORRO PEREZ, M.J. 1995, *Sorption of phenol and parachlorophenol from water using conventional and novel activated carbons*, Water Research 29, 467–472.

SONG, J., ZOU, W., BİAN, Y., SU, F., HAN, R., 2011, *Adsorption characteristics of methylene blue by peanut husk in batch and column models*, Desalination 265, 119–125.

TSENG J., CHANG C., CHANG C., CHEN Y., CHANG C., Jİ D., C. CHİU,P. CHİANG, 2009, *Kinetics and equilibrium of desorption removal of copper from magnetic polymer adsorbent*, Journal of Hazard. Mater. 171, 370–377.

UDİN, T., ISLAM, A., MAHMUD, S., RUKANUZZAMAN M., 2009, *Adsorptive removal of methylene blue by tea waste*, Journal of Hazardous Materials 164, 53–60.

WEBER, W.J., ASCE, J.M., MORRIS, J.C. 1963, *Kinetics of adsorption on carbon from solution in: Proceedings of the American Society of Civil Engineers*, J. Senit Eng. Div. 89, 31–59.

WEİ-LUNG C., Lİ-SHİEN C.,YEN-HSİANG H., CHİH-YANG H., 2011, *Effect of process parameters on the removal of indium ions from aqueous solutions by adsorption onto tea waste*, Fresenius Environmental Bulletin.

XİONGA, L., YANG, Y., MAİA, J., SUNA, W., ZHANG, C., WEİ, D., CHEN, Q., Nİ J., 2010, *Adsorption behavior of methylene blue onto titanate nanotubes*, Chemical Engineering Journal 156, 313–320.

Physicochem. Probl. Miner. Process. 48(2), 2012, 455−462

www.minproc.pwr.wroc.pl/journal/

Physicochemical Problems of Mineral Processing

ISSN 1643-1049 (print)
ISSN 2084-4735 (online)

Received October 31, 2011; reviewed; accepted February 17, 2012

ENHANCEMENT OF COLEMANITE FLOTATION BY ULTRASONIC PRE-TREATMENT

Safak G. OZKAN, Can GUNGOREN

Istanbul University, Eng. Faculty, Mining Eng. Dept., 34320, Avcilar, Istanbul, Turkey

Abstract. Ultrasonic treatment methods are widely used for surface cleaning purposes prior to application of flotation. In this study, enhancement possibility for colemanite recovery was investigated with use of an ultrasonic bath prior to flotation. Representative colemanite ore samples from Hisarcik and Espey open pit mines, located in Emet, Turkey were used for this purpose. Ultrasonic flotation experiments were carried out by using circularly shaped RK-106 model of ultrasonic bath with constant frequency and power, manufactured by Bandelin GmbH in Germany and Denver Sub-2A type flotation machine with an impeller speed of 1200 rpm and 1 cubic decimeter capacity. The reagent for colemanite flotation was Cytec-R825 with variable dosages during conventional and ultrasonic flotation experiments. The results showed that ultrasonic pre-treatment helps desliming and hence yields more borate recovery in floated part with lower borate content in tailing than under conventional flotation conditions by using similar reagent dosages.

keywords: colemanite flotation, ultrasound, ultrasonic pre-treatment, desliming, borates

1. Introduction

Froth flotation process can be influenced by a large number of material, chemical, equipment and operational variables. Changing one of these variables certainly affects the results of flotation, such as grade and recovery significantly. Ultrasound is one of the important treatment methods used to advance the flotation process (Stoev, 1992; Ozkan and Gungoren, 2010).

Chemical effects of ultrasonic treatment in a flotation system are characterized by cavitation and are accompanied by a local increase in pressure and temperature. As solid/liquid interactions are weaker than liquid cohesion forces, solid/liquid interfaces are more amenable to the formation of cavitation. The unsettled conditions occurred at a solid/liquid interface can modify the surface properties of minerals, leading to changes in the adsorption of collectors on minerals and accordingly in their flotation responses. However, dispersive effects occur when ultrasound is applied to a pulp containing a stabilizer such as a surfactant. This phenomenon ends with the formation of an emulsion. Ultrasonic treatment can improve the effectiveness of a reagent due to more uniform distribution in the suspension and also in enhancement of the activity of

http://dx.doi.org/10.5277/ppmp120211

the chemicals used (Celik, 1987; Cilek, Ozgen, 2010, Letmahe et al., 2002; Mitome, 2003; Ozkan and Kuyumcu, 2006, 2007).

In this study colemanite flotation was optimized by conventional evaluation methods such as grade-recovery curves considering some of the material characterization tests, i.e. zeta potential measurements, and the results were compared with ultrasonic flotation data.

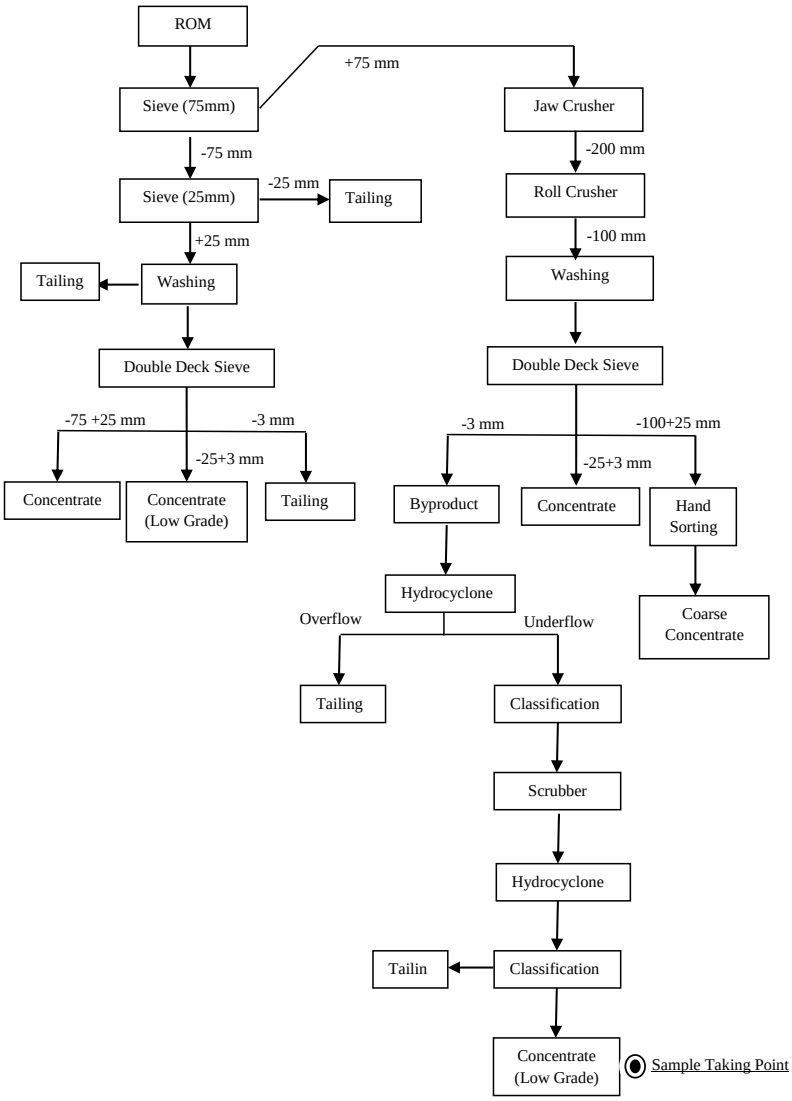

Fig. 1. Simplified processing flow-sheet of the Hisarcik colemanite concentrator (Arslan, 2007; Gungoren, 2009)

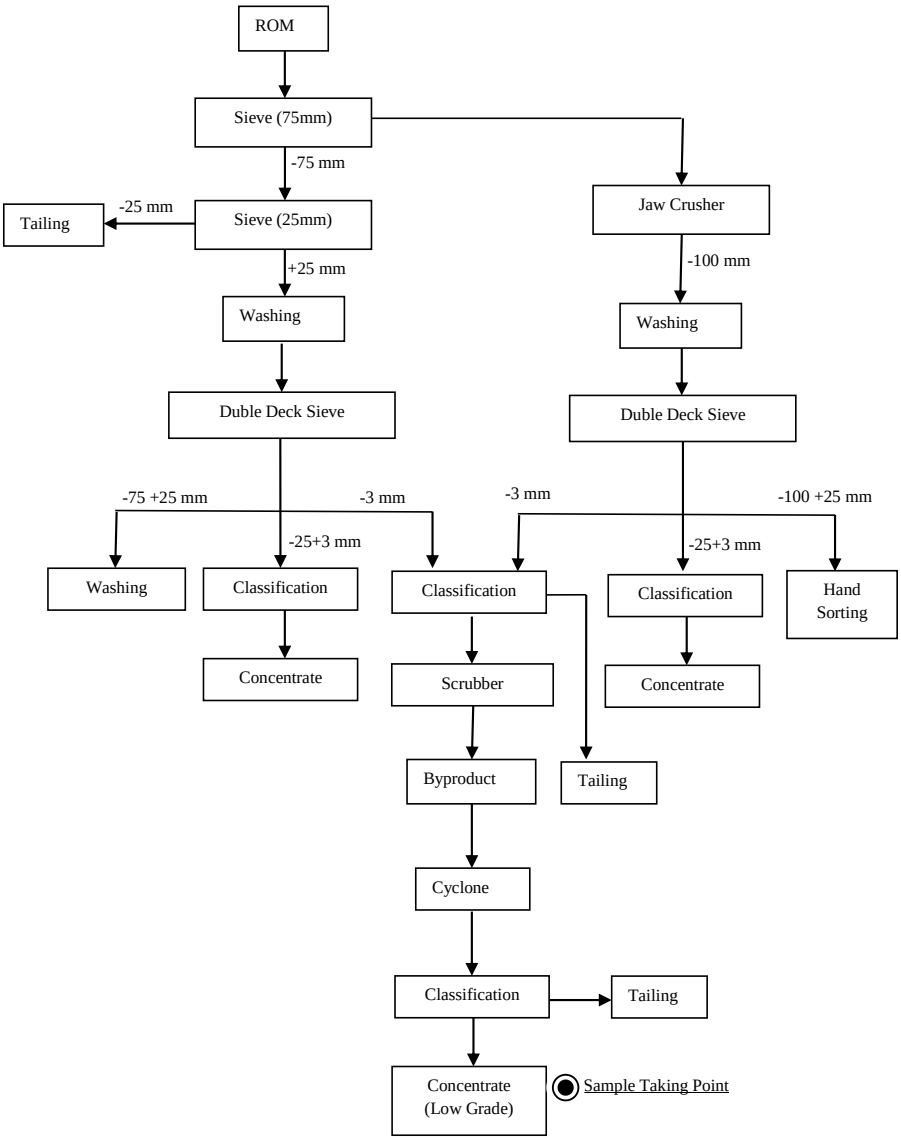

Fig. 2. Simplified processing flow-sheet of the Espey colemanite concentrator (Arslan, 2007; Gungoren, 2009)

2. Material and method

Current colemanite samples were taken from the product stockpiles insufficiently processed in terms of their borate contents by Eti Mines Inc. at Hisarcik and Espey open pit mines, situated in Emet, Kutahya, Turkey. The particle size fraction of the samples was -3 mm. They had insufficient B_2O_3% grades. Current colemanite

processing flow-sheets of both concentrator plants operated by Eti Mines Inc. are shown in Figs. 1 and 2 (Arslan, 2007; Gungoren, 2009). The points of which the current samples were taken are illustrated on the process flowsheets.

The material characterization tests include grinding tests, particle size distrubition, complete chemical and mineralogical analyses as well as zeta potential measurements.

The mineralogical and mineral liberation observations were carried out by an optical binocular microscope. Besides the major colemanite mineral, some clays and arsenic minerals such as orpiment and realgar were observed as gangue minerals. It was also observed that colemanite liberates at minus 250 μm. Because of the possible neagative effects of slime coatings, material at minus 38 μm was decided to be removed before flotation.

Before flotation, grinding tests were performed by a laboratory scale rod mill. About 1 kg sample was ground for the periods of 5, 10 and 20 minutes. Cumulative under size curves of the ground material are shown in Fig. 3. Consequently, optimal grinding time was determined as 8 minutes.

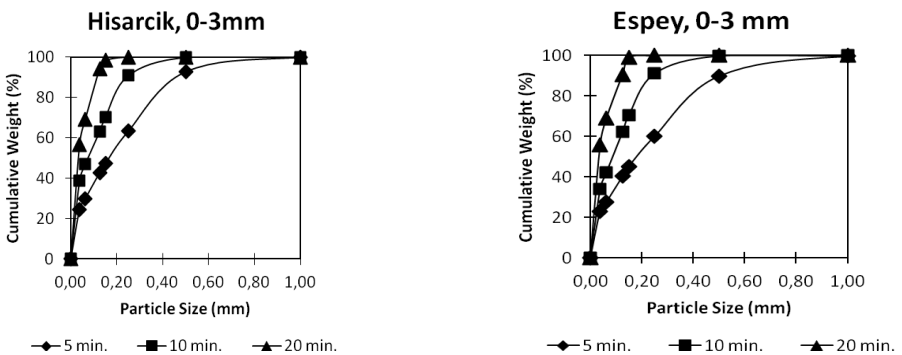

Fig. 3. Cumulative size distributions of the ground samples

The complete chemical analyses of the samples were performed at Eti Mines Inc.'s Emet Boron Works Laboratory and the results are shown in Table 1.

Zeta potentials of conventional and ultrasonically treated pure colemanite, which was previously hand-selected from the Emet deposits, were measured using a Nano Z (ZEN2500) model zeta meter supplied from Malvern Instruments. The device uses a combination of measurement techniques: Electrophoresis and Laser Doppler Velocimetry, called Laser Doppler Electrophoresis. This method is based on the velocity of particle movement in a liquid when electrical field is applied. Hand-selected pure colemanite crystals were ground with a mortar grinder, classified to minus 75 plus 38 micrometer particle size and used during the measurements. Suspensions at different pH values were prepared. Next, a small amount of the representative sample was transferred to the measurement cell. In Fig. 4, the zeta potential variation against various pH values can be seen. It explains the reasons for

selection of an anionic type collector, sodium alkyl sulphonate (Cytec R825) for colemanite flotation.

To reveal the effects of ultrasound applied before flotation, the tests were carried out on conventionally and ultrasonically pre-treated samples separately.

Table 1. Complete chemical analyses results of the investigated samples

Sample	B_2O_3 %	SiO_2 %	MgO %	CaO %	TiO_2 %	Al_2O_3 %	SrO %	K_2O %	Fe_2O_3 %	As ppm	LOI % 900 °C, 15 min
Hisarcik 0-3 mm	32.64	11.35	7.61	21.44	0.06	1.14	0.57	0.55	0.54	750	23.47
Espey 0-3 mm	39.28	8.72	2.68	22.10	0.15	2.28	1.41	0.83	1.24	350	21.04

A Denver Sub 2A flotation machine with one dm^3 cell volume was employed in the experiments. The agitation speed of 1200 rpm and 20% pulp to solid ratio were chosen during the tests. A five percent volumetric concentration of a sodium sulphonate type Cytec R825 collector and alcohol type Ekofol 440 frother were used. The collector was tested in four different dosages: 500, 1000, 1500 and 2000 g/Mg, whereas the frother quantity was kept at 100 g/Mg for all experiments.

A circular profile, 35 kHz single frequency and 120 W single power Bandelin RK106 model ultrasonic bath was used for ultrasonic pre-treatment. Colemanite samples with 20% pulp to solid ratio were sonicated for 10 minutes under above conditions.

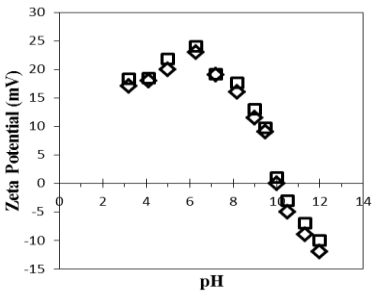

Fig. 4. Zeta potential variation of pure colemanite samples obtained from Emet deposits

3. Experimental results

Concentration tests can be categorized into conventional and ultrasonically pre-treated flotation with variable parameters for comparison and evaluation of the results. The purpose of these tests is to demonstrate and to clarify the grade and recovery differences between conventional and ultrasonicaly pre-treated flotation tests.

The grades and recoveries of flotation products are given in Figs. 5 and 6. B_2O_3 grade and recovery values regard flotation concentrates (floated) and tailings (sinked), whereas Fe_2O_3 % and As_2O_3 % values characterize the tailings (sinked).

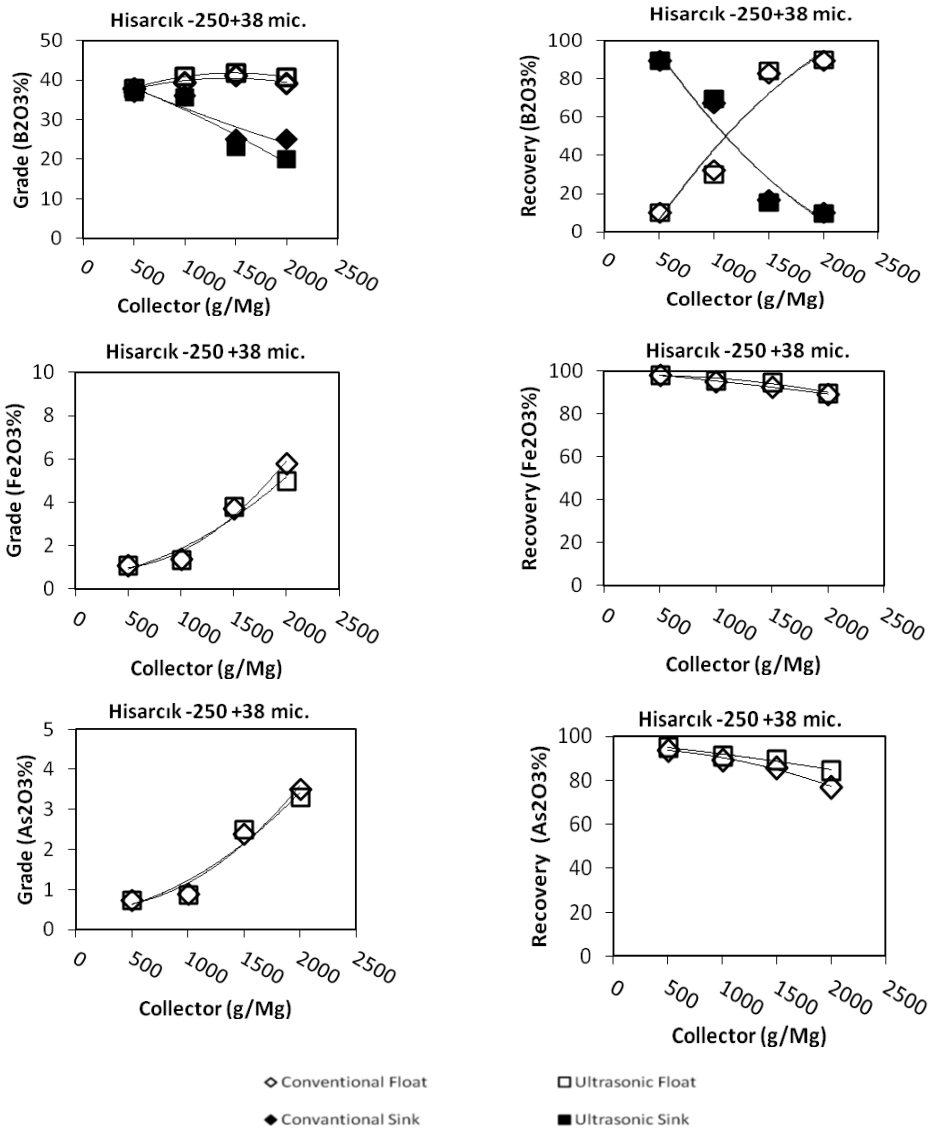

Fig. 5. Grade and recovery values of flotation products for the Hisarcik samples

Figures 5 and 6 show that the B_2O_3 content in the concentrates tends to rise with increasing the amount of collector until 1500 g/Mg for both the Hisarcik and Espey samples achieving recoveries up to 80%. The B_2O_3 grades of ultrasonically pre-treated samples are slightly greater than the conventional ones.

The Fe_2O_3 and As_2O_3 contents in the flotation tailings also go up with increasing collector dosage, though the recoveries decrease.

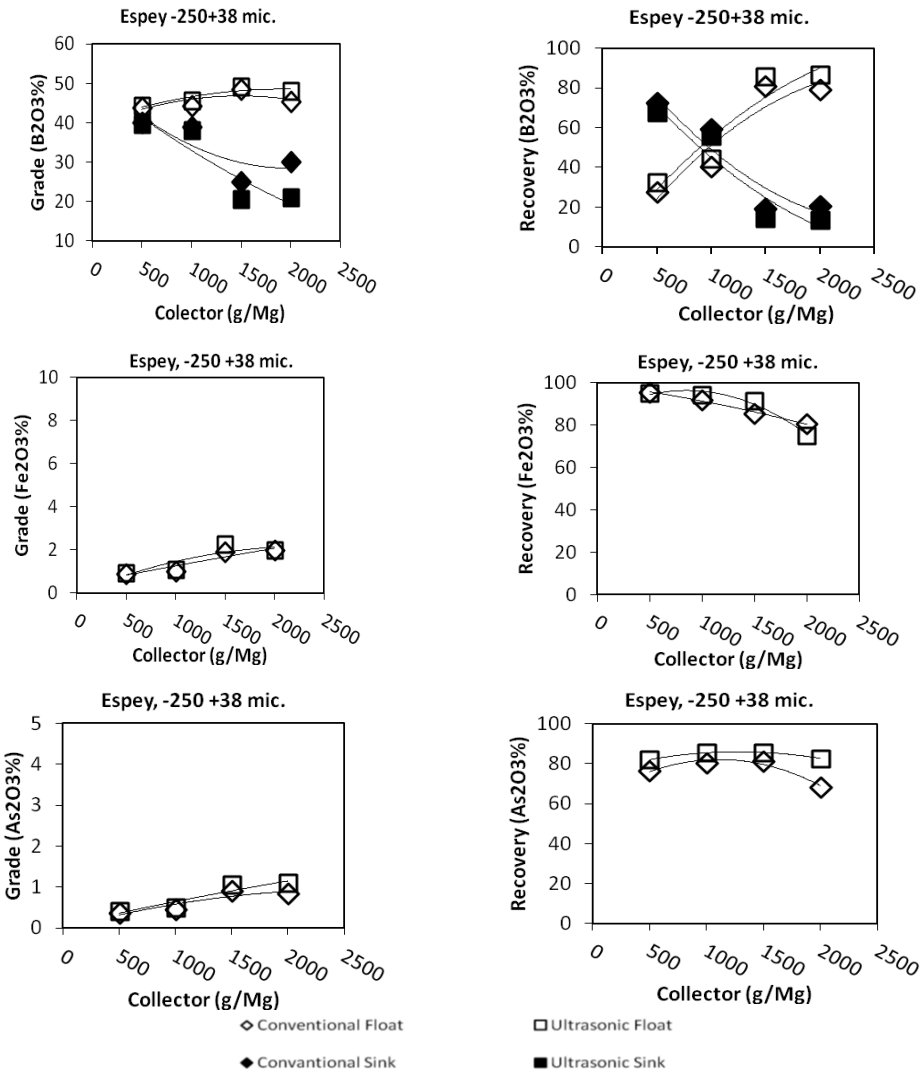

Fig. 6. Grade and recovery values of flotation products for the Espey samples

4. Discussion and conclusions

The results show that ultrasonic pre-treatment gives encouraging flotation results for both Hisarcik and Espey colemanite samples. However, it should be kept in mind that the samples used in this study are not run-of-mine ore. They are low grade concentrates which were tried to get suitable grades during this study. As seen from the B_2O_3 grade-recovery curves from the Figures 5 and 6 that increasing reagent dosages did not necesserally raise the grade and recovery values for the floated

colemanite. Approximately 41% B_2O_3 grade value was reached by desliming only for both samples for particle size of -250+38 μm. In addition, the B_2O_3 % grade value could be increased upto 49% by ultrasonically pre-treated flotation with a recovery of above 80%. Besides, the B_2O_3 grade of the tailings was decreased to around 20% B_2O_3 agaisnt the feed grade B_2O_3 grade of 33% for Hisarcik and 39% for Espey respectively. The optimal results were reached with use of 1500 g/Mg collector dosage.

During flotation, the Fe_2O_3 and As_2O_3 contents of the samples were also investigated. As seen from the Fe_2O_3 and As_2O_3 grade-recovery curves in Figs. 5 and 6 the increasing reagent dosages did not significantly affect the grade and recovery values for sinked tailings. In the concentrates, 0.10% Fe_2O_3 grade could be reached when the feed grade was between 0.70-1.00 % while As_2O_3 grade could be decreased from 0.35% to 0.10%.

It is believed that better results in the ultrasonically pre-treated flotation, than in the conventional flotation, were caused by a cavitation effect of ultrasounds. It is also assumed that the high speed water jets at high pressure and temperature during the sonication remove the clay and slime coatings on the surface of colemanite which obstruct reagent adsorption. Due to the ultrasounds the reagents can absorb more effectively on the surface of colemanite and increase their hydrophobicity.

Acknowledgement

The present work was supported by the Research Fund of Istanbul University, Project No: ACIP-3609, T-2276 and UDP-13658.

References

ARSLAN, M., 2007, *Emet borik asit urununun uretim surecinin iyilestirme analizi*, Afyon Kocatepe University. M.Sc. Thesis, Turkey, (in Turkish).

CELIK, M.S., 1987, *Effect of ultrasonic treatment on the floability of coal and galena*, Sep. Sci. Technol. 24(14), 1159–1166.

CILEK, E.C., OZGEN, S., 2010, *Improvement of the flotation selectivity in a mechanical flotation cell by ultrasound*, Sep. Sci. Technol. 45: 572–579.

GUNGOREN, C., 2009, *Ultrasonik ve mikrodalga enerjilerinin kolemanit flotasyonunda on islem olarak kullanma olanaklarinin arastirilmasi*, Istanbul University, M.Sc. Thesis, Turkey, (in Turkish).

LETMAHE, C., BENKER, B., GUNTHER, L., 2002, *Intensivierung der schaumflotation durch einsatz von ultraschall*. Aufbereitungs Technik 43, 32–40.

MITOME, H., 2003, *Action of ultrasound on particles and cavitation bubbles*, In: Proc. World Congress on Ultrasonics, Paris, 2003, 2342-2346.

OZKAN, S.G., GUNGOREN, C., 2010, *Investigation of ultrasonics use for colemanite flotation*, Conference Proceedings of 10th International Multidisciplinary Scientific Geoconference – SGEM, 20-26 June, Bulgaria, vol. 1, 661–668.

OZKAN, S.G., KUYUMCU, H.Z., 2007, *Design of a flotation cell equipped with ultrasound transducers to enhance coal flotation*, Ultrason. Sonochem. 14(2), 524–529.

OZKAN, S.G., KUYUMCU, H.Z., 2006, *Investigation of mechanism of ultrasound on coal flotation*, Int. J. Miner. Process., 81(3), 201–203.

STOEV, S.M., 1992, *Vibroacoustic improvements of froth flotation*, Innovations in flotation technology, NATO ASI, the Netherlands, series vol. 208, 383–407.

Physicochem. Probl. Miner. Process. 48(2), 2012, 463−473

www.minproc.pwr.wroc.pl/journal/

Physicochemical Problems of Mineral Processing

ISSN 1643-1049 (print)
ISSN 2084-4735 (online)

Received March 9, 2011; reviewed; accepted April 1, 2012

PREPARATION AND CHARACTERISATION OF HYDRATED SILICA/LIGNIN BIOCOMPOSITES

Lukasz KLAPISZEWSKI, Magda MADRAWSKA, Teofil JESIONOWSKI

Poznan University of Technology, Institute of Chemical Technology and Engineering, M. Sklodowskiej–Curie 2, PL-60965 Poznan, Poland, teofil.jesionowski@put.poznan.pl, phone: +48(61)6653720, fax: +48(61)6653649

Abstract. Silica/lignin biocomposites were obtained by a new method proposed and fully characterised. Silica was precipitated from aqueous solution of sodium silicate (as an SiO_2 precursor) and sulphuric acid (as a precipitating agent). The support obtained was subjected to surface functionalisation with aminosilane and then modified with Kraft lignin preliminary activated with sodium periodate solution. The products were characterised by elemental (N, C, H, S) and colorimetric analyses. Adsorption properties of the products were evaluated on the basis of determination of specific surface area, pore volume and pore diameter. The influence of the amount of lignin incorporated into the silica matrix on the physicochemical properties of the biocomposites was proved to be significant. The materials obtained can be used as selective adsorbents of heavy metals or pro-ecological polymer fillers.

keywords: silica/lignin biocomposites, silica, Kraft lignin, modification, physicochemical properties

1. Introduction

Dynamic development of production technologies of new materials has been focused on getting products of specific target properties. A large group of such new materials is based on silica and show a large variety of morphological features. Particularly interesting is production of composites with an addition of organic origin polymer such as for instance lignin. The use of biodegradable materials such as lignin in an inorganic matrix offers a possibility of obtaining a new generation of highly functional biocomposites of prospective economic importance.

Silica belongs to the most abundant natural materials. The most often used methods of its production include: hydrolysis and condensation of tetraalkoxysilanes according to the Stöber method (Stöber, 1968; Ibrahim, 2010), precipitation from sodium metasilicate aqueous solution in polar and nonpolar systems (Jesionowski, 2001, 2002) and high-temperature combustion of silicon halogens in the gas phase (Wypych, 2010). Because of a number of valuable physicochemical properties such as large surface area, high hardness, chemical resistance and high mechanical resistance, silica has been widely used in many branches of industry and in everyday use products.

http://dx.doi.org/10.5277/ppmp120212

Lignin is the second most abundant natural renewable material from the group of polymers and has been for a long time viewed as an attractive material for versatile use (Lora, 2002). Complex chemical structure of lignin, its valuable physicochemical properties and a variety of chemical compositions, have made it a subject of interest of many research groups. Recently, large amounts of lignin has been produced as a side product in the so-called Kraft process (Chakar, 2004; Wallberg, 2006). Lignin, obtained in this process or isolated by some extraction methods, has been used for instance to produce energy (Sannigrahi, 2010), in electrotechnology, electrochemistry (Milczarek, 2009), pharmacy (Tolba, 2011) and in production of modern functional biocomposites of specific properties (Gosselink, 2004).

Increasing cost of energy and the need to protect the natural environment have directed much attention to biodegradable materials based on renewable resources, being environmentally friendly and cheaper. Such interesting new materials are for example silica/lignin biocomposites of a wide range of potential applications. According to the so far published scarce literature on such materials, they can be used as adsorbents of harmful organic compounds or heavy metal ions (Hayashi, 1997; Qu, 2010) or as polymer fillers (Ignat, 2011).

The aim of this study was to obtain a silica/lignin composite in the process of silica (silica was precipitated in a polar system) surface modification with an appropriate lignin solution and a thorough characterisation of the product.

2. Experimental

2.1. Hydrated silica/lignin biocomposite synthesis

Silica used for the study was precipitated in a polar system as a result of reaction between aqueous solution of sodium silicate (Vitrosilicon SA) and 5% sulphuric acid (Chempur®). The reaction mixture was subjected to intense stirring (1800 rev/min) in a high-speed stirrer Eurostar digital made by IKA–Werke GmbH. The reaction was carried out at 85°C. The silica suspension obtained was filtered off under reduced pressure and washed a few times with water. The final white precipitate was dried by the convection method at 105°C for about 24 h. Part of the product was subjected to preliminary surface functionalisation *N*–2–(aminoethyl)–3–aminopropyltrimethoxy-silane to activate the silica surface.

The initial silica and the silica preliminarily modified with silane were subjected to proper functionalisation with Kraft lignin. Two solutions were made. One was labelled as S1. It was lignin dissolved in a dioxane:water (9:1, v/v) mixture. The other was labelled as S2 and it was an aqueous solution of sodium iodate. The S1 solution was placed in a reactor to which S2 was introduced in doses at a constant rate. After introduction of the whole S2 solution, the reaction solution was stirred for 30 minutes. The process of lignin compounds activation was performed with no access of light. To the mixture of solutions, a certain amount of silica (unmodified or modified with the above-mentioned silane) was added and the stirring was continued for 1 hour. The

final product, silica/lignin biocomposite, was moved to a vacuum evaporator to distil off the solvent. The composite was dried for about 24 h at 105°C. The process of SiO_2/lignin biocomposite synthesis is schematically illustrated in Fig. 1.

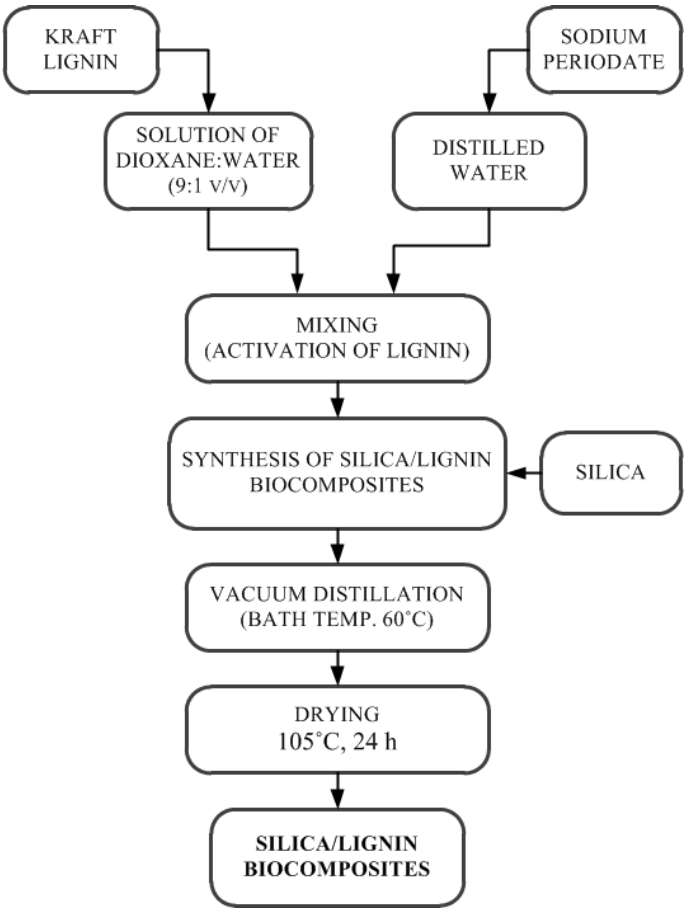

Fig. 1. The simplified scheme for obtaining of silica/lignin biocomposites

2.2. Physicochemical evaluation

The silica/lignin biocomposites were subjected to a thorough physicochemical and dispersive–morphological analysis. The particle size distribution was determined by two different methods and in different ranges using a Zetasizer Nano ZS employing the NIBS technique in the range of 0.6–6000 nm and Mastersizer 2000 employing the laser diffraction technique in the range of 0.2–2000 μm. Both instruments were made by Malvern Instruments Ltd. Elemental composition of the samples (N, C, H, S) was made using a Vario EL Cube made by Elementar, while their colorimetric analyses

were made with a Specbos 4000 colorimeter (YETI Technische Instrumente GmbH). Adsorption properties of some samples were characterised by determination of the specific surface area BET, total pore volume and pore size calculated by the BJH method. Relevant measurements were made on an ASAP 2020 instrument made by Micromeritics Instrument Co.

3. Results and discussion

Table 1 presents the data characterising physicochemical properties of the initial unmodified silica (sample 1) and SiO_2/lignin biocomposites obtained on the basis of this silica (samples 2–8). The particle size distributions were determined by a Zetasizer Nano ZS (in the range of 0.6–6000 nm) and Mastersizer 2000 (in the range of 0.2–2000 μm).

Table 1. Dispersive properties of unmodified silica and silica/lignin biocomposites

Sample No.	Content of lignin in relation to the unmodified silica matrix (wt./wt.)	Dispersive properties				
		Particle size distribution from Zetasizer Nano ZS (nm)	Particle diameter from Mastersizer 2000 (μm)			
			d(0.1)	d(0.5)	d(0.9)	D[4.3]
1	0 (unmodified silica)	44–59 1110–5560	4.63	19.40	43.31	25.12
2	3	91–122 220–295 1480–5560	4.60	16.85	37.33	19.20
3	5	106–190 712–4150	4.60	17.71	38.01	19.80
4	10	79–106 1990–5560	4.74	18.82	40.44	21.03
5	20	79–122 1720–4150	4.50	19.41	42.16	22.72
6	30	79–106 1990–5560	4.33	19.51	42.29	22.92
7	40	79–142 1280–4800	5.38	21.63	44.57	23.75
8	50	79–142 1280–4150	5.24	23.14	48.35	25.43

The primary particles in sample 1 of precipitated and unmodified silica had diameters in the range of 44–59 nm. These particles showed a tendency to form agglomerates of the size 1110–5560 nm in size. As follows from the Mastersizer 2000 results, 10% of the sample particles have diameters smaller than 4.63 μm, while 90% of the sample particles have diameters smaller than 43.31 μm. The particle size distributions obtained for the silica/lignin biocomposites studied are nanometric. The

particles show a tendency to formation of agglomerates and this tendency is the stronger the greater is the content of lignin. The particle size distribution recorded on Mastersizer 2000 indicates that 90% of particles in sample 2 have diameters below 37.33 μm, while 90% of particles in sample 8 (containing 50 weight parts of lignin per 100 weight parts of silica) have diameters below 48.35 μm.

The best dispersive–morphological properties show the biocomposites containing the lowest amount of lignin. The samples containing 30 weight parts by mass or more of lignin (samples 6, 7, 8) show greater inhomogeneity, which is most probably a consequence of the lack of lignin oxidation and its partial degradation. Figure 2 presents dispersive–morphological results for sample 5, containing 20 weight parts by mass of lignin. The particle size distribution obtained on Zetasizer Nano ZS revealed two bands, the first covering the range of 79–122 nm and the second corresponding to agglomerates, covering the range 1720–4150 nm range. The maximum intensity of 19.5% corresponds to particles of the 91 nm in size. The results are confirmed by the SEM image showing the presence of small particles of diameters below 100 nm and greater agglomerate structures.

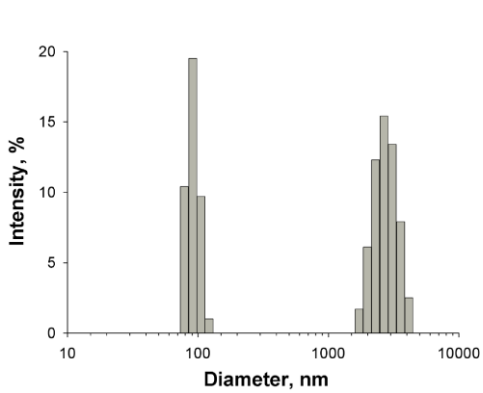

(a)

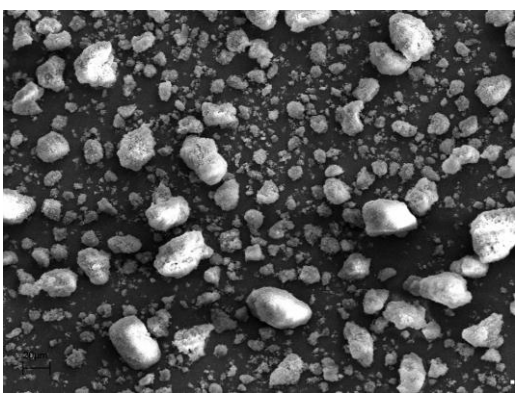

(b)

Fig. 2. (a) Particle size distribution (Zetasier Nano ZS) and (b) SEM microphotograph of silica/lignin biocomposite (sample 5) prepared on the basis of unmodified silica

An additional confirmation of the tendency to agglomerate formation with increasing content of lignin in the silica matrix is the particle size distribution recorded with Mastersizer 2000 (Fig. 3). With increasing content of lignin the particle size distribution peaks are shifted towards greater particle diameters. The greatest contribution of large diameter particles and the lowest contribution of the smallest size ones was observed for sample 8.

Figure 4 presents results of colorimetric analysis of the biocomposite samples, confirming the correctness of the process of modification. The surface functionalisation of the unmodified silica with a lignin solution caused a significant

decrease in the lightness parameter L*. For the unmodified silica (sample 1) L*=93.78, as a result of modification with a lignin solution the value of this parameter decreases: L*=85.68 for sample 2 and L*=46.17 for sample 8. The value of dE* describing a total change in colour, increases with increasing content of lignin in the biocomposite.

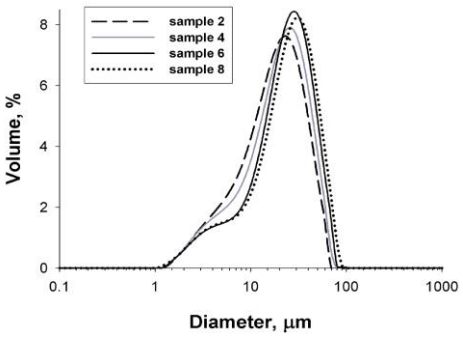

Fig. 3. Particle size distribution (Mastersizer 2000) of silica/lignin biocomposites

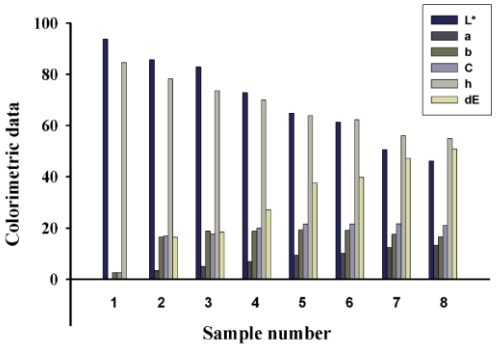

Fig. 4. Colorimetric data of unmodified silica (sample 1) and silica/lignin biocomposites (samples 2–8)

Table 2. Chemical content of unmodified silica (sample 1) and silica/lignin biocomposites (samples 2–8) on the basis of unmodified silica

Sample No.	Elemental content (%)		
	C	H	S
1	0.31	1.28	-
2	1.56	1.37	0.14
3	2.33	1.43	0.20
4	3.42	1.48	0.33
5	5.01	1.53	0.50
6	6.80	1.67	0.66
7	8.94	1.70	0.80
8	10.56	1.86	1.03

Results of elementary analysis (N, C, H, S) of the biocomposite samples based on unmodified silica are given in Table 2. As shown, with increasing content of lignin the contents of carbon, hydrogen and sulphur increase. For example, sample 2 with the lowest content of lignin per unmodified silica (3 wt./wt.) contains 1.56% of carbon and 1.37% of hydrogen. Sample 8, containing 50 weight parts by mass of lignin, has 10.56% of carbon and 1.86% of hydrogen. A small increase in the content of sulphur in the samples with increasing content of lignin is related to the presence of sulphur in the commercial Kraft lignin used in the study.

The above results were compared with those obtained for silica/lignin biocomposites based on silica preliminary modified with N–2–(aminoethyl)–3–aminopropyltrimethoxysilane. The data characterising dispersive properties of samples based on silane modified silica are presented in Table 3.

Table 3. Dispersive properties of silica modified with aminosilane and of silica/lignin biocomposites

Sample No.	Content of lignin in relation to the silica matrix modified with aminosilane (wt./wt.)	Dispersive properties				
		Particle size distribution from Zetasizer Nano ZS (nm)	Particle diameter from Mastersizer 2000 (μm)			
			d(0.1)	d(0.5)	d(0.9)	D[4.3]
9	0 (silica modified with aminosilane)	59–106 1480–5560	5.75	22.66	47.84	22.11
10	3	44–79 1280–4800	4.41	16.12	34.15	18.01
11	5	68–122 2300–5560	4.69	16.20	34.29	18.15
12	10	59–122 1110–5560	4.80	20.31	42.74	23.41
13	20	68–122 712–1480 2670–5560	4.90	21.43	44.22	24.43
14	30	68–91 342–396 1480–4150	4.80	21.45	44.16	23.39
15	40	68–122 531–2670	5.56	23.53	47.19	25.42
16	50	68–106 459–4150	5.01	22.82	48.15	26.08

According to the data presented in Table 3, modified silica (sample 9) shows increased particle size and a greater tendency to agglomeration when compared with the unmodified one (sample 1). In sample 9, 10% of particles have diameter smaller than 5.75 μm, while 90% of particles have diameters smaller than 47.84 μm. In unmodified silica (sample 1) 10% of particles have diameters up to 4.63 μm, while 90% of particles have diameters smaller than 43.31 μm. Modification of silica was responsible for a small shift of the particle size distribution towards larger particle diameters. The above data are corroborated by the results recorded on Zetasizer Nano ZS. The dispersive–morphological features of samples 10–16 based on silane modified silica are similar to those of samples 2–8 based on unmodified silica. With increasing content of lignin, the biocomposite samples show increasing tendency to agglomeration, similarly as it was observed for the samples based on unmodified silica (Table 1).

Figure 5 presents the particle size distribution recorded in the Zetasizer Nano ZS and SEM image of sample 13 (20 weight parts by mass of lignin in relation to silane–grafted silica). Three peaks are obtained: the first corresponds to primary particles and covers the range of 68–122 nm, the second corresponds to aggregations and covers the range of 712–1480 nm and the third in the range of 2670–5560 nm corresponds to agglomerates. The results are confirmed by the SEM image (Fig. 5b) showing the presence of small particles and larger agglomerate clusters. No significant differences in dispersive and morphological properties were found between the samples based on unmodified and silane modified silica. This conclusion is confirmed by the results obtained with Mastersizer 2000 (Fig. 6) showing that with increasing content of lignin the contribution of greater size particles increases.

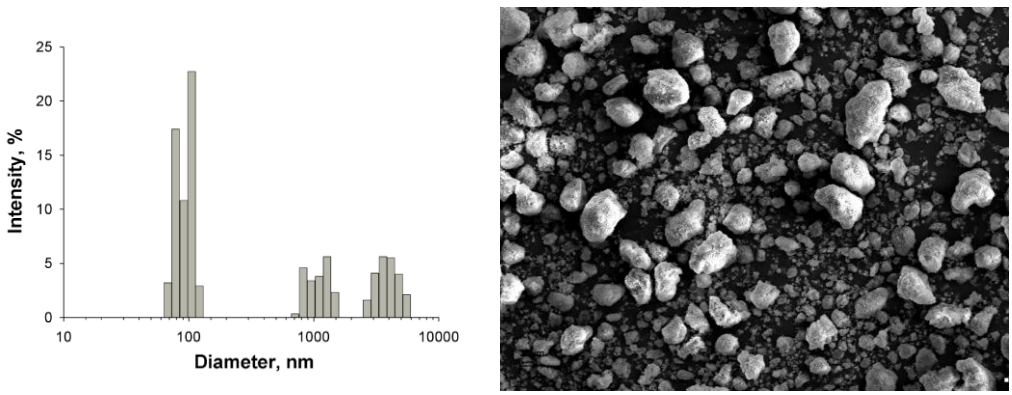

(a) (b)

Fig. 5. (a) Particle size distribution (Zetasier Nano ZS) and (b) SEM microphotograph of silica/lignin biocomposite (sample 13) prepared on the basis of silica modified with aminosilane

As follows from the colorimetric analysis (Fig. 7) with increasing content of lignin in the samples based on modified silica, the lightness L* decreases while the total colour change dE* increases. A comparison of colorimetric results obtained for unmodified and silane modified silica has shown that the silane modification leads first of all to reduction in the lightness L*. For example the lightness of samples 6 (unmodified silica) and 13 (modified silica) containing 20 weight parts by mass of lignin was L*=64.75 and L*=60.19, respectively. This results indicates an increase in the silica affinity to lignin as a result of preliminary silane functionalisation of the former.

Data on the chemical composition of silane modified silica (sample 9) and biocomposites based on modified silica (samples 10–16) are given in Table 4.

As follows from the data, the effect of the preliminary silane modification was an increase in the nitrogen content to 0.61%. Analysis of the data for samples 10–16 has shown an increase in the content of carbon, hydrogen and sulphur with increasing content of lignin. The results are consistent with expectations. Moreover, greater

contents of N, C, H and S in the samples based on silane modified silica illustrates the significance of changes caused by the silane applied.

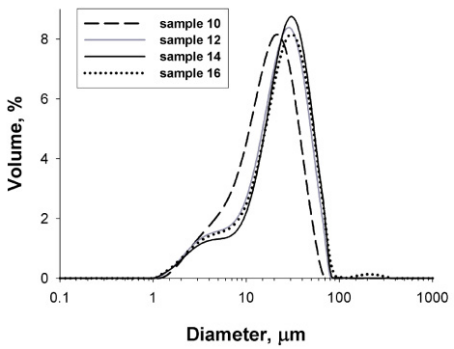

Fig. 6. Particle size distribution (Mastersizer 2000) of silica/lignin biocomposites

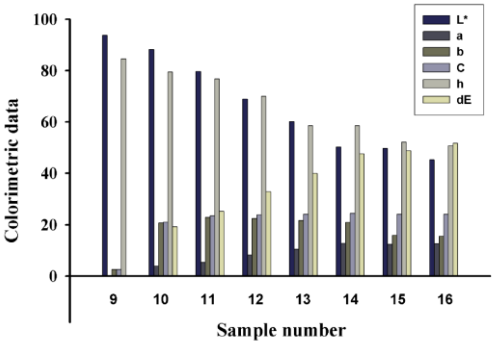

Fig. 7. Colorimetric data of silica modified with aminosilane (sample 9) and silica/lignin biocomposites (samples 10–16)

Table 4. Chemical content of silica modified with aminosilane (sample 9) and silica/lignin biocomposites (samples 10–16) on the basis of silica modified with aminosilane

Sample No.	Elemental content (%)			
	N	C	H	S
9	0.61	1.44	1.48	-
10	0.44	2.60	1.47	0.18
11	0.49	3.45	1.53	0.23
12	0.42	5.04	1.67	0.39
13	0.40	6.70	1.75	0.57
14	0.40	7.97	1.81	0.70
15	0.36	10.15	1.88	0.87
16	0.31	11.33	1.93	1.03

Table 5 presents the data characterising adsorption properties of unmodified silica (sample 1), preliminary silane modified silica (sample 9) and selected silica/lignin biocomposites (samples 4, 8, 12, 16). The specific surface area of these products varies from 108 to 131 m^2/g. Preliminary modification with silane leads to a small increase in the surface area relative to the unmodified silane sample. The mean pore size for all samples are similar and vary from 3.55 to 3.61 nm, which confirms their mesoporous character. Surface functionalisation of silica, either unmodified or modified, with Kraft lignin solution did not affect significantly the adsorption properties of the materials studied

Table 5. Adsorptive properties of silica and silica/lignin biocomposites

Sample No.	BET surface area (m^2/g)	Total volume of pores (cm^3/g)	Mean size of pores (nm)
1	129	0.009	3.55
4	115	0.004	3.59
8	108	0.002	3.61
9	131	0.010	3.55
12	118	0.006	3.58
16	109	0.004	3.55

4. Conclusions

The proposed method of silica/lignin biocomposites synthesis permits obtaining products with well-defined dispersive, morphological and adsorption properties. These properties were found to be significantly influenced by the content of lignin introduced and the modification with the selected aminosilane. With increasing content of lignin in relation of silica matrix (either unmodified or modified) the contribution of greater size particles increases, so does the tendency to agglomeration. The biocomposites with the lowest content of lignin show the best dispersive and morphological properties. As follows from elemental and colorimetric analyses, preliminary silica modification with silane has brought an increase in the surface activity of the material permitting binding a greater amount of lignin at the same weight contributions. Determination of the adsorption properties of the products obtained has confirmed their mesoporous character.

Acknowledgements

This work was supported by Poznan University of Technology research grant no. 32-125/2012–DS.

References

CHAKAR F.S.R., RAGAUSKAS A.J., 2004, *Review of current and future softwood Kraft lignin process chemistry*, Ind. Crop. Prod., 20, 131–141.

GOSSELINK R.J.A., de JONG E., GURAN B., ABÄCHERLI A., 2004, *Coordination network for lignin – standardisation, production and applications adapted to market requirements (EUROLIGNIN)*, Ind. Crop. Prod., 20, 121–129.

HAYASHI J., SHOJI T., WATADA Y., MUROYAMA K., 1997, *Preparation of silica–lignin xerogel*, Langmuir, 13, 4185–4186.

IBRAHIM I.A.M., ZIKRY A.A.F., SHARAF M.A., 2010, *Preparation of spherical silica nanoparticles: Stöber silica,* J. Am. Sci., 6, 985–989.

IGNAT L., IGNAT M., CIOBANU C., DOROFTEI F., POPA V.I., 2011, *Effects of flax lignin addition on enzymatic oxidation of poly(ethylene adipate) urethanes*, Ind. Crop. Prod., 34, 1017–1028.

JESIONOWSKI T., 2001, *Preparation of colloidal silica from sodium metasilicate solution and sulphuric acid in emulsion medium,* Colloid Surf. A, 190, 153–165.

JESIONOWSKI T., 2002, *Effect of surfactants on the size and morphology of the silica particles prepared by an emulsion technique*, J. Mater. Sci., 37, 5275–5281.

LORA J.H., GLASSER W.G., 2002, *Recent industrial applications of lignin: a sustainable alternative to nonrenewable materiale,* J. Polym. Environ., 10, 39–48.

MILCZAREK G., 2009, *Preparation, characterization and electrocatalytic properties of an iodine lignin–modified gold electrode,* Electrochim. Acta, 54, 3199–3205.

QU Y., TIAN Y., ZOU B., ZHANG J., ZHENG Y., WANG L., LI Y., RONG C., WANG Z., 2010, *A novel mesoporous lignin/silica hybrid from rice husk produced by a sol–gel method,* Bioresource Technol., 101, 8402–8405.

SANNIGRAHI P., PU Y., RAGAUSKAS A., 2010, *Cellulosic biorafineries – unleashing lignin opportunities,* Curr. Opin. Environ. Sustain., 2, 383–393.

STÖBER W., FINK A., BOHN E., 1968, *Controlled growth of monodisperse silica spheres in the micron size range,* J. Colloid Interf. Sci., 26, 62–69.

TOLBA R., WU G., CHEN A., 2011, *Adsorption of dietary oils onto lignin for promising pharmaceutical and nutritional applications,* BioResources, 6, 1322–1335.

WALLBERG O., LINDE M., JÖNSSON A.S., 2006, *Extraction of lignin and hemicelluloses from Kraft black liquor,* Desalination, 199, 413–414.

WYPYCH G., 2010, *Handbook of Fillers,* ChemTec Publishing, Toronto 2010.

Physicochem. Probl. Miner. Process. 48(2), 2012, 475−484

www.minproc.pwr.wroc.pl/journal/

Physicochemical Problems of Mineral Processing

ISSN 1643-1049 (print)
ISSN 2084-4735 (online)

Received December 8, 2011; reviewed; accepted February 9, 2012

EVALUATION OF LOW GRADE IRON ORE DEPOSIT IN ERZINCAN-TURKEY FOR IRON ORE PELLET CONCENTRATE PRODUCTION

Osman SIVRIKAYA*,, Ali Ihsan AROL***

* Selçuk University, Mining Engineering Department, 42075 Konya, Turkey, osmansivrikaya@gmail.com

** Middle East Technical University, Mining Engineering Department, Ankara, Turkey, arol@metu.edu.tr

Abstract. In this study the separation possibility of gangue minerals from a low grade magnetite ore with 45% Fe from an iron ore deposit located near Erzincan-Turkey was investigated. The iron ore deposit consists of mainly magnetite mineral. Hematite is the second iron oxide found in the deposit. The gangue minerals contain mainly SiO_2 and Al_2O_3 impurities. The main object of the research is to investigate the production of a concentrate suitable for iron ore pellet production. The concentrate for pellet production should have at least 65% Fe with reasonable gangue contents (SiO_2 <6.0% and Al_2O_3 <1.0%). The Davis tube and low intensity drum type wet magnetic separators were used for upgrading the Fe content and separation of gangue impurities from the iron ore. The results showed that, in order to produce a concentrate with sufficient Fe grade (>65% Fe), the iron ore should be ground to get 45% of material by weight to be finer than 45 μm. The concentrate with over 65% Fe and 90% Fe recovery could be produced with 45% Fe content from the feed material by crushing, grinding and magnetic separation operations.

keywords: iron ore, magnetite, magnetic separation, iron ore pellet

1. Introduction

The main raw material for iron production in the iron-steel industry is iron oxide ore. Natural iron oxide ores can be typically classified as high grade (>65% Fe), medium grade (<65 and >62% Fe) and low grade (<62% Fe) in terms of their Fe contents. The high grade iron ores, which can be used directly in the blast furnace to produce metallic iron, are not abundant in earth's crust to supply the need of iron-steel industry. The exploitation of low grade iron ores is possible after enrichment. The low grade iron ores with considerable amount of gangue minerals, e.g. silica, alumina, calcium and magnesium compounds, require concentration. For concentration, iron ore is crushed and ground for liberation before the implementation of separation techniques. Liberation can mostly be achieved at a very fine particle size and, hence, the concentrate obtained is not suitable to be charged directly into the blast furnace or the DR-plant without converting it into suitably sized agglomerates. The most

http://dx.doi.org/10.5277/ppmp120213

commonly employed agglomeration technique is pelletizing. In pelletizing, a mixture of finely ground iron ore, water and binder is rolled in a mechanical disc or drum to produce agglomerates (green balls or wet pellets). Green pellets then undergo a thermal process, which consists of three stages, namely drying (250 – 400^{o}C), preheating (900 – 1100^{o}C) and firing (1200 – 1300^{o}C) (Sivrikaya and Arol, 2010). Pellets can be charged to reduction furnaces to produce metallic iron.

In previous exploration studies conducted by MTA (General Directorate of Mineral Research and Exploration of Turkey) revealed the existence of four main formations; Kızılkaya, South Kızılkaya, Taştepe and Dönentaş (Yaman, 1985; Yıldırım, 1985). It was also reported that the iron ore deposit consists of mainly magnetite. Hematite is the second iron oxide found in the deposit. The reserve (proven plus possible) of the deposit determined by 95 drilling (12 km in total) done by MTA is given in Table 1.

Table 1. Proven plus possible reserves and average iron grade of Bizmişen iron ore deposit - Kızılkaya, Taştepe and Dönentaş formations (Yaman, 1985; Yıldırım, 1985)

Formation	Reserve, ton	Fe %	SiO_2%	Al_2O_3%	S %
Kızılkaya	10.652.230	54.44	8.23	2.04	1.45
Kızılkaya (South*)	456.700	58.30	-	-	-
Taştepe	2.240.170	43.24	16.29	3.14	0.51
Dönentaş	9.817.789	43.94	12.05	3.52	1.99

* no detailed data for this formation is avaible

The iron ores have been mined from the Taştepe and Kızılkaya formations. No production was carried out from Dönentaş formation. A possible and efficient production method is necessary to exploit iron ore found in this formation since it has remarkable reserve and Fe grade.

In previous concentration investigation conducted by MTA (Yaman, 1985) the iron ore from Taştepe formation was tried to be enriched by magnetic methods. The iron ore was crushed to -1 cm and concentrated by magnetic separation. A concentrate was produced with 54.51% Fe which is suitable for sinter feed. The tailing of this concentration stage was ground to 150 μm (100 mesh) and concentrated by magnetic separator. An upgraded concentrate with 61.99% Fe which was intended to be used for pellet feed, was obtained. However, both products were considered to be not suitable since the first one has a high S content and the second one has a low Fe content. Investigators concluded that a concentration method in which magnetic separation after grinding 80% of the ore to -45 μm should be suitable for this iron ore.

In another study conducted with the iron ore from the Dönentaş formation by MTA (Yıldırım, 1985) the production of lump ore, sinter feed and pellet feed was investigated. It was reported that in the study, lump ore (-22.6+8.0 mm), sinter feed (-8.0 +0.106 mm) and pellet feed (-0.074 mm) concentrates were produced after crushing and grinding by successive stage magnetic separation tests.

In this study in the light of the previous works, the evaluation of the low grade iron ore deposit was performed. Production of concentrates was investigated for iron ore pellet formation by magnetic separation concentration.

2. Material and methods

A 100 kg of the Taştepe formation was obtained. Samples of the Kızılkaya and Dönentaş formations cannot be taken representatively from the mine field. Therefore, these samples were taken from the core samples obtained by drilling done by MTA. Representative samples were taken from the magnetic part of the whole core samples. Seven different core samples (B5, B52, B73, B81, B97, B27 and B31) were divided by sawing and put in separate plastic bags.

The core samples were separately crushed to -10 mm with a jaw crusher and half of samples were split and sealed in labeled plastic bags and saved. The other half was stored as stock material after crushing with a roller crusher to -500 μm. Magnetic enrichment test samples used in concentration experiments were ground up to desired fineness with a centrifuge ball mill. The Fe content of the core representative samples are given in Table 2.

Table 2. Fe content of the core samples used in enrichment tests

Sample Name	Formation	Fe %	
		METU[(1)]	MTA[(2)]
Taştepe	Taştepe	50.27	-
B5	Taştepe	43.00	39.20
B52	Dönentaş	43.98	44.79
B73	Dönentaş	49.85	53.42
B81	Dönentaş	45.10	51.80
B97	Dönentaş	50.82	57.14
B27	Kızılkaya	59.34	60.49
B31	Kızılkaya	42.59	53.78

[(1)]Average Fe content of the representative blended core sample determined at METU (Middle East Technical University)
[(2)]Average Fe content of the formation written in MTA reports (Yaman, 1985; Yıldırım, 1985)

Magnetic separation technique was preferred due to its suitability for magnetic ore and simplicity. The magnetic separation was performed in two stages. At the first stage 8 different samples were ground to different fineness in centrifuge ball mill and concentrated by the Davis tube (Fig. 1). The applied magnetic field of the Davis tube was 0.1 T. About 15-20 g of ground sample was fed to the Davis tube and a concentrate was taken. The liberation of the ore particles is the main parameter affects the concentration efficiency. Therefore, different feeds with different sizes were fed to the Davis tube. The Fe content of the concentrates was determined by the titration method to see the effect of particle size on the Fe content and recovery. The suitable

particle size, which provides 65% Fe grade, was considered as the liberation size for individual test samples.

At the second stage of the investigations, laboratory size low intensity drum type wet magnetic separator (Fig. 2) was used to produce in larger quantities concentrates and to see the suitability of the magnetic drum separator regarding the liberation size determined at the first stage. Representative samples weighing 2 kg were separately taken from Taştepe (B5 and B52 samples) and ground in a ball mill. In addition, a mixed (Mix1) sample was prepared by blending all samples, excluding B27, in equal amount. Since B27 consists of hematite, it cannot be concentrated with the low intensity magnetic separator efficiently. The B27 sample has also relatively high Fe content, so it was thought that it can be used as direct lump feed for metal iron production in reduction operations (blast furnace or DRI furnace). Another mixed sample (Mix2) was prepared by blending all samples to see the effect of the B27 sample on efficiency of separation.

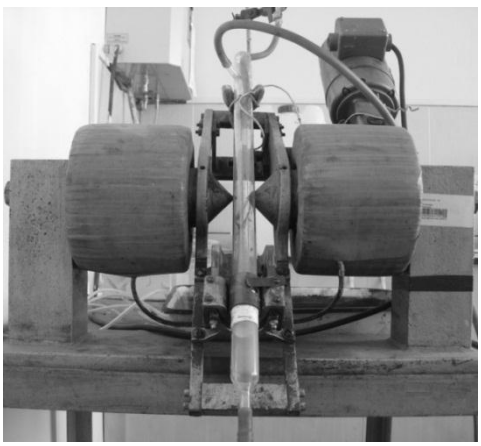

Fig. 1. Laboratory Davis tube magnetic separator

Fig. 2. Laboratory size low intensity drum type wet magnetic separator

The Taştepe, B5, B52, Mix1 and Mix2 samples in 2 kg batch were ground in ball a mill and concentrated in a laboratory size low intensity drum type wet magnetic separator and the concentrates were analyzed. All concentrates, excluding Mix2, were used in pelletizing tests.

A 50^{o} inclined laboratory-scale balling disc (Fig. 3) (390 mm diameter, 100 mm depth, 11 rpm) was used for the pelletizing experiments. A laboratory muffle furnace was used to fire the pellets. Each dry 1 kg concentrate sample was mixed with 0.8% bentonite and 10% water before pelletizing.

The detailed pelletizing procedure was explained in our previous publication (Sivrikaya and Arol, 2011). The green pellets were air-dried overnight and then fired at 1200^{o}C for 2 hours in a muffle furnace at a heating rate of 5^{o}C/min.

Fig. 3. Laboratory size pelletizing disc to produce iron ore pellets

3. Results and discussion

3.1. Magnetic separation test with the Davis Tube

The production of a concentrate with 65% Fe was aimed during the magnetic separation experiments. In the light of the previous results, the liberation was assumed to be at finer particle sizes. In addition, the reference particle size (80% -45 μm) for industrial pellet feed was accepted. Therefore, the enrichment possibility of samples was investigated according to their fineness (-45 μm). The results are given in Figs. 4-6. The results are grouped according to their formation taken from.

The Davis tube enrichment results for the Taştepe and B5 core samples which represent the Taştepe formation are given in Fig. 4. As can be seen from Fig. 4, when the sample is ground to 45%, by weight of -45 μm particles, the Fe grade of concentrate is over 65% Fe.

The B52, B73, B81 and B97 core samples represent the Dönentaş formation. The Davis tube enrichment results for these samples are given in Fig. 5. The results showed that a concentrate with over 65% Fe can be produced if the feed is ground 38-53% by weight -45 μm.

Different results were obtained with B27 and B31 core samples representing the Kızılkaya formation (Fig. 6). A concentrate with over 65% Fe can be produced when the B27 core sample feed is ground to 25% by weight of the -45 μm size fraction. A further grinding (60% -45 μm) increased the grade of the concentrate up to around 68.5% Fe. The B27 core sample consists of hematite and due to oxidation of hematite, this sample gets loose structure and could be ground easily. A direct use of the lump ore is more appropriate since the grade of the B27 sample feed is high (59.34% Fe) and the loses (Table 5) would occur during low intensity magnetic separation for this

type of hematite ores. Therefore the B27 core sample were not used in pelletizing experiments. Davis tube enrichment results for the B31 core sample showed that a concentrate with about 65% Fe can be produced if the feed is ground 90% by weight -45 μm.

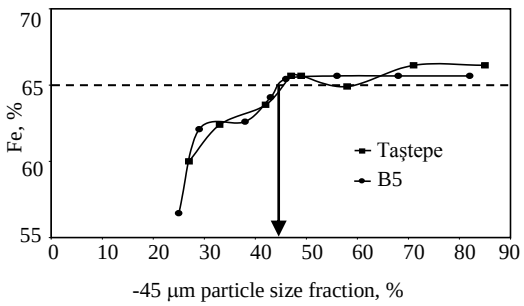

Fig. 4. Davis tube separation results of Taştepe formation according to the content of the -45 μm particle size fraction in the feed sample

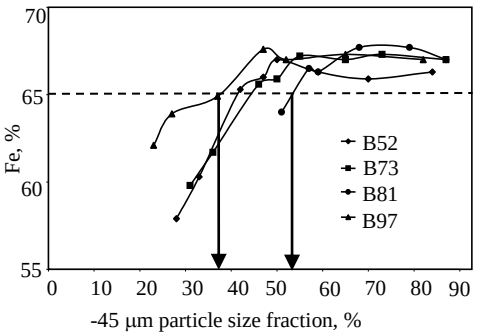

Fig. 5. Davis tube separation results of Dönentaş formation according to the content of the -45 μm particle size fraction in the feed sample

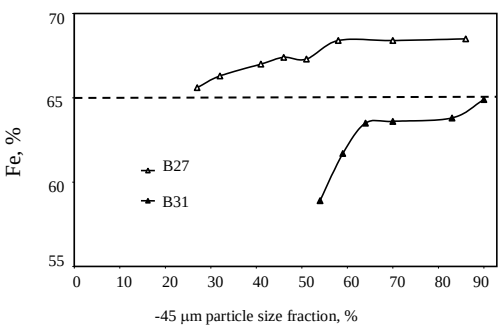

Fig. 6. Davis tube separation results of Kızılkaya formation according to the content of the -45 μm particle size fraction in the feed sample

The results given above show the necessity of fine grinding for the Bizmişen iron ore for enrichment. In order to produce concentrates with sufficient Fe content, the iron ore should be ground to 45-80% by weight of the -45 μm size fraction in the feed. The required particle size for pellets production is assumed to be 80% -45μm. Therefore, two different ground samples about this particle size (80% by weight -45 μm) were analyzed and recoveries as well as efficiency of separation were calculated. The results are given in Table 3.

As can be seen in Table 3, the concentrates with over 65% Fe and 90% Fe recovery could be produced using the Taştepe, B5, B52, B81, B97 and B31 core samples, by magnetic separation. It is a well-known that the recovery should be over 90%. Hence, these results and findings are satisfying. Although the Fe content for the B27 and B73 core samples were found to be high enough, their recovery were not sufficient. The

reason of this is believed to be due to a low magnetic susceptibility of the minerals (hematite and pyrite) present in the two samples. The relatively lower magnetic susceptibility of these minerals leads to loses during low intensity magnetic separation.

Table 3. Grade and recoveries of concentrates produced with Davis tube according to the particle size of feed sample

Formation	Sample name	Particle Size (-45 μm), %	Grade of Fe, %			Recovery by weight, %		Recovery of Fe, %	
			Feed	Concentrate	Tailing	Concentrate	Tailing	Concentrate	Tailing
Taştepe	Taştepe	71.0	50.3	66.3	10.5	71.3	28.7	94.0	6.0
		85.0	50.3	66.3	11.0	71.0	29.0	93.6	6.4
	B5	68.0	43.0	65.6	7.5	61.1	38.9	93.2	6.8
		82.0	43.0	65.6	8.7	60.3	39.7	92.0	8.0
Dönentaş	B52	70.0	44.0	65.9	7.8	62.3	37.7	93.3	6.7
		84.0	44.0	66.3	8.5	61.4	38.6	92.5	7.5
	B73	73.0	49.8	67.3	16.1	65.9	34.1	89.0	11.0
		87.0	49.9	67.0	17.5	65.4	34.6	87.9	12.1
	B81	79.0	45.1	67.7	7.7	62.3	37.7	93.6	6.4
		87.0	45.1	67.0	10.9	61.0	39.0	90.6	9.4
	B97	65.0	50.8	67.3	9.5	71.5	28.5	94.7	5.3
		82.0	50.8	67.0	10.1	71.6	28.4	94.4	5.6
Kızılkaya	B27	70.0	59.3	68.4	39.1	69.1	30.9	79.6	20.4
		86.0	59.3	68.5	44.7	61.5	38.5	71.0	29.0
	B31	83.0	42.6	63.8	7.7	62.2	37.8	93.2	6.8
		90.0	42.6	64.9	10.9	58.7	41.3	89.4	10.6

3.2. Magnetic separation tests with magnetic drum concentrator and pelletizing experiments

The Davis tube experiments showed that the enrichment of the Bizmişen iron ore is possible and the produced concentrates with a sufficient amount of Fe (over 65% Fe). In order to achieve this target the ore should be ground to finer sizes. Since the desired particle size for pellet production is minimum 80% -45 μm, the feed was ground to this fineness and fed to the laboratory size low intensity drum type wet magnetic separator. Different particle sizes were not using the drum separator due to a lack of enough samples.

Five different samples namely Taştepe, B5, B52, Mix1 and Mix2, were used during the drum separator tests. The first three samples were ground and concentrated separately. The latter two were formed by blending all samples Taştepe, B5, B52, B73, B81, B97 and B27 and B31 (14.29% from each samples excluding B27 for Mix1, 12.5% from each for Mix2). All five samples were concentrated separately with the low intensity magnetic separator. Different concentrates and tailings were analyzed

and recoveries as well as efficiency of the separation were calculated. The results are given in Table 4.

Table 4. Grade and recoveries of concentrates produced with magnetic drum separator

Sample Name	Grade of Fe%			Recovery by weight, %		Recovery of Fe, %	
	Feed	Concentrate	Tailing	Concentrate	Tailing	Concentrate	Tailing
Taştepe	50.3	65.3	10.9	72.4	27.6	94.0	6.0
B5	43.0	65.5	7.0	61.6	38.4	93.8	6.2
B52	44.0	65.6	7.2	63.0	37.0	94.0	6.0
Mix 1[(1)]	46.5	64.6	11.0	66.2	33.8	92.0	8.0
Mix 2[(2)]	48.1	66.3	14.0	65.2	34.8	89.9	10.1

[(1)] Taştepe, B5, B52, B73, B81, B97 and B31 core samples were blended in equal amount (14.29%)
[(2)] All core samples were blended in equal amount (12.50%)

Considering the Fe content of all test samples (excluding Mix2), the concentration using the magnetic drum separator was found to give sufficient Fe grade and recovery in the products. The Mix2 sample including the B27 core sample, resulted in low Fe recovery because of the reasons mentioned previously.

The pelletizing experiments with addition of 0.8% bentonite (Meyer, 1980) were carried out with all concentrates excluding Mix2. The green pellets were formed in a laboratory pelletizing disc 9 -16 mm in diameter. The green pellets were fired at 1200^{o}C in a muffle furnace after drying. Detailed elemental analyses were carried out on the products pellets. Elemental analyses with XRF (X-Ray Fluorescence spectrometer analyzer) were done in İSDEMİR (Iskenderun Iron and Steel Co.) and ERDEMİR (Eregli Iron and Steel Co.) and are given in Table 5.

Required limits by a pellet buyer, İSDEMİR, are given in Table 5. According to these results, all components excluding Al_2O_3 of concentrates produced by magnetic separation are suitable to produce blast furnace quality pellets. The reason of relatively high SiO_2 and Al_2O_3 in pellets than in the concentrates is due to the addition of bentonite binder. The high Al_2O_3 problem can be overcome in two ways. In one, the magnetic concentration can be tested with finer particle size to remove the Al_2O_3. In the second method, this type of concentrates can be blended with concentrates containing less of Al_2O_3.

When finer particles are used during concentration, the Fe recovery will decrease (this can be seen in Table 3). Furthermore, concentrates containing very fine particles in the feed for pellet production lead to some operational difficulties and losses. A cost analysis should be done to consider the cost of further grinding, the losses caused by finer particles and low concentration recovery.

In order to determine the presence of valuable component in the tailing of Mix 1, the tailing after magnetic separation was examined by semi-quantitative spectral

analysis. The result was given in Table 6. No significant valuable components were found in the tailing according to this result.

Table 5. Chemical analyses of concentrates produced with magnetic drum separator and pellets produced from these concentrates

Components	Products						
	B5 Concentrate (İsdemir)	B52 Concentrate (İsdemir)	Taştepe Concentrate (İsdemir)	Mix 1 Concentrate (İsdemir)	Mix 1 Concentrate (Erdemir)	Mix 1 Pellet (Erdemir)	Required limits by pellet buyer[(2)]
Total Fe	65.01	65.94	65.16	65.54	65.62	64.06	>65.50
SiO_2	3.41	2.47	2.99	2.75	2.85	3.33	<6.00
Al_2O_3	2.37[(1)]	2.32[(1)]	2.35[(1)]	2.12[(1)]	2.34[(1)]	2.50[(1)]	<1.00
CaO	1.33	1.22	1.35	1.15	1.04	1.03	<3.00
MgO	1.26	1.21	1.25	1.20	1.06	1.07	<1.50
Na_2O	0.079	0.079	0.078	0.076	0.037	0.035	<0.05
K_2O	0.026	0.012	0.029	0.015	0.087	0.047	<0.05
TiO_2	0.064	0.042	0.027	0.038	0.061	0.064	<0.50
Mn	0.11	0.16	0.13	0.15	0.13	0.13	<3.00
P	0.016	0.017	0.016	0.017	0.013	0.012	<0.06
S	0.029	0.10	0.108	0.166	0.095	0.003	<0.01
As	0.0001	0.001	0.0001	0.0001	0.002	0.002	<0.005
Cr	0.0053	0.0046	0.0049	0.005	0.002	0.007	<0.05
Ni	-[(3)]	-	-	-	0.004	0.004	<0.01
Zn	0.0269	0.0475	0.0299	0.0347	0.032	0.043	<0.01
Pb	0.0001	0.001	0.001	0.001	0.001	0.001	<0.01
Cu	0.001	0.0019	0.0039	0.0032	0.006	0.006	<0.01
Sn	-	-	-	-	0.00	0.00	<0.005
Mo	-	-	-	-	0.00	0.00	<0.005
V	-	-	-	-	0.006	0.006	<0.02
LOI	+1.83	+2.01		+1.48	+1.66	+0.06	-

[(1)] Considered high for iron ore pellet production; [(2)] Limits applied by İSDEMİR (Iskenderun Iron and Steel Co.) for acid iron ore pellets (http://www.isdemir.com.tr); [(3)] Under detection limit

Table 6. Result of semi-quantitative spectral analysis of tailing of Mix 1 sample

Components	Fe	SiO_2	Al_2O_3	Ca	Mn	Cu	Ti	Co
%	>10.0	>10.0	>10.0	>1.0	0.4	0.3	0.1	0.04

4. Conclusion

A large part of the Bizmişen iron ore deposit consists of low grade iron ore (mainly magnetite) with high content of impurities (SiO_2 and Al_2O_3). Therefore the direct use of iron ore from this deposit is impossible. The results drawn from study are as follows.

- The liberation size of this low grade iron ore was found to be about 45 μm for the production of concentrates with over 65% Fe content by magnetic separation.
- The concentrates produced cannot be used directly due to their fine particles. Agglomeration process is necessary to produce reduction furnace feed. The concentrate meets the requirements for iron ore pellet production.
- The pelletizing results showed that all components excluding Al_2O_3 of concentrate produced by magnetic separation are suitable to produce blast furnace quality pellets.
- The problem of high content of Al_2O_3 can be overcome by either further grinding applied to achieve better liberation and thus to produce a concentrate with acceptable Al_2O_3 content, or blending with low Al_2O_3 concentrates.

Acknowledgement

The authors would like to thank to Bilfer Mining Inc.-Turkey for financial support for the research.

References

SİVRİKAYA, O., AROL, A.İ., 2010, *Use of Boron Compounds as Binders in Iron ore Pelletization*, The Open Mineral Processing Journal (3), 25–35.

YAMAN, M., 1985, *Pre-concentration Studies of Erzincan-Kemaliye-Taştepe Iron Ore,* MTA Report, Turkey.

YILDIRIM, M., 1985, *Pre-concentration Studies of Erzincan-Kemaliye-Dönentaş Iron Ore,* MTA Report, Turkey .

SİVRİKAYA, O., AROL, A.İ., 2011, *Pelletization of Magnetite ore with Colemanite Added Organic Binders*, Powder Technology 210(1), 23–28.

MEYER, K., 1980, *Pelletizing of Iron Ores*, Springer-Verlag Berlin Heidelberg New York Verlag Stahleisen GmbH, Düsseldorf.

Physicochem. Probl. Miner. Process. 48(2), 2012, 485−494

www.minproc.pwr.wroc.pl/journal/

Physicochemical Problems of Mineral Processing

ISSN 1643-1049 (print)
ISSN 2084-4735 (online)

Received August 4, 2011; reviewed; accepted January 31, 2012

COLOUR REMOVAL FROM AQUEOUS SOLUTION OF TAR-CHROMIUM GREEN 3G DYE USING NATURAL DIATOMITE

Menderes KOYUNCU

Yuzuncu Yil University, Van Vocational Higher School, Department of Textile, Van, Turkey, Tel.: +90 432 2251414; fax: +90 432 2251415, menderes@yyu.edu.tr,

Abstract. Removal of Tar-Chromium Green 3G dye from aqueous solution at different dye concentrations, different temperatures and adsorbent doses has been studied. It was seen that the maximum of 88% adsorption has been achieved from the wastewater using 3.0 g material at 30ºC temperature for shaking time of 60 min.The adsortion isotherms are described by means of the Langmuir and Freudlich isotherms at different temperatures of 25, 30 and 35ºC, and the results were discussed. The equilibrium data satisfied both the Langmuir and Freundlich models. Moreover, thermodynamic parameters such as ΔH, ΔS and ΔG were also studied. It was found that the values of standard free energy (ΔG) and the values of standard enthalpy (ΔH) were negative and entropy (ΔS) was found to be positive. Thermodynamic studies showed that the reaction for uptake by diatomite is exohtermic in nature.The results of this study showed that diatomite could be employed as effective and low-cost materials for the removal of the dye from aqueous solution.

keywords: chromium dyes, adsorption, diatomite, Langmuir and Freundlich model, thermodynamics

1. Introduction

Dyes and pigments from several industrial branches can be emitted into water systems. The presence of dyes in water is highly visible and affects water transparency (Wang and Huiting, 2005). Coloured wastewater is a consequence of batch processes both in the dye manufacturing industries and in the dye-consuming industries. Two percent of dyes that are produced are discharged directly in aqueous effluent, and 10% are subsequently lost during the textile coloration process (Easton, 1995). An indication of the scale of the problem is given by the observation that the annual market for dyes is more than $7 \cdot 10^5$ Mg per year (Robinsonet al., 2001). The main reason for dye loss is the incomplete exhaustion of dyes on to the fibre. The amount of dye lost is dependent upon dyestuff type, the application route and the depth of shade required (Pearce et al., 2003). Untreated disposal of the coloured water into the receiving water body not only causes damage to aquatic life, but also to human beings by mutagenic and/or carcinogenic effect. It can cause severe damage to the

http://dx.doi.org/10.5277/ppmp120214

reproductive system, liver,brain and dysfunction of kidneys. and cause damage to the aesthetic nature of the environment (Baskaralingram et al., 2006). Therefore, the undesirable dye pollutions are required to be removed from wastewaters before being discharged to the environment.

During the past three decades, several physical, chemical and biological decolorization methods such as aerobic and anaerobic microbial degradation, coagulation and chemical oxidation, membrane separation process, electrochemical, dilution, filtration, flotation, softening and reverse osmosis have been proposed (Singh et al., 2003). However, all of these methods suffered with one or another limitation, and none of these were succesful in removing color from the wastewater completely (Dogan et al., 2009).

Amongst the numerous techniques of dye removal, the adsorption process is one of the effective techniques that have been widely used to remove certain classes of pollutants from wastewaters, especially those that are not easily biodegradable. A desired adsorbent should have sufficient adsorption capacity, high thermal and chemical stability, low cost and low environmental impact. The successful implementation of solid-liquid phase dye adsorption requires stable and effective adsorbents from wastewater (Chiou et al., 2004).

For this purpose, recently, some researchers have focused on the use of low cost sorbents. Some low cost materials used as sorbent for dye sorption from wastewaters were as follows, bentonite (Koyuncu, 2009; Tahir and Nassem, 2007), natural and modified diatomite (Yuan et al., 2010; Al-Ghouti et al., 2009; Er et al., 2009; Koyuncu and Kul, 2011), silica (Qiu et al., 2011; Blitz et al., 2007) fly ash (Eren and Acar, 2006), chitosan (Uzun, 2006), and others (Malkoç and Nuhoğlu, 2006; Parap et al., 2006; Marungrueng and Pavasant, 2007).

Diatomite may be thought as other inexpensive materials which can be used as sorbents. Diatomite (SiO_2. nH_2O) is a soft, light colour sedimentary rock formed from accumulation of siliceous crusts of diatoms, which are aquatic organism from algae, and have fosil characteristics. It has a unique combination of physical and chemical properties, which make it applicable as a substrate for adsorption of organic pollutants as filtration medium in a number of industrial uses. Its high permeability and high porosity make it a cheap alternative to activated carbon. The feasibility of using diatomite for removal of color from textile wastewaters was attempted by Erdem et al. (2005) and Hameed (2008).

The aim of the present study is to investigate the effect of initial dye concentration, temperature, and adsorbent dosage on the adsorption of Tar-Chromium Green 3G, the adsorption isotherm and thermodynamics were studied in detail.

2. Materials and methods

2.1. Materials

Diatomite (230 mesh in size) with surface area of 49.040 m^2/g from Çaldıran (Van/Turkey) was used as an adsorbent and the chemical composition of the adsorbent

was obtained with a XRD instrument. According to XRD it contained 76.50% SiO_2, 7.25% Al_2O_3, 3,85% Fe_2O_3, 0.50% TiO_3, 0.45% Na_2O, 0.85% K_2O and 0.43% loss on ignition

The dye was provided by Van Textile Fabrics (Van/Turkey). The molecular structure and formula of Tar-Chromium Green 3G was not provided for commerical reasons. It represents a basic dye.

2.2. Adsorption studies

The adsorption experiment was carried out at natural pH of solutions. Each of 50 cm^3 5mg/dm^3 of dyes solutions was put in five 100 cm^3 erlenmeyer flasks and diatomite adsorbent was added to each of other five erlenmeyers in different adsorbent doses (0.5-5g). Samples of 50 cm^3 of each dyes solutions were shaken with a shaker (New Bounswick Scentific G.24). Working conditions were: 30ºC, 195 rpm for 300 min. The 30ºC, 195 rpm shaking rate was kept as contant and the time variable was 15, 30, 60, 180 and 300 min. The samples were filtrated and analyzed by a UV- vis spectrophotometer(Cintra 202 Duble Beam) set at a wavelength of 480 nm, providing maximum absorbance. The effect of temperature and time variable on adsorption at recorded experimental conditions were also studied. At the end of the each experiment, supernatants were analyzed by UV- vis spectrophotometer (Cintra 202 Duble Beam) set at a wave-length of 480 nm.

The amount of dye adsorbed by diatomite q_e (mg/g), was calculated by the following mass balance relationship

$$q_e = \frac{(C_o - C_e)V}{W}, \tag{1}$$

where q_e is the amount of dye adsorbed (mg/g). C_o and C_e are the initial and equilibrium solution concentrations of dye respectively. V is the volume of the solution, and W is the weight of the adsorbent used.

3. Results and discussion

3.1.Effect of initial dye concentration

The adsorption of Tar-Chromium Green 3G dyes on natural diatomite as a function of concentration was studied at 30ºC by varying concentrations from 5 to 75 mg/dm^3, while keeping all other parameters constant. The adsorption result for the dye is shown in Fig. 1.The results show that the colour removal of Tar-Chromium Green 3G was decreased when the initial dye concentration was inceased. At low concentrations, adsorption sites took more the available dye more quickly. However, at higher concentrations, dye has to migrate to the adsorbent surface by intraparticle diffusion. The percentage of dye removal increased from 5 mg/dm^3 to 45 mg/dm^3 when the initial concentration of dye was from 5 to 75 mg/dm^3 for 3g of adsorbent at equilibrium contact time of 60 min. It indicates that the initial concentration provided

a powerful driving force to overcome the mass transfer resistance between the aqueous and solid phases. Similar observation has been reported by Dogan et al. (2009), and a similar trend was reported for the Cr(VI) removal using Bael Fruit (Anandkumar and Mandal, 2009), a basic dyes, onto live activated sludge (Basıbuyuk and Foster, 2003).

Figure 2 shows that the removal efficiency was increasing sharply in 60 minutes time. The removal of dye is decreasing over next 60 minutes treatment time. The decrease can be explained by a reaching maximum specific holding capacity of diatomite for a system being in the state of adsorption equilibrium between solution and the surface area. Similar adsorption behaviour was reported in the kinetic experiments with trivalent chromium by Gürü et al. (2008) using Tar-Chromium Red-B (Koyuncu and Kul, 2011).

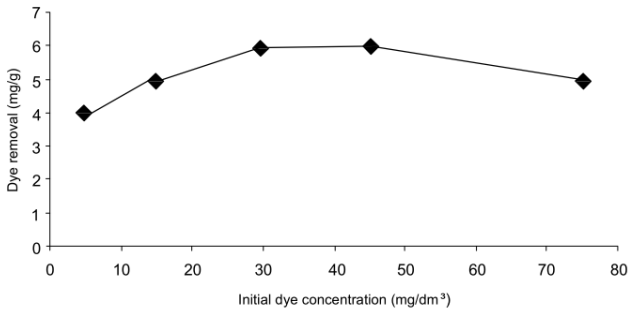

Fig.1. Effect of initial dye concentration on diatomite

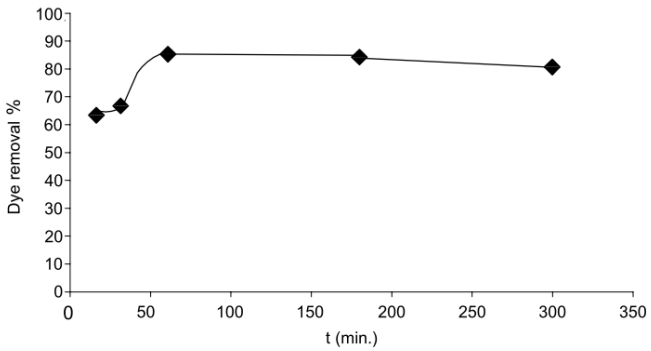

Fig. 2. Removal of Tar-Chromium Green 3G on diatomite for different times, 3 g diatomite, 30ºC, 195 rpm

3.2. Effect of adsorbent mass

Figure 2 shows the removal of Tar-Chromium Green 3G by diatomite at different adsorbent doses (0.5-5g) for the 50 cm^3 of 5 mg/dm^3 of the dye solution. It is evident from the figure that as the mass of the adsorbent dose increases, the percentage of dye removal also increases. This is due to increase in the surface area with a high dosage

of the adsorbent (Gürü et al., 2008). However, it has no impact when more than about 3g diatomite is used. It can be a result of the removal efficiency of dye which decreased with decreasing surface area of adsorbent and increasing particle size and decreasing the external surface area of diatomite.

3.3. Effect of temperature

The rates of adsorption were investigated in the temperature range of 25, 30 and 35ºC for the initial dye concentration of 5 mg/dm^3 at the natural pH. The effect of temperature on the adsorption is shown in Fig. 3. It is observed that at higher temperatures adsorption is lower, and the process was physical adsorption. A decrease of adsorption may be explained by physical adsorption which decreases with increasing temperature, and the adsorption process is exothermic. A similar observation has been reported by other invertigators for Cr(VI) removal (Anandkumar and Mandal, 2009) and trivalent chromium (Gürü et al., 2008) in kinetic experiments with Maxilon Yellow and Maxilon Red (Dogan et al., 2009).

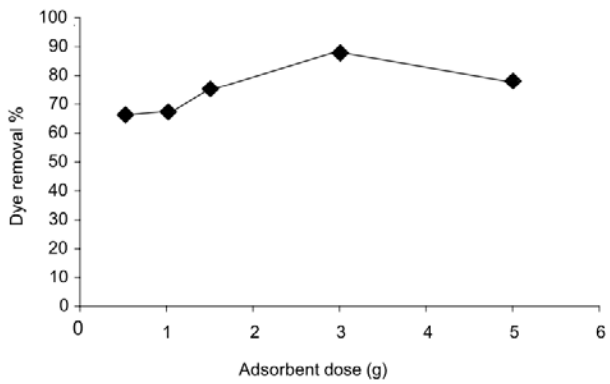

Fig. 3. Effect of adsorbent dosage on the removal of Tar-Chromium Green 3G by diatomite

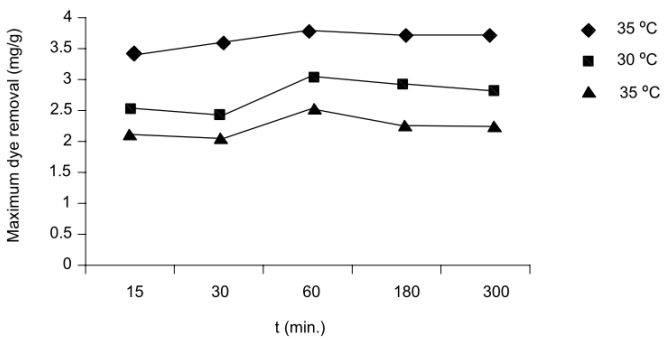

Fig. 4. Effect of temperature on the removal of Tar-Chromium Green 3G by diatomite (conditions: C_o 5 mg/cm^3, natural pH, adsorbent 3.0 g, t = 15 - 300 min)

3.4. Isotherm study

The isotherm analysis of adsorption process were carried out using the Langmuir and Freundlich models at different temperatures.

The Langmuir and Freundlich isotherm parameters were determined for their linear forms. In the case of the Freundlich isoterm:

$$q_e = kC_e^{1/n} \qquad \text{Freundlich isotherm,} \tag{2}$$

$$\ln q_e = \ln k + \frac{1}{n}\ln C_e \qquad \text{Freundlich isotherm (linear form),} \tag{3}$$

where q_e is the amount of dye adsorbed at equilibrium time (mg/g), C_e is the equilibrium concentration of the dye in solution (mg/dm^3), k and n are isotherm constants which indicate the capacity and intensity of the adsorption, respectively.

Figure 4 presents the plots of ln q_e against ln C_e for the adsorption of dye onto diatomite in the range from 25, 30 to 35ºC at natural pH, respectively. Figure 4 shows that the plots for diatomite provide the Freundlich isotherm correlation coefficients 0.980, 0.976 and, 0.973 respectively. On the other hand, the values of n between 2 and 10 show good adsorption (Gürü et al., 2008; Erdem et al., 2005). The values of k and n were calculated from the incercept and slope of the plot of ln qe versus ln Ce, respectively. Therefore, the adsorption of Tar-Chromium Green 3G onto diatomite fits well with the Freundlich models. These constants are given in Table 1. The Freundlich equation frequently gives an adequate description of adsorption data over a restricted range of concentration. The Freundlich equation is suitable for a highly heterogonous surface and adsorption isotherm lacking a plateau, indicating a multi-layer adsorption.

The Langmuir model is as follows:

$$q_e = \frac{Q_o b C_e}{1 + bC_e} \qquad \text{Langmuir isotherm,} \tag{4}$$

$$\frac{C_e}{q_e} = \frac{1}{Q_o b} + \frac{C_e}{Q_o} \qquad \text{Langmuir isotherm (linear form),} \tag{5}$$

where Q_o and b are Langmuir constants, which indicate the adsorption capacity (mg/g) and energy of adsorption, respectively.

Figure 5 shows the plots obtained for diatomite with the Langmuir isotherm correlation coefficients at 25, 30 and 35ºC, 0.998, 0.961 and, 0.935 respectively. The values of Q_o and b are found from the slope and intercept of the plot of C_e/q_e versus C_e, respectively. The constants Q_o, b determined at different temperatures are given in Table 1.

Table 1. Isotherm parameters of textile dye adsorption onto natural diatomite

	Langmuir constants			Freundlich constants		
Temparature	q_m (mg/g)	b(l/g)	R^2	K_f (mg/g)	n	R^2
25^0C	26. 04	0,08	0.998	1.73	5.88	0.980
30^0C	16. 66	0,40	0.932	1.40	3.84	0.976
35^0C	10. 10	0,55	0.917	0.78	3.70	0.973

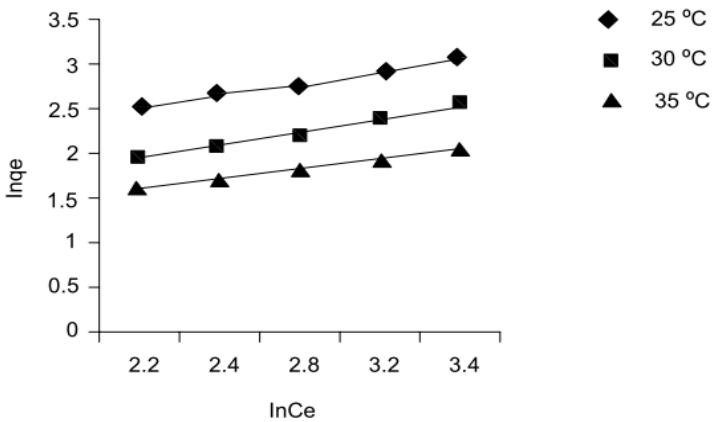

Fig. 5. Freundlich isotherms of the dyes adsorption onto diatomite at different temperatures

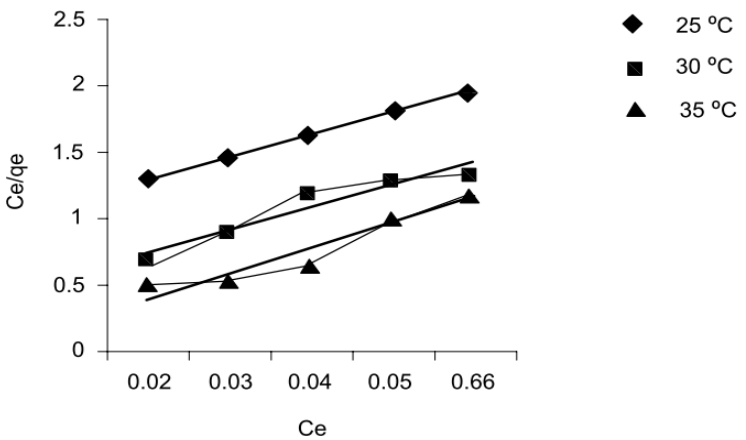

Fig. 6. Langmuir isotherms of the dyes adsorption onto diatomite at different temperatures

3.5. Thermodynamic study

Various thermodynamic parameters such as ΔG, ΔH and ΔS of dyes adsorption on diatomite were determined by using the following equations (Gürü et al., 2008; Ertaş et al., 2010; Nassem and Tahir, 2001):

$$\Delta G = -RT \ln K_c , \tag{6}$$

$$\ln K_c = \frac{-\Delta H}{RT} + \frac{\Delta S}{R}, \tag{7}$$

$$\Delta S = \frac{\Delta H - \Delta G}{T}, \tag{8}$$

$$K_c = \frac{C}{Ce}, \tag{9}$$

where R is the gas constant, K_c is the equilibrium constant, T is the absolute temperature (in Kelvin). C and C_e are the equilibrium constants (concentrations) of dye on adsorbent and in solution, respectively.

The values of ΔH and ΔS were calculated from the slopes and intercepts of the plot of ln K_c versus $1/T$ which are linear. Their plots are shown in Fig. 6 and the thermodynamic parameters are given in Table 2. It is clear from the table that the negative values of ΔG confirm that the dyes adsorption onto diatomite is a spontaneneous process. The negative values of ΔH shows an exothermic process. On the other hand, the positive values of ΔS indicate the randomness at the solid/liquid interface during the adsorption of dye onto diatomite. Similar thermodynamic results have been recorded for adsorption of trivalent chromium onto natural diatomite (Gürü et al., 2008; Ertaş et al., 2010).

Table 2. The thermodynamic parameters for the adsorption of Tar-Chromium Green 3G onto diatomite at different temperatures

Tempareture (K)	K_c	ΔG (kJ/mol)	ΔH(kJ/mol)	ΔS (J/molK)
298	1.772	-1.417	-1.314	0.345
303	2.444	-2.251	-2.308	0.188
308	2.690	-2.532	-2.446	0.282

4. Conclusion

Diatomite, a low cost adsorbent is locally available in Turkey. Diatomite is approximately 500-fold cheaper than commerical activated carbon, CAC. Crystal structure of diatomite contains some ion- exchangeable cations such as Mg^{+2}, Ca^{+2} and Na^{+}. These cations can be exchanged with organic and inorganic cations. The surface charge of diatomaceous earth may arise from chemical reactions. It has a unique combination of physical and chemical properties (high permeability). The high porosity makes it a cheap alternative to activated carbon (Erdem et al., 2005). Therefore, it is suitable material for removal of dyes,

The adsorption isotherms of Tar-Chromium Green 3G on diatomite can be described well by the Langmuir and Freundlich isotherm models. A comparison of the Langmuir and Freundlich models on the overall adsorption showed that the

Tar-Chromium Green 3G and and diatomite was better described by the Freundlich model rather than by Langmuir model. The maximum dye removal was 88% under all experimental conditions studied.

The thermodynamic parameters calculated from the temperature dependent adsorption isotherms indicate that the adsorption process is spontaneous and exothermic.

References

ANANDKUMAR, J., MANDAL, B., 2009, *Removal of Cr (VI) from aqueous solution using bael fruit (Aegle marmelos correa) shell as an adsorbent*, J. Hazard. Mater. 168, 633–640.

BASİBUYUK, M., FOSTER, C. F., 2003, *An examination of the adsorption characteristics of a basic dye (Maxilon Red BL –N) on to live activated sludge system*, Process Biochem. 38, 1311–1316.

BASKARALİNGAMA, P., PULİKESİA, M., ELANGOB, D., RAMAMURTHİA, V., SİVANESAN, S., 2006, *Adsorption of acid dye onto organobentonite*, J. Hazard. Mater. 128, 138–144.

BLITZ, I.P., BLITZ, J.P., GUN'KO, V.M., SHEERAN, D.J., 2007, *Functionalized silicas: Structural characteristics and adsorption of Cu (II) and Pb (II)*, Colloids and Surfaces A: Physicochem. Eng. Aspects. 307, 83–92.

CHİOU, M.S. HO, P.Y. AND Lİ, H.Y., 2004, *Adsorption of anionic dyes in acid solutions using chemically cross- linked chitosan beads*, Dyes and Pigments 60, 69–84.

DOĞAN, M. KARAOĞLU, M.H.. ALKAN, M., 2009, *Adsorption kinetics of maxilon yellow 4GL and maxilon red GRL dyes on kaolinite*, J. Hazard. Mater. 165, 1142–1151.

EASTON, J.R. 1995, *The dye maker's view*, in: Colour in Dyehouse Effluent, COOPER, P. (Ed.), Bradford, Society of Dyers and Colourists, UK, 9–21.

ER, L., XİANGYİNG, Z., YUEHUA, F., 2009, *Removal of chromium ion (III) from aqueous solution by manganese oxide and microemusion modified diatomite*, Desalination, 238, 158–165.

ERDEM, E., ÇÖLGEÇEN, T., DONAT, R., 2005, *The removal of textile dyes by diatomite earth*, J. Colloid Interface Sci. 282, 314–319.

EREN, Z., ACAR, F.N., 2006, *Adsorption of reactive black 5 from an aqueous solution: equilibrium and kinetic studies*, Desalination 194, 1–10.

ERTAŞ, M., ACEMİOĞLU, B., ALMA, M.H., USTA, M., 2010, *Removal of methylene blue from aqueous solution using cotton stalk, cotton waste and cotton dust*, J. Hazard. Mater. 183, 421–427.

Al-GHOUTİ, M.A., KHRAİSHEH, M.A., AHMAD, M.N., ALLEN, S.. 2009, *Adsorption behaviour of methylene blue onto jordanian diatomite: A kinetic study*, J. Hazard. Mater. 165, 589–598.

GÜRÜ, M. VENEDİK, D. AND MURATHAN, A. Removal of trivalent chromium from water using low-cost natural diatomite, jhazmat. 160 (2008), pp. 318-323.

HAMEED, B.H., 2008, *Equilibrium and kinetic studies of methyl violet sorption by agricultural waste* , J. Hazard. Mater.154, 204–212.

UZUN, İ., 2006, *Kinetics of the adsorption of reactive dyes by chitosan*, Dyes anp Pigments 70, 76–83.

KOYUNCU, M, .KUL, A.R., 2011, *Removal of Tar- chrome red-B dye by adsorption onto natural diatomite*, Journal of Chemical and Pharmaceutical Research 3, 297–303.

KOYUNCU, M., 2009, *Adsorption properties of basic dyes (maxilon red GRL and maxilon yellow GRL) onto bentonite*, Asian J. Chem. 21, 5458–5464.

MALKOÇ, E, NUHOĞLU, Y., 2006, *Fixed bed studies fort he sorption of chromium (VI) onto tea factory waste*, Chem. Eng.Sci. 61, 4363–4372.

MARUNGRUENG, K., PAVASANT, P., 2007, *High performance biosorbent (Caulerpa lentillifera) for basic dye removal*, Biores.Tech. 98, 1567–1572.

MURATHAN, A. BENLİ, S., 2005, *Removal of* Cu^{2+}, Pb^{2+} *an* Zn^{2+} *ions from aqueous solutions on diatomite via adsorption in fixed beds*. Fresen. Environ. Bull. 14, 468–472.

NASSEM, R., TAHİR, S.S, 2001, *Removal of Pb (II) from aqueous/acid solutions by using bentonite*, Water Res. 35, 3982–3986.

PARAB, H., JOSHI, S.; SHENOY, N., LALI, A.; SARMA, U.S.; SUDERSANAN, M.; 2006, *Detemination of kinetic and equilibrium parameters of the batch adsorption of Co (II) Cr(III) and Ni(II) onto coir pith*, Process Biochem. 41, 609–615.

PEARCE, C.I., LLOYD, J.R., GUTHRİE, J.T., 2003, *The removal of colour from textile waste water using whole bacterial cells. A review*, Dyes and Pigments 58, 179–196.

QİU, J., WANG, Z., Lİ, H., XU, L., PENG, J., ZHAİ, M., YANG, C., Lİ, J., WEİ, G., 2009, *Adsorption of Cr(VI) using silica- based adsorbent prepared by radiation-induced grafting*, J. Hazard. Mater. 166, 270–276.

ROBİNSON, T., MULLAN, G., MARCHANT, R., NİGAM, P., 2001, *Remediation of dyes in textile effluenta critical on current treatment technologies with a proposed alternative*, Bioresour. Technol., 77, 247–254.

SİNGH, K.P.,MOHAN, D., SİNHA, S., TONDON, G.S., GOSH, D., 2003, *Color removal from wastewater using low-cost activated carbon derived from agricultural waste material*, Ind. Eng. Chem. Res. 42, 1965–1976.

TAHİR, S.S., NASSEM, R., 2007, *Removal of Cr (III) from tannery wastewater by adsorption onto bentonite clay*, Sep. Purif. Technol. 53, 312–321.

WANG, S., HUİTİNG, L., 2005, *Dye adsorption on unburned carbon: Kinetics and equilibrium*, J. Hazard. Mater. 26, 71–77.

YUAN, P., LİU, D., FAN, M., YANG, D., ZHU, R., GE, F., ZHU, J., HE, H., 2010, *Removal of hexavalent chromium [Cr(VI)] from aqueous solutions by the diatomite supported/unsupported magnetite nano particles*, J. Hazard. Mater. 173, 614–621.

Physicochem. Probl. Miner. Process. 48(2), 2012, 495−512

www.minproc.pwr.wroc.pl/journal/

Physicochemical Problems of Mineral Processing

ISSN 1643-1049 (print)
ISSN 2084-4735 (online)

Received April 3, 2012; reviewed; accepted May 1, 2012

EFFECT OF AUTOCORRELATION ON THE PROCESS CONTROL CHARTS IN MONITORING OF A COAL WASHING PLANT

Adem TASDEMIR

Department of Mining Engineering, Division of Mineral Processing, Eskişehir Osmangazi University, 26480, Eskişehir, Turkey, atasdem@ogu.edu.tr, Tel: +90 222 239 37 50 Ext: 3438

Abstract. Traditional statistical process control charts assume that generated process data are normally and independently distributed, i.e. uncorrelated. This research presents the effect of autocorrelation on process control charts to monitor the two quality characteristics of fine coals produced in a coal washing plant for power plant, namely moisture content and ash content. Individual (X) and moving range charts (MR) were constructed to monitor 10 months data. It was determined that even though both data values obey the normal distribution, there is a moderate autocorrelation between their observations. For simulating the autocorrelated data, ARIMA time-series models were used. It was found that X/MR charts showed many false alarms due to the autocorrelation. The ARIMA (1, 0, 1) for moisture content and ARIMA (0, 1, 2) for ash content were determined to be the best models to remove autocorrelation. Compared to large number of false alarms on conventional X/MR charts and on charts applying the Western Electric rules, which assume the data independence, there were much less unusual points on the X/MR charts of residuals (Special Cause Charts). Usage of residual based control charts is suggested when the data are autocorrelated.

keywords: coal, autocorrelation, statistical control charts, special cause charts, ARIMA models

1. Introduction

Statistical process control (SPC) has been proposed firstly by Dr. Shewhart in 1931 and then, many SPC charts have been developed and improved to use for different process data. In its basics form, a control chart compares process observations with a pair of control limits (Karaoğlan and Bayhan, 2011). One of the essentials of producing high quality low cost product is to adopt and apply the SPC correctly. SPC is a tool for achieving and improving quality standards. The most important and sophisticated tool of SPC is control charts.

SPC is widely used to monitor, control and improve quality in many industrial processes (MacCharty and Wasusri, 2002). The SPC has been also used in mining and mineral processing field to monitor the grade variations and to ensure the product specifications. In a review study, MacCharty and Wasusri (2002) summarize the usage of non-standard applications of statistical process control charts. Some application

http://dx.doi.org/10.5277/ppmp120215

examples of SPC can be given from the literature for mining/mineral processing industry (Ankara and Bilir, 1995; İpek et al., 1999; Bhattacherjee and Samanta, 2002; Bayat and Arslan, 2004; Aykul et al., 2005; Vapur et al., 2005; Elevli and Behdioğlu, 2006; Ankara and Yerel, 2008; Vapur, 2009; Elevli, 2009; Aykul et al., 2010; Yerel and Ankara, 2011). However, the information related to the application of SPC in mineral industry is still limited when compared to other industrial areas.

Traditional SPC techniques are based on the assumption that generated data generated are normally and independently distributed. However, the independency assumption is not realistic in practice (Demirkol, 2008). Therefore, the assumption of normality and indepence of data must be satisfied in order to apply SPC for a process (Bhattacherjee and Samanta, 2002).

In the continuous industries processes most data are autocorrelated (Le, 1998). Since observations for many processes exhibit autocorrelation that may be the result of dynamics that are inherent to the process, the autocorrelation is more likely to be observed in processes when observations are closely spaced in time (Lu and Reynolds, 2001). Such autocorrelations can occur for a number of reasons. One reason is because of current automated measurement and recording technology, subgroup samples may be taken with a high frequency, with consecutive samples being similar in nature and hence statistically correlated. Other samples of correlated subgroups occur when items made by a worker exhibit similar characteristics due to the way the machine is handled, the process shows seasonal patterns due to materials or weather, or the alertness of a worker changes over time (Le, 1998).

The effect of autocorrelation on the performance of process control charts have been shown by many researhers (Alwan and Roberts, 1998; Lu and Reynolds, 1999; Montgomery and Mastrangeko, 1991; Atienza et al., 1997; Reynolds and Lu, 1997; Zhang, 1997). Results of these studies have shown that traditional SPC methods are strongly affected by data autocorrelation. Under autocorrelation conditions, the traditional control charts will become ineffective and many false alarms may occur on the charts. Consequently, there has been considerable research in recent years on designing SPC procedures suitable for autocorrelated processes.

In the case of autocorrelation, a very high false alarm rate will cause process personnel to waste effort in unproductive searches for special causes. This can lead to a loss of confidence in the control chart, and even to process monitoring being discontinued. Thus, autocorrelation should not be ignored when designing control charts, because failure to properly account for autocorrelation can greatly reduce or eliminate the effectiveness of control charts (Lu and Reynolds, 2001).

For these reasons, some modifications for traditional control charts are necessary. As an alternative to traditional control charts which plot the original observations, a number of papers have suggested fitting a time series model (Alwan and Roberts, 1988; Reynolds and Lu, 1997; Lu and Reynolds, 1999; Lu and Reynolds, 2001). The residuals obtained from time series model are then plotted on standard control charts.

To apply these methods, a time series model of the process is required (Apley and Lee, 2003).

Alwan and Roberts (1988) introduced the first residual control chart, namely special cause chart (SCC). A residual Shewhart chart was developed by them and it is called as the special control chart (SCC). The SCC is an individual control chart (individual control chart is constructed by plotting single observations and setting control limits on these observations) applied to the residuals. Therefore, the SCC is also known as the X residual chart in the literature. In residual charts, an appropriate time series model is fitted to the autocorrelated observations and the residuals are plotted in a control chart (Demirkol, 2008).

Even though the assumptions required for the applicability of SPC methods are known to be essential, their existence may questionable in mining industry (Bhattacherjee and Samanta, 2001). When the literature is reviewed, the impact of autocorrelation on SPC have been considered in mineral applications by only few studies (Samanta and Bhattacherjee, 2001; Bhattacherjee and Samanta, 2002; Samanta, 2002; Elevli et al., 2009). Indeeed, the observations in these studies are assumed to normally distributed and independent that is uncorrelated.

Turkey has 8.3 billion tons of lignite coal reserves (Arslan, 2006). Since 80% of Turkish lignite coal reserves has a heating value of below 2500 kcal/kg, large amount of them are used in power plants. Moisture and ash contents of coals are the two important quality characteristics that determine properties of coals burning in power plants. Substantial amount of low quality coals which have high ash and moisture contents are transformed into energy by burning them in power plants (Tekir et al., 2009). In a power plats that burns lignites, moisture and ash contents are the key quality indicators monitored. Therefore, lowering the ash contents of lignites to the desired levels is an essential entity to reduce problems and costs associated with the ash. Coals having high ash and moisture contents cause serious problems such as incrasing the costs of operation, transportation and burning of coal together with disposing the ash to dams in power plants (Tekir et al., 2009). For these reasons, coal fines produced in a coal washing plant should have desired moisture and ash content limits in order to be used as feeding material for a power plant. To control the coal qualities produced in washing plants, it is necessary to monitor the coal characteristics by applying an effective method such as statistical process control.

The aim of this paper is to investigate individual X control charts based on the original observations or on residuals obtained by the time series of ARIMA models for moisture and ash contents of fine coal products that are produced for power plant as a feeding material in Tunçbilek washing plant. Autocorrelated observations were characterized by ARIMA models and special control charts (SCC) were utilized to monitor the residuals, based on the ARIMA model forecast values. The performance of the standard Shewhart chart, which ignores subgroup correlations for the two coal quality variables, is compared with the X charts of residuals.

2. Statistical process control charts

Statistical Process Control (SPC) charts are graphical presentations of the sample quality for one parameter measured in control samples. In a basic the SPC chart, three horizontal lines, the center line and two control limits, are plotted on a control chart, which show the mean value and three standard deviations distance from either side of the mean value, respectively (an example is given in Fig. 1). If the plotted observatios fall outside the limits, the process is consired to be out of control. The process needs to be stopped and inspected for causes when the out of control points are detected (Carson and Yeh, 2008).

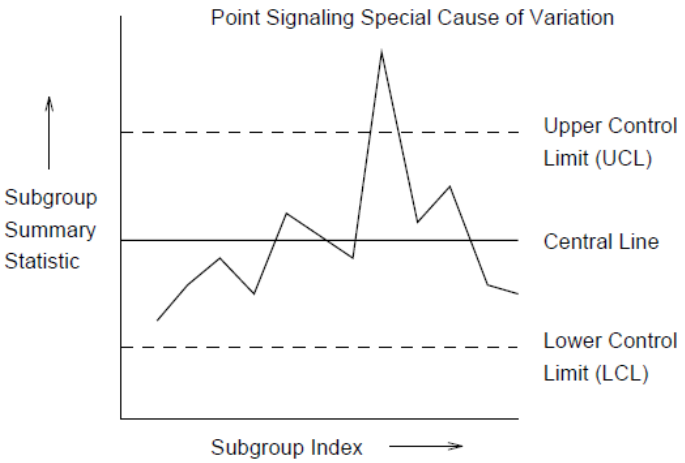

Fig. 1. A traditional Shewhart control chart

2.1. X/MR charts for individual observations

In many situations, the sample size used for process control is $n = 1$; that is, the sample consists of an individual unit. In such situation, the individuals control chart (also called as X chart or I chart) is used. Mean of the individual values for m individual observations gives us the center line of the X control chart as:

$$\overline{X} = \frac{1}{m}\sum_{i=1}^{m} X_i = \frac{X_1 + X_2 + X_3 + \ldots + X_m}{m}. \tag{1}$$

The control chart for individuals uses moving range of two successive observations to estimate the process variability and it is also known as MR chart (Montgomery and Runger, 2011). The moving range is defined as $MR_i = |X_i - X_{i-1}|$ and for m observations the average moving range ($\overline{MR}$) is:

$$\overline{MR} = \frac{1}{m-1}\sum_{i=2}^{m} \left| X_i - X_{i-2} \right|. \tag{2}$$

An estimate of standard deviation (σ) is:

$$\sigma = \frac{\overline{MR}}{d_2} = \frac{\overline{MR}}{1.128}. \tag{3}$$

Here, d_2 is a constant depending on the sample size, n, (Montgomery and Runger, 2011). It is 1.128 for $n = 2$.

The center line (CL_X) and upper control limit (UCL_X) and lower control limit (LCL_X) for a control chart for individuals is (Montgomery and Runger, 2011):

$$UCL_X = \overline{X} + 3\frac{\overline{MR}}{d_2} = \overline{X} + 3\frac{\overline{MR}}{1.128} = \overline{X} + 2.66\overline{MR}, \tag{4}$$

$$CL_X = \overline{X}, \tag{5}$$

$$LCL_X = \overline{X} - 3\frac{\overline{MR}}{d_2} = \overline{X} - 3\frac{\overline{MR}}{1.128} = \overline{X} - 2.66\overline{MR}. \tag{6}$$

Since each moving range is the range between two consecutive observations. It should be noted that there are only m-1 moving ranges. The parameters for a control chart of moving range are defined as follows:

$$UCL_{MR} = D_4\overline{MR} = 3.267\overline{MR}, \tag{7}$$

$$CL_{MR} = \overline{MR}, \tag{8}$$

$$LCL_{MR} = D_3\overline{MR} = 0. \tag{9}$$

D_3 and D_4 are constants depending on the sample size, n. It is possible to establish a control chart on the MR using D_3 and D_4 for $n = 2$ (Montgomery and Runger, 2011). The LCL_{MR} for this moving range chart is always zero because $D_3 = 0$ for $n = 2$. The D_4 equals to 3.267 for $n = 2$ while determining the UCL_{MR}.

For a simple control chart in Fig. 1 control limits were plotted as warning lines from the action limits of 3σ. In this figure, only measurements that are plotted further than 3σ from the central line indicate an out-of-control process. However, additional warning limits in Shewhart charts are commonly used in practice, since they help the analyst to recognize possible changes in the process before it shifts out of 3σ (Carson and Yeh, 2008). For example, when two consecutive out of 2σ samples are detected, this can indicate some changes in the process. Therefore, it is advisable to perform some rechecks of the process at this point.

It is known that the Shewhart control chart is insensitive to small shifts in the process parameter. To enhance the ability for the chart to detect small shifts more quickly, one way is to add sensitive rules in the chart (Chang and Wu, 2011). Several frequently used rules suggested by the Western Electric (1956) are (Montgomery and Runger, 2011):

1. One or more points fall outside the 3σ control limits,
2. Two of three consecutive points fall outside the 2σ warning limits,
3. Four of five consecutive points fall beyond the 1σ limits,
4. Eight points in a row fall one side of the center line.

The above rules are always referred to runs rules. In the sequel, a control chart that uses several rules simultaneously is referred to a compound control chart. It should be noted that rule 1 in included in all compound control charts. Also note that these rules can only be applied to one side of the center line. There are more rules for detecting small shifts and these can be added to control.

In this study, the four rules listed above were used when considering additional warning limits by Western electric rules. These plots searches and identifies any unusual patterns in the data. This is often helpful in detecting processes which are slowly drifting away from target, even though no points may fall outside the control limits.

3. Time series models

The methodology of ARIMA estimation and model selection is a classical topic covered in most textbooks on time series analysis such as Montgomery et al. (2008). Therefore, we will not duplicate the descriptions of already well documented methodologies. We will give only practical information in this context to the models.

3.1. Autoregressive Process (AR)

Most time series consist of elements that are serially dependent in the sense that one can estimate a coefficient or a set of coefficients that describe consecutive elements of the series from specific, time-lagged (previous) elements. This can be summarized in the following Eq. 10:

$$X_t = \delta + \phi_1 X_{t-1} + \phi_2 X_{t-2} + \ldots + \phi_p X_{t-p} + \varepsilon_t \,, \tag{10}$$

where X_t is response (dependent) variable at time t; $X_{t\text{-}1}$, $X_{t\text{-}2}$, $X_{t\text{-}\mathrm{p}}$ response variable at time lags t-1, t-2,…t-p, respectively; ϕ_1, ϕ_2, ϕ_p, denote estimated coefficients, ε_t is an error term at time t, and $\delta = \left(1 - \sum_{i=1}^{p} \phi_i\right)\mu$ with μ denotes the process mean.

It should be noted that an autoregressive process will only be stable if the parameters are within a certain range for example, if there is only one autoregressive parameter, then it must fall within the interval of $-1<\phi_1<+1$. Otherwise, past effects would accumulate and the values of successive X_t's would move towards infinity, that is, the series would not be stationary. If there is more than one autoregressive parameter, similar (general) restrictions on the parameter values can be defined (Montgomery et al., 2008).

3.2. Moving Average process (MA)

Independent from the autoregressive process, each element in the series can also be affected by the past error (or random shock) that cannot be accounted for by the autoregressive component, that is:

$$X_t = \mu + \varepsilon_t - \theta_1\varepsilon_{t-1} - \theta_2\varepsilon_{t-2} - \ldots - \theta_q\varepsilon_{t-q}\,, \tag{11}$$

where X_t is the time series, μ is the mean of the series, ε_{t-I} denotes random noise term with mean 0 and variance σ_ε^2 at time t. θ_1, θ_2, θ_q, are the moving average model parameters. The value of q is called the order of the MA model.

3.3 Autoregressive Moving Average model (ARIMA)

The ARIMA model which combines the autoregressive and moving average parameters and includes differencing in the model was introduced by Box and Jenkins (1976) (Montgomery et al., 2008). This equation was used to forecast one-step ahead disturbances, according to data characteristics of stationary or non-stationary as shown in Eq. 12.

$$\Delta_d X_t = \mu + \phi_1\Delta_d X_{t-1} + \phi_2\Delta_d X_{t-2} + \ldots + \phi_p\Delta_d X_{t-p} + \varepsilon_t - \theta_1\varepsilon_{t-1} - \ldots - \theta_q\varepsilon_{t-q}\,, \tag{12}$$

Three types of parameters in the model are: the autoregressive parameters (p), the number of differencing passes (d), and moving average parameters (q). The Box and Jenkins models are summarized as the ARIMA (p, d, q); so, for example, a model described as (0, 1, 2) means that it contains 0 (zero) autoregressive (p) parameters and 2 moving average (q) parameters which were computed for the series after it was differenced once (documentation.statsoft.com).

The input series needs to be stationary for ARIMA. It should have a constant mean, variance, and autocorrelation through time. Therefore, the series are first differentiated until they are stationary. Sometimes the series also require log transformation of data to stabilize the variance. The d parameter indicates the number of times the series needs to be differenced to achieve stationarity (documentation.statsoft.com). The necessary level of differencing is determined by examining the plot of the data and autocorrelogram. Significant changes in level (strong upward or downward changes) usually require first order non seasonal (lag=1) differencing; strong changes of slope usually require second order non seasonal differencing. When the estimated autocorrelation coefficients decline slowly at longer lags, first order differencing is usually needed (documentation.statsoft.com). Some time series may require little or no differencing, and over differenced series produce less stable coefficient estimates It is needed to decide how many autoregressive (p) and moving average (q) parameters are necessary to yield an effective but has the fewest parameters and greatest number of degrees of freedom among all models that fit the data model of the process. The number of p or q parameters very rarely need to be greater than 2 in practice (documentation.statsoft.com).

The ARIMA models may also include a constant in addition to the standard *p* and *q* parameters. The interpretation of a constant that is statistically significant depends on the model fitted. The expected value of the constant is *m*, the mean of the series, when there are no AR parameters in the model. The constant represents the intercept, if there are the AR parameters in the series. If the series is differenced, then the constant represents the mean or intercept of the differenced series. If the series investigated is differenced once, and there are no the AR parameters in the model, then the constant represents the mean of the differenced series, and therefore the linear trend slope of the undifferenced series (documentation.statsoft.com).

4. Methodology

The objective of this paper is to investigate effect of autocorrelation on the performance of the Shewhart individual control charts based on original observations or residual charts. This procedure was applied for the data obtained from moisture and ash contents of coal fines which are produced at the Tunçbilek coal washing plant and used as power plant feeding in Tunçbilek, Turkey. The used data were for the -18+0.5 μm size coal fines, called middling product, which is concentrated by dense medium cyclones. The mixture material containing magnetite as dense medium and coals, that sunk in the first dense medium cyclone are feed to second dense medium cyclone flowsheet, having 1800 g/Mg dense medium, for the final separation of -18+0.5 μm coals from schist. The middling product is obtained from and an overflow of cyclone and schist are separated from the underflow of the cyclone. The middling products are then separated from magnetite, dried and sent to the power plant as a feeding material. Daily moisture and ash content data from January 2011 to October 2011 for middling product were supplied from the plant. Totally 242 measurements were obtained and used in the study.

These data were imported into the statistical software package. Trial version of Statgraphics Centurion XVI and Minitab 16 softwares were used to construct different control charts for statistical analyses. First, individual X and moving range (MR) charts assuming normality and independence of observations and X/MR charts applying the Western electric rules to detect the small shifts were generated to monitor the two quality characteristics. Normality and independence of data were checked by applying statistical methods. Since strong autocorrelations were determined for both quality values, the most suitable time series models to remove the autocorrelation between the observations were selected by applying the ARIMA methods. Then, special cause charts (X and MR charts of residuals obtained from ARIMA models) were also generated. Finally, performance of the Shewhart charts of individual observations is compared with the performance of special cause charts for the two coal quality measurements to control the unusual points.

5. Results and discussions

5.1. Control charts for individual coal quality observations

A major drawback of the Shewhart variable charts is its dependency on normality assumption. First, the normal probability plots were generated. When the distribution of the variable is normal, the observed values show a near-linear distribution in the linear line drawn of the chart. The resulted plots including statistical information are given in Fig. 2. As seen in these plots, observed data distribution are almost linear indicating that both variables obey the normal distribution function. The data of the two coal characteristics have been also checked for normality by applying the Anderson-Darling normality test. The Anderson-Darling values were 0.659 and 0.249 for moisture and ash content of coals, respectively. Also *p* values of both variables were higher than 0.05, suggesting that the data came from a process with normal distribution. The result indicates that the first normality assumption needed for applying the standard Shewhart control charts was satisfied.

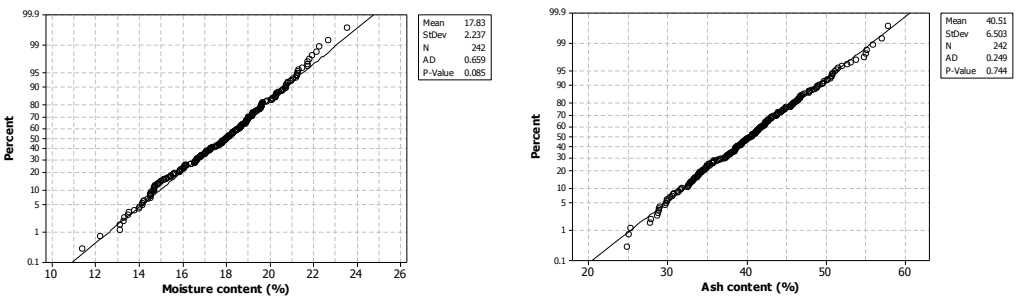

Fig. 2. Normal probability plots of moisture and ash contents

The *X* and MR control charts of individual data for moisture content and ash contents are given in Fig. 3 and Fig. 4 respectively. The calculated control chart parameters are given in Table 1. The charts are designed to determine whether the data come from a process which is in a state of statistical control. The control charts are constructed under the assumption that the data come from a normal distribution with a mean equal to 17.83 for moisture content, 40.51 for ash content and a standard deviation equal to 1.19 for moisture content, 3.76 for ash content. Of the 242 individual observations shown on the charts, 25 are beyond the 3σ control limits on the *X* chart while 3 are beyond the limits on the MR chart for moisture content. On the other hand, 20 points are beyond the 3σ control limits on the *X* chart while 2 points are beyond the limits on the MR chart. Since the probabilities of seeing 25 or more points for moisture content and 20 or more points for ash content beyond the limits just by chance is 0.0. When the data come from the assumed distribution and they are not autocorrelated, we can declare the process to be out of control at the 95% confidence level.

When the Western electric rules were applied to the two coal quality characteristics, much more unusual points were determined in these charts as shown in Figs. 3 and 4. When these plots are examined, we can see that the efficiency of warning limits for detection of process shifting toward out-of-control state is increased when applying the Western Electric rules. Two hundred and 171 unusual runs have been detected for moisture content and ash content, respectively. The plots show observations at which the unusual pattern was detected as well as the particular rule which was violated. For example, rule 3 was violated for point 5 in the moisture content of X chart and for point 18 in the ash content X chart. At these locations, there were groups of 4 out of 5 points beyond 1.0 sigma, all on the same side of the centerline.

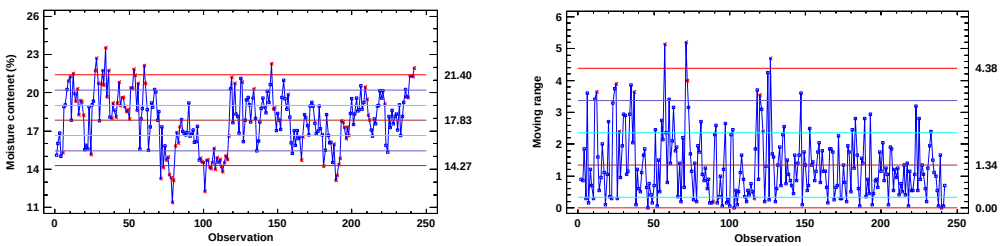

Fig. 3. *X*/MR charts of moisture content and unusual points by Western electric rules

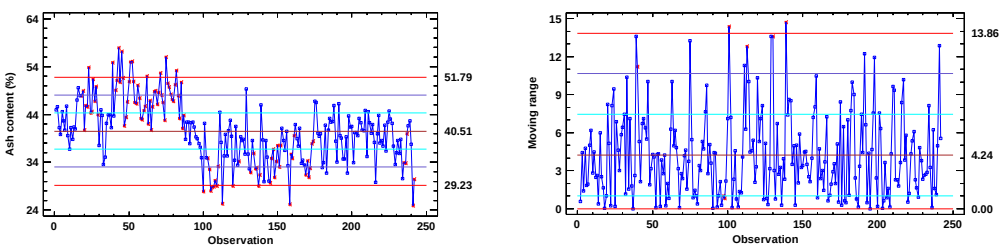

Fig. 3. *X/MR* charts of ash content and unusual points determined by Western electric rules

Table 1. Shewhart chart parameters of moisture and ash contents of coals

X /MR Chart parameters	Moisture content (%)	Ash content (%)
UCL_X	21.39	51.79
$\overline{X}$	17.83	40.51
LCL_X	14.27	29.23
UCL_{MR}	4.38	13.86
$\overline{MR}$	1.34	4.24
UCL_{MR}	0.0	0.0
$1\sigma = \overline{MR}/d_2$	1.19	3.76
2σ	2.37	7.52
3σ	3.56	11.28

Since the normality assumptions are satisfied by the normality tests, the performance of the individual control charts which are discussed so far is valid when the moisture and ash contents of coals are independent. However, if the data are autocorrelated, these findings can result in many wrong decisions about the process. Therefore, whether there is any autocorrelation between the consecutive observations of the two quality characteristics, or not, is tested in the following section.

5.2. Testing autocorrelation of coal characteristics

In addition to normality, independence of data must also be satisfied in order to apply SPC for the processes. Autocorrelation means the correlation between data observed, builds up automatically. If two variables are related in such a way that a change in one variable is reflected by a change in the other variable, the two variables are said to be correlated (Stapenhurst, 2005). Data are autocorrelated if each value is correlated to the previous one. Autocorrelation is a problem because the control charts, and indeed most statistical analyses, assume that the data are not autocorrelated. A quick and simple method of checking for autocorrelation is to draw a scatter diagram of each value, X_i, against the previous value X_{i-1} (Stapenhurst, 2005). Figure 5 shows the scatter diagram of moisture and ash contents of fine coals used in this study. It is clear that there are considerable positive correlations between the two consecutive data values of both variables. In the autocorrelated series of observation, each individual observation is dependent upon previous observation (Singh and Prajapati, 2011). This also exists for the two coal quality values and the degree of autocorrelation should be determined and also these autocorrelations must be removed by an appropriate ARIMA time series model before constructing statistical control charts.

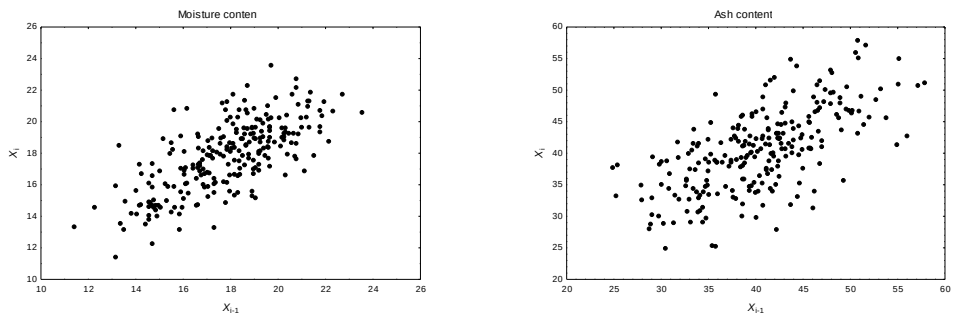

Fig. 5. Scatter diagrams showing autocorrelation for moisture and ash contents

It is possible to calculate the autocorrelation between consecutive values, that is, of lag 1. It is also possible to calculate the autocorrelation of lag 2 (i.e. between values two observations apart) or any number of observations apart (Stapenhurst, 2005). The correlation coefficient can be calculated for lags 1, 2, 3, etc. and it should steadily decrease. For some value *n*, the correlation coefficient will not be significant and this gives us the minimum time that should be allowed between sampling.

To check this, autocorrelation and partial autocorrelation function plots were generated for 25 lags. The sample Autocorrelation Function (ACF) and the sample Partial Autocorrelation Function (PACF) which are representative of the autocorrelation structure across periods of the time series, displayed in Fig. 6 for the moisture content time series (top plots) which show relatively stationary characteristics and for the ash content time series (bottom plots) which show some characteristics of a non-stationary process. There is a high degree of correlation (r = 0.7) for moisture content and (r = 0.6) for ash contents of consecutive data points. The sample ACF of moisture content decays linearly and the corresponding PACF indicates the most important contribution at the first lag. The sample ACF of ash content decays very slowly and the corresponding PACF shows one very significant contribution at lag 1 and then two contributions at lags 2 and 3.

Due to these facts it is likely to see an increased number of false alarms in both Shewhart control charts. Continuing to use a control chart that signals too often can be counter-productive because a real signal may be ignored as just another false alarm.

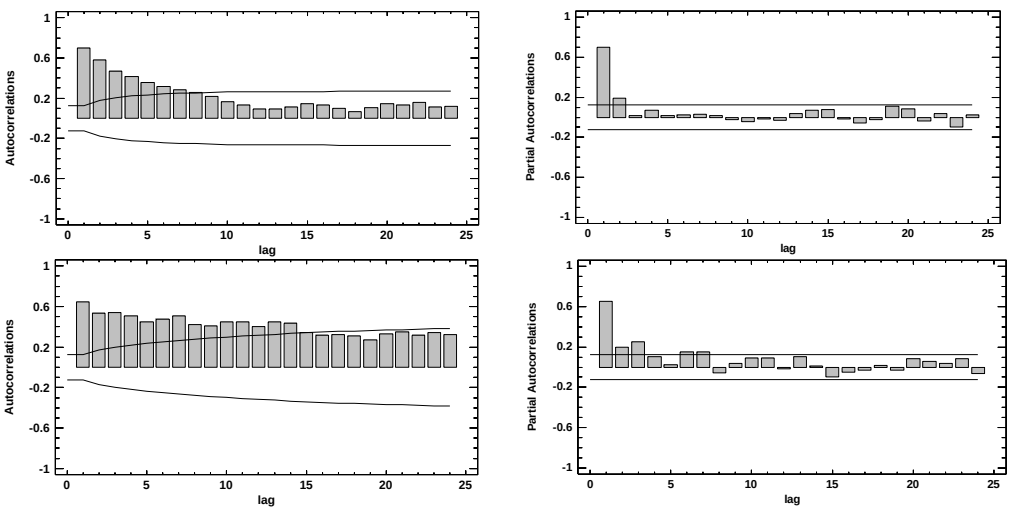

Fig. 6. ACFs and PACFs of moisture (top plots) and ash (bottom plots) contents

5.3. ARIMA fits and residuals

To remove the autocorrelations of two quality characteristics, ARIMA time series models that fit the best to the moisture and ash contents were determined by Statgraphics software. We use the ARIMA procedure in Statgraphics software to estimate the models for moisture and ash contents.

Tables 2 and 3 show the values of model fit statistics used for the ARIMA model selection for the moisture content and ash content respectively. In these tables, A, B, C, D and E denote the ARIMA models that can be suitable for the two quality characteristics. The five ARIMA models in the list are those that fit best, among

dozens that were fit. The most suitable model between them was selected by applying the selection criteria. The procedure fits each of the models indicated and selects the models that give the smallest value of the selected criterion. There are six criteria to choose from: (1) the root mean squared error (RMSE), (2) the mean absolute error (MAE), (3) the mean absolute percentage error (MAPE), (4) the mean error (ME), (5) the mean percentage error (MPE), (6) the Akaike Information Criterion (AIC).

Each of the statistics is based on the one-ahead forecast errors, which are the differences between the data value at time *t* and the forecast of that value made at time *t*-1. The first three statistics measure the magnitude of the errors. A better model will give a smaller value. The last two statistics measure bias. A better model will give a value close to 0. This table compares the results of fitting different models to the data.

The model with the lowest value of the Akaike Information Criterion (AIC) was chosen as the best describing model in this study. The AIC is calculated from:

$$AIC = 2\ln(RSME) + 2c/n, \tag{13}$$

where *RSME* is the root mean squared error during the estimation period, *c* the number of estimated coefficients in the fitted model, and *n* the sample size used to fit the model. The AIC is a function of the variance of the model residuals, penalized by the number of estimated parameters. In general, the model will be selected that minimizes the mean squared error without using too many coefficients (relative to the amount of data available).

The models with the lowest value of AIC are ARIMA (1,0,1) with a constant for the moisture content and ARIMA (0,1,2) for ash content though several other models are very similar, as presented in Table 2 and Table 3. Therefore, the ARIMA models are preferred for our data in this research.

Table 2. ARIMA model fit statistics for moisture content

Model	RMSE	MAE	MAPE	ME	MPE	AIC
(A)	1.56223	1.24302	7.09856	0.0137352	-0.713845	0.917022
(B)	1.5634	1.24791	7.1247	0.0160021	-0.705291	0.91852
(C)	1.56514	1.24187	7.09152	0.0129439	-0.715767	0.929005
(D)	1.56633	1.24641	7.11658	0.0119596	-0.722733	0.930528
(E)	1.57798	1.23127	6.99972	0.0646808	-0.372863	0.937088

A: ARIMA(1,0,1) with constant; B: ARIMA(2,0,0) with constant; C: ARIMA(1,0,2) with constant; D: ARIMA(2,0,1) with constant; E: ARIMA(2,1,1)

Table 3. ARIMA model fit statistics for ash content

Model	RMSE	MAE	MAPE	ME	MPE	AIC
(A)	4.62662	3.67199	9.47837	-0.168696	-1.69922	3.08018
(B)	4.63186	3.67325	9.5009	-0.178473	-1.74001	3.08245
(C)	4.63362	3.66381	9.425	-0.00738307	-1.29087	3.09147
(D)	4.618	3.61403	9.35612	-0.10959	-1.65678	3.09298
(E)	4.63713	3.66895	9.46142	-0.16297	-1.67918	3.09299

A: ARIMA(0,1,2); B: ARIMA(1,1,1); C: ARIMA(0,1,2) with constant; D: ARIMA(1,0,2) with constant; E: ARIMA(1,1,2)

Parameters of ARIMA (1,0,1) model for moisture and ARIMA (0,1,2) model for ash content are given in Table 4. The output summarizes the statistical significance of the terms of the forcasting model. The terms with *p*-values less than 0.05 are statistically significantly different from zero at the 95.0% confidence level. For the ARIMA (1,0,1) model, the *p*-value for the AR(1) term is less than 0.05, so it is significantly different from 0. The *p*-value for the MA(1) term is less than 0.05, so it is significantly different from 0. The *p*-value for the constant term is less than 0.05, so it is significantly different from 0. The estimated standard deviation of the input which noise is equal to 1.56364. As the evidence of Fig. 6, ACF of the time series values falls down fairly quickly for the moisture content, then the time series values can be considered stationary. Therefore, the moisture values were not need to be differentiated. For the ARIMA (0,1,2) model, the *p*-value for the MA (1) and MA(2) terms are less than 0.05, so they are significantly different from 0. The estimated standard deviation of the input which noise is equal to 4.62806. This model does not contain a constant. As seen in ACF of ash content it goes down very slowly, the time series values of ash content were considered non-stationary (Fig. 6). The ARIMA (0,1,2) model means that the data are differenced once and a second-order moving average term is included, with no intercept.

We obtained the moisture content model in the form:

$$X_t = 2.709 + 0.849X_{t-1} + 0.284\varepsilon_{t-1} \text{ with the AIC of 0.917.}$$

We also obtained the ash content model in the form:

$$X_t = X_{t-1} + 0.574\varepsilon_{t-1} + 0.215\varepsilon_{t-2} \text{ with the AIC of 3.08.}$$

Table 4. Summaries of parameters of ARIMA models

ARIMA (1,0,1) with constant model for moisture content				
Parameter	Estimate	Standard Error	t-value	p-value
AR(1)	0.848526	0.0504203	16.829	0.000000
MA(1)	0.284025	0.0867921	3.27247	0.001224
Mean	17.8889	0.446367	40.0767	0.000000
Constant	2.70971			
ARIMA (0,1,2) model for ash content				
Parameter	Estimate	Standard Error	t-value	p-value
MA(1)	0.574255	0.0627454	9.15215	0.000000
MA(2)	0.215334	0.0633602	3.39857	0.000794

Figure 7 shows the actual and fitted plots of individual observations comparatively. As seen in these figures, the fitted values by ARIMA models were very close to the actual quality characteristics for both variables.

Figure 8 shows the residual autocorrelations and residual partial autocorrelations for moisture and ash contents respectively. As seen in these plots, the autocorrelation removed successfully by applying the ARIMA models and there are no autocorrelations between residual values of two coal quality characteristics. Also, as shown in Fig. 9, the residuals obtained from ARIMA models obey the normal

distribution very well. Since the normality and independence assumptions were satisfied by the ARIMA model residuals, the standard Shewhart charts can be applied conveniently to monitor the moisture and ash contents.

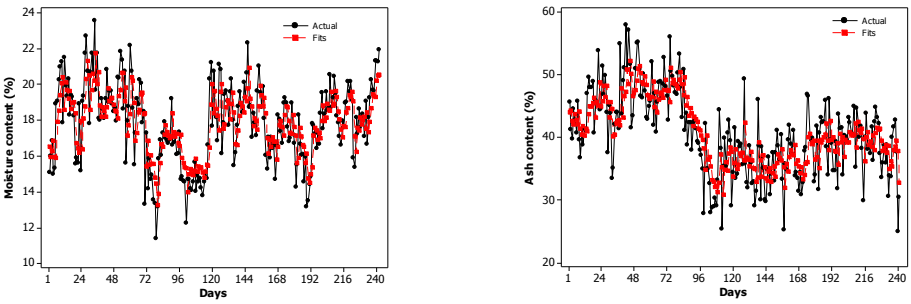

Fig. 7. Actual and fitted moisture contents by ARIMA (1, 0, 1) with constant model and ash contents by ARIMA (0,1,2) model

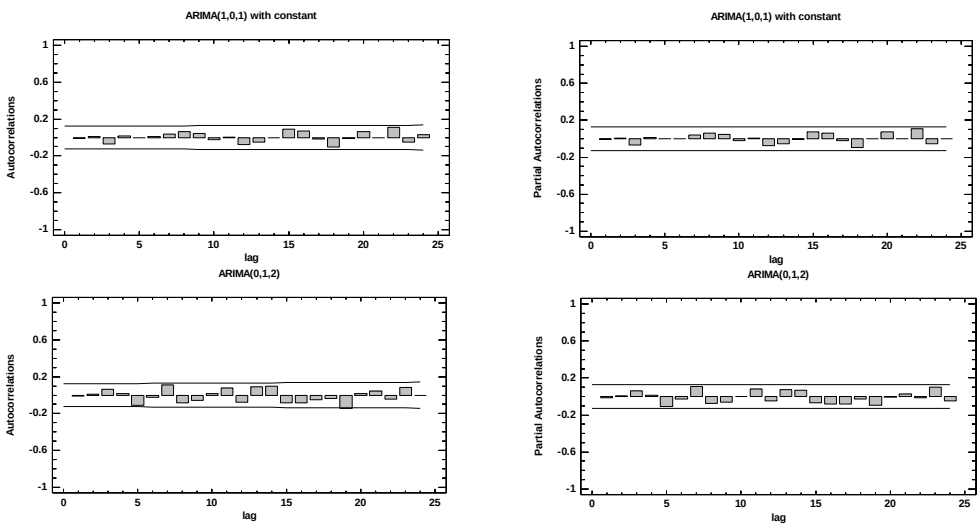

Fig. 8. ACFs and PACFs of residuals for moisture content by ARIMA (1,0,1) with constant model and for ash content by ARIMA (0,1,2)

5.4. X/MR Charts for monitoring forecast residuals

Figure 10 shows the X and MR charts of residuals for individual moisture and ash contents. Even applying the Western electric rules, the number of out-of control points signaficantly reduced the false alarms. There are only 5 and 6 unusual points in X charts of moisture and ash contents, respectively. There is only one point exceeding 3σ limits for moisture and no out-of control point for ash content. On the other hand these numbers are 2 and 3 on the MR charts for the moisture and ash contents, respectively.

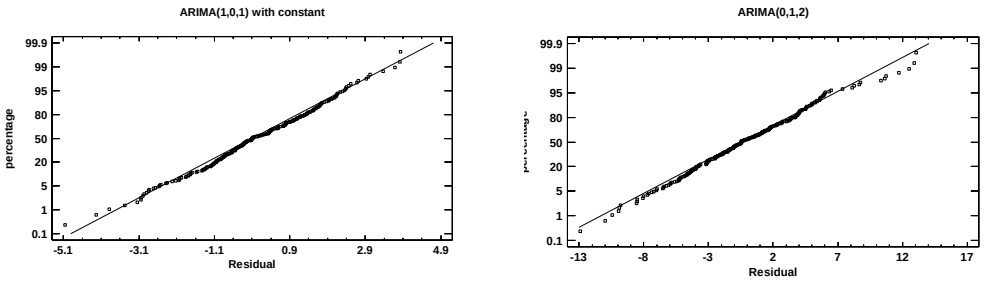

Fig. 9. Normal probability plots of residuals obtained by ARIMA models for moisture and ash contents

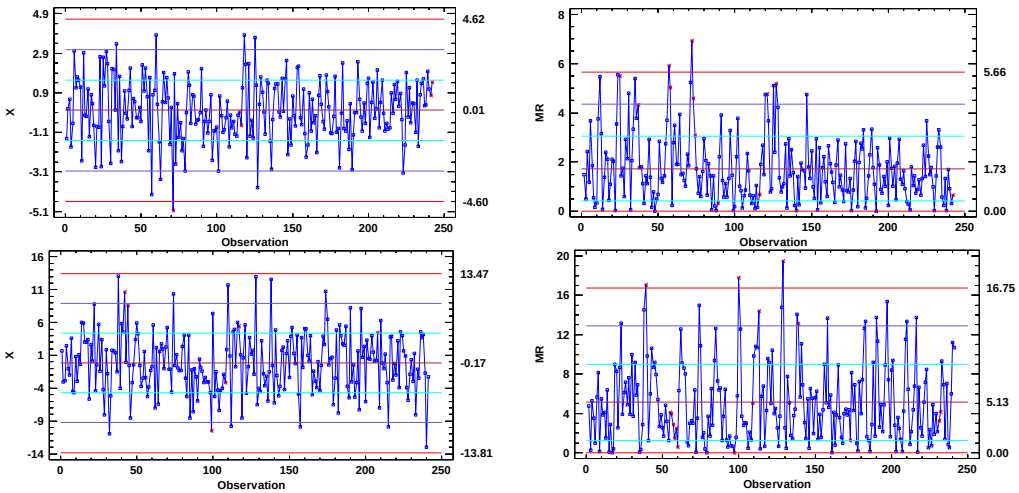

Fig. 10. The *X* and MR charts of residuals (special cause charts) for moisture (top plots) and ash (bottom plots) contents

It is known from literature that these charts would immediately lack the robustness when the observations violated the conditions, and the problem was that most industrial processes are continuous and correlated. When the data were highly correlated, the traditional charts would signal the high rate of false alarms. Alwan and Roberts (1995) analyzed sample applications of control charts and showed that about 85% displayed incorrect control limits were due to the autocorrelation in the data. They pointed out that there would be lots of false prediction or missing alarms when the autocorrelations were ignored. According to results obtained from this study, ignoring autocorrelation in coal data also causes false out-of control points in the SPC charts.

6. Conclusions

Obeying the normality is not enough for applying the SPC charts to monitor two discussed here coal quality characteristics. The results of this study also showed that

autocorrelation strongly affected performance of the SPC charts in case of coal washing data. It was determined that the data of daily moisture and ash contents of the coal washing plant were moderately autocorrelated. For this reason, much more out-of control points on the traditional Shewhart charts, which assumes the independence of observations with normaly distributed data, were detected for both variables.

The series of daily values of moisture contents are best described by ARIMA (1,0,1), with a constant model. The ARIMA (0,1,2) model is recommended to be used for generating time series of ash contents. Reduced number of out-of control points in the residual control charts showed us the importance of autocorrelation in coal industry and this autocorrelation should be removed before constructing a control chart to monitor the quality characteristics. It is also shown that the Shewhart control charts of residuals which are independent and normally distributed and obtained from ARIMA models are more appropriate to find the true unusual points otherwise huge amount of wrong out-of control points are recorded. These situations might cause wrong decisions to monitor the process since most of the data points which are in control actually detected as out-of control. Therefore, usage of uncorrelated data may cause misleading results about the process.

It may also possible to make make preventive and corrective actions for the quality characteristics of coal by the ARIMA models since these models can forecast for the future using past data of the processes.

Acknowledgements

The author greatefully acknowledges the Tunçbilek coal washing plant for supplying the data used in this research.

References

ALWAN, L.C., ROBERTS, H.V., 1988, *Time-series modeling for statistical process control*, Journal of Business and Economic Statistics 6, 86–95.

ALWAN, L.C., ROBERTS, H.V., 1995, *The problem of misplaced control limits*, Journal of Royal Statistical Societyi Series C 44(3), 269–278.

ANKARA, H., BİLİR, K., 1995; *Kriblaj tesisinde kalite denetimi*, Madencilikte Bilgisayar Uygulamaları Sempozyumu, 235–240 (in Turkish).

ANKARA, H., YEREL, S., 2008, *Use of range control charts in determination of variability in surface parallelisms of plates*, Journal of Scientific & Industrial Research 67, 1078–1082.

APLEY, D.W., LEE, H.C., 2003, *Design of exponentially weighted moving average control charts for autocorrelated processes with model uncertainty*, Technometrics 45(3), 187–198.

ARSLAN, V., 2006, *Dry coal cleaning methods*, Madencilik 45(3): 9–18 (in Turkish).

AYKUL, H., AKÇAKOCA, H., EDİZ, G.,TAKSUK, M., 2005, *Garp linyitleri işletmesi termik santral kömürleri için istatistiksel süreç kontrol analizi*, Türkiye 19, Uluslararası Madencilik Kongresi, 313–321 (in Turkish).

AYKUL, H., EDİZ, İ. G., AKÇAKOCA, H., ERARSLAN, K., TAKSUK, M., DİXON-HARDY, D. W., 2010, *Statitistical process control for coal fired power plant system*, Journal of the Energy Institute 83, 41–47.

BAYAT, O., ARSLAN, V., 2004, *Statistical analysis in Turkish chromite mining*, Scandinavian Journal of Metallurgy 33, 322–327.

BHATTACHERJEE, A., SAMANTA, B., 2002, *Practical issues in the consruction of control charts in mining applications*, The Journal of The South African Institute of Mining and Metalllurgy, 173–180.

CARSON, P. K., YEH, A. B., 2008, *Exponentially weighted moving average (EWMA) control charts for monitoring an analytical process*, Ind. Eng. Chem. Res. 47, 405–411.

CHANG, Y. M., WU, T. L., 2011, *On average run length of control charts for autocorrelated processes*, Methodol. Comput. Appl. Probab. 13, 419–431.

DEMİRKOL, Ş., 2008, *Comparison of control charts for autocorrelated data*, Master Thesis, Graduate School of Natural and Applied Sciences of Dokuz Eylül University.

ELEVLİ, S., BEHDİOĞLU, S., 2006, İstatistiksel Proses Kontrolü Teknikleri İle Kömür Kalitesindeki Değişkenliğin Belirlenmesi, Madencilik 45(3), 19–26 (in Turkish).

ELEVLİ, S., 2006, *Coal quality control with control charts*, Coal Preparation 26(4), 181–199.

ELEVLİ, S., 2009, *Control charts for autocorrelated colemanite data*, Journal of Scientific & Industrial Research 68, 11–17.

HTTP://DOCUMENTATION.STATSOFT.COM/STATISTICAHelp.aspx?path=TimeSeries/TimeSeries/Overview/Arima/ARIMAARIMAMethodology.

İPEK, H., ANKARA, H., ÖZDAĞ, H., *The application of statistical process control*, Minerals Engineering 12(7): 827-835.

KARAOĞLAN, A.D., BAYHAN, G.M., 2011, *Performance comparison of residual control charts for trend stationary first order autoregressive processes*, Gazi University Journal of Science 24(2), 329–33.

LE, K.H., 1998, *A statistical control chart for process with correlated subgroups*, The Korean Communications in Statistics 5(2), 373–381.

LU, C.W., REYNOLDS, M.R., 2001, *CUSUM charts for monitoring an autocorrelated process*, Journal of Quality Technology 33, 316–334.

MACCHARTY, B.L., WASUSRI, T., 2002, *A review of non-standard applications of statistical process control (SPC) charts*, International Journal of Quality & Reliability Management 19(3), 295–320.

MONTGOMERY, D.C., JENNINGS, C.L., KULAHÇI, M., 2008, *Introduction to time series analysis and forecasting*, Wiley Sries in Probability and Statistics.

MONTGOMERY, D. C., RUNGER, G.C., 2011, *Applied statistics and probability for engineers*, Fifth Edition, John Wiley&Sons, Inc.

SAMANTA, B., BHATTACHERJEE, A., 2001, *An investigation of quality control charts for autocorrelated data*, Mineral Resources Engineering 10, 53–69.

SAMANTA, B., 2002, *Multivariate control charts for grade control using principal-component analysis and time series modelling*, Trans. Inst. Min. Metall. (Sect A: Min Technol) 307, 149–157.

SCHMID, W., SCHÖNE, A., 1997, *Some properties of the EWMA control chart in the presence of autocorrelation*, The Annals of Statistics 25(3): 1277–1283.

STAPENHURST, T., 2005, *Mastering statistical process control*, A handbook for performance improvement using cases, Elsevier.

TEKİR, U., ARSLAN, V., AKAR, G., 2009, *Dry beneficiation of fine coals from soma basin with pneumatic air table*, The Jornal of Ore Dressing 11(22), 33–38.

VAPUR, H., BAYAT, O., AKYOL, F., 2005, *Eti Gümüş A.Ş. Liç Prosesinde İstatistiksel Proses Kontrolü Uygulaması*, Türkiye 19. Uluslararası Madencilik Kongresi, 347-356 (in Turkish).

VAPUR, H., 2009, *Applicability of statistical process control for flotation of metals complex*, Asian Journal of Chemistry 21(1), 655–665.

YEREL, S., ANKARA, H., KONUK, A., ÖZDAĞ, H., 2007, *Preventive maintance policy supported by a quality control chart and Kolmogorov-Smirnov tests: Emet colemanite mineral processing plant, Turkey*, Minerals & Metallurgical Process 24, 152–156.

YEREL, S., ANKARA, H., 2011, *Process control for a coal washing plant using a range control chart and multidimensional, scaling analysis*, Energy Sources, Part A 33, 1028–1034.

Physicochem. Probl. Miner. Process. 48(2), 2012, 513−531

www.minproc.pwr.wroc.pl/journal/

Physicochemical Problems of Mineral Processing

ISSN 1643-1049 (print)
ISSN 2084-4735 (online)

Received April 13, 2011; reviewed; accepted May 10 , 2012

EFFECTS OF DIFFERENT MESH SCHEMES AND TURBULENCE MODELS IN CFD MODELLING OF STIRRED TANKS

Mohsen KARIMI, Guven AKDOGAN, Steven M. BRADSHAW

Department of Process Engineering, Stellenbosch University, Private Bag X1, Matieland 7602, Stellenbosch, South Africa. Tel: +27 21 808 3860, Fax: +27 21 808 2059; Email: karimi@sun.ac.za

Abstract. This paper focuses on the effects of grid schemes and turbulence models on the CFD modelling of stirred tanks. The economical grid was determined by examining the dimensionless wall distance and the skewness of elements. The grid independency study ensured that the independency of numerical predictions. Also, three categories of turbulence models were compared for prediction of flow pattern. The grid sensitivity study highlighted that the quality of control volumes in the bulk and near the wall regions are significant for obtaining the consistent solutions. It was also found that for the prediction of velocity components and the turbulent quantity the RANS based models are more efficient.

keywords: stirred tank, computational fluid dynamics, turbulence models, grid sensitivity

1. Introduction

Mechanically stirred vessels are broadly used in a wide range of unit operations such as flotation cells in mineral processing plants, blending of liquids and crystallization in chemical engineering reactors. Owing to their extensive range of use, a reliable method of simulating the hydrodynamics of flow instead of correlating the overall performance to the operational and geometrical conditions would be beneficial for the industries.

Computational Fluid Dynamics (CFD) provides a numerical method in which thorough information on the hydrodynamics of fluid flow can be extracted. The flow pattern is then used to understand the details of the process itself. Thus, it would be expected that an accurate CFD simulation of the fluid flow leads to improved understanding of the mixing sub-processes occurring in mechanically stirred vessels.

Since the unsteady nature of turbulent flow inside stirred tanks is affected by many parameters such as the geometry of rotational system, the local vortices, the gas dispersion and so on, an accurate simulation of the flow pattern is rather complex. To tackle this intricate problem one may investigate the factors such as the grid resolution, the discretization scheme, the impeller rotation modelling method, and the turbulence models. At the same time, the enhancement of CFD packages is an on-going progress, and each new version of solvers is equipped with more features aimed

http://dx.doi.org/10.5277/ppmp120216

at accurately capturing more details of the fluid flow behaviour. As a consequence, a computationally efficient and accurate CFD model for a stirred tank must be updated to assess the effects of new options encompassed in recent CFD solvers. In the insight of previous works that considered different aspects of CFD modelling of a stirred tank, this research is scoped to update and optimize the CFD methodology for stirred tanks as realistic as possible, while it should be computationally inexpensive.

The potential of CFD for modelling of unbaffled stirred tanks has been reported in several papers. The applicability of numerical modelling was demonstrated by comparison of the simulated results with the laser-Doppler velocimeter data (Armenante et al., 1997; Dong et al., 1994a, b). In these early papers, the standard k-ε and the Algebraic Stress Model (ASM) were used as turbulence models and the rotation of impeller was modelled by either adapting the LDV measurements or by the Multiple Reference Frames (MRF) method.

Oshinowo et al. (2000) showed that MRF is an efficient choice for the modelling of impellers in the baffled stirred tanks. The sensitivity of the solution to the different grids was also investigated. They compared the predicted tangential velocities with the three turbulence models including the standard k-ε, the RNG k-ε and RSM. They concluded that the steady-state modelling with the MRF is a valuable tool in the analysis and design of stirred tanks when the single phase turbulent flow occurs.

Bakker (Bakker and Oshinowo, 2004; Bakker et al., 2000) investigated whether the Large Eddy Simulation (LES) can predict the large-scale chaotic structures in stirred tanks. A single radial pumping impeller and a single axial pumping pitched blade turbine were simulated. The results showed that both impeller configurations had qualitatively good agreement with the experimental data (Myers et al., 1997).

Another approach for modelling of impellers, the Sliding Mesh method (SM), was compared with the MRF by Lane et al. (2000). The computational time, accuracy of mean velocities and the turbulence parameters were the main variables of comparison. A half slice model of a 294 mm diameter baffled stirred tank was discretized by 48, 39 and 60 cells in the axial, radial and azimuthal directions. An important finding was that the MRF method was more computationally efficient than the SM. They also found that both methods had similar results for the prediction of the velocities. For turbulence characterizations, the MRF provided an improvement in the predictions.

Yoon et al. (2001) modelled the motion of impellers using Particle Image Velocimetry (PIV) data as boundary conditions around the impeller. A 3D grid of 51,840 cells for 60° sector of a 145 mm diameter cell was used to compute the flow. They provide a method to describe the impeller-induced flow in the stirred tank.

Influences of different impeller modelling methods, discretization schemes, and turbulence models on the CFD modelling of stirred tanks were investigated by Aubin et al. (2004). The mean axial and radial flow patterns were slightly affected by the choice of SM or MRF for modelling of the impeller. The higher order of discretization schemes were recommended for the simulation of turbulent flow inside the stirred tank. Applying the Reynolds Stress Model (RSM) as the turbulence model led to a

diverged solution. The Standard and the Renormalization-group k-ε models did not show significant differences in predicting the mean radial and axial velocity fields. The authors suggested that correct prediction of the single phase flow quantities is necessary for an accurate multiphase modelling of stirred tanks.

Deglon and Meyer (2006) used the MRF for modelling of the impeller rotation in conjunction with the standard k-ε turbulence model for studying the turbulence effects. The flow pattern in a half of a cylindrical tank agitated with a standard six-blade Rushton turbine was simulated over four different grids using the QUICK discretization scheme. A range of impeller speeds corresponding to the laminar and turbulent flow regimes were tested. They showed that although the flow field can be predicted with a coarse mesh, an accurate prediction of turbulence in stirred vessels is computationally intensive and needs both fine grid resolution and a high-order discretization method.

One of the recent work addressing numerical issues in the CFD simulation of the fluid flow in stirred tanks was performed by Coronoe (2010). This work aimed at verifying the effect of numerical issues on the RANS-based predictions of the single phase flow in stirred tanks. The effects of grid sizes and discretization schemes were considered for modelling of the mean velocity, the turbulent dissipation, and the homogenization with the standard k-ε turbulence model and the MRF method. This work revealed that the effect of numerical uncertainties may be minimized with sufficiently fine grid resolution. They argued that due to the limitation of the turbulence model the detailed explanation of turbulence quantities cannot be achieved. They also mentioned that the effects of the numerical inaccuracies would be more important in the multiphase modelling of stirred tanks.

Reviewing the previous literature revealed that the standard k-ε is a computationally affordable turbulence model and it is generally accepted for the modelling of stirred tanks. The Multiple Reference Frames (MRF) yields better results than the Sliding Mesh method to model the impeller motion in terms of both computational time and agreement with the experimental data. Although the previous works shed some light on how to deal with the common aspects of the numerical issues on the CFD modelling of stirred tanks, CFD solver developments led to the question of whether the available methodology of numerical simulation of the stirred vessel is still reliable or it should be updated. Thus, this paper is intended to fill this gap. To accomplish this goal, the optimized mesh was selected through different criteria including the value of y+ on the problematic regions near the walls to capture the small eddies, skewness of elements, and the grid independence study. Then, turbulence models were categorized into three different groups. The performance of each category was compared with the experimental data.

2. Methodology

The Reynolds averaged continuity and the Reynolds averaged Navier-Stokes equations (RANS) have been resolved in this work to model the highly turbulent flow inside the agitated vessel. They can be written as follow:

$$\frac{\partial \rho}{\partial t} + \rho \frac{\partial \langle u_i \rangle}{\partial x_i} = 0 , \tag{1}$$

$$\frac{\partial \left(\rho \langle u_i \rangle\right)}{\partial t} + \frac{\partial \left(\langle u_i \rangle \langle u_j \rangle\right)}{\partial x_j} = \frac{\partial \langle p \rangle}{\partial x_i} + \frac{\partial}{\partial x_j}\left(\mu \frac{\partial \langle u_i \rangle}{\partial x_j}\right) + \frac{\partial}{\partial x_j}\left(\tau_{ij}^{\mathrm{Re}}\right) + \rho g_i , \tag{2}$$

where u is the velocity component, ρ is the liquid density, p is the pressure, μ is the fluid viscosity, and g is the gravitational acceleration. The term τ_{ij}^{Re} denotes the Reynolds stress and signifies the effects of turbulent velocity fluctuations on the mean flow. To close Eqs. (1) and (2) the Reynolds stress must be modelled. There are different turbulence models to achieve closure for the above partial differential equations. In the following sections the fundamentals of these models are briefly explained and referenced.

2.1. RANS based turbulence mode

The RANS-based turbulence models are recommended (ANSYS Inc, 2009) to reduce the required computational effort and resource. They are divided into the four different categories including: one-equation model, two-equation models, three-equation models, and Reynolds Stress Model (RSM). Except the latter, the other RANS-based turbulence models apply the Boussinesq hypothesis (Hinze, 1975) that relates the Reynolds stresses to the mean velocity gradients:

$$\tau_{ij}^{\mathrm{Re}} = u_t \left(\frac{\partial u_i}{\partial x_j} + \frac{\partial u_j}{\partial x_j}\right) - \frac{2}{3}\left(\rho k + \mu_t \frac{\partial u_k}{\partial x_k}\right)\delta_{ij} . \tag{3}$$

In this equation μ_t is the turbulent viscosity, k is the turbulent kinetic energy and δ_{ij} is the Kronecker delta. The Boussinesq theory assumes the turbulent viscosity is an isotropic scalar.

The RANS-based turbulence models have been divided according to the number of additional transport equations essential to resolve the flow field.

2.1.1. One-equation model

The Spalart-Allmaras is a relatively simple one-equation model that solves one transport equation for the turbulent kinematic viscosity. The details of equations of this model are explained by Spalart and Allmaras (1992).

2.1.2. Two-equation models

This group of turbulence models has become the standard approach for industrial applications and is of particular interest for engineering problems where turbulence effects are significant such as stirred vessels. As the definition states, to capture the

turbulence effects, two extra transport equations must be solved for this type of turbulence model. Models such as the k- ε and its variants and the k-ω model and its variant fall into this class. From two additional transport equations, one of the variables is turbulent kinetic energy, *k*. The second one depends on what type of two-equation turbulence models is used. The second transported variable can be thought of as the determination factor of turbulence. The common options for the two-equation models are the turbulent dissipation, ε, or the specific dissipation, ω.

- Standard k-ε model

The advantages of using the Standard k-ε model such as robustness and reasonable accuracy account for the numerous applications of this model in the simulation of stirred tanks. The standard k-ε model is a semi-empirical model that solves the turbulent kinetic energy (k) and its turbulent dissipation (ε) for fully turbulent flow. The details of the transport equations were explained by Launder and Spalding (1972).

- RNG k-ε model

The RNG k-ε model is derived from the standard k-ε model carrying out a mathematical technique called "renormalization group" (RNG). In this turbulence model some refinements for accurate results have been outlined. Adding an extra term in the "ε" equation improves the accuracy for rapidly strained flows. Besides, the effects of swirl on the turbulence are included in the RNG k-ε model, enhancing the precision for swirling flow. Orszag et al. (1993) have documented a complete application of the RNG concept for turbulence modelling.

- Realizable k-ε model

This turbulence model is a relatively new approach to resolve the Reynolds stresses (Shih et al., 1995). Its differences from the standard k-ε model are twofold: a new formulation for the turbulent viscosity and a vorticity-based new transport equation for the turbulent dissipation, ε. These modifications are reported to provide superior performance for swirling flow.

- Standard k-ω model

The standard k-ω model used in this paper is based on the Wilcox k-ω model (Wilcox, 1998). Wilcox has derived this empirical turbulence model based on the transport equations for turbulence kinetic energy (k) and the specific turbulent dissipation (ω).

- Shear-Stress Transport (SST) k-ω model

Blending the robust formulation of the k-ω model in the inner parts of boundary layer with the applicability of the k-ω model in the bulk flow is the backbone of this model. The SST k-ω turbulence model was developed by Menter (1994).

- Transition SST model

The transition SST model is another derivative of the k-ω model taking advantage of two more transport equations, one for intermittency and one for the transition onset criteria.

2.1.3. Three-equation model

- k-kl-ω transition model

Since the k-kl-ω model has three transport equations for the turbulent kinetic energy, the laminar kinetic energy, and the inverse turbulent time scale (ω), it is considered as a three-equation model. This model benefits from predicting the boundary layer development and the calculating transition onset. Using this model one can effectively address the evolution from laminar flow to turbulence in the boundary layer.

2.2. Large Eddy Simulation (LES)

The entire concept of the Large Eddy Simulation (LES) model is based on eddies that are the main characteristics of the turbulent flow. In this model, the motion of large eddies is resolved directly, while the small eddies are implicitly modelled using a sub-grid scale model. Thus, a filtering operation should be conducted to separate the velocity field into two resolved parts; large eddies and a sub-grid part. Filtering the time-dependent Navier-Stokes equations results in a set of the solved part (large scale) and the residuals (small scale). The filtered equations are expressed as:

$$\frac{\partial \rho}{\partial t} + \rho \frac{\partial \overline{u_i}}{\partial x_i} = 0\,, \tag{4}$$

$$\frac{\partial \overline{u_i}}{\partial t} + \frac{\partial \left(\overline{u_i}\,\overline{u_j}\right)}{\partial x_j} = -\frac{1}{\rho}\frac{\partial \overline{p}}{\partial x_t} + \frac{\partial}{\partial x_j}\left(\mu \frac{\partial \overline{u_i}}{\partial x_j}\right) - \frac{\partial \tau_{ij}^{sgs}}{\partial x_j} + g_i\,, \tag{5}$$

τ_{ij}^{sgs} is the stress tensor composed of all the information about small scales. It can be related to the eddy viscosity by the following equation:

$$\tau_{ij}^{sgs} = -\mu_t\left(\frac{\partial \overline{u_i}}{\partial x_j} + \frac{\partial \overline{u_j}}{\partial x_i}\right). \tag{6}$$

In this research, solving the eddy viscosity, μ_t, has been conducted by three different methods: Smagorinsky-Lilly (Smagorinsky, 1963), WALE model (Nicoud and Ducros, 1999), and dynamic kinetic energy (Kim and Menon, 1997).

2.3. Detached Eddy Simulation

The DES model is a hybrid turbulence model that applies the RANS model to solve the flow near the wall, and other regions far from the walls are computed by the LES approach. In the modelling of stirred tanks in this study three combinations of RANS models with the LES have been considered including the Spalart-Allmaras, realizable k-ε and the SST k-ω (Shur et al., 1999). It should be noted here that computational

cost of using DES model is greater than the RANS computational cost, but less than the LES.

3. Numerical approach

The 3D unsteady flow of water inside a 293 mm diameter unbaffled tank agitated by a six-blade impeller with 73 mm clearance (Fig. 1) was simulated using CFD package ANSYS FLUENT 12.1. Since the finite volume method is implemented in this solver, the computational domain, adopted from (Armenante et al., 1997), was discretized into different cells. To conduct the MRF method for modelling of impeller motion, recommended by Lane et al. (2000) and Deglon and Meyer (2006), the entire vessel was divided into the bulk flow region and the rotational zone. In this way, governing equations are solved in a rotating reference frame to handle the impeller rotation, while in the rest of the vessel the flow is calculated by solving the RANS equations in a stationary reference frame. The SIMPLE algorithm coupled the continuity and momentum equations to derive the pressure field inside the tank, and the momentum discretization was computed by a second-order upwind method. It should be mentioned that to perform the LES and DES turbulence models the discretization scheme was altered to the bounded central differencing method. In this study, the impeller speed was 450 rpm. A 45° sector of vessel was simulated using periodic boundary conditions.

Different time steps corresponding to 5, 10, 12 and 15 degrees of rotational angle of the impeller have been simulated. Each simulation was initialized with the standard k-ε turbulence model for 10 revolutions of the impeller. All the simulations were performed on an Intel Corei7 CPU 1.6 GHz workstation in this study.

One of the main issues that have been considered in this article is how sensitive the CFD results are to the various mesh schemes. The grid density should be dense enough to embody all the underlying flow features. To explain this effect, different grids have been built up. In each case, different numbers of elements in the two separate regions, the bulk flow and the rotational zone, have been distinguished. The details of each structured hexagonal mesh are described in Table 1. The number of elements in the three directions of cylindrical coordinate system is shown in Table 1.

In order to capture the time-dependent fluctuations of turbulence inside the boundary layer, y+ value was taken into account. These parameters are defined as the dimensionless distance from the wall to the first grid point. The value of y+ is computed for the boundary cells on the specified wall zones. Then, those cells with the y+ values within a specified range will be marked for refinement during the solution process. The y+ can be computed by the following equation:

$$y+ = \frac{u^* y}{\nu}, \tag{7}$$

where u^*, the friction velocity can be defined by Eq. (8), y is the distance to the wall and ν is the kinematic viscosity:

$$u^* = \sqrt{\frac{\tau_w}{\rho}}, \tag{7}$$

where τ_w is the wall shear stress and ρ is the fluid density at the wall.

Skewness has also been used in this study to investigate the quality of each control volume. As is shown in Table 1, even the maximum skewness is in the excellent range of commonly used for the mesh quality (ANSYS Inc, 2009).

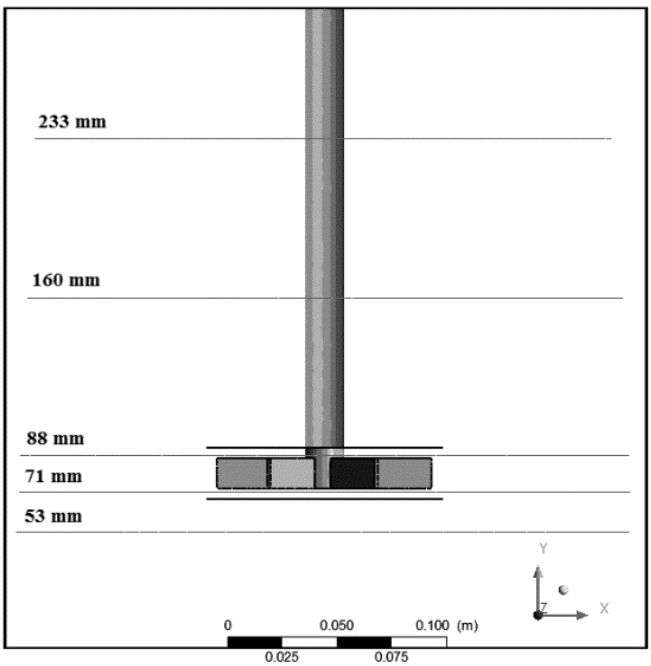

Fig. 1. Schematic of the whole vessel adapted from Armenante et al. (1997)

Table 1. Properties of the mesh schemes used in this article

Case#	Bulk flow			Rotational zone			No. Cells		Skewness		
	ρ	φ	z	ρ	φ	z	Original	Adapted	Min	Max	Ave
C1	31	20	65	11	20	5	40,300	59,375	0.0125	0.1086	0.0242
C2	40	24	78	14	24	6	74,880	110,762	0.0104	0.1429	0.0190
C3	48	29	94	17	29	8	130,848	176,306	0.0050	0.0990	0.0211
C4	58	35	113	20	35	10	229,390	296,478	0.0041	0.1077	0.0168
C5	70	42	126	24	42	12	370,440	472,129	0.0034	0.1260	0.0210
C6	84	50	139	29	50	14	583,800	704,818	0.0029	0.1436	0.0208
C7	92	60	154	35	60	17	850,080	1,024,317	0.0015	0.1606	0.0309

* the numbers in the ρ,φ, and z columns represent the number of elements in each direction of cylindrical coordinate system

4. Results and discussion

4.1. Grid study

As the grid determines the control volume on which all governing equations for the stirred tank are resolved, the numbers of cells directly affect the solution accuracy and the required CPU time. One of the main aspects of this study is to examine the influences of different cell numbers on the prediction of flow behaviour. Therefore, finding the optimized number of cells wherein almost all the local turbulent events are captured, yet the computational time is affordable, is one of the focal points of this work. Meanwhile, the quality of an efficient mesh should be good enough so that the solution is not affected by the bad-quality elements. Owing to the facts mentioned above, the skewness and values of the y+ were utilised for surveying the mesh quality in the bulk flow and the viscous layer near the wall.

4.1.1. Systematic study of y+

In the turbulent flow in a stirred tank, the mean flow is strongly affected by the turbulence. The numerical results for this type of flow depend on the mesh size. It would be expected that a sufficiently fine mesh for the regions where the mean flow is influenced by the existence of the rapid changes and the shear layers with large strain rates can resolve the flow field pattern. Values of y+ can be an indicator for checking the near-wall mesh quality. Two different wall functions namely, the standard wall function, which is the most widely used in the industrial flows and the enhanced wall treatment, appropriate for the fine mesh schemes, were applied for capturing the near-wall flow features. It is recommended (ANSYS Inc, 2009) that for using the standard wall function, the value of y+ in the first cell should be within the logarithmic law layer, whereas the enhanced wall treatment requires y+ as low as possible ($y+<5$). Testing the value of y+ at all bounding walls showed that the most problematic area is the blade region. Figure 1 shows the value of y+ on the centre line of the blade for different number of meshes. It is clearly shown that the highest value in all cases is at the tip and close to the impeller-shaft junction point.

To reduce the value of y+ on the blade, the solution-adaptive mesh refinement feature of ANSYS FLUENT was used. In this way, additional cells can be added where they are needed, which is in this case on the tip and close to the shaft. The main advantage of this method is that one can locally increase the number of cells based on the solution and analyse the impacts of supplementary cells on the results without regenerating of the mesh. Different refinement methods have been applied on the problematic areas. After comparing different adaptation methods, results of the best refinement that decreases the value of y+ more than other approaches are depicted in Fig. 2. The number of cells after refinement is reported in Table 1.

In order to assess how much the extra cells change the maximum y+ value on the blade, the simulations were repeated after the refinement. All other simulation parameters were kept constant. The values of y+ on the centre line of the blade are

displayed in Fig. 2. Except for the first case, maximum y+ value on the blade in all the other cases is significantly decreased.

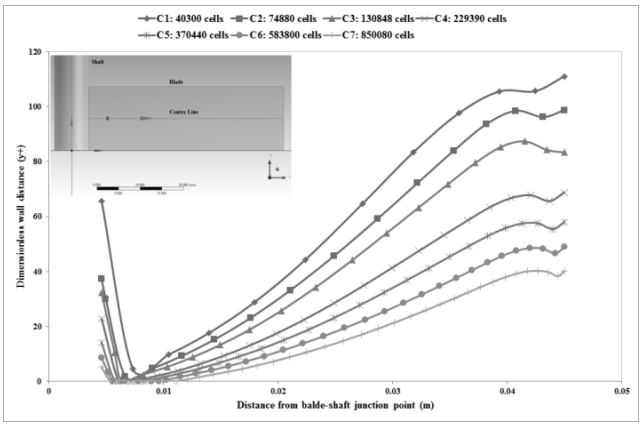

Fig. 2. Value of y+ on the centre line of blade for seven different cases before refinement. C1 to C7 represent the number of cells before refinement for case1 to case7 described in Table 1

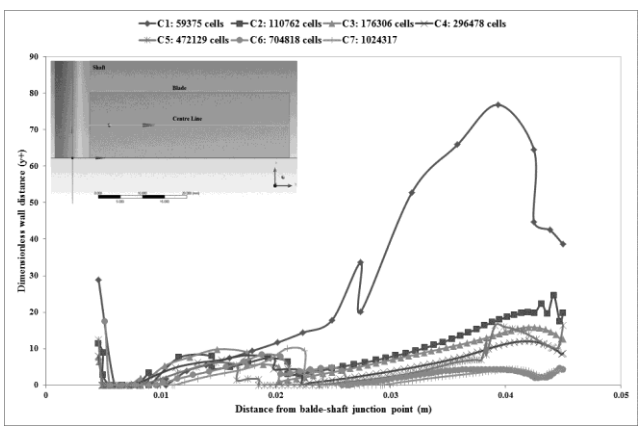

Fig. 3. Value of y+ on the centre line of blade for seven different cases after refinement. C1 to C7 represent the number of cells after refinement for case1 to case7 described in Table 1

It can also be seen from Fig. 2 that for case 6 and case 7 the values of y+ are coincident. Thus, adding more cells did not lead to improvement in the value of y+. To elaborate more on this behaviour the maximum y+ on the centre line for the seven different cases is plotted with respect to computational time in Fig. 3. The number of cells in Fig. 3 is adopted after the refinement. Although the reduction rate of y+ maximum on the blade for the first three cases (i.e. C1 with 59375 cell, C2 with 110762 cells and C3 with 176306 cells) is too high, it is clearly demonstrated that beyond certain number of cells the maximum value of y+ does not differ significantly. Since the computational time and number of cells are following a linear correlation,

using high number of cells results in increasing the required CPU time without reducing the maximum y+. Also, an extreme case with 2 million cells was investigated and the effect on the y+ was found to be insignificant while the computational time was around 48 hours. The systematic study of y+ suggests that successful computation of turbulent flow close to the walls of the stirred tank can be achieved by a grid density between 500,000 to 700,000 cells. Figure 4 illustrates the contour plot of y+ for the case with 704, 818 cells. The final refined surface mesh on the blade is also shown in this figure.

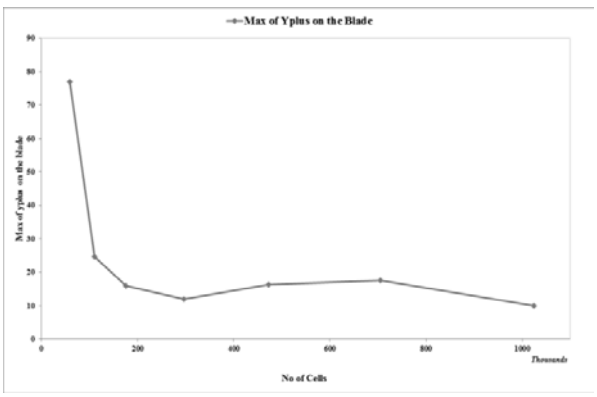

Fig. 4. Maximum y+ value on the centre line of the blade for seven different cases

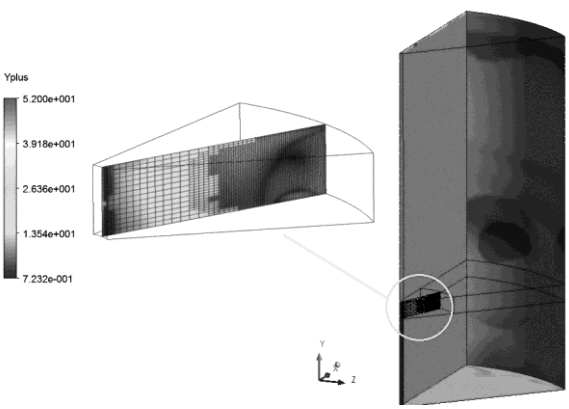

Fig. 5. Contour plot of y+ value for 45° sector and blade

4.1.2. Grid independence study

Any small fluctuations of velocity and other features of the flow within the tank should be captured by an efficient mesh scheme. However, a very fine mesh refinement leads to increased computational time. Thus, a grid independence study has been performed to find optimize number of cells for which the solution is independent.

To achieve this aim, four points on five planes in different parts of the vessel were defined (Fig. 5). As shown in Fig. 5, the planes covered all the hydrodynamically significant zones of the tank such as lower bottom of the vessel, top and bottom of the impeller and two planes for the upper parts of the vessel. The points are also situated in the locations where the data close to the impeller, shaft, middle of vessel and close to the wall can be derived. After running the simulations for seven cases (Table 1) the values of the velocity components (tangential, radial and axial) and the turbulent kinetic energy were collected for all the nominated points, shown in Fig. 5, to quantify how much each of these components vary over the wide-ranging numbers of cells. Because of space constraints, only the results of tangential velocity and turbulent kinetic energy in the middle of each plane, depicted by the balls in Fig. 5, are shown here.

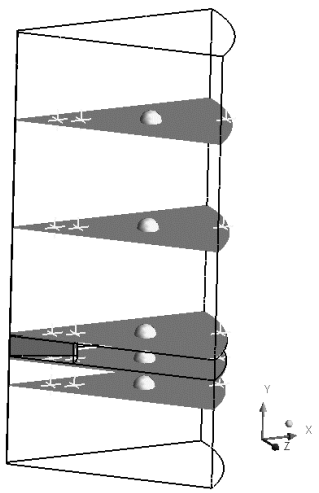

Fig. 6. Locations of points and planes for the grid sensitivity test (the whole vessel and 45º sector)

Figures 7 and 8 show the variations of tangential velocity and turbulent kinetic energy at the selected points for the different numbers of cells. It is clearly demonstrated here that there exists a specific grid size beyond which both the velocity components and the turbulent quantities show little variation. It is seen in Fig. 6 a-c and e that variations of tangential velocity are negligible after the number of 472,000 elements (case 5), although for the plane 160 mm from the bottom of vessel (Fig. 6d) this observation is seen for 704,000 cells.

From Fig. 8 it can be seen that increasing the number of cells to 1000,000 means that one can detect only very small eddies inside the computational domain and the mean quantity of turbulent kinetic energy does not change significantly. It must be noted that the simulated data (the velocity components and the turbulent kinetic energy) for the other points were also checked but results, for the sake of brevity, are not included in the present paper.

Therefore, in order to have the precise and computationally economical solution the y+ systematic study in combination with the grid independence study should be conducted. The results of these two examinations show that the adopted grid system applied in the case 6 (Table 1) can computes the flow close to the boundary layers, while at same time the general phenomenon of the bulk flow can be predicted thoroughly. As a result the methodology used for case 6 (Table 1) was chosen to investigate the effects of different turbulence models in the simulation of flow field within the stirred vessel.

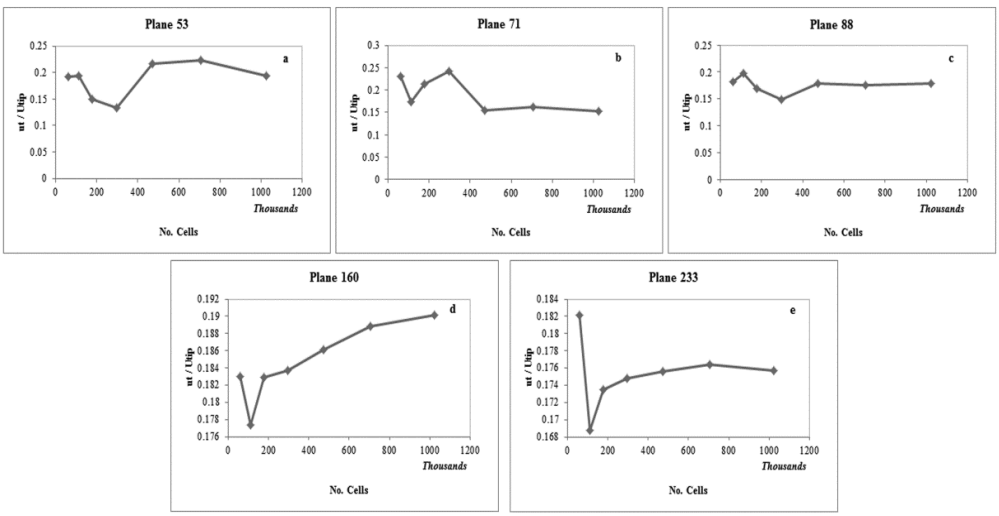

Fig. 7. Tangential velocities for the mid-points in five different palnes, shown in Fig. 6, for different grids

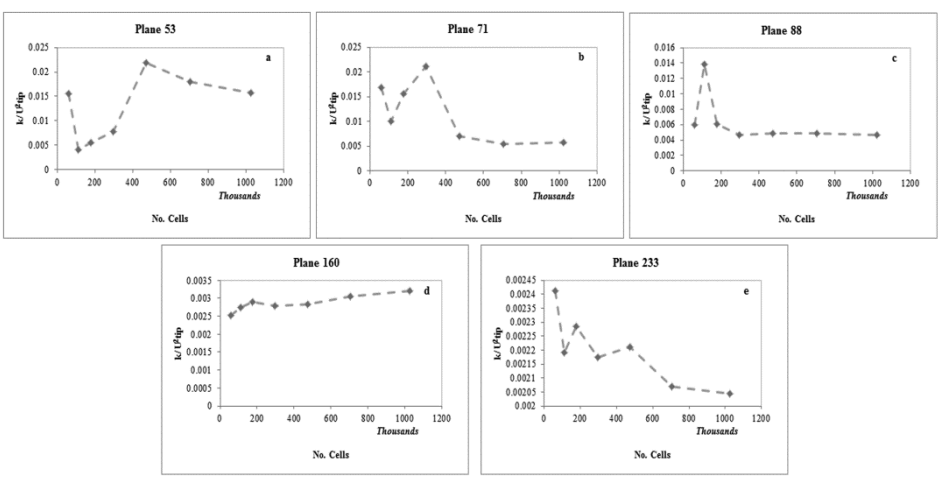

Fig. 8. Turbulent kinetic energy for the mid-points in five planes for different grids

4.2. Turbulence models study

There is no generally accepted turbulence model that can be applied in all types of engineering flow simulation problems. Therefore, a comparison of different turbulence models for prediction of flow inside the stirred tank is another aim of this work. To attain this objective all the turbulence models available in ANSYS FLUENT 12.1 were categorized into various groups based on their methodology of calculation of the term τ_{ij}^{Re} in Eq. (2). Also, the experimental data, adopted from Armenante et al. (1997), were used to compare the performance of each turbulence model for estimation of the velocity components and the turbulence quantity. The selected results for each group are discussed in the following sections.

4.2.1. Validation of RANS turbulence models

As discussed in the methodology section, this type of turbulence model implements the Boussinesq assumption that relates Reynolds stresses to the mean velocity gradient. Because this group of turbulence models solves the averaged flow quantities they are computationally preferable.

For the validation of each model, the velocity components (tangential, radial and axial) as well as the turbulent kinetic energy were compared with the experimental data over five different planes (Fig. 5). It should be mentioned among all the RANS models, using the Reynolds Stress Model (RSM) led to diverged solutions. Attempt to remedy this by decreasing the under-relaxation factors, initializing with the other turbulence models, gradually increasing the angular velocity and varying the time step were unable to achieve a converged solution.

Figure 9 shows the tangential velocity profile predicted by the RANS models together with the experimental data. It is clear that the choice of turbulence models plays an important role in the simulation of the flow inside the stirred tank. Among the models with the scalar assumption of turbulent viscosity, the k-ε RNG and the Transition-SST turbulence models provided a better fit to the experimental data. Although the Transition-SST predicted the maximum of velocity closer to the experimental data, the general trend of the k-ε RNG data for the rest of the vessel compared well with the experimental data.

Comparing the axial and the radial velocity profiles on the other planes showed that the performances of the above mentioned models, the k-ε RNG and the Transition-SST, were better than other RANS models. Transition SST for predicting the axial velocity was the efficient option, while the radial velocity profiles predicted with the k-ε RNG were more accurate. In the regions with high turbulence, i.e. the impeller discharge zone and the bottom of the vessel, the prediction of turbulent kinetic energy with the three-equation turbulence model, k-kl-ω, was significantly improved and the transition SST worked better for the top part the vessel where the flow was not influenced too much due to the rotation of the impeller.

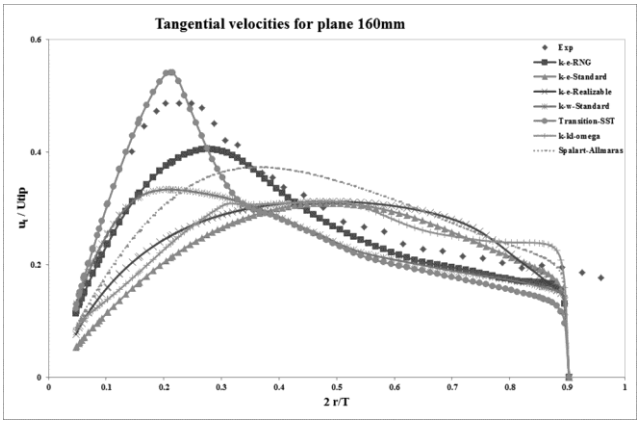

Fig. 9. RANS predictions of tangential velocity compared with experimental data for plane 160

4.2.2. Validation of Large Eddy Simulation (LES)

The tangential velocity profile on plane 160 predicted by the LES is compared with the experimental data in Fig. 10. In order to assess the performance of LES model for calculation of eddy viscosity, μ_t (Eq. (6)), three approaches have been applied. As is demonstrated in Fig. 10, these three subgrid-scale models have very good agreement with the LDV results. The maximum of velocity at the tip is slightly over-predicted by the Smagorinsky-Lilly and the WALE approaches, though it is captured by the "kinetic energy transport" method. This conclusion is also valid for the other planes.

To predict the axial velocity the WALE model provides results comparable to the "kinetic energy" alternative and both of them have captured the trends of the axial velocity measurements.

The radial velocity profile predictions with these three subgrid-scale models fit the measurements fairly well, and none of the subgrid-scale models has any merit in terms of having closer agreement with the experimental data. As the fluctuation range of this velocity component is very narrow, having exact fit with the experimental data is computationally very expensive. It is interesting to note that among the three subgrid-scale models one may select the "kinetic energy" method to justify the term optimized methodology, i.e. having both adequate agreement with experimental data and reasonable computational cost.

4.2.3. Validation of Detached Eddy Simulation (DES)

The Detached Eddy Simulation model draws advantages from the RANS models to predict the flow behaviour close to the wall and the LES in the rest of the stirred tank. Three RANS models involving the Spalart-Allmaras, realizable k-ε, and SST k-ω in combination with the LES have been tested to simulate the flow pattern inside the vessel. As a case to illustrate the performance comparison, Fig. 11 shows the tangential velocity profile on the plane 160 mm from the bottom of the tank. There is

not much difference among these three turbulence models, nevertheless the maximum velocity predicted by the combination of LES/realizable k–ε was in better agreement with the experimental data.

Generally, for prediction of the radial and axial velocity components, the above-mentioned combination fits the LDV data fairly well. Comparison of the simulated turbulent kinetic energy with the experimental data showed that the Detached Eddy Simulation method was not suitable to predict the measured data. Its under-predictions of turbulent kinetic energy are problematic for its use as a turbulence model for a stirred tank.

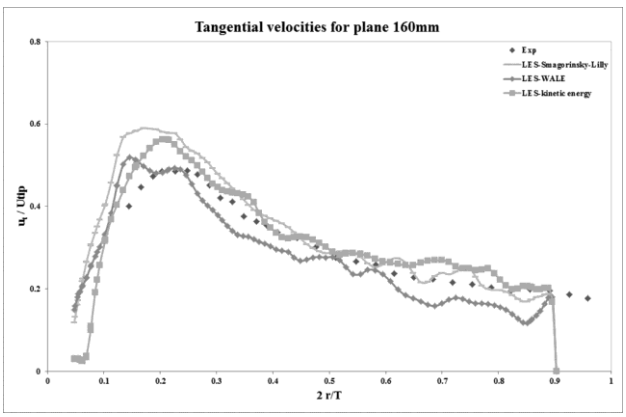

Fig. 10. LES predicitons of tangential velocity compared with experimental data for plane 160

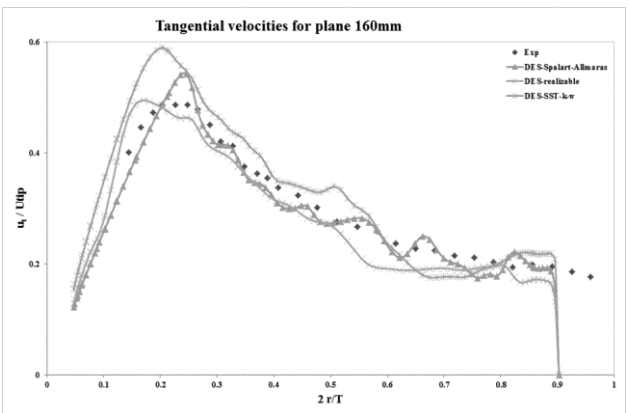

Fig. 11. DES predictions of tangential velocity compared with experimental data for plane 160

4.2.4. Comparison of different turbulence models

Validation of each turbulence model in the previous sections showed that the choice of turbulence model was an inseparable part in the simulation of stirred tanks.

The models in which the Boussinesq hypothesis is applied found to be more adequate for the stirred tank modelling. The Spalart-Allmaras, k-ε family, k-ω family are computationally efficient and inexpensive. The Spalart-Allmaras was found to be the least expensive model in this paper. However, LES, based on the modelling of the large-scale eddies, needed longer CPU times to obtain a stable solution compared to the RANS model. The advantage of using the RANS/LES hybrid model might be that the computational cost falls between LES and RANS models.

All the three groups of turbulence models have also been compared with experimental data. To accomplish this comparison, the optimized model was selected in such a way that two criteria of having short computational time and acceptable agreement with the experimental data were satisfied. Figure 12 is an example of comparing the turbulence models for prediction of the tangential velocity on the plane 160 mm from bottom of the tank. As can be seen, LES over-predicts the maximum of velocity, while RNG k-ε suffers from under-prediction. However, the maximum of tangential velocity on this plane is correctly captured with the DES turbulence model.

Other components of velocity and the turbulent kinetic energy predicted by the optimized model of each group on all planes were compared with the experimental data. The comparisons showed that the tangential velocity can be modelled with the renormalization group of k-ε turbulence model. Although the LES was successful for the computation of the radial and the axial velocity in some of the planes, its agreement with the experimental data did not show improvement over that achieved by RANS models such as RNG k-ε and transition SST. To predict the turbulent kinetic energy efficiently two of the RANS models, the three-equation model and the transition SST, had acceptable agreement. The Detached Eddy Simulation model, on the other hand, tended to under-predict the turbulent quantity which made it unsuitable candidate for the CFD problem of stirred tanks.

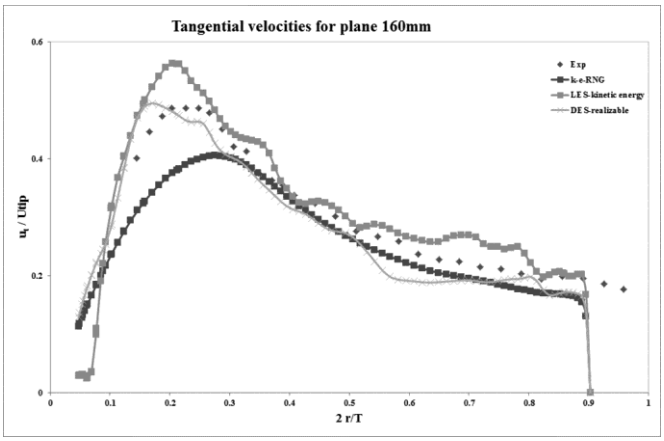

Fig. 12. Comparison of turbulence models with experimental data for tangential velocity on plane 160

5. Conclusion

Two underlying aspects of the numerical simulation of stirred tanks, namely the efficient grid scheme and the choice of suitable turbulence models, have been investigated. Through various criteria we have established the meshing methodology which ensures both results' independency and adequate agreement with experimental data. The widely used skewness factor was also tested to understand the optimal cell size in the bulk flow. The value of the y+ showed the problematic elements near the wall boundary conditions. Solving the problematic elements was carried out using different refinement methods to locally increase the number of cells. The grid independence study suggested that the solutions tend to converge at around 700,000 cells by which most characteristics of the turbulent flow can be captured.

In this study, the performances of RANS, LES and DES turbulence models for prediction of velocity components and turbulent kinetic energy have been investigated and compared with experimental data.

It was found that the RNG k-ε and the transition SST turbulence model produced better agreement for both velocity components and turbulent quantity. Likewise, the LES turbulence model in conjunction with the "kinetic energy" as subgrid-scale model was found to capture the trends of velocity components. However, the required CPU time for having converged solution made this model computationally intensive. Application of DES as the turbulence model for the stirred tank also gave accurate results for all the velocity components. It should be noted that the turbulent kinetic energy was under predicted.

Overall, this study demonstrated that for the consistent solution one needs to investigate the quality of mesh near the walls and the independency of the results from the number of cells. In addition, RANS turbulence models which implemented the Boussinesq hypothesis such as RNG k-ε and transition SST yielded better simulation of the flow behaviour inside the stirred tank. These recommendations might also be useful for the multiphase modelling of stirred tanks.

References

ANSYS Inc, 2009, *ANSYS FLUENT 12.0 Theory Guide*. ANSYS Inc,.

ARMENANTE, P.M., LUO, C., CHOU, C.-C., FORT, I., MEDEK, J., 1997, *Velocity profiles in a closed, unbaffled vessel: comparison between experimental LDV data and numerical CFD predictions*, Chemical Engineering Science 52(20), 3483–3492.

AUBIN, J., FLETCHER, D.F., XUEREB, C., 2004, *Modeling turbulent flow in stirred tanks with CFD: the influence of the modeling approach, turbulence model and numerical scheme*, Experimental Thermal and Fluid Science 28(5), 431–445.

BAKKER, A., OSHINOWO, L.M., 2004, *Modelling of Turbulence in Stirred Vessels Using Large Eddy Simulation*, Chemical Engineering Research and Design 82(9), 1169–1178.

BAKKER, A., OSHINOWO, L.M., MARSHALL, E., 2000, *The use of Large Eddy Simulation to study stirred vessel hydrodynamics*, In 10th European Conference on Mixing, 247–254.

CORONEO, M., MONTANTE, G., PAGLIANTI, A., MAGELLI, F., 2011, *CFD prediction of fluid flow and mixing in stirred tanks: numerical issues about RANS simulation*,Computer & Chemical Engineering 35(10), 1959–1968.

DEGLON, D.A., MEYER, C.J., 2006, *CFD modelling of stirred tanks: Numerical considerations*, Minerals Engineering 19(10), 1059–1068.

DONG, L., JOHANSEN, S.T., ENGH, T.A., 1994a, *Flow induced by an impeller in an unbaffled tank--I. Experimental*, Chemical Engineering Science 49(4), 549–560.

DONG, L., JOHANSEN, S.T., ENGH, T.A., 1994b, *Flow induced by an impeller in an unbaffled tank--II. Numerical modelling*, Chemical Engineering Science, 49(20), 3511–3518.

HINZE, J.O., 1975. *Turbulence*, Mc-Graw-Hill Publishing Co, New York.

KIM, W.-W., MENON, S., 1997, *Application of the localized dynamic subgrid-scale model to turbulent wall-bounded flows*, American Institute of Aeronautics and Astronautics.

LANE, G.L., SCHWARZ, M.P., EVANS, G.M., 2000, *Comparison of CFD methods for modelling of stirred tanks*, In 10th European Conference on Mixing, 273–280.

LAUNDER, B.E., SPALDING, D.B., 1972, *Lectures in Mathematical Models of Turbulence*, Academic Press, London, England.

MENTER, F.R., 1994, *Two-Equation Eddy-Viscosity Turbulence Models for Engineering Applications*, AIAA 32(8), 1598–1605.

MYERS, K.J., WARD, R.W., BAKKER, A., 1997, *A digital particle image velocimetry investigation of flow field instabilities of axial flow impellers*, Journal of Fluids Engineering 119, 623–632.

NICOUD, F., DUCROS, F., 1999, *Subgrid-Scale Stress Modelling Based on the Square of the Velocity Gradient Tensor*, Flow, Turbulence, and Combustion 62(3), 183–200.

ORSZAG, S.A., YAKHOT, V., FLANNERY, W.S., BOYSAN, F., CHOUDHURY, D., MARUZEWKI, J., PATEL, B., 1993, *Renormalization Group Modelling and Turbulence Simulations*, In International Conference on Near-Wall Turbulent Flows, Tempe, Arizona.

OSHINOWO, L., JAWORSKI, Z., DYSTER, K.N., MARSHALL, E., NIENOW, A.W., 2000. *Predicting the tangential velocity field in stirred tanks using the Mulkle Reference Frames (MRF) model with validation by LDV measurements*, In 10th European Conference on Mixing, 281-288.

SHIH, T.-H., LIOU, W.W., SHABBIR, A., YANG, Z., ZHU, J., 1995, *A new k-ε eddy viscosity model for high reynolds number turbulent flows*, Computers & Fluids 24(3), 227–238.

SHUR, M., SPALART, P., STRELETS, M., TRAVIN, A., 1999, *Detached-Eddy Simulation of an Airfoil at High Angle of Attack*, In 4th Int. Symposium on Eng. Turb. Modeling and Experiments, Corsica, France.

SMAGORINSKY, J., 1963, *General Circulation Experiments with Primitive Equations. I*, The Basic Experiment. Month. Wea. Rev 91, 99–164.

WILCOX, D.C., 1998, *Turbulence Modelling for CFD*, DCW Industries Inc., La Canada, California.

YOON, H.S., SHARP, K.V., HILL, D.F., ADRIAN, R.J., BALACHANDER, S., HA, M.Y., KAR, K., 2001. *Integrated experimental and computational approach to simulation of flow in a stirred tank*, Chemical Engineering Science 56(23), 6635–6649.

Physicochem. Probl. Miner. Process. 48(2), 2012, 533−544

www.minproc.pwr.wroc.pl/journal/

Physicochemical Problems of Mineral Processing

ISSN 1643-1049 (print)
ISSN 2084-4735 (online)

Received January30, 2012; reviewed; accepted May 4, 2012

DETERMINATION OF TURBULENCE AND UPPER SIZE LIMIT IN JAMESON FLOTATION CELL BY THE USE OF COMPUTATIONAL FLUID DYNAMIC MODELLING

Oktay SAHBAZ*, Umran ERCETIN, Bahri OTEYAKA*****

*Dumlupinar University, Department of Mining Engineering, Kutahya, Turkey, Tel.: +90 537 3862002; Fax.: +90 274 2652066; osahbaz@mail.dumlupinar.edu.tr
**Dumlupinar University, Department of Mechanical Engineering, Kutahya, Turkey
***Osmangazi University, Department of Mining Engineering, Eskişehir, Turkey

Abstract. In the coarse particle flotation, turbulence which can be treated as energy dissipation rate, is one of the most significant parameters effecting the recovery and grade. Therefore, determination of energy dissipation rate is very beneficial for delineation of coarse particle flotation and determining the maximum floatable particle size in any cell. In this study, Computational Fluid Dynamic (CFD) modelling for the Jameson cell has been carried out to determine the high turbulent regions and the effect on the upper floatable size limit. The CFD modelling has been utilized for determining the flow characteristics and hydrodynamic behaviour of the Jameson flotation cell. In parallel with this purpose the turbulence map of the cell has been determined and energy dissipation rate determined by using the CFD modelling. According to the result acquired from the CFD modelling, there are two main turbulent regions which are mixing zone in the upper part of the downcomer and critical region at the separation tank. While the high turbulence at the mixing zone supplies fine bubbles and fast collection of particles, the turbulence at the separation tank causes the main detachment of the bubble-particle aggregate. Then, the increase in turbulence in the tank causes the decrease of the maximum floatable size of particles. In addition, the average energy dissipation rate in the critical region has been determined and used for estimation of the maximum floatable particle size in the Jameson cell. Moreover, the effect of hydrophobicity has been discussed.

keywords: Jameson cell, coarse particle flotation, turbulence, CFD modelling

1. Introduction

Flotation is a dynamic process used for separation of hydrophobic minerals from hydrophilic ones. The size of particles is one of the most important parameters in flotation. While the flotation recovery of intermediate particles is high, the recovery of both fine and coarse particles is usually remarkably low (Trahar, 1981). Thus, particle size versus recovery figures leads to the inverted U-shape curves (Trahar, 1981; Nguyen, 2003). The reason of low recovery of coarse particle is mostly the turbulence within the cells (Schulze, 1982; Oteyaka and Soto, 1995; Drzymala,

http://dx.doi.org/10.5277/ppmp120217

1994a). Even though particles may have high hydrophobicity, they cannot be reported as a "float" due to the instability of the aggregate as a result of high turbulence. On the other hand, the low recovery of fine particles can be attributed to low collision probability of fine particles (Schulze, 1989; Çinar et al., 2007). Therefore, new and modified conventional technologies are under investigations to increase flotation performance of fine and coarse particles (Rodrigues and Rubio, 2007; Uçurum and Bayat, 2007; Jameson, 2010; Şahbaz, 2010;). Moreover, determination of particle size limits in flotation cells is prepossessed (Nguyen, 2003; Gonjito et al., 2007; Kowalczuk et al., 2011).

The Jameson cell is relatively new flotation device used especially in the flotation of fine particles (<100 μm) with a high performance (Evans et al., 1995; Cowburn et al., 2006; Cinar et al., 2007). However, the collision probability of fine particles increase in the Jameson cell due to the fine bubble (400-700 μm) generation in the upper part of the downcomer, called the mixing zone, which is one of the main parts of the cell and primary contacting zone of bubble and particle (Evans et al., 1995). On the contrary, the performance of the Jameson cell shows tendency to decrease with the increase of particle size due to turbulence (Cowburn et al., 2006; Cinar et al., 2007). However; due to operational and maintenance issues, it is becoming necessary to recover the coarse particle by using the Jameson cell in existing mineral processing plants (Cowburn et al., 2006). In some applications of coal flotation the feed size can be greater than 500 μm for the Jameson cell (Cowburn et al., 2006). Therefore, the turbulent region causing the detachment should be determined and maximum floatable particle size should be ascertained in the cell.

Computational fluid dynamic (CFD) modelling, which has been recently applied to flotation cells to elucidate complexity of the hydrodynamic characteristics of cells, has been used in flotation science by Koh et al. (2000), Koh and Schwarz (2003 and 2006), Lane et al. (2002), Liu and Schwarz (2009), Sahbaz (2010) etc. In CFD modelling, a flotation cell is discretized into particular finite volumes where local values of flow fields are calculated. The detailed understanding of flows using this approach allows determination of flow characteristics by means of velocity magnitude, pressure changes, turbulence dissipation rate etc. Also this information provides the possibility for investigating where the attachment and detachment occur (Koh et al., 2000; Koh and Schwarz, 2003; 2006). The CFD modelling has become a popular method as it yields informative results and insights to mechanisms, and because of the relatively low labour and equipment costs involved as a result of ever-increasing computer speed and capacity (Liu and Schwarz, 2009). Finally, the CFD modelling seems to be a very useful tool for determination of turbulence, resulting from energy dissipation rate, and related particle size limits in flotation.

In the present study, the turbulence has been quantitatively determined and its effect on the upper particle size limits in the Jameson flotation cell has been ascertained by using the CFD modelling. Furthermore, the effect of particle hydrophobicity on maximum floatable particle size has been elucidated.

2. Material and method

2.1. Material

In the present study high purity quartz (95%±1%, obtained from Muğla-Milas Region in Turkey) sample was used.

The particle size range of the sample "as received" was -1+0.5 mm. The sample was ground in a porcelain mill and sieved for the experiments in different relatively coarser size groups, which are -150+106 μm, -180+150 μm, -212+180 μm, -250+180 μm and -300+250 μm.

In the experiment, dodecylamine (DDA) was used as a collector. Different amounts of DDA were used to assure required contact angle of 50º and 78º resulting from the 180 g/Mg and 1000 g/Mg DDA, respectively. Aerofroth 65 (AF65) frother, received from Cytec Industries, was added in the form of droplets using a disposable syringe. The amount of AF65 used in the experiments was 10 ppm. The flotation experiments were carried out at natural pH of 8-9 using the domestic tap water.

2.2. Experimental method

The Jameson cell which was used in this study has two main parts, which are "downcomer" with the diameter of 20 mm and "separation tank" with a diameter of 200 mm. The upper part of the downcomer was equipped with a nozzle (Fig. 1) having 4 mm aperture to supply a high pressure water jet and mixing zone at the upper part of the downcomer.

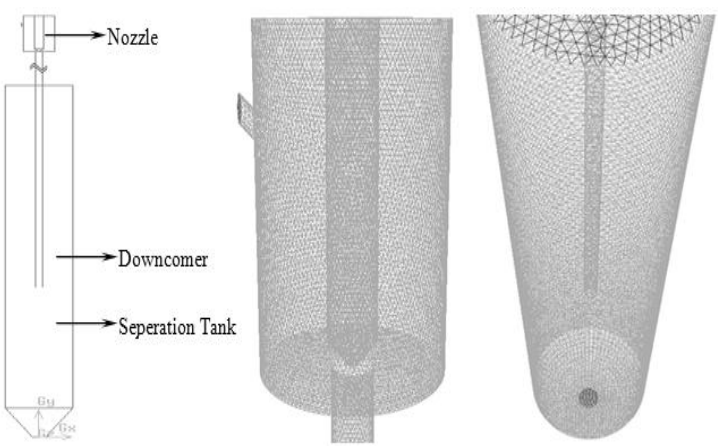

Fig. 1. Meshed view of nozzle, downcomer and separation tank

A conditioned slurry has been pumped (110 kPa) into the downcomer which is the primary contacting zone of particle with bubbles. Air is sucked into downcomer because of the venturi effect of the plunging jet. The sucked air is broken up into fine bubbles produced due to the shearing action of the water jet. Then, micro processes of

flotation, which are encountering, collision, attachment and detachment, start and turbulent region with a high rate occurs at the tip of the nozzle. The three phase mixture is transported into the separation tank due to the gravity flow under high pressure. The second turbulent region occurs at the exit of the downcomer during transportation. This turbulence can be accepted as the turbulence causing the majority of detachment. Therefore, the turbulence, which occurs during the operation must be satisfactorily understood to describe the flotation of coarse particles in the Jameson cell.

During the study all parameters of experiments, such as feeding velocity, solid ratio, air to pulp ratio, have been tried to be kept at optimum conditions considering the previous studies carried out by Evans et al. (1995), Harbort et al. (2002), Çınar et al. (2007), and Sahbaz et al. (2008; 2010).

3. Theory

3.1. The maximum floatable particle size

Flotation of particle depends on the balance of forces acting on bubble-particle aggregate. These forces are the attachment forces between bubble and particle in relation to detachment forces in the environment (Ralston et al., 1999; Pyke et al., 2003; Kowalczuk et al., 2011). The main forces operating at the moment of spherical particle – gas phase rupture are given in Table 1 (Drzymala, 1994b; Pyke et al., 2003; Kowalczuk et al., 2011).

The more realistic force balance for a spherical particle in the liquid/gas interface can be written as in Eq.1 (Kowalczuk et al, 2011):

$$F_{c\max} + F_b + F_h - F_p - F_g - F_a = 0, \tag{1}$$

The sum of the forces is zero at equilibrium. At the equilibrium, particle has the same chance to sink or float. If attachment forces are greater than the detaching forces, particles can float. Therefore; maximum floatable particle size in flotation can be determined by the ratio of the attachment and detachment forces. The probability of stabilisation or destabilisation of the bubble–particle aggregate is based on the Bond number, B_o (Schulze, 1993):

$$B_o = \frac{F_{det}}{F_{att}}, \tag{2}$$

In this equation, the parameter "*a*", which is used to determine the inertia force, is hard to determine. Additional acceleration, *a*, determines the detachment forces and depend on the structure and intensity of the turbulent flow field, therewithal on the energy dissipation in a given volume of apparatus (Schulze, 1993). It can be calculated by using the maximum energy dissipation (ε) and aggregate size (D_{agr}) (Pyke et al, 2003):

$$a = 29.6 \frac{\varepsilon^{2/3}}{\left(D_{agr}\right)^{1/3}}, \tag{3}$$

where aggregate size is

$$D_{agr} = d_b + d_p . \tag{4}$$

Thus, the final equation (5) is obtained to determine the additional acceleration by using Eq. (3) and Eq.(4):

$$a = 29.6 \frac{\varepsilon^{2/3}}{\left(d_b + d_p\right)^{1/3}} . \tag{5}$$

In addition, the detachment contact angle, θ_d, in the equations (Table 1) refers to experimental (advancing) contact angle (Kowalczuk et al, 2011).

The maximum floatable size of any particle can be found by using the Bond number calculating the values of forces acting on bubble-particle aggregate by iteration. All terms can be found easily, except for energy dissipation rate, ε, in the cells. The CFD study is one of the useful methods to determine the energy dissipation rate in the flotation cells.

Table 1. Main forces acting on aggregate

Symbol	Force	Equation and Explanation	Effect of force
F_{cmax}	The maximum capillary force	$F_{c\max} = \frac{1}{2}\pi d_{\max}\sigma(1-\cos\theta_d)$ where d_{max} is a maximum floatable particle size, θ_d is a detachment contact angle, and σ is a surface tension	Attachment
F_b	Buoyancy force	$F_b = \frac{1}{8}\pi d_{\max}^3 \rho_l g\left(\frac{2}{3}+\cos\frac{\theta_d}{2}-\frac{1}{3}\cos^3\frac{\theta_d}{2}\right)$ where ρ_l is a liquid density, g is a gravity constant	Attachment
F_h	Hydrostatic pressure force	$F_h = \frac{1}{4}\pi d_{\max}^2\left(1-\cos\theta_d\right)\rho_l g R$ where R is a bubble radius	Attachment
F_p	Pressure in the gas bubble force	$F_p = \frac{1}{4}\pi d_{\max}^2\left(1-\cos\theta_d\right)\frac{\sigma}{R}$	Detachment
F_g	Gravity force	$F_g = \frac{1}{6}\pi d_{\max}^3 \rho_p$ where ρ_p is a particle density	Detachment
F_a	Inertia force	$F_a = ma$ $F_a = \frac{1}{6}\pi d_{\max}^3 \rho_p a$ where a is an additional acceleration	Detachment

3.2. CFD modelling

The required simulation results for the Jameson flotation system has been numerically modelled using the commercial the CFD code of Fluent. The geometry of the Jameson cell has been defined and a grid has been generated using Gambit 2.4.6 which is the pre-processor for geometry modelling and mesh generation. For all cases studied in this paper, mixtures of triangular and quadrilateral elements have been generated. The computational domain and grid structure in 3D flow field is shown in Fig. 1. The Fluent 6.3.26 commercial computer program for modelling fluid flow, has been used to carry out the modelling of the experimental process. Computations have been performed using Eulerian multiphase approach, for turbulent flows depending on water and air inlet velocity in thr 3D space. The CFD simulations have been performed using a pressure based steady-state segregated implicit solver. A standard k-ε mixture model has been employed for flow simulation. Pressure based implicit solver with green-gauss node based has been used. The relationship between velocity and pressure corrections has been calculated using a simple algorithm. A second order upwind discretization scheme has been employed for momentum, turbulent kinetic energy, turbulent dissipation rate and for volume fraction. Gravitational acceleration has been included in the computation and the governing equations for flow and turbulence have been solved iteratively until convergence has been obtained. The inlet velocities of air and water have been entered as 1.4 m/s, volume fraction of air has been set as 43.75%. Outlets have been adjusted as outflow and ratio of the outlets are 20% at mixing outlet and 80% at water outlet. The simulation has been converged after more than 2500 iterations. Grid independence tests for different mesh sizes have been carried out. It was found that the solution has not been affected by the mesh quantity.

4. Results and discussion

The CFD predictions have helped to figure out a complex flow field within the Jameson cell. It has been used to visualize the main turbulent regions within the cell. In addition, values of energy dissipation rates have been determined by the use of the the CFD modelling. Thus, the maximum floatable sizes of particles having contact angles of 50^0 and 78^0 have been revealed by the use of the CFD results and the force balance.

The CFD results include turbulence intensity values which indicate that there are two main turbulent regions in the Jameson cell (Fig. 2). It is seen in Fig. 2 that these regions arise from the upper part of the downcomer and at the exit of the downcomer. The turbulence intensity of 1% or less can be considered as low, while the turbulence value greater than 10% can be considered as high (Fluent 6.3 User's Guide). The turbulence intensity at the tip of the nozzle (mixing zone) and downcomer has exceeded the scale and was more than 10% in Fig. 2. But this turbulence may not cause the main detachment because of the compact design and nature of the system.

The high turbulence occurring in the mixing zone is responsible for fine bubble generation (< 1 mm) and faster bubble-particle connection (Evans et al., 1995). In addition to this, detached particles have various chances to attach to bubble again and again along with the downcomer. However, the level of micro-turbulence in the separation tank, as predicted by k-epsilon turbulence model, is highest at the region of the downcomer exit (Fig. 2.). The turbulent region at the exit of the downcomer can be considered as critical region where the main detachment occurs (Harbort et al., 2002; Sahbaz, 2010). The part about 20-25 cm deep from the downcomer exit is the critical part causing the bubble-particle detachment (Fig. 2). Thus, the intensity of turbulent in this critical region in separation tank determines the maximum floatable size of particles (Sahbaz et al., 2010). Turbulence intensity increased to the value of 23% at this region and decreased along with the separation tank (Fig. 2). The degree of intensity finally diminished to less than 1% around the froth phase (upper part) of the separation tank (Fig. 2).

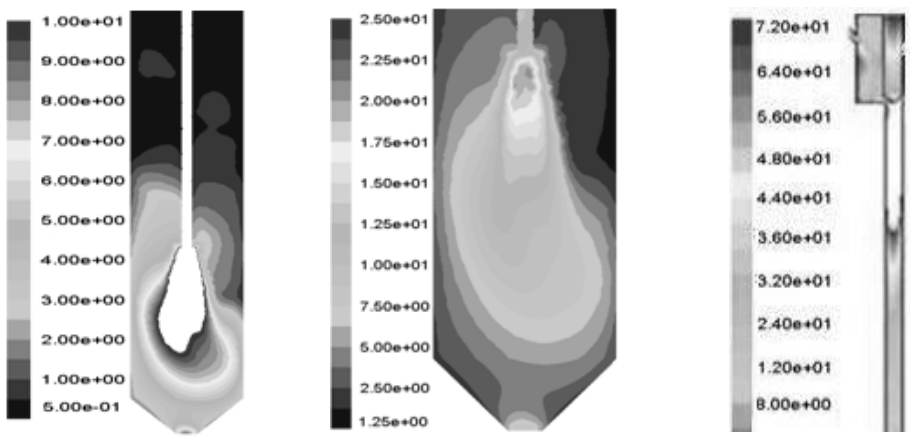

Fig. 2. Contours of turbulence intensity, %

Furthermore, the local turbulent energy dissipation rates are obtained by the CFD modelling of the Jameson cell. The CFD modelling provides a realistic approach to flotation models without additional assumptions on turbulent energy dissipation rates (Evans et al, 2008). Energy dissipation rates obtained from the CFD predictions has also given satisfactory results to comprehend the flow characteristics in the cell (Fig. 3). Furthermore, the value of the energy dissipation rate gives the detachment force acting on bubble particle aggregate within the explicit regions. According to the result obtained from the CFD simulation, the rate of energy dissipation increases at the exit of downcomer and starts to decrease along with the separation tank (Fig. 3). Based on the turbulent dissipation rate, the aggregate stability is mostly disturbed in the separation tank. The local dissipation rate changes between 2.1 m^2/s^3 and 0.075 m^2/s^3 (Fig 3). The calculation performed by the use of the exact volume, in which the main detachment zone determined in Fig 4. is about 0.9 m^2/s^3 (Fig.4-b) according to the

CFD solutions (Fig.4). Thus, the maximum floatable particle size for the laboratory scale Jameson cell can be determined by using this result.

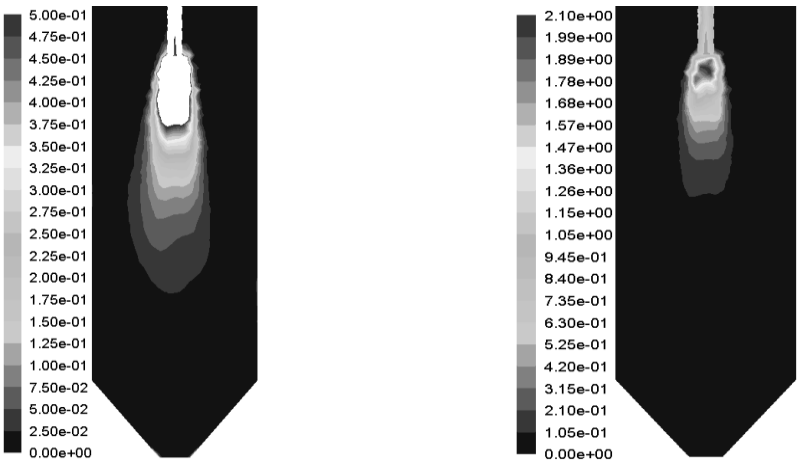

Fig. 3. Energy dissipation rate, m^2/s^3

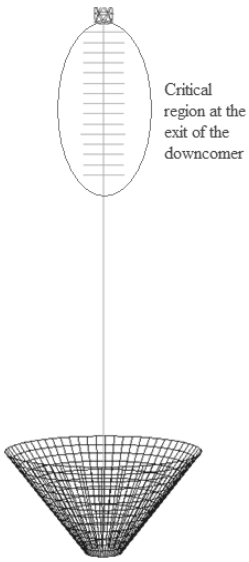

Fig. 4. The critical region determination by the use of the CFD modelling

The relation between theoretical maximum floatable size of particle, d_{max}, and energy dissipation rate is shown in Fig. 5. According to Fig. 5, there is an inverse relation between d_{max} and energy dissipation rate as expected. The figure also shows the same trend for d_{max} having different contact angle values. In addition, Fig. 5 indicates that the capture of large particles is favoured by a low energy dissipation rate

and high contact angles. Finally, theoretical d_{max} for the average dissipation rate have been determined as 260 μm and 345 μm for the contact angle of 50^0 and 78^0, respectively (Fig. 5).

The experimental results which were also published by Şahbaz (2010) are shown in Fig.6. It is seen that the recovery decrease with the particle size increase for both low and high contact angle values (Fig.6). In the same turbulent conditions, the only way of recovery increase of coarse particle is the increase of hydrophobicity. But, even if hydrophobicity is increased, there is still a limitation for floatable particle size. That means that as long as the particle size increases in flotation, the recovery starts to diminish at a critical point. Therefore; there is a d_{max} in every environment and determination of it is beneficial for the operations.

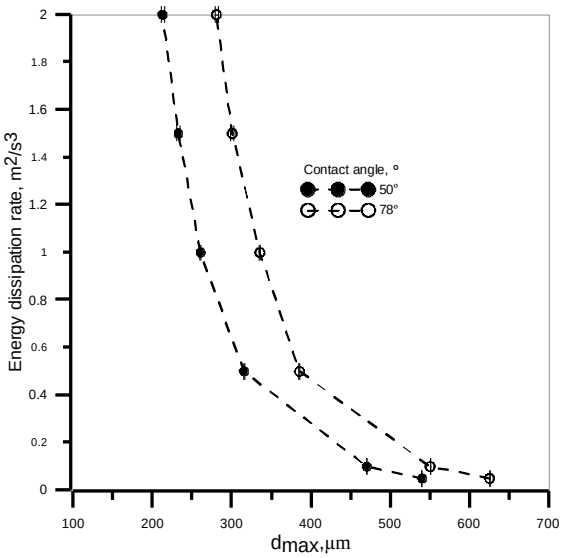

Fig. 5. Relation of d_{max} and energy dissipation rate

d_{max} is defined as the size for which the recovery of floatable particles is equal to 50% (d_{50}). It is a good measure of d_{max} because at that point the particle has equal chance to float and to sink. This was discussed and applied by different authors including Schulze (1977), Drzymala (1994, 1999), Chipfunhu et al. (2011), and Kowalczuk et al. (2011). Therefore, the maximum floatable particle has been found as 235±20 μm and 330±20 μm for the particles having contact angle of 50^0 and 78^0, respectively (Fig. 6).

According to Figs. 5 and 6 there is a close relationship between theoretical and experimental results. Especially these results are nearly the same for the coarser sizes (Figs. 5 and 6). It is possible to speak of a good compliance of high hydrophobicity values between simulation and experimental results (Figs. 5 and 6). It is natural for d_{max} value to increase with the increase of hydrophobicity. Thus, degree of attachments

forces has increased and the recoverable particle size is also increased. However, it can be seen in those figures that there is still a small differences between the experimental and theoretical results for both sizes, specifically for finer ones. The main reason of these differences comes from the difficulty of determination of all detachment regions in the cell. It has been seen that at the turbulent region, particles with a low hydrophobicity are affected more than expected by the model. Bubble-particle aggregate is more prone to detach while passing through the critical region at the exit of the downcomer. This situation causes some differences between CFD simulation results and practical values. As a result, while particles of a size around 250 μm can float in Jameson cell at a low hydrophobicity value; it can reach to 330 μm at a high contact angle value (Figs. 5 and 6).

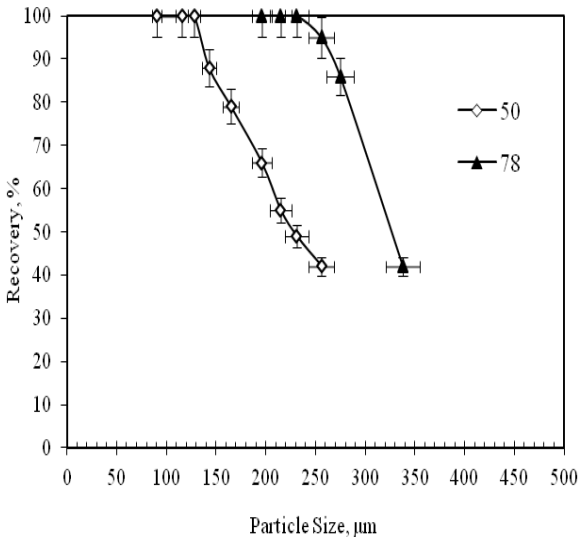

Fig. 6. Experimental results (Şahbaz et al., 2010)

5. Conclusions

In this study, CFD modelling for the Jameson cell has been carried out to determine the hydrodynamic behaviour and effect of turbulence on the upper floatable size limit. The study shows that there are two main turbulent regions which are mixing zone in the upper part of the downcomer and critical region at the separation tank. While the high turbulence at the mixing zone causes fine bubble generation and fast collection of particle, the turbulence at the separation tank causes the main detachment of the bubble-particle aggregate. Thus, the increase in turbulence in the tank causes the decrease the maximum floatable size of the particle.

According to the CFD simulation the turbulence intensity is higher at the exit of the downcomer than in the whole separation tank. Value of energy dissipation rate within the cell changes between 2.5 m^2/s^3 and 0,025 m^2/s^3. In addition to this, the local energy dissipation rate within the critical region is around 0.9 m^2/s^3. This means that the maximum floatable particle size within the cell is approximately 250 μm and 350 μm for the contact angle rate of 50^0 and 78^0, respectively. The experimental results have been confirmed by the theoretical results.

Acknowledgement

The authors are thankful to Prof. Dr. Greame J. Jameson for his great support during the design of laboratory scale Jameson cell. And we are also thankful to Dr. Ali Ucar for his advices during the experimental part of this study.

References

CHIPFUNHU, D., ZANIN, M., GRANO,S., 2011, *Flotation behaviour of fine particles with respect to contact angle*, Chemical Engineering Research and Design, 2011, Article in Press.

ÇINAR, M., ŞAHBAZ, O., ÇINAR, F., KELEBEK, Ş. AND ÖTEYAKA, B., 2007, *Effect of Jameson cell operating variables and design characteristics on quartz-dodecylamine flotation system*, Minerals Engineering, 20, 1391–1396.

COWBURN, J., HARBORT, G., MANLAPIG, E. POKRAJCIC, Z., 2006, *Improving the recovery of coarse coal particles in Jameson cell*, Minerals Engineering, 19, 609–618.

DRZYMALA, J., 1994a, *Characterization of materials by Hallimond tube flotation, Part 1. Maximum size of entrained particles*, Int. J. Miner. Process, 42, 139–152.

DRZYMALA, J., 1994b, *Hydrophobicity and collectorless flotation of inorganic materials*, Adv. Colloid Interface Sci., 50, 143–185.

EVANS, G.M., ATKINSON, B., JAMESON, G.J., 1995, *The Jameson Cell. Flotation Science and Engineering*, ed. Matis K.A., Marcel Dekker Inc., 331–363.

EVANS, G.M., DOROODCHI, E., LANE, G.L., KOH, P.T.L., SCHWARZ, M.P., 2008, *Mixing and gas dispersion in mineral flotation cells*, Chemical Engineering Research and Design, 86, 1350–1362.

FLUENT 6.3 User's Guide, Fluent Inc., Centerra Resource Park, 10 Cavendish Court, Lebanon, NH 03766, USA, 2006.

GAMBIT User's Guide, Fluent Inc., Centerra Resource Park, 10 Cavendish Court, Lebanon, NH 03766, USA, 2006.

GONJITO, F.C., Fornasiero, D., Ralston, J., 2007, *The limits of fine and coarse particle flotation*, The Canadian Journal of Chemical Engineering, 85, 739–747.

HARBORT, G.J., MANLAPIG, E.V. ve DEBONO, S.K., 2002, *Particle collection within the Jameson cell downcomer*, Trans. IMM Section C, 111/Proc. Australas IMM, V. 307.

JAMESON, G.J., 2010, *New directions in flotation machine design*, Minerals Engineering, 23(11–13), 835–841.

KOH, P.T.L., MANICKAM, M., M.P. SCHWARZ, 2000, *CFD simulation of bubble- partıcle collisions in mıneral flotation cells*, Minerals Engineering, 13, 1455–1463.

KOH, P.T.L., SCHWARZ, M.P., 2003, *CFD modelling of bubble-particle collision rates and efficiencies in a flotation cell*, Minerals Engineering, 16, 1055–1059.

KOH, P.T.L., M.P. SCHWARZ, 2006, *CFD modelling of bubble–particle attachments in flotation cells*, Minerals Engineering, 19, 619–626.

KOWALCZUK, P., SAHBAZ, O., DRZYMALA, J., 2011, *Maximum size of floating particles in different flotation cells*, Minerals Engineering, 24, 766–771.

LANE, G.L., SCHWARZ, M.P., EVANS, G.M., 2002, *Predicting gas–liquid flow in a mechanically stirred tank*, Applied Mathematical Modelling, 26, 223–235.

LUI, T.Y. SCHWARZ, M.P., 2009, *CFD based modelling of bubble particle collision efficiency with mobile bubble surface in a turbulent environment*, International Journal of Mineral Processing, 90, 45–55.

NGUYEN, A.V., 2003, *New method and equations for determining attachment tenacity and particle size limit in flotation*, International Journal of Mineral Processing, 68, 167–182.

ÖTEYAKA, B., SOTO, H., 1995, *Modelling of negative bias column for coarse particles flotation*, *Minerals Engineering*, 8, 91–100.

ÖTEYAKA, B., 1993, *Modelisation D'une Colonne De Flottation Sans Zone D'ecume Pour La Separation Des Particules Grossieres*, PhD Thesis, Universite Laval, Quebec, Canada, 1993.

PYKE, B., FORNASIERO, D., RALSTON, J., 2003, *Bubble particle heterocoagulation under turbulent conditions*, Journal of Colloid and Interface Science, 265, 141–151.

RALSTON, J., FORNASIERO, D. HAYES, R., 1999, *Bubble-particle attachment and detachment in flotation*, International Journal of Mineral Processing, 56, 133-164.

RODRIGUES, R.T., RUBIO, J., 2007, *DAF–dissolved air flotation: Potential applicationsin the mining and mineral processing industry*, International Journal of Mineral Processing, 82,1–13.

ŞAHBAZ, O., ÖTEYAKA, B., KELEBEK, Ş., UÇAR A. ve DEMIR, U., 2008, *Separation of unburned carbonaceous matter in bottom ash using Jameson cell*, Separation and Purification Technology, 62, 103–109.

SAHBAZ, O., 2010, *Modification of downcomer in Jameson Cell and its effect on performance*. Ph.D. Thesis, Dumlupinar University, Department of Mining Engineering, Turkey, 2010.

SCHUBERT, H., 1999, *On the turbulence-controlled microprocesses in flotation machines*, International Journal of Mineral Processing, 56, 257–276.

SCHULZE, H.J., 1977, *New theoretical and experimental investigations on stability of bubble/particle aggregates in flotation: a theory on the upper particle size of floatability*, International Journal of Mineral Processing, 4, 241–259.

SCHULZE, H.J., 1982, *Dimensionless number and approximate calculation of the upper particle size of floatability in flotation machines*, International Journal of Mineral Processing, 9, 321–328.

SCHULZE, H.J., 1989, *Determination of adhesive strength of praticles within the liquid/gas interface in flotation by means of a centrifuge method*, Journal of Colloidal and Interface Science, 128(1).

SCHULZE, J.H., 1993, *Flotation as a heterocoagulation process: possibilities of calculating the probability of flotation*. Coagulation and Flocculation and Applications. Dekker, New York, ed. Dobias, B., 1993, 321–353.

TRAHAR, W.J., 1981, *A rational interpretation of the role of particle size in flotation*, International Journal of Mineral Processing, 1981, 8, 289–327.

UÇURUM, M., BAYAT O., 2007, *Effects of operating variables on modified flotation parameters in the mineral separation*, Separation and Purification Technology, 55 (2), 173–181.

Physicochem. Probl. Miner. Process. 48(2), 2012, 545−554

www.minproc.pwr.wroc.pl/journal/

Physicochemical Problems of Mineral Processing

ISSN 1643-1049 (print)
ISSN 2084-4735 (online)

Received April 7, 2012; reviewed; accepted May 5, 2012

DEPENDENCE OF MINE REVENUE ON THE GRADE OF COPPER CONCENTRATE

Jerzy MALEWSKI*, Malgorzata KRZEMINSKA**

* Wroclaw University of Technology, Wyb. Wyspianskiego 27, 50-370 Wroclaw, jerzy.malewski@pwr.wroc.pl
** KGHM Polska Miedź S.A. Oddział Zakłady Wzbogacania Rud, Polkowice

Abstract. The paper presents a method of calculating the Net Smelter Return or Revenue (NSR) formula for copper ore mines based on heuristic models of functional relationships between concentration of metals in ore and copper concentrates, the operational efficiency, and the metal prices in the global markets. A method has been proposed to identify these relationships as well as a way of estimating their parameters. The NSR optimization calculations have been performed for the data coming from the mining and smelting practise of KGHM Polska Miedź S.A., which demonstrate its practical usefulness in assessing the efficiency of production based on the current quality of ore, the efficiency of its beneficiation, and the market prices of metals.

keywords: NSR, copper grading, recovery, costs, revenue, modelling

1. Introduction

The Net Smelter Return or Revenue (NSR) method is commonly used to analyse the economic impact of the degree of concentration of enriched minerals in light of processing costs and metal market prices (Czeczott, 1937; Paulo and Strzelska-Smakowska, 2000; Wills, 2006). It involves calculating the profits achievable from the sale of the main product of the mine, i.e. the concentrate after deducting the processing costs. It is an important piece of information for the mine, which may be a criterion for optimizing extraction and beneficiation of ore according to the quality of the concentrates. This method also provides the basis for the structure of settlement contracts between the mine and the smelter, but it can also be used as a tool for studying the efficiency of investment projects (Płaneta et al., 2000) or optimization projects (Krzemińska, 2012).

In such a settings the mine, i.e. mining units and the processing plant taken together represent one side of the settlements, while the smelter is on the other side. Combining ore excavation and beneficiation into one technological body is due to the fact that shipment of ore over great distances to the processing plant and then to the smelter without beneficiation would be, for obvious reasons, completely uneconomical. Therefore, the processing plant is usually an integral part of the mine,

http://dx.doi.org/10.5277/ppmp120218

whereas smelters can be located anywhere in the world because they are not dependent on a specific mine and can operate safely through the concentrates markets or by entering into direct contracts with specific providers. The global mining practise is such that about half of that industry operates without processing while the other half operates in the form of mining and smelting groups (Fig. 1).

In the Polish copper industry metal production is organized in terms of technology and management as a mining and smelting group, which is functionally divided into extraction, ore beneficiation, and smelting divisions (Monografia KGHM, 2007). The divisions settle their mutual accounts according to the volume and quality of the main product, but not financially. Consequently, it is interesting to determine what maximum revenue can be achieved by the mine (extraction + ore beneficiation plant) from mining production (quality of the ore and concentrate) considering the processing costs and the price movements on the global market of non-ferrous metals. For this purpose we will use own structure of the NSR settlement formula built on relationships between the quality of ore, quality and yield of the concentrates, processing costs, and finally, metal prices in the open market.

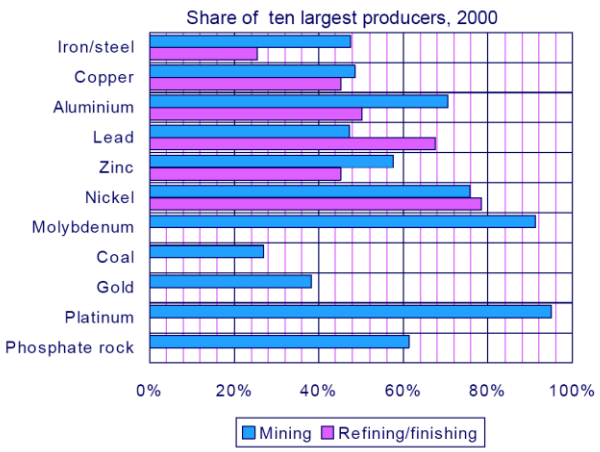

Fig. 1. The structure of production of the 10 largest producers of raw materials. Source: MMSD, CRUI report 2001

Figure 2 shows the revenue limits at each stage of production. In this article we will confine ourselves to the analysis of the cost and quality relationships between the mine and the Ore Beneficiation Plant (OBP) on one hand and the smelter on the other hand. However, it is also possible to put extraction on the one side and the OBP with the smelter on the other side, where the potential revenue of mining would be called Net Smelting & Processing Revenue (NSPR).

The final beneficiary of the mining and smelting production is the investor, whose expected benefit from the investment is the revenue after deducting total production costs, i.e. Net Smelting & Processing & Mining Revenue (NSPMR). The volume

calculated this way is useful for analyzing the efficiency of investment projects, e.g. at the stage of the feasibility study.

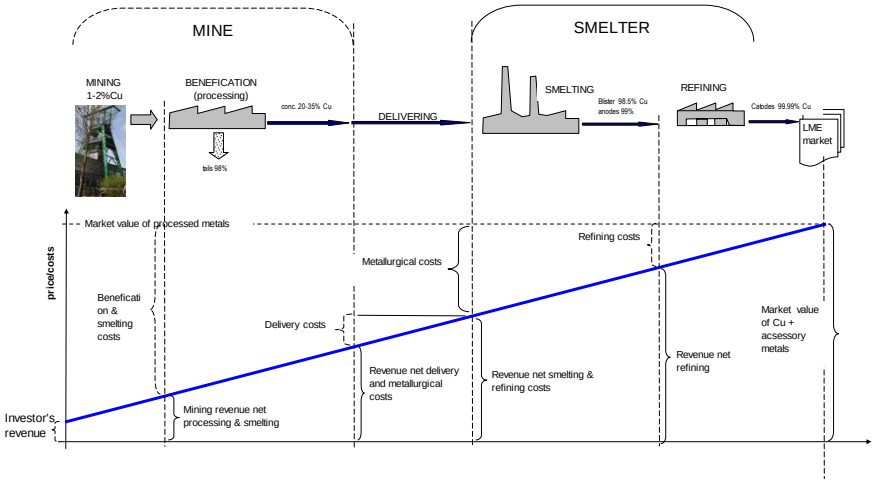

Fig. 1. The diagram of the expected revenue from final production

2. The structure of the NSR formula

The NSR formula determines how much income can be obtained from the sales of the main product at a given stage of production taking into account its current quality/price and the processing costs at subsequent operations to the final level of quality acceptable in the open market. It is commonly known (Strzelska-Smakowska and Paulo, 1995; Wills, 2006) as the following expression:

$$NSR = [\sum_i (\beta_i \cdot \delta_i \cdot p_i) - (MC + DC) - P + B] \cdot \gamma_1, \quad (1)$$

where

NSR – net smelter return measured in $ per 1 Mg of ore,
β_i - share of i-component (metal) in the main product (concentrate) (grade)
δ_1 - payable part of metal in concentrate
p_i - price of the i-component in the open market
$MC=TC+RC$- metallurgical charge
TC - treatment (smelting) charge dependent on quality of concentrate.
RC - refining charge, $/unit of metal
DC- cost of delivery ex-recipient
P - penalties for the presence of harmful components (according to contract terms)
B - bonuses for the presence of desirable components (according to contract terms)
$\gamma_1=1-\gamma_2$ denotes yield of the concentrate from the feed (ore),

where γ_2- yield of tailings, and $\gamma_0=1$ - amount (unit) of feed (ore).

Formula (1) may additionally introduce costs of chemical analyses of quality testing, and other contractual limitations.

3. Concept of calculation

In the optimization analyses the basic problem is to identify the relationship between the efficiency of beneficiation operations (recovery) (ε) and the concentration of the enriched minerals. In the case of complex ores the producer may be interested in any one component (metal, mineral), but not each one is the subject of beneficiation even though it will be recovered in subsequent smelting operations. This is precisely the case that will be considered in this work on the example of copper production technology at KGHM Polska Miedź S.A.

Under the qualitative and quantitative calculations of the yield of the main component (Cu) depending on the efficiency of the beneficiation operations we use a relationship that is well-known in the processing, which is derived from the mass balance of the processing operation (Drzymala, 2007):

$$\varepsilon = \frac{\beta}{\alpha} \cdot \gamma_1, \tag{2}$$

where α is a metal (Cu) content in the feed (ore) or concentrate, β is a metal (Cu) content in the concentrate.

The second relationship useful for further calculations will be the empirical hypothesis (Malewski, 2008) of a relationship between Cu recovery and the desired concentration of that metal in the concentrate which we will write down as follows:

$$\varepsilon = 1 - \left[\frac{\beta - \alpha}{\beta_{\max} - \alpha} \right]^A, \tag{3}$$

where:

$A=f(\pi,z,t)$ is a function of current values of the operation parameters $\{\pi\}$, environmental variables{z} and duration of the beneficiation operation t,.

β_{max} – limit of the metal (Cu) content in processed minerals,

α, β – as in (2); γ_1 as in (1).

So, from (3) we can determine recovery for a given quality of concentrate and then from (2) calculate actual concentrate yield, or after appropriate transformations we obtain a formula for yield of the main component in the concentrates as follows

$$\gamma_1 = \frac{\alpha}{\beta} \cdot \left[1 - \left(\frac{\beta - \alpha}{\beta_{\max} - \alpha} \right)^A \right], \quad \alpha \le \beta \le \beta_{\max}. \tag{4}$$

Parameter *A* in formula (3) can be determined experimentally by using a series of observations $\{\varepsilon\}$ and $\{\beta\}$ or by using the hypothesis that it will progress as in Fig. 3a. Then, by knowing the current value ε and β parameter *A* can be adjusted iteratively for compliance of the calculated result with the measured one.

The hypothesis (3) also has a physical meaning because it determines the limits of metal beneficiation depending on its stoichiometric concentration in the mineral. Confirmation of the shape of that function in practical ranges β can be found in many studies and publications (Strzelska-Smakowska and Paulo, 1995; Łuszczkiewicz and Chmielewski, 2006; Wills, 2006; Drzymała, 2007).

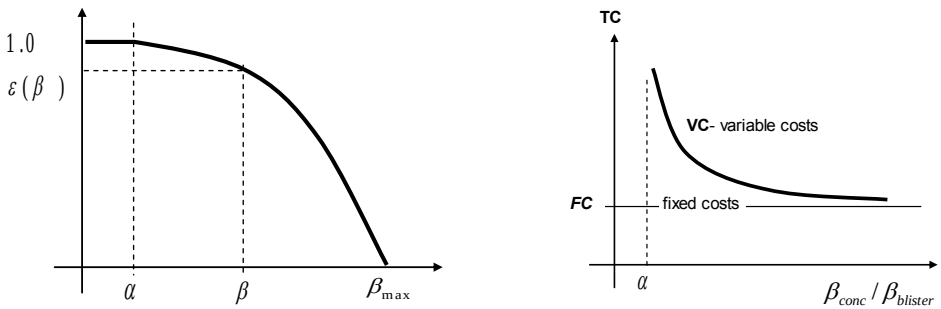

(a) (b)

Fig. 3. Models/hypotheses: (a) efficiency of industrial beneficiation of copper minerals, (b) cost of smelting of concentrates depending on the metal content in the concentrate

4. Costs of production

Calculation of formula (1) requires costs of processing of the concentrates to the form of pure metals as the metallurgical costs impact on revenue charge. At the metallurgical stage there are two operations: one is smelting of copper matte and fire refining to the anode copper (99% Cu), second - is electrolytic refining to commercial purity (99.99% Cu). The smelting *TC* and refinery *RC* charge will depend strictly on the amount of Cu in concentrate.

Determining the functional dependence of the metallurgical processing costs on the results of the preceding technological operations is a relatively difficult issue without performing appropriate experiments on real objects. In such case certain heuristic models of those relationships may be useful, as presented in Fig. 3b. This is energy dependence relationship extracting amount β [%] metallic Cu by smelting 1 Mg of concentrate. The model in general form may be of the type:

$$\frac{TC}{TC^*} = C \cdot \left(\frac{\beta}{\beta^*}\right)^{-k} + D, \tag{5}$$

where

β, β*- actual and observed grade of concentrate, respectively,

$C=VC^*/TC^*$ – constant, representing relative variable treatment costs,
$D=FC/TC^*$– constant, representing relative fixed treatment cost,
TC^* – observed treatment costs
k –curve form factor determined experimentally by iteration in a way similar to how it was described in the case of formula (3).

If $\beta=\beta^*$ and $TC=TC^*$ then from formula (5) we have $C+D=1$.

The metallurgical costs, however, depend on the presence of components harmful to the refining technology or the environment. Therefore, the formula (1) introduces optionally the penalty component (P) for the presence of undesirable components in the concentrate.

Content and recovery of precious metals from refining tailings is usually beyond the control of concentrates production but could theoretically be the subject of considering more sophisticated technology for this aim on the stages of deposit exploitation or ore beneficiation.

The content of accessory metals will be taken into account in our *NSR* equation in a simplified manner from the relationship:

$$\frac{\beta_i}{\beta_i^*} \approx b_{Cu} = \frac{\beta_{Cu}}{\beta_{Cu}^*}. \tag{6}$$

Thus, $\beta_i \approx b_{Cu} \cdot \beta_i^*$ is a current grade β_i of i-component proportionally to the relative change of copper grade of concentrate.

The same approach is applied to calculate the i-component of ore for the need of current ore value calculation, i.g. $\alpha_i \approx a_{Cu} \cdot \alpha_i^*$.

5. Sample calculations

Now, we will perform calculations to optimize the quality of the concentrate for the content of copper and/or accessory metals using the previously derived relationships. We will use industrial data of metals content in the operations streams throughout the copper production cycle. Input data for calculations are presented in Table 1.

Treating the data in Table 1 as empirical (α_i^*, β_i^*), we will calculate the relative yield of the concentrate γ_1. Taking $\alpha_{Cu}^*=1.67\%$, $\beta_{Cu}^*=25.76$, $\varepsilon_{Cu}^*=88\%$ and assuming metal content in the mineral $\beta_{max}^*=70\%$ applying iterative method we will assess the parameters of the function (3) that it crosses the empirical point as shown in Fig. 4.

Knowing the relationship as described above and comparing it to (4) we will calculate the yields $\gamma_{Cu}=f(a_{Cu} \cdot \beta_{Cu})$ for the current values of copper grading in the concentrate and in the ore.

The next task is the estimation of smelting costs. Using approximation method as above for the parameters as in Table 2 we will obtain the result presented in Fig. 4.

When we have the dependence models and assessment of their parameters, we can simulate revenue limits from production of concentrates for the mine and processing plant complex. Figures 6-7 show the results of such calculations for a practical scope

of metal grading in ore and concentrate. The NSR values are presented with reference to the values of metals in the concentrate in two variants: (a) without accessory metals, and (b) taking those metals into account in the revenue calculation. Penalties (*P*) for undesirable components and bonuses (*B*) for desirable ones are neglected in these examples.

Table 1. The data adopted for calculations. Component grades of the main product of operations. Prices on the LME of 23 Dec. 2011

Concentrate Factor	Components	Mine	Concentrator	Smelter	Market
CF(i)	Metal		Grade, %		Price $/Mg
15.43	Cu	1.67000	25.76000	98.50	7 590
13.00	Ag	0.00462	0.06010	0.23	942 581
15.00	Au	0.00002	0.00034	0.00	51 838 710
11.11	Pb	0.19777	2.19713	8.57	0
11.16	As	0.14492	1.61666	4.85	0
1.60	C	4.49703	7.19495	0.00	0
1.75	H2O	4.87000	8.51000	0.00	0
	ε_{Cu}	100.00	88.00	98.50	
	γ_1	100.00	5.70	1.42	

Table 2. Parameters and calculations of $\beta=f(\alpha_{Cu}^{*}, \beta_{Cu}^{*})$ function

α	β	$\varepsilon(\beta)$	γ_1
1.67%	25.76%	0.880	0.057
β_{max}=0.7	1.67%	1.000	1.000
	15%	0.962	0.107
A=2	20%	0.928	0.072
	25%	0.883	0.059
	30%	0.828	0.046
	35%	0.762	0.036

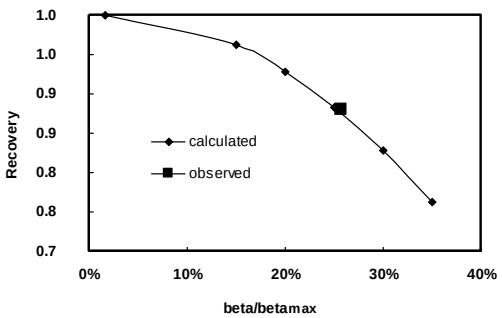

Fig. 4 Approximation of the recovery function $\varepsilon_{Cu}=f(\beta_{Cu})$ for the parameters A=2 and β_{max}=70%. The square marks the empirical value

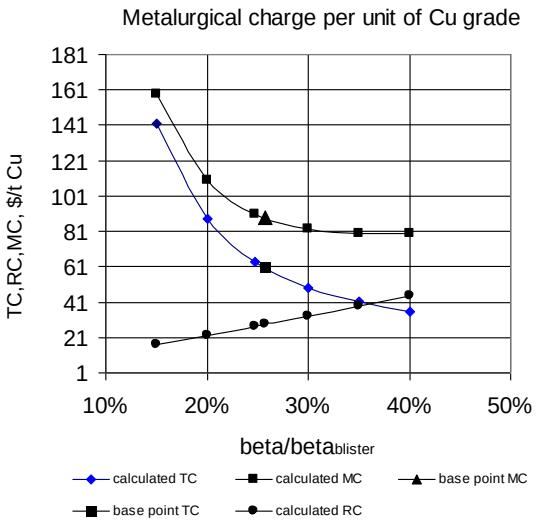

Fig. 5. Base (base point) and calculated costs of treatment (TC), refining (RC) and total metallurgical costs (MC) according to the data and parameters in Table 2

Table 3. Parameters of TC function and calculations of metallurgical costs

β	*TC*	*RC*	*MC*
	\$/Mg concentrate		
15%	142	17	158
20%	88	22	110
25%	63	27	91
25.76%	60	28	88
30%	49	33	82
35%	41	39	79
40%	35	44	79
k	C	D	
2	0.7	0.3	
β^*	TC^*	RC^*	
25.76%	60	110	

6. Conclusions

Calculations of the *NSR* revenue show that there is a certain optimum region of mining operations (α) and beneficiation (β) at which we achieve the greatest benefits from the concentrates. This method of analysis will be useful to establish or modify contractual terms in settlements between the mine and the smelter but the results of the calculations do not mean at all that the component concentrations that are optimal in the formula will be optimal at the investor level (the *NSPM* formula), that is after taking into account the costs of mining and beneficiation, which obviously depend on

the quality of mineral and the desired quality of ore and concentrates. This is a topic worthy of further investigation in that interesting field of study.

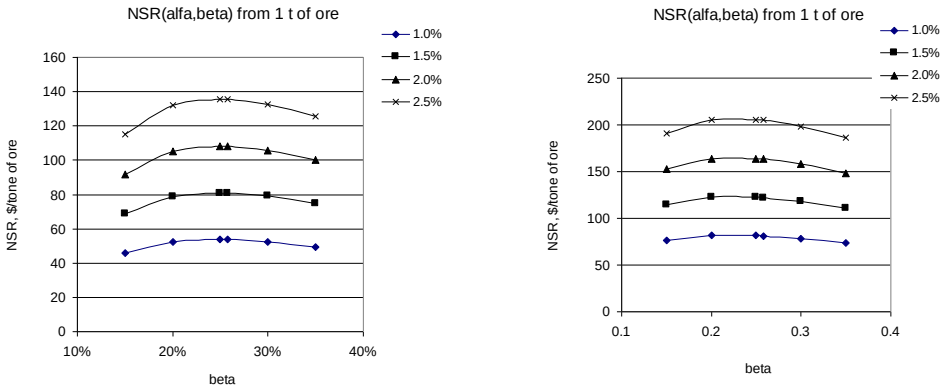

Fig. 6. The NSR revenue of the mine for different quality of ores and concentrates: (a) paid (δ=0.95) copper only, (b) paid (δ=0.95) Cu and accessory metals: Ag and Au

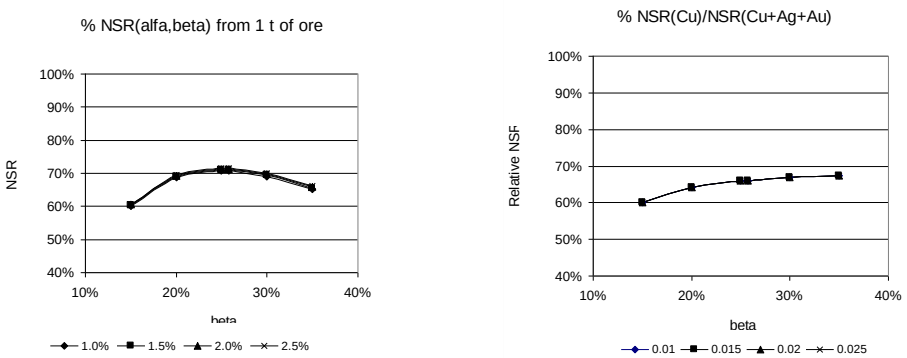

Fig. 7. (a) Relative NSR (only Cu in concentrate)/(value of Cu in ore), (b) Relative NSR (concentrate Cu)/NSR (concentrate Cu+Ag+Au)

References

CZECZOTT, H., 1937, *Przeróbka mechaniczna użytecznych ciał kop*alnych. Część II, Nakładem Komitetu Wydawniczego Dzieł ŚP. Prof. Henryka Czeczotta, Kraków (in Polish).

DRZYMAŁA, J., 2007, *Mineral processing: Foundations of theory and practice of mineralurgy*, Ofic. Wyd. PWr., Wrocław.

KRZEMIŃSKA, M., 2012, *Analiza efektywności procesów wzbogacania rud miedzi w pracach naukowych i publikacjach krajowych*, Górnictwo i Geologia 2012, Pr. Nauk. Inst.Gor. PWr.. (in Polish, in press).

ŁUSZCZKIEWICZ, A., CHMIELEWSKI, T., 2006, *Technologia chemicznej modyfikacji produktów pośrednich w układach flotacji siarczkowych rud miedzi*, Rudy i Metale Nieżelazne 51(1), 2-10 (in Polish)

MALEWSKI, J., 2008, *Metoda analizy efektywności produkcji miedzi ze złóż LGOM*, Praca statutowa 2006-2008, (unpublished, in Polish).

MMSD, 2001, *Development of the minerals cycle and the need for minerals*. A report prepared for the International Institute for Environment and Development, RSIC Ref No: 0097/November 2001

Monografia KGHM Polska Miedź S.A. Praca zbiorowa (pod red. A. Piestrzyńskiego), Lubin 2007

PAULO A., STRZELSKA-SMAKOWSKA B., 2000, *Rudy metali nieżelaznych i szlachetnych*, AGH, Uczelnianie Wydawnictwa Naukowo-Dydaktyczne, Kraków (in Polish).

PŁANETA, S., WIRTH, H., KUDEŁKO, J., GROTOWSKI, A., OFMAN, P., 2000, *Metoda oceny techniczno-ekonomicznej projektów geologiczno-górniczych*, Cuprum 14, 45-47 (in Polish).

WILLS, B.A., 2006, *Mineral processing technology*, Elsevier Sci & Techn Books, 2006.

Physicochem. Probl. Miner. Process. 48(2), 2012, 555−566

www.minproc.pwr.wroc.pl/journal/

Physicochemical Problems of Mineral Processing

ISSN 1643-1049 (print)
ISSN 2084-4735 (online)

Received December 17, 2011; reviewed; accepted May 10, 2012

FLOCCULATION PERFORMANCE OF FINE PARTICLES IN TRAVERTINE SLIME SUSPENSION

Eyup SABAH, Ceyhun ACIKSOZ

Afyon Kocatepe University, Engineering Faculty, Department of Mining Engineering, 03200 Afyonkarahisar, Turkey, Tel.: +90 272 228 14 23/1320; Fax:+90 272 228 14 22, esabah@aku.edu.tr

Abstract. The flocculation performance of new generation of flocculants (Magnafloc 5250 and 6250) possessing unique molecular architecture (UMA) and conventional polyacrylamide based SB 1836 was investigated for the solid-liquid separation of travertine processing wastewater. The settling rate and turbidity values were considered as the performance criteria. Based on the settling rate and turbidity values the anionic UMA flocculant 6260 showed better performance compared to the other anionic flocculants, SB 1836, which is currently used in the travertine processing plant, and the UMA flocculant 5250. The results obtained from this study clearly indicated that the type of the flocculants showed no significant effect on the adsorption of the polymers on the travertine particles at natural pH. The settling rates of the travertine particles and the turbidity of the suspensions were greatly affected by the surface charge of the flocculants at high and low pH regimes. The flocculation tests results with the medium charge flocculants (Magnafloc 5250 and SB 1836) were slightly affected by pH, and resulted in poor performance in terms of turbidity.

keywords: travertine processing, wastewater, flocculation, settling rate, turbidity

1. Introduction

The use of natural stones such as marble and travertine in construction industry has been growing rapidly during the last few years. Particularly, there is a significant increase in production level for both domestic consumption and export markets in Turkey. However, processing of marble and travertine for the end use generates fine dust. In addition, a significant amount of water is used for cutting, shaping, and polishing operations. For this reason recovery and reuse of water from these processes has become an important topic of interest from both environmental and a dust suppression point of view.

Although thickeners may be utilized to settle and remove particles less than 75 μm, some colloidal particles (<1 μm) may still remain in water which adversely affects surface polishing and cause plugging in pipes (Acar, 2001; Önenç, 2001). Sedimentation, another method used to dewater travertine processing wastes is often applied with addition of water soluble polymers which accelerate the settling of

http://dx.doi.org/10.5277/ppmp120219

particles. An effective solid–liquid separation of tailings is crucial for producing good quality circulating water and also for obtaining an underflow with high percentage of solids which in turns enhances the performance of mineral processing equipment in plant and tailing dam.

Developments of future flocculants including polyacrylamide-based ones is likely to be based on the "molecular architecture" concept. That will enable to produce the flocculants of required performance to meet the increasing and changing demands of solid–liquid separation processes in mineral industry. The UMA^{TM} approach is an unconventional way of thinking in polymer design and presents multiple pictures (Pearse et al., 2001). For example, highly branched and reactive polymer chains produce flocculant solutions containing a proportion of semi-particulate entities and polymer chains reticulated in three dimensions which produce flocs of different characteristics than those formed by conventional flocculants. Another aspect of UMA technology is manipulation of the molecular mass distribution to produce fractions that have greater activity in efficient flocculation. Benefits to be seen from this approach are better overall dosage efficiency, better clarification at a given settling rate and better rheological properties of settled solids than shown with conventional flocculants in terms of higher solids concentrations for a given yield stress (Pearse, 2003).

The aim of this study was to investigate the type and concentration of flocculants for solid-liquid separation of travertine processing wastewater. The new generation flocculants (Unique Molecular Architecture) were used to obtain a high settling velocity, hence a solid waste at high solid ratio, and finally circulation water with low turbidity. The settling rate and turbidity values were considered as the performance criteria. The characterization of the particles and the process water were also performed.

2. Experimental

2.1. Materials

The travertine processing wastewater used for the flocculation tests was obtained from a local travertine company in Afyonkarahisar region in Turkey. Figure 1 shows the sample port on the plant schematic diagram. The representative samples were taken according to TSE 5667-10. Three high molecular weight polyacrylamide based polymers were used for the flocculation tests. The detailed characteristics of the polymers used for the tests are presented in Table 1. HCl and NaOH (analytical grade) solutions were used to adjust the suspension pH.

Table 1. Basic characteristics of polymers

Commercial name	Type	Molecular Weight	Charge density (%)	Supplier	Effective pH range
SB 1836	anionic	high	40* (medium)	Snf Floerger	4-12*
Magnafloc 5250	anionic	high	30* (medium)	Ciba	4-10*
Magnafloc 6260	anionic	high	49.4* (high)	Ciba	4-10*

* According to the manufacturer description

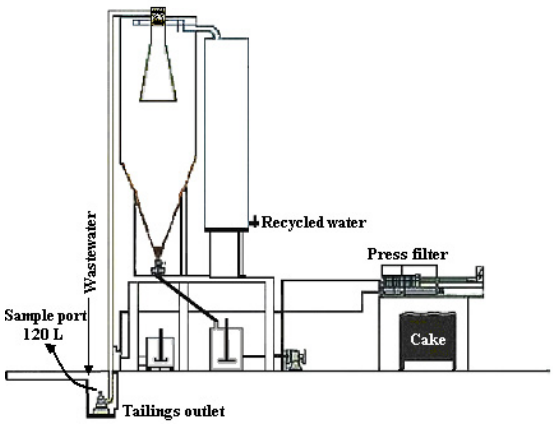

Fig.1. A schematic illustration of travertine processing plant

2.2. Methods

The hardness and cation (Mg^{2+} and Ca^{2+}) concentrations in water were determined by volumetric methods. The chemical composition of the particles was analyzed by X-ray fluorescence. The size distribution of the sample was determined using Malvern Mastersizer Particle Size Analyzer. The mineral composition of the travertine particles was determined by X-ray diffraction (XRD), using Rigaku-Giger Flex diffractometer. The zeta potential measurements for the travertine fines were conducted by Zeta-Meter 3.0, which is equipped with a microprocessor unit capable of directly measuring the average zeta potential and its standard deviation. The pH measurements were conducted with a WTW 526 pH Meter. The zeta potential experiments were carried out at 0.1% solid ratio.

A stock solution (0.1% w/v) of polymer was prepared using distilled water for the flocculation tests. A diluted solution (100 mg/dm^3) was prepared from this stock solution, and used throughout the flocculation tests. The sedimentation experiment was initiated by taking the representative suspension from the slurry. Then, the suspension was placed in a 500 cm^3 mixing cylinder with a glass stopper, and continuously agitated using a mixer at 350 rpm (DIN 12217, 2003). A specified amount of flocculant was then added to the suspension. The suspension was vigorously shaken three times. The height of the sediment bed was measured at selected time intervals after the agitation was completed (DIN 23007, 1985). After 15 min of settling of the suspension, an aliquot of the supernatant was taken for turbidity measurements using a WTW Turb 550 turbidimeter.

The operating conditions were adjusted at the required levels according to the Box-Behnken experimental design and the results have been interpreted by SPSS 15.0 software package to evaluate optimum parameter values.

3. Results and discussion

3.1. Characterization of travertine samples

3.1.1. Mineralogical and chemical analyses

The X-ray diffraction (XRD) and chemical analysis (Table 2) revealed that the travertine sample is predominately composed of calcite.

Table 2. Chemical compositions of travertine fines

CaO %	MgO %	Fe_2O_3 %	SiO_2 %	Al_2O_3 %	Na_2O %	K_2O %	LOI %
55.27	0.42	0.06	0.32	0.05	0.27	0.06	43.55

3.1.2. Particle size distribution

As shown in Fig. 2 more than 90% of the sample is composed of particle with the diameter less than 38 μm. The average particle size was found to be 10.3 μm.

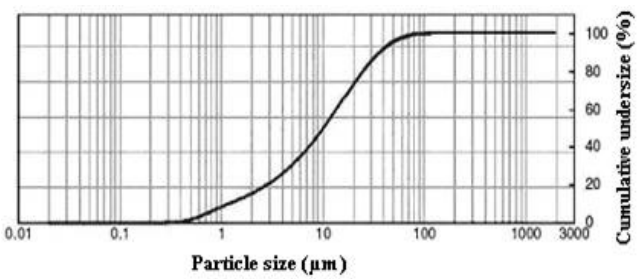

Fig. 2. Particle size analysis of travertine fines

3.1.3. Zeta potential

Zeta potential is a measure of surface charge acquired on particles in a liquid. Zeta potential provides important information about the behavior of particles in dispersing medium and stability of the dispersion. Figure 3 shows the zeta potential of the sample as a function of pH. In these experiments, NaOH and slaked lime ($Ca(OH)_2$) were used to adjust the pH of the suspension. The zeta potential value of the particles at natural pH (8.23) was found to be -13.7 mV. As shown in Fig. 3, the tailings exhibit negative charge at all pH values with no apparent point of zero charge (pzc) when NaOH was used to adjust the pH. However, the negative charge of the particles reversed and became positive at high pH values (11-12) when $Ca(OH)_2$ was used to adjust the suspension pH. As shown in the speciation diagram for Ca^{2+}, in aqueous solution Ca^{2+} concentration is higher at the pHs 11-12. In addition, $CaOH^+$ concentration increases with pH increasing from 10 to 12. The concentration of Ca^{2+} and $CaOH^+$ has a profound effect on the zeta potential of travertine fines acquiring

negative charge in water. The increasing concentration of $Ca^{2+}$and $CaOH^{+}$ ions in the suspension caused the zeta potential values to shift toward more positive values due to Ca^{2+} and $CaOH^{+}$ adsorption on negatives sites of the travertine surfaces. Generally, polyvalent ions (e.g. CO_3^{2-}, Mg^{2+}, Ca^{2+}) tend to change the surface charge by adsorption onto oppositely charged surface sites on travertine fines. On the other hand, the zeta potential of travertine fines in the presence of monovalent cations such as Na^{+} did not show similar trend. The increase in the concentration of OH^{-} ions with the increasing pH also increases the negative charge of the travertine particles, hence the zeta potential values shift toward more negative values.

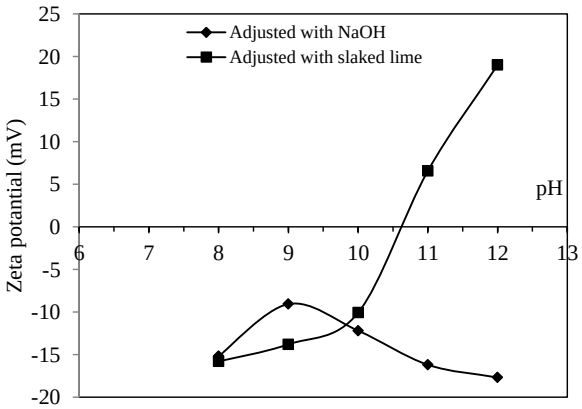

Fig. 3. Zeta potential of the travertine fines as a function of pH

3.2. Characterization of travertine suspensions

The ionic composition of water is important in flocculation of fine and colloidal particles. When hardness of water is less than 9^0F, interaction between polymer molecules and colloidal particles weakens due to relation between hardness of water and effectiveness of a flocculant. Therefore, not only an inferior settling rate but also low turbidity is observed (Sabah and Erkan, 2006).

The flocculation experiments were carried out with the travertine processing water. The hardness of the travertine processing water from which tailings are dewatered is 26ºF. This is well above the proposed limiting value and falls within the class of very hard waters because of high bivalent ion concentration (29.7 mg/dm^3 Mg^{2+} and 54.4 mg/dm^3 Ca^{2+}). These colloidal suspensions usually exhibit relatively high conductivity.

Figure 4 shows the effect of pH on settling behavior of the particles in the travertine processing wastewater at 1.1% (w/w) solid ratio without any flocculants.

According to ASTM D-4187 Standard Test Method (1990), if zeta-potential of colloids in water or waste slurry is above -60 mV, the stability of the system is

classified as 'perfect'. The maximum zeta potential values for the travertine slurry for this work was reported to be –17.7 mV and +19 mV at pH 7 and 12 respectively. Therefore, the stability of the travertine processing slurry is considered to be weak and could be improved by using coagulation or flocculation. The settling rate and the turbidity results shown in Fig. 6 also confirm this behavior.

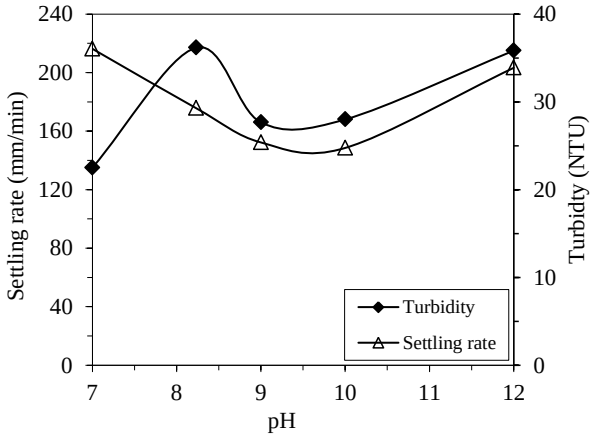

Fig. 4. Influence of pH on settling rate and turbidity for original travertine processing wastewater without flocculants

3.3. Flocculation tests

Figures 5a and b show the effect of flocculant dosage on the settling rate and the turbidity using two new generation flocculants (Magnafloc 5250 and 6260) along with a conventional flocculant SB 1836. As seen in Fig. 5a, the settling rate of the particles gradually increases with an increase in flocculant dosage for all flocculants. On the other hand, it was observed that the travertine suspensions can have similar clarity of supernatant with lower flocculant addition as shown in Fig. 5b. Based on these results, an optimum flocculant dosage at 900 mm/min setting rate occurs at 37.5 g/Mg of solids. This settling rate is higher compared to the settling rates for the same size coal settling speeds and wastes from ceramic processing plants (Cengiz et al., 2004).

These results indicate that the best settling performance for the fine particles was obtained with Magnafloc 6260 flocculant in terms of both settling rate and supernatant turbidity. An optimum flocculant dosage for Magnafloc 6260 appears to be about 12.5 g/Mg-solids. This concentration resulted in a turbidity of 6.25 NTU and a settling rate of about 558.6 mm/min. It is interesting to note that although the flocculant and the travertine fine particles are negatively charged, a higher sedimentation performance was achieved. The possible mechanism for polymer adsorption on the fine particles may be listed as follows: (i) the presence of the polymer COO^- pendant group,

although leads to a more expanded polymer chain conformation at natural pH, apparently mitigates the adsorption onto the negatively charged travertine particles. (ii) at low concentrations of Magnafloc 6260 (12.5 g/Mg of solids), the high settling rates and low turbidities were achieved due to chemical bonding between metal sites on the travertine surfaces and the flocculants' high charge density anionic groups.

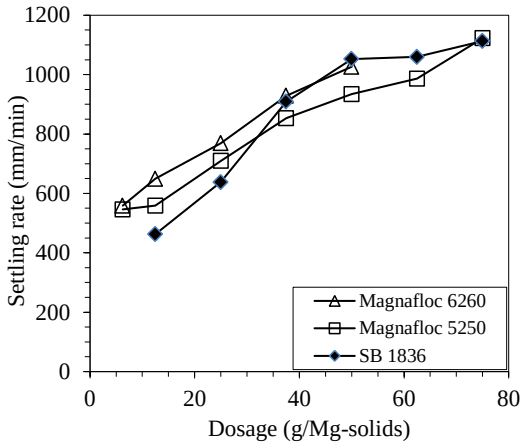

(a)

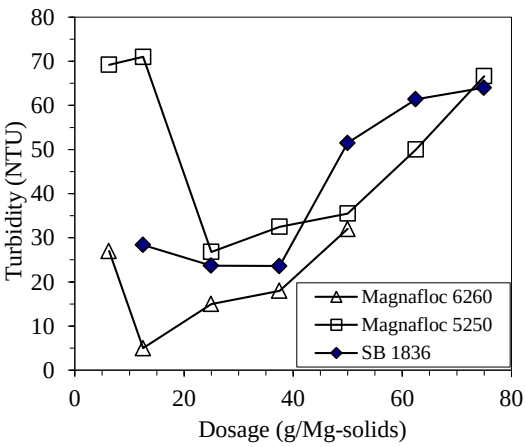

(b)

Fig. 5. Effects of polymer type and dosage on the settling rate (a) and turbidity (b) (solid concentration: 4%, pH 8.23)

Figure 3 clearly shows that the surface charge of travertine fines is low at natural pH of 8.23. Under these circumstances, the acceleration of particle aggregations should be expected. As a result, the bigger aggregates will settle faster due to gravity. Therefore, all flocculants showed good performance with regard to settling rate and turbidity. On the other hand, Magnafloc 5250 which has a relatively low charge density compared to other flocculants showed a dispersive effect at low dosages. In

such systems, with negatively charged particles, this is an expected behavior with polymers of high molecular weight and low to high charge density. At low concentrations of Magnafloc 6260 (12.5 g/Mg of solids), the high settling rates and low turbidities were achieved due to chemical bonding between metal sites on the surface of the travertine fines and the flocculants' high charge density anionic groups.

The type of the flocculant showed significant effect on the adsorption of the flocculants on the travertine particles at natural pH, as seen in Fig. 6a and b. However at pH values lower or higher than the natural pH these flocculants show different performance in terms of settling rates and turbidity. This behavior is understandable since each polymer has different chemical structure and different affinity for a given particle surface.

The settling rate and the turbidity of the travertine fine particles was significantly affected by the charge density of the flocculants at high and low pH values. The suspensions with low turbidities were obtained at low and high pH values with the use of high surface charge density Magnafloc 6260 floculant. The flocculation tests with Magnafloc 5250 (medium charge density) were slightly affected by pH, and hence exhibited a poor sedimentation performance in terms of turbidity. However, the flocculation tests with the conventional flocculant SB 1836 (medium charge density) showed an unstable behavior with a pH dependent flocculation of colloidal particles.

The high charge density Magnafloc 6260 formed small and compact flocs in the travertine process water at natural pH. This caused a decrease in the settling rate of the travertine fine particles with a clear supernatant. The decrease in the settling rate is due to the decrease in the number of carboxyl groups of the anionic polymer which can be hydrolyzed in the acidic pH. It is plausible that the intra molecular bonds between carboxyl groups may cause the polymer molecule to form a ring shape and thus weakening the bridge formation. The suspension pH can change charge characteristics of polymer chain and their conformation in solution and thus may directly affect the flocculation power of polymer (Foshee et al., 1982; Reuter and Hartan, 1986). The flocculation power of anionic polymers by bridging decreases as the polymer molecules are in a random coil conformation in sections, whereas at relatively high pH the configurations of the polymer extends due to electrostatic repulsion between the charged groups on the polymer chain. Taylor et al. (2002) and Sworska et al. (2000) reported that the addition of Ca^{2+} and Mg^{2+} ions prior to the addition of the flocculant improves the clarity of the supernatant in alkaline environment in the presence of stable clay suspensions.

Obtaining a fairly clear supernatant (with low turbidity) is important since water used in cutting and polishing operation is generally recycled. In order to achieve a suspension with a lower turbidity, the suspension pH was adjusted using slaked lime. The tests results with Magnafloc 6260 indicated that the best flocculant performance can be achieved by utilizing lime for the adjustment of the suspension pH. The lime resulted in much lower turbidity (0.33 NTU) and also reduced the required flocculant dosage (25 g/ton-solids). However, the settling rate decreased to 371 mm/min which is

tolerable level. These results indicate that Ca^{2+} adsorption at the travertine-H_2O interface involves the transfer of Ca^{2+} ions into Stern plane without the release of an equivalent number of protons into the diffuse layer and bulk solution. The subsequent decrease in the zeta-potential due to adsorption of Ca^{2+} ions may be related to unstable colloidal suspension and very small, dispersed floc particles in the presence of Ca^{2+} solutions when lime was used as pH modifier. This may imply that if lime solutions were to be added to the travertine slime suspension prior to Magnafloc 6260 addition, there is a good probability that the flocculation would be "activated" because of the presence of Ca^{2+} ions in the system. In addition, Ca^{2+} ions may also act as bridges between the anionic sites on the ionized polymer chain and travertine fines at pH 9 as shown in Fig. 7

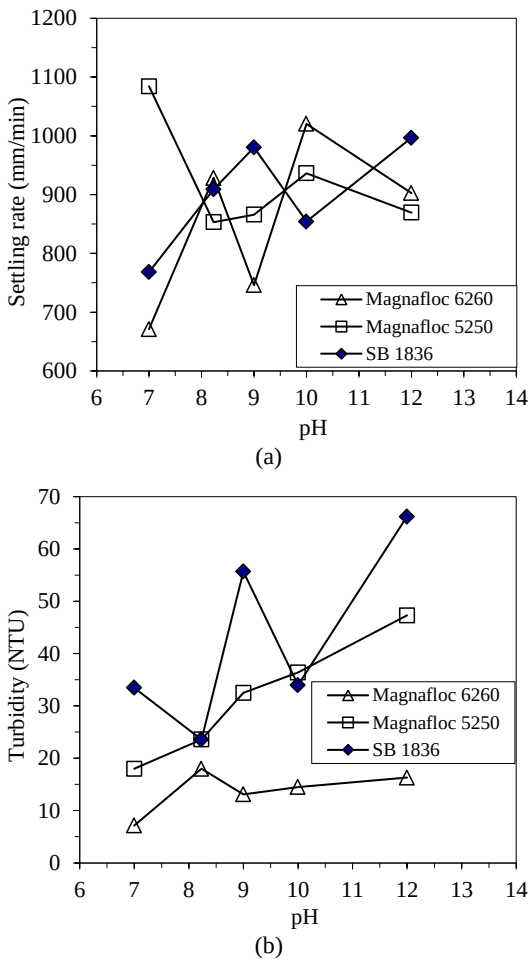

Fig. 6. Effect of suspension pH on settling rate (a) and turbidity (b) at optimum polymer dosages (solids concentration: 4%, pH 8.23, dosage 37.5 g/Mg of solids)

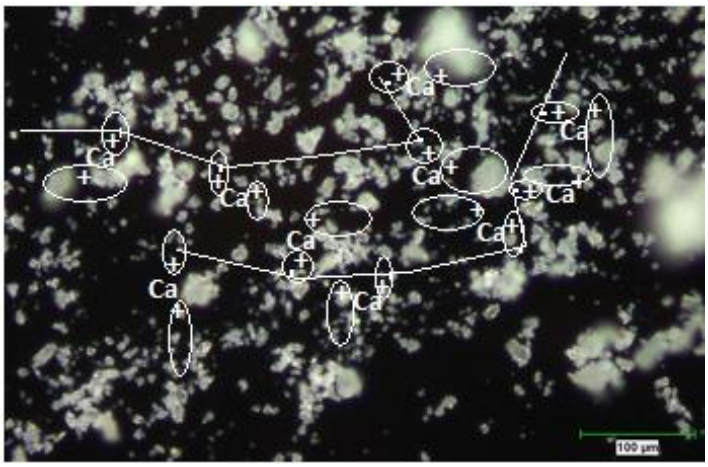

Fig. 7. Schematic illustration of Ca^{2+} activation on adsorption of high molecular weight anionic flocculant onto a negatively charged suspended travertine fines

3.4. Modeling of settling rate and turbidity

The regression analysis was chosen to determine the relationship between the response functions (settling rate and the turbidity) and the operating conditions (dosage and pH). A two factor matrix three level Box-Behnken design was used to determine the response (settling rate and turbidity). Two significant variables of flocculation performance are flocculant dosage and pH. When the number of tests at the central points is three, the total number of tests required for the two variables comes out to be $3^2+2+2=13$ for the Box-Behnken design (Souzaa et al., 2005). The variables and their levels used in this study are shown in Table 3.

Table 3. The level of variables chosen for the Box-Behnken design.

Variable		Variable level		
		Low	Center	High
		-1	0	+1
Dosage, g/Mg of solids	x_1	6,25	37,5	75
pH	x_2	7	9	12

For the three-level two-factorial Box-Behnken experimental design, a total of 13 experimental runs are needed. Using the relationships in Table 3, the levels of the variables for each of the experiments in the design matrix were calculated as given in Table 4.

For the settling rate of travertine:

$SR_{SB\ 1836}= 77 + 10.3\cdot D + 44.3\cdot pH$; $R^2 = 0.832$

$SR_{MG\ 5250}= 579 + 8.41\cdot D - 4.5\cdot pH$; $R^2 = 0.778$

$SR_{MG\ 6260}= 182 + 8.35\cdot D + 31.3\cdot pH$; $R^2 = 0.702$.

For the turbidity of travertine:

$T_{SB\ 1836}$= - 43.3 + 0.738·D + 6.38·pH; R^2 = 0.681

$T_{MG\ 5250}$=30.9 + 0.087·D-1.72·pH; R^2 = 0.022

$T_{MG\ 6260}$=13 + 0.056·D + 0.13·pH; R^2 = 0.012.

Table 4. The level of variables x_1 and x_2

Run no.	Dosage (g/Mg of solid)	pH
1	0	1
2	0	-1
3	-1	0
4	1	-1
5	1	0
6	0	0
7	-1	1
8	0	0
9	-1	-1
10	0	0
11	0	0
12	0	0
13	1	1

$SR_{SB\ 1836}$ is the settling rate (mm/min) of the travertine suspension with SB 1836, $SR_{MG\ 5250}$ is settling rate (mm/min) of the travertine with Magnafloc 5250, $SR_{MG\ 6260}$ settling rate (mm/min) of the travertine with Magnafloc 6260, $T_{SB\ 1836}$ turbidity (NTU) of the travertine with SB 1836, $T_{MG\ 5250}$ turbidity (NTU) of the travertine with Magnafloc 5250, $T_{MG\ 6260}$ turbidity (NTU) of the travertine with Magnafloc 6260, D polymer dosage in flocculation tests (6.25-75 g/Mg) and pH (7-12) is pH solution in flocculation tests.

The match of predicted values with the actual data points indicates a good fit (R^2 value of 0.832, 0.778, and 0.702 with SB 1836, Magnafloc 5250, and Magnafloc 6260, respectively) of the equation for settling rate of travertine. For the turbidity of travertine, the predicted values and the observed data points, indicating a poor fit with SB 1836 (R^2 value of 0.681) and a very poor fit with Magnafloc 5250 and Magnafloc 6260 (R^2 value of 0.022 and 0.012, respectively) of the equations.

4. Conclusions

The results from the zeta potential experiments for the fine particles indicated that the particles are negatively charged at all pH values with no apparent point of zero charge. On the other hand, the zeta potential of the particles measured using slaked lime showed positive charge at high pH values. This can be attributed to the specific adsorption of the dissolved ions such as Ca^{2+} and $CaOH^{+}$ on the particles.

In terms of the settling rate and turbidity, the UMA Magnafloc 6260 anionic polymer showed a better flocculation performance compared to UMA Magnafloc 5250 and conventional SB 1816 at natural pH of travertine suspension.

The polymer charge density at high and low pH regimes played a crucial role in the flocculation of the travertine particles. On the other hand, the medium charge density polymers (Magnafloc 5250 and SB 1836) were slightly affected by pH, and exhibited a very bad performance in terms of the turbidity. In the case of the pH dependant flocculation of colloidal particles, conventional flocculant SB 1836 presented an unstable behavior.

The decrease in the polymer dosage and turbidity (0.33 NTU) can be achieved by Magnafloc 6260 when slaked lime is used to adjust the suspension pH due to the presence of Ca^{2+} ions in the system.

Acknowledgements

The financial support of Scientific Research Commission (BAPK) of Afyon Kocatepe University is greatly acknowledged.

References

ACAR, H., 2001, *Particular points in construction and operation of the water recycling system for marble processing plant*, 3th Marble Symposium, Afyonkarahisar-Turkey, 289-296.

ASTM D4187-82, 1990, Methods of Test for Zeta Potential of Colloids in Water and Waste Water.

CENGIZ, İ., SABAH, E., ERKAN, Z.E., 2004, *A Study on the Flocculation Performance of Conventional and UMA (Unique Molecular Architecture) Technology Polymers*, Madencilik. 43(1), 15–23.

DIN 23007, 1985, *The German Institute for Standardization. Flocculants for Process Water*, Beuth-Vertrieb GmbH, Berlin.

DIN 12217, 2003, *The German Institute for Standardization. Doors - Operating Forces - Requirements and Classification*, Beuth-Vertrieb GmbH, Berlin.

FOSHEE, W.C., SWAN, W.J., KLİMPEL, R.R., 1982, *Improvement in Coal Preparation. Water Classification Through Polymer Flocculation*, Miner. Eng. 34, 93–97.

ÖNENÇ, D. İ., 2001, *The Blocks Becoming Powder and The Hopes*, Marble. 7 (30), 66–68.

PEARSE, M.J., WEIR, S., ADKINS, S.J., MOODY, G.M., 2001, *Advances in Mineral Flocculation*, Miner. Eng. 14 (11), 1505–1511.

PEARSE, M. J., 2003, *Historical Use and Future Development of Chemicals for Solid–Liquid Separation in the Mineral Processing Industry*, Miner. Eng. 16, 103–108.

REUTER, J.M., HARTAN, H.G., 1986, *Structure and Reaction Kinetics of Polyelectrolytes and Their Use in Solid–Liquid Processing*, Aufbereitungs-Technik. 11, 598–606.

SABAH, E., ERKAN, Z.E. 2006, *Interaction Mechanism of Flocculants with Coal Waste Slurry*, Fuel. 85, 350–359.

SOUZAA, A.S., WALTER, N.L., SERGIO FERRIA, L.C., 2005, *Application of Box–Behnken design in the optimization of an on-line pre-concentration system using knotted reactor for cadmium determination by flame atomic absorption spectrometry*, Spectrochim. Acta B. 60, 737–742.

SWORSKA, A., LASKOWSKI, J.S., CYMERMAN, G., 2000, *Flocculation of the Syncrude Fine Tailings: Part I. Effect of pH, Polymer Dosage and Mg^{2+} and Ca^{2+} Cation*, Int. J. Miner. Process. 60, 143–152.

TAYLOR, M.L., MORRİS, G.E., SELF, P.G., SMART, R.C., 2002, *Kinetics of Adsorption of High Molecular Weight Anionic Polyacrylamide onto Kaolinite*. J. Colloid. Interf. Sci. 250, 28–36.

TS 5667-10, 2002. *Sampling methods of wastewater*, Turkish Standard Institution.

Physicochem. Probl. Miner. Process. 48(2), 2012, 567−578

www.minproc.pwr.wroc.pl/journal/

Physicochemical Problems of Mineral Processing

ISSN 1643-1049 (print)
ISSN 2084-4735 (online)

Received April 11, 2012; reviewed; accepted May 1, 2012

EFFECTIVE PROCESSING OF LOW-GRADE IRON ORE THROUGH GRAVITY AND MAGNETIC SEPARATION TECHNIQUES

Ahmed A. S. SEIFELNASSR*, Eltahir M. MOSLIM, Abdel-Zaher M. ABOUZEID*****

*Suez Canal University, Faculty of Engineering, Dept. Mining, Suez, Egypt
** Omdurman Islamic University, Faculty of Engineering Sciences, Dept. Mining, Khartoum, Sudan
*** Cairo University, Faculty of Engineering, Dept. Mining, Giza, Egypt, abdel.abouzeid@gmail.com

Abstract. This study investigates the effectiveness of gravity and magnetic concentration techniques for the beneficiation of a Sudanese iron ore, the newly discovered Wadi Halfa iron ore deposit. It is a low-grade type of ore with high silica content, more than 45% SiO_2, and an average iron content of about 35% Fe. Based on the fact that there are appreciable differences in specific gravity and magnetic susceptibility between the desired iron minerals and the gangue minerals, it was suggested that gravity separation and/or magnetic separation may be useful to concentrate this type of ore. These two techniques were adopted for the beneficiation of the Wadi Halfa low-grade iron ore. As a result of the fine dissemination of the iron minerals and the most abundant gangue mineral, quartz, the optimum degree of grinding is around 150 micrometers. The rougher tests of both the gravity separation and magnetic separation produced concentrates of about 44% Fe. Each of these two concentrates was cleaned in a second stage of processing using high intensity magnetic separator. Final iron concentrates, assaying about 64% Fe at a recovery of about 70%, were achieved.

keywords: Wadi Halfa iron ore, low-grade iron ore, gravity concentration, magnetic concentration, combined gravity/magnetic concentration

1. Introduction

With increasing global demand of iron ores due to the huge requirement of steel all over the world, important iron ore producing countries have increased their production by initiating steps to utilize the low-grade iron ores, fines, and slimes. The main difficulty in processing and utilization of low-grade iron ores primarily stems from their mineralogical characteristics as well as the soft nature of some ores and their high silica content. Thus, beneficiating the low-grade iron ores to remove the gangue minerals and enhancing their grade is an attractive proposition today. Among the known iron deposits in Sudan, many are of low-grade which require beneficiation to produce an acceptable feed for steel making plants.

Wadi Halfa iron ore, in Northern Sudan, is one of these types. The problem in up-grading this deposit is two-fold. Firstly, the iron minerals occur as a mixture of

http://dx.doi.org/10.5277/ppmp120220

goethite and hematite in an oolitic pisolitic texture. Secondly, the iron minerals are finely disseminated in silica and silicates. This requires fine grinding to obtain adequate degree of liberation of the desired iron mineral and the gangue constituents. The location of Wadi Halfa iron ore deposit, in the Northern State, is bounded by latitude 21º 45' and 22º 00' N and longitudes 31º 15' and 31º 45' E. The iron ore deposits of this area are located on both sides of Lake Nasser. The ore exists in several layers in stratified succession. The iron ore tonnage is estimated for only one layer of the deposit to be about 400-800 Tg (teragrams or million tons) at an average assay of 36% Fe. Since the ore is multi-layered, the tonnage given could be an underestimation of the whole reserves. In addition, the western part of the area is not yet assessed but it could add some additional reserves (Ali et al., 2004; Moslim, 2010).

The processing of this particular iron ore is worthy to be considered for many reasons. It's occurrence beside the Nile River; hence water will be available in terms of quantity and quality. Electricity is underway in the near future when the national grid reaches Halfa from Merawe Dam. Railway line connects Halfa to the rest of the country. Skilled labor is available in the area**.**

The most commonly used beneficiation methods for iron ores are the gravity and magnetic separation methods. Recovery of valuables from natural ores by gravity concentration process is one of the oldest and most economic techniques (Brut, 1999). Although in the twentieth century gravity concentration has been partially replaced by other techniques, notably, flotation and magnetic separation, they have not made it obsolete. Gravity separation techniques are widely used in mineral beneficiation practices for its low-cost, ease of operation, and eco-friendly nature. They are based on the differential settling velocities of the constituting particle of the ore.

The settling velocity of particles is governed jointly by weight (volume and density), buoyancy, and drag forces. The most commonly used gravity techniques for beneficiation of iron ores are shaking tables, jigs (Roy, 2009) and spirals. Upgrading iron ores by jigging has been an emerging trend (Mukherjee, 2006). Flowing film gravity concentration using Wilfley table is a powerful technique for the recovery of fine iron minerals. Many theoretical and experimental investigations of Wilfley table performance have been reported (Gaudin, 1987; Mansar, et al., 1999; Shivamohan, and Forssberg, 1985). Tabling efficiency is quite high when the specific gravity difference between valuable and gangue minerals is high (Samykina et al., 2005). In addition, for upgrading iron ores, magnetic separation may be preferred solely or in combination with gravity separation, depending on the ore characteristics (Svoboda, and Ross, 1989; Svoboda, 1994; Svoboda and Fujita, 2003).

Beneficiation of Camdag iron (oolitic) hematite ore containing limonite-hematite or goethite-limonite using gravity separation and high intensity magnetic separation, increases the grade of ore about 5-7% in concentrates with about 60% recovery by both methods (Guney et al., 2000). Abouzeid (1967) studied the possibility of using high intensity magnetic separator for the beneficiation of El-Gedida iron ore. An ore sample containing 51.6% Fe, 8.76% SiO_2 and 3.06% BaO was used for the study. He

found that high intensity magnetic separator tests were limited to very close range of sizes between 2 and 0.125 mm. The final magnetic product assayed 61% Fe at an iron recovery of 90.3%. However, 5% by weight was obtained as middling assaying 31.4% Fe. These middling products, together with the fine fraction minus 0.125mm which constitute 35% by weight of the whole sample, were not possible to be upgraded by magnetic separation. The barite-riche iron ore of the same deposit was treated by anionic flotation using Na-DDS as a collector for floating barium sulfate, and sodium silicate as a depressant for iron minerals (Mossallam, 2004). The feed size fraction for the flotation cell was -250+80 μm assaying 36.5% Fe and 23% BaO. After several cleaning stages by flotation, an iron concentrate assaying 62% Fe with less than 2% BaO at a recovery of 71.3% was obtained.

Rowayshed (1983) studied the possibility of using high intensity magnetic separator for beneficiation of El-Gedida. He found that high intensity magnetic separator is limited by a much-closed range of sizes less than 2 mm, neither the coarse nor the very fine sizes can be treated by this method. The dominant iron minerals present in this ore are the hydrated minerals, goethite and hydro-goethite, which are difficult to treat through the high intensity magnetic separator.

Fatma et al. (1999) studied the beneficiation of an iron ore sample containing 44% Fe, 1.59% SiO_2 and 20% BaO. By magnetic separation, two products of iron ore and barite concentrates were obtained by using a high intensity magnetic separator. The fine fraction (-0.125 mm) is about 20% by weight assaying 54.6% Fe, and 3.91% BaO, which needs further cleaning to reduce the barite content to meet the smelter specifications (52% Fe, and 2% BaO). The size (0.74 +0.106 mm) fraction, after concentration by H.I.M.S., still contains 41.9% Fe and 11.55% BaO. After cleaning several times using H.I.M.S, an iron concentrate assaying 58.48% Fe, and 0.73% BaO is obtained. Final iron concentrate was obtained assaying 64.2% Fe, and 0.24% BaO.

Faraghaly (2002) studied an iron ore containing 23.5% Fe and 34% BaO using a dry high intensity magnetic separator for the processing of a feed size fraction of -1+0.125 mm (about 69% by weight of the original feed size). A concentrate containing 56.78% Fe and 1.61% BaO at a recovery of 82.76% was obtained. Reduction roasting process was carried out on the fine fraction (-0.125mm) which represents about 31% by weight of the head sample. A concentrate assaying 56.78%Fe, and 1.61%BaO, with recovery of 82.76% was obtained.

The iron ore at Wadi Halfa is intercalated with Nubian sedimentary rock faces and overlies these rocks. The stratigraphy of the area from bottom to top is composed of whitish to violet clayey sandstone, followed by iron-bearing rocks (usually varied in thickness), conglomerates, and then ferruginous layes intercalated with Nubian sandstone, which is usually capped with oolitic ironstone. The stratigraphy is repetitive in nature indicating several or multiple depositional sedimentary cycles. Chemically and structurally, the oolitic iron ore of Wadi Halfa can be classified into three types. These are: 1) hematitic oolitic type is red in color because hematite is domination in the ore. It is fine grained and is always found at the base of the iron

oolitic form colony, 2) oolitic goethitic iron ore which is black in color indicates supergene sedimentary conditions associated with the precipitation of the iron ore, 3) brown oolitic iron formation is an intermediate species between the above two mentioned types in terms of composition and color (Ali et al., 2003).

It is worth mentioning that the Wadi Halfa iron ore deposit was discovered recently by the Geological Research Authority of Sudan (GRAS) (Ali et al., 2004). No beneficiation studies have been reported concerning this deposit until now.

The main objective of this study is to investigate the amenability of Wadi Halfa (Northern Sudan) low-grade iron ore for upgrading by gravity and magnetic separation techniques. The main parameters affecting the effectiveness of a shaking table (exploiting the difference in specific gravity of the main ore constituents), and a high intensity magnetic separator (exploiting the differences in magnetic susceptibility of the ore constituents) were investigated

2. Experimental

Ore sample. A composite sample of about 200 kg was collected from the iron ore deposit at Wadi Halfa area. The sample was collected from different pits in the deposit area to represent, to some extent, the actual deposit. It was crushed, well mixed, and quartered to small samples of about 1 kg each. Representative samples were prepared for chemical analysis and mineralogical studies.

Feed preparation. Some of the samples were ground in a ball mill to different degrees of fineness: -500 μm, -350 μm, and -150 μm to be used in the beneficiation experiments. These fractions were deslimed using a hydro-cyclone at a cut size of 20 μm, which made the feed fractions to be: -500+20 μm, -350+20 μm, and -150+20 μm.

Beneficiation techniques. A laboratory shaking table of dimensions 50 cm x 120 cm was used to exploit the difference in specific gravity between the iron minerals and the gangue minerals. Also, as a result of the significant difference in magnetic susceptibility between the desired and no desired minerals, a High Intensity Magnetic Separator (H. T. Readings, PTY LTD, Series No. 88.1) was used as an alternative technique for upgrading this type of iron ore.

3. Results and discussion

3.1. Characterization of the ore

Mineralogy of the ore. Using X-Ray Differential Analysis, it was found that the iron ore sample consisted of goethite, hematite, quartz, calcite kaolin, and feldspar. The major constituents were goethite as an iron mineral and quartz as a gangue mineral, and the rest were minor minerals. Under the optical microscope, it was observed that the iron minerals and quartz are finely disseminated. The ore exists in the form of oolitic and pesolitic texture.

Chemical analysis. Table 1 gives the chemical analysis of the iron ore sample used in this research work. It is clear that the iron content is relatively low, in the range of

36% Fe, and the major gangue mineral is quartz, in the range of 48% SiO_2. The rest of the undesired constituents is less than 2% each.

Table 1. Chemical analysis of Wadi Halfa iron ore sample

Constituent	Fe_2O_3	Fe (Total)	SiO_2	CaO	MgO	MnO	Al_2O_3	SO_4	P_2O_5
Percent	45.3	36.1	47.5	1.6	0.3	0.3	1.8	nil	0.1

Desliming of the ore sample. The three ball mill products: -500 μm, -350 μm, and -150 μm were deslimed using a hydro-cyclone to remove the -20 μm particles. Table 2 shows the results of the desliming tests. The slimes fraction ranges from 6% by weight in the coarse size fraction, -500 μm, to 10% by weight in the fine size fraction, -150 μm, with rejected amounts of 2.5% Fe and 8.0% Fe, respectively.

Table 2. Classification of the feed fractions

Size fraction, μm	Fraction weight, %	Assay, Fe %	Metal distribution, %
-500+20	94.3	36.7	97.5
-20	5.7	34.7	02.5
Total	100.0	36.6	100.0
-350+20	92.4	37.0	94.7
-20	7.6	31.9	5.3
Total	100	36.6	100
-150+20	90.5	37.7	92.0
-20	9.5	30.0	08.0
Total	100	36.9	100

Liberation study. The degree of liberation of the iron minerals was studied by the point counting technique. Polished sections of the different size fractions were prepared and studied under the microscope in reflected light mode. Both the free particles of iron minerals and the grains of iron minerals locked with gangue minerals in the microscope view were counted, and the percentage of free iron minerals grains relative to the sum of the two types of particles was calculated. Table 3 gives the counting results and the degree of liberation of the iron minerals

Table 3. Degree of liberation of Wadi Halfa iron ore as a function of size fraction

Size fraction, μm	No. of free iron minerals grains	No. of locked grains	Total number (free +locked)	Degree of liberation, %
-500+20	2957	2254	5211	56.7
-350+20	3053	960	4013	76.1
-150+20	2396	235	2631	91.1
-105+20	2408	105	2513	95.8

The above counts suggest that the degree of liberation increases as the grain size gets finer, which is obvious.

Concentration of the Wadi Halfa iron ore. Gravity and magnetic separation techniques seem to be two suitable candidates for upgrading this type of iron ore due

to the significant differences in specific gravity and magnetic susceptibility between the desired and no desired constituents in the ore. The important parameters in both of these techniques were investigated to find out if one of them or both could be applied to concentrate the Wadi Halfa iron ore. The following is a brief discussion of the results obtained throughout this study.

3.2. Gravity separation

Effects of the two important operating parameters of the shaking table,-feed size range and table tilt were investigated. The following summarizes the obtained results.

Effect of feed size range. The feed size ranges used in this study were +500-20 μm, -350+20 μm, and -150+20 μm. Table 4 summarizes the effect of the feed size fraction to the table on the assay and metal distribution of the iron concentrate.

Table 4. Effect of feed size fraction on the efficiency of tabling (table tilt is 5 degrees)

Size fraction, μm	Product	Product weight, %	Assay, Fe %	Metal distribution %	Metal distribution relative to original sample, %
-500+20	Concentrate	70.0	38.8	74.3	72.5
	Tailing	30.0	31.4	25.7	25.1
	Total	100	36.7	100.0	97.6
-350+20	Concentrate	72.6	41.5	82.3	77.9
	Tailing	27.4	23.6	17.7	16.8
	Total	100.0	36.5	100.0	94.7
-150+20	Concentrate	72.5	44.9	86.7	79.9
	Tailing	27.5	18.2	13.3	12.1
	Total	100	37.6	100.0	92.0

The assay of the concentrate obtained using the coarse feed is not significantly different from that of the feed. The assay of the concentrate as well as the metal recovery continued to increase as the feed size fraction decreased. The assay increased from 38.8% Fe to 44.9% Fe and the recovery increased from 74.3% to 86.7% as the feed size fraction decreased from -500+20 to -150+20 μm, respectively. These effects are logical because the degree of liberation increases as the size fraction decreases (Fig. 1).

Effect of angle of table inclination (table tilt). The tilt angle was changed between 3º and 5º. Table 5 presented the results as a function of the table tilt angle.

The optimum tilt angle is 5º. At 5º table inclination large amount of middling particles are driven towards the concentration end of the table, which increased the recovery and decreased the assay. At higher tilt angle, the wash water washes away large amounts of the iron-bearing particles towards the tailing section of the table (Fig. 2).

The above results show that the optimum parameter values for using the shaking table as a roughing stage for concentrating this type of iron ore are: feed size fraction of -150+20 μm when the table tilt angle was 5º. At these parameter values, the

concentrate assay was 44.9%Fe and the stage recovery was 86.7%. Taking the lost material in desliming into consideration, the overall recovery was 79.9%.

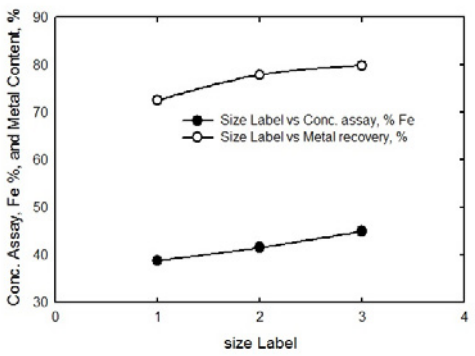

Fig. 1. Concentrate assay and metal recovery as a function of the feed size fraction to the table. The size labels are: 1 for -500+20 μm, 2 for -350+20 μm, and 3 for -150+20 μm

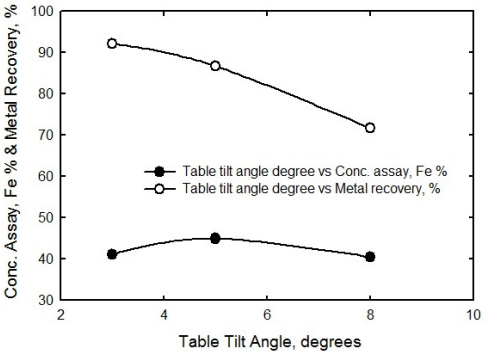

Fig. 2. Concentrate assay and metal recovery as a function of the table tilt angle

Table 5: Effect of Table inclination. Feed size fraction is -150+20 μm

Table inclination, degree	Product	Product weight, %	Assay, Fe %	Metal distribution, %	Metal distribution relative to original sample, %
3	Concentrate	83.8	41.1	92.1	79.2
	Tailing	16.2	18.0	07.9	06.8
	Total	100	37.4	100.0	86.0
5	Concentrate	72.5	44.9	86.7	79.9
	Tailing	27.5	18.2	13.3	12.1
	Total	100.0	37.6	100.0	92.0
8	Concentrate	66.0	40.5	71.7	66.0
	Tailing	34.0	31.0	28.3	28.3
	Total	100.0	37.3	100.0	94.3

3.3. Magnetic separation

Three parameters affecting the performance of the high intensity magnetic separator, feed size fraction, magnetic field intensity, and drum rotating speed were investigated. The effect of each of these operating parameters will be discussed in the following paragraphs.

Effect of feed size fraction. The feed size fractions used in this study were: -500+20 μm, -350+20 μm, and -150+20 μm. Table 6 summarizes these results.

Table 6: Effect of feed size fraction on efficiency of magnetic separation at 0.3 Ampere and 100 rpm

Size fraction μm	Product	Product weight, %	Assay Fe %	Metal distribution, %	Metal distribution relative to original sample, %
-500+20	Magnetic	65.1	38.8	74.3	72.5
	Non-magnetic	34.9	31.4	25.7	25.1
	Total	100	36.7	100.0	97.6
-350+20	Magnetic	75.3	41.5	82.3	77.9
	N0n-magnetic	24.7	23.6	17.7	16.8
	Total	100.0	36.5	100.0	94.7
-150+20	Magnetic	81.5	42.4	92.4	84.9
	Non-magnetic	18.5	16.0	7.8	7.1
	Total	100.0	36.5	100	92.0

As it was observed in the gravity separation, the optimum results were obtained at feed size fraction of -150+20 μm, where the iron assay of the concentrate was 42.4% Fe at a recovery of 92.2%. Again, this is because the finer the size fraction, the more is the liberation of the desired minerals from the gangue minerals (Fig. 3). However, the selectivity was low because of the high percentage of silica.

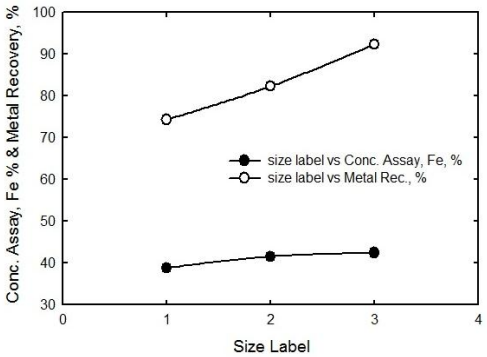

Fig. 3. Effect of feed size fraction on the concentrate assay and metal recovery using high intensity magnetic separator. The size labels are: 1 for -500+20 μm, 2 for -350+20 μm, and 3 for -150+20 μm

Effect of electric current intensity to the electromagnetic coil. The current intensity to the coil is an indication to the magnetic field intensity, as the current increases the field intensity increases. The range of the current variation in the magnetic separator that was used is from 0.1 to 0.5 Amperes. Table 7 and Figure 4 give the results of the effect of the current intensity on the assay and recovery of the concentrate.

From Table 7, it can be seen that the assay of the concentrate decreases with increasing the magnetic field intensity. This result is due to the degree of selectivity as a function of the field intensity. At low field intensity only the high magnetically susceptible particles are picked up by the rotating drum, which produces a relatively high grade concentrate (45.0% Fe) at low recovery (79.6%). The low recovery is due to the fact that a large portion of the locked particles goes with the non-magnetic fraction. The optimum result was obtained at a current intensity of 0.3 Ampere.

Table 7. Effect of magnetic field intensity. The magnet drum runs at 100 rpm

Current Ampere	Product	Product weight, %	Assay Fe %	Metal distribution, %	Metal distribution relative to original sample, %
0.1	Magnetic	66.0	45.0	79.6	73.2
	Non-magnetic	34.0	22.5	20.4	18.8
	Total	100.0	37.4	100.0	92.0
0.2	Magnetic	76.5	42.7	87.3	80.3
	Non-magnetic	23.5	20.2	12.7	11.7
	Total	100.0	37.4	100.0	92.0
0.3	Magnetic	81.5	42.4	92.2	84.8
	Non-magnetic	18.5	16.0	07.8	07.2
	Total	100.0	37.5	100.0	92.0
0.4	Magnetic	82.0	41.9	91.8	84.4
	Non-magnetic	18.0	17.0	08.2	07.6
	Total	100.0	37.4	100.0	92.0
0.5	Magnetic	83.0	41.2	91.7	84.3
	Non-magnetic	17.0	18.3	08.3	07.7
	Total	100	37.3	100.0	92.0

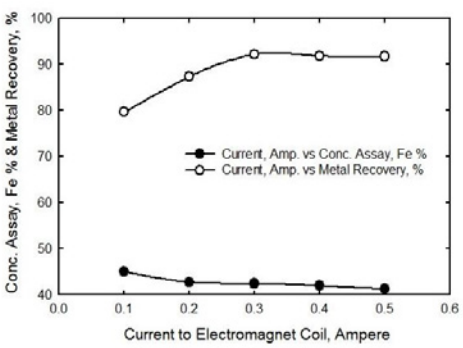

Fig. 4. Iron assay and metal recovery of the concentrate as a function of current intensity to the electromagnetic coil at this current intensity, the magnetic intensity

Effect of the drum rotational speed. The drum rotational speed was varied from 60 to 220 rpm. The main effect of the drum rotational speed is the induced centrifugal force to the flowing particles which is a function of the particle mass. However, because of the nature of the main ore constituents, iron minerals and quartz, during size reduction, the quartz particles are coarser than the iron minerals particles although less in density than the iron minerals. Also the particle weight (density multiplied by volume) is a main parameter in this case because of the gravitational force acting on the individual particles. This means that there are several forces which act on the flowing particles, namely, centrifugal force, gravitational force, and magnetic force. A combined effect of these acting forces determines the optimum operating conditions in this case. As a result of this combination of forces, the optimum result, as represented by the concentrate assay and recovery, was obtained at drum revolution of 100 rpm (Table 8 and Fig. 5).

The above results show that the conditions under which the optimum concentrate was obtained, using the high intensity magnetic separator, are feed particle size of -150+20 μm, electric current intensity of 0.3 A, and 100 rpm drum rotational speed.

This concentrate assays 42.4% Fe, at a metal recovery of 92.2%. However, as we have seen from the presented results of both the gravity separation and the magnetic separation processes, the concentrate assay under optimum operating conditions is low, 44.9% Fe, at a recovery of 86.7% in the case of the gravity separation process and 42.4% Fe, at a recovery of 92.2% in the case of the magnetic separation process. These results suggest that a cleaning stage of the concentrate obtained from the first stage may improve the assay of the final product. Based on this conclusion, the concentrates obtained from the shaking table and from the high intensity magnetic separator were, separately, subjected to a second run on the high intensity magnetic separator.

Table 8. Effect of drum speed (current to the electromagnetic coil 0.3 Ampere, feed particle size fraction is -150+20 micrometers)

Drum speed rpm	Product	Product weight, %	Assay Fe %	Metal distribution, %	Metal distribution relative to original sample, %
60	Magnetic	84.0	40.3	91.2	83.9
	Non-magnetic	16.0	20.0	08.8	08.1
	Total	100.0	37.1	100.0	92.0
100	Magnetic	81.5	42.4	92.2	84.8
	Non-magnetic	18.5	16.0	07.8	07.2
	Total	100.0	37.5	100.0	92.0
140	Magnetic	56.0	43.0	64.2	59.1
	Non-magnetic	44.0	30.5	35.8	32.9
	Total	100	37.5	100.0	92.0
180	Magnetic	41.3	44.3	49.5	45.5
	Non-magnetic	58.7	31.9	50.5	46.5
	Total	100.0	37.0	100.0	92
220	Magnetic	36.2	44.3	43.2	39.7
	Non-magnetic	63.8	33.0	56.8	52.3
	Total	100.0	37.1	100.0	92.0

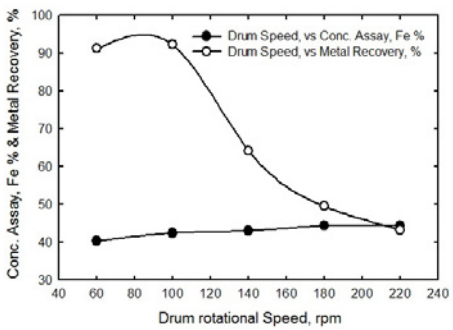

Fig. 5. Effect of drum rotational speed on the performance of the magnetic separator

3.4. Cleaning of the Rougher Concentrates

The rougher concentrates obtained from the shaking table as well as the magnetic separator were both relatively low in grade. The shaking table concentrate assayed 44.9% Fe at metal recovery of 86.7%, and the magnetic separator concentrate assayed

42.4% Fe at metal recovery of 92.2%. These two rougher concentrates were passed through the high intensity magnetic separator, at its optimum operating conditions (current to the coil is 0.3 Ampere, drum rotation speed 100 rpm), for cleaning. Table 9 presents the results of the cleaning stage of the shaking table concentrate. The final assay of the concentrate is 65.4% Fe, at an overall metal recovery of 69%.

The rougher concentrate from the magnetic separator was passed again on the high intensity magnetic separator, at its optimum operating conditions, for cleaning. The cleaned concentrate assayed 63.5% Fe at an overall metal recovery of 67.7%. Table 10 shows the results of the cleaning stage for the magnetic separator rougher concentrate.

Table 9. Cleaning of the table concentrate using the high intensity magnetic separator (magnetic field intensity is at 0.3 A, drum speed 100 rpm)

Product	Product wt. %	Assay Fe %	Metal distribution, %	Metal distribution relative to original sample, %
Magnetic	60.1	65.4	87.2	69.0
Non-magnetic	39.9	14.5	12.8	10.2
Total	100	45.0	100	79.2

Table 10. Cleaning of the magnetic rougher concentrate (magnetic field intensity at 0.3 A, drum speed 100 rpm)

Product	Product wt. %	Assay Fe %	Metal distribution,%	Metal distribution relative to original sample, %
Concentrate	53.2	63.5	79.7	67.7
Tailing	46.8	18.4	20.3	17.3
Total	100.0	42.4	100.0	85.0

4. Conclusions

The low-grade iron ore sample obtained from the Wadi Halfa iron ore deposit, North of Sudan, was analyzed mineralogically and chemically. The major mineral constituents were hydrated iron minerals and quartz. The trace constituents were calcium, magnesium, aluminum, manganese, and phosphorus oxides. The average iron assay was about 36% Fe, and the silica content was about 57% SiO_2. Three samples were ground such that the first sample passed 500 μm, the second passed 350 μm, and the third passed 150 μm. Each of the three samples were deslimed to remove the -20 μm fraction, such that the feed size ranges to be tested were -500+20 μm, -350+20 μm, and -150+20μm. The ore was beneficiated using the shaking table and the high intensity magnetic separator. The beneficiation took place in two stages: roughing and cleaning. The optimum operating conditions for the table were: feed size fraction of -150+20 μm and table tilt angle of 5^o, and those of the magnetic separator were: feed size fraction of -150+20 μm, 0.3 Ampere, and drum rotational speed of 100 rpm. The rougher concentrates from both the gravity separation and the magnetic separation were, separately, subjected to the second stage of concentration, the cleaning stage. In the cleaning stage, the rougher concentrates were passed on the high intensity magnetic separator at its optimum operating conditions: 0.3 Ampere and 100 rpm

drum speed. The cleaned concentrate obtained by using the shaking table followed by magnetic separator assayed 65.5% Fe, at a recovery of 69.0%, and the cleaned concentrate obtained by passing the ore twice on the magnetic separator assayed 63.5% Fe, at a recovery of 67.7%. The obtained results suggest that the Wadi Halfa iron ore could be beneficiated using either of the two routes: gravity separation (shaking tables) followed by high intensity magnetic separation, or two stage high intensity magnetic separation.

References

ABU-ZEID, A.M., 1967, *A contribution to the beneficiation of El-Gedida iron ore*, Bahariya Oases, Egypt, M.Sc. Thesis, Faculty of Engineering, Cairo University.

ALI, M.N.W., et al., 2004, *A study on the Oolitic Iron Ore Mineralization of Wadi Halfa*, Arab Mining Conference, University of Amman, Jorden.

ALI, M.N.W., BABIKER, M. E., ELTAYEB, H., HAROUN, A., 2003, *A study on the oolitic iron ore mineralization of Wadi Halfa*, Geolocal Rasearch Authority of Sudan, Report.

BURT.R, 1999, *The role of gravity concentration in modern processing plants*, Minerals Engineering 12, 1291–1300.

FARAGHALY, M.G., 2002, *Beneficiation of El-Gedida Barite Iron Ore*, Journal of Engineering Science 30, 779–812.

FATMA, H.A., ARAFA, M.A., 1999, *Concentrate from an Egyptian baritic iron ore*. Proceedings of the 6th international conference on Mining, Petroleum, and Metallurgy, Faculty of Engineering, Cairo University, Feb. 1999.

GAUDIN, A.M., 1987, *Principles of Mineral Dressing*, New Delhi, Tata McGraw-Hill Publishing Company Limited, Mohan Makhijani at Rekha Printers Pvt. Ltd.

GUNEY, A. et al., 2000, *The Beneficiation of Camdag Iron Ore* . ITU Mining Faculty ,Mining Eng. Dep. Min and Coal proc. Section ,80626, Maslak, Istanbul, Turkey.

MOSLIM, E. M., 2010, *Beneficiation Studies on low grade iron ore, Wadi Halfa area, Northern Sudan*. Ph.D. Thesis, Faculty of Engineering Sciences, Omdurman University, Sudan.

MANSAR, R.J., BARLEY, R.W., WILLS, B.A., 1991, *The shaking table concentrator — The influence of operating conditions and table parameters on mineral separation — The development of a mathematical model for normal operating conditions*, Minerals Engineering 4, 369–381.

MUSSALLAM, F. K., 2004, *Fundamental Studies on Upgrading Iron Ores in Egypt*, M Sc Thesis, Faculty of Petroleum and Mining Engineering, Suez Canal University.

MUKHERJEE, A.K. BHATTACHARJEE, D., MISHRA, B.K., 2006, *Role of water velocity for efficient jigging of iron ore*, Minerals Engineering 19, 952–959.

ROY, S., 2009, *Recovery improvement of fine iron ore particles by multigravity separation*. The Open Mineral Processing Journal 2, 17–30.

ROWAYSHED .S.A., 1983, *Beneficiation of El-Bahariya Oasis Low grade Iron Ores*, M.Sc. Thesis, Faculty of Engineering, Al-Azhar University, Cairo, p.103

SAMYKINA, E., SURKOV, A., EPPELBAUM, L., SEMENOV, S., 2005, *Do old spoils contain large amounts of economic minerals?* Minerals Engineering, 18, 643–645.

SHIVAMOHAN, R., FORSSBERG, E., 1985, *Principles of tabling*, International Journal of Mineral Processing 15, 281–295.

SVOBODA, J., ROSS, V.E., 1989, *Particle capture in the matrix of magnetic separator*, International Journal of Mineral Processing 27, 75–94.

SVOBODA, J., 1994, *The effect of magnetic field strength on the efficiency of magnetic separation*, Mineral Engineering 7, 747–757.

SVOBODA, J., FUJITA, T., 2003, *Recent developments in magnetic methods of material separation*, Minerals Engineering 16, 785–793.

Physicochem. Probl. Miner. Process. 48(2), 2012, 579−589

www.minproc.pwr.wroc.pl/journal/

Physicochemical Problems of Mineral Processing

ISSN 1643-1049 (print)
ISSN 2084-4735 (online)

Received March 15, 2012; reviewed; accepted May 7, 2012

ANALYSIS OF SELECTED METHODS OF BENEFICIATING COAL SLURRIES DEPOSITED IN IMPOUNDMENTS

Jan SZPYRKA, Marcin LUTYNSKI

Silesian University of Technology, Faculty of Mining and Geology, Department of Mineral Processing and Waste Utilization, Gliwice, Poland, jan.szpyrka@polsl.pl, marcin.lutynski@polsl.pl

Abstract. The paper presents research results of the possibility to beneficiate coal slurries deposited in 21 impoundments located in the region of Silesia, Poland. Coal slurries of particle size diameter below 1 (0.5) mm were subjected to beneficiation tests with the use of the following methods: centrifugal separator, hydrocyclone, Reichert spiral separator and flotation. Applied methods showed significant differences in obtained results. The most effective method was flotation where yield was on average 64% with concentrate of high calorific value. In case of centrifugal separator and Reichert type spiral average yield was 22% and 25%, respectively. In case of hydrocyclone classifier-separator, a high yield of low quality concentrate was obtained. The study revealed that such impoundments have a high energetic potential which can be effectively used by applying a proper beneficiation technology.

keywords: coal slurry, tailings, impoundments, gravity separation

1. Introduction

The most common gravity separation methods are used successfully for particle size fractions larger than 0.1 mm. Nevertheless, below this limit with appropriate technological parameters and with the use of appropriate equipment (application of additional centrifugal force) an effective separation of finer particle sizes with high density difference is carried out. A summary of gravity separation methods taking into account particle sizes is presented in Table 1.

The latest technology of gravity separation using devices that allow to obtain high centrifugal forces significantly reduce particle size lower limit suitable for effective separation. These technologies which employ equipment of Mozley, Falcon, Knelson and Kelsey are not in use currently in Poland.

Results of coal slurries beneficiation tests from twenty one impoundments are presented in the paper. The tests were performed at the Technological Laboratory of Department of Mineral Processing and Waste Utilization within the framework of development project N R09 0006 06/2009 entitled “Identification of energetic potential of coal slurries in the national fuel balance and technological development strategy of their usage”. The project is implemented by the Institute of Mechanized

http://dx.doi.org/10.5277/ppmp120221

Construction & Rock Mining in Warsaw in cooperation with the Department of Mineral Processing and Waste Utilization of the Silesian University of Technology (Blaschke et al. 2011, Baic and Blaschke 2010).

The purpose of the Project is quantitative and qualitative identification of coal slurries deposited in impoundments located in the area of mining activity. Coal slurry impoundments are the effect of long term activity of coal beneficiation plants. Material deposited there consists of slurries and post-flotation muds of particle size smaller than 1 (0.5) mm. Up to the thirties i.e. the time of development and introduction of froth flotation technology small size fraction gangue was difficult to remove using conventional beneficiation methods which, as a result, was significantly lowering the coke quality. Therefore, particle size smaller than 1 mm were treated as a waste. The same situation was in the case of steam coal as it was impossible to burn small particles in stoker-fired boilers.

Nevertheless, the coal slurries deposited in impoundments have an energetic potential that should be effectively utilized. Recovering the coal matter is one of such methods, effective use of the energetic potential (Lutyński and Blaschke 2009; Hycnar et al. 2005; Hycnar and Bugajczyk 2004; Karbownik and Haber 1999).

Table 1. Gravity separation chart. Adapted from (Abols and Grady, 2006)

Equipment type	Feed particle size [μm]								
	10	20	50	100	200	500	10^3	10^4	10^5
Inline pressure jig									
Diaphragm jig									
Dense medium separators									
Dense medium cyclones									
Mozley Multi-Gravity Separator									
Spirals									
Fan-shaped trough separators									
Frue vanners									
Centrifugal separators									
Falcon separators									
Knelson separators									
Kelsey Centrifugal jig									
Reichert cones									

2. Description of tests

Beneficiation tests of coal slurries were carried out in our laboratory on a semi-technical scale. Three different separation methods were tested:

— centrifugal force separation method with the use of hydrocyclone classifier-separator and centrifugal separator (Honaker et al. 1994; Driessen 1945),
— wet gravity separation method with the use of Reichert spiral separator LD4 (Atesok et al. 1993),
— physicochemical method – flotation (Tao et al. 2002).

Beneficiation tests of coal slurries were carried out with a hydrocyclone classifier-separator of ø150 mm diameter located at the Technological Laboratory of our Department. The feed of selected density was pumped to the hydrocyclone with overflow in order to maintain constant hydrostatic pressure. Before proceeding to the tests with proper samples, several tests on waste material of similar properties were carried out. The purpose of preliminary tests was to determine the range of appropriate feed density and the feed flow rate. It was found that the preferred density of the beneficiated material is 150 g/dm^3. The testing device was equipped with electromagnetic flowmeter FM 300 DN25 SPT. The testing device is designated for separation of slurries with the upper particle size limit of 1(2) mm.

Results of coal slurry beneficiation tests carried out in the hydrocyclone are presented in Table 2 and Table 3.

In gravity separation methods the quality of concentrate is lowered by the finest gangue fraction (<0.1 mm) that passes with larger and lighter coal particles to concentrates. Improvement of concentrate quality can be achieved by removing sludge from the feed or by removing the sludge from the concentrate. Sludge can be removed in the hydrocyclone. Therefore, the concentrate from the hydrocyclone was used as the feed in the beneficiation tests in the centrifugal and spiral separator.

Centrifugal separator uses a centrifugal force to separate material. It is designated to beneficiate slurries with the upper particle size limit of 1(2) mm. Vortex is created by rotating blades on a vertical shaft driven by an electric engine with transmission belt which allows changing the rotation speed. Set of blades is rotating in the cone-shaped bowl where the feed is introduced under hydrostatic pressure. Feed slurry enters centrally and is distributed outwards at the base of the cone by centrifugal force and then flows up the inclined surface of the bowl, segregating in the process, with high specific gravity particles on the outside closest to the bowl surface and low density particles on the inside which discharge over the lip at the top of the bowl.

The feed of proper density (100-150 g/dm^3) is pumped to the cone which provides a constant hydrostatic pressure. Received products are collected by gravity in two tanks.

Beneficiation tests were carried out for two feed densities of 100 and 150 g/dm^3. Due to favorable outcome only test results for the feed density of 150 g/dm^3 are presented in the paper (see Table 4).

In case of spiral separator, a Reichert LD4 type separator was used. The testing device consists of feed tank, LD4 spiral separator with two trough of six coils and a dewatering screen.

Table 2. Quality parameters of coal slurry products classification in hydrocyclone classifier-separator of diameter 150 mm. Slurry density 150 g/dm^3

Impoundment	underflow		overflow		feed
	Yield g_k [%]	Ash content A^a [%]	Yield g_o [%]	Ash content A^a [%]	Ash content A^a [%]
1	47.5	31.64	52.50	35.93	33.89
2	55.58	26.12	44.42	47.53	35.63
3	49.52	39.64	50.48	45.94	42.82
4	50.03	57.45	49.97	68.84	63.14
5	59.66	71.63	40.34	74.01	72.59
6	51.05	42.51	48.95	55.30	48.77
7	77.35	43.87	22.65	53.63	46.08
8	63.4	56.87	36.6	62.17	58.81
9	57.89	25.13	42.11	44.34	33.22
10	44.23	46.22	55.77	61.82	54.92
11	52.08	43.91	47.92	47.96	45.85
12	50.58	32.2	49.42	24.00	28.15
13	59.24	24.21	40.76	34.78	28.52
14	57.43	22.36	42.57	34.88	27.69
15	45.61	30.96	54.39	42.80	37.4
16	47.57	34.88	52.43	38.28	36.66
17	50.5	34.21	49.5	38.07	36.12
18	50.74	35.67	49.26	37.29	36.47
19	43.79	48.63	56.21	62.90	56.65
20	47.50	44.06	52.5	51.77	48.11
Av.	53.10	39.60	46.94	48.11	43.57

The feed was supplied by gravity from a tank with a high-speed stirrer and further agitated with air from a compressor. Rotation of stirrer and air-lift prevent from sedimentation of feed in the tank and provide constant feed density.

Initial tests were carried out in order to determine the preferred range of feed density, feed flow rate and to adjust settings of feed driving blades and product collectors.

Tests were carried out on samples from seventeen and nineteen impoundments with two feed densities (300 g/dm^3 and 400 g/ dm^3). Favorable results were observed for feed density of 400 g/ dm^3. Results are presented in Table 5.

Laboratory flotation tests of coal slurries were carried out in laboratory froth flotation cells with volume of 1 dm^3. The density of the coal slurry was 100 g/dm^3.

It should be mentioned that the experience of the Department employees shows that in case of flotation process, results obtained in the laboratory differ significantly from the results obtained in industrial flotation cells.

Two flotation agents which are in common use in coal beneficiation plants, were used for the tests. Initial tests were performed in order to determine the optimum amount of flotation agent. Further tests were carried out for flotation agent

concentration of 0.4, 0.5 and 0.6 kg per Mg of dry material. Best results were obtained for the concentration of flotation agent of 0.6 kg per Mg of dry material.

Table 3. Quality parameters of concentrate (underflow from hydrocyclone classifier-separator) obtained for classification of 0.1 mm sorted particle size

Impoundment	Concentrate (underflow)				
	Yield	Ash content	Hydroscopic moisture	Sulfur content	Calorific value
	γ_k %	A^a [%]	W^{ex} [%]	$S_c{}^a$ [%]	Q^a [%]
1	47.50	31.64	6.65	1.34	18121
2	55.58	26.12	6.43	0.76	20362
3	49.52	39.64	5.30	1.02	17281
4	50.03	57.45	4.41	0.58	9295
5	59.66	71.63	4.59	0.66	8576
6	51.05	42.51	5.32	0.96	15990
7	77.35	43.87	1.33	3.42	16277
8	63.40	56.87	1.22	2.04	12027
9	57.89	25.13	2.89	0.70	24234
10	44.23	46.22	4.09	1.09	13444
11	52.08	43.91	1.50	1.05	17972
12	50.58	32.2	2.19	0.35	24363
13	59.24	24.21	1.99	0.61	24,557
14	57.43	22.36	2.02	0.83	25501
15	45.61	30.96	1.88	0.86	21415
16	47.57	34.88	2.21	0.85	21085
17	50.50	34.21	1.69	1.12	21161
18	50.74	35.67	2.22	1.06	21844
19	43.79	48.63	3.30	0.82	12008
20	47.50	44.06	2.12	0.74	18022
Av.	53.10	39.60	3.16	1.04	16950

Tests were conducted on samples from all impoundments. A positive flotation test result was assumed when 80% of the samples had a positive flotation effect. In case of samples from one impoundment a positive test was considered when 66% of the samples had a yield greater than 30% and the ash content in concentrate was lower than 25%. These criteria were fulfilled for the samples from 12 impoundments. Results of tests for the flotation agent 2 which was considered as preferable are presented in Table 6.

3. Results of investigation

Results of tests carried out were summarized in Tables 2 to 8. In Tables 7 and 8 a comparison of selected results from different separation methods is shown. Presented results are both for concentrate and tailings. It seems that obtained results indicate the efficiency of selected method (Fig. 1). In Figures 2 and 3 washability curves for the two most favorable results of hydrocyclone separation are presented.

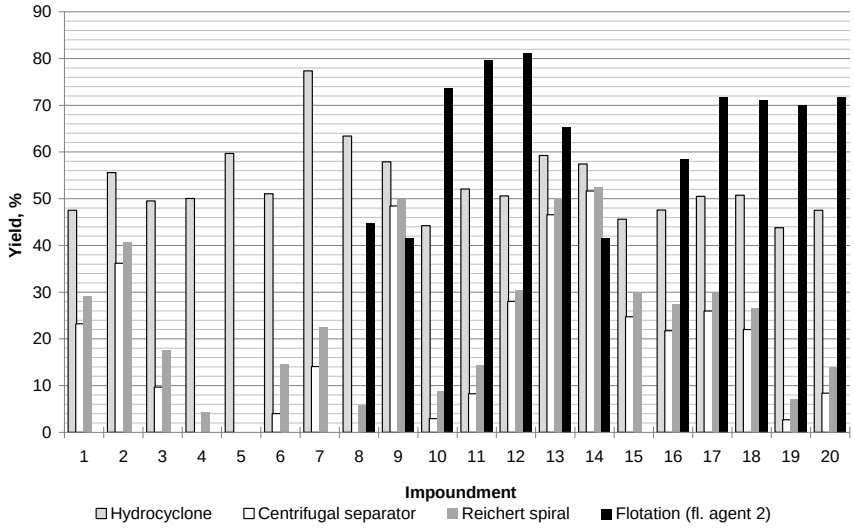

Fig. 1. Comparison of concentrate yields obtained with each separation method

Table 4. Concentrate parameters after sludge removal in centrifugal separator for feed density of 150 g/dm^3

Impoundment	Concentrate				Tailings				Concentrate yield with regard to the feed
	Yield	Ash content	Calorific value	Hydroscopic moisture	Yield	Ash content	Calorific value	Hydroscopic moisture	
	γ_o [%]	A^a [%]	Q^a [kJ/kg]	W^{ex} [%]	γ_o [%]	A^a [%]	Q^a [kJ/kg]	W^{ex} [%]	γ_{kc} [%]
1	48.88	21.14	18916	5.32	51.12	41.68	14199	4.09	23.22
2	65.08	20.68	20654	5.46	34.92	36.26	16158	6.12	36.17
3	19.54	20.31	22042	4.11	80.46	44.33	14065	3.99	9.68
4	-	-	-	-	-	-	-	-	-
5	-	-	-	-	-	-	-	-	-
6	7.84	22.06	21043	5.71	92.16	44.25	14409	4.51	4.00
7	18.20	21.59	25840	1.26	81.8	48.83	14015	1.19	14.08
8	-	-	-	-	-	-	-	-	-
9	83.67	20.47	24104	2.51	16.33	49.01	13403	1.84	48.44
10	6.59	21.68	18965	4.72	93.41	47.95	12260	4.25	2.91
11	15.84	19.93	25046	1.73	84.16	48.42	14723	1.78	8.25
12	55.41	20.47	24095	1.93	44.59	46.78	15914	2.51	28.03
13	78.61	21.14	24164	2.06	21.39	35.49	19068	2.25	46.57
14	89.92	21.56	24315	2.31	10.08	29.50	20484	1.12	51.64
15	54.23	20.46	24430	2.23	45.77	43.40	16531	2.60	24.73
16	45.68	21.51	24043	1.96	54.32	46.12	15398	2.22	21.73
17	51.41	21.86	23802	2.39	48.59	47.28	15173	2.49	25.96
18	43.33	21.15	24281	2.06	56.67	46.77	15604	2.38	21.99
19	6.12	22.35	18519	6.13	93.88	50.34	12165	4.38	2.68
20	17.62	21.82	24124	2.83	82.38	48.82	15294	2.64	8.37
Av.	41.64	21.19	22846	3.22	58.35	44.42	15227	2.96	22.26

Table 5. Parameters of separation of concentrate after sludge removal beneficiated in six coils LD4 of Reichert spiral separator for the feed density of 400 g/dm^3

Impoundment	Concentrate				Tailings				Yield	Concentrate yield with regard to the feed
	Yield	Ash content	Calorific value	Hydroscopic moisture	Yield	Ash content	Calorific value	Hydroscopic moisture	Ash content	
	γ_o [%]	A^a [%]	Q^a [kJ/kg]	W^{ex} [%]	γ_o [%]	A^a [%]	Q^a [kJ/kg]	W^{ex} [%]	A^a [%]	γ_{kc} [%]
1	61.15	21.10	18825	5.64	38.85	48.23	12680	3.19	31.64	29.05
2	73.12	22.14	20271	5.51	26.88	36.95	15950	6.18	26.12	40.64
3	35.62	21.86	21523	4.40	64.38	49.48	12480	3.79	39.64	17.64
4	8.69	22.07	21042	4.83	91.31	60.82	7114	3.10	57.45	4.35
6	28.43	22.81	20760	5.72	71.57	50.34	12581	4.16	42.51	14.51
7	29.14	21.20	25843	1.22	70.86	53.19	12113	1.19	43.87	22.54
8	9.21	23.81	24258	1.13	90.79	60.22	9479	1.59	62.17	5.84
9	86.12	20.47	24335	2.36	13.88	54.04	11518	2.65	25.13	49.85
10	19.63	21.45	19136	4.71	80.37	52.27	11272	4.17	46.22	8.68
11	27.47	22.31	24241	1.70	72.53	52.09	13545	1.80	43.91	14.31
12	60.25	20.33	24459	1.90	39.75	50.19	14831	2.63	32.20	30.47
13	84.38	22.52	23763	2.08	15.62	33.34	19879	2.21	24.21	49.99
14	91.33	21.84	24333	2.19	8.67	27.84	21879	2.19	22.36	52.45
15	65.61	23.26	23352	2.10	34.39	45.65	15528	2.97	30.96	29.92
16	57.63	22.27	23666	2.15	42.37	52.03	13192	2.03	34.88	27.41
17	58.73	21.46	24035	2.31	41.27	52.35	13581	2.62	34.21	29.66
18	52.35	21.39	24195	2.25	47.65	51.36	14012	2.23	35.67	26.56
19	16.11	20.82	18756	5.83	83.89	53.97	11486	4.23	48.63	7.05
20	29.42	21.35	24256	2.67	70.58	53.53	14008	2.67	44.06	13.97
Av.	47.07	21.81	22687	3.19	52.93	49.36	13533	2.93	35.66	24.99

Table 6. Coal slurry flotation results, flotation agent # 2

Impoundment	Feed ash content A^a, %	Product	Yield %	Ash content in products A^a %	Calorific value of concentrate, Q^a kJ/kg
8	50.8	C T	44.8 55.1	22.7 73.3	24 687
9	60.9	C T	41.5 58.5	31.2 82.9	20 670
10	27.2	C T	73.7 26.3	14.5 65.8	27 620
11	28.6	C T	79.6 20.4	15.9 80.3	27 120
12	28.6	C T	81.1 18.9	16.4 81.1	26 880
13	48.0	C T	65.3 34.7	29.4 82.9	21 525
14	60.9	C T	41.5 58.5	31.2 82.9	24 520
16	44.3	C T	58.4 41.6	23.6 76.8	24 670
17	36.7	C T	71.7 28.3	19.2 79.8	25 875
18	36.2	C T	71.1 28.9	19.5 76.7	25 810
19	37.3	C T	70.0 30.0	19.3 77.4	25 845
20	36.5	C T	71.7 28.3	21.3 76.3	25 465

C – concentrate, T – tailings

Table 7. Comparison of selected coal slurry concentrate parameters beneficiated by different methods

Imp.	Hydrocyclone			Centrifugal separator, 150 g/dm^3			Reichert spiral, 400g/dm^3			Flotation, flotation agent # 2		
	Yield γ_k %	Ash content A^a [%]	Calorific value Q^a [%]	Yield γ_k %	Ash content A^a [%]	Calorific value Q^a [kJ/kg]	Yield γ_k %	Ash content A^a [%]	Calorific value Q^a [kJ/kg]	Yield γ_k %	Ash content A^a [%]	Calorific value Q^a [kJ/kg]
1	47.50	31.64	18121	23.22	21.14	18916	29.05	21.10	18825	-	-	-
2	55.58	26.12	20362	36.17	20.68	20654	40.64	22.14	20271	-	-	-
3	49.52	39.64	17281	9.68	20.31	22042	17.64	21.86	21523	-	-	-
4	50.03	57.45	9295	-	-	-	4.35	22.07	21042	-	-	-
5	59.66	71.63	8576	-	-	-	-	-	-	-	-	-
6	51.05	42.51	15990	4.00	22.06	21043	14.51	22.81	20760	-	-	-
7	77.35	43.87	16277	14.08	21.59	25840	22.54	21.20	25843	-	-	-
8	63.40	56.87	12027	-	-	-	5.84	23.81	24258	44.8	22.7	24 687
9	57.89	25.13	24234	48.44	20.47	24104	49.85	20.47	24335	41.5	31.2	20 670
10	44.23	46.22	13444	2.91	21.68	18965	8.68	21.45	19136	73.7	14.5	27 620
11	52.08	43.91	17972	8.25	19.93	25046	14.31	22.31	24241	79.6	15.9	27 120
12	50.58	32.2	24363	28.03	20.47	24095	30.47	20.33	24459	81.1	16.4	26 880
13	59.24	24.21	24.557	46.57	21.14	24164	49.99	22.52	23763	65.3	29.4	21 525
14	57.43	22.36	25501	51.64	21.56	24315	52.45	21.84	24333	41.5	31.2	24 520
15	45.61	30.96	21415	24.73	20.46	24430	29.92	23.26	23352	-	-	-
16	47.57	34.88	21085	21.73	21.51	24043	27.41	22.27	23666	58.4	23.6	24 670
17	50.50	34.21	21161	25.96	21.86	23802	29.66	21.46	24035	71.7	19.2	25 875
18	50.74	35.67	21844	21.99	21.15	24281	26.56	21.39	24195	71.1	19.5	25 810
19	43.79	48.63	12008	2.68	22.35	18519	7.05	20.82	18756	70.0	19.3	25 845
20	47.50	44.06	18022	8.37	21.82	24124	13.97	21.35	24256	71.7	21.3	25 465
Av.	53.10	39.61	16950	22.26	21.19	22846	24.99	21.81	22687	64.2	22.02	25057

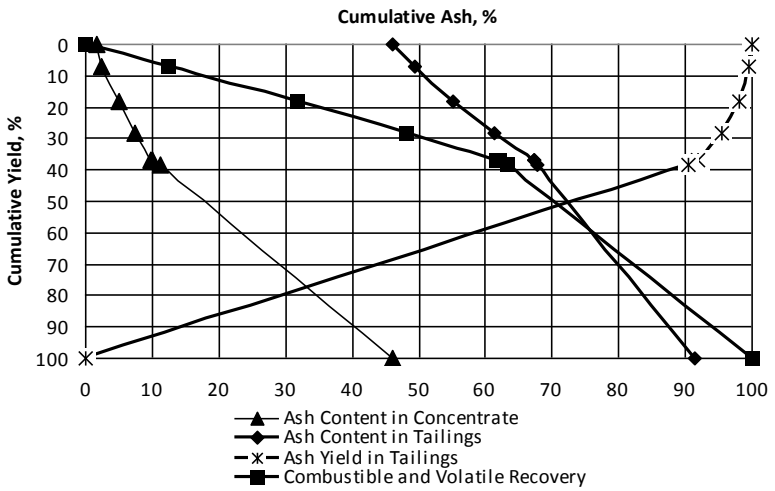

Fig. 2. Washability (Henry) curves of coal slurry from impoundment 9

Table 8. Comparison of selected coal slurry tailings parameters from different separation methods

Imp.	Hydrocyclone		Centrifugal separator, 150 g/dm^3		Reichert spiral 400g/ dm^3		Flotation, flotation agent # 2	
	Yield γ_k %	Ash content A^a [%]	Yield γ_k %	Ash content A^a [%]	Yield γ_k %	Ash content A^a [%]	Yield γ_k %	Ash content A^a [%]
1	52.50	35.93	51.12	41.68	70.95	48.23	-	-
2	44.42	47.53	34.92	36.26	59.36	36.95	-	-
3	50.48	45.94	80.46	44.33	82.36	49.48	-	-
4	49.97	68.84	-	-	95.65	60.82	-	-
5	74.01	74.01	-	-	85.49	50.34	-	-
6	55.30	55.30	92.16	44.25	77.46	53.19	-	-
7	53.63	53.63	81.8	48.83	94.16	60.22	-	-
8	62.17	62.17	-	-	50.15	54.04	55.1	73.3
9	44.34	44.34	16.33	49.01	91.32	52.27	58.5	82.9
10	61.82	61.82	93.41	47.95	85.69	52.09	26.3	65.8
11	47.96	47.96	84.16	48.42	69.53	50.19	20.4	80.3
12	24.00	24.00	44.59	46.78	50.01	33.34	18.9	81.1
13	34.78	34.78	21.39	35.49	47.55	27.84	34.7	82.9
14	34.88	34.88	10.08	29.50	70.08	45.65	58.5	82.9
15	42.80	42.80	45.77	43.40	72.59	52.03	-	-
16	38.28	38.28	54.32	46.12	70.31	52.35	41.6	76.8
17	38.07	38.07	48.59	47.28	73.44	51.36	28.3	79.8
18	37.29	37.29	56.67	46.77	92.95	53.97	28.9	76.7
19	62.90	62.90	93.88	50.34	86.03	53.53	30.0	77.4
20	51.77	51.77	82.38	48.82	75.01	49.36	28.3	76.3
Av.	46.90	48.11	58.35	41.68	75.01	48.23	35.8	78.02

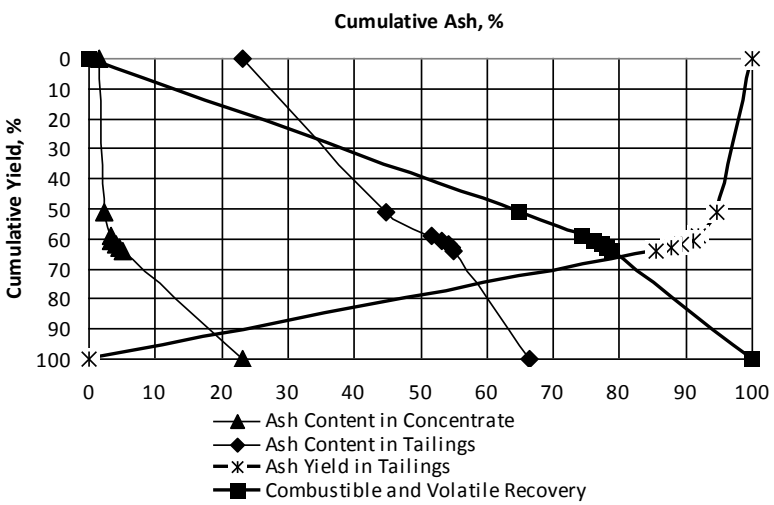

Fig. 3. Washability (Henry) curves of coal slurry from impoundment 13

4. Conclusions

Four separation methods presented in the paper show significant differences in results. The most effective method is the froth flotation where yield was on average 64%, calorific value of the concentrate was approximately 25 MJ/kg and the ash content approximately 22%. Moreover, tailings showed high ash content. Performed tests reported that due to flotation agent used this method cannot be applied to all tested coal slurries. Thus, if this method is to be applied for fine particle size coal tailings, other more efficient flotation agents must be applied (Laskowski 2004).

Much less favorable results were obtained with the centrifugal separator and Reichert type LD4 spiral separator. In material used in these types of separators particle size below 0.1 mm was initially separated in the hydrocyclone. The average yield for the Reichert spiral was 25% and for the centrifugal separator 22%. The calorific value of the concentrate was 22.687 MJ/kg and 22.846 MJ/kg, respectively, and ash content 25% and 22%, respectively. Low ash content was observed in tailings which was approximately 48% and 58% for the Reichert spiral and centrifugal separator respectively.

In case of hydrocyclone separation of particle below 0.1 mm in size, a significant yield (53%) was obtained, while the quality was low. The concentrate had a high ash content (39.6%) and low calorific value (16.95 MJ/kg) whereas tailings had low ash content (48.11%). Thus, the separation was inefficient due to the fact that the concentrate had approximately 38% particles smaller than 0.1 mm fraction and according to the study of Szpyrka and Lutyński (2012) these particle have a high ash content.

In conclusion, it should be noted that there is a possibility to upgrade fine coal particles. This process is of great importance because of considerable amount of coal deposited in impoundments. An alternative for fine coal beneficiation is a direct combustion in fluidized bed furnaces. Such furnaces are designed and manufactured taking into account individual characteristics of the fuel, i.e. particle size and quality parameters. Some of the materials tested fulfill these criteria (Blaschke 2005, Grudziński 2005).

References

ABOLS, J.A., GRADY, P.M., 2006, *Maximizing Gravity Recovery through the application of multiple gravity devices*. Vancouver, Gekko Systems.

ATESOK, G., YILDIRIM, I., CELIK, M.S., 1993, *Applicability of the Reichert spiral for cleaning bituminous and lignitic coals, a pilot scale study*,Int. J. Miner. Process.40(1–2), 33–44.

BAIC, I., BLASCHKE, W., 2010, *Identyfikacja mułów węglowych i strategia rozwoju technologicznego w zakresie ich gospodarczego wykorzystania.* Paliwo-bezpieczeństwo środowisko. Innowacyjne Techniki i Technologie Instytut Techniki Górniczej KOMAG. Gliwice.

BLASCHKE, W., RÓG, L., OSTATKIEWICZ, A., 2011, *Jakość produktów odpadowych wydzielanych w procesach wzbogacania energetycznego węgla kamiennego*. Przegląd Górniczy 5, 42–46.

BLASCHKE, W., 2005, *Określenie wartości mułów węglowych zdeponowanych w osadnikach ziemnych*. Materiały VII Ogólnopolskiej Konferencji Naukowej pt. Kompleksowe i szczegółowe problemy inżynierii środowiska. Politechnika Koszalińska. Koszalin.

DRIESSEN, M.G., 1945, *The use of centrifugal force for cleaning fine coal in heavy liquids and suspensions with special reference to the cyclone washer*, Journal Institute Fuel.

GRUDZIŃSKI, Z., 2005, *Analiza porównawcza jakości mułów węgla kamiennego pochodzących z bieżącej produkcji i zdeponowanych w osadnikach ziemnych*. Materiały VII Ogólnopolskiej Konferencji Naukowej pt**.** Kompleksowe i szczegółowe problemy inżynierii środowiska. Politechnika Koszalińska. Koszalin.

HONAKER, R.Q., PAUL, B.C., WANG, D., HUANG, M., 1994, *The Application of Centrifugal Washing for Fine Coal Cleaning*, Preprint, SME Meeting, Albuquerque, New Mexico, February 14-17, 94–259.

HYCNAR, J.J., FOLTYN, R., OKULSKI, T., BLASCHKE, S.A., 2005, *Kierunki energetycznego wykorzystania drobnoziarnistych odpadów z wydobycia i wzbogacania węgla kamienneg*o. VII Konferencja Naukowa Kompleksowe i szczegółowe problemy inżynierii środowiska. Politechnika Koszalińska. Koszalin - Ustronie Morskie.

HYCNAR, J.J., BUGAJCZYK, M.,, 2004, *Kierunki racjonalnego zagospodarowania drobnoziarnistych odpadów węglowych*. Polityka Energetyczna. Wydawnictwo IGSMiE PAN. Tom 7. Zeszyt Specjalny. Kraków.

KARBOWNIK, A., HABER, M., 1994, *Wykorzystanie mułów węglowych a ochrona środowiska*. Karbo 10.

Laskowski J. S., Testing flotation frothers, Physicochemical Problems of Mineral Processing, 38 (2004) 13-22

LUTYŃSKI, A., BLASCHKE, W., 2009, *Aktualne kierunki zagospodarowania odpadów przeróbczych węgla kamiennego*. Przegląd Górniczy 10, 33–35.

SZPYRKA, J., LUTYŃSKI, A., 2012, *Właściwości fizyko-chemiczne mułów węglowych zdeponowanych w osadnikach ziemnych*. Innowacyjne i przyjazne dla środowiska techniki i technologie przeróbki surowców mineralnych. Bezpieczeństwo – jakość – efektywność. Instytut Techniki Górniczej KOMAG. ISBN 978-83-60708-59-0. Gliwice, 259–274.

TAO D., LI B, JOHNSON S., PAREKH B.K., 2002, A flotation study of refuse pond coal slurry. Fuel Processing Technology 76(3), 201–210.

Physicochem. Probl. Miner. Process. 48(2), 2012, 591−598

www.minproc.pwr.wroc.pl/journal/

Physicochemical Problems of Mineral Processing

ISSN 1643-1049 (print)
ISSN 2084-4735 (online)

Received February 26, 2012; reviewed; accepted May 3, 2012

INFLUENCE OF ACID ACTIVATION ON THE ION-EXCHANGE PROPERTIES OF MANISA-GORDES CLINOPTILOLITE

Abdulkerim YORUKOGLU

MTA Genel Mudurlugu, Mineral Research and Exploration General Directorate, Dumlupinar Bulvari No:139, 06800-Ankara, Turkey, kerim@mta.gov.tr

Abstract. In this study, the possibilities of using Manisa-Gördes district tuffs having important deposits rich of clinoptilolites have been investigated for the removal of heavy metal ions from industrial wastewaters. Adsorption of ammonium and metal cations such as Pb^{++}, Cu^{++}, Cd^{++} and Zn^{++} ions from aqueous solution onto sulphuric, hydrochloric and nitric acid activated samples were studied. Experimental data were obtained from batch equilibrium tests on samples activated at different acid concentrations at two different size fractions. It has been found that selectivity of the zeolite is sequentially $Pb^{++} > NH_4^+ > Cu^{++}$, $Cd^{++} > Zn^{++}$. Experimental results show that the NH_4^+ ion exchange capacity of 95 meq/100 g for the raw material can be increased to 140 meq/100 g after activation with sulphuric acid. In general, acid activation was observed to increase the ion exchange capacity, sulphuric acid responding better than hydrochloric and nitric acids.

keywords: zeolite, clinoptilolite, acid activation, ion exchange

1. Introduction

Natural zeolite minerals are hydrated aluminosilicates of alkaline and alkaline-earth cations with indefinitely extending three dimensional network of (Si, Al)O_4 tetrahedral linked to each other by sharing all of the oxygen. Their structure contain channels and pores that are occupied by mobile cations and water molecules. Due to their structural characteristics, natural zeolites especially clinoptilolites are used for many purposes related with their ion exchange, adsorption, dehydration and rehydration properties (Castaldi et al., 2008; Girgin et al., 1996; Englert and Rubio, 2005; Wang and Peng, 2010, Cincotti et al., 2001; Korkuna et al., 2006).

Clinoptilolites are capable of exchanging alkaline and alkaline-earth cations in aqueous solutions and studies have been conducted on the waste water and nuclear waste treatment for the removal of some harmful cations (Ata and Girgin, 1994; Erdem et al., 2004; Curkovic et al., 1997; Toprak and Girgin, 2000; Gunay et al., 2007; Motsi et al., 2009; Ouki and Kavannagh, 1999; Abusafa and Yucel, 2002; Borai et al., 2009). They offer advantages over organic-ion exchangers due to their high chemical, thermal and radiation stabilities. Their ion-exchange and adsorption

http://dx.doi.org/10.5277/ppmp120222

properties can be improved by thermal and acid activation methods (Girgin et al., 1996; Wang and Peng, 2010; Curkovic et al., 1997; Inglezakis, 2005; Modale et al., 1995; Toprak and Girgin, 1999) .

This study was aimed at determining the cation-exchange capacity of Manisa-Gördes clinoptilolites for Pb^{+2}, NH_4^+, Cu^{+2}, Ca^{+2} and Zn^{+2} after activation with H_2SO_4, HCl and HNO_3.

2. Experimental

2.1. Chemicals and reagents

Merck grade HCl, H_2SO_4 and HNO_3 were used in the acid-activation experiments. Solutions used in ion exchange tests were prepared using CH_3COONH_4, $Cu(CH_3COO)_2 \cdot H_2O$, $Pb(CH_3COO)_2 \cdot 3H_2O$, $Zn(CH_3COO)_2 \cdot 2H_2O$, $Cd(CH_3COO)_2 \cdot 2H_2O$ and KCl (analytical grade Merck reagents).

2.2. Preparation and characterization of the sample

Clinoptilolite-rich tuff samples taken from Manisa-Gördes region was used in the experiments. Representative samples were crushed using jaw, cone and roll crushers, and then wet screened to -0,3 mm. After washing with distilled water and acetone, -707 +595 μm and -500 +298 μm fractions were obtained in ion-exchange experiments.

The chemical composition of the sample determined by XRF analysis (Rigaku RIX-3000 Spectrometer) is given in Table 1.

Table 1. Chemical composition of the sample used

Component	%
SiO_2	71.29
Al_2O_3	13.55
Fe_2O_3	1.15
CaO	2.45
MgO	0.70
Na_2O	0.60
K_2O	3.50
LOI	6.43

XRD analysis (Rigaku Geiger Flex X–ray) shows that the main mineral is clinoptilolite and cristobalite is present in minor quantities (Fig. 1a). XRD patterns of the sample treated between 100-1000ºC (Fig. 1b) show lowering in the peak intensities of clinoptilolite lattice concentration and thermal collapse of the framework at 800^0C . The TG/DTA data (Rigaku TAS 100 Thermo flex TG 8110) is in agreement with the

XRD results showing continuous hydration up to 700^{0}C with release of water and an exothermic event at around 924ºC due to the collapse of the structure (Fig. 2).

Considering the K, Na, Ca, Mg contents of the sample, theoretical cation exchange capacity was calculated as 120.74 meq/100g. Also, specific surface area, pore diameter, pore volume and the density (Quantachrome Nova 2000) of the sample were determined as 43.91 m^2/g, 0.018 μm, 0.1717 cm^3/gr, 2.12 g/cm^3, respectively.

Figure 3 shows the electronmicroscopic view of the sample (FEI Qanta 400 MK2 electronmicroscope) where macro and micropores can clearly be seen between the clinoptilolite crystals (Fig. 3d).

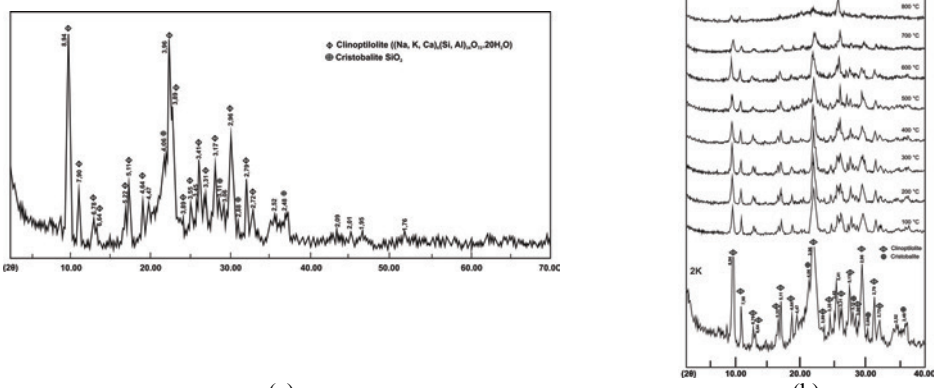

(a) (b)

Fig. 1. a)XRD pattern of the sample b) XRD patterns of the sample between 100–1000ºC

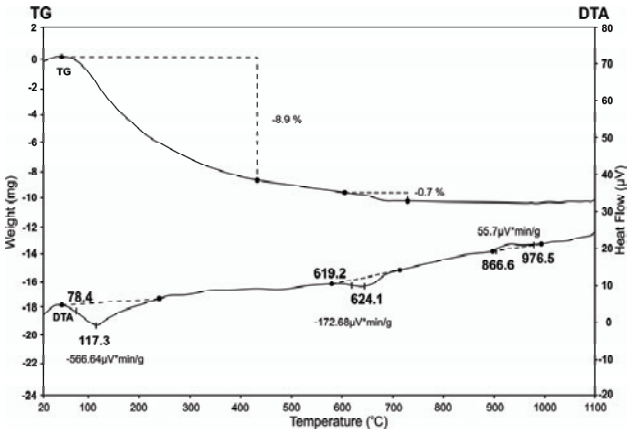

Fig. 2. TG/DTA curves of the sample

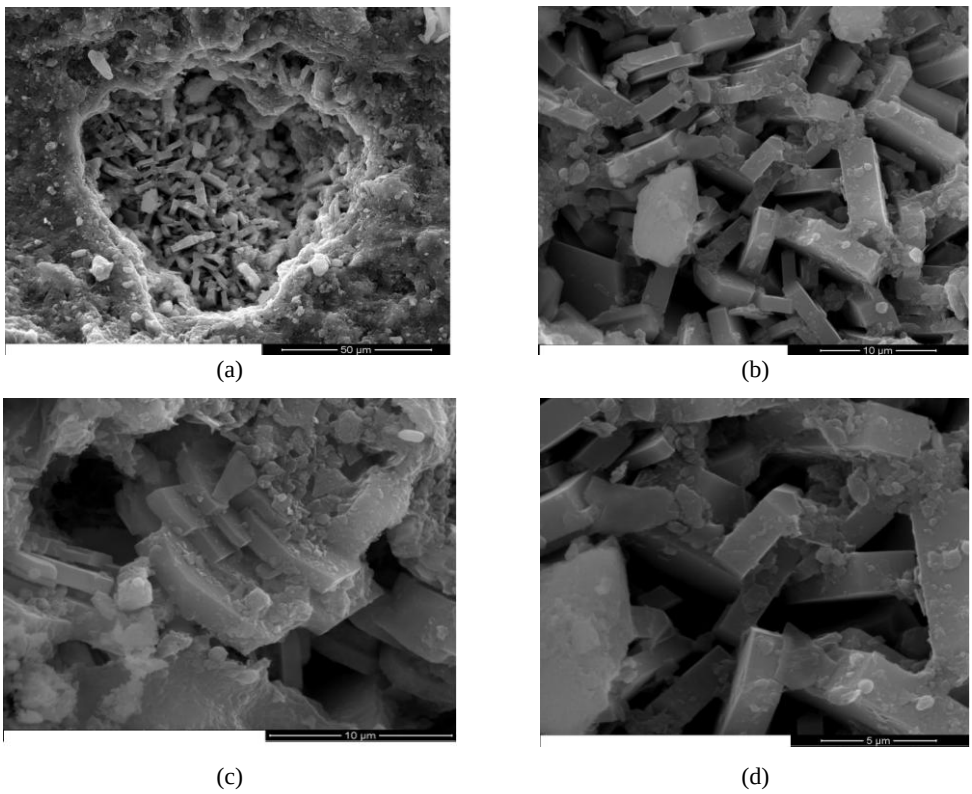

(a) (b)

(c) (d)

Fig. 3. An electronmicroscopic view of Manisa-Gördes clinoptolite (a) ~1000x magnification, (b) ~4000x magnification, (c) ~6000x magnification, (d) ~8000x magnification

2.3. Acid activation and ion exchange tests

In the acid activation experiments, the sample was treated with acid solutions of varying concentrations (0.1, 0.5, 1.0, 2.0 M) for one hour at room temperature. Following filtration, the samples were washed with water, then with acetone and finally were dried at 105ºC for 24 hours.

In the cation exchange tests, 1 gram of sample was treated with 100 cm^3 of solution for 8 hours in a 250 cm^3 beaker with mechanical agitation at constant speed to keep all the particles in suspension. After completion of the reaction, the samples were separated by filtration and rinsed with methanol. For the stripping of exchanged cations, loaded samples were treated with 100 cm^3 of KCl solution for 8 hours, filtered and the solutions were analyzed. As the adsorption of Pb^{+2} on clinoptilolite was irreversible, the samples were exchanged with K^+ before treatment with Pb^{+2} solution and the extent of Pb^{+2} exchange was determined by K^+ analysis in the solution.

Ammonium ion was determined by colorimetric method and the other ions were analyzed using the atomic absorption spectrophotometric method.

The batch technique was used for measurement of cation exchange capacity of samples (Sub-Committee, 1994) and the cation exchange capacities (CEC) in meq/100g were determined using equation:

CEC (meq/100g) = (milimoles of sorbed ion / 100g sample) · (cation valence).

3. Results and discussion

The NH_4^+ exchange capacities for the raw sample were determined as 94 meq/100g and 100 meq/100 g for sample sizes of +595 μm and +298 μm, respectively. The effect of particle size and acid concentration were considered in the ion exchange experiments and the results for acid activated samples are given in Fig. 4.

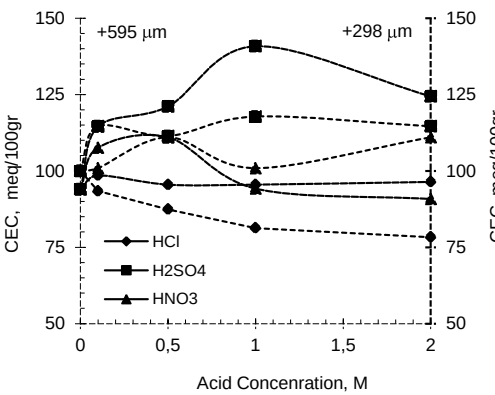

Fig. 4. NH_4^+ exchange capacity of the acid activated samples

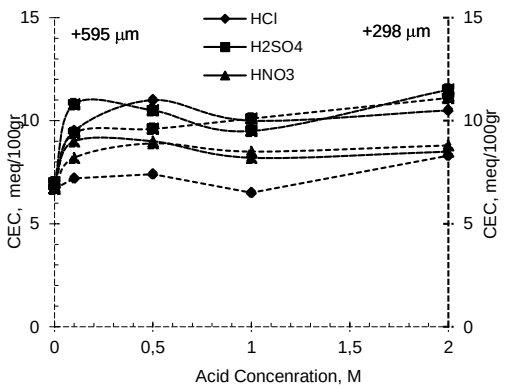

Fig. 5. Zn^{2+} exchange capacity of the acid activated samples

Although HCl does not have a significant effect on the ion exchange capacity for +595 μm sample, ion exchange capacity decreases from 93.4 meq/100 g to 78.3 meq/100 g for +298 μm sized sample. The highest value obtained for 0.1 M HCl activated sample for both sizes was determined as 98.5 meq/100 g. Ion exchange capacity values for +595 μm sample activated with 0.1 and 0.5 M HNO_3 were reached to 107.6 meq/100 g and 111 meq/100 g, respectively. But, upon increase of the acid concentration in the activation, ion exchange capacities were decreased considerably. Compared to others, better results were obtained with the sample activated using 1 M H_2SO_4 and the CEC value was reached to 140.8 meq/100 g for both sizes.

Zn^{++} exchange capacity of the raw sample for both sizes were quite close to each other being around 7 meq/100 g. Considering the Zn^{++} exchange capacities for acid activated samples (Fig. 5) HCl and HNO_3 activated samples showed slight increases in the exchange capacities. Best results again were obtained with H_2SO_4 activated sample and the highest value reached was 11.5 meq/100 g for +595 μm size when the

activation was done using 2 M H_2SO_4. For all the acid activated samples better results were obtained for +595 μm sample.

Pb^{++} exchange capacities for the raw samples were determined as 25.6 meq/100 g for +595 μm and 26.7 meq/100 g for +298 μm sizes. It can be seen from Fig. 6 that acids did not show big differences. The values varied between 27 meq/100 g to 31.3 meq/100 g on 595 μm sample, except 0.1 M HCl with which the value reached was 20.1 meq/100 g. It seems that particle size does not have any effect on ion exchange capacity for Pb ion. The best value obtained on +595 μm sized sample was around 31.3 meq/100 g for samples activated with 0.1 M HNO_3 and 2 M H_2SO_4.

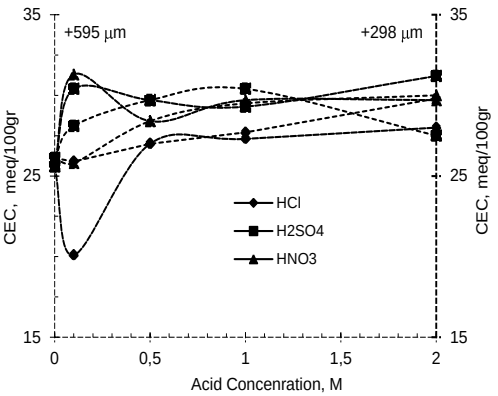

Fig. 6. Pb^{++} exchange capacity of the acid activated samples

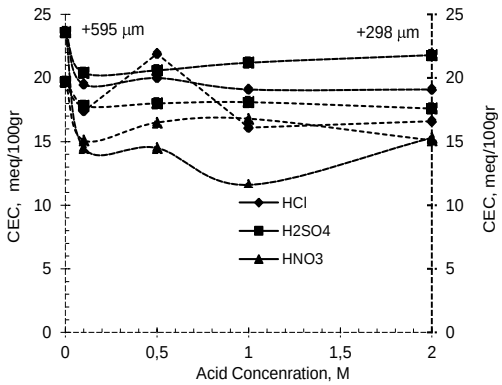

Fig. 7. Cu^{++} exchange capacity of the acid activated samples

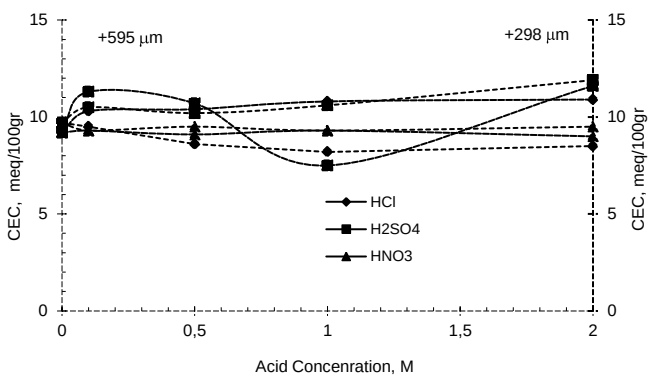

Fig. 8. Cd^{++}exchange capacity of the acid activated samples

For Cu^{++} ion, ion exchange capacity was 23.6 meq/100 g for +595 μm raw sample which was better than that of +298 μm sample. Also, this value was the highest compared to the acid activated ones (Fig. 7). Accordingly, although H_2SO_4 activation gives better results, acid activation does not improve the Cu^{++} exchange capacity of the raw material.

Cd^{++} exchange capacities for the raw material were found as 9.2 meq/100 g for +595 μm and 9.7 meq/100 g for +298 μm sizes. No significant changes were observed for acid activated samples (Fig. 8) and a value of 11.9 meq/100 g with +298 μm sample was reached for the sample activated using 2 M H_2SO_4.

4. Conclusions

Ion exchange tests using NH_4^+, Zn^{++}, Pb^{++}, $Cu^{++}$and Cd^{++} ions show that Manisa-Gördes clinoptilolites have exchange capacities for these ions in the order Pb^{++} >NH_4^+ > Cu^{++}, Cd^{++} > Zn^{++}. This determination is very similar to what had been stated for heavy metals before (Concotti et al. 2001, Modela et al. 1995).

Acid activation generally affected the cation exchange capacities positively. If it is necessary to take a concise look to the results obtained separately, better cation exchange capacity values were reached at both particle sizes with every three acids for NH_4^+, except one that the cation capacity values decreased as M concentration of HCl increased at 298 μm sample. After acid activation, while the cation exchange capacities for Pb and Zn increased, the values somewhat dropped for Cu, especially when HNO_3 used. On the other hand, it can be said for Cd that activation showed just very slight effect. It can be concluded that better results were usually obtained with H_2SO_4.

The results obtained in the batch experiments are worthy. However, in order to determine the industrial applicability, pilot size tests should also be conducted.

References

ABUSAFA, A., YUCEL H., 2002, *Removal of 137 Cs from aqueous solutions using different cationic forms of a natural zeolite: Clinoptilolite,* Sep. Purif. Technol., 28 (2), 103– 116.

ATA, S., GIRGIN İ., 1994, Ion exchange property of Bigadiç clinoptilolite for lanthanum, Progress in Mineral Processing Technology, Balkema, 397–400.

BORAI, E.H., HARJU, R., MALINEN, L., PAAJENEN, A., 2009, *Efficient removal of cesium from low-level radioactive liquid waste using natural and impregnated zeolite minerals*, Journal of Hazardous Materials, 172, 416–422.

CASTALDI, P., SANTONA, L., ENZO, S., MELIS, P., 2008, *Sorption processes and XRD analysis of a natural zeolite exchanged with Pb^{2+}, Cd^{2+} and Zn^{2+} cations*, Journal of Hazardous Materials, 156, 428–434.

CINCOTTI, A., LAI, N., ORRU, R., CAO, G., 2001, *Sardinian natural clinoptilolites for heavy metals and ammonium removal: experimental and modeling*, Chem. Eng. J., 84 (3), 275–282.

CURKOVIC, L., STEFANOVIC S.C., FILIPAN, T., 1997, *Metal ion- Exchange by natural and modified zeolites*, Water Res., 31, 1379–1382.

ENGLERT, A.H., RUBIO, J., 2005, *Characterization and environmental application of a Chilean natural zeolite*, International Journal of Mineral Processing, 75, 21–29.

ERDEM, E., KARAPINAR, N., DONA, R., 2004, *The removal of heavy metal cations by natural zeolites*, Journal of Colloid and Interface Science, 280, 309–314

GIRGIN İ., GÜNDOĞDU M. N., ATA, S., YÖRÜKOĞLU, A., 1996, *Oil decolorization properties of the Emirler clinoptilolite (Bigadiç, Turkey)*, Mineral Deposita, 31, 584–588.

GÜNAY, A., ARSLANKAYA, E., TOSUN İ., 2007, *Lead removal from aqueous solution by natural and pretreated clinoptilolite: Adsorption equilibrium and kinetics*, Journal of Hazardous Materials, 146, 362–371.

INGLEZAKIS, V.J., 2005, *The concept of "capacity" in zeolite ion-exchange systems*, Journal of Colloid and Interface Science 281, 68–79.

KORKUNA, O., LEBODA, R., SKUBISZEWSKA-ZEEBA, J., VRUBLEVS'KA, T., GUN'KO, V.M., RYCZKOWSKI, J., 2006, *Structural and physicochemical properties of natural zeolites: clinoptilolite and mordenite*, Microporous and Mesoporous Materials 84, 243–254.

MONDALE, K.D., CARLAND, R.M., APLAN, F.F., 1995, *The comparative ion exchange capacities of natural sedimentary and synthetic zeolites*, Minerals Engineering 8, 535–548.

Motsi, T., Rowson N.A., Simmons M.J.H., 2009, *Adsorption of heavy metals from acid mine drainage by natural Zeolite*, International Journal of Mineral processing 92, 42–48.

OUKI, S.K., KAVANNAGH M., 1999, *Treatment of metals-contaminated wastewaters by use of natural zeolites*, Wat.Sci.Tech., 39, 115– 122.

SUB-COMMITTEE MEMBER from Okutama Kogyo Co Ltd., Tokyo Japan., 1994, *Method for Measurements of Cation Exchange Capacity (CEC), "Natural Zeolite and its Utilization"* Edit No:111 committee CSPTS Jacarta SPS, 319–325.

TOPRAK R., GIRGIN İ., 2000, *Aktifleştirilmiş klinoploliteile deri sanayi atık sularından kromun giderilmesi*, Turk J. Engin. Environ. Sci., 24, 343–351.

TOPRAK, R., GIRGIN, İ., 1999, *Balıkesir – Bigadiç klinoptilolitlerinin adsorplama özelliklerinin iyileştirilmesi için anorganik asitlerle aktivasyonu,* Yerbilimleri, 21, 201–209.

WANG, S.,PENG, Y., 2010, *Natural zeolites as effective adsorbents in water and wastewater treatment*, Chemical Engineering Journal, 156, 11–24.

Physicochem. Probl. Miner. Process. 48(2), 2012, 599−606

www.minproc.pwr.wroc.pl/journal/

Physicochemical Problems of Mineral Processing

ISSN 1643-1049 (print)
ISSN 2084-4735 (online)

Received April 13, 2012; reviewed; accepted May 4, 2012

LEACHING CHARACTERISTICS OF EAF AND AOD STAINLESS STEEL PRODUCTION DUSTS

Antti KEKKI, Jari AROMAA, Olof FORSEN

Aalto University, Department of Materials Science and Engineering, PO Box 16200, FI-0076, Aalto, Finland, email: antti.kekki@aalto.fi

Abstract. In this paper sulfuric acid leaching of four different stainless steel production flue dusts is studied. The main objective is to study and compare the valuable metal Zn, Cr, Ni, Fe, Mo dissolution present in the EAF 1&2 (electric arc furnace) and AOD 1&2 (argon oxygen decarburization converter) dusts. The effect of sulfuric acid concentration, temperature and liquid-to-solid ratio are tested for maximum and selective Zn leaching into solution for recycling purposes. Leaching tests were done in 0.1 M, 0.5 M and 1.5 M sulfuric acid, at temperatures of 30ºC, 60ºC and 90ºC with liquid-to-solid ratios L:S = 10 and 20 under 1 bar pressure for 120 minutes. Maximum Zn dissolution yield was achieved with 1.5M, 90ºC, L:S = 10 where the Zn dissolution yield varied from 65% to almost 100%, depending on the dust type (AOD, EAF) and production line (1 or 2). At the same time Cr was leached 7 – 17%, Ni 37 – 48%, Fe 48 – 89% and Mo 82 – 100%. The best zinc selectivity vs. Cr, Ni, Fe, Mo was achieved with 0.5 M, 30ºC and L:S 10. The Zn dissolution varied between 33 – 72%, Cr 2 – 4%, Ni 6 – 9%, Fe 2 – 9% and Mo 1 – 55%. Higher temperature and acid concentration resulted in faster dissolution of metals. AOD dust in both lines 1 and 2 has better valuable metal recycling possibilities than EAF dust due to better maximum Zn dissolution and better selective dissolution of Zn vs. Cr, Ni, Fe, Mo.

keywords: stainless steel dust leaching, EAF, electric arc furnace AOD, argon oxygen decarburization converter, hydrometallurgy, recycling

1. Introduction

Various amounts of wide range metal containing dusts are generated in separate parts of stainless steel process. In electric arc furnace (EAF), for example, about 1-2% of the charge is turned into dust (Steinlechner and Antrekowitsch, 2010; Tsakiridis and Oustadakis, 2010). Both the EAF and AOD dusts contains various amounts of chromium, nickel, iron, zinc and other heavy metal oxides and the weight percent of these elements usually varies from batch to batch basis (Nyirenda, 1991; Machado and Brehm, 2006; Tsakiridis and Oustadakis, 2010). Due to stricter environmental regulation laws and high price of stainless alloying elements, the valuable segment (Cr, Ni, Mo) of the stainless steel dusts are in the interest to be recycled back to

http://dx.doi.org/10.5277/ppmp120223

process, and the rest, small part of the harmful materials that are now landfilled, to be neutralized or minimized.

Today, most part of the carbon steel and stainless steel dusts are treated in separate plants mainly by pyrometallurgical methods to recover majority of the valuable materials (Zn, Cr, Ni, Mo) for re-use. However, some part of the flue dusts are still stored as landfill, mainly in developing countries (Nasmyth and Cooper, 2010; Ruetten 2010; Steinlechner and Antrekowitsch, 2010).

Hydrometallurgical methods instead of pyrometallurgical ones can offer energy savings and lower CO_2 emissions. Still, many hydrometallurgical processes have been investigated in the past three decades but virtually none of them have passed to wider industrial scale use. The main problem in steel dust leaching is the low yield and separability of zinc. Usually over 50% of Zn in the dusts exists in zinc ferrite structure $ZnFe_2O_4$ (franklinite) which makes the selective leaching of Zn without Fe difficult, whereas ZnO (zincite) phase does not cause problems and dissolves easily (LeClerc et al., 2003; Havlik et al., 2005; Havlik et al., 2006; Langová and Matýsek, 2010). Depending on its current price, the recovery method and amount in the dust, zinc is a valuable material resource for recycling to primary zinc production but a major impurity if recycled back to stainless steel process with Cr, Ni, Mo and Fe. Zinc is a volatile component which recirculates and adds up in the furnace and ventilation system (Nyirenda, 1991). In hydrometallurgical research, Zn - Fe separation and zinc recovery especially from carbon steel dusts, mainly from EAF dusts, has been the most researched topic. However, very few research projects have been focused on other types of dusts, i.e. AOD dust, or in general, on stainless steel dusts to recover Cr, Ni, Mo and Fe. Thus, a developed method to recover these valuable elements by hydrometallurgical means is relatively unknown. This might be due to the fact that stainless steel dust recycling by pyrometallurgical methods is well established and the value and concentration of the recovered elements has been sufficiently high to offset the high-energy consumption, the generation of worthless residues to landfill and high CO2 emissions (Nyirenda, 1991; Tsakiridis and Oustadakis, 2010).

There are numerous reports of EAF carbon steel dust leaching and treatment experiments in atmospheric pressure with sulfuric acid but the results vary greatly depending on the dust composition and leaching conditions (Nyirenda, 1991; Cruells et al., 1992; Strobos and Friend, 2004; Havlik et al., 2005; Shawabkeh, 2010; Tsakiridis and Oustadakis, 2010). Hydrochloric acid is found to be a quite effective lixiviant for the steel dusts zinc ferrite spinel (Baik and Fray, 2000). Jha et al. (2001) have done a review of different hydrometallurgical dust treatment processes for zinc recovery from industrial wastes. Havlik et al. (2004), Nyirenda (1991) and Zunkel (2001) discuss generally hydrometallurgical methods and problems encountered in carbon steel (EAF) dust treatment. For example, it is known fact that Cl and F are detrimental elements with very small ppm level amounts in the liquid phase if considering recycling zinc back to Zn primary metallurgy. The same problems and methods apply to some extent also in stainless steel dust treatment, for example

leaching harmful Zn as an impurity from the recyclable solids (Cr, Ni, Mo, Fe) and waste liquid management.

The main focus of the present work is on four stainless steel production dusts (EAF 1&2 and AOD 1&2) and the dissolution characteristics of Zn, Cr, Ni, Mo and Fe with sulfuric acid. The main objective at this first stage is to i) maximize zinc extraction into solution for recovery and ii) selectively leach maximum amount of zinc leaving the valuable elements Cr, Ni, Fe, Mo in the solid residue for further treatment and possible recycling back to stainless process.

2. Experimental

Four stainless steel production dust materials, from EAF 1&2 furnace and AOD 1&2 converter, were used for the leaching experiments. These dusts were collected from bag house filter containers behind each furnace or converter. These dusts are a mixture of different production batches, so each dust is a representative sample of an average dust composition.

The chemical composition of received stainless steel production dusts is presented in Table 1. The chemical analysis was done by a standardized method with molten sodium peroxide and atomic emission spectrometry (ICP-AES) for the most typical metals and earth alkaline metals in the dust. The main elements are Fe, Zn, Cr, Ca, Ni and Mn. Calcium is present due to its presence in fluxes and slag.

The chemical and mineralogical composition of dust depends on the batch feed material and the operating parameters of furnace or converter during production. In carbon steel EAF dusts, the zinc amount is typically from 15 to 35 wt.%, or even up to 40%, which is generally much higher than in dusts generated in stainless steel production (Havlik et al., 2004, 2006) (Table 1.)

Table 1. Chemical composition of received dust material from stainless steel production

Sample	wt-%	Zn	Fe	Cr	Ni	Mo	Mn	Mg	Ca	K	Pb	Cd	Cu	Al	S
EAF1		8	23	10	1.5	0.02	3	2	10	1.3	0.6	0.1	0.3	0.9	0.5
EAF2		6	20	10	2.6	0.1	3	1	13	1.4	1	0.3	0.5	1	0.4
AOD1		10	33	10	0.7	0.03	3	1.3	5	0.9	0.1	0	0.2	0.1	0.1
AOD2		5	26	10	2.9	1.3	3	2.5	15	0.8	0.5	0	0.3	0.2	0.2

Leaching experiments were done in a 1000 cm^3 glass reactor in a temperature controlled water bath with a cap that had sealable holes for dust material feed, thermometer, stirrer (300 rpm) and a condenser for water evaporation (Fig. 1). Total volume of 600 cm^3, 0.1 M, 0.5 M and 1.5 M sulfuric acid was used for the leaching experiments. The dust sample weight was 60 g and 30 g for liquid-to-solid ratios of 10 and 20, respectively. The temperature was 30ºC, 60ºC and 90ºC and the liquid samples for chemical analysis were taken and after 10, 20, 60 and 120 minutes.

The samples (10 cm^3) were filtered and sealed before sending them to multi-element ICP-AES analysis.

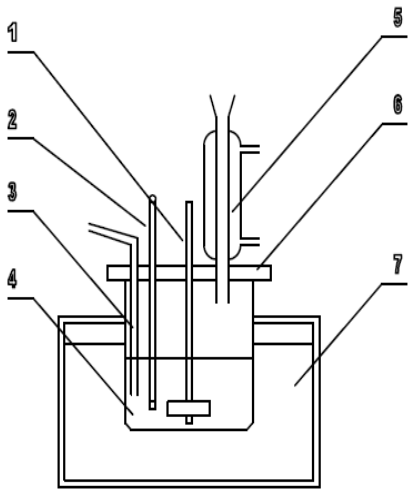

Fig. 1. Schematic picture of the leaching reactor. 1-stirrer, 2-thermometer, 3-sample off take, 4-glass reactor, 5-vapour cooler, 6-reactor cover, 7-temperature controlled water bath

3. Results and discussion

High acid concentration 1.5 M and high temperature 90 ºC results in faster leaching and higher yield of elements into solution versus 0.5 M and 30ºC (Fig.2) for all tested dust materials. With 0.1 M acid concentration the total dissolution was even lower or the elements did not dissolve at all.

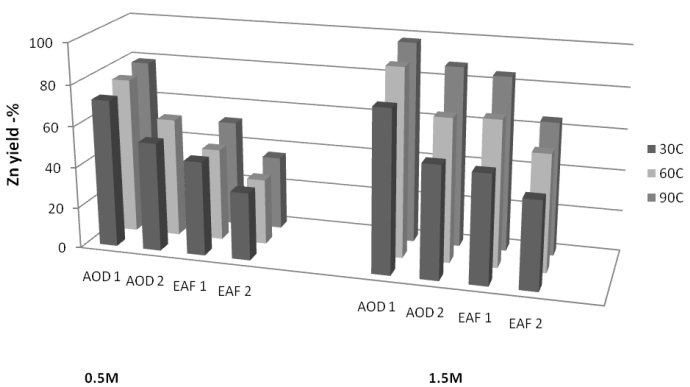

Fig. 2. The effect of temperature and acid concentration (in mol/dm^3) on Zn dissolution (L:S=10, 120 min)

The temperature and acid concentration effect trend is clear, except for 0.5 M, 90ºC AOD 2 dust where Zn probably started to precipitate. Thermodynamically certain elements dissolution depends on pH and Eh, so the pH increase in AOD 2 dust has probably reached Zn precipitation pH limit.

Between L:S 10 or L:S 20 liquid-to-solid ratios we did not notice a clear trend for Zn dissolution (Fig. 3). This could be due to the fact that with both L:S 10 and L:S 20 ratios there were enough free acid left and pH remained sufficiently low for Zn dissolution during the experiment. However, for Fe, it seems that with L:S 20 Fe dissolves somewhat faster and results in slightly higher yield than L:S 10. Exception is 0.5 M, L:S 10, 30ºC EAF 2 dust where acid-alkaline reactions seem to increase the system's pH into an area where Fe starts to precipitate (Fig. 3). This effect is not seen at 1.5 M, 90ºC (Fig. 4). Fe precipitation is a beneficial effect where zinc selectivity into solution is an objective

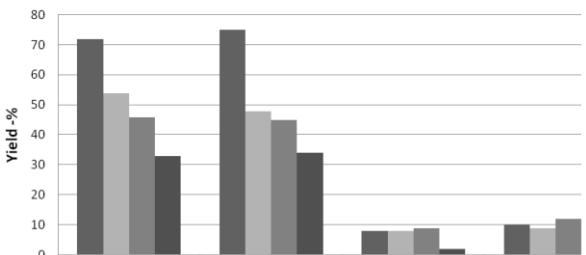

	Zn L:S 10	Zn L:S 20	Fe L:S 10	Fe L:S 20
AOD 1	72	75	8	10
AOD 2	54	48	8	9
EAF 1	46	45	9	12
EAF 2	33	34	2	18

Fig. 3.The effect of liquid-to-solid ratio on Zn and Fe yields, 0.5 M, 30ºC, 120 min

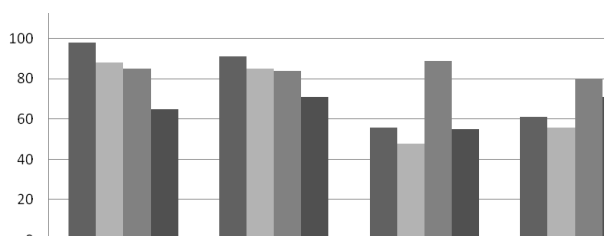

	Zn L:S 10	Zn L:S 20	Fe L:S 10	Fe L:S 20
AOD 1	98	91	56	61
AOD 2	88	85	48	56
EAF 1	85	84	89	80
EAF 2	65	71	55	71

Fig. 4.The effect of liquid-to-solid ratio on Zn and Fe yield -%, 1.5 M, 30ºC, 120 min

For all dusts, maximum Zn dissolution yield was achieved with 1.5M, 90ºC, and L:S = 10 where the Zn dissolution yield varied from 65% to almost 100%. At the same time: Cr was leached 7 – 17%, Ni 37 – 48%, Fe 48 – 89% and Mo 82 – 100% (Fig. 5.). The best zinc selectivity vs. Cr, Ni, Fe, Mo was achieved with 0.5 M, 30ºC, and L:S 10. Zinc dissolution varied between 33 – 72%, Cr 2 – 4%, Ni 6 – 9%, Fe 2 – 9% and Mo 1 – 55% (Fig. 6.).

A large variation of the yield results is probably due to chemical and mineralogical differences between the original dusts. Additionally, another important factor to affect the yield is to control the dissolution and precipitation reactions by careful pH control.

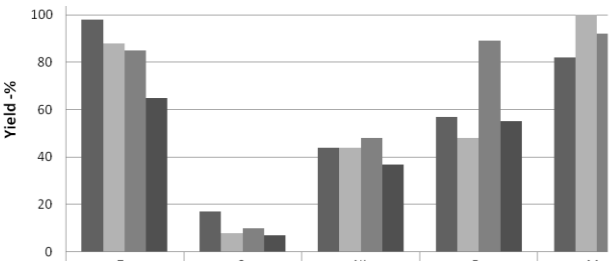

	Zn	Cr	Ni	Fe	Mo
AOD 1	98	17	44	57	82
AOD 2	88	8	44	48	100
EAF 1	85	10	48	89	92
EAF 2	65	7	37	55	99

Fig. 5. Maximum extraction yields for Zn, 1.5 M, 90ºC, L:S 10, 120 min

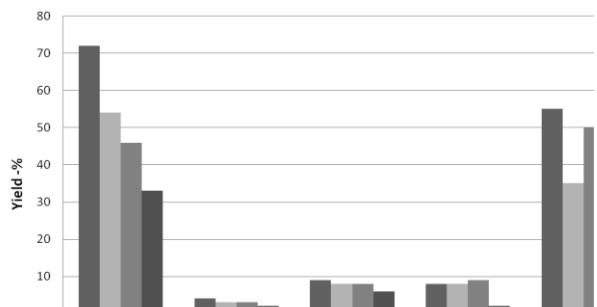

	Zn	Cr	Ni	Fe	Mo
AOD 1	72	4	9	8	55
AOD 2	54	3	8	8	35
EAF 1	46	3	8	9	50
EAF 2	33	2	6	2	1

Fig. 6. Best selectivity (Zn vs. Cr, Ni, Fe, Mo, 0.5 M, L:S 10, 120 min)

4. Conclusions

Sulfuric acid leaching of different stainless steel production flue dusts was studied. The main objective was to study valuable metals (Zn, Cr, Ni, Fe, Mo) dissolution yields for the dusts. The effect of sulfuric acid concentration, temperature and liquid-to-solid ratio were tested for maximum and selective Zn extraction into solution. The aim was to maximize zinc extraction for recovery and selectively leach maximum amount of zinc leaving the valuable elements Cr, Ni, Fe, Mo in the solid residue for further treatment.

Higher temperature and acid concentration resulted in faster dissolution and increased yield. Used L:S ratio and chemical composition of a dust has a presumable

effect on pH and, by that, on dissolution of a certain element. The AOD dust in both sample lines 1&2 had better maximum and selectivity results for Zn. The differences in leaching results were presumably from variations in chemical and mineralogical composition between the dusts. Nonetheless, experiments for more efficient selectivity with minimal amount of Fe and as high amount of Zn as possible in liquid phase are still needed for better valuable element (Zn, Cr, Ni, Fe, Mo) recycling possibilities. Understanding chemical and mineralogical effect on leaching is equally important.

Acknowledgement

This work has been done in the METDUST project of the ELEMET research program funded by FIMECC Oy. The financial support of TEKES, OutokumpuOyj, OutotecOyj and New Boliden Oyj (Kokkola) is gratefully acknowledged

References

BAIK, D.S., FRAY, D.J., 2000, *Recovery of zinc from electric-arc furnace dust by leaching with aqueous hydrochloric acid, plating of zinc and regeneration of electrolyte*, Trans. Inst. Min. Metall Sec. C 109: 121−128.

CRUELLS, M., ROCA, A., NUÑEZ, C., 1992, *Electric arc furnac flue dusts: characterization and leaching with sulphuric acid*, Hydrometallurgy 31, 213−231.

HAVLIK, T., FRIEDRICH, B., STOPIC, S., 2004, *Pressure leaching of EAF dust with sulphuric acid*, Erzmetall 57, 113−120.

HAVLIK, T., SOUZA, B.V.,. BERNARDES, A.M, SCHNEIDER, I.A.H., MISKUFOVA, A., 2006, *Hydrometallurgical processing of carbon steel EAF dust*., Journal of Hazardous Materials B135, 311−318.

HAVLIK, T., TURZAKOVA, M., STOPIC, S., FRIEDRICH, B., 2005, *Atmospheric leaching of EAF dust with diluted sulphuric acid*, Hydrometallurgy 77, 41−50.

JHA, M.K., KUMAR, V., SINGH, R.J., 2001, *Review of hydrometallurgical recovery of zinc from industrial wastes, Resources*, Conservation & Recycling 33, 1−22.

LANGOVÁ, S., MATÝSEK, D., 2010, *Zinc recovery from steel-making wastes by acid pressure leaching and hematite precipitation*, Hydrometallurgy 101: 171-173.

LECLERC, N., MEUX, E., LECUIRE, J.-M., 2003, H*ydrometallurgical extraction of zinc from zinc ferrites*, Hydrometallurgy 70, 175−183.

MACHADO, J.G.M.S., BREHM, F.A., 2006, *Chemical, physical, structural and morphological characterization of the electric arc furnace dust*, Journal of Hazardous Materials B136, 953−960.

NASMYTH, M., COOPER, G., 2010, *Feed materials and process options*. Lead-Zinc 2010. L. C. A. Siegmund, C. Green, N. Piret, G. Richards and R. Stephens. Vancouver, Canada, John Wiley & Sons, Inc. New Jersey: 291−306.

NYIRENDA, R.L., 1991, *The processing of steelmaking flue-dust: a review*, Minerals Engineering 4, 1003−1025.

RUETTEN, J., 2010, *Different ways of using waelz oxide - overview and evaluation*. Lead-Zinc 2010. L. C. A. Siegmund, C. Green, N. Piret, G. Richards and R. Stephens. Vancouver, Canada, John Wiley & Sons, Inc. New Jersey: 841−849.

SHAWABKEH, R.A., 2010, *Hydrometallurgical extraction of zinc from Jordanian electric arc furnace dust*, Hydrometallurgy 104, 61−65.

STEINLECHNER, S., ANTREKOWITSCH, J., 2010, *Simultaneous recovery of various metals from zinc containing residues on a reducing metal bath*. Lead-Zinc 2010. A. Siegmund, L. Centomo, C. Green, N. Piret, G. Richards and R. Stephens. Vancouver, Canada, John Wiley & Sons, Inc. Hoboken, New Jersey: 889−897.

STROBOS, JG., FRIEND, J.F.C., 2004, *Zinc recovery from baghouse dust generated at ferrochrome foundries*, Hydrometallurgy 74, 165−171.

TSAKIRIDIS, P.E., OUSTADAKIS, P., 2010, *Hydrometallurgical process for zinc recovery from electric arc furnace dust (EAFD), Part I: Characterization and leaching by diluted sulphuric acid*, Journal of Hazardous Materials 179(1−3), 1−7.

ZUNKEL, D.A.D., 2001, *Recovering zinc and lead from electric arc furnace dus*t: *A 2001 processing and technology status update*. European Metallurgical Conference, Friedrichshafen, Germany, GDMB.

Physicochem. Probl. Miner. Process. 48(2), 2012, 607−618

www.minproc.pwr.wroc.pl/journal/

Physicochemical Problems of Mineral Processing

ISSN 1643-1049 (print)
ISSN 2084-4735 (online)

Received March 19, 2012; reviewed; accepted May 6, 2012

FLOTATION OF SERPENTINITE AND QUARTZ USING BIOSURFACTANTS

Agnieszka M. DIDYK, Zygmunt SADOWSKI

Wroclaw University of Technology, Chemical Engineering Department, Wybrzeze Wyspianskiego 27, 503-70 Wroclaw, Poland, agnieszka.didyk@pwr.wroc.pl, zygmunt.sadowski@pwr.wroc.pl

Abstract. Biosurfactants produced by *Bacillus circulans* and *Streptomyces* sp. were used for biomodification of both serpentinite and quartz surfaces. The biosurfactants produced by bacteria possess the ability to decrease the surface tension of water from 72 to 28.6 mNm^{-1} (*Bacillus circulans*) and to 29.3 mNm^{-1} (*Streptomyces* sp.).

This paper demonstrated biomodification of quartz and serpentinite surfaces by the biosurfactants adsorption. The effect of biosurfactants adsorption onto mineral surface properties was investigated by microflotation. Additionally, IR-ATR spectroscopy was used for characterisation of the biomodificated surfaces of quartz and serpentinite. Flotation experiments indicated that these biosurfactants effectively changed the properties of mineral surfaces and the separation of minerals can be realized.

keywords: biosurfactant; flotation; surface tension; quartz, serpentinite

1. Introduction

Biosurfactants are amphiphilic compounds produced by microorganisms that exhibit surface activity. These metabolite products can be categorized into four groups (i) lipopeptides, (ii) lipoproteins, (iii) glycolipis, (iv) phospholipids. In comparison to synthetic surfactants, biosurfactants possess several advantages such as a low irritancy, high biodegrability and low toxicity. For these reasons, they are ecologically acceptable.

Biosurfactants are applied in pharmaceutical, cosmetic, detergent and food industries (Banat et al., 2000). A spectacular application of biosurfactants is the microbial enhanced oil recovery (MEOR) and viscosity reduction of heavy crude oil for pipeline transport. Biosurfactants enhance emulsification of hydrocarbons and accelerate oil remediation.

Application of biosurfactants as bioreagents in mineral processing operations (bioflotation or bioflocculation) is a new way for upgrading minerals (Rao et al., 2010). In recent years, several studies have been carried out on the use of biosurfactants as flotation reagents. Knowledge of adsorption of biosurfactants at the solid-liquid interface is essential for understanding the basic mechanism of flotation and lubrication. Adsorption of biosurfactant on a substratum surface alters

http://dx.doi.org/10.5277/ppmp120224

hydrophobicity of the surface and causes a facilitation of microbial adhesion. For mineral processing, bioflotation is very important to understand the role of metabolic products in biomodification of the mineral surface.

Chemoautotrophic bacteria such as *Acidithiobacillus ferrooxidans*, *Acidithiobacillus thiooxidans,* and *Leptospirillum ferrooxidans*, which usually live in aqueous acid solution in mines, are able to depress sulfide minerals. It is a result of surface oxidation. Selective flotation of complex sulfide ores, particularly chalcopyrite, sphalerite, and pyrrotite using xanthate as collector, needs application of bioreagents (Pecina et al., 2009).

Bacteria attach to the surface by a complex of exopolysaccharides, called glycocalyx, forming a biofilm. The colonization of the surface by bacteria can lead to modification of the surface property (Das et al., 2009).

Magnesium silicate can be used for storage of CO_2 by mineral carbonation. Dissolution of natural serpentinite in acids and precipitation of magnesium carbonate require quartz to be removed. Carbonation of natural serpentinite seems to be an interesting alternative to geological reservoirs for storage of CO_2 (Teir et al., 2009).

Serpentinite can be used as a conventional raw material in the ceramic industry. Mechanical resistance of serpentinite depends on the quantity of quartz in the raw materials (Diaz, Torrecillas 2007).

The aim of this paper was to investigate flotation of quartz and serpentinite in the presence of biosurfactants and nickel ions as an activator.

2. Materials and methods

2.1. Microorganisms and biosurfactant production

Bacteria were isolated from soil samples. Soil samples were collected from a gas station soil. The samples were collected in sterilized glass bottles. The isolation procedure was carried out using the serial dilution-agar plating technique. Two pure cultures (*Bacillus circulans* and *Streptomyces* sp.) were selected. The strains were grown on a liquid mineral salt medium consisting of K_2HPO_4 (7 g/dm^3), KH_2PO_4 (3 g/dm^3), $MgSO_4 \cdot 7H_2O$ (0.1 g/dm^3) $(NH_4)_2SO_4$ (1 g/dm^3), Yeast extract (0.5 g/dm^3), saccharose (10 g/dm^3) and glycerin. Microorganisms were cultures in 500 cm^3 shake flasks containing 250 dm^3 of medium. The cultures were incubated in a rotary shaker at the temperature of 26 °C. The cell growth and surface tension were monitored with respect to time. The cultures from the end of exponential growth phase were centrifuged (3500 rpm for 25 min) and the cell-free culture broth was used as the broth for flotation experiments. The cell concentration was determined by the optical density measurements at wavelength 550 nm (OD_{550}) using a spectrophotometer.

2.2. Mineral samples

Mineral samples of quartz and serpentinite ($Mg_3(Si_2O_5)OH_4$) were obtained from Osiecznica mine and Grochow mine, respectively. Both mines are located in Lower Silesia (Poland).

The mineral samples were dry ground using a porcelain ball mill and then wet sieved. The +125 - 250 μm fraction was used for microflotation experiments. The particle size distribution of the sample was determined using Malvern Mastersizer 2000. The particle size analysis showed that the mean diameters for quartz and serpentine were 231.1 μm and 227.5 μm, respectively. The specific surface area of the samples was measured using FlowSorb II 2300, according to the BET method. Helium and nitrogen was used as the gas mixture. The BET surface area was found to be 0.19 g m^{-2} for quartz and 7.62 g m^{-2} for serpentine. The X-ray powder diffraction analysis indicated that the sample of quartz was of high purity.

2.3. Microflotation experiment

The flotation experiments have been conducted using a glass Hallimond tube (height of 43 cm, diameter of 3.8 cm, and total volume of column about 500 cm^3). Pure nitrogen at a flow rate of 50 cm^3/min for 20 min was used for flotation. For flotation tests, 1 g of mineral samples of size +125 - 250 μm was added to 0.12 dm^{-3} total volume suspensions. The suspension containing biosurfactants or anionic surfactant sodium dodecyl sulphate (SDS was purchased from POCh) was transferred to the microflotation tube and floated. Flotation recovery was calculated as the ratio of floated to unfloated material.

Before flotation, mineral samples were activated with a variable concentration of hexahydrate nickel chloride solution ($5 \cdot 10^{-4}$ M, 10^{-3} M $3 \cdot 10^{-3}$ M, $5 \cdot 10^{-3}$ M, 10^{-2} M, $5 \cdot 10^{-2}$ M respectively) for 1 hour. The biosurfactants and SDS were conditioned with activated mineral for 2 hour.

2.4. Surface tension measurement

The surface tension of the culture broth was measured using a Krüss 12 T (Kruss Optische-Mechansche Werkstatten, Hamburg, Germany) ring tensiometer as a qualitative indicator of biosurfactant production. The surface tension measurements were carried out at temperature of 20 ± 1^0C. All of the measurements were repeated five times and their average values were plotted.

2.5. Zeta potential measurements

The zeta potential of mineral samples were measured using Malvern ZetaMaster. The mineral samples (< 40 μm) were dispersed in a 1 mM NaCl solution (indifferent electrolyte) and the pH was adjusted using diluted solutions of HCl and NaOH. All experiments were conducted with the pH progressively changed from pH 10 to 1.5, with a 15 min equilibration time at each new pH value. The zeta potential profiles for serpentinite and quartz were carried out in the absence and presence of biosurfactants (broth solution).

3. Experimental studies

Separation of pure bacterial surfactant from the broth is complicated. For this reason the whole fermented solution as a mixture of biosurfactants and metabolic products was used. In this study, the microorganism growth and surface tension changes during the incubation period are presented in Figs. 1 and 2 for the *Bacillus circulans* and *Streptomyces* sp. The reduced surface tension of broth was an indicator of biosurfactant production. The cultures growth was controlled by measuring the changes in culture medium turbidity as a function of the bacteria cell density. Figure 1 shows that the highest bacterial cell density appears at cultivation time of 20 h. In this period a sharp drop in surface tension value (from 49.0 to 30.48 mNm^{-1}) was observed. Under the studied conditions the stationary phase of growth was reached and microbial surfactants synthesis was noticed. The highest surface tension reduction of the broth was achieved after 24 h (28.4 mNm^{-1}). The surface tension value remains unchanged for further cultivation, which indicates that culture was stable.

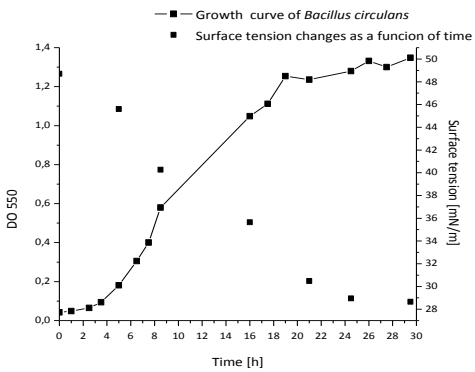

Fig. 1. Growth curve of *Bacillus circulans* and broth surface tension changes as a function of time

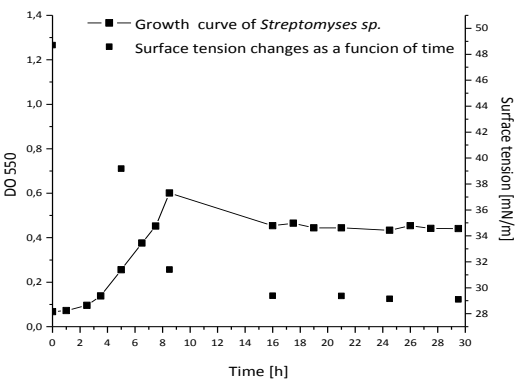

Fig. 2. Growth curve of *Streptomyces* sp. and broth surface changes as a function of time

Figure 2 illustrates that the highest turbidity of the culture medium correlated with cell density was noticed after about 8 hours from inoculation. In this period the culture moved from the logarithmic phase of growth to stationary phase and the strain of *Streptomyces* sp. started production of biosurfactants. Moreover, the surface tension value at the equilibrium phase reached 29.7 mNm^{-1} and stayed strongly reduced to the end of the experiments.

Biosurfactants have amphiphilic nature. For this reason, the biosurfactant molecules adsorb readily at the solid-liquid interface and results in biomodification of the mineral surfaces. Physical adsorption is realized by electrostatic interactions between the biosurfactant head group and oppositely charged surface. Chemisorption demands chemical interaction between surfactant and mineral (Gallos et. al., 2007). In this paper microbial surfactants adsorption onto quartz and serpentine surfaces in the

presence of several of nickel ions concentrations as an activator was investigated. Also, a possible use of biosurfactants as a quartz and serpentinite collector or modifier was examined by microflotation tests. Results of quartz and serpentinite flotation using SDS, *Streptomyces sp*. broth and *Bacillus circulans* broth as the collector are presented in Figs 3-5, respectively. Nickel chloride at concentrations of $5 \cdot 10^{-4}$ M, 10^{-3} M, $3 \cdot 10^{-3}$ M, $5 \cdot 10^{-3}$ M, 10^{-2} M, and $5 \cdot 10^{-2}$ M was used as an activator of mineral surface. The pH value maintained during the flotation experiments was in the range of 5.9-7.6, which was constant for samples with *Streptomyces sp*. broth, *Bacillus circulans* broth and SDS, respectively. Figures 3-5 show a strong effect of the activator concentration on the rate of quartz and serpentinite flotation.

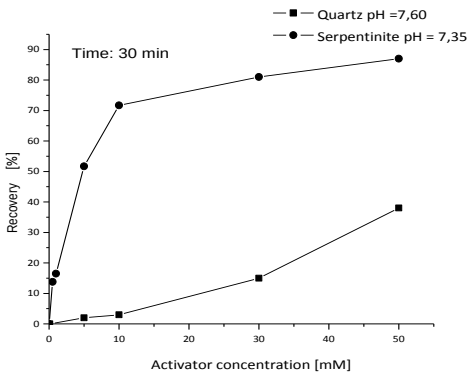

Fig. 3. Flotation recovery of quartz and serpentinite using SDS ($5 \cdot 10^{-3}$ M) as collector in a function of activator concentration (Ni^{2+} ions)

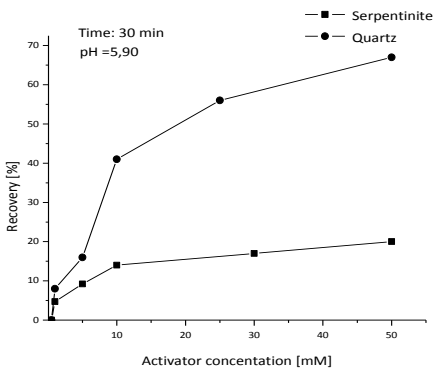

Fig. 4. Flotation recovery of quartz and serpentinite using *Bacillus circulans* broth as collector in a function of activator concentration

The microflotation tests in the present of SDS clearly show that both minerals flotation recovery increases when the concentration of the activator ions increases. At pH close to 8 adsorption of $Ni(OH)^+$ ions takes place on the silica and serpentinite surfaces and their amount increases with the concentration of $NiCl_2$. The presence of these ions on the silica and serpentinite surfaces results in the appearance of local positive charges. That allows interacting with the anionic surfactant molecules and thereby increasing surface hydrophobicity. The stable surface structure of quartz favors physical adsorption of the collector. Anionic nature of SDS and positive charge of the activated quartz surface cause that the collector is electrostatically attracted to the surfaces. That allows to carry out silica flotation process with yield of 37% at the concentration of activator ions about $5 \cdot 10^{-2}$ M. One can see that at the same activator concentration the recovery of serpentine reaches a value of 87% (Fig. 3). It is related to a different mechanism of adsorption. In the case of serpentinite SDS interacts both with Ni^{2+} ions (physical adsorption) and the surface ions Mg^{2+} (chemical adsorption). Moreover, the observed differences between the recovery of quartz and serpentinite can be caused by different specific surface areas of used minerals.

An analysis of experimental results of activated silica and serpentinite (Fig. 4-5) flotation indicates that for both medium broths the flotation yield increases with increasing activation ions concentration. The flotation profile is similar to the flotation using anionic collector. It can be concluded, according to the previous assumptions, that the two cultivation media contain anionic biosurfactants in their composition. Biomolecules were able to adsorb onto mineral surfaces, causing their modification. In the case of culture medium derived from *Bacillus circulans*, the flotation recovery of silica reached a high value of 68%, while the yield of the silica flotation using the broth from *Streptomyces sp*. is more than twice lower (30%).

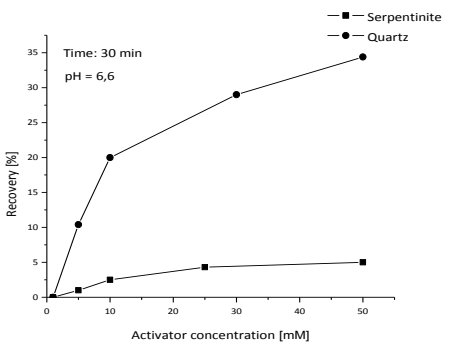

Fig. 5. Flotation recovery of quartz and serpentinite using *Streptomyces sp.* broth. as collector as a function of activator concentration

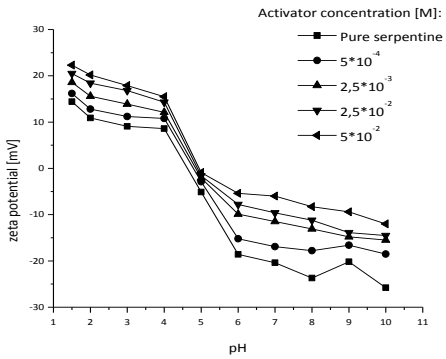

Fig. 6. Zeta potential of activated quartz and pure serpentinite as a function of pH (indifferent electrolyte 1 mM NaCl solution)

Figures 4 and 5 show the results of flotation experiments using activated serpentinite. As for silica, we are dealing with biomodification of mineral surface. However, in this case, the flotation recovery is much lower. The analysis of the results indicates that serpentinite flotation using culture medium from *Bacillus circulans* gave flotation yield about 18%, while flotation testes carried out after the interaction with broth solution from *Streptomyces sp*. made it possible to obtain only 5% recovery. As one can see, there are large differences in the flotation recoveries of both minerals. Therefore, it seems possible to selectively float quartz from serpentinite. The obtained lower bioflotation results, when compared to the flotation test with SDS, can be attributed to the fact that broths containing polysaccharides, proteins and organic acids make the surface of serpentine and quartz more hydrophilic. Moreover, large yields differences between quartz and serpentinite flotation for the same medium broth result from differences in interacting of broth compounds with activated mineral surfaces (interaction and complex formation between Mg^{2+} and broth compounds could occur), and consequently from the different adsorption degrees of these elements on both mineral surfaces.

Differences in the flotation yields for serpentinite and quartz resulting from the application of different broths can be caused by different composition of the broth, as well as differences in pH values of the flotation feed solutions.

The flotation data are in accordance with the zeta potential evaluation. The zeta potential and isoelectric point of serpentine and quartz were measured for pure mineral samples and for samples in the presence of biosurfactant as a surface modifier.

Figures 6 and 7 show the changes of the zeta potential as a result of the activation of the mineral surface. In the presence of Ni^{2+} ions significant changes in the value of zeta potential is observed. Increasing amount of activator ions at the particle surface increased the zeta potential values. Moreover, the isoelectric point (IEP) of pure quartz is around 2.5, which is close to the IEP values reported in literature (Kosmulski, 2009). The IEP of serpentinite was above 4.3. The isoelectric point of serpentine is strongly dependent on the mineralogical composition of the mineral. The presence of activator ions (Ni^{2+}) caused the IEP of both minerals to increase. Figure 8 depicts the result of electrokinetic measurements for biomodified serpentinite and quartz.

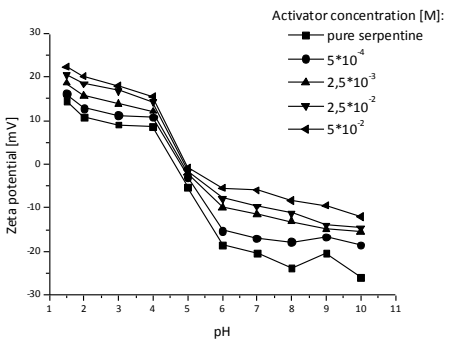

Fig. 7. Zeta potential changes of pure and activated serpentinite as a function of pH (indifferent electrolyte: 1 mM NaCl solution)

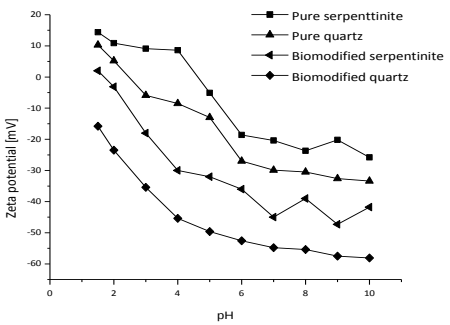

Fig. 8. Zeta potential changes of biomodified (broth of *Bacillus circulans*) minerals as a function of pH (indifferent electrolyte: 1 mM NaCl solution)

Surfactant molecules from the bulk can adsorb on the particle and control the surface charge as well as the hydrophobic character of the surface. The surface became more hydrophobic resulting in changing the surface properties of mineral and zeta potential values. It can see that the pH of IEP for both minerals has shifted towards lower pH. The zeta potential values of serpentinite and quartz were decreased when the broth from *Bacillus circulans* was added. Moreover, the zeta potential profiles for both minerals after interaction with the metabolite solution were similar.

Additionally, the IR-ATR spectroscopy and optical microscope were used for the characterization of surface properties of pure samples of quartz and serpentinite before and after interaction with biosurfactants.

Figure 9 and 10 illustrate IR-ATR spectroscopy spectra of activated surfaces of silica and serpentine. Silica is the final products of silicates decomposition caused by water and carbon dioxide. A general formula of silica (SiO_2) does not fully reflect the interactions between atoms. The structure of quartz surface shows a large amount of OH groups. It can be noticed that the most important role in the adsorption process on the mineral surface is played by siloxane bonds (≡ Si-O-Si ≡) and silanol groups (Si-OH) (Mesquita, 2003). In the spectrum of Ni^{2+} ions activating silica, six characteristic vibrations were observed (Fig. 9). The absorption peak at 650 cm^{-1} corresponds to the stretching vibrations of diatomic O-H units. The absorption bands at 777.62 - 794.40 cm^{-1} are characteristic for the symmetric stretching vibration of the ≡ Si-O-Si ≡ bond. The peak at 1062.93 cm^{-1} represents vibrations of the ≡ Si-O-Ni- bond and peak at 1082.51 cm^{-1} is due to asymmetric stretching vibration of the Si-O-Si bond. Finally, the absorption pick at 1163.63 cm^{-1} is from vibrations of the valence Si-O bond.

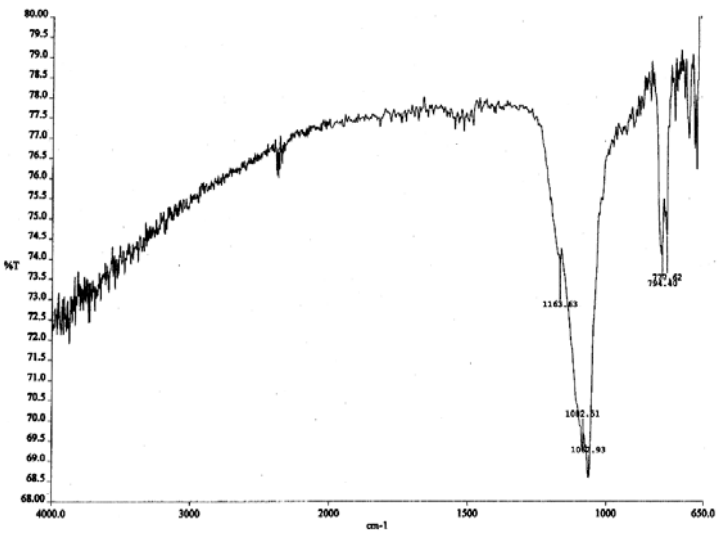

Fig. 9. ATR-IR spectrum of quartz surface activated by Ni^{2+} ions

Serpentinite ($Mg_3(Si_2O_5)OH_4$) is a layered silicate, which belongs to the group of clay materials. The spectrum of activated serpentinite (activation using nickel ions) contains four characteristic bands (Fig. 10). Adsorption band at 672.35 cm^{-1} corresponds to the vibrations of O-H bonds. Peak at 885.11 cm^{-1} represents deforming vibrations of Si-OH groups. The IR band at about 963.48 cm^{-1} is attributed to the stretching vibrations of ≡ Si-OH bonds, and the band at 1011.88 cm^{-1} is characteristic for the vibrations of ≡ Si-O-Ni- bond.

In this paper the changes in the IR spectra of activated minerals, as a result of biomodification, were examined. Figures 11 and 12 illustrate the IR-ATR spectra of silica and serpentine after the biomodification process. The broth from *Bacillus*

circulans was used for biomodification. The spectrum of biomodified silica shows some significant differences compared to the spectra of silica activated by Ni^{+2} ions.

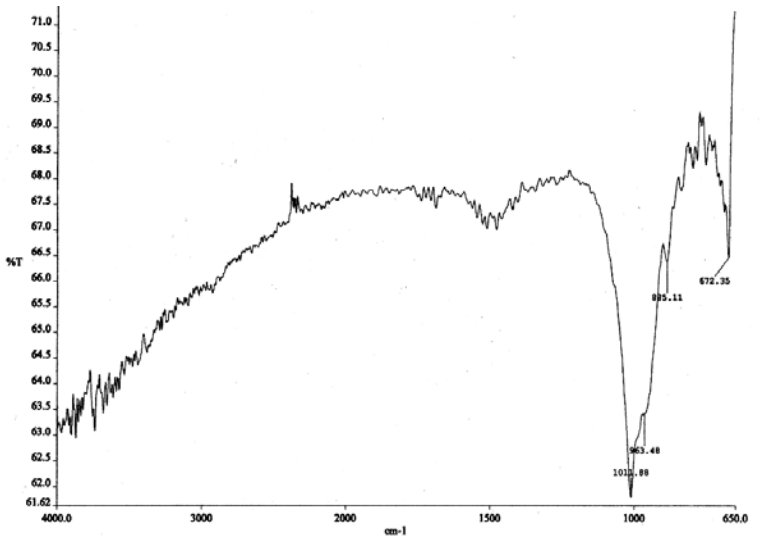

Fig. 10. ATR-IR spectra of serpentine surface activated by Ni^{2+} ions

The adsorption band at 1170.78 cm^{-1} corresponds to vibrations of valence Si-O bond. The peak at 700.38 cm^{-1} represents the vibrations of O-H bonds. It is less intense compared to the band observed for the activated silica. A weaker band was observed at 1053.11 cm^{-1}.It is characteristic for the vibrations of ≡Si-O-Ni- bond. Additionally, the IR spectrum of biomodified silica has showed two new bands. These bands did not exist in the case of activated mineral. The first band at 797.64 cm^{-1} represents the symmetric stretching vibrations of the ≡Si-OH bonds. The second adsorption peak at 700.38 cm^{-1} is attributed to rocking vibrations of - (CH_2) n - $(n \geq 4)$ bonds. Moreover, the IR spectra of silica which was biomodified by broth from *Streptomyces sp*. show similar changes when compared to the spectrum of silica biomodified by *Bacillus circulans.*

The IR spectrum of biomodified serpentine is presented at Fig. 12. The distinct changes in the absorption frequency profile can be observed for the spectra of the activated mineral. The adsorption peak at 683.98 cm^{-1} is due to vibrations of O-H bond. However, it is less intense than the frequency corresponding to the activated serpentinite.

A weaker band, apparent at 1015.48 cm^{-1}. It corresponds to the vibrations of ≡ Si-O-Ni- bonds. Additionally, we can see the band, which does not occur in the spectrum of the activated serpentine. The adsorption peak at 746.06 cm^{-1} represents the rocking vibration of the -(CH_2) n - $(n \geq 4)$ bond. Finally, the IR band at 834.55 cm^{-1} is attributed to the vibration of $C(CH_3)_3$ bonds. Furthermore, the IR-ATR spectrum was collected for biomodified serpentinite by the contact with the broth received from

Streptomyces sp. The observed changes in the IR spectrum of minerals were exactly the same as for the biomodification using *Bacillus circulans*.

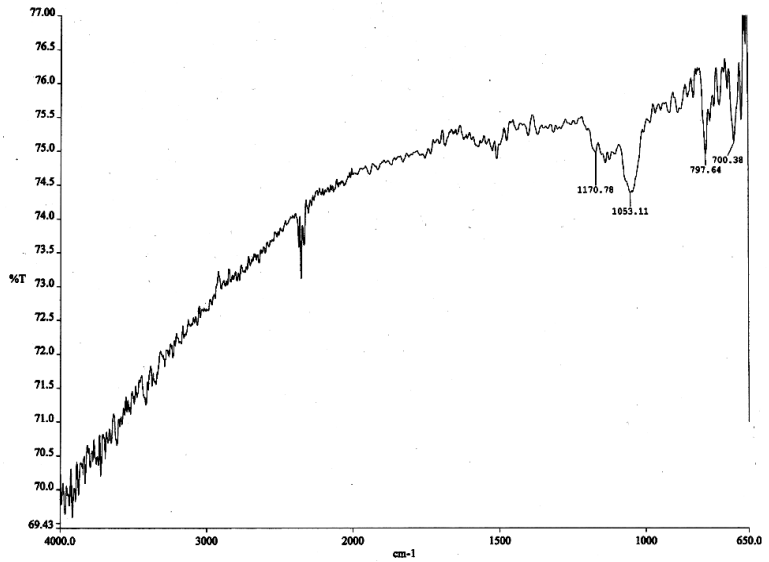

Fig. 11. ATR-IR spectrum of quartz surface biomodified by adsorption of *Bacillus circulans*

It was shown that biomodification of both minerals causes significant changes of the spectra. The intensity reduction of adsorption bands corresponding to vibrations of ≡Si-O-Ni- bonds was noted. It indicates that the biosurfactants adsorption on the minerals surface occurs through the ≡Si-O-Ni- center. Similarly, the intensity decrease of the band, characteristic to the vibration of O-H group, is probably due to the adsorption of biological surfactants onto the mineral surfaces.

Moreover, the appearance of new adsorption bands for biomodified silica and serpentine surfaces correspond to the hydrophobic tails of adsorbed biosurfactants.

By comparing the spectra of the biomodified silica and serpentine surface it can be concluded that many new groups appear onto the modified surface of serpentinite. Generally, the profile changes in the surface structure of both minerals, caused by biomodification using culture media, are similar. However, full explanation of biosurfactants adsorption mechanism onto the silica and serpentinite surfaces requires further detailed studies.

4. Conclusions

In this paper biomodification of quartz and serpentinite by biosurfactants adsorption was investigated. Biosurfactants from *Bacillus circulans* and *Streptomyces sp.* served as modifying agents for serpentinite and quartz flotation. The application of these modifying agents makes the separation process possible.

1. Biosurfactants adsorption is a result of interactions of hydrophilic parts of biomolecules with nickel center on the surfaces of minerals or with magnesium center on the serpentinite surface.
2. Flotation recovery of modified quartz and serpentine increases with increasing activating ion concentration. The maximum flotation yield (68%) corresponds with the maximum Ni^{2+} ion concentrations. This correlation was obtained for the activation process using silica and the culture medium of *Bacillus circulans.*
3. Adsorption of nickel ions on the mineral surfaces changes the value of zeta potential and isoelectric point. An increase of the activator concentration caused an increase in zeta potential values.
4. Biomodification of both investigated mineral surfaces caused a decrease of zeta potential values.
5. Biomodification of quartz and serpentinite caused important changes in the ATR-FTIR spectra of their surfaces. The appearance of new bands in the adsorption spectra of modified serpentine correspond to the presence of hydrocarbon groups on the mineral surface.
6. Most changes in the silica and serpentine surfaces as a result of biomodification have a similar nature.

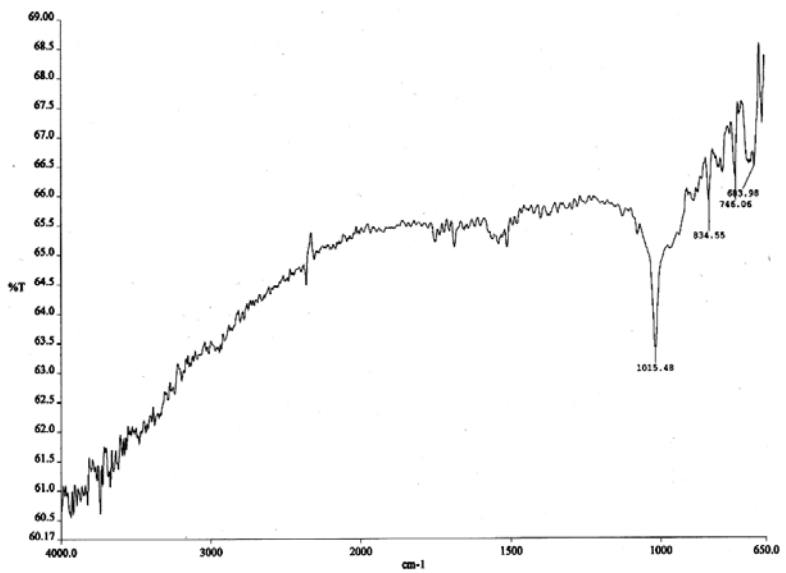

Fig. 12. ATR-IR spectrum of serpentine surface biomodified by adsorption of *Bacillus circulans*

Acknowledgement

This research was funded by the Dean of Faculty of Chemistry, Wroclaw University of Technology. The authors thank to Dr. I. Maliszewska for providing valuable comments in the field of microorganisms.

References

BANAT, M.I., MAKKAR S.R., CAMEOTRA S.S., 2000, *Potential commercial application of microbial surfactantas*, Appl. Microbial Biotechnol., 53,495−508.

CASAS BOTERO E.A., TOREM L.M., SOUZA DE MESQUITA M.L., 2007, *Fundamental studies of Rhodococcus opacus a as a biocollector of calcite and magnesite*, Minerals Engineering, 20, 1026−1032.

DAS P., MUKHERJEE S., SEN R., 2009, *Antiadhesive action of a marine microbial surfactant*, Colloids Surfaces B: Biointerfaces, 71, 183−186.

De MESQUITA S.M.L., LINS F.F., TOREM L.M., 2003, *Interaction of a hydrophobic bacterium strain in a hematite-quartz flotation system*, Int. J. Miner. Process. 71, 31−44.

DIAZ A.L., TORRECILLAS R., 2007, *Porcelain stoneware obtained from the residual muds of serpentinite raw materials*, J. European Ceramic Society, 27, 2341−2345.

GALLIOS G.P., DELIYANNI E.A., PELEKA E.N., K.A. MATIS, 2007, *Flotation of chromite and serpentine*, Separation and Purification Technology, 55, 232−237.

KOSMULSKI M., 2009, *Complication of PZC and IEP of sparingly soluble metal oxides and hydroxides from literature*, Advances Colloid Inter. Sci., 152, 14−25.

PECINA T.E., RODRIGUEZ M., CASTILLO P., DIAZ V., ORRANTIA E., 2009, *Effect of Leptospirillum ferrooxidans on the flotation kinetics of sulphide ores*, Minerals Engineering 22, 462−468.

RAO H.K., VILINSKA A., CHERNYSHOVA V.I., 2010, *Minerals bioprocessing: R and D needs in mineral biobeneficiation*, Hydrometallurgy, 104, 465−470.

TEIR S., ELONEVA S., FOGELHOLM C-J., ZAVENHOVEN R., 2009, *Fixation of carbon dioxide by producing hydromagnesite from serpentinite*, Applied Energy, 86, 214−218.

Physicochem. Probl. Miner. Process. 48(2), 2012, 619−630

www.minproc.pwr.wroc.pl/journal/

Physicochemical Problems of Mineral Processing

ISSN 1643-1049 (print)
ISSN 2084-4735 (online)

Received March 21, 2012; reviewed; accepted April 23, 2012

SYNTHESIS OF HEPTA(ISOBUTHYL)ETHYLTRIETHOXYSILYL-OCTASILSESQUIOXANE AND ITS APPLICATION AS A MODIFIER OF BOTH HYDRATED AND EMULSION SILICAS

Karolina SZWARC-RZEPKA*, Filip CIESIELCZYK*, Monika ZAWISZA*, Michał KACZMAREK*, Michał DUTKIEWICZ, Bogdan MARCINIEC**, Hieronim MACIEJEWSKI***, Teofil JESIONOWSKI***

* Poznan University of Technology, Faculty of Chemical Technology, Institute of Chemical Technology and Engineering, M. Skłodowskiej–Curie 2, PL-60965, Poznan, Poland, E–mail: Teofil.Jesionowski@put.poznan.pl, phone: +48(61)6653720, fax: +48(61)6653649

** Adam Mickiewicz University, Faculty of Chemistry, Department of Organometallic Chemistry, PL-60780, Grunwaldzka 6, Poznan, Poland

*** Poznan Science and Technology Park, Rubież 46, PL-61612 Poznan, Poland

Abstract. Hepta(isobuthyl)ethyltriethoxysilyloctasilsesquioxane was synthesized by hydrosilylation of hepta(isobuthyl)vinyloctasilsesquioxane with triethoxysilane, over Karstedt catalyst and tetrahydrofuran. Hybrid systems of silica and monofunctional silsesquioxane (SiO_2/POSS) were obtained by solvent evaporation, using emulsion silica (ES) and hydrated silica (HS), obtained by precipitation in emulsion or water media. For their surface modification hepta(isobuthyl)ethyltriethoxysilyloctasilsesquioxane was used. The hybrids were characterized by dispersion analysis (NIBS method and laser diffraction technique) and morphological analysis (transmission electron microscopy) as well as wettability profiles in an aqueous system. The adsorptive properties of the hybrids were evaluated on the basis of surface area BET, pore volume and size. The effectiveness of modification of the hybrid fillers was tested by FTIR and ^{29}Si CP MAS NMR.

keywords: silica, surface modification, silsesquioxanes cage, hybrid nanofillers

1. Introduction

Polyhedral Oligomeric Silsesquioxanes or POSS make an important group of organic-inorganic hybrid materials. They occur in many varieties differing in the size of cages, the number and type of side groups (Iyer, 2007). Particularly stable is T_8 silsesquioxane in which the organic groups R are attached to the inorganic fragments of each vertex of a silsesquioxane cage containing Si–O–Si group (Wallace, 2000).

The chemistry of silsesquioxanes is dominated by the chemistry of T_8 and its derivatives, which is related to its easy synthesis, easy isolation from the reaction mixture and high yields of the processes in which it is involved when compared to those of the other POSS (Janowski, 2008). POSS show many interesting properties

http://dx.doi.org/10.5277/ppmp120225

such as thermal stability, easy chemical modification and tendency to formation of nanometric size particles (Madhavan, 2009).

POSS containing 8 silicon atoms in its molecule (T_8) is most often used in synthesis of polymers (Tang, 2009; Lin, 2009), in dentistry (Wu, 2009), microelectronics and optics (Matisons, 2010). Silicas modified with cage POSS have been so far used only for determination of catalytic properties of metallocenes (Bianchini, 2005).

The main aim of this work was the synthesis of hepta(isobuthyl)-ethyltriethoxysilyloctasilsesquioxane and its application as a modifier of hydrated and emulsion silicas. Moreover, the influence of such modification process on the physicochemical properties of hybrid fillers obtained was evaluated.

2. Experimental

2.1. Synthesis of hepta(isobuthyl)ethyltriethoxysilyloctasilsesquioxane

Hepta(isobuthyl)ethyltriethoxysilyloctasilsesquioxane (K-POSS) was synthesized in the hydrosilylation reaction of previously synthesized hepta(isobuthyl)-vinyloctasilsesquioxane (Żak, 2009) with triethoxysilane (Fig. 1). The process was carried out in the presence of a Karstedt catalyst and THF as a solvent. Hepta(isobuthyl)vinyloctasilsesquioxane (5 g, 5.9 mmol), triethoxysilane with 10% excess (1.1 g, 6.7 mmol) together with 100 cm^3 of THF as a solvent were placed in a three necked, round bottom flask equipped with a thermometer, condenser and magnetic bar. The Karstedt catalyst (3.7 mg, $4.07 \cdot 10^{-7}$ mol Pt) was added at room temperature and the solution was heated to 60°C and kept at this temperature overnight. Then, the solvent and the excess of triethoxysilane were evaporated under vacuum to give the product as white powder (5.8 g, 98% of theoretical yield).

To control the course of synthesis and to verify the products structure the spectra: ^{1}H NMR (300 MHz), ^{13}C NMR (75 MHz) and ^{29}Si NNR (59 MHz) were recorded on a Varian XL 300 spectrometer at room temperature using C_6D_6 as solvent. All chemicals were used as received from suppliers without any further purification.

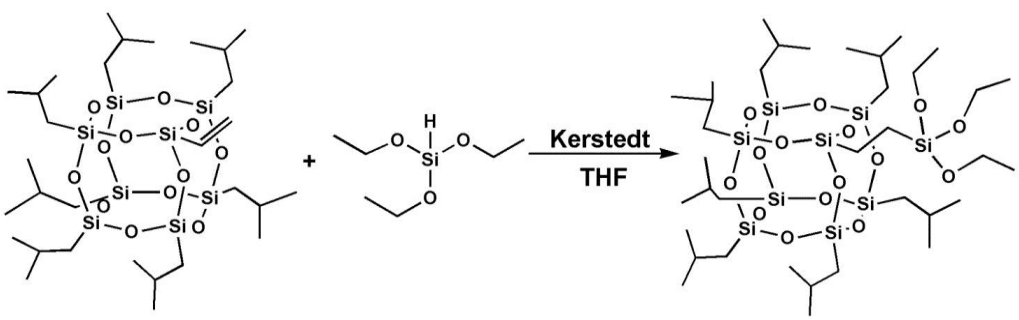

Fig. 1. Synthesis of hepta(isobuthyl)ethyltriethoxysilyloctasilsesquioxane (K-POSS)

2.2. SiO_2/POSS hybryd synthesis

The process was begun with production of silicas on a large laboratory scale. Two types of silica were prepared, obtained in the emulsion (ES) or in the aqueous (HS) system. The idea of production of silica fillers was presented in detail by Jesionowski (2003, 2009). The SiO_2/POSS hybrids were obtained by solvent evaporation. At first a fraction of ES or HS silica was introduced into the reactor and then on the silica surface a mixture made of a monosubstituted silsesquixane cage and 30 cm^3 toluene was introduced in doses by the atomization method. The modifying substance was introduced in the amounts of 3, 5 or 10 weight parts by mass of SiO_2. After introduction of the whole portion of the mixture, the contents were moved into a flask of 500 cm^3 in capacity and placed in a vacuum evaporator Rotavapor RII made by Büchi Labortechnik AG to perform the modification and to evaporate the solvent. Finally the product was subjected to convection drying at 120°C for 48h (chamber drier SEL–I3, made by Memmert). The idea of synthesis of hybrid fillers is schematically presented in Fig. 2.

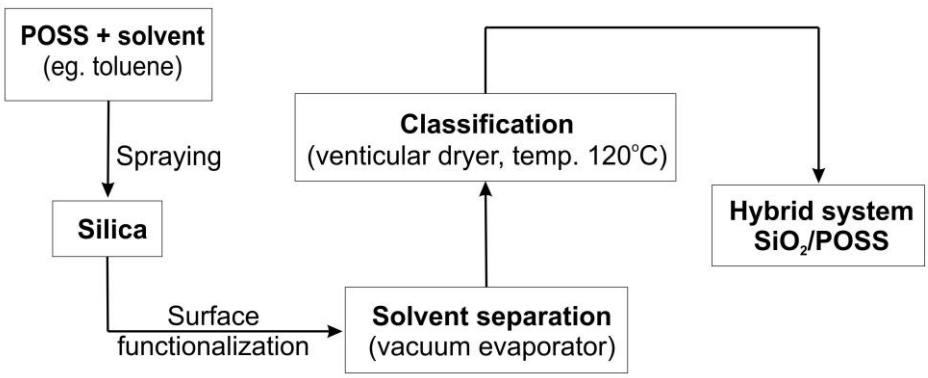

Fig. 2. A scheme of synthesis of SiO_2/POSS hybrids

The final product was characterized by a number of methods. The particle size distributions of the samples were measured using Zetasizer Nano ZS and Mastersizer 2000, both made by Malvern Instruments Ltd., enabling measurements in the range 0.6–6000 nm (NIBS method) and 0.2–2000 μm (laser diffraction technique). Microstructure of the samples was analyzed by using the transmission electron microscopy images (Joel 1200 EX II). The wettability with water was measured by a tensiometer K100 made by Krüss equipped with necessary attachments. For selected hybrid systems the nitrogen adsorption/desorption isotherms were recorded using an ASAP 2020 analyzer, made by Micromeritics Instrument Co. On the basis of the isotherms the specific surface area BET (S_{BET}) was calculated and the pore size (S_P) and volume (V_P) were found from BJH equation. The effectiveness and degree of

modification of SiO_2 with POSS were estimated using the FTIR IFS 66v/S spectrophotometer made by Bruker. The ^{29}Si CP MAS NMR spectra analysis of unmodified and modified silicas was conducted with a DSX spectrometer (Bruker).

3. Results and discussion

Results of NMR analysis of the silsesquioxane product confirmed its structure:
^{1}H NMR (C_6D_6, 298K, 300 MHz) ppm: 0.78–0.92 (CH_2), 1.02–1.09, 1.23–1.38 (CH_3), 1.93–2,14 (CH), 4.32–4.54 (–OCH_2),
^{13}C NMR (C_6D_6, 298K, 75.5 MHz) ppm: 6.3 (CH_2Si), 13.4 ($SiCH_2$), 18.8 (CH_3), 22.5, (CH_2), 23.9 (CH), 26.2 (CH_3), 53.3 (OCH_2),
^{29}Si NMR (C_6D_6, 298K, 59,6 MHz) ppm: -64.6, -66.9, -67.7, -68.2.

Functionalization of silica was performed with monosubstituted hepta-(isobuthyl)ethyltriethoxysilyloctasilsesquioxane (K-POSS). Table 1 presents the data characterizing dispersive and physicochemical properties of the hybrids obtained.

Table 1. Dispersion characterization and physicochemical properties of the hybrid systems made of hydrated silica (HS) and hepta(isobuthyl)ethyltriethoxysilyloctasilsesquioxane

Sample No.	Amount of POSS modifiers (wt./wt.)	Polydispersity index (PdI)	Diameters from Zetasizer Nano ZS (nm)	Diameters from Mastersizer 2000 (μm)			
				d(0.1)	d(0.5)	d(0.9)	D[4.3]
1	–	0.514	91–220 3090–6440	5.91	15.40	30.64	17.18
2	3	0.663	122–342	5.84	28.68	83.06	66.00
3	5	0.543	122–342	5.72	28.48	91.58	76.00
4	10	0.749	91–220 1110–3580	6.03	31.93	96.57	79.00

The hybrids obtained were subjected to particle size determination to check a possible relation between the degree of agglomeration and the amount of the modifier used. Moreover, for the unmodified silicas and the hybrids, the TEM images were recorded.

Analysis of Table 1 data for the hybrid made with HS has revealed that sample 3, obtained with 5 weight parts by mass of K-POSS shows the lowest degree of agglomeration. Moreover, the polydispersity index for this sample is 0.543. The particle size distribution measured for sample 3 shows only one band covering the particle diameters from the range 122–342 nm. The same range of particle diameters was also found for sample 2, although the maximum volume contributions of particles were different for these two samples. The greatest tendency towards agglomeration was noted for sample 4, which is related to the use of the greatest amount of the modifier for its preparation

The sizes of particles in samples 2–4, measured by Mastersizer 2000 (Table 1), varied in practically the same ranges of diameters. In sample 3 obtained with 5 weight

parts by mass of K-POSS (sample 3) 10% of particles had diameters not greater than 5.72 μm and 50% of particles had diameters not greater than 28.48 μm and 90% not greater than 91.58 μm. The mean diameter of particles in this sample D[4.3] corresponded to agglomerations of the maximum diameter of 76.00 μm. TEM images of samples 2, 3 and 4 obtained with 3, 5 and 10 weight parts by mass of K-POSS (Fig. 3) inform about their inhomogeneous structure and the presence of primary particles and secondary agglomerates. Particles of irregular shapes making larger clusters are observed for samples 2 and 3, (Figs. 3b, c). Despite the worse dispersion parameters, sample 4 (Fig. 3d) has particles of the greatest refinement, they are much smaller and the clusters they make are also small.

The hybrid systems obtained by functionalization of emulsion silica (ES) with K-POSS show much different dispersive and morphological character. The relevant data are presented in Table 2. As follows from these data, sample 7 (ES grafted with 5 weight parts by mass K-POSS) is characterised by the greatest degree of homogeneity, which is confirmed by the particle size distribution measured by Zetasizer Nano ZS. The polydispersity index of this sample is 0.219. Sample 7 also shows the lowest tendency towards agglomeration (Fig. 4b). Its particles have spherical shape and their adhesion to irregular K-POSS particles is rather strong.

Samples 6 and 8 obtained with 3 and 10 weight parts by mass of K-POSS have definitely inhomogeneous character, their particles are greater and their polydispersity indices are higher. The differences in dispersion characteristics are illustrated by TEM images (Fig. 4b,d). These samples have spherical shape particles, making primary and secondary agglomerations. Because of significant hydrophobicity of these samples, no measurements of particle size distribution by the laser diffraction method were made. The SiO_2/POSS hybrid systems obtained by mechanical method were characterized by much different dispersive and morphological properties (Szwarc 2012). The final products obtained by the mechanical method with the use of mortar mill, were made of particles with diameters of the order of 200 nm, despite the use of micrometric hydrated silica as the matrix for functionalization.

Table 2. Dispersion and physicochemical characterization of hybrid systems made of emulsion silica and hepta(isobuthyl)ethyltriethoxysilyloctasilsesquioxane (K-POSS)

Sample No.	Amount of POSS modifiers (wt./wt.)	Polydispersity index (PdI)	Diameters from Zetasizer Nano ZS (nm)
5	–	0.252	255–712
6	3	0.268	531–1480
7	5	0.219	255–1280
8	10	0.447	825–2300

At the next step of hybrids characterization they were subjected to a water wettability analysis. Figure 5 presents the wettability profiles of the initial hydrated

silica and the hybrids based on HS obtained with the use of 3, 5 and 10 weight parts by mass of K-POSS (samples 1–4), while Fig. 6 shows the wettability profiles of ES and the hybrids made of ES and K-POSS (samples 5–8). The greatest tendency to water absorption was found for sample 1, while the lowest amount of water was absorbed by sample 4, modified with 10 wt./wt. of K-POSS. The character of the wettability profiles indicates that with increasing amount of the modifying monofunctional POSS, the hydrophobic character of the product increases

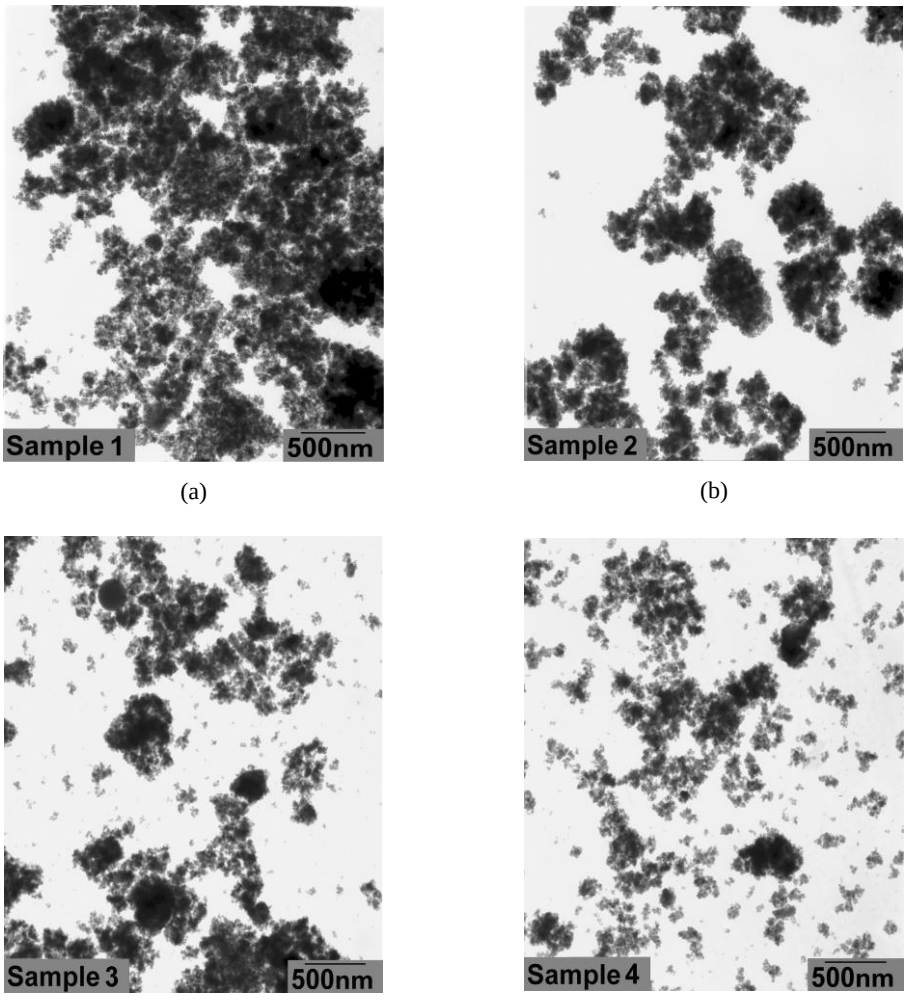

Fig. 3. TEM microphotographs of (a) pure hydrated silica and hybrid modified with (b) 3, (b) 5, and (d) 10 weight parts by mass of hepta(isobuthyl)ethyltriethoxysilyloctasilsesquioxane (K-POSS)

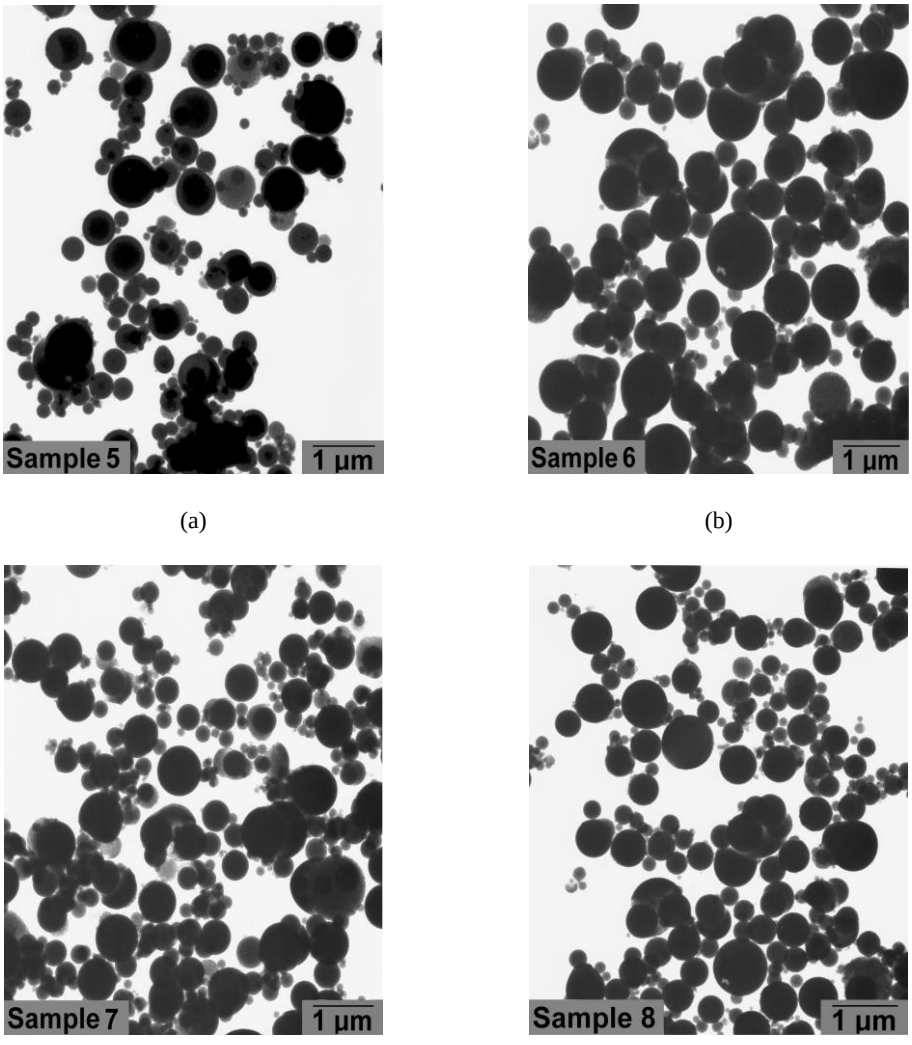

Fig. 4. TEM microphotographs of (a) pure emulsion silica and hybrid modified with (b) 3, (b) 5, and (d) 10 weight parts by mass of hepta(isobuthyl)ethyltriethoxysilyloctasilsesquioxane (K-POSS)

The hybrids with K-POSS based on silica precipitated from the emulsion system show similar tendencies to water absorption, although sample 5 has the highest sorption capacity expressed by a mass increase of 0.32 g. The smallest mass increase was noted for sample 8, obtained with the use of 10 wt./wt. of K-POSS. It should be emphasised that the initial silicas differed significantly in hydrophilic character. Hydrated silica absorbed about 50% more water than emulsion silica.

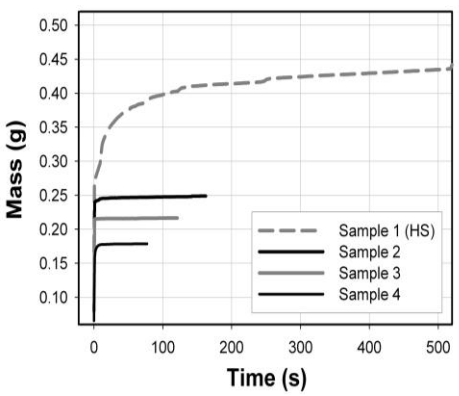

Fig. 5. Wettability profiles obtained for hydrated silica (HS) and selected SiO_2/POSS hybrids

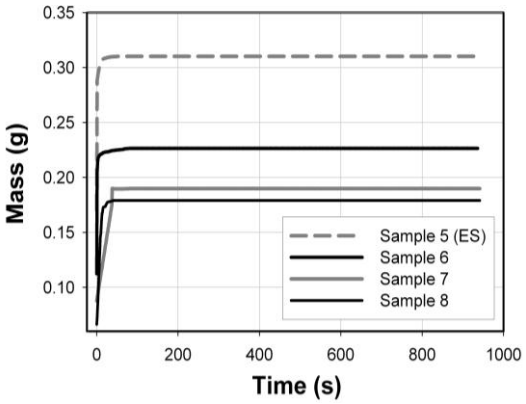

Fig. 6. Wettability profiles obtained for emulsion silica (ES) and selected SiO_2/POSS hybrids

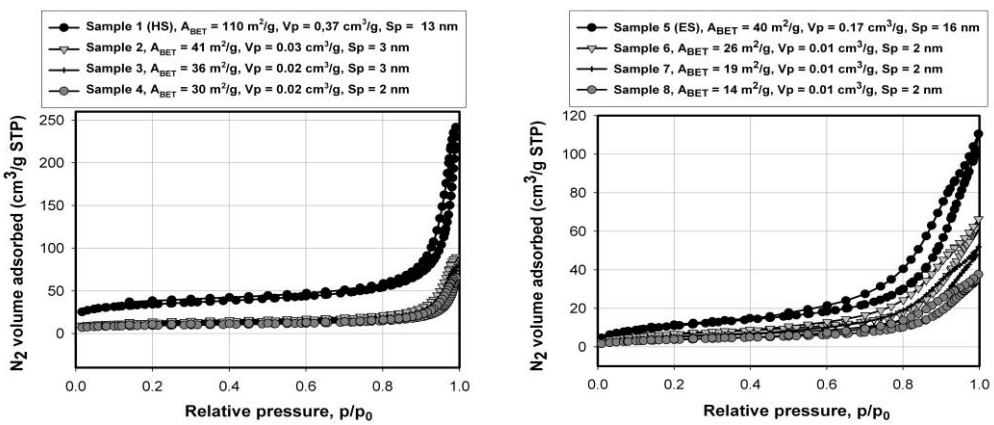

(a) (b)

Fig. 7. Nitrogen adsorption/desorption isotherms and adsorptive properties for: (a) unmodified HS (sample 1), (b) unmodified ES (sample 5) and silicas modified with 3, 5 or 10 weight parts by mass of hepta(isobuthyl)ethyltriethoxysilyloctasilsesquioxane (K-POSS)

To evaluate the adsorptive properties of the samples studied, they were subjected to determination of nitrogen adsorption/desorption isotherms. Analysis of the isotherms permitted determination of the surface area as well as pore volume and diameters (see Fig. 7). Figure 7 presents the nitrogen adsorption/desorption isotherms for the unmodified hydrated silica (HS) and emulsion silica (ES) samples and for the hybrids modified with 3, 5 or 10 wt./wt. of K-POSS. The isotherms show a systematic increase in the volume of adsorbed nitrogen with increasing relative pressure till reaching a maximum value of 240 cm^3/g for sample 1 at $p/p_0=1$ (Fig. 7a). For hybrids the

increase in the volume of adsorbed nitrogen after the threshold value ($p/p_0 = 0.7$) is not so steep and the maximum values for $p/p_0 = 1$ are much lower. Also the specific surface area, pore volume and pore size were drastically lower than those for unmodified samples, e.g. $A_{BET} = 30$ m^2/g for sample 4 modified with 10 wt./wt. of K-POSS. A similar effect is observed for the hybrids based on ES; for the unmodified silica the specific surface area (A_{BET}) was 40 m^2/g and for sample 8 it has decreased to 14 m^2/g (Fig. 7b). These changes are consequences of blocking the active centres on the SiO_2 surface by the molecules of silsesquioxane. The pore size determined proves the mesoporous character of the hybrids obtained.

Figure 8 presents the FT-IR spectra of the unmodified silicas (HS and ES) and the hybrids obtained after the silicas modifications with 10 wt./wt. of K-POSS.

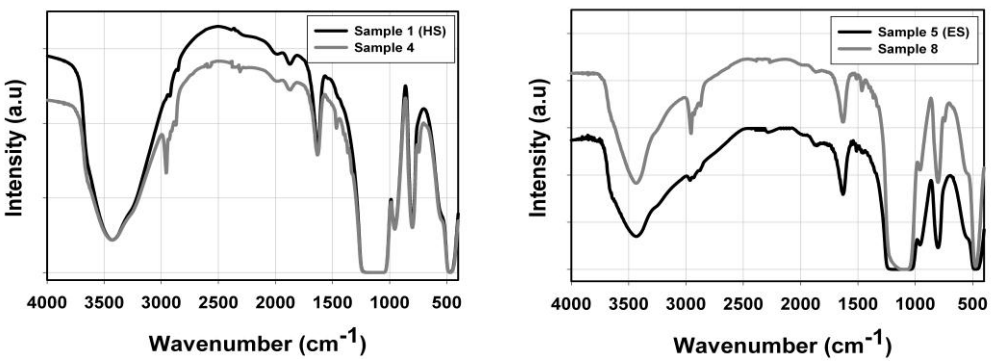

Fig. 8. FT-IR spectra of unmodified silicas (samples 1 and 5) and the hybrids obtained by their modification with 10 wt./wt. of K-POSS (samples 4 and 8)

The FT-IR spectra (Fig. 8) revealed signals typical of K-POSS used for silica surface modification. In the range 3700–3200 cm^{-1} the spectra show the signals corresponding to the stretching vibrations of hydroxyl groups from the adsorbed water molecules. In each spectrum there was a signal assigned to δ(C–H) in the range 2900–2850 cm^{-1}. At 1350 cm^{-1} there is a band assigned to the bending vibrations of γ(C–H) groups. The bands appearing in the range 1500–1450 cm^{-1} and 860–700 cm^{-1} are characteristic of the vibrations of Si–C bond. Strong bands at 1100 cm^{-1} and 500 cm^{-1} correspond to the stretching vibrations of Si–O–Si. At about 850 cm^{-1} there is a band assigned to δ(C–C) from isobutyl groups of K-POSS. Comparing the spectra presented in Fig. 8a and 8b, no significant differences were found in the content of characteristic functional groups in the filler structure, irrespective of the type of silica used.

The effectiveness of silica modification with K-POSS was verified by the ^{29}Si CP MAS NMR spectra, which are presented in Figs. 9 and 10.

The ^{29}Si CP MAS NMR spectrum of unmodified HS (Fig. 9) shows two signals at −110 and −100 ppm. The main signal at −110 ppm is assigned to three siloxane groups

and one silanol group (Q^3), while the signal at −100 ppm corresponds to four siloxane bridges (Q^4, ≡Si–O–Si≡). The spectra of samples modified with K-POSS besides the Q^3 and Q^4 signals also have a band assigned to T^3 group at −67 ppm. Although the presence of T^2 and T^3 structures testifies to the chemical modification of SiO_2 surface, we cannot draw such conclusions as no changes in the intensities of Q^3 and Q^4 signals were observed as a result of functionalization with K-POSS.

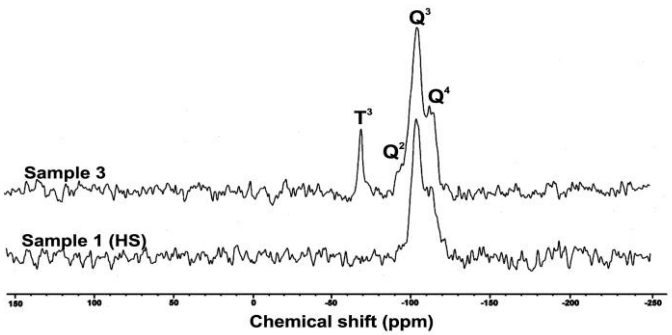

Fig. 9. ^{29}Si CP MAS NMR spectra of unmodified HS (Sample 1) and silica functionalized with 5 wt./wt. K-POSS (Sample 3)

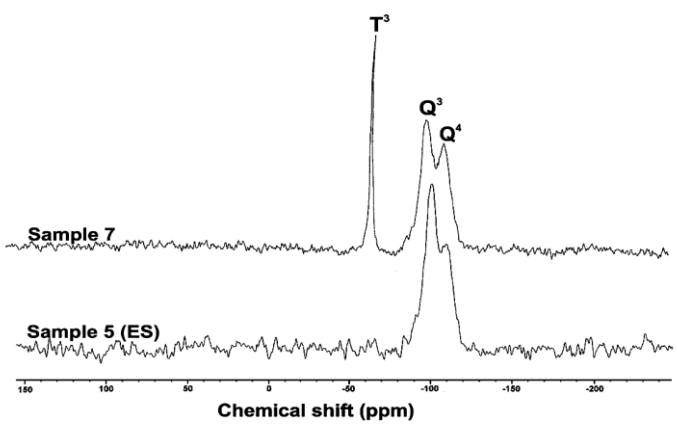

Fig. 10. ^{29}Si CP MAS NMR spectra of unmodified ES (sample 5) and silica functionalized with 5 wt./wt. of K-POSS (sample 7)

The spectrum of unmodified ES (sample 5) reveals three characteristic signals at –110, –100 and –99 ppm. The latter small signal is assigned to the double silanol groups, to the so-called silicon site Q^2. The spectrum of sample 7 shows additionally the T^3 structure (–67 ppm), characteristic of condensation of the modifier (K-POSS) with the silica support. As a result of silica functionalization, a change in the intensity

of signals corresponding to the silanol (Q^3 –100 ppm) and siloxane (Q^4, –110 ppm) groups, which could indicate that chemical adsorption have taken place. However, because of the lack of T^2 structure, we can conclude only about the adhesion of cage POSS to the silica surface.

Recently, the interest in the hybrid systems has been increasing. A combination of inorganic matrix with organic-inorganic cage POSS gave products showing a number of interesting physicochemical and dispersive-morphological properties.

Modification of silica supports gives changes in the dispersive and morphological properties and enhances the hydrophobic character of the products. The process of silica modification with K-POSS proved effective as evidenced by the results of FTIR, NMR analysis and adsorption parameters. Functionalization of silica with selected POSS compounds permits controlling of the physicochemical properties of the products to meet specific target demands.

4. Conclusions

The proposed method of silica modification involving solvent evaporation has brought products of homogeneity lower than that of the initial silicas. Functionalization of the silica surface with hepta(isobuthyl)ethyltriethoxy silyloctasilsesquioxane (K-POSS) gave products containing greater size particles, showing a tendency to formation of primary and secondary agglomerates. Much better dispersive properties were obtained for the products based on the amorphous hydrated silica.

With increasing amount of the monosubstituted POSS used for functionalization, the products obtained showed increasingly higher hydrophobic character.

The functionalization with K-POSS also resulted in a significant reduction of the surface area BET, e.g. from 110 m^2/g for the unmodified hydrated silica to 30 m^2/g for the hybrid filler (sample 4). The same tendency was noted for the emulsion silica. The other parameters characterizing adsorptive properties such as the pore diameters and pore volume as well as the amount of nitrogen adsorbed, were also much decreased.

The proposed method of silica modification with K-POSS had advantageous effect on the physicochemical parameters as evidenced by the FT-IR results.

Analysis of ^{29}Si CP MAS NMR spectra confirmed no chemical interactions between the silica support and the K-POSS modifier. The results indicated the condensation phenomenon and strong adhesion of the modifier to the support.

Acknowledgement

The study was realized within the Development Project POIG 01.03.01-30-173/09 Nanosil from the European Fund of Regional Development within the operation programme Innovative Economy.

References

BIANCHINI D., GALLAND G.B., DOS SANTOS J.H.Z., WILLIAMS R.J.J., FASCE D.P., DELL'ERBA I.E., QUIJADA R., PEREZ M., 2005, *Metallocene supported on a Polyhedral*

Oligomeric Silsesquioxane–modified silica with high catalytic activity for ethylene polymerization, Journal of Polymer Science: Part A: Polymer Chemistry, 43, 5465–5476.

IYER S., ABU–ALI A., DETWILER A., SEHIRALDI A., 2007, *Transparent polymer – Polyhedral Oligomeric Silsesquioxane composities*, ACS Symposium Series (Science and Technology of Silicones and Silicone–Modified Materials), Cleveland, 964, 313–325.

JANOWSKI B., PIELICHOWSKI K., 2008, *Polimery nanohybrydowe zawierające poliedryczne oligosilseskwioksany*, Polimery, 53, 87–98.

JESIONOWSKI T., 2009, *Preparation of spherical silica in emulsion systems using the co–precipitation technique*, Materials Chemistry and Physics, 113, 839–849

JESIONOWSKI T., ŻURAWSKA J., KRYSZTAFKIEWICZ A., POKORA M., WASZAK D., TYTUS W., 2003, *Physicochemical and morphological properties of hydrated silicas precipitated following alkoxysilane surface modification*, Applied Surface Science 205, 212–224.

LIN P., KHARE R., 2009, *Molecular simulation of cross–linked epoxy and epoxy–POSS nanocomposite*, Macromolecules, 42, 4319–4327.

MADHAVAN K., GNANASEKARAN D., REDDY B.S.R., 2009, *Synthesis and characterization of poly(dimethylsiloxane–urethane) nanocomposites: Effect of (in)completely condensed silsesquioxanes on thermal, morphological, and mechanical properties*, Journal of Applied Polymer Science, 114, 3659–3667.

MATISONS J., 2010, *Applications of Polyhedral Oligomeric Silsesquioxanes*, Springer, New York.

SZWARC K., SIWINSKA–STEFANSKA K., MARCINIEC B., JESIONOWSKI T., 2012, *Synthesis and characterisation of SiO2/POSS hybrid systems obtained using the mechanical method*, Physicochemical Problems of Mineral Processing, 48, 181–192.

TANG Y., LEWIN M., 2009, *Migration and surface modification In polypropylene (PP)/polyhedral oligomeric silsequioxane (POSS) nanocomposites*, Polymers Advanced Technologies, 20, 1–15.

WALLACE W.E., GUTTMAN C.M., ANTONUCCI J.M., 2000, *Polymeric silsesquioxanes: degree–of–intramolecular–condensation measured by mass spectrometry*, Polymer 41,2219–2226.

WU J., MATHER P.T., 2009, *POSS Polymers: Physical properties and biomaterials applications*, Journal of Macromolecular Science, Part C: Polymer Reviews, 49, 25–63.

ŻAK P., PIETRASZUK C., MARCINIEC B., SPÓLNIK G., DANIKIEWICZ W., 2009, *Efficient functionalisation of cubic monovinylsilsesquioxanes via cross–metathesis and silylative coupling with olefins in the presence of ruthenium complexes*, Advanced Synthesis and Catalysis, 351, 2675–2682.

Physicochem. Probl. Miner. Process. 48(2), 2012, 631−643

www.minproc.pwr.wroc.pl/journal/

Physicochemical Problems of Mineral Processing

ISSN 1643-1049 (print)
ISSN 2084-4735 (online)

Received April 2, 2012; reviewed; accepted April 16, 2012

SYNTHESIS OF $Mg(OH)_2$ FROM MAGNESIUM SALTS AND NH_4OH BY DIRECT FUNCTIONALISATION WITH POLY(ETHYLENE GLYCOLS)

Agnieszka PILARSKA, Iwona LINDA, Marcin WYSOKOWSKI Dominik PAUKSZTA, Teofil JESIONOWSKI

Poznan University of Technology, Faculty of Chemical Technology, Institute of Chemical Technology and Engineering, M. Sklodowskiej-Curie 2, PL-60965 Poznan, Poland, teofil.jesionowski@put.poznan.pl, phone: +48(61)6653720, fax: +48(61)6653649

Abstract. Synthesis of magnesium hydroxide using different magnesium salts and ammonium hydroxide is described. The reaction was performed in the presence of non-ionic compounds representing the group of poly(ethylene glycols) as modifiers. Dispersive properties of the products were characterised by polydispersity index, particle size, as well as SEM and TEM images. Adsorptive properties of the products were evaluated on the basis of their specific surface area, pore volume and diameter determination. Physicochemical characterisation of the products was extended by the degrees of their surface coverage with PEG, calculated on the basis of elemental analysis and specific surface area BET. Crystalline structures of the products were determined by the WAXS method and then using the Scherrer formula the crystallite size was calculated for selected samples. Wettability profiles in aqueous systems were measured and selected samples were subjected to TG/DTA analyses. The properties of the products were found to be significantly dependent on the molecular mass of PEG and type of magnesium salt used.

keywords: $Mg(OH)_2$, poly(ethylene glycols), particle size distribution, surface morphology, adsorptive properties, crystal structure, elemental analysis, TG/DTA analysis

1. Introduction

Magnesium hydroxide is a very attractive compound because of a wide range of its important applications. Besides, $Mg(OH)_2$ is one of the most important precursors of magnesium oxide. It is used as a neutraliser of acidic pollutants of water and gases, filler in paper industry, antibacterial agent, and fertiliser additive (Dziubek, 1984; Giorgi, 2005; Dong, 2010). One of its interesting properties is the diversity of its microstructure. It crystallises as needles, plates, rods, tubes and flowers (Yan, 2005; Wang, 2011;Song, 2011). Its non-toxic character and high thermal stability make it an attractive additive to polymers used to restrict polymers flammability. The appearance of many papers on $Mg(OH)_2$ indicate increasing interest in this inorganic filler. The main subject of these papers are new methods of synthesis of nano-$Mg(OH)_2$ and ways

http://dx.doi.org/10.5277/ppmp120226

of modification of the $Mg(OH)_2$–polymer system aimed at improvement its compatibility (Lv, 2007; Chen, 2009; Jurkowski, 2010; Gul, 2011).

Recently, much attention has been paid to the methods of synthesis of nanomolecular $Mg(OH)_2$. The methods proposed include: precipitation, solvo- and hydrothermal, microwave, electrochemical, sol-gel and the method based on watering of the commercial MgO with the use of dolomite and sea water (Ding, 2001; Du 2009; Yildirim, 2010; Bae, 2011; Pilarska, 2011). The above-mentioned methods, except precipitation, need a long time, complex and expensive equipment, which means that the process of magnesium hydroxide production becomes economically unattractive. The method based on precipitation is easy to conduct also on an industrial scale. It permits control of the particle size and is rather inexpensive. No wonder that it has been intensely studied in a number of research groups (Jiang, 2009; Meshkani, 2009; Meshkani, 2010).

According to the recent literature reports, the properties of the final product, in particular its morphology, are closely related to the type of precursor and the precipitating agent. Much interest is devoted to the use of modifiers. Modification of the reaction system, understood as direct participation of an additional organic or inorganic chemical substance in the process of synthesis, is undertaken to modify the original properties of the product, including its surface properties. Modifications of this type are most often applied upon precipitation of magnesium hydroxide (Wang, 2007; Huang, 2008; Wang, 2009; Pilarska, 2011). Functionalisation of the surface of fillers is aimed first of all at control of the shape and size of particles and at making the product more hydrophobic to permit binding of inorganic fillers with organic polymer matrices (Rothon, 2003).

This paper reports the synthesis of $Mg(OH)_2$ of plate morphology realised by the method of precipitation with the use of magnesium salts, ammonium hydroxide and non-ionic compounds from the group of poly(ethylene glycols) as modifiers. The influence of molecular weight and type of magnesium precursor on the dispersive-morphological and physicochemical properties of the products has been mainly analysed.

2. Experimental

The substrates used for the synthesis of magnesium hydroxide were: hydrated magnesium sulfate ($MgSO_4 \cdot 7H_2O$, analytical grade), magnesium chloride ($MgCl_2 \cdot 6H_2O$), magnesium nitrate ($Mg(NO_3)_2 \cdot 6H_2O$, analytical grade), ammonium hydroxide (NH_4OH, analytical grade) as a precipitation agent (all made by POCh SA.) and non-ionic compounds from the group of poly(ethylene glycols): PEG 200, PEG 400, PEG 8000 and PEG 20000 (purchased from Sigma-Aldrich), as solutions of appropriate concentration. Magnesium hydroxide was obtained from a 5 % solution of a given magnesium salt and a solution of ammonium hydroxide prepared to maintain the stoichiometric amount of reagents. Precipitation was carried out at 60°C. A technological scheme of the process is shown in Fig. 1.

Portions of 200 cm^3 of a given magnesium salt solution and 200 cm^3 of ammonium hydroxide were simultaneously dosed into 50 cm^3 of water with a modifier, placed in a reactor of 500 cm^3 in capacity, equipped with a high speed stirrer (1800 rpm) (Eurostar Digital, IKA Werke). The reagents were vigorously stirred. The reagents were dosed by a peristaltic pomp of Ismatec ISM833A type, at a constant rate of 2.3 cm^3/min. The reactor was placed in a thermostat (MP14, Julabo), to control and keep a constant temperature. The precipitate was washed out, filtered and subjected to conventional drying at 105ºC for about 8 h.

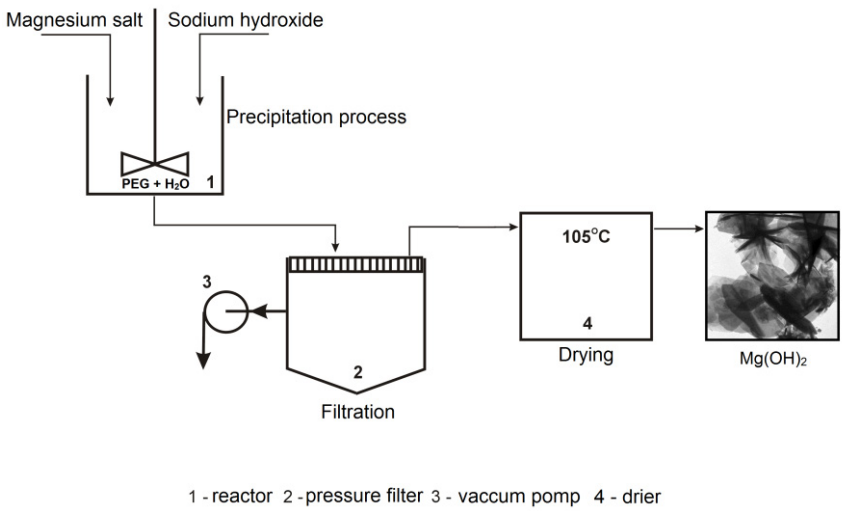

Fig. 1. Technological scheme of $Mg(OH)_2$ synthesis from a magnesium salt and ammonium hydroxide with a modifier

The particle size of the precipitate was measured by Zetasizer Nano ZS (0.6–6000 nm) and Mastersizer 2000 (0.2–2000 μm) made by Malvern Instruments Ltd., operating by the NIBS method and laser diffraction techniques, respectively. The Zetasizer Nano ZS instrument was also used for determination of the polydispersity index (PdI), which is a measure of the sample homogeneity. The morphology and microstructure of the products were characterised on the basis of observations by a scanning electron microscope Zeiss EVO 40 and a transmission electron microscope (Joel 1200 EX II). The adsorption activity of the products was evaluated on the basis of specific surface area BET, pore volume and pore diameter measurements performed using the ASAP 2020 instrument made by Micromeritics Instrument Co. Selected samples were subjected to elemental analyses (Elementar model Vario EL III), whose results together with the surface area BET allowed calculation of the degree of coverage with the modifier. Analysis of the products wettability in water systems was made using the K100 tensiometer with a special instrumentation made by Krüss. The crystalline structure of selected magnesium hydroxide samples was determined by

WAXS. The X-ray diffractograms were recorded by a computer-controlled horizontal diffractometer, equipped with a HZG-3 type goniometer. From the Scherrer formula the crystallite size in the samples was calculated. Selected samples of the products were also subjected to thermal analyses TG/DTA (Jupiter STA 449F3 – Netzsch).

3. Results and discussion

Table 1 presents the dispersive and adsorptive properties of magnesium hydroxide samples precipitated during a simultaneous dosing of reagents prepared in stoichiometric amounts into the aqueous system at the rate of 2.3 cm^3/min at 60°C.

Table 1. Physicochemical properties of magnesium hydroxide precipitated with the use of 5% solution of a magnesium salts, ammonium hydroxide in stoichiometric amount and a 2% solution of one of the following non-ionic compounds PEG 200, 400, 8000, 20000

Sample No.	Precipitation process conditions		Dispersive properties		Adsorptive properties		
	Type of salt	Mean molecular weight of PEG	PdI	Particle diameter from Zetasizer Nano ZS (nm)	BET surface area (m^2/g)	Total volume of pore (cm^3/g)	Mean size of pore (nm)
S_unmod.	magnesium sulfate	–	0.225	21 – 106	21	0.01	2.7
1S_mod.		200	0.688	59 – 220	28	0.01	2.6
2S_mod.		400	0.346	59 – 142	42	0.22	28.2
3S_mod.		8000	0.435	68 – 459	30	0.01	2.6
4S_mod.		20000	0.387	79 – 255	32	0.01	2.7
Cl_unmod.	magnesium chloride	–	0.196	220 – 396	3.3	0.02	2.8
1Cl_mod.		200	0.287	51 – 459	10	0.01	3.5
2Cl_mod.		400	0.312	122 – 459	8	0.01	3.5
3Cl_mod.		8000	0.571	68 – 2670	12	0.02	3.6
4Cl_mod.		20000	0.496	59 – 342	6	0.01	3.1
N_unmod.	magnesium nitrate	–	0.365	106–255; 1110–1990	3	0.01	1.5
1N_mod.		200	0.380	33 – 396	4	0.01	2.2
2N_mod.		400	0.428	51 – 825	4.5	0.01	2.6
3N_mod.		8000	0.520	79 – 3090	7	0.01	2.5
4N_mod.		20000	0.321	68 – 190	6	0.01	2.1

The following magnesium salts, in 5% solutions, were used: magnesium sulfate (samples S_unmod., 4S_mod.), magnesium chloride (samples Cl_unmod., 4Cl_mod.) and magnesium nitrate (samples N_unmod., 4N_mod.) with an addition of a 2% solution of a modifier of different molecular mass PEG 200, 400, 8000, 20000 – for each salt. The modification was performed to obtain the products with particles of smaller size than that of unmodified sample, hydrophobic character and larger surface areas.

As follows from the above results, the particles of each modified sample were greater than those of unmodified samples or more or less of the same size. No reduction in the particle size upon modification was observed. The smallest diameters (59–459 nm) were noted for the samples precipitated from the solution of magnesium sulfate, the same samples also showed the most homogeneous and regular morphology (Fig. 2a). The samples obtained with magnesium chloride or magnesium nitrate revealed the presence of particles of diameters reaching 3090 nm (sample 3N_mod.). The increase in the particle diameters is particularly well seen in the samples obtained with magnesium nitrate (Fig. 2c). An analysis of dispersive and adsorptive properties of the products obtained with magnesium chloride and magnesium nitrate has shown a positive effect of modification with PEG 200 and PEG 20000. Dispersive properties and microstructure of the modified samples determined their specific surface area. For all the modified samples (see Table 1) the specific surface area BET is greater than in their unmodified correspondents. The best adsorptive parameters were found for the samples obtained with magnesium sulfate, S series, in particular sample 2S_mod., modified *in situ* with PEG 400, whose surface area BET was 42 m^2/g, which was twofold greater than that of sample S_unmod. Unusually, a high value of the pore volume (0.22 g/cm^3) and pore diameter (28.2 nm), indicated mesoporous structure of this material. Figure 3 presents the nitrogen adsorption/desorption isotherm for sample 2S_mod and the pore size distribution. According to the IUPAC classification it is a type IV isotherm with a hysteresis loop H3 type, which is related to the capillary condensation in mesopores between two planes. Sample 2S_mod. is the best candidate to be an adsorbent, catalysts support or a catalyst, among all samples studied in this experiment.

The inorganic salts $MgCl_2$, $MgSO_4$ or $Mg(NO_3)_2$ are commonly used as precursors of magnesium hydroxides. According to the literature, $Mg(OH)_2$ obtained in the reaction with ammonium hydroxide has particles in the form of hexagonal plates (Dong, 2010; Wang, 2011). TEM microphotographs (Fig. 4a) show the particles of magnesium hydroxide with plate-like structures (2S_mod. sample). In samples obtained with magnesium chloride (1Cl_mod., Fig. 4b) – the particles are of star-like shape. In a recent work (Wang, 2011) on magnesium hydroxide precipitated with the use of the same reagents (i.e. magnesium chloride and ammonium hydroxide) the same morphology was described as a broom shape. Wang (2011) presented in details the mechanism of formation of such unusual shapes. He claims that in these samples the process of nucleation depends considerably on the relation of surface diffusion and surface integration in the crystal growth process. In the same paper Wang (2011) analysed also the influence of a modifier (poly(ethylene glycol), PEG 12000) on the phenomenon of plate formation at different reaction temperatures (determining the way of PEG adsorption). At 60ºC and 80ºC magnesium hydroxide particles develop as plates as PEG is adsorbed exclusively on the (001) crystalline surface. Restricted growth of $Mg(OH)_2$ crystals along the (001) surface leads to formation of plates. At lower temperatures PEG adsorption leads to formation of needles. These

morphological features can determine the type of application of the products obtained (catalysis, adsorption, flame retardancy).

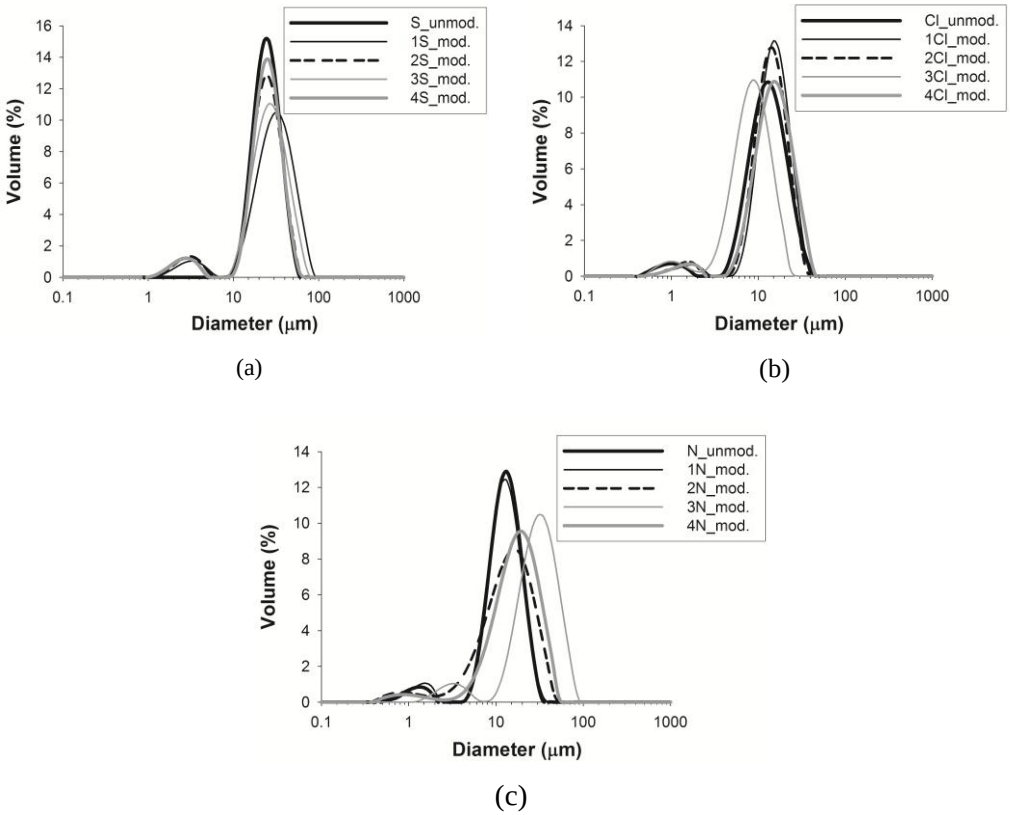

Fig. 2. Particle size distribution (Mastersizer 2000) of magnesium hydroxides obtained with the use of: (a) magnesium sulfate, (b) magnesium chloride and (c) magnesium nitrate

Physicochemical characterisation of the products was supplemented with X-ray diffraction studies. The X-ray diffraction patterns shown in Fig. 4 reveal the maxima typical of the crystalline structure of brucite $Mg(OH)_2$, identified by the program X-RAYAN (Marciniak, 1999). The X-ray patterns were almost the same for the products obtained with the same magnesium salt irrespective of the molecular mass of the PEG applied. Changes in the shape of the peaks were clearly related to the type of magnesium salt used. The structure of brucite is much better developed for samples Cl_mod. (Fig. 5b) and N_mod., than in sample S_mod, as indicated by the height and shape of relevant diffraction maxima. The differences in the crystalline structure are confirmed by the different sizes of crystallites in the samples in selected directions. For example the crystallite size calculated from the Scherrer formula for the direction perpendicular to (001) plane (maximum at $2\theta=18.5°$), for samples 1Cl_mod. and

1N_mod., reach about 35 nm, while the crystallite size in sample 1S_mod. is of about 12 nm. Similarly for the direction perpendicular to the (101) plane (maximum at 2θ=37.9°), the crystallite size in samples 1Cl_mod. and 1N_mod. is of an order of 40 nm (39 nm and 43 nm, respectively), while for sample 3S this size is almost twice smaller (18 nm). The above values are comparable with literature data (Ding, 2001; Klug, 2001; Wang, 2011).

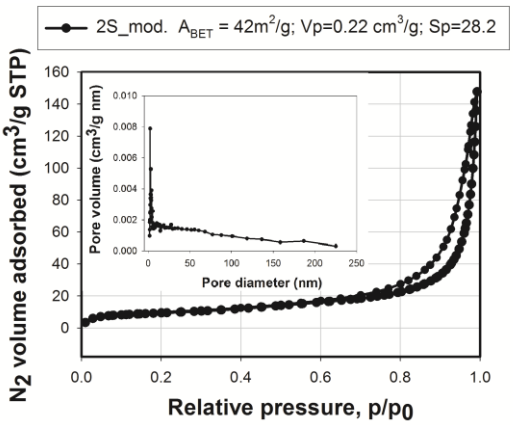

Fig. 3. Nitrogen adsorption/desorption isotherm and pore size distributions of magnesium hydroxide 2S_mod. grafted by PEG 400

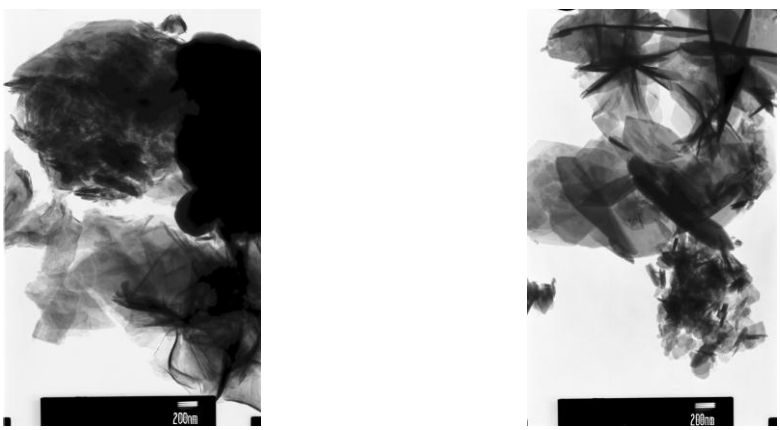

(a) (b)

Fig. 4. TEM images of magnesium hydroxides (a) 2S_mod. and (b) 1Cl mod. obtained with the use magnesium sulfate and magnesium chloride

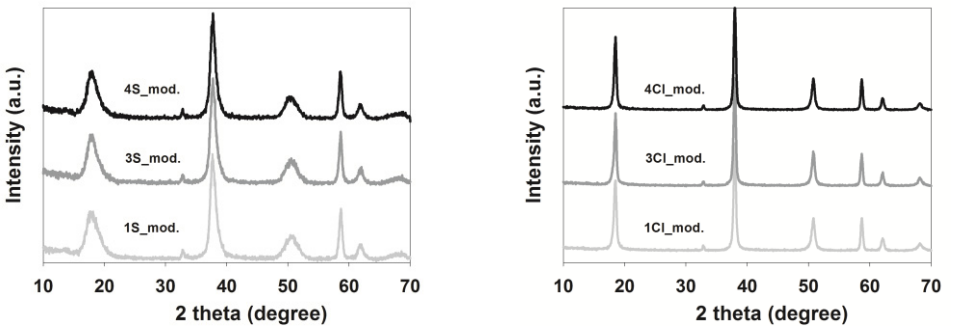

(a) (b)

Fig. 5. X-ray diffraction patterns of magnesium hydroxides obtained with the use of (a) magnesium sulfate and (b) magnesium chloride and with addition of different non-ionic compound from the group of poly(ethylene glycols)

The modifier is also applied in order to endow the samples of magnesium hydroxide with hydrophobic properties, which is essential to enhance their stability and extend their application possibilities as active fillers. The hydrophilic surface of $Mg(OH)_2$ nanoparticles is highly unfavourable for their dispersion in polymers. Poor compatibility between $Mg(OH)_2$ and polymer causes degradation in the mechanical and physical properties of the composites. Literature provides examples of facile methods to synthesize hydrophobic $Mg(OH)_2$ nanoparticles with good dispersibility and compatibility in organic phase with the use of octadecyl dihydrogen phosphate (ODP), oleic acid, poly(methyl methacrylate) (PMMA) etc. (An 2009, Yan 2009). Figures 4a, b, and c present the wettability profiles recorded for the samples precipitated with the use of the three magnesium salts studied and 2% solutions of PEG of different molecular weight. The highest tendency towards water absorption was observed for strongly hydrophilic unmodified hydroxides, while the lowest tendency towards water absorption was recorded for samples modified with PEG 200 (1S_mod., 1Cl_mod., 1N_mod.) PEG 400 (1S_mod.) and PEG 20000 (4Cl_mod.), irrespective of the salt used for precipitation. As follows from the calculated degree of coverage (see Table 3), PEG 200 undergo permanent absorption forming most probably a compact protective layer. Moreover, PEG 200 is built of shorter carbon chains and contains a lower number of hydroxyl groups. Significant hydrophobicity of samples modified with PEG 20000 (4Cl_mod., Fig. 4b) can be explained by favourable changes in magnesium hydroxide microstructure it causes (see Table 1).

The results of elemental analysis presented in Table 2 show that almost in all samples the contents of carbon and hydrogen increased in proportion to the molecular mass of the PEG applied. The differences in the contents of carbon and hydrogen in the samples modified with PEGs of the shortest and longest carbon chains are not significant. For example the content of carbon in sample 1N_mod. (PEG 200) is 0.595%, while in sample 4N_mod. (PEG 20000) it increases only to 0.735%. Much

more pronounced dependence on the molecular weight of PEG is observed for the degree of coverage of magnesium hydroxide surface with the modifier, calculated on the basis of elemental analysis results and the specific surface area. The coverage degree (Table 2) takes the highest value for samples modified with PEG 200 and for those modified with PEG 20000 it takes a value by one order of magnitude lower. Such a rapid decrease in the degree of coverage with increasing length of the modifier means that the adsorption of long-chain PEGs is rather ineffective. Among the samples analysed, the highest degree of coverage was obtained for PEG 200. The results of elemental analysis are well correlated with those of wettability (Figs. 5a, b, c). A high degree of coverage of magnesium hydroxides modified with PEG 200 can explain their strongest hydrophobicity (samples 1S_mod., 1Cl_mod., 1N_mod.). The observation that adsorption of PEGs of short carbon chains is the most effective is corroborated by the dispersive, adsorptive and surface properties of the samples modified with them.

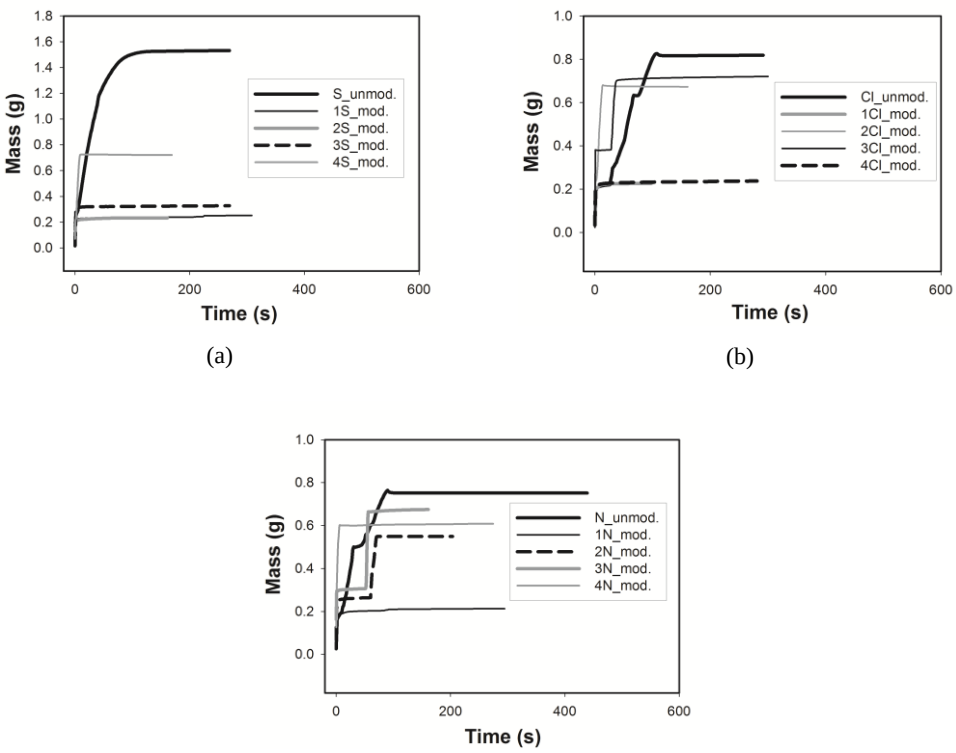

Fig. 6. Wettability profiles of magnesium hydroxides obtained with the use of: (a) $MgSO_4$, (b) $MgCl_2$ (c) $Mg(NO_3)_2$

Another interesting observation was that the highest degree of coverage was calculated for the samples precipitated with the use of magnesium chloride and magnesium nitrate, which is related to small surface area BET of these samples. The degree of coverage found for the sample precipitated with magnesium sulfate having smaller surface area is considerably lower.

Table 2. Elemental content of carbon and hydrogen in modified samples of magnesium hydroxide precipitated with the use of magnesium sulfate and magnesium chloride and the calculated degree of their coverage with PEG compounds

Sample No.	Elemental content (%)		Coverage degree (μmol/m^2)
	C	H	
S_unmod.	–	–	–
1S_mod.	1.177	6.135	7.467
2S_mod.	1.276	6.335	4.091
3S_mod.	1.480	6.675	3.683
4S_mod.	1.613	6.878	0.106
Cl_unmod.	–	–	–
1Cl_mod.	0.784	2.825	31.325
2Cl_mod.	0.919	2.893	18.426
3Cl_mod.	0.821	2.924	10.194
4Cl_mod.	1.107	3.056	0.446
N_unmod.	–	–	–
1N_mod.	0.595	2.568	26.023
2N_mod.	0.645	2.825	14.124
3N_mod.	0.690	2.937	9.036
4N_mod.	0.735	2.989	0.323

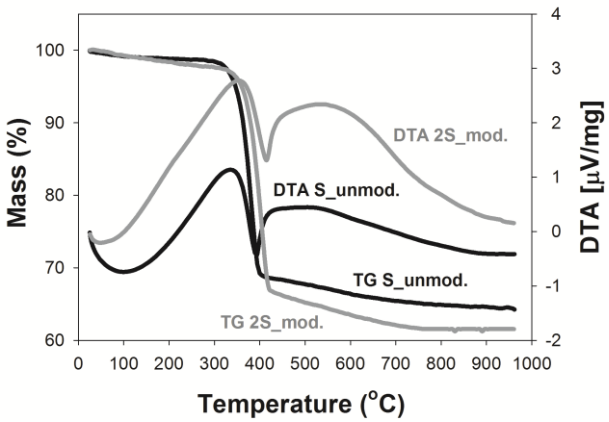

Fig. 7. TG/DTA curves of magnesium hydroxides S_unmod. and 2S_mod.

The products obtained were also subjected to TG/DTA thermal studies in order to establish the character of chemical and structural transformation induced by high temperature and to compare mass changes between the modified and unmodified samples. Figure 6 presents the TG/DTA curves recorded for the unmodified sample (S_unmod.) the sample modified by a 2% PEG 400 solution (sample 2S_mod.). The DTA curve recorded for the unmodified sample shows an exothermic effect appearing in the range 99 to 330ºC, corresponding to the loss of physically bound water. The endothermic effect appearing in the range from 420 to 900°C corresponds to decomposition of magnesium hydroxide and reorganisation of $Mg(OH)_2$ structure to that of pure crystalline form of MgO (Wang, 2007), accompanied by the loss of constitutional water. The rapid mass decrease corresponding to this endothermic effect was manifested in the TG results. The DTA curve recorded for the modified sample is slightly shifted towards higher temperatures. The corresponding TG results point to a greater, by about 4%, mass loss for the modified sample, which confirms the presence of the modifier.

4. Conclusions

Functionalisation of magnesium hydroxide (precipitated with the use of a magnesium salt and ammonium hydroxide) with non-ionic compounds from the group of poly(ethylene glycols) has not brought favourable changes in the dispersive properties of the products. The size of particles in the modified samples was greater or comparable to that in the unmodified magnesium hydroxide. The modification with PEG has resulted in increased specific surface areas BET of all samples. Relatively large specific surface area was obtained for the samples synthesized with the use of magnesium sulfate. The best dispersive properties (particle size range from 59 to 142 nm) and adsorptive properties (surface area BET of 42 m^2/g) were found for sample 2S_mod., modified with PEG 400. Introduction of the modifying PEG compounds to the reaction system *in situ* has brought beneficial changes in the character of the products' surface. The majority of modified samples were observed to show reduced ability to absorb water (to about 0.2 g). Particularly high reduction in water absorbability was found for the samples modified with G 200 (1S_mod., 1Cl_mod., 1N_mod.) and PEG 400 (2S_mod., 2Cl_mod.). The increased hydrophobicity of these samples can be related to the degree of coverage of their surface with the modifier (which reaches the highest values for PEGs of the shortest carbon chains) and with microstructural changes. Because of large BET surface area of the samples precipitated with the use of magnesium sulfate (1S_mod., 4S_mod.) the coverage of their surfaces with the modifier is smaller than that for the other samples

Acknowledgements

This work was supported by Poznan University of Technology research grant No. 32-125/2012–DS.

References

AN D., WANG L., ZHENG Y., GUAN S., GAO X., TIAN Y., ZHANG H., WANG Z., LIU Y., 2009, *In situ preparation and surface modification of magnesium hydroxide* nanoparticles, Colloids Surf. A: Physicochem. Eng. Aspects, 348, 9–13.

BAE T.H., LIU J., THOMPSON J.A., KOROS W.J., JONES C.W., NAIR S., 2011, *Solvothermal deposition and characterization of magnesium hydroxide nanostructures on zeolite crystals*, Micropor. Mesopor. Mat., 139, 120–129.

CHEN X., YU J., GUO S., LU S., LUO Z., HE M., 2009, *Surface modification of magnesium hydroxide and its application in flame retardant polypropylene composites*, J. Mater. Sci., 44, 1324–1332.

DING Y., ZHANG G., WU H., WANG L., QIAN Y., 2001, *Nanoscale magnesium hydroxide and magnesium oxide powders: control over size, shape, and structure via hyrothermal synthesis*, Chem. Mater., 13, 435–440.

DONG C., CAIRNEY J., SUN Q., MADDAN O.L., HE G., DENG Y., 2010, *Investigation of $Mg(OH)_2$ nanoparticles as an antibacterial agent*, J. Nanopart. Res., 12, 2101–2109.

DONG H., DU Z., ZHAO Y., ZHOU D., 2010, *Preparation of surface modified nano-$Mg(OH)_2$ via precipitation method*, Powder Technol., 198, 325–329.

DU G.X, ZHENG S.L., 2009, *Preparation of plate-shape nano-magnesium hydroxide from asbestos tailings*, J. Phys.: Conf. Ser., 188, 1–9.

DZIUBEK A.D., 1984, *Oczyszczanie wody i ścieków w środowisku alkalicznym*, Ochrona Środowiska, 34, 9–18.

GIORGI R., BOZZI C., DEI L., GABBIANI C., NINHAM B.W., BAGLIONI P., 2005, *Nanoparticles of $Mg(OH)_2$: synthesis and application to paper conservation*, Langmuir, 21 8495–8501.

GUL R., ISLAM A., YASIN T., MIR S., 2011, *Flame-retardant synergism of sepiolite and magnesium hydroxide in a linear low-density polyethylene composite*, J. App. Polym. Sci., 121, 2772–2777.

HUANG H., TIAN M., YANG J., LI H., LIANG W., ZHANG L., LI X., 2008, *Stearic acid surface modifying $Mg(OH)_2$: mechanism and its effect on properties of ethylene vinyl acetate/$Mg(OH)_2$ Composites*, J. App. Polym. Sci., 107, 3325–3331.

JURKOWSKI B., JURKOWSKA B., RYDAROWSKI H., 2010, *Palność materiałów polimerowych*, Wydawnictwo Politechniki Poznańskiej, Poznań.

JIANG W., X. HUA X., HAN Q., YANG X., LU L., WANG X., 2009, *Preparation of lamellar magnesium hydroxide nanoparticles via precipitation method*, Powder Technol., 191, 227–230.

KLUG H.P., ALEXANDER L.E., 2001, *X-Ray diffraction procedures*, Wiley/Interscience, New York.

LV J., LIU W., 2007, *Flame retardancy and mechanical properties of EVA nanocomposites based on magnesium hydroxides nanoparticles/microcapsulated red phosphorous*, J. App. Polym. Sci., 105, 333–340.

MARCINIAK H., R. DIDUSZKO R., 1999, *Program X-RAYAN to X-ray analysis and identification*, Warszawa.

MESHKANI F., M. REZAEI M., 2009, *Facile synthesis of nanocrystalline magnesium oxide with high surface area*, Powder Technol. 196, 85–88.

MESHKANI F., REZAEI M., 2010, *Effect of process parameters on the synthesis of nanocrystalline magnesium oxide with high surface area and plate-like shape by surfactant assisted*, Powder Technol., 199, 144–148.

PILARSKA A., JESIONOWSKI T., 2011, *Synthesis of MgO in magnesium hydroxide carbonatisation process*, Physicochem. Probl. Miner. Process, 46, 83–94.

PILARSKA A., SZWARC K., PAUKSZTA D., JESIONOWSAKI T., 2011, *The effect of modifiers and precipitation conditions on physico-chemical properties of $MgCO_3$ and their calcinates*, Physicochem. Probl. Miner. Process., 47, 79–90

SONG X., SUN S., ZHANG D., WANG J., YU J.,2011, *Synthesis and characterization of magnesium hydroxide by batch reaction crystallization*, Front. Chem. Sci. Eng., 5, 416–421.

WANG D.A, ZHENG Y, GUAN S., GAO X., TIAN Y., ZHANG H., WANG Z., LIU Y., 2009, *In situ preparation and surface modification of* $Mg(OH)_2$ *nanoparticles*, Colloids Surf. A: Physicochem. Eng. Aspects, 348, 9–13.

WANG P., LI C., GONG H., WANG H., LIU J., 2011, *Morphology control and growth mechanism of magnesium hydroxide nanoparticles via a simple wet precipitation method*, Ceram. Int., 37, 2061–2066.

WANG W., QIAO X., CHEN J., LI H., 2007, *Facile synthesis of magnesium oxide nanoplates via chemical precipitation*, Mater. Lett., 61, 3218–3220.

YAN C., XUE G., ZOU L., YAN X., WANG W., 2005, *Preparation of magnesium hydroxide nanoflowers*, J. Cryst. Growth, 282, 448–454.

YAN H., ZHANG X., WEI L., LIU X., XU B., 2009, Hydrophobic magnesium hydroxide nanoparticles via oleic acid and poly(methyl methacrylate) – grafting surface modification, Powder Technol., 193,125–129.

YILDRIM M., AKARSU H., 2010, *Preparation of magnesium oxide (MgO) from dolomite by leach – precipitation – pyrohydrolysis process*, Physicochem. Probl. Miner. Process, 44, 257–272.

Physicochem. Probl. Miner. Process. 48(2), 2012, 645−654

www.minproc.pwr.wroc.pl/journal/

Physicochemical Problems of Mineral Processing

ISSN 1643-1049 (print)
ISSN 2084-4735 (online)

Received April 15, 2012; reviewed; accepted May 10, 2012

THE ROLE OF PARTICLE SIZE AND SOLID CONTENTS OF FEED ON MICA-FELDSPAR SEPARATION IN GRAVITY CONCENTRATION

Murat KADEMLI[*], Ozcan Y. GULSOY[**]

* Hacettepe University, Hacettepe Vocational School of Higher Education, kademli@hacettepe.edu.tr
** Hacettepe University, Department of Mining Engineering

Abstract. In the present study, the role of particle size of mica with flaky shape on the separation efficiency of mica from feldspar by the shaking table and Reichert spiral (Model HG7) concentrators were investigated. An albite ore containing mica from the Cine region of Turkey was treated under various test conditions. During the study, particle size distribution, solids content of the feed and flow rate of the feed were changed in the spiral tests. Then, the flow rate of the feed was kept constant as 1 dm^3/s in the shaking table tests. It was observed that mica could be separated from feldspar, owing to its laminar morphology. Accordingly, the particle size, directly related to the laminar morphology of mica, is the most effective parameter in the separation process. The best results were obtained with spiral concentrators, which met the requirements of the glass industry.

keywords: shaking table, spiral, mica, shape factor, gravity concentration

1. Introduction

Mica is the primary source of iron in feldspar minerals, which causes colouring in ceramic and glass. The most common method for separating mica from feldspar is flotation. Nevertheless, flotation has some disadvantages such as detrimental effects on the environment because of chemical use, high investments and operation costs (Akar, 1994; Bayraktar et al., 1999; 2002; Celik et al., 1998; 2001). The separation does not always take place under conditions which are convenient for the concentration criterion. In order to allow for the differences in the particle shape, the concentration criterion must be multiplied by the shape ratio factor (Burt, 1984). When there is a marked difference in particle shape, the concentration criterion, which is the density of the heavy species minus the density of suspending fluid, divided the density of light species minus density of suspending fluid, approaches 1.0. Typical of this is the separation of mica from quartz and feldspar (Browning, 1973).

Mica and feldspar are close to each other in respect to their density. The densities of feldspar and mica minerals are approximately 2.65 and 2.7-3.4 g/cm^3, respectively (Ipekoglu and Asmatulu, 1996). As mentioned by Iverson (1932) the difference

http://dx.doi.org/10.5277/ppmp120227

between their densities is not sufficient in achieving the efficient separation of these minerals by using gravity methods. Coarse mica grains are nearly equi-dimensional and spherical. However, in fine sizes the flaky shape character of the mica minerals is revealed. Mica normally takes the form of numerous single flakes, which are pliable, resilient and tough, and can be separated like the pages of a book (Schoement, 1989). This physical characteristic of the mineral has been responsible for its separation by gravity from feldspar. This distinguishing property of fine mica particles was first reported by Iverson (1932). He managed to separate mica from feldspar by tabling. Later, Adair et al. (1951) also showed the possibility of concentration of mica in the Humphrey spiral. Therefore, this method is considered as an alternative method to mica flotation.

The purpose of this study was to investigate the separation characteristics of mica from feldspar in a shaking table and the Reichert spiral by determining the role of the shape factor of mica in terms of particle size distribution and feed solids content on the separation efficiency. Industrial scale equipments were used in this study, in order for the results to be applied to the industry directly.

2. Materials and methods

The Na-feldspar (albite) samples were obtained from a feldspar deposit in the Cine Akmaden, which is in the Southwest of Turkey. The chemical composition of the samples used in the tests is given in Table 1. The samples were crushed with a jaw crusher to 2 cm of size, and then were gradually reduced with a roll crusher. The particles, finer than 74 μm, were removed by dry screening in order to prevent their adverse influence on the separation. Five samples with different size fractions and grades were prepared and tested (Table 2). The particle size distributions were given in Fig. 1.

Table 1. Chemical composition of feldspar sample

Content	%
SiO_2	65.01
Al_2O_3	20.09
Fe_2O_3	0.73
MgO	0.20
CaO	1.82
Na_2O	10.20
K_2O	0.48
TiO_2	0.25
L.O.I	0.42
Total	99.40

First of all, the tests were carried out in the Reichert spiral (HG7). The spiral was operated in a closed circuit, which included a tank and a pump. There were two splitters at the discharge. The position of the outer splitter was not suitable for

controlling product streams due to the occurrence of a big gap largely free of particles between the tailing and the concentrate streams during the tests (Fig. 2). Therefore, this splitter was fixed for all conditions in the main series of the tests. The position of the inner splitter was adjusted to ¼, ½ and ¾ of the maximum opening (16 mm, L). Samples were fed into a spiral. Feldspar minerals, in the samples in the form of pulp, were moved close to the centre of the spiral, whereas the mica minerals were moved to the wall side of the spiral.

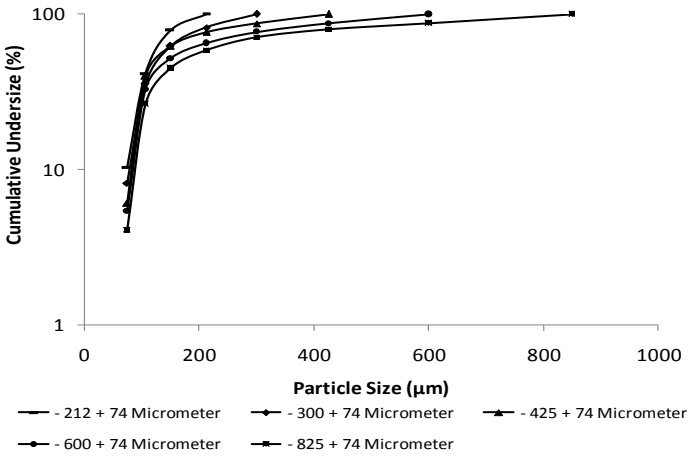

Fig. 1. Particle size distributions of feed sample

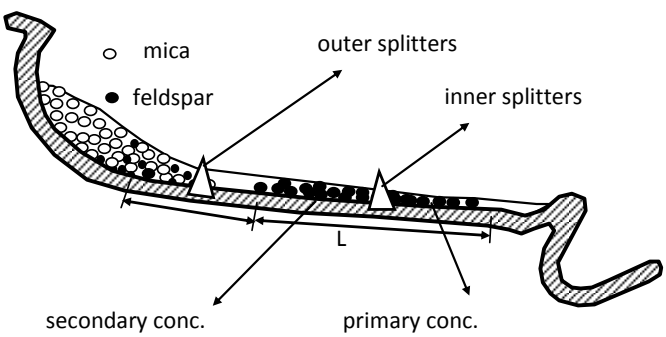

Fig. 2. The view of the spiral discharge

At the beginning of the tests, primary and secondary concentrates, and tailing were obtained as shown in Fig. 2. The Fe_2O_3 grades of the concentrates were determined by chemical assaying. The results showed that there was no significant difference between the primary and secondary concentrates.

Table 2. Chemical compositions of spiral feed and fines (–74 μm) fractions

Size fraction (μm)	Wt. % (Fines, -74μm)	Fe_2O_3 % (Fines, -74μm)	Fe_2O_3% (Feed)
-850 +74	4.20	0.03	0.74
-600 +74	5.28	0.06	0.74
-425 +74	7.10	0.07	0.76
-300 +74	8.54	0.08	0.77
-212 +74	10.25	0.12	0.78

Therefore, only one set of concentrate data representing the average characteristics of the two concentrates, and one set of the tailing data were used in the evaluation of the effect of particle size, solids % of feed and flow rate of feed on separation process. It was also not necessary to take a middling stream by using a second splitter in the separation process. Particle size distributions were:- 850 + 74 μm, - 600 + 74μm, - 425 + 74 μm, - 300 + 74 μm and – 212 + 74 μm. Pulp solids contents for these particle sizes were 15%, 20% and 25% by weight and flow rates were 1 dm^3/s, 1.5 dm^3/s and 2 dm^3/s in all tests. The 45 different conditions were tested and results of chemical assays were evaluated. Accordingly, the flow rate was fixed to its best value as 1 dm^3/s. The favourable conditions were tested in shaking table and results were compared to spiral concentrator.

The shaking table was operated as batch processes. There were two determined discharge units in the equipment. The positions of the discharge units were fixed for taking products as a primary concentrate, secondary concentrate and tailing. Samples were fed into the shaking table; the samples were moved in specific directions, which the mica minerals were moved with water in a vertical direction to the movement of the table because of the flaky shape while the feldspar minerals were followed table movement (Fig.3).

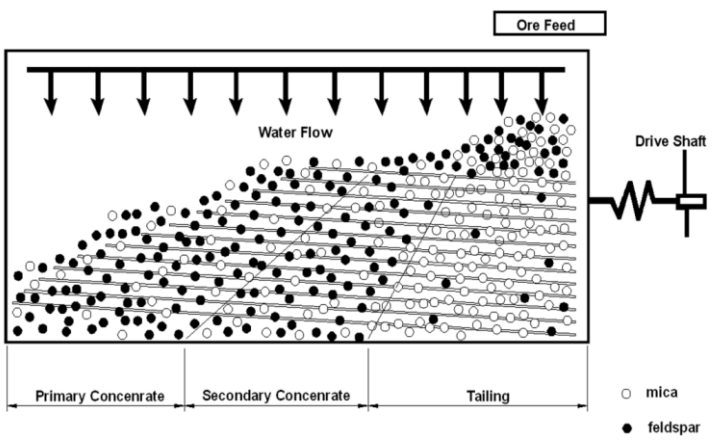

Fig. 3. The view of the shaking table discharge

Samples were taken simultaneously of primary and secondary concentrates and tailings during the tests in both concentrators. Prior to each test, the equipment was discharged, cleaned, and then operated in a manner appropriate to the new feed and solid contents. In order to make a comparison between the two methods, the concentrates of the shaking table were treated in the same way, one set of concentrate data representing the average characteristics of the two concentrates, as spiral concentrator. This enables the process to be used and controlled easily on the plant-scale

3. Results and discussions

In this study, the effect of the solids density of feed, the flow rate of feed and the flaky shape of mica, which depends directly on particle size, on the separation efficiency of mica from feldspar in a spiral concentrator were investigated. The favourable conditions were tested in shaking table by keeping flow rate constant at the value of 1 dm^3/s. The particle size distributions were varied between and -850 +74 μm and -212 +74 μm and solids % of feed were varied 25% to 15% by weight. These ranges stayed within the normal industrial operational limits of both equipments.

In the spiral concentrator, the major parts of the water in the feed were accumulated at the outside of the separation surface, carrying most of the flaky mica with it. The feldspar particles were moved predominantly to the inner part of the surface, forming a natural gap between the concentrate and the tailing streams. Therefore, the outer splitter was not very effective in controlling the concentrate quality. During the separation, the outer splitter was roughly adjusted by a visual judgement of the best position. The chemical analysis of the concentrate results for both concentrators (spiral and shaking table) are shown in Table 3.

Table 3. Fe_2O_3 grade of concentrates and mass recovery

	Particle Size (μm)	15% Solids Grade (%)	20% Solids Grade (%)	25% Solids Grade (%)	15% Solids Mass Recovery (%)	20% Solids Mass Recovery (%)	25% Solids Mass Recovery (%)
Spiral	-212+74	0.07	0.11	0.17	70.74	69.85	67.70
	-300+74	0.11	0.19	0.26	72.86	72.34	71.10
	-425+74	0.29	0.41	0.50	75.66	74.88	74.07
	-600+74	0.62	0.78	0.84	79.81	78.38	77.57
	-850+74	0.85	0.85	0.85	82.08	81.15	79.20
Shaking Table	-212+74	0.27	0.32	0.34	76.88	79.21	81.39
	-300+74	0.31	0.34	0.38	79.29	82.39	83.51
	-425+74	0.42	0.56	0.61	81.43	85.48	87.71
	-600+74	0.69	0.81	0.80	83.12	87.06	89.92
	-850+74	0.83	0.82	0.82	85.88	89.64	90.08

The minimum and maximum sizes of operating particle were determined according to the specifications of the spiral and shaking table used in the tests. Thus, three

different solid contents that were 15%, 20% and 25% by weight, were selected and performed. The effects of the solid content on the Fe_2O_3 grade of concentrate, Fe_2O_3 removal, and the mass recovery were investigated for each feed size. The results are shown in Figs. 4–6 for the spiral concentrator and Fig. 7 for the shaking table.

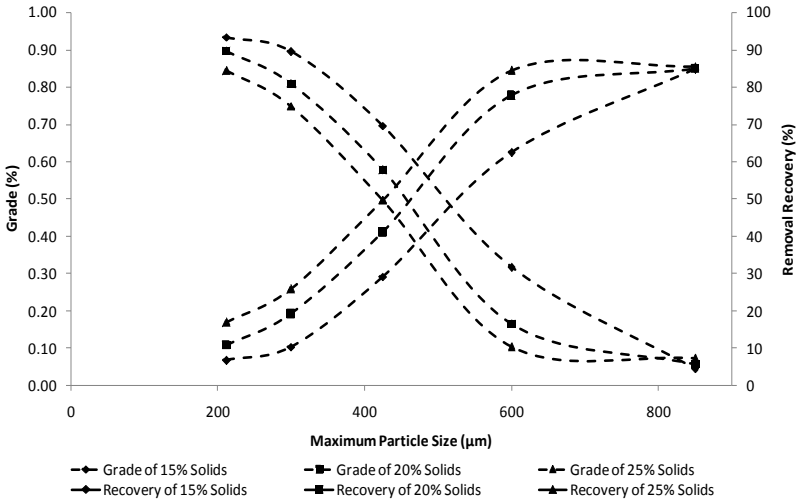

Fig. 4. A relationship between grade, recovery and maximum particle size in spiral concentrator at 1 dm^3/s flow rate

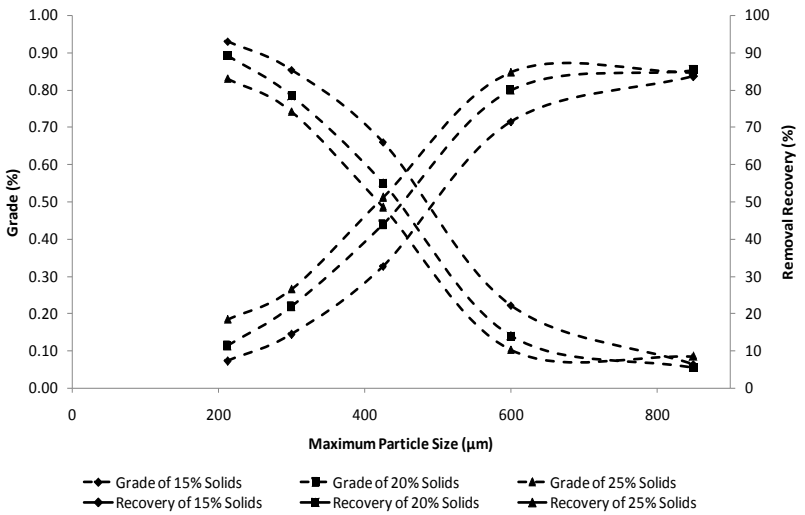

Fig. 5. A relationship between grade, recovery and maximum particle size in spiral concentrator at 1.5 dm^3/s flow rate

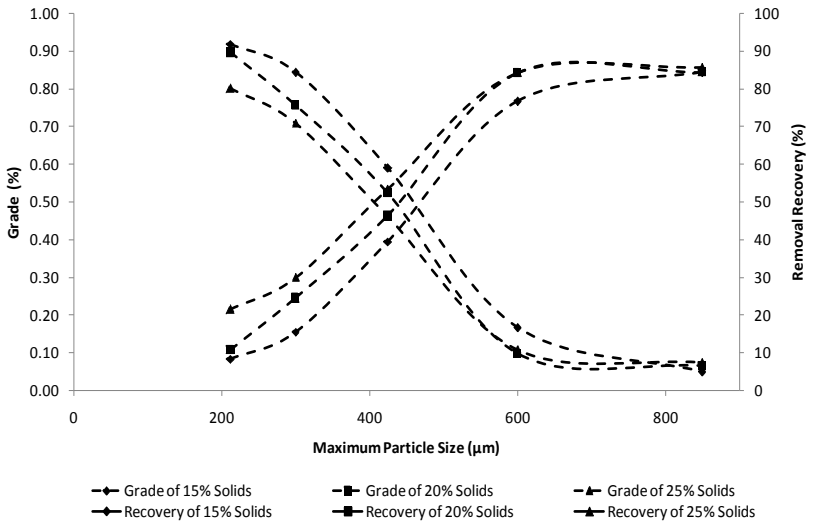

Fig. 6. A relationship between grade, recovery and maximum particle size in spiral concentrator at 2 dm^3/s flow rate

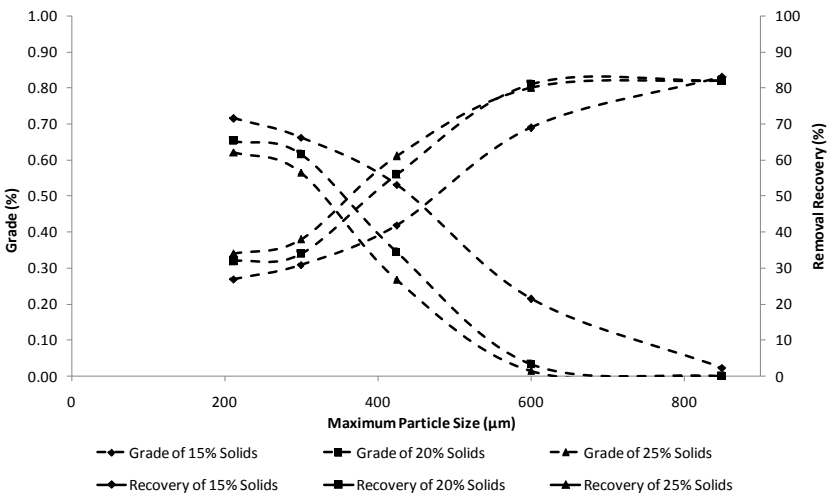

Fig. 7. A relationship between grade, recovery and maximum particle size in shaking table at 1 dm^3/s flow rate

From Figs. 4-7 it can be seen that the particle size distribution is the most effective parameter in the separation in both methods. In general, the separation efficiency of the gravity concentration methods is better for coarse particles than fine particles because the gravity force is more effective on coarse particles. However, the coarse

mica grains are nearly equi-dimensional, and the difference in the specific gravity is not sufficient to make the separation of these minerals possible in this case. On the other hand, the flaky shape character of the smaller mica particles made the separation of the mica from the feldspar possible in the fine particle sizes. This situation is not related to the differences in the degree of liberation since mica was in the form of liberated particles even in the coarse fractions.

The Fe_2O_3 grade of the concentrate and the Fe_2O_3 removal and recovery of the feldspar were directly related to the change in the particle size. An increase in the particle size occurs with the Fe_2O_3 grade of the concentrate (Table 3) and decreases with the Fe_2O_3 removal. The removal recovery was calculated from equation:

$$RR = \left[1 - \frac{C_c}{F_f}\right] \cdot 100, \tag{1}$$

where *RR* is removal recovery (%), *C* mass of concentrate (kg), *F* mass of feed (kg), *c* Fe_2O_3 content in concentrate (%), *f* Fe_2O_3 content in feed (%).

The mass recovery decreased slightly with the finer particle size since the amount of particles carried by water to the tailings stream increased. This behaviour was observed in both concentrators. According to Table 3, increasing the solids % of the feed increased the Fe_2O_3 grade of the concentrate and decreased the mass recovery, except for the feed top size fraction of - 850 μm + 74 μm. As well as reducing the separation efficiency, an increase in the solids content slightly reduced the amount of concentrate.

In classical gravity concentration, the purpose of separation is to get maximum grade of metallic ore with maximum possible mass recovery. In this case, most important terms are Fe_2O_3 content of concentrate, removal recovery and mass recovery. That is why the purpose of separation is to remove Fe_2O_3 from the feldspar minerals and to get the minimum Fe_2O_3 contents, the best Fe_2O_3 removal and mass recovery values in order to meet the glass industry requirements. So, the lower Fe_2O_3 content is favourable for this kind of separation. The spiral concentrate has 0.07% Fe_2O_3 content with a 93% Fe_2O_3 removal recovery and approximately 70% mass recovery, whereas the shaking table concentrate has 0.27% Fe_2O_3 content with a 72% Fe_2O_3 removal recovery and approximately 76% yield. Although the mass recovery of shaking table is higher than spiral concentrator, % Fe_2O_3 content and Fe_2O_3 removal recovery do not meet the desired specifications of glass industry.

The results showed that the spiral concentrator is more favourable than the shaking table for this kind of separation process. According to the concentrators operating principles, the spiral concentrator has a very significant advantage such as the centrifugal force contribution. The most favourable results of both concentrators are given in Fig. 8.

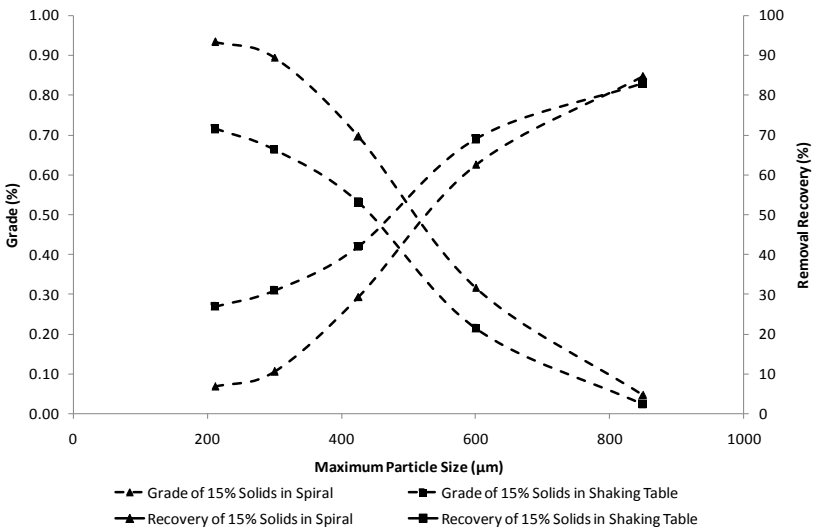

Fig. 8. Comparison of both concentrators in their best conditions

4. Conclusions

In this investigation, the role of mica flaky shape characteristics, which is achieved by decreasing the particle size of the feed, flow rate and the effect of the solids % in the feed on the mica separation from feldspar mineral, were examined. The results revealed that the increasing in particle size had an extreme effect on separation efficiency. Separation was not possible when the particle sizes were - 850 µm + 74 µm or - 600 µm + 74 µm.

The separation efficiency of the mica removal increased as the particle size distribution got finer, the most suitable particle size fraction being - 212 µm + 74 µm in both concentrators. In the spiral, the Fe_2O_3 content of the concentrate was reduced from 0.73% to 0.07% with 93% removal of the Fe_2O_3 and mass recovery of approximately 70%, whereas the Fe_2O_3 content of the concentrate was reduced from 0.73% to 0.27% with a 72% removal of the Fe_2O_3 and a mass recovery of approximately 76% in the shaking table concentrator.

The most favourable results were obtained in the spiral concentrator. There was a certain separation occurring in the shaking table, but the values did not meet the required specifications for the glass industry. On the other hand, the iron content, which was obtained in the spiral tests, met these specifications. Firing buttons with a pale pink colour confirmed these results.

It appeared that the particle size needed to be reduced to minus 212 µm in order to ensure that the mica had a flaky shape characteristic, which had the desired distinctive behaviour in these concentration processes.

Although the effect on the separation efficiency of the solids in the feed was less pronounced than that of the particle size, the increasing solids significantly reduced the separation efficiency. Only the concentrate obtained with the minimum solids (15%) met the desired specification.

References

ADAIR, R., MC DANIEL, W.T., HUDSPETH, W.R.,1951, *A new method for recovery of flake mica*, Min. Eng. 3, 252- 254.

AKAR, A., 1994. *Evaluation of Gördes Köprübaşı district feldspar industrial raw material deposits,* in: *5th Progress in Mineral Processing Technology Symposium*, ed. H. Demirel and S. Ersayın. Balkema Inc., Rotterdam 243-249.

BAYRAKTAR, I., ERSAYIN, S., GULSOY, O.Y., EKMEKCİ, Z., CAN, N.M.,1999. *Temel seramik ve cam hammaddelerimizdeki (feldispat, kuvars ve kaolin) kalite sorunlari ve cozum onerileri*, in: *3rd. Industrial Mineral Symposium*. Izmir, Turkey 22-33.

BAYRAKTAR, I., GULSOY, O.Y., CAN N.M., ORHAN, E.C., 2002. *Feldispatlarin zenginlestirilmesi*, in : *4th Industrial Mineral Symposium*, Izmir, Turkey 97-105.

BROWNING, J.S.,1973, *Mica Benefication*, U.S. Bureau of Mines Bulletin, 662, 21 – 22.

BURT, O.R., 1984. *Gravity Concentration Technology*, Elsevier Science Publishers, Amsterdam, Chap. 13.

CELIK, M.S., CAN, I., EREN R.H.,1998. *Removal of titanium impurities from feldspar ores by new flotation collectors*, Miner. Eng. 12, 1201-1208.

CELIK, M.S., PEHLIVANOGLU, B., ASLANBAS, A., ASMATULU, R., 2001, *Flotation of coloured impurities from feldspar ores*, Miner. and Metall. Proces. 18, 101-105.

IPEKOĞLU, B., ASMATÜLÜ, R., 1996.*The recovery studies of pure mica for paint industry,* in: *Changing Scopes in Mineral Processing*, Balkema Inc.,Roterdam 415-420.

IVERSON, H.G.,1932, *Separation of feldspar from quartz*, Eng. and Min. J., April, 227-229.

SCHOEMENT,J.J.,1989, *Mica and Vermiculite in South Africa,* J.S. Afr. Inst. Metall., 89, 1-12.